Particulate Reinforcement of Elastomers at Small Strains

Lewis Blair Tunnicliffe

A thesis submitted for the award of Doctor of Philosophy

The School of Engineering and Materials Science

Queen Mary University of London

Mile End Road,

LONDON E1 4NS

March 2015

Abstract

A series of particulate reinforced natural rubber composites are prepared using both model (glass sphere) and commercial (carbon black and precipitated silica) reinforcing filler materials having a range of surface activities.

Small strain reinforcement and viscoelastic behaviour of the model (glass sphere-filled) microcomposites are found to be well described by hydrodynamics and temperature-insensitive stiffening mechanisms such as strain amplification and elastomer occlusion. This means that the energy applied to the model materials during small strain deformations is entirely stored and dissipated within the elastomer phase.

For carbon black-filled natural rubbers such mechanisms are no longer found to completely describe the levels of reinforcement and viscoelastic behaviour. This is the case particularly for high surface area carbon blacks of small aggregate size. For carbon blacks, additional mechanisms of reinforcement are identified and associated with the formation of a filler network and with effects at the polymer-filler interface.

For all the compounds considered in this study, no direct experimental evidence is found for the formation of significant volumes of interphase polymer exhibiting retarded chain dynamics near the filler surface.

The observation of a secondary dissipation process in rubbery region small strain dynamic mechanical and creep measurements of carbon black-natural rubber compounds where the polymer filler interaction is particularly poor (where the carbon black surface is graphitised) indicates that there may be a significant slippage of polymer chain segments at the filler-elastomer interface. There is some limited evidence from small strain creep testing to indicate that this process also occurs in commercial carbon black-filled compounds but to a much reduced extent. To the best of the author's knowledge this is the first time that such processes have been observed in carbon black filled elastomers.

Declaration

I, Lewis Blair Tunnicliffe, confirm that the research included within this thesis is my own work or that where it has been carried out in collaboration with, or supported by others, that this is duly acknowledged below and my contribution indicated. Previously published material is also acknowledged below.

I attest that I have exercised reasonable care to ensure that the work is original, and does not to the best of my knowledge break any UK law, infringe any third party's copyright or other Intellectual Property Right, or contain any confidential material.

I accept that the College has the right to use plagiarism detection software to check the electronic version of the thesis.

I confirm that this thesis has not been previously submitted for the award of a degree by this or any other university.

Signature:

Date:

Details of collaborations:

Raman Spectroscopy and surface free energy determination (Chapter 3) were performed in collaboration with Dr Mike Morris, Cabot Corporation, Billerica, MA.

^{1}H-Multiple Quantum (MQ)-NMR work (Chapter 4) was performed in collaboration with Dr Juan Lopez Valentín, Grupo de Elastomeros, ICTP, CSIC, Madrid.

Broadband dielectric spectroscopy (Chapter 6) was performed in collaboration with Menglong Huang, Soft Matter Group, QMUL, London.

Details of publications:

LB Tunnicliffe, MD Morris, J Kadlcak, Y Shi, AG Thomas, JJC Busfield, *Flocculation and Viscoelastic Behaviour of Carbon Black-filled Natural Rubber*, Macromolecular Materials and Engineering, 2014, DOI: 10.1002/mame.201400117

LB Tunicliffe, M Huang, AG Thomas, JJC Busfield, *The Glass Transition and Segmental Relaxations of Particulate-Filled Natural Rubber*, European Polymer Journal, In Press

LB Tunnicliffe, JL Valentín, A González-Jiménez, AG Thomas, JJC Busfield, *Network Structures and Interfacial Properties of Filled, Peroxide-Crosslinked Natural Rubber,* European Polymer Journal, Submitted

LB Tunnicliffe, JL Valentín, A González-Jiménez, AG Thomas, JJC Busfield, *Inhomogeneities in the Network Structures of Peroxide-Crosslinked Natural Rubbers*, In preparation

LB Tunnicliffe, AG Thomas, JJC Busfield, *Carbon Black Reinforcement of Natural Rubber at Small Strains*, In preparation

Details of conference proceedings:

LB Tunnicliffe, AG Thomas, JJC Busfield, *Energy Losses in Filled Rubber at Small Strains*, Proceedings of Constitutive Models for Rubber VII, Jerrams and Murphy Eds., 2011

LB Tunnicliffe, AG Thomas, JJC Busfield, *The Effect of fillers on Crosslinking, Swelling and Mechanical Properties of Peroxide-Cured Rubbers*, Proceedings of Constitutive Models for Rubber VIII, Gil-Negrete and Alonso, Eds., 2013

Details of oral conference presentations:

German Rubber Institute, KHK, Hannover, 8/11/2014 - *Mechanisms of particulate reinforcement of elastomers at small strains*

American Chemical Society, 186th Technical Meeting of the Rubber Division, Nashville, 15/10/2014 - *Mechanisms of particulate reinforcement of elastomers at small strains*

International Rubber Conference, Beijing, 17/09/2014 - *Carbon black reinforcement and flocculation in natural rubber melts*

14th Dresden Polymer Discussion on Reinforcement of Polymer Melts and Networks, 27/05/2014 - *Carbon black reinforcement and flocculation in natural rubber melts*

Rubbercon, Manchester, 14/05/2014 - *Mechanisms of particulate reinforcement of elastomers at small strains*

Tire Technology International, Cologne, 16/02/2014 - *Mechanisms of particulate reinforcement of elastomers at small strains*

American Chemical Society, 184th Technical Meeting of the Rubber Division, Cleveland, 15/10/2013 - *Viscoelasticity of Filled Elastomers at very small strains*

European Conference on Constitutive Models for Rubber, San Sebastian, 20/06/2013 – *The Effect of fillers on Crosslinking, Swelling and Mechanical Properties of Peroxide-Cured Rubbers*

Tire Technology International, Cologne, 7/02/2013 - *Viscoelasticity of Filled Elastomers at very small strains*

Institute of Materials, Minerals and Mining, Rubber in Engineering Group, London, 18/12/2012 - *Viscoelasticity of Filled Elastomers at very small strains*

German Rubber Institute, KHK, Hannover, 8/11/ 2012 - *Linear-Viscoelastic Energy Dissipation at the Filler-Matrix Interface in Carbon Black-Rubber Nanoomposites*

American Chemical Society, 182nd Technical Meeting of the Rubber Division, Cincinnati, 11/10/2012 - *Linear-Viscoelastic Energy Dissipation at the Filler-Matrix Interface in Silica-Rubber Nanocomposites*

European Conference on Constitutive Models for Rubber, Dublin, 20/09/2011 – *Energy Losses in Filled Rubbers at Small Strains*

Acknowledgements

I would like to thank Professors James Busfield and Alan Thomas for their supervision of my work, inspirations and encouragements. I thank all the members of the Soft Matter group for their assistance and camaraderie. In particular I would like to thank Menglong Huang for our many interesting discussions and shared frustrations on the topics of filler reinforcement and dielectric spectroscopy. I would like to express my gratitude to the support staff in SEMS and I would like to thank the funding partners for this work; EPSRC and Sibelco - in particular the support of Drs Kevin Young and John Stuart both formerly of Sibelco.

Much of this work would not have been possible if not for the kind assistance of various people and organisations who allowed me access to specialised equipment for rubber and particle preparation/analysis. I would like to thank the Tun Abdul Razak Research Centre for allowing access to their internal mixing facilities, Alpha Technologies for allowing access to the rubber process analyser used in Chapter 5 and Cabot Corporation for supply of some of the materials for this work and for the Raman and surface energy analysis work they kindly performed on my carbon black samples. In particular I would like to thank Dr Juan López Valentín and Antonio Gonzaléz of the Grupo de Elastomeros, CISC, Madrid for introducing me to the multiple quantum NMR technique used in the Chapter 4 of this thesis, their hospitality during my stay in Madrid and their efforts in our collaborative work.

I would like to again express my gratitude to James Busfield for allowing me to attend so many conferences during my PhD which enabled me to talk to many other researchers with different points of view and experience of this subject. These conversations were instrumental in the forming of the conclusions reached in this thesis. In particular I would like to thank the following for informative conversations at various conferences and meetings: Dr Lorenzo Botto, Dr Andrew Chapman, Dr Vince Coveney, Prof. Alan Gent, Dr Laurent Guy, Dr Geoffrey Lin, Dr David Lowe, Dr Alan Muhr, Dr Mike Morris, Dr Julien Ramier, Dr Christopher Robertson and Dr Andrew Tinker. Finally I would like to thank my wife and my family for their support and faith in me.

Lewis Tunnicliffe

Contents

List of Figures

List of Tables

List of Symbols and Abbreviations

Key symbols used in this thesis are defined here. Arbitrary symbols for dimensions, shape factors and so forth are defined in the main body of text.

Symbols:

A	Ampere
A_{H}	Helmholtz free energy
a_T	WLF shift factor
B_0	Magnetic field
C_1	WLF constant
C_2	WLF constant
C_p	Capacitance
D	Diffusion coefficient
Da	Daltons
D_{Res}	Residual dipolar coupling
d	Interplanar spacing (XRD)
d_f	Fractal dimension
E	Tensile modulus
E_a	Activation energy
e	Change on an electron
eV	Electron volt
F	Tension, force
f	Frequency
f_S	Shape factor
f_v	Fractional free volume
G	Gauss
G	Shear Modulus
G_A	Elastic modulus of cluster-cluster aggregates
$\bar{G}$	Force constant of bonds between filler aggregates
G^*	Complex modulus

G'	Storage modulus, dynamic elastic modulus
G''	Loss modulus, dynamic viscous modulus
g	Gram
g	Gravitational acceleration
Hz	Frequency
$H(\tau)$	Relaxation spectrum
$\mathbf{h}$	Plank's constant
I	Inertia
I_D	Intensity of Raman D band
I_{DQ}	Double quantum build-up curve
I_G	Intensity of Raman G band
I_{nDQ}	Normalised double quantum build-up curve
I_{Q}	Quantum spin number
I_{ref}	Double quantum reference curve data
I_x	Second moment of area for a rectangular beam
$I_{\sum \mathrm{MQ}}$	Summatory of multiple quantum
i	$\sqrt{-1}$
J	Joule
J	Compliance
K	Kelvin
$\mathbf{k}$	Boltzman constant
L	Inductance
L_A	In-plane crystal dimension in nm
L_C	c-axis crystal dimension
l	Length
M_C	Molecular weight between crosslinks
m	Metre
m	Kraus Equation power exponent
mol	Mole
N	Newton
N	Number of moles
N_B	Number of filler aggregates in a cluster
N_C	Chemical network density (Maier-Göritz model)

N_L	Labile bonded chain network density (Maier-Göritz model)
N_{L0}	Number of isolated interaction sites per unit volume (Maier-Göritz model)
N_{St}	Stable bonded chain network density (Maier-Göritz model)
n	Refractive index
P	Pressure
Pa	Pascal
P_0	Nucleus angular momentum
$P(x)$	Probability as a function of x
p_e	Momentum of an electron
phr	Parts per hundred rubber
ppm	Parts per million
R	Ideal gas constant
R	Resistance
$R(T,\omega)$	Reinforcement
r	Radius
S	Entropy
S_b	Chain order parameter
$S^{'}$	In-phase dynamics torque
s	Second
T	Temperature
T_g	Glass Transition Temperature
T_Q	Torque
$T_g^{\omega}(Z)$	Local T_g at a distance, Z, from the filler surface
T_2	NMR relaxation constant
t	Time
tanδ	Tangent of the phase angle
t_1	Life time of polymer-filler bond (Yarin-Graham model)
t_0	Pre-exponential constant (Yarin-Graham model)
t_*	Characteristic time of Brownian segmental motion (Yarin-Graham model)
U	Internal Energy
V	Volt

V	Molar volume
V_{A}	Accelerating voltage
$V_f(T)$	Free volume
V_0	Glassy state volume
v_{e}	Electron speed
v_{P}	Poisson's ratio
W	Work
X	Strain amplification factor
Z	Impedance
Z'	Real part of the impedance
Z''	Imaginary part of the impedance
z	Distance from filler surface
α	Alpha relaxation
α_f	Thermal expansion coefficient
β	Line broadening coefficient (XRD)
Γ	Amount of water absorbed on filler surface in mol/g
γ	Shear strain
$\dot{\gamma}$	Strain rate
γ_{g}	Gyromagnetic ratio
γ_{s}	Total surface free energy
$\gamma_{\mathrm{s}}^{\mathrm{d}}$	Dispersive part of the surface free energy
$\gamma_{\mathrm{s}}^{\mathrm{p}}$	Polar part of the surface free energy
Δ	Logarithmic decrement
ΔG_e	Entropic free energy
ΔG_m	Free energy of mixing
ΔG	Free energy of dilution of a crosslinked rubber
δ	Phase angle
ε_0	Permittivity of free space
ε'	Real part of the permittivity
ε''	Imaginary part of the permittivity
ζ	Constant with units of dimension which relates to the nature of the attachment of polymer chains at the interface
η	Viscosity

Θ	Fractional site coverage constant (Maier and Göritz model)
θ	Angle (Bragg angle for XRD)
λ	Extension Ratio
λ_{WL}	Radiation wavelength (XRD)
μ	Magnetic moment
ν	Crosslink density
ξ	Filler aggregate cluster size
π	Pi
π_e	Spreading pressure of water
ρ	Density
ρ_{DC}	DC resistivity
σ	Tensile stress
σ_{DC}	DC conductivity
σ_{NMR}	Nuclear shielding constant
τ	Shear stress
τ	Polymer segmental relaxation time (used only in Chapter 6)
τ_{DQ}	Double quantum build-up time
τ_{rel}	Relaxation time
τ_{ret}	Retardation time
Φ	Absorption/desorption constant (Maier and Göritz model)
φ	Volume fraction
φ_C	Critical volume fraction (percolation threshold)
φ_2	Volume fraction of rubber in swollen material
φ^*	Effective volume fraction
χ	Polymer-solvent interaction parameter
Ω	Total number of chain conformations
ω	Angular frequency
°C	Degrees Centigrade

Abbreviations:

^{13}C-MAS-NMR	Carbon 13 - Magic Angle Spinning - Nuclear Magnetic Resonance
^{1}H-DQ-NMR	Proton - Double Quantum - Nuclear Magnetic Resonance

^{1}H-NMR	Proton - Nuclear Magnetic Resonance
2D	Two Dimensional
3D	Three Dimensional
AC	Alternating Current
ACF	Auto Correlation Function
AFM	Atomic Force Microscope
AG	Aggregate Growth
ASTM	American Society for Testing and Materials
BDS	Broadband Dielectric Spectroscopy
BET	Brunauer-Emmet-Teller
BR	Bound Rubber
CB	Carbon Black
CBS	N-Cyclohexyl-2-Benzothiazol Sulphenamide
CCA	Cluster-Cluster Aggregate
CS	Conventional Silica
CS-TEVS	Conventional Silica - Triethoxy Vinyl Silane
CTAB	Cetyl Trimethyl Ammonium Bromide
CV	Conventional Vulcanisation
DBP	Dibutyl Phthalate
DBPA	Dibutyl Phthalate Absorption
DC	Direct Current
DCP	Dicumyl Peroxide
DMA	Dynamic Mechanical Analysis
DQ	Double Quantum
DSC	Differential Scanning Calorimetery
EFM	Electric Force Microscopy
EPDM	Ethylene Propylene Diene Terpolymer
EPR	Electron Paramagnetic Resonance
E-SBR	Emulsion Styrene Butadiene Rubber
ETC	Environmental Test Chamber
EV	Efficient Vulcanisation
FEM	Finite Element Model
FID	Free Induction Decay

FNE	Finite Network Extensibility
GO	Graphene Oxide
HAF	High Abrasion Furnace
HDS	Highly Dispersible Silica
HDS-TEVS	Highly Dispersible Silica - Triethoxy Vinyl Silane
HN	Havriliak-Negami function
IGC	Inverse Gas Chromatography
IIR	Butyl Rubber
IR	Synthetic cis-poly Isoprene
LALLS	Low Angle Laser Light Scattering
MD	Molecular Dynamics
MDR	Moving Die Rheometer
MQ	Multiple Quantum
mSBR	Meleated Styrene Butadiene Rubber
MT	Mid Thermal
MWS	Maxwell-Wagner-Sillars polarisation
NMR	Nuclear Magnetic Resonance
NR	Natural Rubber
P2VP	Poly-2-vinylpyrrolidone
P4VP	Poly-4-vinylpyrrolidone
PB	Poly Butadiene
PDMS	Poly Dimethyl Siloxane
PEA	Poly Ethyl Acrylate
PFVD	Percolation of Free Volume Distribution
PMMA	Poly Methyl Methacrylate
PS	Polystyrene
PSi	Precipitated Silica
PVA_C	Poly Vinyl Acetate
QMUL	Queen Mary University of London
RDC	Residual Dipolar Coupling
RPA	Rubber Process Analyser
SAF	Super Abrasion Furnace
SBR	Styrene Butadiene Rubber

SEF	Stored Energy Function
SEM	Scanning Electron Microscope
SEV	Semi Efficient Vulcanisation
SFE	Surface Free Energy
SIC	Strain Induced Crystallisation
SMR CV(60)	Standard Malaysian Rubber, Constant Viscosity, 60 Mooney Units
SSA	Specific Surface Area
S-SBR	Solution Styrene Butadiene Rubber
STA	Simultaneous Thermal Analysis
TARRC	Tun Abdul Razak Research Centre
TEM	Transmission Electron Microscope
TEVS	Triethoxy Vinyl Silane
TGA	Thermogravimetric Analysis
TSDC	Thermally Stimulated Depolarisation Currents
TTS	Time Temperature Superposition
VFT	Vogel-Fulcher-Tammann
VTG	Van de Walle, Tricot and Gerspacher
VPR	Butadiene-Styrene-Vinyl Pyridine Rubber
WLF	Williams-Landel-Ferry
XRD	X-ray Diffraction

Chapter 1

Introduction

After the invention of the vulcanisation process, which transformed rubber from essentially a novelty into a commercial engineering material, perhaps the most significant technological advancement of the material was the discovery in 1904 of the reinforcing effect of incorporating carbon black particulates. At a technological level, filler reinforcement has played a key role in the development of engineering components with improved lifetimes and performance properties and in the case of the passenger tyre, improved safety, wear performance and fuel efficiency.

From a scientific perspective, despite the mass usage of particulate-reinforced elastomer materials, the exact mechanisms by which fillers modify the properties of crosslinked rubbers across a broad spectrum of temperature, frequency and strain conditions, remain unresolved. One of the main reasons for this is the physical complexity of the filled elastomer material which is structured across a broad range of length scales, from individual polymer chain segments on the scale of a nanometre to filler particle cluster-cluster agglomerates which can span hundreds of nanometres up to the micrometer length scale.

The work presented in this thesis is an attempt to examine the phenomenology and underlying mechanisms of filler reinforcement under small strain conditions. By employing small strain testing, some of the complexity of the physics of the material, namely the phenomenon of dynamic yielding of the filler cluster-cluster agglomerates (filler structure), can be ignored and the data interpretation can be correspondingly simplified. The materials examined in this investigation are carbon black-natural rubber composites. Precipitated silica is also used as a comparison material in some chapters due to scientific interest generated from its increased use as a reinforcing material in 'green' tyre technology.

Chapter 2 gives a critical overview of the relevant literature pertaining to the physics of rubber elasticity and the state-of-the-art in the understanding of filler reinforcement mechanisms. The literature review attempts to highlight gaps in the current levels of understanding and

point out topics of disagreement in the literature in order to formulate an experimental project. It is clear from the literature review that an experimental programme should attempt to characterise the key aspects of the composite material namely; the elastomer network structure, the filler particulates (and filler network) and the interface/interphase between the elastomer and filler.

Chapters 3-8 detail the main experimental work of the thesis. Chapter 3 characterises the filler particles in terms of surface area, surface activity and particle morphology. A range of carbon black materials are used varying in size and structure, and an analogous series of thermally deactivated (graphitised) carbon blacks are prepared where the surface activity of the particles is significantly reduced. Precipitated silica filler is used as a comparison material, incorporating a silane modification of the filler surface.

Chapter 4 details an attempt to characterise the nature of the elastomer network in both unfilled and filled compounds. This is achieved using a range of complimentary experimental techniques and demonstrates the significant effect the filler particles can have on the crosslinking yield in the filled compounds depending on the surface area and activity of the filler.

Chapter 5 addresses the phenomenology and microstructural origins of the increase in small strain elastic modulus (reinforcement) of elastomers upon incorporation of filler. This chapter initially considers the reinforcement of simple model microcomposites (natural rubber filled with micrometer diameter glass spheres) and then extends the study to consider what happens when carbon blacks of decreasing aggregate size are used as the reinforcing phase. The existence of percolating filler networks is confirmed using electrical testing and is shown to be highly dependent on the particle size and surface activity of the particulates. The structural dynamics of these filler networks are probed using melt rheology measurements.

Chapter 6 attempts to verify the existence of immobilised or glassy polymer interphase material in the carbon black and silica-filled compounds. This is highlighted in the literature review as a potentially dominant effect in the reinforcement of elastomer networks. No evidence for a substantial quantity of interphase material could be detected using a range of complimentary experimental techniques. The implications of this finding are discussed in detail.

Chapter 7 first revisits the model microcomposites introduced in Chapter 5 and demonstrates that the small strain viscoelasticity of these compounds can be understood in very simple terms by considering the deformation energy to be stored and dissipated entirely within the elastomer phase. In order to very precisely determine the small strain viscoelastic properties of the carbon black filled compounds, a torsion pendulum device is constructed and is shown to collect data which are very consistent with previous literature. This equipment is used to demonstrate that when the surface activity of the carbon black is significantly reduced through thermal treatment, a secondary dissipation effect is observed in rubbery region far above the glass transition. This is evidenced as a significant increase in the small strain tanδ with increasing temperature both above and below the filler percolation threshold. This appears to be consistent with similar observations in the literature where poor polymer-filler interactions are considered but is (to the best knowledge of the author) the first time that such effects have been observed for carbon black-based fillers.

In Chapter 8 this effect is probed in more detail using small strain creep testing. The small strain creep response of the compounds shows that a reduction in surface activity of the carbon blacks results in a significant increase in creep inelasticity. Examination of the time dependence of the creep data indicates that it can be separated into a logarithmic time dependence typical of the inelasticity of a polymer network and a linear time dependence which can be described as Newtonian viscous flow.

The conclusion reached is that this effect may be related to a viscous sliding of elastomer chain segments at the filler-polymer interface which is exaggerated for the case of graphitised carbon black due to the increase in the surface concentration of low surface energy graphitic planes.

Chapter 2

Literature Review

Précis

The topics of elastomer physics and filler reinforcement of elastomers have been extensively studied for over 100 years. Despite the vast bodies of work which have been published on these topics, there is still a lack of a complete understanding of the precise mechanisms of filler reinforcement. This targeted literature review is an attempt to highlight the key developments in the understanding of the physics of rubber elasticity and viscoelasticity and to critically review the state of the art in the understanding of the phenomenon of filler reinforcement. This literature review serves as a basis for identifying areas where new contributions to the subject can be made.

2.1. A Brief History of Rubber

Nowadays, goods derived from rubbery polymers play an integral part of daily life for most people. From pencil erasers to car tyres, the unique chemical and physical properties of rubbers have been widely exploited by a range of industries.

One of the earliest reports of rubber being utilised by mankind came following Columbus' voyage to the Caribbean where he reported native peoples playing with balls of a soft, elastic substance (the mesoamerican ball game - see Figure 2.1). Such rubber toys were then demonstrated to the court of Emperor Charles V in 1524 by a group of Aztecs [1, 2]. Jean Marie de la Condamine reported to the Royal Academy of Sciences in 1751 his observations of natives tapping and coagulating *Hevea* latex to produce shoe soles and waterproofed fabrics during his voyage through the Amazon rainforest [2, 3].

Around this time the new material gained its common English name 'rubber' from Joseph Priestley's observation in 1770 of its ability to remove lead pencil marks from paper [2]. In French the name 'caoutchouc' was derived from the native Amazonian expression 'caa-o-chu' meaning 'weeping tree' and remains in common use within the French language (the German term 'kautschuk' being derived from the French) [2]. During the 18th and early 19th centuries the uses of rubber remained rather limited. For example, Charles Macintosh's invention of the waterproof coat was limited by the rubber's inherent stickiness during warm weather and rigidity during the cold seasons [1].

Thomas Hancock developed the process of mastication processing of rubber in 1820. His original device survives to this day (Figure 2.2). However it was not until the discovery of the sulphur vulcanisation process almost simultaneously by Thomas Hancock (patented May 21st) and Charles Goodyear (patented June 15th) in 1844 during the industrial revolution that the full industrial potential of rubber began to be realised [2]. Utilisation of *natural* or *Hevea* rubber obtained from the latex of the *Hevea Brasiliensis* tree increased dramatically during the 19th century - between 1830 and 1860 the worldwide consumption of rubber increased 240 % - creating an economic boom for Brazilian plantations before plantations were subsequently established in various regions of the British Empire from 1877 [1]. The advent of the motorcar and the invention by John Boyd Dunlop of the pneumatic tyre further increased rubber consumption.

Figure 2.1: An image of a preserved rubber ball used in the Mesoamerican ball game by the Olmecs. This particular ball dates from 1600 BC (Image from BBC4 programme: 'Lost Kingdoms of Central America' [4])

Figure 2.2**:** Thomas Hancock's original rubber masticator. Now on display at the Tun Abdul Razak Research Centre (TARRC), Hertfordshire, UK

The discovery that incorporation of carbon black into rubber leads to dramatic improvements in rubber properties was first achieved by SC Mote in 1904 but only came to prominence some 8 years later when the Goodrich Company commercialised the process [2, 5].

Synthetic rubbers were developed over the first half of the 20th century in a response to both the fluctuating prices of natural rubber and the necessities of the two world wars. The most widely used of the synthetic rubbers is Styrene Butadiene Rubber (SBR). In 2008 SBR accounted for 41 % of total worldwide consumption of rubber polymer compared with 36 % for natural rubber [6]. Synthetic rubbers offer material selection solutions for problems where, for example, increased hysteresis or improved chemical resistance are required.

2.2. What is a Rubber?

A material displays rubber-like properties when the following conditions are satisfied [6, 7]:

- It is a high molecular weight material (typically polymeric) above its glass transition temperature
- In the unstrained state the material is amorphous or negligibly crystalline
- The polymer chains have weak inter-chain interactions
- The material is lightly crosslinked or is of suitably high molecular weight for crosslinking through physical entanglements to occur

A brief review of a few of the important types of engineering rubbers is now presented.

2.2.1. Natural Rubber (NR)

NR is obtained from the latex of the *Hevea Brasiliensis* tree. Latex, a colloidal suspension of rubber particles of between 30-40 % rubber by weight, is collected via 'tapping' of the tree and is then coagulated and processed in order to remove impurities and kill bacteria [8]. Natural rubber can be supplied in latex form (with rubber particulates of diameters in the range 0.1 - 1.0 μm) typically for use in the 'wet' rubber industries such as rubber gloves or condoms or in processed bale form where the rubber is completely dewatered for use in 'dry' rubber industries such as tyres.

NR primarily constitutes polymerised isoprene - specifically cis-1,4-polyisoprene, shown in Figure 2.3, produced as a result of biosynthetic reactions within the tree [7, 9]. However a number of organic and inorganic impurities are also present in the final product. The concentrations of these impurities depend on the grade of NR but typically constitute a few percent by mass. The majority of the impurities are proteins from the tree and are the reason that some people suffer from allergies from latex gloves and condoms. NR is a linear polymer, the chain molecular weight of which is between 200,000-500,000 Da [8, 9]. However this figure is strongly affected by the biosynthesis, meaning NR is subject to natural variations in average molecular weight and molecular weight distributions which do not affect the synthetic rubbers. The melting point of NR crystals is about 35 °C and the kinetics of crystallisation at room temperature are slow, so in the unstrained state at room temperature NR generally displays little crystallinity [10].

Crystallisation issues can occur when NR is stored for a long time and/or in colder environments. Upon the application of strain however, the melting point of the crystals increases leading to the well known strain-induced crystallisation effect (SIC) [7, 11, 12]. SIC is a self-reinforcing mechanism and is the primary reason that NR displays such a high tensile strength when compared with other non-crystallising rubbers. NR has a glass transition temperature in the range of -75 to -50 °C depending on the test method and testing conditions [9]. NR is used in a wide range of rubber goods including tyres, shock mounts, seals, isolators and bearings [8].

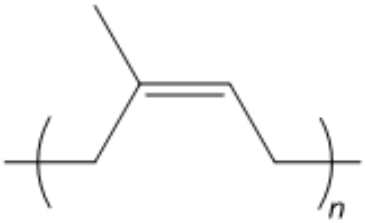

Figure 2.3**:** The chemical structure of cis-1,4-polyisoprene, the primary component of natural rubber. *n* refers to the number of repeat units

2.2.2. Synthetic cis-poly isoprene (IR)

IR is synthetically produced cis-1,4-polyisoprene. IR contains none of the non-polymer impurities present in NR and also exhibits a narrower molecular weight distribution. These result in slightly reduced mechanical properties due, in part, to the lack of the slight reinforcing

effects imparted by the protein component and also to the narrow molecular weight distribution which suppresses SIC [13]. IR can be used interchangeably with NR and is often preferred where a greater consistency in processing rheology is required [8].

2.2.3. Styrene Butadiene Rubber (SBR)

SBR is the most widely used synthetic, general purpose rubber and was developed during the second world war in both Germany and the USA in response to the loss of NR supplies from the far east. SBR is produced via the Ziegler-Natta catalysed, free radical-based polymerisation process through either an emulsion-based synthetic route (E-SRB) or a solution-based synthesis (S-SBR) [14].

SBR is a random co-polymer meaning that it lacks the stereo regularity required for either strain-induced or low temperature crystallisation (Figure 2.4) [7]. As such the resulting tensile properties of SBR are inferior to those of NR as illustrated in Figure 2.5 which plots typical stress-strain behaviour for unfilled, crosslinked NR and SBR. The inferior mechanical properties of SBR mean that a reinforcing agent must be used in combination with the polymer.

The glass transition of SBR typically varies from -50 to -10 °C depending, primarily on the vinyl content of the polymer. Typical SBR vinyl contents are around 23 % by mass [8]. Due to its relatively high glass transition temperature SBR tends to be used in applications requiring more hysteretic components. For example SBR is blended with other rubbers in car tyre treads to improve traction and abrasion resistance by increasing tread energy dissipation. SBR is also used for conveyor belts, shoe soles and various moulded rubber goods [8].

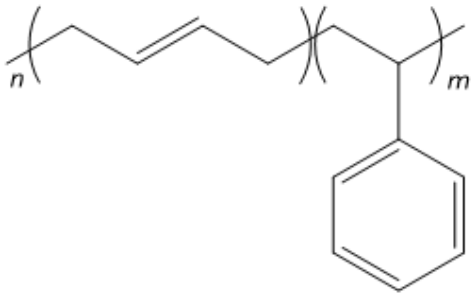

Figure 2.4**:** The chemical structure of styrene butadiene rubber (SBR). SBR is a random copolymer and *n* and *m* in the diagram refer to the number of repeat units

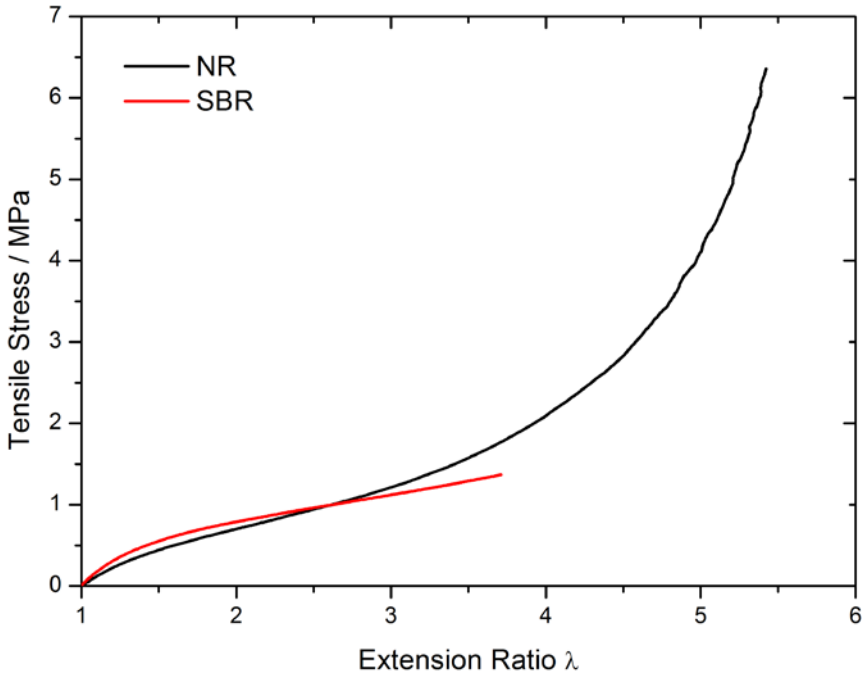

Figure 2.5**:** Tensile mechanical properties of crosslinked, unfilled NR and SBR. Although the stress-strain behaviour is similar up to λ = 4, the asymptotic upturn in stiffness displayed by the NR compound results in part from the self-reinforcing behaviour of strain-induced crystallites

2.2.4. Butyl Rubber (IIR)

IIR is prepared by copolymerisation of isoprene as a minor component with polysiobutylene. The doping of isoprene units into the main chain permits crosslinking of the normally saturated polyisobutylene (Figure 2.6). Typically IRs contain 0.5-3.0 mole % unsaturation. IIR exhibits a tightly packed molecular structure resulting in a low gas permeability and finds uses where its gas barrier properties can be exploited, for example as inner tubes and liners, tyre curing bladders and seals [8]. Butyl rubber has an unusually low resilience (at operating temperatures) given its relatively low T_g of around -70 °C [15].

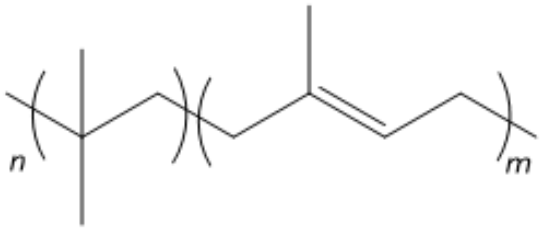

Figure 2.6**:** The **c**hemical structure of butly rubber (IIR). IIR is a random copolymer and *n* and *m* in the diagram refer to the number of repeat units

2.3. Physics of the Mechanical Behaviour of Rubbers Part I. Quasi-Static Elasticity

Many of the original investigations into the mechanical properties of rubber materials were performed under quasi-static loading conditions [7, 16] - meaning that the strain rates employed for testing were slow enough to largely ignore time-dependent effects.

When testing unfilled rubber and elastomer samples under such conditions it becomes apparent that rubber is:

(I) a relatively soft, compliant material,

(II) a highly extensible material,

(III) a highly elastic material (at least when well above the glass transition temperature and at low strain rates) and

(IV) displays a non-linear relationship between engineering stress and strain.

Typical mechanical data are presented in Figure 2.7. Here the engineering stress is defined as force divided by un-extended sample cross-sectional area and extension ratio is 1 + the strain. Note that the marked non-linearity at smaller strains is primarily due to geometric effects. If the true stress were considered then much of the non-linearity at lower strains would disappear.

Early observations made by Gough (1805) and later by Joule (1859) highlighted the remarkable thermo-elastic properties of rubbers (summarised in Treloar [7]):

(I) rubber strips contract when held under constant load and subject to heating,

(II) when held at constant extension ratio and heated, the resulting measured force increases as a function of temperature, and

(III) when subjected to extension, rubber samples evolve heat.

The data of Joule and of James and Guth are reproduced in Figure 2.8 from Treloar [7] and illustrate the evolution of heat with extension. The observation of these effects allowed for the interpretation of the mechanical properties of rubbers in terms of well-established thermodynamic concepts.

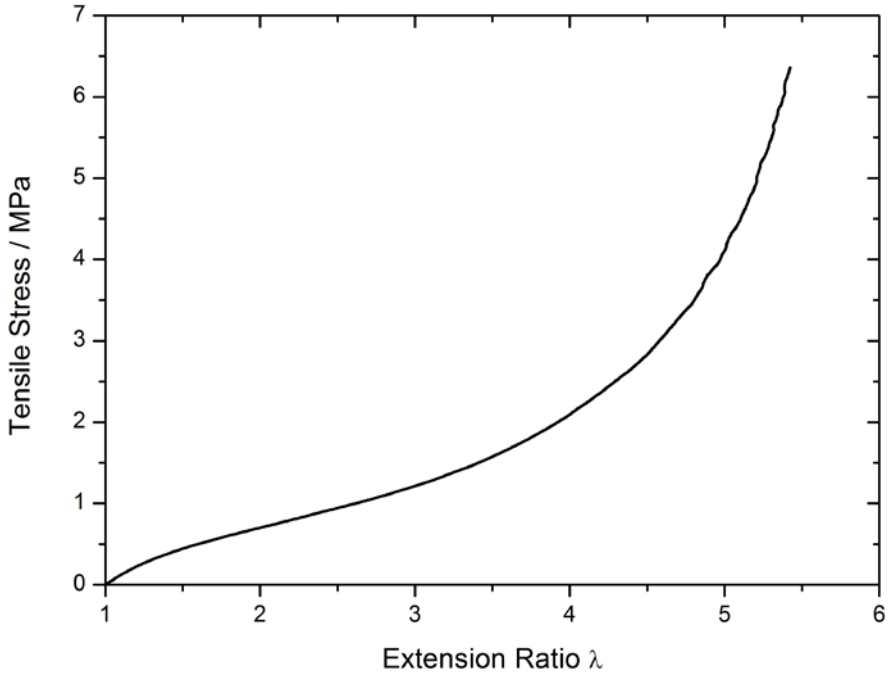

Figure 2.7: Typical stress-strain behaviour of NR crosslinked with 2 phr dicumyl peroxide (data taken from Chapter 4 of this thesis)

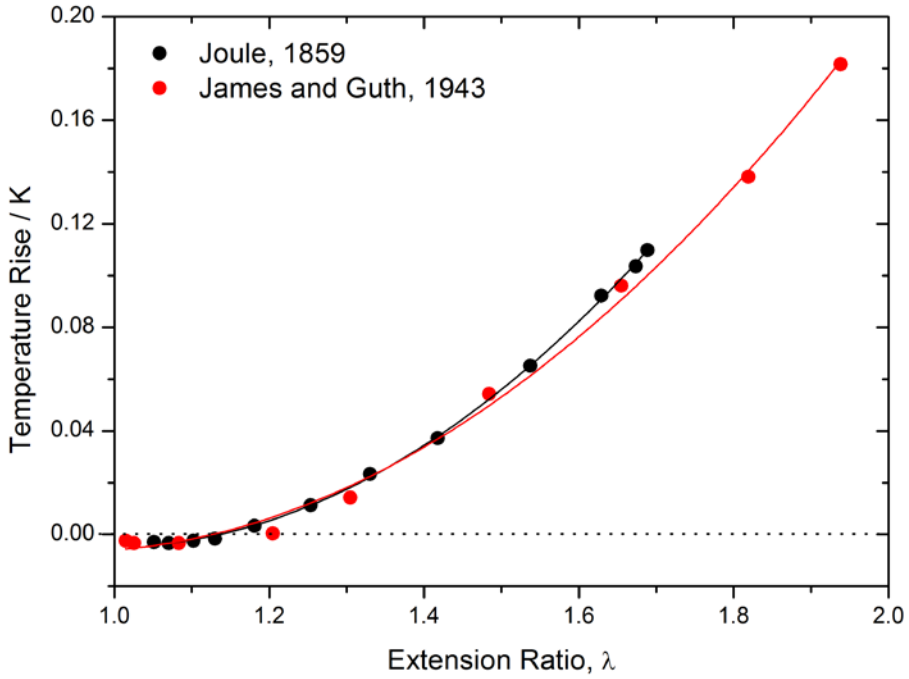

Figure 2.8: Thermo-mechanical behaviour of rubber from Joule and later James and Guth (Digitised from Treloar [7])

2.3.1. Thermodynamic Features of Rubber Elasticity

The kinetic theory of rubber elasticity derives relationships between measurable experimental parameters such as temperature, force and length and thermodynamic quantities of entropy and internal energy. The result of the thermodynamic analysis of rubber elasticity (which is derived in full in Treloar [7], Gent [15] and Young and Lovell [14]) is the following relationship, where F is the tension on a piece of extended rubber, U is the internal energy, l is the sample length and T is the temperature [7, 9]:

$$F = \left(\frac{\partial U}{\partial l}\right)_T + T\left(\frac{\partial F}{\partial T}\right)_l \qquad 2.1$$

This means that the tension on a piece of strained rubber is proportional to the temperature (i.e. the modulus of unfilled rubber increases with a rise in temperature). The force term can be related to entropy, S, by:

$$\left(\frac{\partial S}{\partial l}\right)_T = -\left(\frac{\partial F}{\partial T}\right)_l \qquad 2.2$$

It is also possible to discriminate the contributions to rubber elasticity arising from internal energy and entropic changes. Obtaining the entropy and internal energy terms for a given extension ratio by plotting the stress versus temperature (Figure 2.9) allows an equilibrium stress/strain curve to be compiled in terms of the relative contributions from internal energy and entropy at each extension. Figure 2.10 reproduces the data of Anthony, Caston and Guth to illustrate this [7]. Note that Figure 2.10 has been corrected for the effects of material thermal expansion on the actual extension ratios. Their results show that the contribution to quasi-static elasticity from changes in internal energy are minimal. For the case of rubbers, elasticity results from perturbations of the entropy associated with the crosslinked, macromolecular structure. This is in contrast to most other types of materials whose elasticity can be broadly related to internal energy changes through the stretching of molecular bonds. The limitations of this entropic approach are encountered at large deformations with the onset of finite network extensibility and, in certain rubbers, strain-induced crystallisation effects [7].

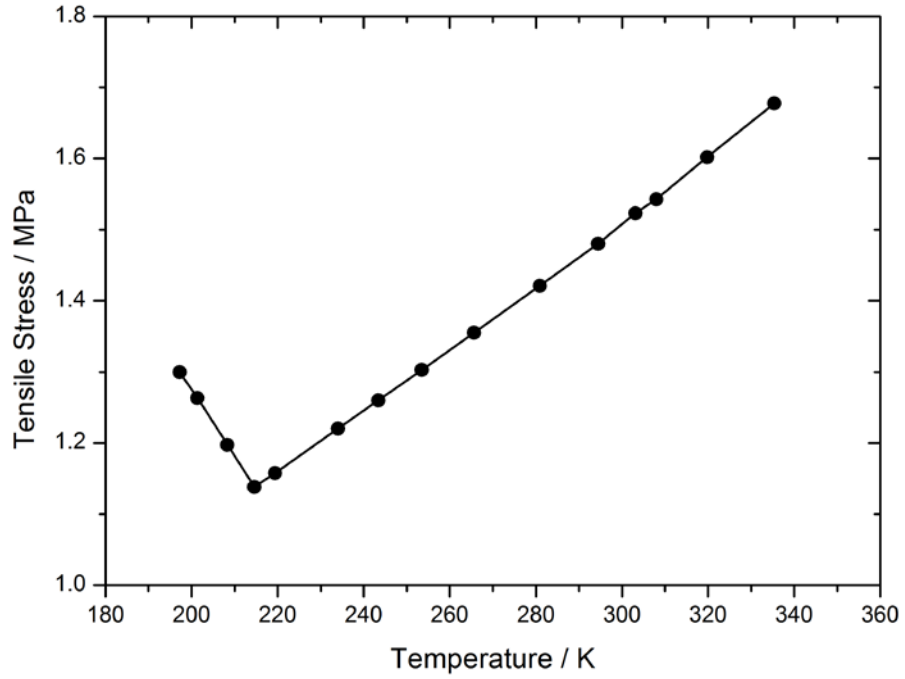

Figure 2.9: Stress as a function of temperature for NR at 350% extension. Such plots allow the determination of the internal energy and entropic contributions to elasticity (Digitised from Treloar [7])

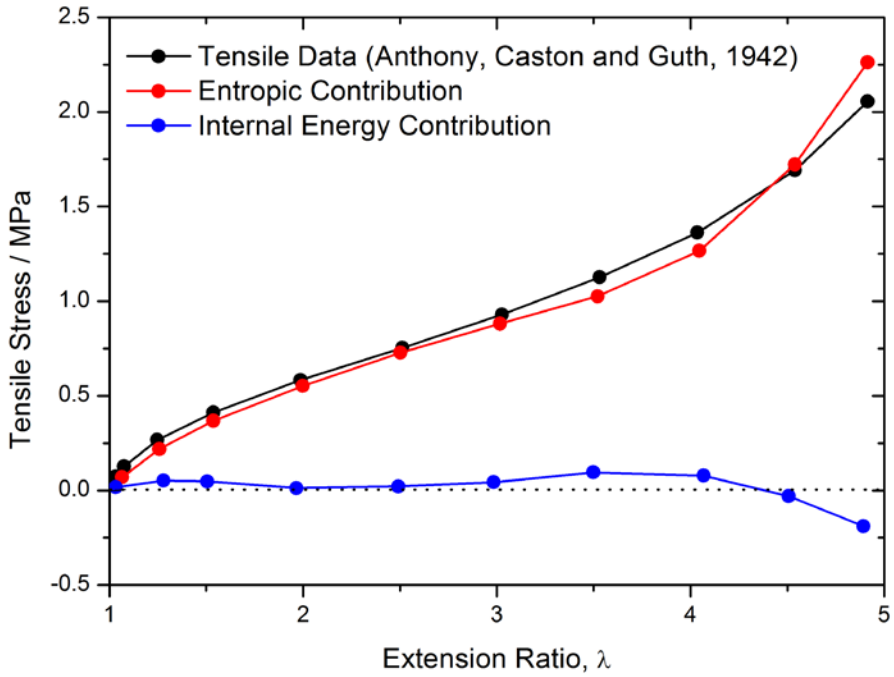

Figure 2.10: The data of Anthony, Caston and Guth, showing the mechanical behaviour of NR in terms of contributions from internal energy and entropy (Digitised from Treloar [7])

2.3.2. The Elasticity of a Single, Freely Jointed Chain

In order to develop a molecular-level description of rubber elasticity it is necessary to make assumptions about the nature of the polymer chain statistics. Chain segments are assumed to undergo free rotation around 'bonds'. In reality these may be actual covalent bonds connecting the chemical repeat units or may relate to rotation between individual Kuhn segments (physically rigid segments) of the polymer backbone. Although the structure of real polymers may differ at an atomistic level from that of the idealised chain (for example steric restriction of free rotation), given a suitably high degree of polymerisation the statistical properties of the freely jointed chain are eventually recovered meaning that this is a valid assumption to make. For such idealised chains the root mean square displacement, $\left(\overline{r^2}\right)^{\frac{1}{2}}$, between chain ends is found to be [7]:

$$\left(\overline{r^2}\right)^{\frac{1}{2}} = l(2n)^{\frac{1}{2}} \tag{2.3}$$

where r is the end-to-end displacement, l is the length of the chain and n is the number of chain segments. If the chain is represented by chain end A isolated at the origin, O, of a 3D Cartesian coordinate system and chain end B which can move freely and randomly throughout space (Figure 2.11) then the probability density distribution of point B occupying a unit of volume, $P(x, y, z)$ has been shown by Kuhn and by Guth and Mark [7] to be given by a Gaussian distribution function (illustrated in Figure 2.11).

Due to the spherical symmetry of the Gaussian distribution function, the probability distribution, P, along the x-axis can be given as

$$P(x)dx = \left(\frac{b}{\pi^{\frac{1}{2}}}\right)\exp(-b^2x^2)dx \tag{2.4}$$

where the constant b is:

$$b^2 = \frac{3}{2}nl^2 \tag{2.5}$$

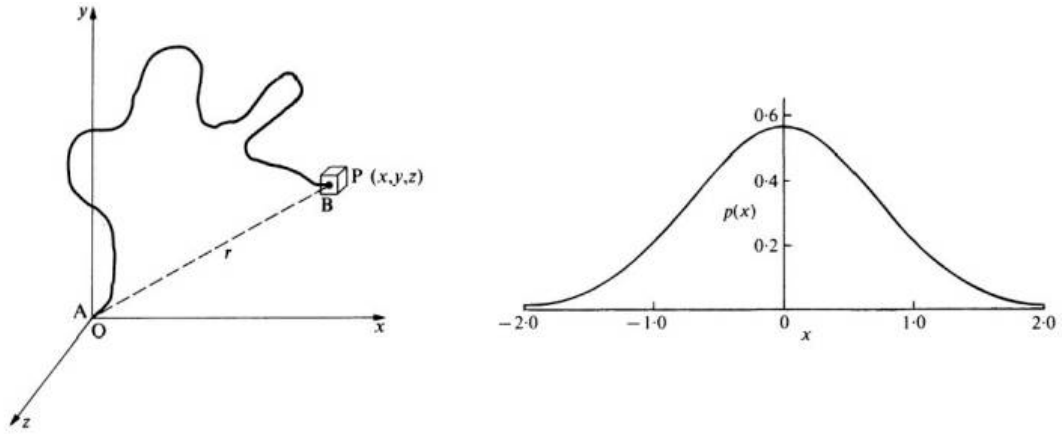

Figure 2.11**:** Left) freely jointed chain moving in 3D with one end of the chain tethered to the origin. Right) the corresponding Gaussian distribution function (From Treloar [7])

This results in a peak in probability per unit volume at the origin. Taking into account the three dimensional nature of the problem it is necessary to express the probability within a spherical shell volume. This is given as

$$P(r)dr = \left(\frac{b^3}{\pi^{\frac{3}{2}}}\right)\exp(-b^2r^2)4\pi^2dr \qquad 2.6$$

The resulting probability per incremental spherical shell of volume is illustrated in Figure 2.12. Now the peak in probability occurs at a finite distance from the origin.

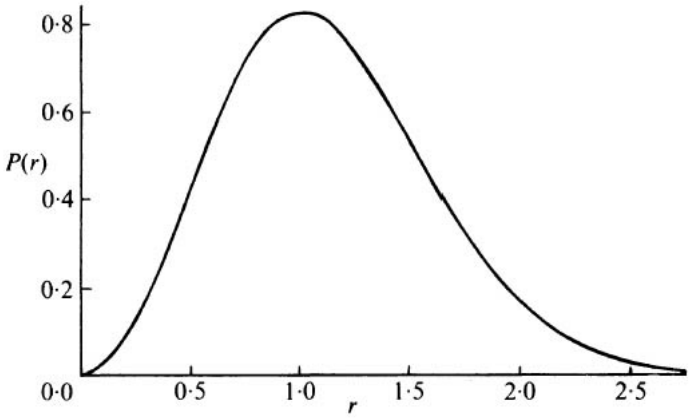

Figure 2.12**:** Probability distribution of the location of the chain end per unit of volume (From Treloar [7])

The entropy, S, associated with such a chain under moderate extensions (so that the distribution remains Gaussian) is derived using statistical thermodynamics as being proportional to the logarithm of the total number of chain conformations, Ω. This allows the entropy to be expressed as Equation 2.7:

$$S = \mathbf{k}\ln\Omega \tag{2.7}$$

$$S = \mathbf{k}\{\ln(c) - b^2r^2 + \ln d\tau\} \tag{2.8}$$

where c is a constant, $d\tau$ is the volume element and $\mathbf{k}$ is the Boltzmann constant. If the volume is assumed to be constant then

$$S = c - \mathbf{k}b^2r^2 \tag{2.9}$$

where c is a constant. The corresponding force can be calculated by considering the change in work, W, which is equivalent to the change in Helmholtz free energy, A_{H}, with increasing *r*.

$$F = \frac{\mathrm{d}W}{\mathrm{dr}} = \frac{\mathrm{d}A_{\mathrm{H}}}{\mathrm{dr}} = -\mathrm{T}\frac{\mathrm{d}S}{\mathrm{dr}} \tag{2.10}$$

Inserting the derivative with respect to r of the chain entropy term gives

$$F = 2\mathbf{k}Tb^2r \tag{2.11}$$

This gives the statistically averaged force as a function of end-to-end distance.

2.3.3. The Elasticity of a Network of Chains

In order to describe the elasticity of a network of chains in a similar way, a number of assumptions about the nature of the network must be made. It is assumed that the chains between crosslinking points can be described by Gaussian statistics as outlined above, that the deformation of the crosslinking points is affine, and that the total entropy of the network is described by a linear combination of the constituent chain entropies. The difference in entropy, ΔS, between the relaxed, S, and extended chains, S' can therefore be given by

$$\Delta S = S' - S = -\mathbf{k}b^2\{(\lambda_1^2 - 1)x_0^2 + (\lambda_2^2 - 1)y_0^2 + (\lambda_3^2 - 1)z_0^2\} \quad 2.12$$

where λ is the extension ratio along a given axis (x, y, z) and x_0, y_0 and z_0 are the relaxed coordinates. The total entropy change for a network of elastomer chains is then

$$\Delta S = \sum S' - \sum S = -\mathbf{k}b^2\left\{(\lambda_1^2 - 1)\sum x_0^2 + (\lambda_2^2 - 1)\sum y_0^2 + (\lambda_3^2 - 1)\sum z_0^2\right\} \quad 2.13$$

Given that the distribution is symmetric in 3D and the initial end to end distances, r_0, are random, it is possible to write

$$\sum x_0^2 = \sum y_0^2 = \sum z_0^2 = \frac{1}{3}\sum r_0^2 \quad 2.14$$

Hence

$$\Delta S = -\frac{1}{3}N\mathbf{k}b^2\overline{r_0^2}(\lambda_1^2 + \lambda_2^2 + \lambda_3^2 - 3) \quad 2.15$$

Where N is the number of chains. Recalling and combining Equation 2.3 and Equation 2.5 gives $\overline{r_0}^2 = \frac{3}{2b^2}$ which implies that that the unstrained chain end to end distance is equivalent to an analogous set of free chains. Insertion of this into Equation 2.15 simplifies the change in entropy term to

$$\Delta S = -\frac{1}{2}N\mathbf{k}(\lambda_1^2 + \lambda_2^2 + \lambda_3^2 - 3) \qquad 2.16$$

In terms of work of deformation, W, this is then

$$W = \frac{1}{2}N\mathrm{k}T(\lambda_1^2 + \lambda_2^2 + \lambda_3^2 - 3) \qquad 2.17$$

where

$$N\mathbf{k}T = \frac{\rho\mathbf{R}T}{M_C} = G \qquad 2.18$$

where ρ is the density of the rubber, T is temperature, M_C is the chain molecular weight between crosslinks and G is the small strain shear modulus of the material. This therefore provides a method to predict the stress-strain behaviour for any unfilled rubber in any mode of deformation from a molecular concept of entropic elasticity as the differentiation of the stored energy function (SEF) results in a stress-strain curve.

The SEF derived from statistical elasticity is called the Neo-Hookean SEF. A fit of the Neo-Hookean SEF to experimental data is shown in Figure 2.13. As can be seen the fit is very good at low extensions but somewhat overestimates the stiffness at moderate strains and underestimates it at the highest extensions. The overestimate in the moderate strain region is generally attributed to non-elastic network defects which are not taken into account in the statistical theory. At higher extensions the assumption that chain statistics follow a Gaussian distribution becomes less and less valid as a significant non-symmetrical bias is placed on the

chains. The additional stiffening effect imparted by strain-induced crystallisation effects at large strains in some polymers are also not accounted for in the model.

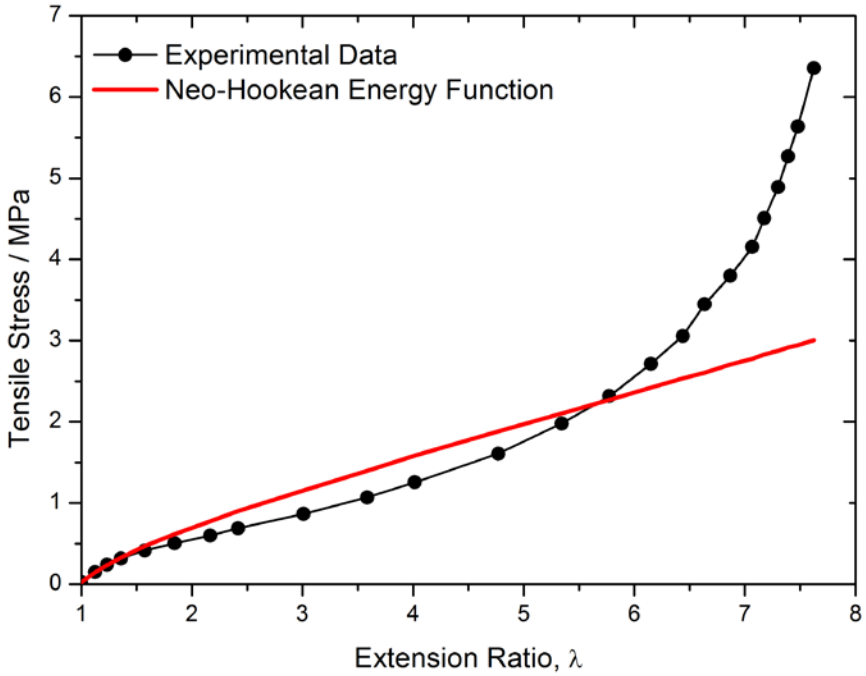

Figure 2.13: Comparison of the Neo-Hookean stored energy function with experimental data for crosslinked NR - (Digitised from Treloar [7])

2.4. Physics of the Mechanical Behaviour of Rubber Part II: Viscoelasticity

2.4.1. Inelastic Effects in Rubbers under Static Loadings

The previous section was concerned with non-linear elasticity apparent under quasi-static loading conditions where relations between load and displacement are assumed to be reversible. However in reality rubbers are viscoelastic materials meaning that their mechanical properties can be characterised by both elastic and inelastic (viscous) contributions which are subject to a temperature and frequency dependence [6, 14, 17, 18]. Under static loads and strains the inelastic component is typified by creep and stress relaxation responses respectively. This is illustrated in Figure 2.14. For unfilled rubbers these effects can be related directly to the timescales of polymer chain relaxations as will be shown in the next section. Note that creep behaviour is typically reported as material compliance as a function of time where the compliance is defined as $J(t) = \gamma/\tau$ where γ is the shear strain and τ is the applied shear stress.

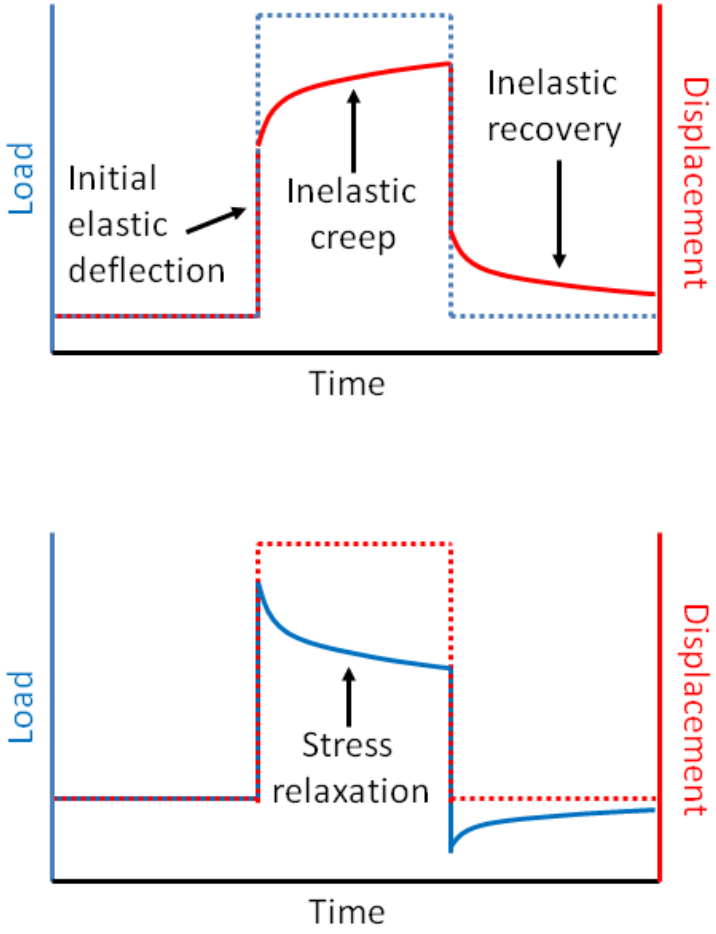

Figure 2.14: Creep and relaxation effects in rubbers. Dashed lines correspond to the applied excitation (load or displacement), solid lines to the material response.

The phenomenology of inelastic effects can be described using either the Maxwell or Kelvin-Voigt models. The Maxwell model describes the relaxation of stress in response to an applied strain using a spring and dashpot in series where σ_0 is the initial stress apparent after instantaneous application of a deformation, t is the time and τ_{rel} is the characteristic relaxation time [17].

$$\sigma(t) = \sigma_0 \exp\left(\frac{-t}{\tau_{rel}}\right) \qquad 2.19$$

Similarly the creep in strain following an applied stress is given by the Kelvin-Voigt model using a spring and dashpot in parallel where τ_{ret} is the characteristic retardation time.

$$\gamma(t) = \frac{\sigma}{G}\left(1 - \exp\left(-\frac{t}{\tau_{ret}}\right)\right) \qquad 2.20$$

or, since $J = 1/G = \gamma/\sigma$,

$$J(t) = J\left(1 - \exp\left(-\frac{t}{\tau_{ret}}\right)\right) \qquad 2.21$$

A combination of Maxwell and Kelvin-Voigt models is called a 'Standard Linear Solid' and is able to capture both creep and relaxation behaviour of polymers in a single model. The time scale of the creep or relaxation process is characterised by a relaxation or retardation time in the Maxwell and Kelvin-Voigt models.

The use of a single relaxation or retardation time to describe static inelastic effects is often insufficient to account for experimental data. In a microstructural sense, relaxation and molecular motion of polymer chains takes place over a wide range of timescales (Figure 2.15). This gives rise to the logarithmic dependence of creep and relaxation effects on time.

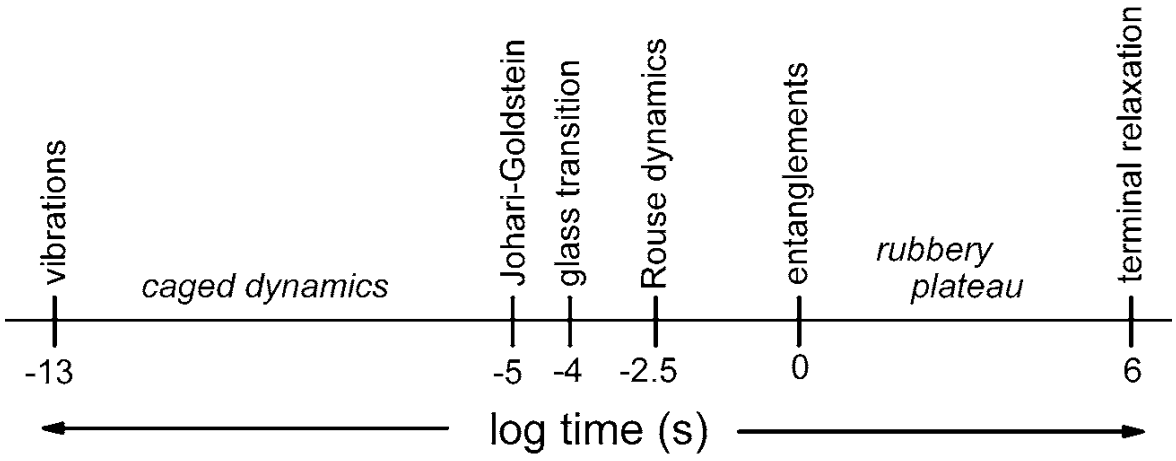

Figure 2.15: Timescales of molecular motions in polymeric materials. Note that for the case of crosslinked rubbers, the terminal relaxation (viscous flow) is not apparent (From Science and Technology of Rubber [9])

Such inelastic effects can have consequences for industrial applications where static loads are applied, for example in engine mounts or bearings. Crosslinking of rubbers significantly reduces the inelastic effects observed under static loadings. For example, long term creep in uncrosslinked rubber results in steady state polymer flow whereas flow in crosslinked rubbers is restricted by the crosslinked network [18]. For crosslinked rubbers acceleration in creep rates at long timescales is often observed. However, this is related to chemical degradation of the network at long timescales and elevated temperatures (chemical creep) rather than to physical polymer processes [15].

2.4.2. Inelastic Behaviour of Rubbers under Dynamic Excitations

The viscoelastic nature of rubber becomes especially important under dynamic excitations. In fact, dynamic loading experiments are more frequently used to characterise viscoelasticity than static loading tests. Although in practise elastomer components are usually subject to complex dynamic loadings, here we consider dynamic loadings as idealised, sinusoidally varying stresses and strains. Consider, for example, the application of a sinusoidal dynamic shear strain of constant amplitude and frequency to a linear elastic and to a Newtonian material (Figure 2.16).

Here the stress responses are dictated by the appropriate constitutive laws. Hooke's Law describes the response of a perfectly elastic material with the shear stress response proportional to and in phase with the applied shear strain, γ.

$$\tau = G\gamma \tag{2.22}$$

where G is the shear modulus.

Newtonian viscous behaviour described by a constant viscosity, η, produces a stress, proportional to the time derivative of strain (the strain rate, $\dot{\gamma}$), and out of phase with the applied strain by 90°.

$$\sigma = \eta\left(\frac{\mathrm{d}\gamma}{\mathrm{dt}}\right) = \eta\dot{\gamma} \tag{2.23}$$

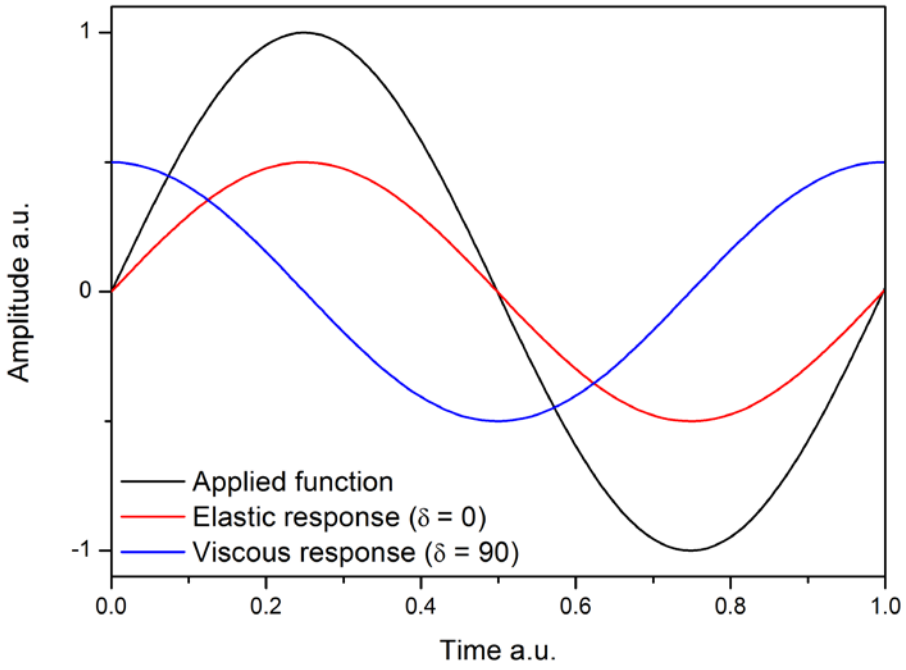

Figure 2.16: Elastic and viscous responses to a dynamic excitation. The applied excitation (black line) may be either a load or displacement. The response functions for Hookean (red line) and Newtonian (blue line) responses are also plotted

The phase angle, δ, is characteristic of the viscoelastic nature of the material under dynamic loading, bounded by extremes of δ = 0° for elastic and δ = 90° for viscous responses. Viscoelastic materials such as rubbers and elastomers have phase angles which lie somewhere between the two extremes depending on the test conditions (temperature, frequency, amplitude). The applied strain can be expressed according to

$$\gamma(t) = \gamma_0 \sin(\omega t) \qquad 2.24$$

where ω is the deformation frequency. The sinusoidal stress response incorporates a phase lag as

$$\tau(t) = \tau_0 \sin(\omega t + \delta) \qquad 2.25$$

Using the trigonometric relation for the sine of the sum of two angles this can be rewritten as

$$\tau(t) = (\tau_0 \cos\delta)\sin(\omega t) + (\tau_0 \sin\delta)\cos(\omega t) \quad 2.26$$

Defining the in phase part as the storage (G') and out of phase part as the viscous (G'') moduli gives

$$G' = \frac{\tau(t)}{\gamma(t)}\cos\delta \quad 2.27$$

$$G'' = \frac{\tau(t)}{\gamma(t)}\sin\delta \quad 2.28$$

This gives the stress response as a function of time as

$$\tau(t) = \gamma_0[G'\sin(\omega t) + G''\cos(\omega t)] \quad 2.29$$

The complex modulus, G^*, is then defined as

$$G^*(\omega) = G'(\omega) + iG''(\omega) \quad 2.30$$

The ratio of the viscous modulus to storage modulus gives the tangent of the phase angle which is often reported as the material hysteresis.

$$\tan\delta = \frac{G''}{G'} \quad 2.31$$

Changing the testing conditions allows for the characterisation of material mechanical properties in terms of viscoelastic parameters (G', G'', $\tan\delta$) over a wide range of frequencies,

temperatures and amplitudes. This is routinely accomplished using Dynamic Mechanical Analysis (DMA). An example DMA experiment is shown in Figure 2.17. Here a crosslinked, unfilled elastomer is examined at small dynamic strains (0.1 %) over a temperature range from (200-240 K) at a deformation frequency of 1 Hz. Dramatic changes are observed in the viscoelastic parameters as the sample passes through the glass transition.

Often it is the frequency dependence rather than temperature dependence of rubber viscoelasticity which is of interest. For example, the deformations associated with wet braking in passenger car tyres are in the kHz-MHz frequency range. However the typical upper frequency range for DMA equipment is around 200 Hz. Fortunately the Time-Temperature Superposition (TTS) Principle for polymers allows the upper and lower frequency ranges of DMA to be substantially extended (at least for linear viscoelastic strains above the glass transition). TTS developed from the experimental observation that the mechanical behaviours of polymers at low temperatures are similar to those observed under higher testing frequencies, and correspondingly high temperature behaviour equates to lower frequency behaviour [17]. Figure 2.18 illustrates the TTS principle.

Here data is collected over the range of available experimental frequencies and over a series of isothermal temperatures. Horizontal shifting of the individual frequency sweeps against a reference temperature data set (typically T_g + 40 °C) produces a viscoelastic mastercurve which is independent of temperature and covers many orders of magnitude in frequency. Willams, Landel and Ferry [17] proposed that the shift factor, a_T, could be given by

$$\log a_T = -\frac{C_1(T - T_0)}{C_2 + (T - T_0)} \qquad 2.32$$

where C_1 and C_2 are material constants and T_0 is the reference temperature. Viscoelastic mastercurves can be produced from a range of mechanical experiments, typically forced oscillation or creep.

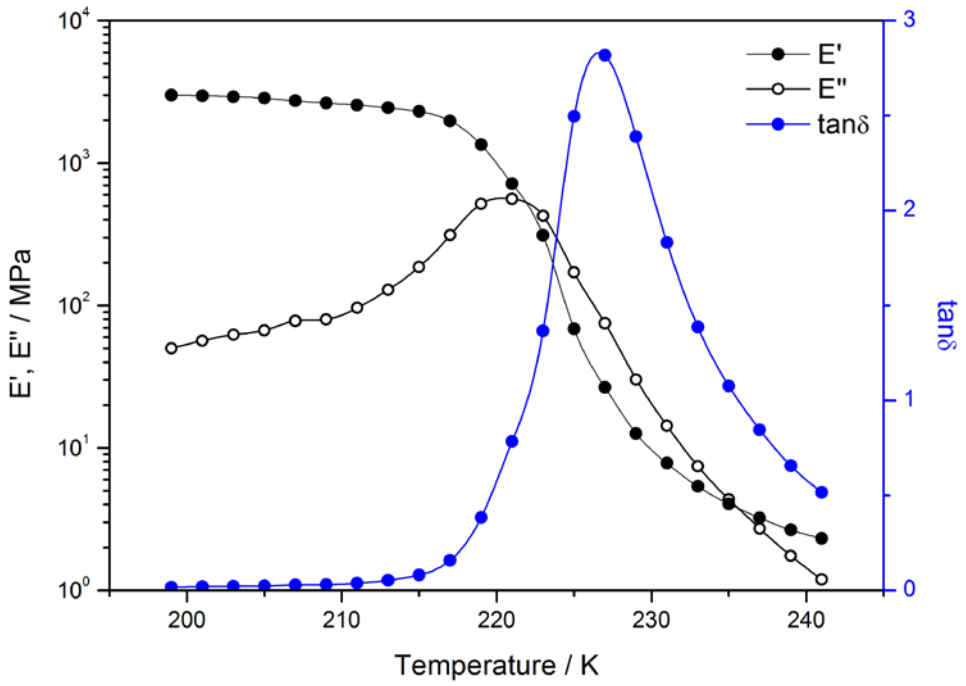

Figure 2.17: Dynamic mechanical analysis of a crosslinked rubber (NR crosslinked with 2 phr dicumyl peroxide) as a function of temperature. The glass transition is apparent as the sudden decay in the storage modulus and peak in viscous dissipation

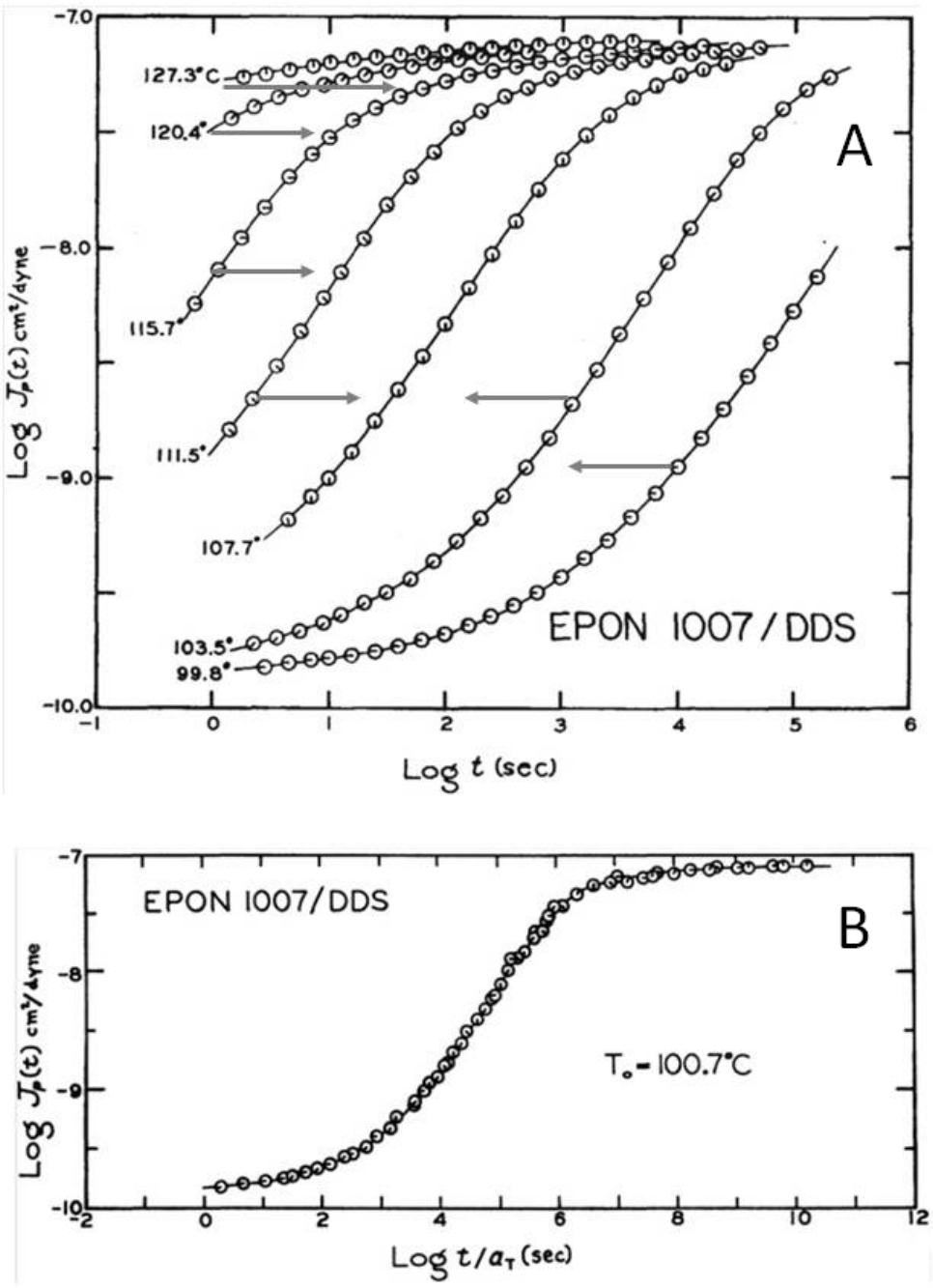

Figure 2.18: Data and principle of Time-Temperature Superposition. A) creep compliance data for EPON 1007/DDS epoxy resin recorded at 7 different temperatures. The arrows show the shifting direction relative to the reference temperature (100.7 °C). B) the resulting creep compliance mastercurve covering 10 orders of magnitude in time. (From Science and Technology of Rubber [9])

A typical viscoelastic mastercurve is presented for an unfilled, uncrosslinked rubber at small strain in Figure 2.19 [9]. Three key regions are apparent. At the highest frequencies the storage modulus is at a maximum, corresponding to the glassy, elastic region. The storage modulus drops dramatically (typically 2-3 orders of magnitude) and the viscous modulus passes through a maximum as the frequency is reduced; corresponding to the glass transition region. At lower frequencies, for the uncrosslinked elastomer, the terminal flow regime is eventually recovered; with an observed relaxation of the storage and viscous moduli. Such mastercurves are often more complex for the case of semi-crystalline polymers or polymer blends; where additional relaxation processes are apparent. Figure 2.19 also highlights a limitation of the TTS principle. The inset shows the superposition of the loss tangent around the T_g where the peak height decreases with increasing temperature - meaning superposition cannot be achieved. This arises from the relatively similar timescales of relaxation for segmental and Rouse (Gaussian chain) dynamics (Figure 2.15) which possess different temperature dependencies [9, 18].

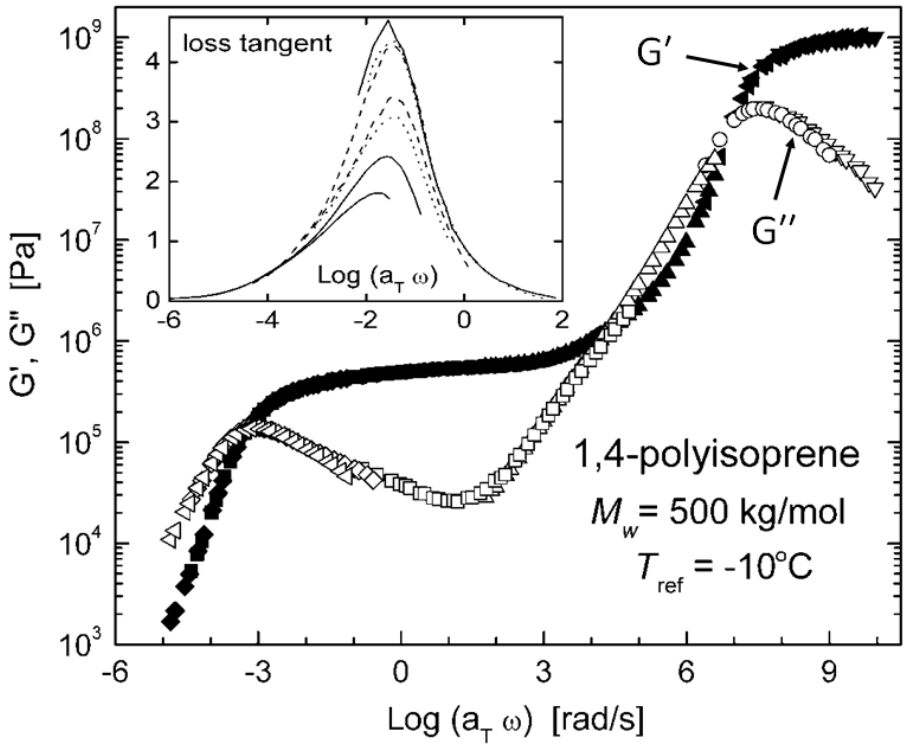

Figure 2.19**:** Example mastercurves for an uncrosslinked polyisoprene rubber. Inset: the breakdown of superposition of the loss tangent in the transition zone (From Science and Technology of Rubber [9])

The phenomenology of viscoelastic mastercurves can be broadly described using the Kelvin-Voigt and Maxwell models of viscoelasticity. For example the frequency response of the Maxwell (controlled strain) model is:

$$G'(\omega) = G\frac{(\omega\tau_{rel})^2}{1+(\omega\tau_{rel})^2} \quad 2.33$$

$$G''(\omega) = G\frac{\omega\tau_{rel}}{1+(\omega\tau_{rel})^2} \quad 2.34$$

where G is the modulus of the spring component in the glassy state and τ_{rel} is the relaxation time of the material.

At low frequencies the moduli of the Maxwell models tend to zero. A more realistic model is the standard linear solid model which includes a finite modulus at low frequency by incorporating an additional spring in parallel. This is plotted in Figure 2.20.

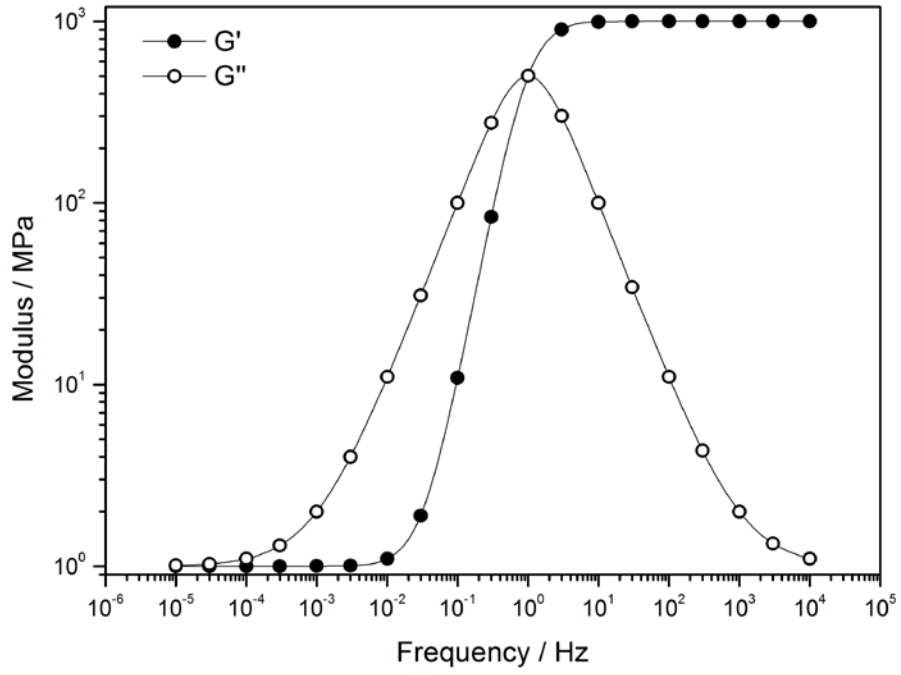

Figure 2.20: The storage and loss components of a standard linear solid model. Note that Equations 2.33 and 2.34 are plotted to include a finite modulus of 1 MPa at low frequency and a glassy storage modulus of 1 GPa

In most cases it is not possible to describe the frequency dependence of experimental results using a single elastic and relaxation term. Although the Maxwell model is strictly phenomenological, it is clear that more than one microstructural relaxation time contributes to the observed mechanical response (for example in the range of timescales observed during linear viscoelastic creep or stress relaxation experiments). In such cases the generalised Maxwell model can be used to describe the total relaxation process as the linear combination of a series of discrete phenomenological relaxation times [17].

$$G'(\omega) = \sum_{i=l}^{n} p_i G_i \frac{(\omega\tau_{rel})^2}{1 + (\omega\tau_{rel})^2} \quad 2.35$$

$$G''(\omega) = \sum_{i=l}^{n} p_i G_i \frac{(\omega\tau_{rel})}{1 + (\omega\tau_{rel})^2} \quad 2.36$$

where p_i is the probability of a specific relaxation taking place. Taking this a step further, it is possible to describe a continuous spectrum of relaxation times, $H(\tau)$, according to

$$G'(\omega) = \int_{-\infty}^{+\infty} H \frac{(\omega\tau_{rel})^2}{1 + (\omega\tau_{rel})^2} d\ln\tau \quad 2.37$$

$$G''(\omega) = \int_{-\infty}^{+\infty} H \frac{(\omega\tau_{rel})}{1 + (\omega\tau_{rel})^2} d\ln\tau \quad 2.38$$

Thus it is theoretically possible to describe both the linear viscoelastic spectrum and static inelastic effects through a knowledge of the material's unique relaxation (or retardation) spectrum. Relaxation spectra can be extracted from a range of mechanical experiments, typically mastercurve data and static creep. The inter-conversion between experiment and spectra and from stress to strain control is outlined in detail by Ferry [17] as are several approximate numerical methods for extracting such spectra from experimental data.

2.5. The Glass Transition

The glass transition is a phenomenon associated with amorphous polymers and glass-forming liquids and can be characterised by a dramatic increase in mechanical properties (modulus or viscosity) as it is approached from the melt either by lowering of the temperature or through an increase in deformation frequency (as shown in Figure 2.17 & Figure 2.19 in the viscoelasticity section). As such, the thermodynamic location of the glass transition is one of the key factors determining the mechanical properties of rubbers and elastomers. Similar changes in viscosity are observed upon phase transitions is other materials. However, unlike conventional phase transitions, the glass transition appears to be a second order effect; meaning that upon passing through the transition no discontinuity is observed in the temperature dependence of the volume, enthalpy or entropy of the material [6, 14]. In fact, in both the glassy and rubbery regimes, the polymer is still in the same thermodynamic state. Therefore it is important to distinguish the terms 'glassy state' and 'rubbery state' and references to transitions between them as distinct from their typical thermodynamic connotations. The exact physical nature of the glass transition is still an open issue in condensed matter physics. Several physical explanations for the glass transition are outlined below.

2.5.1. Chain Relaxation and Free Volume Concepts

One way of conceptualising the glass transition is by considering the temperature dependence of polymer chain segmental relaxation times. Above the T_g, in the rubbery region, fast segmental motions (α or segmental relaxations) are apparent, and for the case of uncrosslinked melts, global or terminal translation of chains throughout the melt. Upon passing through the T_g into the glassy state the fast motions are gradually suppressed as energetic barriers to segmental motions increase due a reduction in both the available free volume and thermal energy of the chains [9]. In the glassy state chain motions are essentially 'frozen out', leaving the polymer in a non-equilibrium, glassy condition. Very slow relaxations are still apparent, such as those responsible for physical aging effects in which the glass slowly moves towards equilibrium [18-20].

The temperature dependence of these relaxation effects is related to the temperature dependence of the free volume of the polymer material - that is the volume within the bulk material which is not occupied by polymer chains. The total volume of a polymer material,

$V(T)$, can be defined as a linear combination of the molecular volume of the polymer, V_0, and the free volume, $V_f(T)$.

$$V(T) = V_0 + V_f(T) \quad 2.39$$

The existence of such free volume can be inferred by the dissolution of a non-crosslinked glassy polymer in a suitable solvent, for example polystyrene in benzene [6]. The total volume of such a solution is found to be less than the linear combination of polymer and solvent volumes - thus the free volume of the polymer phase is apparent. It is proposed that the ability of polymer chains to undergo bond and segmental rotation and translation is directly related to the amount of free volume in the bulk material.

Often the free volume is considered in terms of the temperature dependence of the fractional free volume defined as $f_v = V_f(T)/V$. The fractional free volume in the glassy state, f_g, is given as $f_g = V_f^*/V$, where V_f^* is the free volume below the T_g. Above the T_g a contribution to the free volume arises from the thermal expansion of the melt according to:

$$V_f = V_f^* + \left(T - T_g\right)\left(\frac{\partial V}{\partial T}\right) \quad 2.40$$

Dividing through by the total volume, V, gives the fractional free volume in terms of its thermal expansion coefficient, α_f.

$$f_V = f_g + \left(T - T_g\right)\alpha_f \quad 2.41$$

The temperature dependence of free volume in a typical polymer material is illustrated in Figure 2.21. Above the T_g the free volume is seen to increase with temperature.

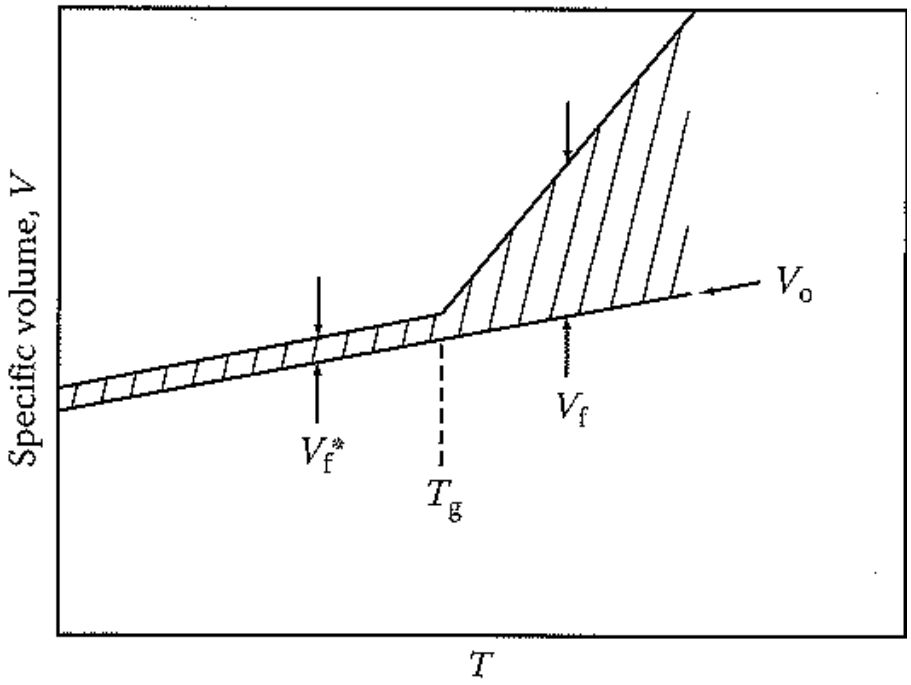

Figure 2.21: Temperature dependence of the free (specific) volume of a polymeric material. Below T_g the free volume is constant. Above T_g the free volume fraction increases as a function of temperature (From Science and Technology of Rubber [9])

2.5.2. Percolation of Free Volume Distribution Model

Recently a new conceptualisation of the free volume model of the glass transition has been proposed which has a bearing on the reinforcement of elastomers by particulate fillers and also observed T_g effects in polymer thin films. The 'Percolation of Free Volume Distribution (PFVD) Model' proposed by Long and Lequeux [21] and Merabia, Sotta and Long [22-24] amongst others describes thermally-induced local density (free volume) fluctuations within van der Waals liquids. Percolation of these dynamically slow, rigid domains at lower temperatures leads to the observed glass transition. By comparing the percolation of such slow domains in bulk 3D and confined 2D geometries several aspects of the T_g can be qualitatively described.

This process is illustrated schematically in Figure 2.22 where a 'bulk' sample is schematically represented as a percolated network of slow domains (solid squares). Under these conditions the bulk material is below T_g. Taking a thin section through the material (that is a thin film of polymer), it can be seen that the slow domains are no longer percolated - therefore the thin film remains above the T_g.

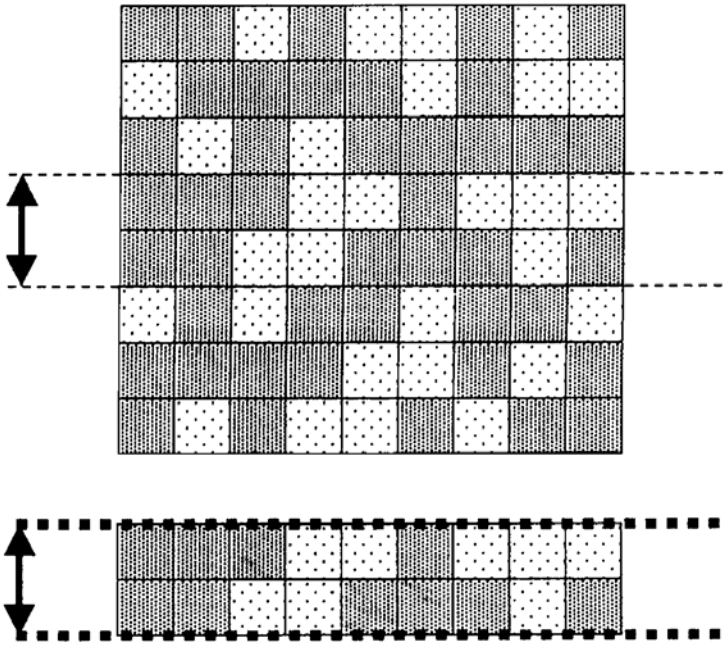

Figure 2.22: Illustration of the PFVD model of the glass transition in the bulk (top - percolated slow domains (solid squares) = glassy behaviour) and in a thin film (bottom - non-percolated slow domains = liquid behaviour) (From Long and Lequeux [21])

2.5.3. Experimental Determination of the Glass Transition

A number of different experimental techniques can be used to examine the glass transition. Typically these involve measurement of the mechanical or thermodynamic properties of the polymer as a function of temperature and/or frequency.

- Mechanical Methods
  - Static mechanical analysis has been used to examine the glass transition temperature especially during the early days of rubber research. Measurement of the modulus, various stress-strain parameters or damping characteristics as a function of temperature can determine the T_g temperature and gives an indication the scale of the change in mechanical properties associated with the T_g. Figure 2.23 shows the rebound resilience of various rubber balls as a function of temperature [7]. A minimum in the resilience response corresponds to high levels of damping at T_g.
  - DMA is now a more regularly reported method for determining the T_g than static mechanical analysis. Typically, the small strain viscoelastic properties are recorded as a function of temperature. The sudden three order of magnitude

change in storage modulus and corresponding peak in viscous modulus are indicative of the T_g (Figure 2.17). Various methods are used to extract a single value for the T_g from this data such as the onset temperature for the change in G', the peak value of G'' or the peak value in tanδ [9]

- Enthalpic and Volumetric Methods:
  - Differential Scanning Calorimetry (DSC) is a technique widely used for the examination of thermal transitions and processes for all types of materials. In polymer science it is used for evaluations of the degree of polymer crystallinity, high temperature decomposition and T_g [25]. The principle of DSC is addressed in more detail in the Appendix. As the T_g is a second order process no corresponding endo- or exo-thermic processes are observed in the thermal trace. Instead, a step change in the heat capacity or heat flow is detected (Figure 2.23). This can be evaluated in a range of different ways, for example by defining an onset temperature or taking the midpoint in the step change.
  - Volume methods. A variety of experimental techniques such as dilatometry [26] and ellipsometry [27] can be used to examine the temperature dependence of the volume of polymer materials. A second order transition is observed at the T_g which can be evaluated by extrapolation of linear fits to the glassy and rubbery behaviour. Figure 2.23 shows the evaluation of volume-temperature trends for polystyrene over a range of applied pressures.
- Broadband dielectric spectroscopy (BDS) is a powerful tool which can be used to study many different aspects of polymer dynamics - including the T_g [18]. BDS is best summarised here as an electrical analogue of DMA, whereby an alternating field is applied across a sample and the temperature and frequency and varied. DBS is sensitive to electrical dispersions which occur at the frequencies related to their mechanical analogues. Thus it is possible to observe the segmental α relaxation which underpins the T_g as a strong dispersion peak in the out of phase component of the permittivity. BDS is reviewed in detail in the Appendix.
- Other methods of determining the T_g which will not be examined in detail here include magnetic resonance techniques [28], neutron and X-ray scattering [29] and fluorescent marker techniques [30].

One interesting issue faced when determining the T_g is rate dependence. Particularly for the case of DMA and DSC measurements where thermal ramps are used, the precise location of the T_g can shift several degrees depending on the ramp rate [25]. This is due to differences in the timescale of approach to the T_g resulting in different levels of non-equilibrium in the glassy state [9].

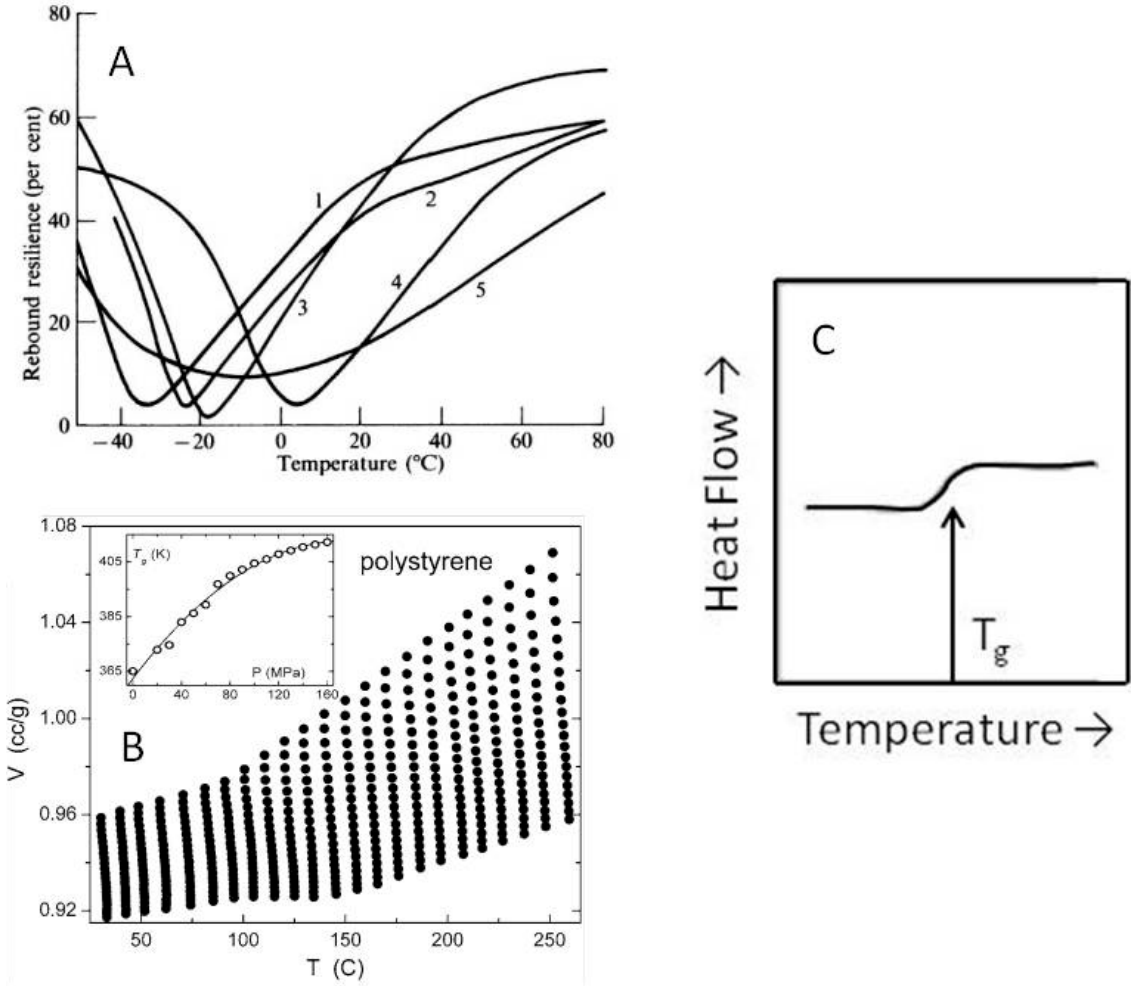

Figure 2.23: A) The variation of rebound resilience with temperature for various rubbers (1 = NR, 2 = SBR, 3 = Neoprene, 4 = Butadiene acrylonitrile, 5 = Butyl) (From Treloar [7]). B) Temperature dependence of the volume of polystyrene over a range of pressures (From Science and Technology of Rubber [9]). C) DSC trace showing the step change in heat capacity at the T_g (Adapted from Thermal Analysis of Rubbers and Rubbery Materials [25])

2.6. Crosslinking of Rubbers and Solvent Swelling of Elastomers

Up to this point, only passing references have been made to the chemical crosslinking of rubber. The process of crosslinking of typical diene rubbers introduces stable, covalent bonds between individual rubber chains; forming a continuous macromolecular network. This is commonly achieved by using either sulphur-based chemistry or organic peroxides.

2.6.1. Sulphur Vulcanisation

Sulphur vulcanisation is the most widely used method for crosslinking elastomers. In the basic vulcanisation system, the rubber polymer is combined with elemental sulphur, a chemical activator (typically zinc oxide combined with a fatty acid) and an accelerator (often a sulphenamide compound). The precise chemistry of the sulphur vulcanisation system is very complex and still not completely defined [31]. As the majority of the work in this thesis is performed on peroxide-crosslinked samples, a detailed overview of sulphur crosslinking chemistry is not presented.

The number of sulphur atoms involved in individual crosslinks is called the sulphur rank. The average sulphur rank of crosslinks can be varied by changing the sulphur to accelerator ratio. A relative increase in accelerator concentration promotes more efficient consumption of the elemental sulphur meaning that the resulting crosslinks will have a lower sulphur rank [9]. Vulcanisation systems are ranked according to their sulphur consumption efficiency and classed as either conventional (CV), semi-efficient (SEV) or efficient (EV) vulcanisation. The sulphur rank of the crosslinks impacts the mechanical properties of vulcanisates in a complex way. This is believed to be due to the ability of the polysulphidic crosslinks to yield under applied stress and then recombine through free radical recombination in the strained state [31].

Network structures resulting from sulphur cures are often very complex with sulphur being combined in crosslinks of different rank and also with polycyclic sulphidic compounds being attached to a single chain. During the vulcanisation process, cis-to-trans isomerisation of chain backbones may also occur. In addition, significant amounts of non-network material remain in the vulcanisate following the vulcanisation process. A schematic of such modifications is presented in Figure 2.24.

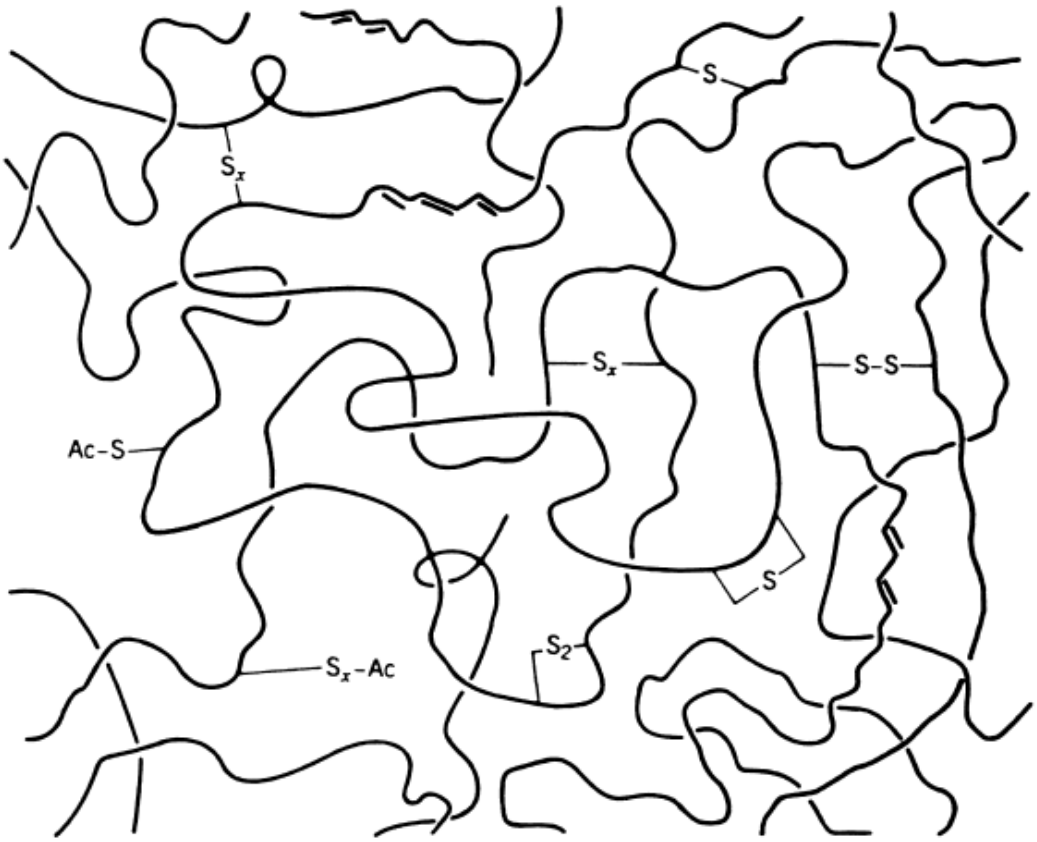

Figure 2.24: Schematic representation of a typical network structure obtained from accelerated sulphur crosslinking. This idealised network consists of poly, di or mono sulphidic crosslinks between chains, sulpidic closed loops which may be formed on the backbone of a single chain, non-crosslinking sulphur atoms which are bonded to an isoprene chain and a partially converted accelerator molecule, regions of trans-isomerism on the polyisoprene network chains, chain dangling ends, closed loops and trapped entanglements. S represents sulphur atoms, Ac represents accelerator molecules (From Science and Technology of Rubber [9])

2.6.2. Peroxide Crosslinking

Peroxide cure systems are widely used as an alternative to sulphur-based cures where improved aging resistance and compression set of cured compounds is required or for crosslinking saturated polymers [15]. Additionally, peroxide cures have been used as simplified model cure systems with the potential for a stoichiometric equivalence between curative and crosslink density [32, 33]. Peroxide cures also result in reduced non-network material in the final cured elastomer compared with sulphur cures.

The mechanism of peroxide crosslinking of NR has been studied by a number of authors [34-36] and has been reviewed by Dluzneski [37]. It has been proposed that, in its simplest form, the peroxide crosslinking reaction can be described by a combination of proton abstraction, radical addition and chain scission mechanisms.

The proton abstraction route is detailed in Figure 2.25 A-C. The initial step (A) involves thermally-induced homolytic scission of the peroxide curative (in this case dicumyl peroxide) to form 2 alkoxy precursor free radicals. Subsequently the precursor radicals are able to abstract an α proton from the NR backbone (B) to form a chain macro-radical. Combination of 2 macro-radicals forms a carbon-carbon, inter chain crosslink (C). Following this route, there is a 1:1 molar equivalence between the peroxide and the concentration of crosslinks.

Alternatively, under certain conditions, the alkoxy precursor radical can add directly to the NR backbone double bond. Addition follows the anti-Markovnikov rule since the free radical is stabilised at the most alkylated carbon (Figure 2.26). This process generates an additional free radical which is able to 'polymerise' in the local area [37].

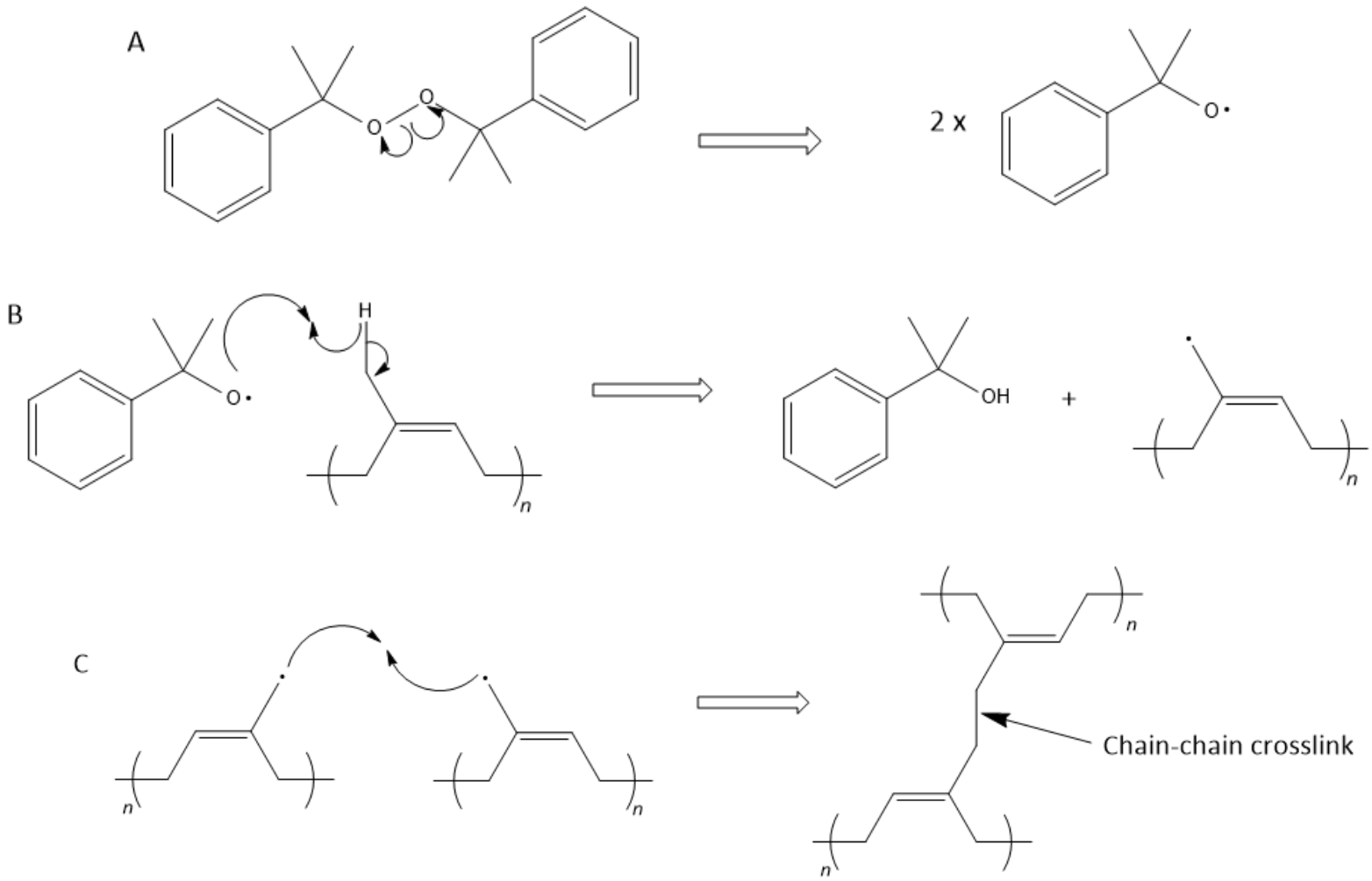

Figure 2.25: Abstraction mechanism of crosslink formation (Adapted from [37])

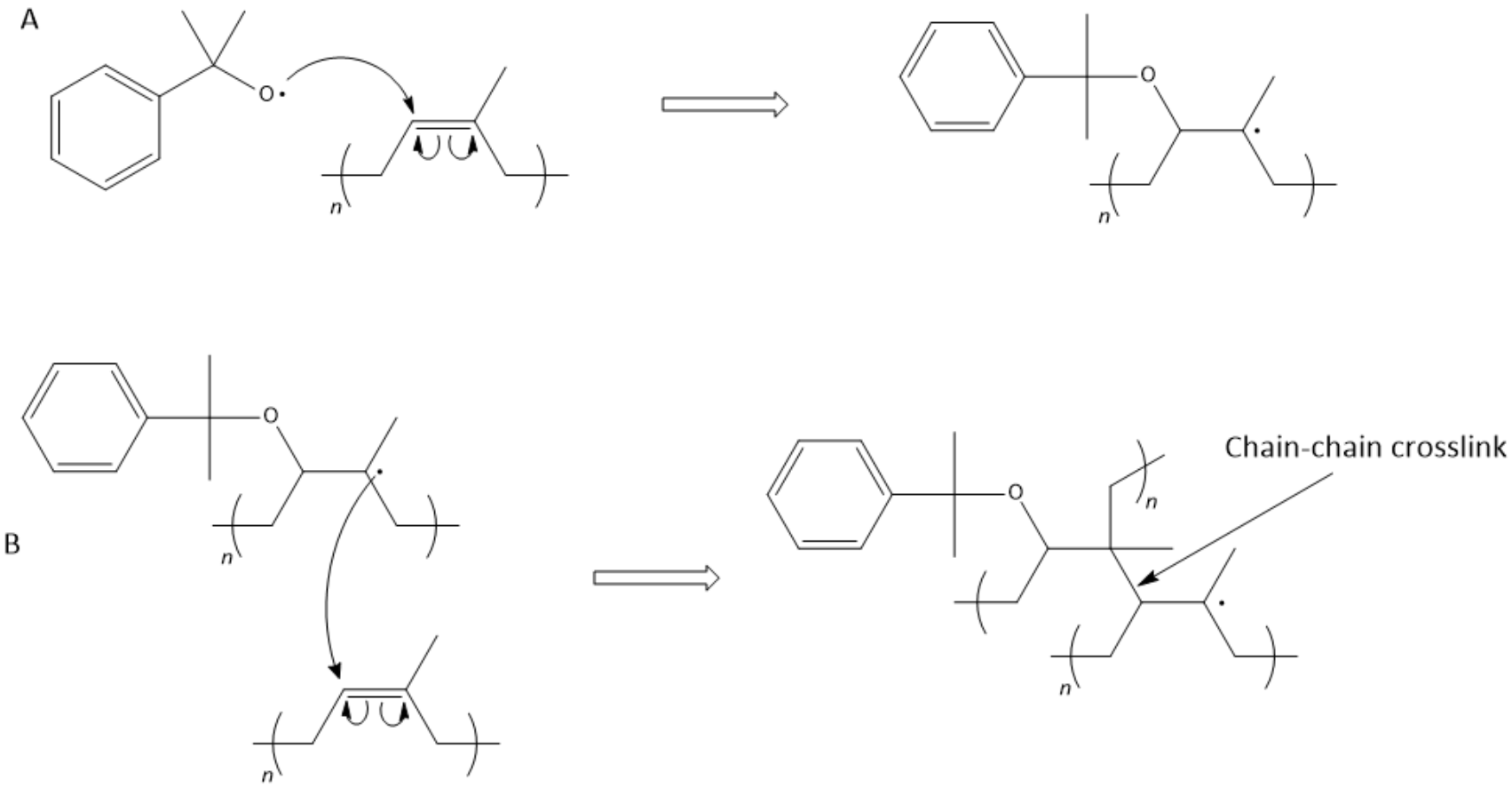

Figure 2.26: Addition mechanism of crosslink formation (Adapted from [37])

2.6.3. Equilibrium Solvent Swelling

While linear polymers dissolve in suitable amounts of solvent given enough time, crosslinked rubbers are noted for their swelling behaviour [7, 15]. The swelling process is time dependent - that is, it takes a finite amount of time for the polymer-solvent mixture to reach equilibrium. Flory and Huggins addressed the issue of dissolution of linear polymers in solvents and this was modified by Flory and Rehner to account for crosslinked polymers [7, 14]. The total free energy of dilution of crosslinked rubbers, ΔG, is given as a linear combination free energies

$$\Delta G = \Delta G_m + \Delta G_e \tag{2.42}$$

Here ΔG_m is the free energy associated with mixing of the solvent with the polymer in the uncrosslinked state and ΔG_e is the free energy change associated with expanding the crosslinked rubber network. ΔG_e can be determined directly from the statistical theory [7]. The stored energy density function for isotropic expansion - as is the case for unconstrained swelling - can be written as

$$W = \frac{\rho \mathbf{R} T}{2M_C}(\lambda_1^2 + \lambda_2^2 + \lambda_3^2 - 1) = \frac{3\rho \mathbf{R} T}{2M_C}\left(\varphi_2^{-2/3} - 1\right) \tag{2.43}$$

where φ_2 is the volume fraction of rubber in the swollen compound, ρ is the density of the rubber, $\mathbf{R}$ is the ideal gas constant and T is the temperature. The free energy change upon swelling is defined as $\partial W / \partial n_1$where n_1 is the number of moles of solvent swollen into the elastomer. φ_2 is defined in terms of n_1 as

$$\varphi_2 = \frac{n_2 V_2}{n_1 V_1 + n_2 V_2} \tag{2.44}$$

where n_2 and V_2 are the number of moles and molar volume of rubber in the swollen compound and V_1 is the molar volume of solvent. Substituting this into Equation 2.43 and differentiating with respect to n_1 gives ΔG_e

$$\Delta G_e = \frac{\rho \mathbf{R} T}{M_C} V_1 \varphi_2^{1/3} \quad 2.45$$

ΔG_m is defined by the Flory-Huggins expression [14] as

$$\Delta G_m = \mathbf{R}T \left[\ln(1-\varphi_2) + \left(1 + \frac{1}{x}\right)\varphi_2 + \chi \varphi_2^2 \right] \quad 2.46$$

where x is the degree of polymerisation and χ is the polymer-solvent interaction parameter, giving ΔG as

$$\Delta G = \mathbf{R}T \left[\ln(1-\varphi_2) + \left(1 + \frac{1}{x}\right)\varphi_2 + \chi \varphi_2^2 + \frac{\rho V_1}{M_C} \varphi_2^{1/3} \right] \quad 2.47$$

At equilibrium a balance should exist between entropic and mixing terms such that ΔG = 0. The degree of polymerisation in crosslinked rubbers is also large. This results in the Flory-Rehner Equation.

$$\ln(1-\varphi_2) + \varphi_2 + \chi \varphi_2^2 + \frac{\rho V_1}{M_C} \varphi_2^{1/3} = 0 \quad 2.48$$

Often the modified expression for the entropic contribution given by Flory [7] is used and the result is

$$\ln(1-\varphi_2) + \varphi_2 + \chi \varphi_2^2 + \frac{\rho V_1}{M_C} \left(\varphi_2^{1/3} - \frac{\varphi_2}{2} \right) = 0 \quad 2.49$$

This result therefore allows the determination of the average molecular weight between network crosslinks by experimental evaluation of the equilibrium solvent swelling behaviour of elastomers. However a number of factors limit the precision of this approach:

- The value of the polymer solvent interaction parameter, χ, has been shown to depend not only on the polymer-solvent pair but also on the value of φ_2 in the swollen rubber [38].

- The description of entropic elasticity used here to derive ΔG results from the assumption of affine deformation within the network. This means that the network points between chains are held at fixed points relative to each other during deformation. However James and Guth [7] proposed a different scenario whereby the positions of network junctions are permitted to fluctuate relative to each other during deformation - the non-affine or phantom network model - which would lead to a slightly different derivation for ΔG. The physical reality of the situation probably lies somewhere in between the two [7, 38].
- If swelling experiments are performed using gravimetric rather than volumetric techniques then the value of rubber density is required in order to calculate φ_2. For sulphur-vulcanised rubbers this value does not necessarily correspond to the density of the uncrosslinked rubber as the presence of non-network material must be taken into account [38].
- For swelling of sulphur-vulcanised rubbers the precise value for the equilibrium level of swelling is complicated by time dependent photo-oxidative degradation of the sulphidic crosslinks leading to an apparent slow linear increase in swelling capacity at longer timescales [38].

2.7. Fillers

While the properties of unfilled elastomers are interesting from a scientific perspective, such materials often do not possess the required properties for most engineering applications. For example, often very stiff elastomer materials are required, with higher damping and strength properties than are found in unfilled materials - for example in car tyre applications. In fact, some non-strain crystallising elastomers such as SBR are almost unusable in their unfilled form. The use of finely divided particulates to modify the properties of elastomers has therefore become a key technology within the rubber industry. Many different types of particles are used as reinforcing fillers to varying levels of effectiveness depending on factors such as particle size, morphology and surface activity. In this section the two most common types of filler particle, carbon black and precipitated silica are reviewed in detail.

2.7.1. Carbon Black

Carbon Black (CB) was one of the first types of particles noted for its reinforcing properties [2, 5] when incorporated into rubbers. The typical elemental composition of CB is primarily carbon, with oxygen, sulphur and hydrogen present as minor constituents [39]. CB is produced via the combustion of vaporised hydrocarbons under strictly controlled conditions. A schematic of the furnace production process is reproduced from Klüppel [40] and given in

Figure 2.27. The hydrocarbon mixture is injected and vaporised, mixed with air, combusted and then quenched by water. Early in the combustion process spherical primary particles of CB are formed and increase in size due to surface deposition of carbon - indicated as surface growth (SG) in the diagram. Primary particles rapidly coalesce to form small aggregates which continue to undergo surface growth. Aggregate growth (AG) occurs when two or more of these aggregates come into contact forming larger aggregates. During this process the surface growth mechanism continues to solidify the particles and increase their size and mass. Eventually the process is quenched and particles are recovered from the reactor. Varying factors such as the quench time, furnace temperature and feedstock injection rate alter the physicochemical properties of the recovered CBs [39, 40].

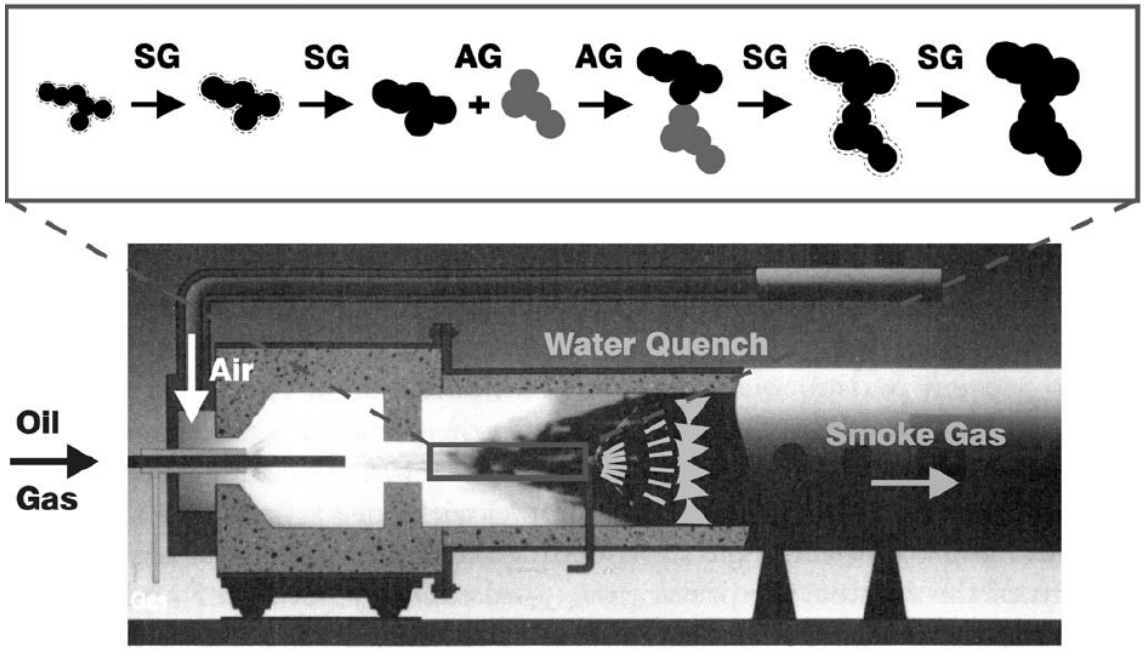

Figure 2.27: Schematic of a carbon black production furnace with a schematic of the aggregate growth mechanism. SG refers to the surface growth mechanism and AG refers to the aggregate growth mechanism (from Klüppel [40])

The resulting structures are generally aciniform in morphology (like a bunch of grapes) made up of many primary particles fused together. Figure 2.28 are transmission electron microscopy images of carbon black aggregates of various grades. The typically branched morphology can be clearly distinguished. The many 'structure' types of the carbon black aggregates are schematically illustrated in Figure 2.29. Higher structures generally refer to more branched, anisotropic morphologies [41].

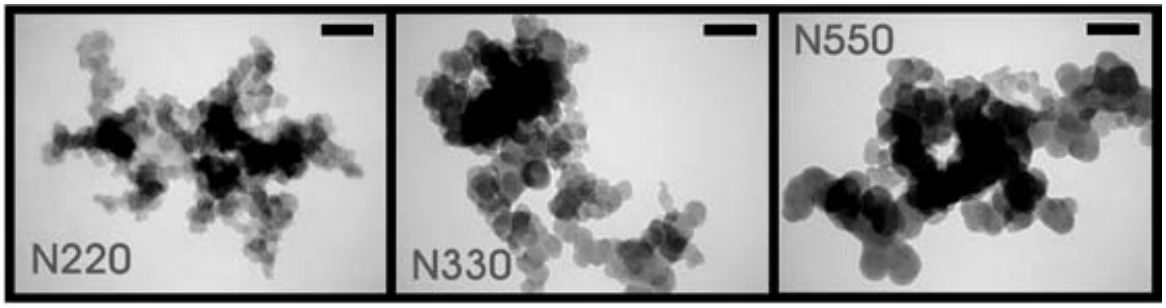

Figure 2.28: TEM images of carbon black aggregates of varying particle size and morphology. The scale bar corresponds to 100 nm (from Klüppel [40])

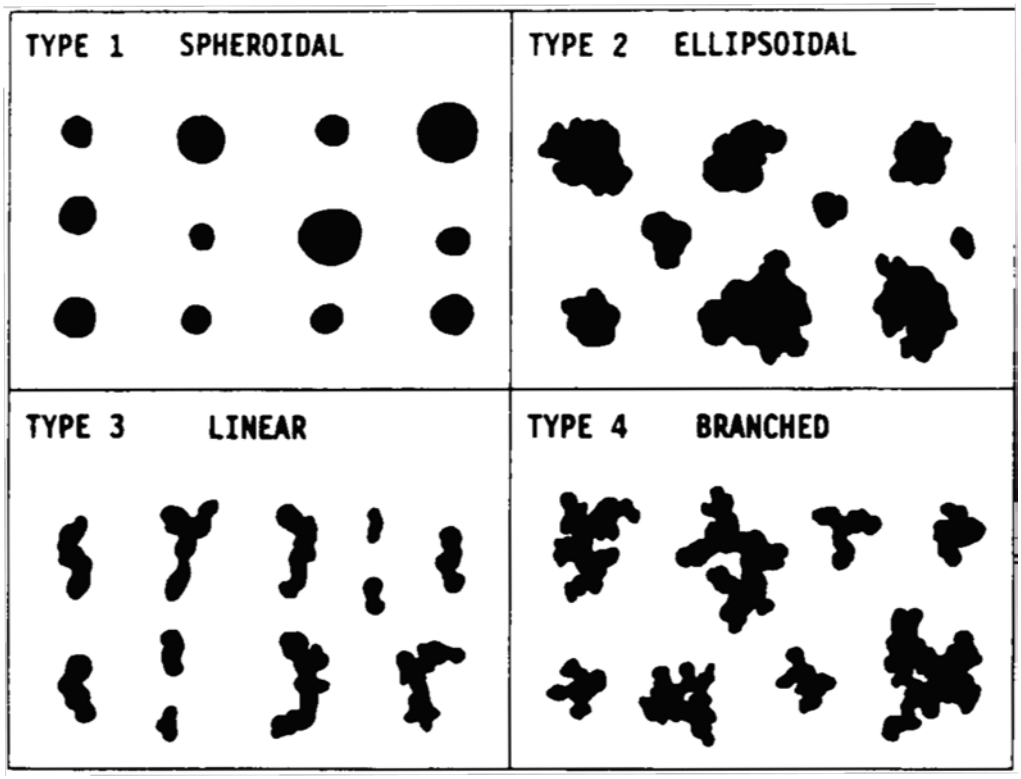

Figure 2.29: Qualitative characterisation of carbon black 'structure' (from Gruber and Herd [41])

CBs are ASTM graded [42] according to both their primary particle size and aggregate structure. A typical ASTM CB grading is assigned as follows:

- The first letter of the grade corresponds to the degree to which the CB interacts with the sulphur cure system. For rubber applications the letter N designates 'non-interacting, or normal curing' and the letter S indicates 'slow curing'.
- The first number relates to the average primary particle size (1-7 = 10 - 700 nm diameter).

- The final two numbers are related to CB structure. In general, a higher number indicates a higher level of structure.

For example, N110 is a non-interacting carbon black with an average primary particle diameter of 10 nm and a relatively low structure. The slight exception to this trend is the case of N990 grade CB. N990 exhibits no aggregate structuring and instead consists of isolated spherical particles with a diameter of around 250 nm. As such N990 is one of the largest particle size CBs with the lowest surface area and is the least reinforcing grade.

Reported values for surface areas of CBs are usually determined specific to the surface absorption of a probe gas or liquid. Inert gases such as argon and nitrogen are routinely used to determine surface area via the Brunauer-Emmett-Teller (BET) isotherm method (see the Appendix for theoretical background). Larger probe liquids such as iodine or cetyltrimethylammonium bromide (CTAB) are often used to provide surface areas which may better correspond with the surface area of filler accessible to the rubber polymer. Typical BET and CTAB surface areas for a range of CB grades are given in Table 2.1.

Table 2.1: Primary particle diameters (note that this is not the total aggregate size) and specific surface areas of various CB grades. BET SSA refers to nitrogen specific surface area and CTAB refers to cetyltrimethylammonium bromide specific surface area (Reproduced from Donnet [39])

ASTM Grade	Mean particle diameter / nm	BET SSA / $m^2.g^{-1}$	CTAB / $m^2.g^{-1}$
N110	18	138	127
N220	21	116	111
N330	30	83	84
N550	56	41	43
N660	67	36	35
N762	107	26	28
N990	285	9	9

An industry standard measure of carbon black structure is given by the dibutyl phthalate (DBP) absorption capacity of the carbon black in units of ml DBP per 100 g of carbon black. A plot of the DBP capacity of a range of carbon blacks against their nitrogen surface area is given in Figure 2.30.

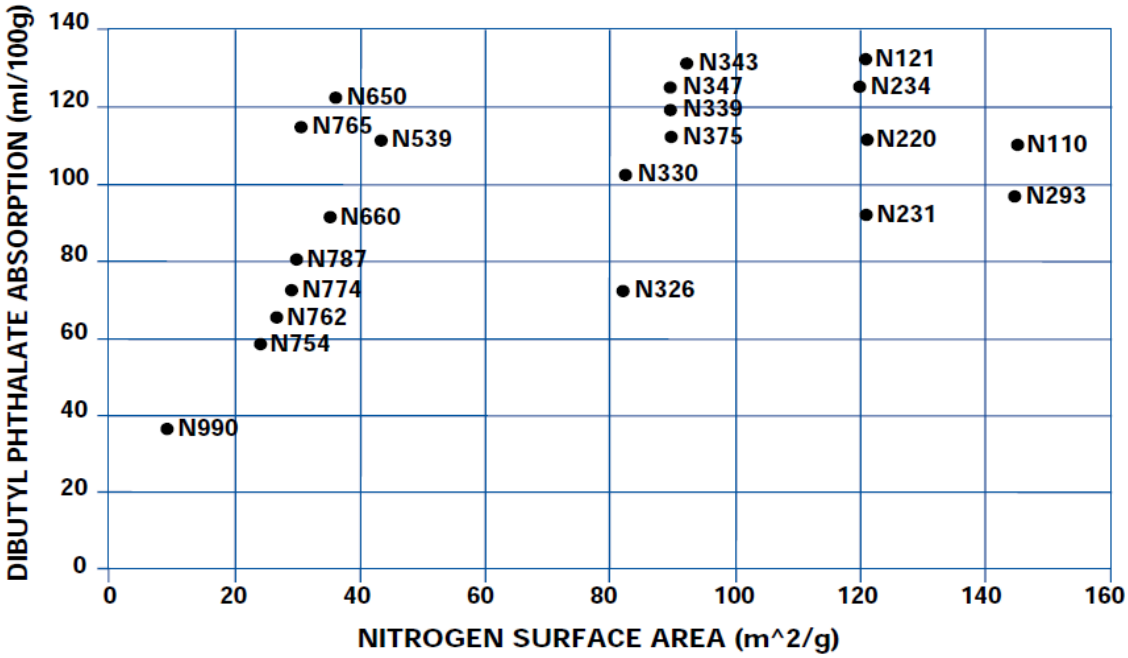

Figure 2.30: DBP absorption levels (structure) versus nitrogen BET surface area for a range of carbon black grades (From Cancarb N990 technical data sheet [43])

The nature of the CB surface activity is dictated by the industrial production method. The spatial distribution of free energy at the surface of regular tyre grade carbon blacks is highly heterogeneous [39, 44, 45]. Surface free energy is defined as the excess in energy present at the surface of a material over the energy within the bulk material and is covered in more detail in the Appendix.

Depending on the grade of carbon black there exist, to varying extents, regions of amorphous carbon interspersed with graphitic crystal layers and edges [39, 45-47]. Schröder et al. [44] used inverse gas chromatography to identify four discrete types of energetic sites: isolated at the lateral surface of the graphitic crystals; the amorphous carbon regions between crystallites; at the crystallite edges; and within slit-shaped cavities between graphitic layers present on the surfaces of a range of different carbon blacks. Example surface energy distributions for various CBs are presented in Figure 2.31. Here the total distribution is deconvoluted into the four separate contributions which are related to structures at the surface of the carbon blacks. In addition to physical surface activity, oxygen-containing chemical functionalities such as carboxyl, quinonic, phenol and lactone groups have been identified on the carbon black surface [39]. Both physical and chemical activities have been investigated in terms of physical interaction with polymer chains and also crosslinking chemistry [39, 48].

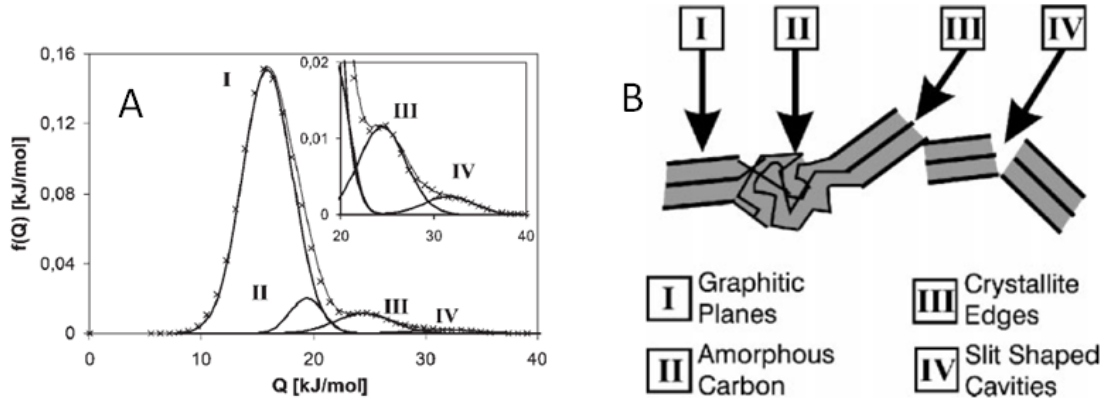

Figure 2.31: A) surface free energy distribution for N220 deconvoluted into 4 distinct contributions. Note, the ordinate is the frequency of free energy. B) assignment of the energetic contributions to the surface morphology of carbon black (From Schröder [44])

Thermal treatments (graphitisation) have previously been used to produce carbon blacks which have retained their particle morphology but have a dramatically altered surface energy profile [46, 49-52]. During the graphitisation process carbon black is exposed to high temperatures, often between 1000 and 3000 °C, under an inert atmosphere. This results in a reduction of the high energy sites on the particle surface by crystallisation of amorphous carbon regions producing a growth of graphitic layers and results in a net reduction in the surface concentration of crystallite edges [39, 44, 53]. Graphitised carbon black is therefore useful as a model material where the filler-rubber interactions have been severely reduced versus the unmodified carbon black.

An example of the effect of the graphitisation process on the surface properties is given in Figure 2.32 from Göritz et al. [46]. Here the surface morphology of carbon black was images using scanning tunnelling microscopy (STM) before and after graphitisation. The appearance of flat plateau areas on the carbon black surface is the result of the formation of graphitic crystallites which present a much lower surface free energy to the polymer phase once compounded.

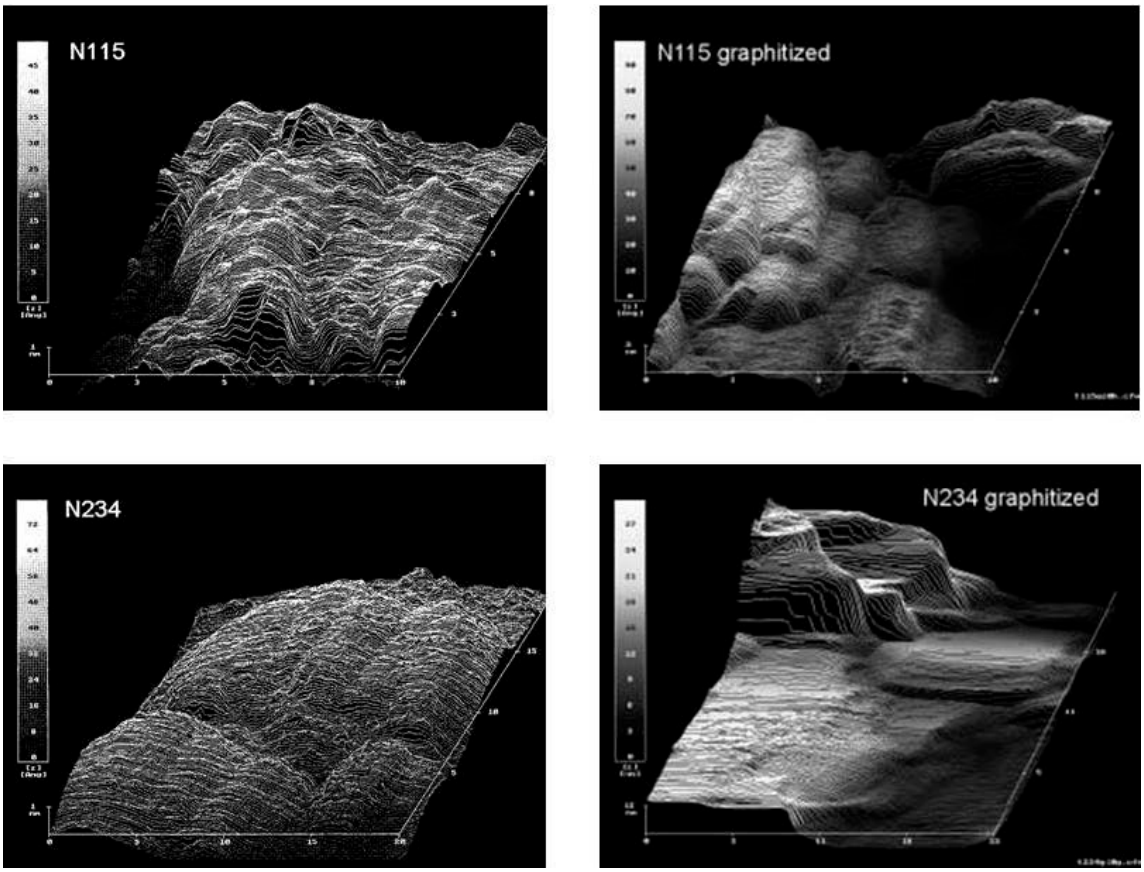

Figure 2.32: Scanning tunnelling microscopy images of the topology of the surfaces of N115 and N234 carbon black (left) and their graphitised analogues (right). The *x* and *y* dimensions are 20 nm. The *y*-axis scale bar corresponds to 1 nm. (From Göritz et al. [46])

Carbon blacks are typically provided in a pelletised form, and incorporation into rubber is usually achieved in an internal mixer prior to the addition of curatives [54]. Due to its highly energetic surfaces, CB generally interacts well with most rubber polymers. During mixing, carbon black dispersion throughout the rubber polymer is achieved more efficiently than when using polar surface fillers such as silicas or clays. Re-agglomeration (flocculation) of filler is also less pronounced than with silicas.

2.7.2. Precipitated Silica

Precipitated silicas (PSi) are the second most commonly used type of filler particle after carbon black. PSis are an amorphous form of silica produced via acidification of sodium silicate under controlled conditions [55, 56]. Figure 2.33 illustrates this process. Sodium silicate and sulphuric acid are first mixed and continually agitated. Initially primary particles with diameters of a few 10s of nanometres are formed and tend to cluster together to create chemically bonded aggregate structures similar in geometry to those of carbon black. Subsequent filtering, drying and milling stages also influence the structure of the precipitated silica [56].

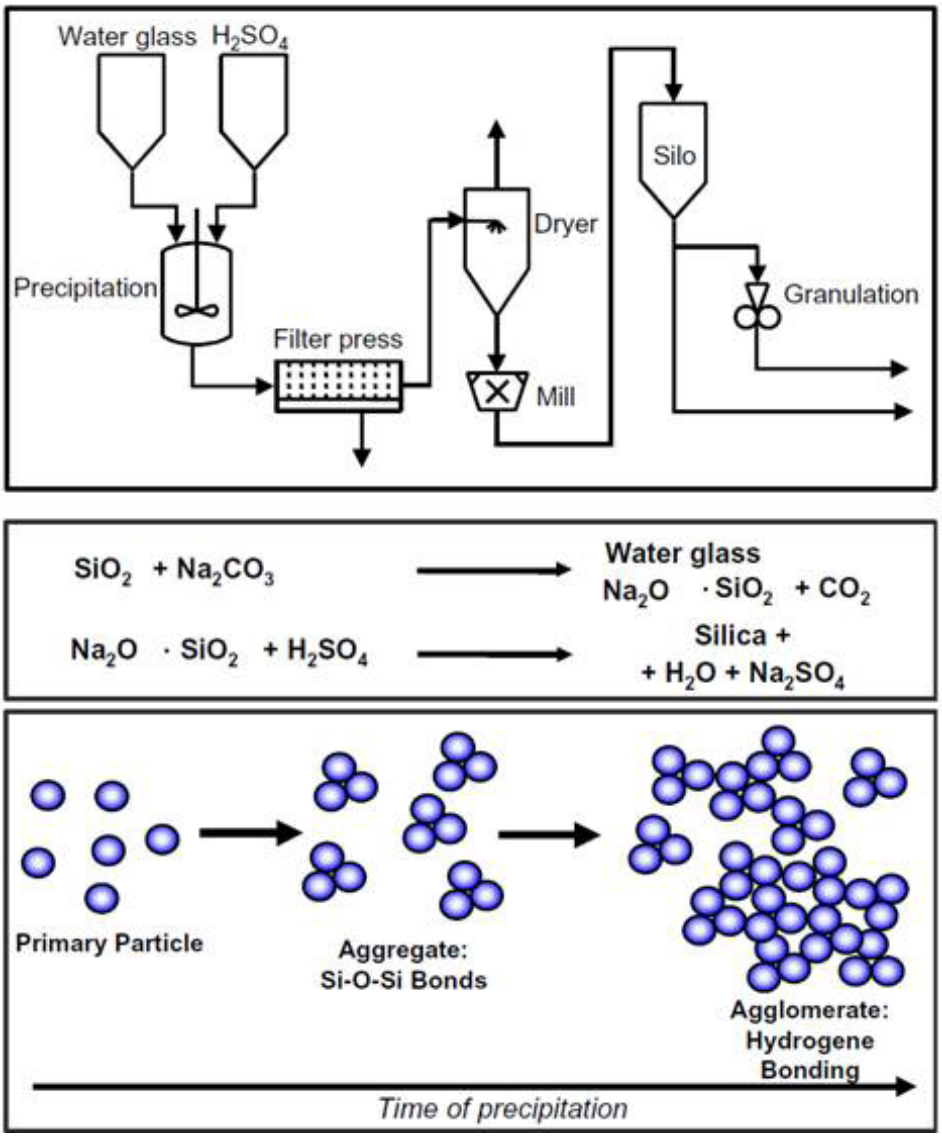

Figure 2.33: Top) schematic of the process for synthesis of precipitated silica. Middle) chemistry of the synthesis process. Bottom) schematic of the aggregate growth mechanism (From Lugginsland [56])

Although the morphology of such PSi is qualitatively similar to carbon black, the surface chemistry is very different. PSi is populated with polar hydroxyl (silanol) groups with a typical surface density of 5 nm^{-2} [57-59]. Three different types of surface silanol groups have been identified: isolated, geminal and vicinal in addition to oxygen-bridged siloxane groups [55, 58] (Figure 2.34). Being produced via an aqueous method, PSi usually contain a few percent of moisture by mass. Typically this water is present as a 'shell' of moisture in close proximity to the silica surface and held in place by strong hydrogen bonding. This surface moisture has been shown to affect the compounded dispersion state of silica and also can also interact with cure systems [60, 61]. The nature of surface moisture in cured compounds has been studied in detail using dielectric spectroscopy [62].

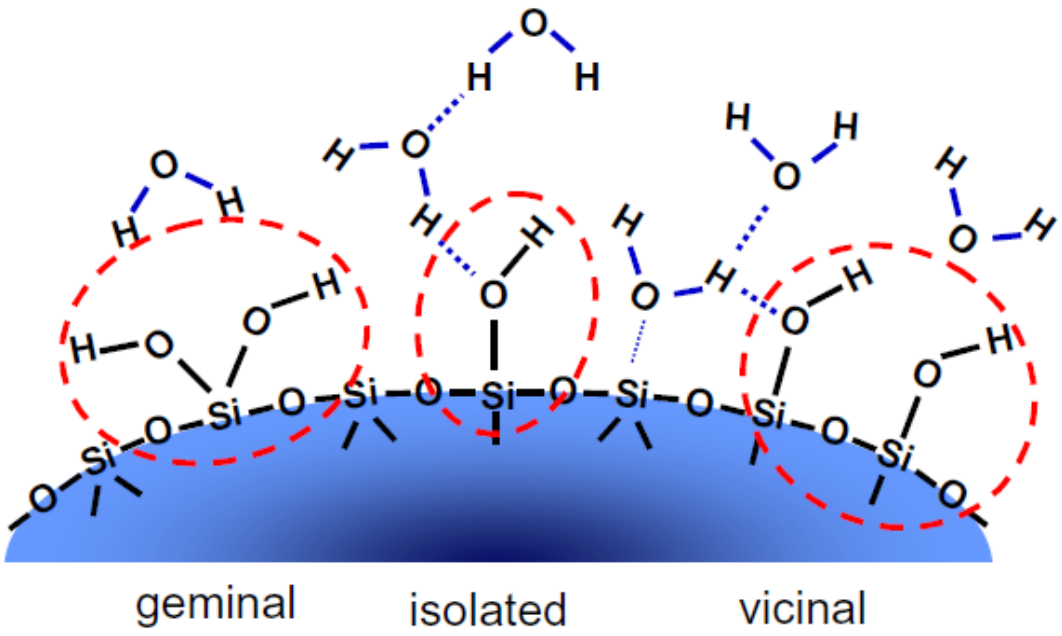

Figure 2.34: Schematic of three types of silanol groups present on the surface of precipitated silica (From Lugginsland [56])

The morphology of precipitated silica varies according to production method and is not strictly graded in the same way as carbon black. Very generally PSi can be split into two categories; conventional silica (CS) and highly dispersible silica (HDS) [56]. HDS is generally used in tyre tread formulation and usually has a high surface area in comparison with carbon blacks, ranging from 100 to 200 m^2/g. As the name suggests HDS consists of very fine aggregates (~ 50 nm) which are more readily dispersed throughout the rubber upon compounding. The polar, hydroscopic nature of the silica surface presents an issue when it comes to the compounding of silicas. In general the polarity difference between the silica surface and most diene rubbers makes effective dispersion of raw silicas very difficult [45, 47].

Furthermore during high temperature vulcanisation, re-agglomeration or flocculation of the filler aggregates detrimentally affects the state of dispersion [63, 64]. Hydrogen bonding between silica aggregates further promotes the formation of an agglomerated filler structure. Highly aggregated filler structures tend to result in very high values of hysteresis at larger strains due to dissipative breakdown of the structure. Therefore the surface chemistry of PSi has a negative impact on the degree of macro and micro scale filler dispersion. This can be overcome by using an organosilane dispersing or coupling agent to modify the surface of the silica [5, 56, 65].

2.7.3. Silane Chemistry

Bi-functional organosilanes are now regularly used in the passenger tyre industry to overcome processing issues arising from the polar nature of the silica surface and to improve the interaction between polymer and filler [45]. Typically the silane performs two functions. Firstly, during the initial mixing stage, one functionality of the silane reacts with silanol groups on the silica surface and covalently bonds to the filler surface. This modifies the polarity of the filler and typically improves dispersion in non-polar rubbers and suppresses flocculation effects during vulcanisation (due to a reduction in the concentration of silanol groups on the silica surface available for hydrogen bonding). Secondly during the vulcanisation step a second functionality of the silane reacts directly with the polymer chains to couple the filler surface to the polymer phase [5, 66].

Therefore silica fillers are usually mixed with rubbers in a two step process. The initial reaction of the silane with the silica surface requires a minimum temperature and mix duration be reached in order to promote and complete the chemical reaction [67, 68]. The exact temperature range depends on the particular silane in question. The reaction of silane with silica typically proceeds via condensation of suitable leaving groups (ethoxy, methoxy) with silanol groups. This leads to the evolution of volatile alcohol during the mix stage. The second silane functionality and reaction chemistry depends on the cure system used. Figure 2.35 details the reaction of triethoxyvinyl silane (TEVS) with the surface of precipitated silica.

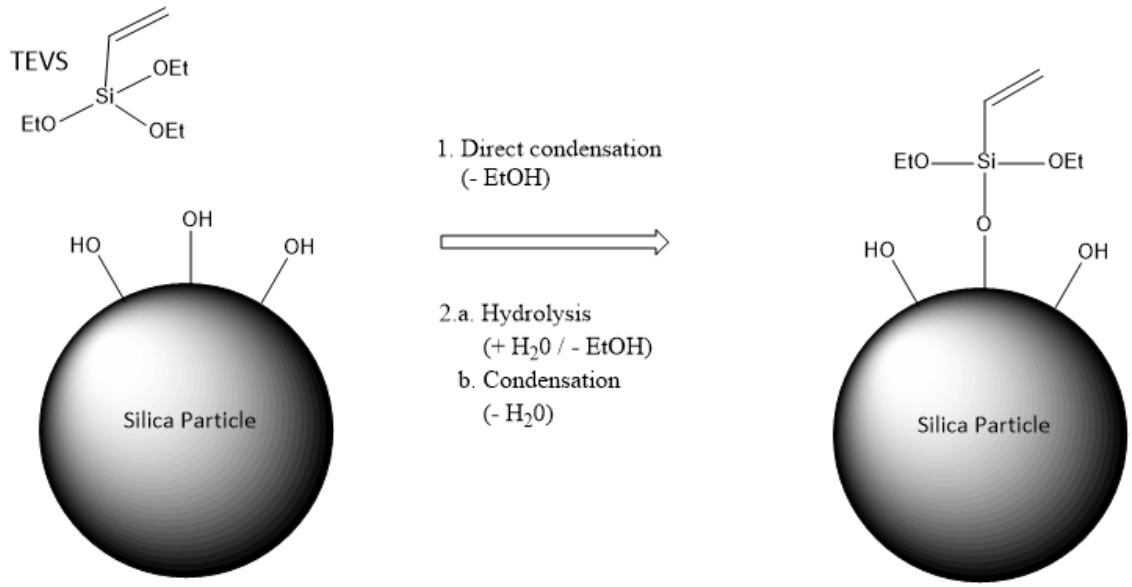

Figure 2.35: Schematic of the reaction of triethoxyvinylsilane (TEVS) with the surface silanol functionality of precipitated silica

The reaction proceeds either through direct condensation of the ethoxy functionality with the surface silanols or through an intermediate hydrolysis step. Both of these reaction routes lead to the liberation of ethanol as a by-product. The second stage coupling proceeds via free radical addition to the vinyl functionality during the peroxide crosslinking step to form a stable bond between the elastomer network and the silica filler.

2.7.4. Comparison of Carbon Black and Silica Performance in Car Tyre Treads

Since the patent filed by Michelin for 'Green Tyre' technology in 1992 [69], the use of precipitated silica as a partial filler substitute for carbon black in passenger tyre treads has increased dramatically. At a technological level, the combination of silane chemistry with highly dispersible silica is able to modify the viscoelastic properties of rubber beyond the limits associated with carbon black fillers. In car tyre technology, performance factors can be associated with specific regions of the tread material's viscoelastic spectrum. For example Figure 2.36 illustrates the frequencies associated with rolling resistance and wet grip deformations [70]. Often the frequencies of interest - especially wet grip frequencies - are outside the limits of typical dynamic testing equipment. As such the time temperature superposition principle (TTS) is used to approximate the corresponding temperatures associated with the frequencies of interest (though in reality the application of TTS to highly filled systems is often inappropriate - as will be seen in the following section). As such, dynamic temperature sweeps are used to rapidly characterise the hysteresis at the relevant temperatures.

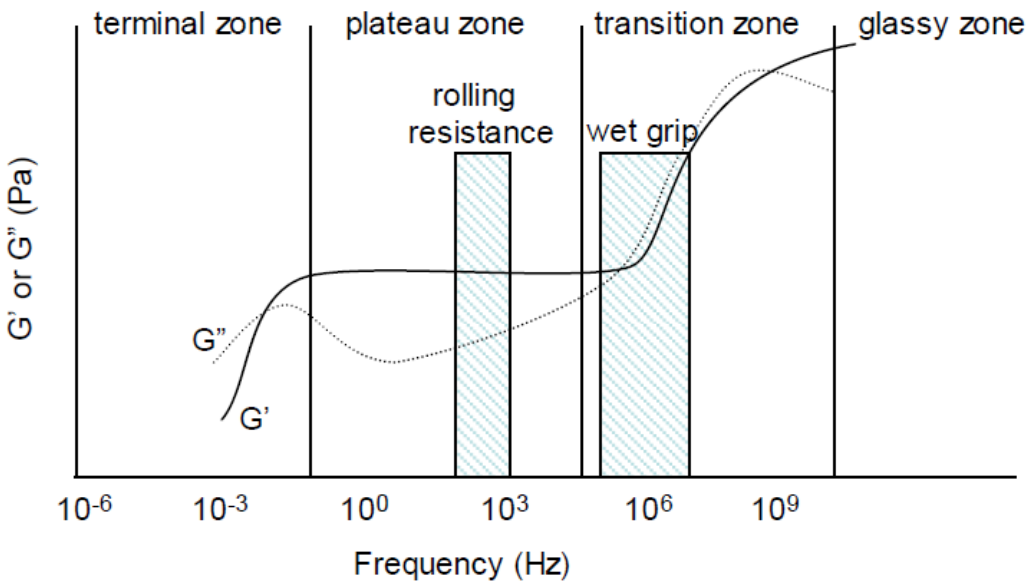

Figure 2.36: Schematic of the dependence of the dynamic moduli on the deformation frequency. Frequencies corresponding to rolling resistance and wet grip performance are highlighted (from Mihara [71])

Figure 2.37 demonstrates the use of a temperature sweep to characterise the viscoelastic performance of car tyre treads. The arrows indicate wet grip braking generally improving with more hysteretic compounds in the transition region and rolling resistance (fuel economy) improving with more elastic compounds in the rubbery region [47]. As such there is a need to develop compounds which are as viscous as possible in the transition region and as elastic as possible in the plateau, rubbery region - without detriment to the abrasion properties of the tread. Precipitated silica compounds are generally found to improve both of the performance factors while maintaining wear resistance in comparison with carbon black.

2.7.5. Other Types of Reinforcing Fillers

Various other types of reinforcing filler are used to a lesser extent. These include organoclays, precipitated carbonates and other minerals such as talc and kaolinite-based clays. Recent research has also focused on applications of carbon nanotubes, expanded graphite and graphene oxide in various types of rubber [72-79].

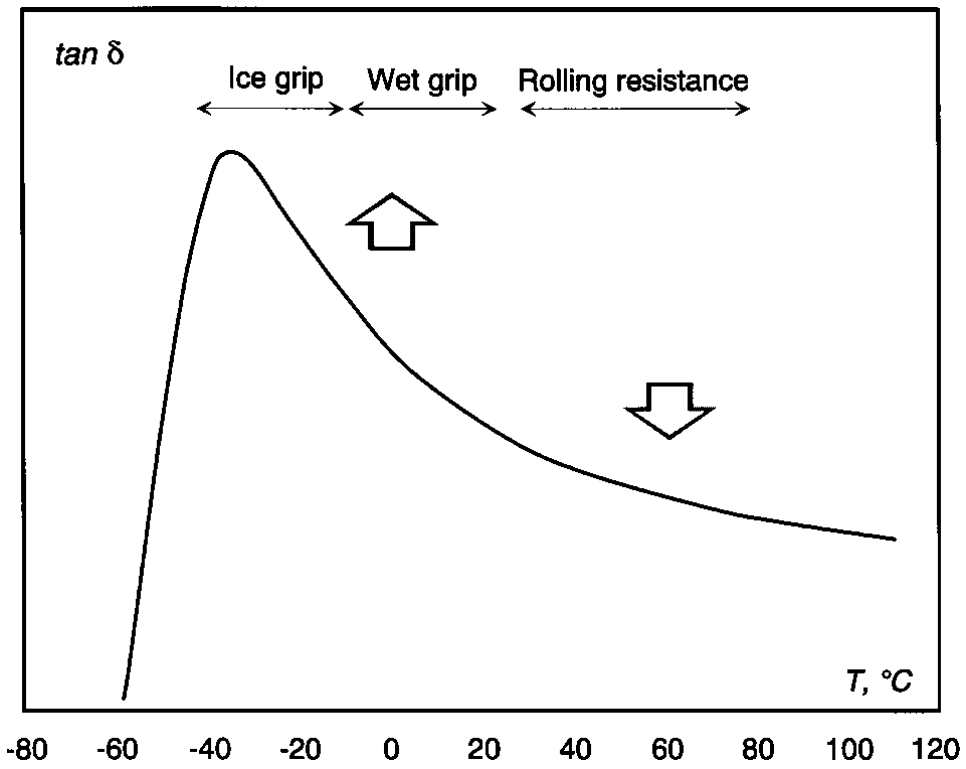

Figure 2.37: Schematic of the temperature dependence of the loss tangent for a typical filled vulcanisate. The temperature regions corresponding to ice and wet grip and rolling resistance are indicated. The large arrows indicate improved tyre performance (From Wang [47])

2.8. Phenomenology of Filler Reinforcement

This section of the review chapter focuses on the characteristic phenomenology associated with particle reinforcement of rubber. The discussion of underlying microstructural mechanisms is left to later sections.

As has been commented upon by a number of researchers, the term 'reinforcement' actually encompasses a broad range of modifications to the various physical properties of elastomers imparted by the incorporation of filler materials. For example, Dannenberg [50] noted that *'Increased reinforcement has been defined as increased stiffness, modulus, rupture energy, tear strength, tensile strength, cracking resistance, fatigue resistance and abrasion resistance*'.

So it appears that the definition of the term 'reinforcement' depends on one's point of view. For example, early research into rubber materials tended to focus on the quasi-static, finite strain mechanical properties of the material, simply because this data was readily accessible using the experimental equipment available at the time. As such many of the earlier investigations into filler reinforcement attempted to explain reinforcement in terms of finite strain, quasi-static mechanisms - typically at room temperature [16, 80-82].

More recently, advances in experimental equipment - specifically the development of the dynamic mechanical analyser [83, 84] - has allowed researchers to probe reinforcement effects across a wide range of temperatures and frequencies - from the glass to the rubber region. This had led to the development of a general understanding of the phenomenology of 'reinforcement' across a spectrum of temperatures, timescales and strains (especially in the linear region) which is a prerequisite to the development of microstructural theories of reinforcement. These phenomenological features are reviewed here.

2.8.1. Quasi-static reinforcement: elastic stiffening, strength and stress softening

Figure 2.38 demonstrates the stiffening and the greatly increased tensile strength imparted by the incorporation of carbon black filler particles into NR. One particularly interesting aspect of quasi-static stress-strain properties of reinforced elastomers is that the onset of the stiffening inflexion (associated with SIC and/or finite network extensibility) occurs at lower strains than in the corresponding unfilled materials due to the strain amplification effect [85].

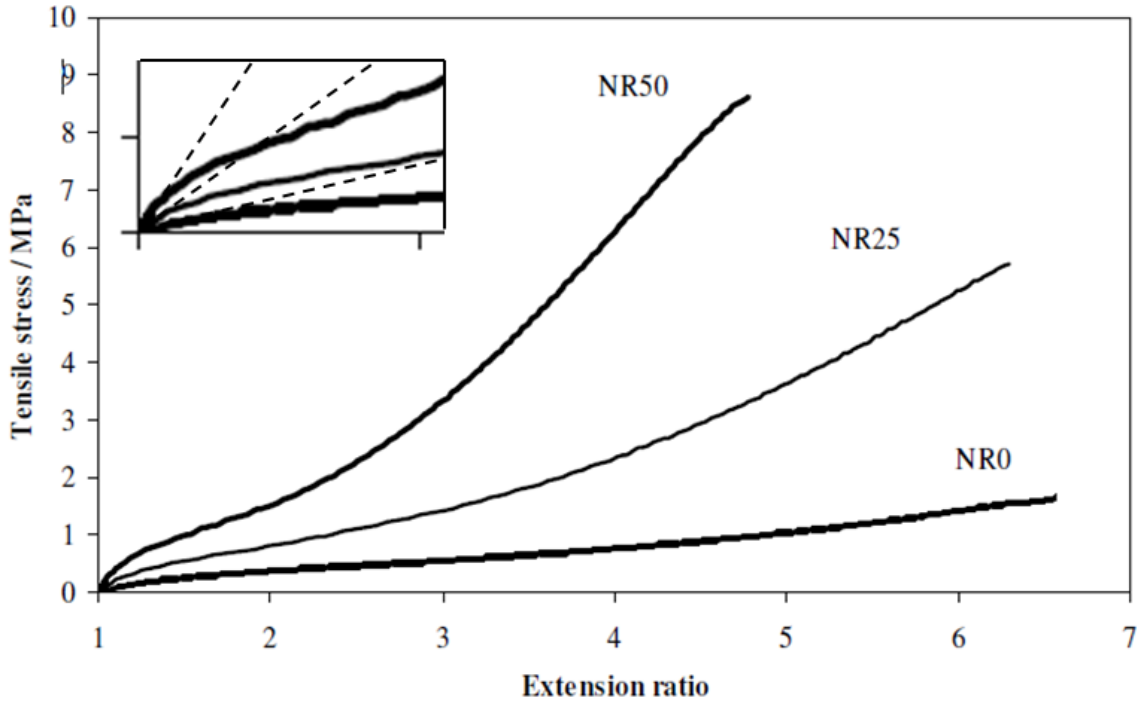

Figure 2.38: Contrasting tensile properties for unfilled NR and NR loaded with 25 and 50 phr of N330 carbon black. Inset: expanded view of the lower strain properties between λ = 1 and 2. Dashed lines are guides to show the increase in low strain modulus with increasing filler loading (Adapted from Suphadon [86]).

As can be seen in the inset of Figure 2.38, the low strain modulus is observed to increase with increasing filler concentration. This phenomenon is shown again in Figure 2.39 which plots the low strain shear modulus of various filled compounds normalised to that of the unfilled control compound against the volume fraction of carbon black filler. As can be seen the type of carbon black filler (surface area, structure) can have a dramatic effect on the scale of small strain stiffening. By examining small strain, linear properties in this way it is possible to evaluate these stiffening effects in terms of hydrodynamics (see the following section).

The large strain properties of filled rubbers (tensile strength and elongation at break) are found to pass through a maximum as a function of filler loading (Figure 2.40).

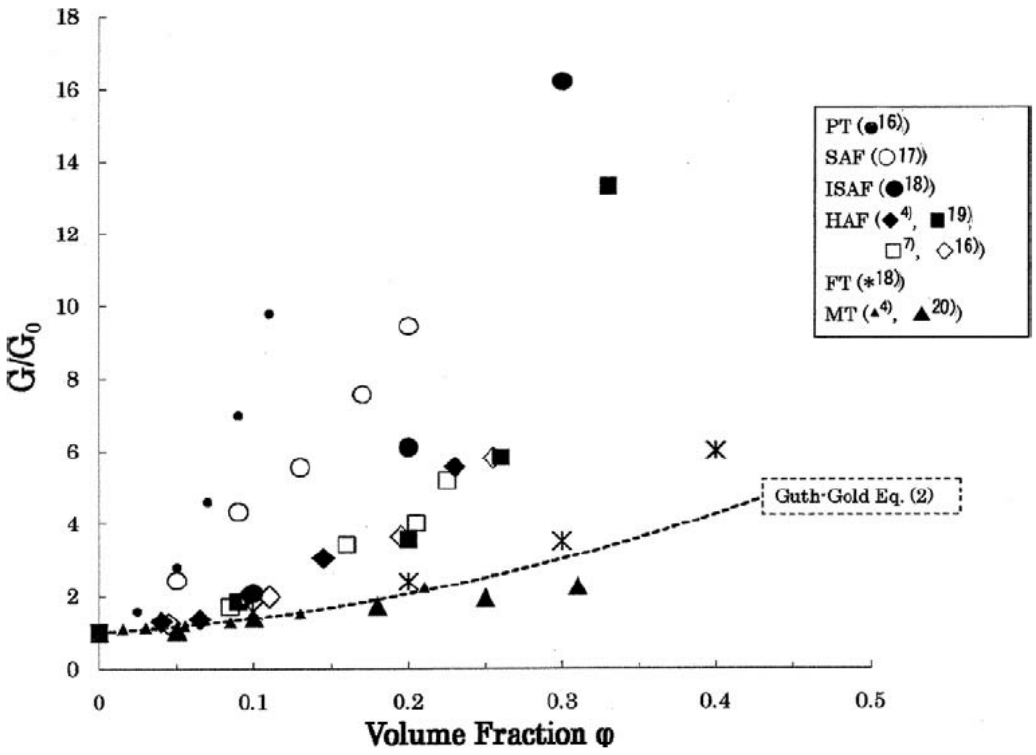

Figure 2.39: Small strain shear moduli of various carbon black-filled compounds plotted versus the volume fraction of filler. Trends for a range of different carbon black grades and the Guth-Gold theoretical relationship are shown. The data reference system used in the legend corresponds to that found in the source paper rather than this thesis (From Fukahori et al. [87])

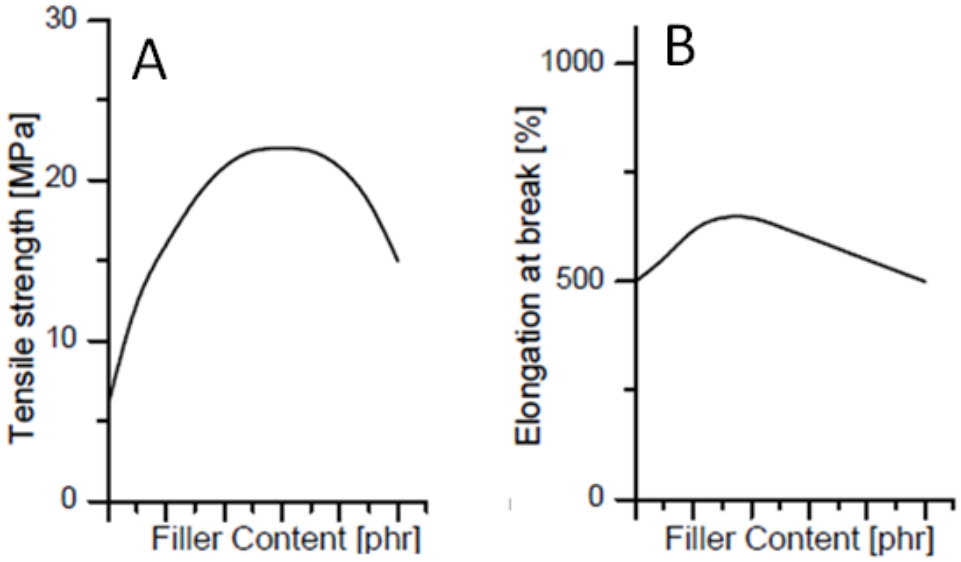

Figure 2.40: Schematic of the general trends found for the dependence of tensile strength (A) and elongation at break (B) on the loading of filler (in units of phr). (From Ten Brinke [88])

Strain softening and hysteresis effects which are apparent upon successively increasing extensions and retraction of highly filled elastomer samples were extensively studied by Mullins [16] after whom the effect is now named. The 'Mullins effect' is shown in Figure 2.41 with the strain being increased after each successive cycle. It is noteworthy that after each straining cycle, when the sample is loaded to strains above the maximum strain of the previous cycle, the mechanical behaviour of the initial equilibrium stress-strain curve is recovered; that is the first time that the material is exposed to a given level of strain it behaves as it would upon initial extension - irrespective of the strain history. This had led to a number of researchers considering the Mullins effect as a strain-dependent transformation of harder regions within the sample into soft regions [24, 40, 89]. This is clearly connected to reorganisations on the microstructural level which are addressed in the following sections. The Mullins effect also demonstrates the dramatic increase in quasi-static hysteresis as a function of applied strain for filled elastomers. For the case of unfilled elastomers at temperatures above their T_g, hysteresis is generally much lower and at the highest strains is associated with chain and crosslink rupture and SIC.

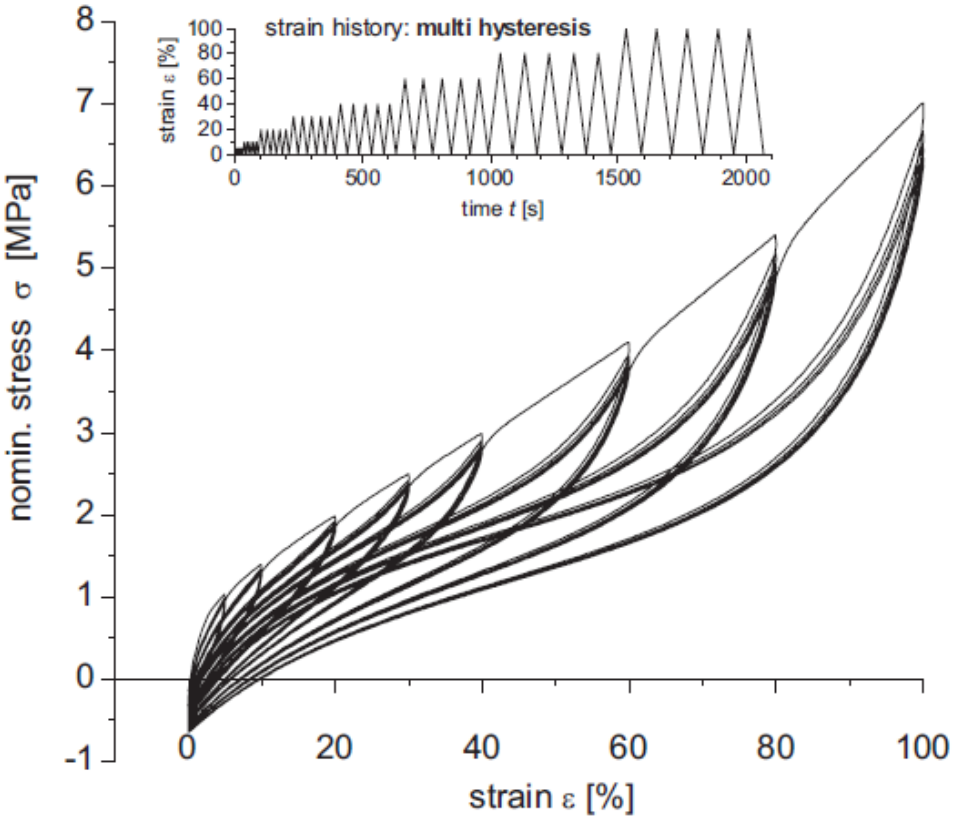

Figure 2.41: The Mullins stress softening effect observed in carbon black reinforced EPDM under cyclic tensile deformations (from Lorenz et al. [90])

2.8.2. Dynamic reinforcement: linear and non-linear viscoelasticity

If the effects of reinforcement are considered under linear viscoelastic conditions (typically less than 0.1 % strain), then three key phenomena are apparent:

Firstly, if the small strain, temperature domain elasticity of filled and unfilled rubbers is considered, then within the rubbery region, a marked change in the temperature dependent elastic response is seen upon systematic loading of rubber with filler. In the unfilled state or at low filler loadings, the elastic response is an increasing function of temperature as defined by the principle of entropic elasticity - see Equation 2.1. For highly filled rubbers this trend is reversed and entropic elasticity is lost or masked.

Secondly, in the transition region, an apparent broadening of the main T_g relaxation is observed for highly filled rubbers when compared with their unfilled counterparts (Figure 2.42). As highlighted by Robertson et al. [91], this filler-induced magnification of the storage modulus in the transition region is not reflected in the temperature dependence of the loss modulus and therefore results in changes to the shape and magnitude of the peak in tanδ which do not reflect the dynamics of the polymer phase (Figure 2.43).

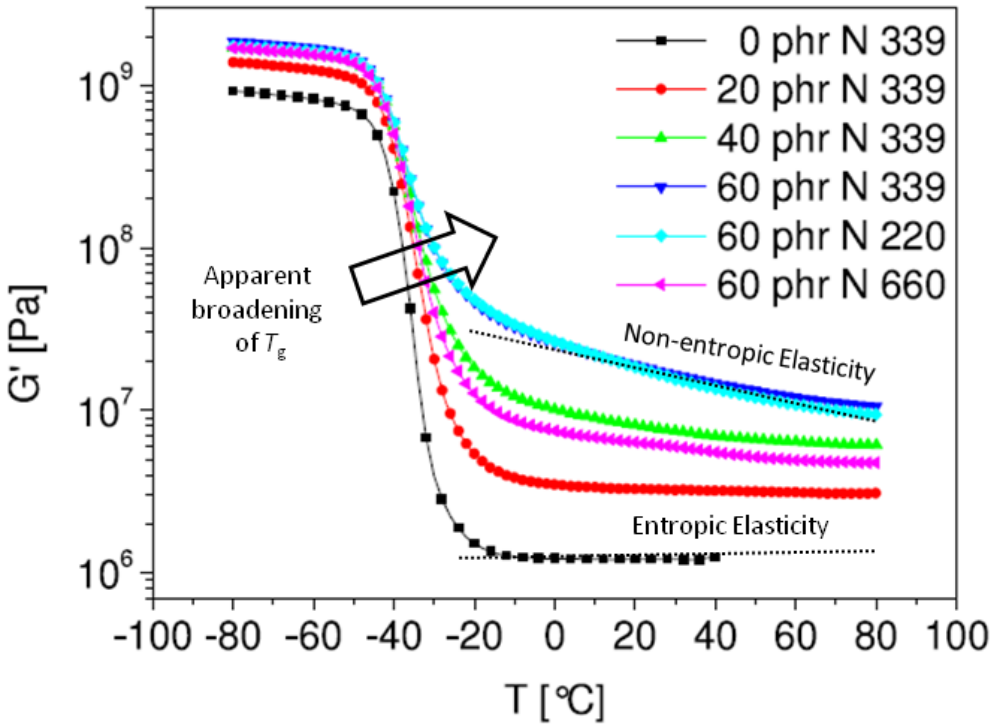

Figure 2.42: Temperature-domain, small strain linear elasticity of S-SBR and S-SBR filled with various types of carbon black at different loading levels. An apparent broadening of the T_g is observed in the transition region and a systematic change in the temperature dependence of the storage modulus is observed in the rubbery region upon increasing the loading and surface area of the carbon black (Adapted from Fritzsche and Klüppel [92])

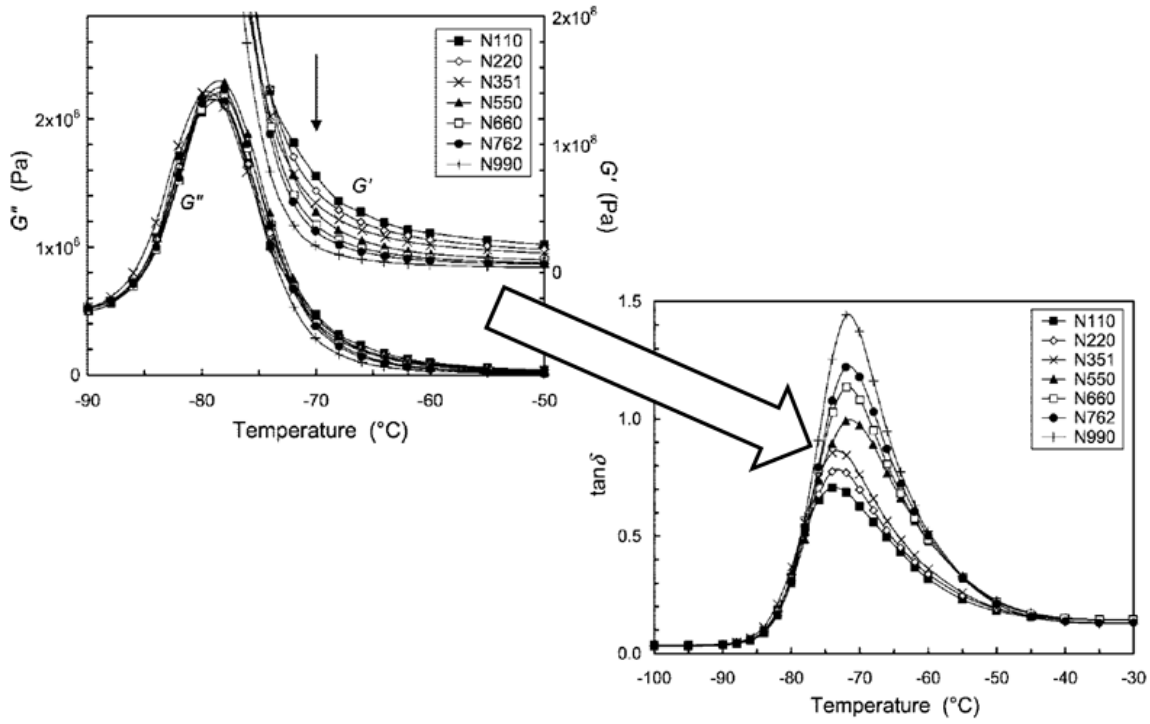

Figure 2.43: Viscoelastic data for carbon black filled compounds in the transition region. The filler induced amplification of the storage modulus is not accompanied by a similar change in the loss modulus. This results in changes to the tanδ peak - which can no longer solely be considered as reflecting the glass transition in such systems (Adapted from Robertson et al. [91])

These effects can be viewed from a different perspective by considering the reinforcement - or amplification - of the small strain storage modulus - which is found to be highly temperature dependent. Berriot et al. [28] defined the 'reinforcement' at small strains as $R(T,\omega) = G'_{Filled}/G'_{Unfilled}$. Figure 2.44 shows dynamic data for silica-filled polyethylacrylate (PEA) rubber and details this reinforcement plotted as a function of temperature as an inset. A peak in stiffness is apparent immediately following the T_g which then decays as a function of temperature. This peak in reinforcement depends upon a number of factors such as the filler particle size, surface area and degree of filler loading [91]. This temperature dependence of the reinforcement also reflects the loss of entropic elasticity in the rubbery region seen in highly filled rubbers.

Finally, for highly filled elastomers the Time-Temperature Superposition (TTS) principle usually fails to collapse temperature domain data onto a single viscoelastic mastercurve. Typically data for filled samples requires vertical as well as horizontal shifting and, even when this is performed, the resulting mastercurves can show 'feathering' between individual data sets where agreement is incomplete. An example of such a mastercurve is given in Figure 2.45

taken from Klüppel [93]. Here a mastercurve is presented for unfilled, crosslinked SBR and also for silica-filled SBR. TTS is successful for the unfilled compound but when filler is introduced, although the mastercurve is reasonably well constructed in the transition region it is less precise towards the lower frequency end of the spectrum. The fact that the linear viscoelastic behaviour of filled samples cannot be entirely accounted for in terms of elastomer dynamics is a key indicator that additional temperature and/or frequency-dependent processes must be contributing to bulk viscoelasticity.

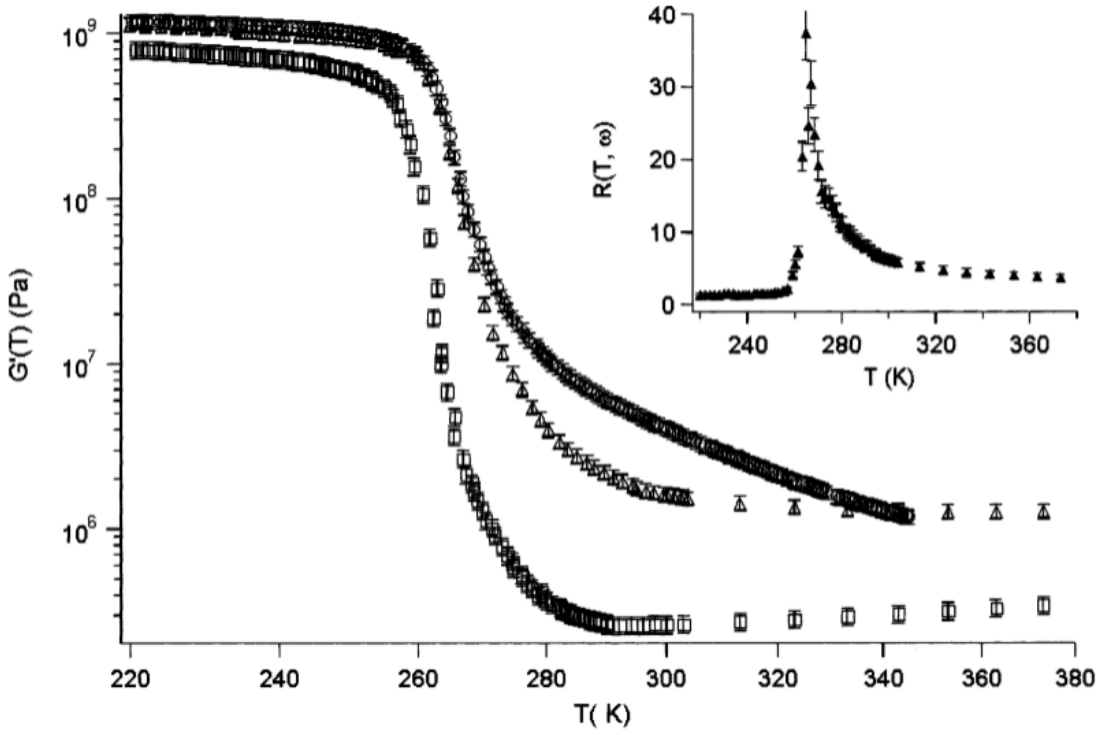

Figure 2.44: Dynamic elastic moduli and (inset) reinforcement as a function of temperature for silica-filled and unfilled PEA. Volume Fraction, ϕ, Key: □ = 0.00, △ = 0.16, ○ = 0.18 (From Berriot et al. [28])

If the dynamic strain is systematically increased then the limit of linear viscoelasticity is found typically at around 0.1 % strain. Beyond this limit significant non-linearities in the strain response of the viscoelastic moduli become apparent. Fletcher and Gent [83, 94] published some of the first detailed reports on this topic but it was the extensive work of Payne in the 1960's [84, 95-102] which started to connect the observed non-linearities to microstructural mechanics. Subsequently such effects are colloquially called the 'Payne Effect' but in fact are apparent for a range of other complex fluid systems such as filled greases and oils, clay suspensions, suspensions of carbon blacks and silicas in paraffin oils and colloidal dispersions in general [100, 103].

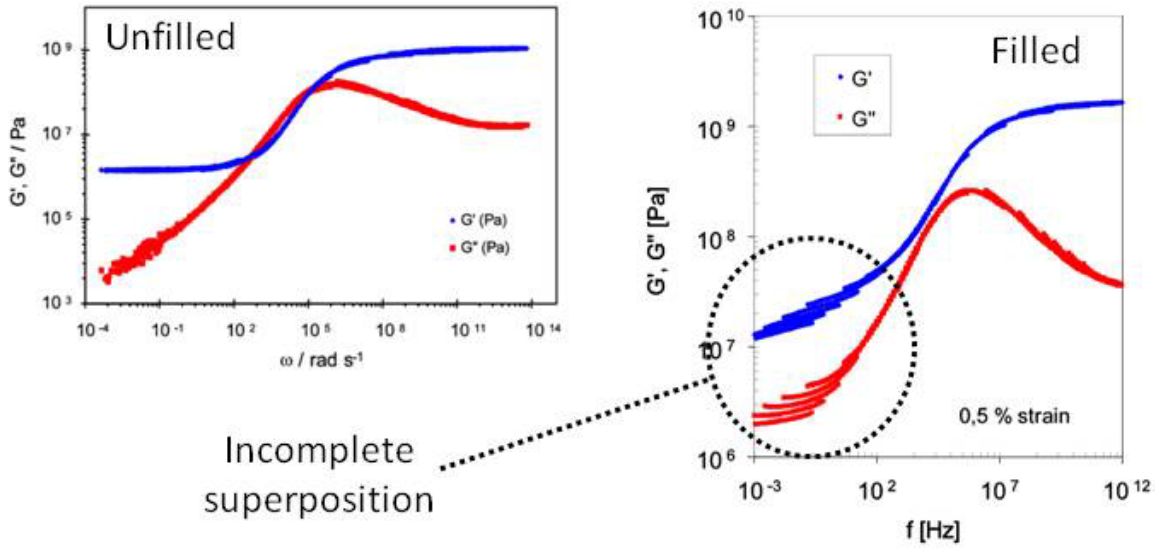

Figure 2.45: Small strain TTS performed on unfilled (left) and filled (right) S-SBR. Incomplete superpositioning of the isothermal data in the case of the filled material is indicative of additional time-temperature dependent processes present within the composite (Adapted from Klüppel [93])

The Payne Effect is illustrated in Figure 2.46 which reproduces some of Payne's original measurements of the dynamic storage moduli as a function of strain for carbon black-filled butyl rubber. Here, above the limit of linear viscoelasticity the storage modulus decays as a sigmoidal function of the logarithm of strain while a corresponding peak in the loss modulus (and therefore tanδ) appears over roughly the same strain range. The Payne Effect magnitude ($\Delta G'$) depends on the type and loading of filler and decreases with increasing temperature (Figure 2.47).

A further interesting feature of the Payne Effect is the so-called Payne effect harmonic paradox [104, 105]. In the non-linear regime it would be usual in most complex fluid systems to see the non-linear nature of the material manifest as higher harmonics in the dynamic response to applied sinusoidal deformations or loads (that is, a distinctly non-sinusoidal response). Instead for filled rubbers the response contains little contribution from higher order harmonics. So the Payne Effect is actually a description of different linear material responses at different strains .

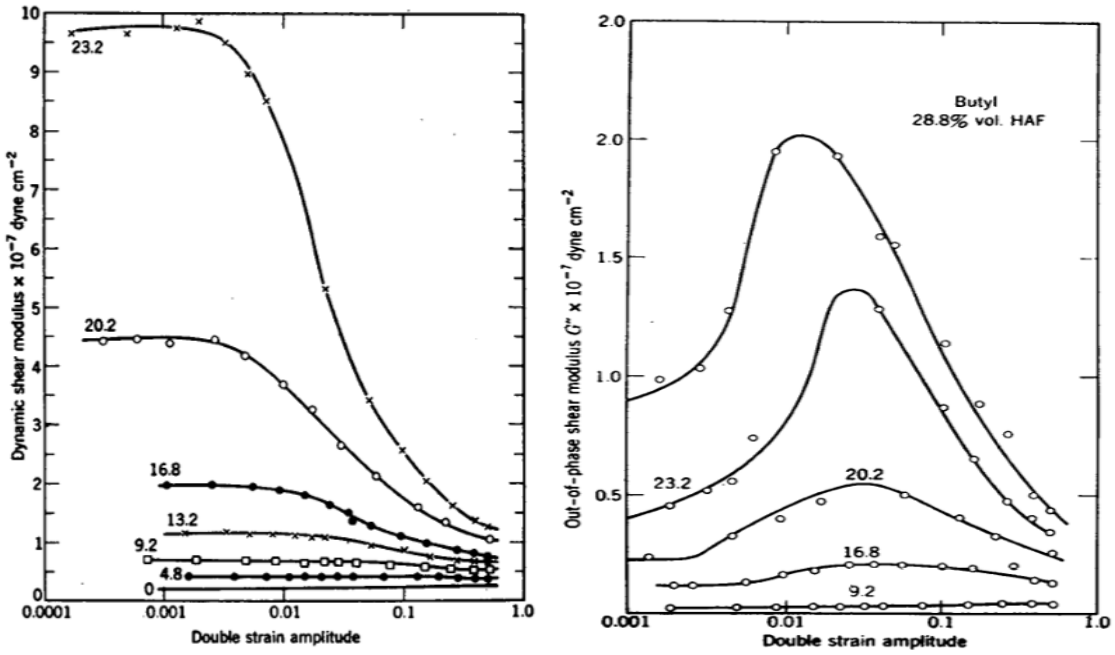

Figure 2.46: Payne's original data detailing the strain dependence of the dynamic elastic and viscous moduli for butyl rubber filled with various volume percentages of HAF carbon black (From Payne [84])

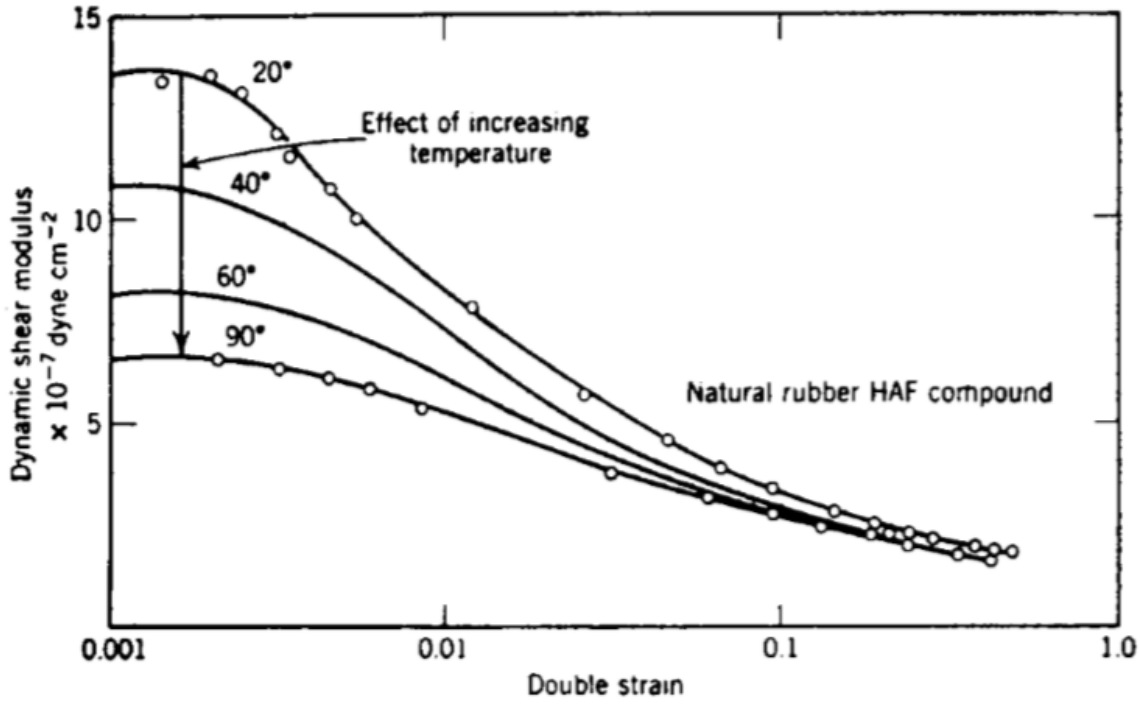

Figure 2.47: The temperature dependence of the magnitude of the Payne effect (From Payne and Whittaker [102])

2.8.3. The 'bound rubber' phenomenon

Bound rubber is a well known phenomenon associated with the reinforcement of rubber. Specifically it is defined as the amount of polymer which cannot be extracted by a suitable solvent from a filler/rubber mixture prior to the addition of curatives and subsequent crosslinking. When an uncrosslinked mix of rubber and filler is submerged in excess solvent the polymer phase slowly dissolves into the solvent. However when equilibrium is reached, a gel-like substance is recovered containing carbon black and undissolved polymer (sometimes bound rubber is referred to as carbon gel). The amount of undissolved polymer (bound rubber) is dependent on the initial filler loading, the filler surface area and filler surface activity and can therefore be seen as indicative of the reinforcing potential of the filler.

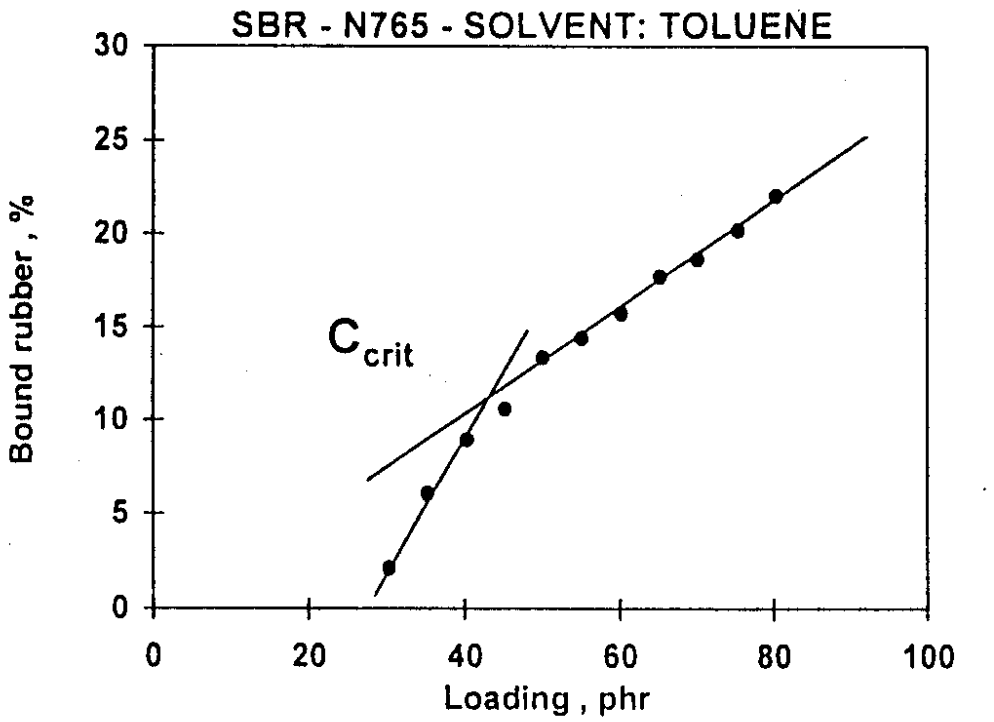

Figure 2.48: Plot of bound rubber versus the loading of carbon black for the indicated polymer-filler-solvent combination. C_{crit} refers to the loading of carbon black at which a consistent gel is formed (From Wolff [5])

Figure 2.48 plots the extracted bound rubber values for the polymer-filler-solvent combination indicated versus the mass loading of the filler. The change in gradient apparent in the trend corresponds to the filler loading required for the formation of a carbon gel C_{crit}. Figure 2.49 plots the C_{crit} values for a range of different carbon blacks when combined with SBR rubber.

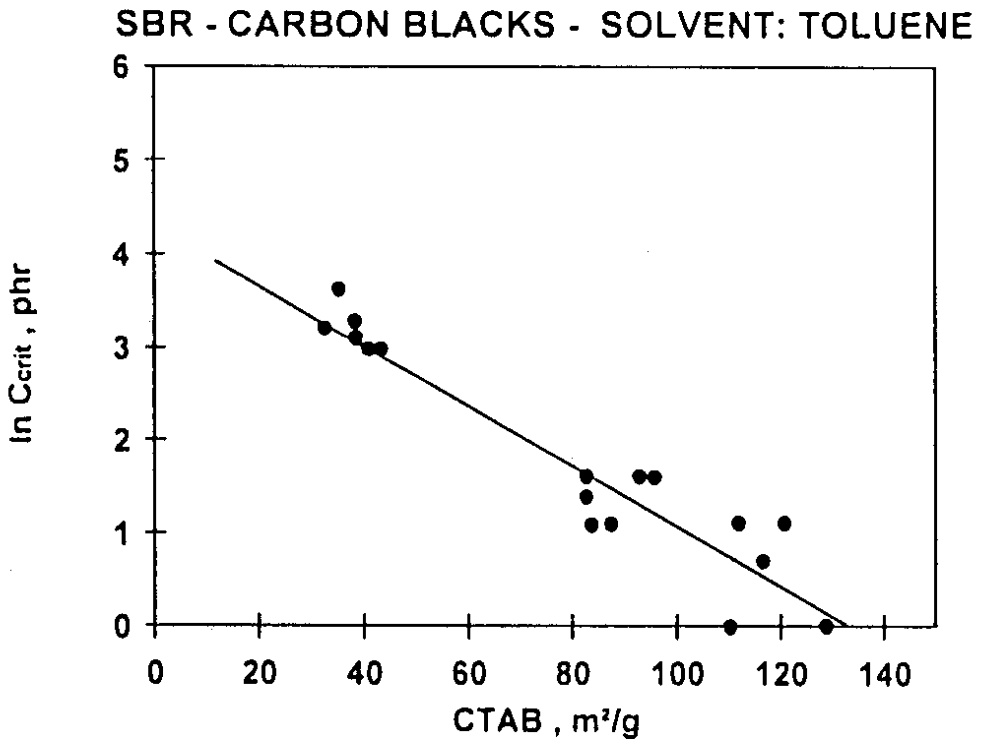

Figure 2.49: Plot of ln(C_{crit}) versus the cetyltrimethylammonium bromide-specific surface area of various carbon black fillers. Higher surface area fillers show an earlier onset of gel formation in terms of filler loading (From Wolff [5])

In addition to these filler-specific parameters (surface area, activity and loading), bound rubber is also sensitive to a range of other factors such as extraction temperature, extraction solvent, compounding temperature, filler dispersion state and storage time prior to extraction which makes it a useful tool for probing various aspects of filler reinforcement.

The molecular origins of the bound rubber phenomenon have long been debated, with suggestions that it is formed via adsorbed polymer chains bridging between filler particles. Meissner [106] has developed a statistical treatment of the phenomenon while Leblanc has focussed on the specific interactions required at carbon black surfaces required to produce bound rubber [107-109]. Leblanc attributes the trapping of polymer segments at the filler surface to topological constraints imposed of the chains by the 'rough' surface of the carbon black composed of terraces of graphitic planes. An illustration of his concept is given in Figure 2.50.

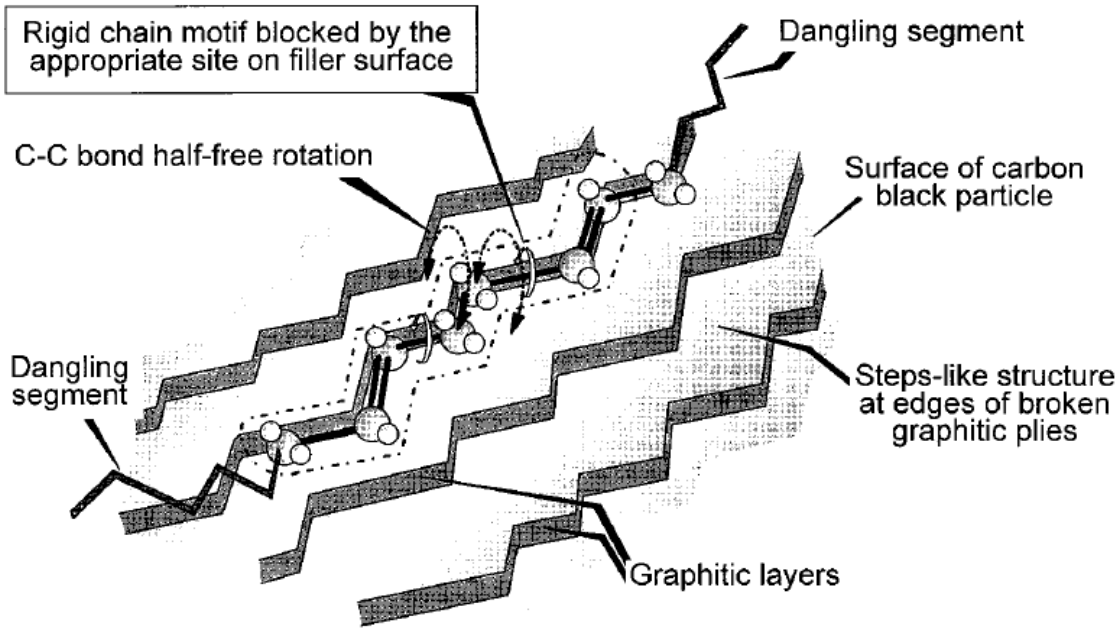

Figure 2.50: Schematic proposed by Leblanc of the topological restriction imposed on polymer chains by direct contact with the microstructurally 'rough' surface of carbon black (From Leblanc [108])

2.9. Mechanisms of Filler Reinforcement

2.9.1. Hydrodynamics

Einstein [110] derived the analytical hydrodynamic solution for the problem of viscosity increases in Newtonian fluids when rigid particles are incorporated at infinite dilution. A number of assumptions are implicit in this derivation:

- The rigid inclusions are very stiff compared with the viscous matrix
- The boundary condition between inclusion and matrix is non slip
- The inclusion concentration is small enough to assume that a single particle in isolation represents the bulk behaviour
- The inclusion morphology is spherical
- The viscous matrix is a Newtonian liquid

The resulting Einstein viscosity equation (Equation 2.50) describes the increase in viscosity in sparingly filled Newtonian fluids as a function of the volume fraction of filler where η is the viscosity of the filled fluid, η_0 is the viscosity of the unfilled fluid and φ is the volume fraction of filler material.

$$\frac{\eta}{\eta_0} = 1 + 2.5\varphi \quad 2.50$$

The equivalence between the viscous problem addressed by Einstein and the elastic problem considered for reinforced elastomers was exploited by Smallwood [111] who derived an identical solution to the Einstein viscosity equation for elastic bodies (Equation 2.51) where E and G are the tensile and shear moduli respectively. Smallwood found good experimental agreement with his theory between the increase in small strain modulus of reinforced elastomers under limited conditions (low volume loadings and larger filler particle sizes with spherical morphologies). The Einstein-Smallwood hydrodynamic equation rapidly breaks down when considering higher volume loadings, highly structured fillers and finite strains [87, 111, 112].

$$\frac{\eta}{\eta_0} = \frac{E}{E_0} = \frac{G}{G_0} = 1 + 2.5\varphi \quad 2.51$$

Guth and Gold [113, 114] introduced a higher power, φ^2 term expansion of the hydrodynamic relation to account for closer, though still idealised, particle packing and interactions of particle stress fields. They proposed a coefficient for the φ^2 term of 14.1 obtained through a fitting process. More rigorous, analytical derivations by Batchelor and Green [115] and later Chen and Acrivos [116, 117] gave coefficients of 5.1 and 5.0 respectively. Equation 2.52 gives the φ^2 expansion using the coefficients derived by Chen and Acrivos.

$$\frac{\eta}{\eta_0} = \frac{E}{E_0} = \frac{G}{G_0} = 1 + 2.5\varphi + 5.0\varphi^2 \quad 2.52$$

Guth [113] proposed a modified hydrodynamic equation to account for anisotropic filler stiffening by incorporating a shape factor, f_S, into the relation.

$$\frac{\eta}{\eta_0} = \frac{E}{E_0} = \frac{G}{G_0} = 1 + 0.67 f_S \varphi + 1.62 f_S^2 \varphi^2 \quad 2.53$$

Such analytical equations predict for the stiffening of a soft elastic material by rigid filler inclusions of varying morphologies and low volume loadings at small strains. In fact these hydrodynamic equations are found to significantly underestimate the stiffening imparted for all but the largest, simplest morphology filler particles at low volume concentrations. The limitations of the analytical hydrodynamic approach have been pointed out by a number of authors:

- Filler particles are very rarely spherical in morphology [118]
- Industrially relevant volume fractions are often much higher than the values for which these equations were derived
- The packing of filler particles is best described by fractal packing concepts rather than the simplified spherical packing geometries inherent in the hydrodynamic derivations [119]
- The boundary condition between filler and elastomer phases is open to debate [29]
- Elastomer trapped between tightly packed filler aggregates is shielded from strain under low strain conditions and behaves as a rigid body, thereby increasing the effective volume loading of the rigid phase [120, 121]
- Hydrodynamics assumes that the stored energy density upon deformation is isolated in the elastomer phase. At higher volume loadings of the more structured filler particles, it has been proposed that some of the deformation energy is stored in the resulting percolated filler structure [92, 122]

Although it is theoretically possible to analytically account for some of these effects by expanding the hydrodynamic series to higher power terms, the complexity of the derivation required means that this is not feasible. Some researchers have used finite element techniques to test the applicability of hydrodynamics concepts at higher volume loadings with non-spherical particles and random placements within the matrix. These efforts are covered in more detail in the following section. Recently Huber and Vilgis [123] have extended the Einstein-Smallwood equation to take into account the fractal geometry of structured carbon black filler particles and have also considered different boundary conditions for the case of spherical particles.

One important outcome of the hydrodynamic approach is that there is no temperature dependence to the stiffening effect. Therefore the observation by Berriot et al. [28] of highly temperature dependent reinforcement at small strains indicates that other temperature-dependent reinforcement mechanisms must be present (see Figure 2.44)

2.9.2. Strain amplification and elastomer occlusion

Mullins and Tobin [81] proposed the concept of strain amplification whereby the random placement of rigid filler particles within an elastomer matrix gives rise to non-affine deformations on the mesoscale upon deformation which can be greater (or less) than that of the globally applied strain. Mullins and Tobin introduced a strain amplification factor, X, to quantify the average increase in mesoscale strain resulting from the introduction of filler. They found that X corresponds to the Guth-Gold relationship for the case of rubber filled with N990 (spherical) carbon black up to a volume fraction of 0.20.

More recently, finite element simulations of the mesoscale deformation of elastomers filled with randomly placed particles (Bergström and Boyce [124], Jha et al. [125], Busfield et al. [126], Gusev and Rozman [118]) have demonstrated the overstraining of certain regions of elastomer upon small macroscopic deformations (Figure 2.51). Furthermore, finite element analyses of three dimensional representations of real filler dispersions (determined experimentally using a microtomography technique) embedded in an hyperelastic continuum [127] performed by Akutagawa et al. have demonstrated the significant presence of regions of strain amplification (Figure 2.52 & Figure 2.53).

The same mechanism which underpins strain amplification is also responsible for a shielding or occlusion of rubber from the globally applied strain. Medalia [120, 121] proposed that rubber could be occluded from the global strain by becoming trapped between tightly packed filler aggregates or within the fractal aggregate structure itself (Figure 2.54). At small strain this results in an increase in the total effective volume of rigid phase, φ^*, thereby amplifying the hydrodynamic stiffening effect. Medalia proposed that the occluded volume could be estimated from the type of carbon black structure and void volume measurements [120]. Again the later simulations of Bergström and Boyce and of Akutagawa et al. demonstrated the contribution to rigid volume reinforcement made by occluded elastomer (Figure 2.52 & Figure 2.53).

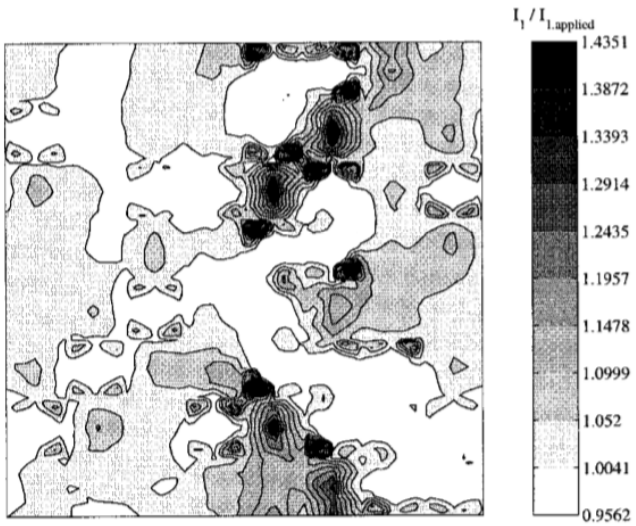

Figure 2.51: Stochastic 2-D FEM simulation of rigid particles embedded in an hyperelastic continuum. The local strain map (left) reveals regions of strain amplification ($I_I/I_{I\ Applied} > 1$) and matrix occlusion ($I_I/I_{I\ Applied} < 1$). The applied strain is -0.2 (From Bergström and Boyce [124])

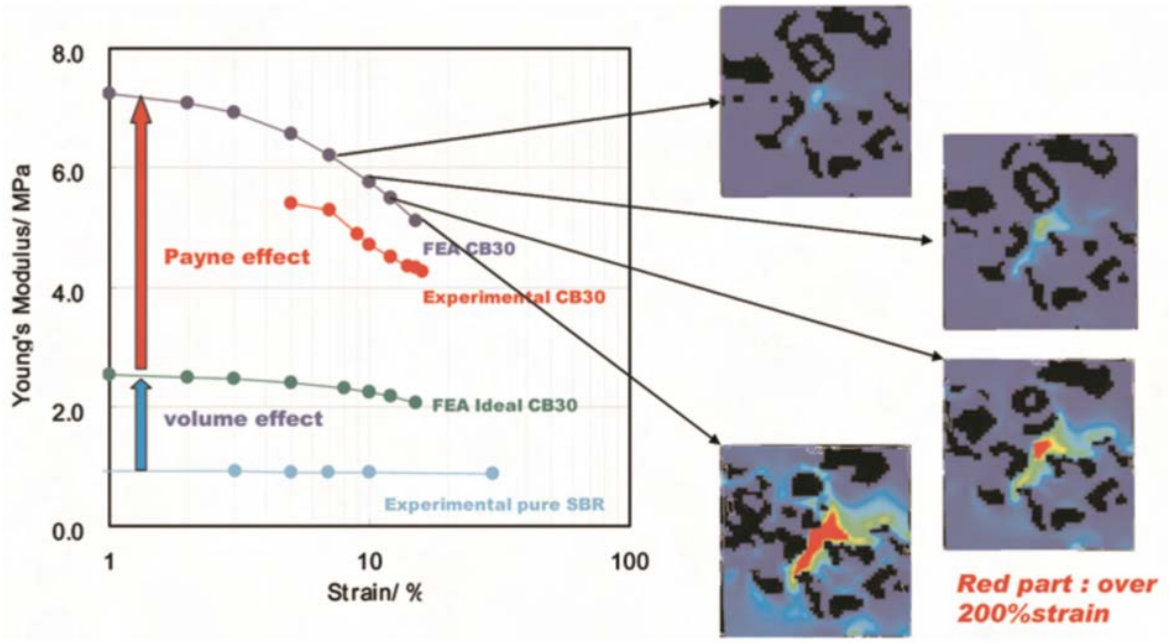

Figure 2.52: Evolution of local strain amplification as a function of strain for FEA simulations of real filler dispersions embedded in an hyperelastic matrix. The pictures show 2D snapshots of strains within the elastomer matrix. Black areas are rigid fillers and red areas correspond to the regions of highest strain (From Akutagawa et al. [127])

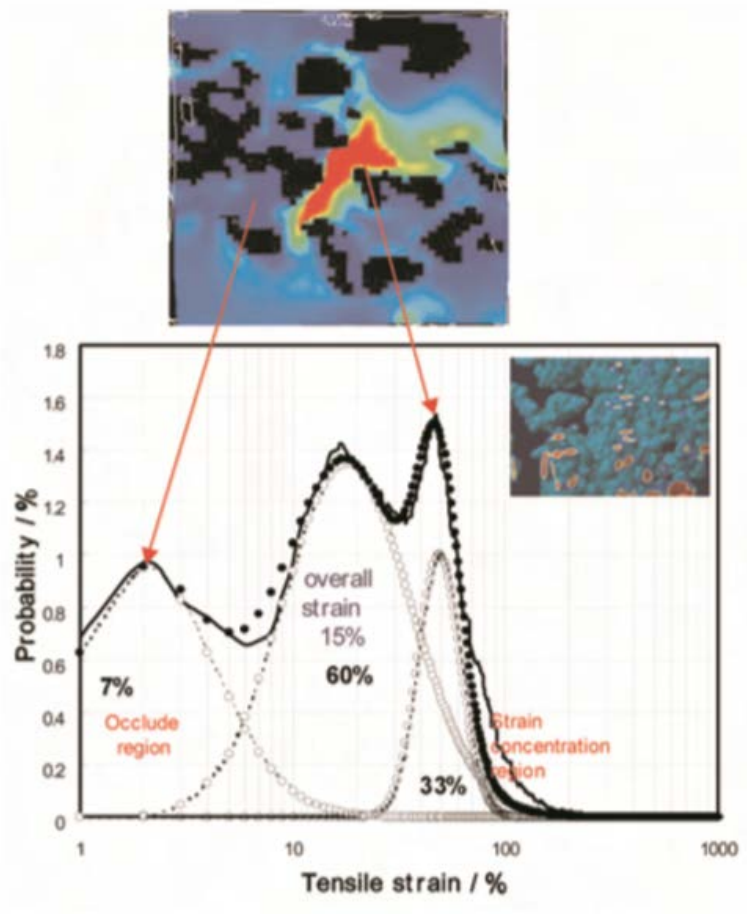

Figure 2.53: Probability distribution of strains within FEA simulation at 15 % globally applied strain. Note: 7 % occlusion of rubber and 33 % strain amplification (From Akutagawa et al. [127])

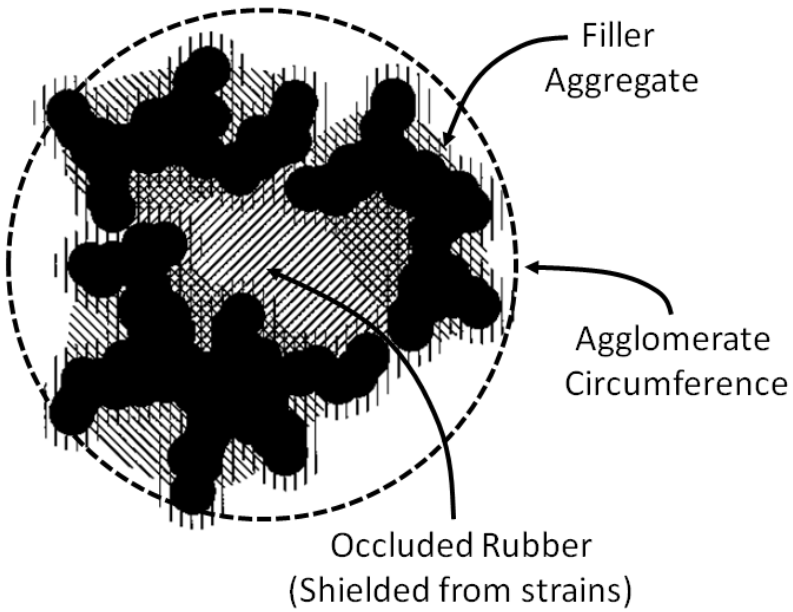

Figure 2.54: Schematic of Medalia's occluded rubber concept (Adapted from Wang [47])

2.9.3. Filler Networking

2.9.3.1.Filler networks in crosslinked rubber

The concept of filler networking and network breakdown has been used to explain several features of elastomer reinforcement and has been extensively investigated due to its inherent link with bulk material hysteresis. The first part of this section considers the filler network as it is found in the crosslinked material and product. Secondly, mechanisms of network formation in the melt are considered before several attempts to model filler networks and network breakdown are reviewed.

Fletcher and Gent [83, 94] published one of the first reports detailing the non-linear decay of dynamic storage modulus with increasing strain. They proposed that a successive breakdown of connected filler aggregates throughout the rubber phase was responsible for the observed strain softening. Payne explored this concept in greater detail in a series of seminal papers [84, 95-102]. He determined the dependence of the magnitude of the Payne effect on the filler volume loading, the filler type (surface area, morphology) and the state of dispersion of the filler phase throughout the rubber network. Payne also demonstrated that increasing surface area of carbon black at a constant volume fraction generally results in a larger small strain modulus and greater magnitude of the Payne effect (Figure 2.55).

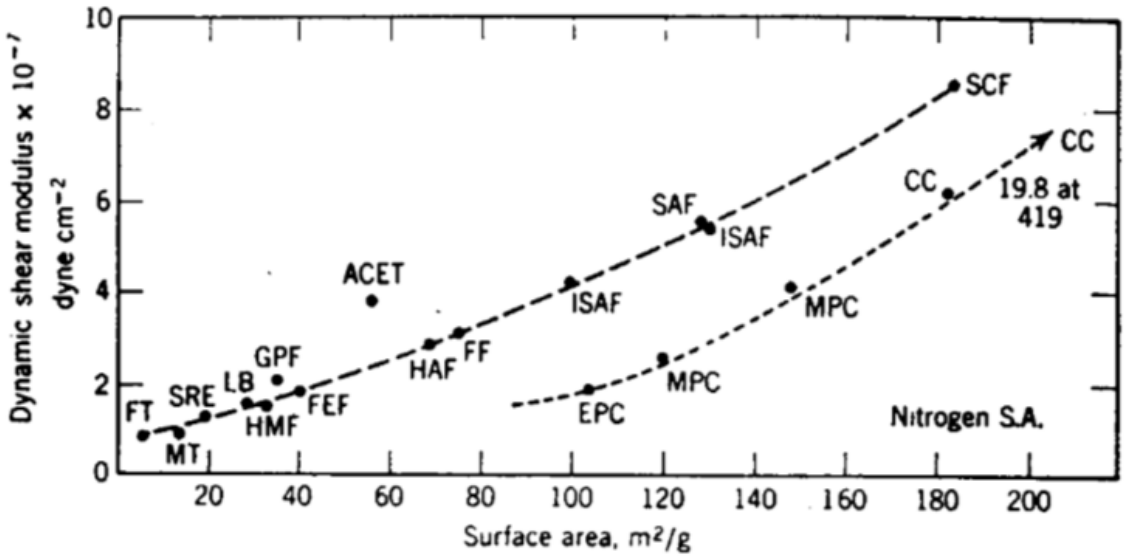

Figure 2.55: Dependence of the small strain dynamic elastic modulus of butyl rubber filled carbon blacks of varying nitrogen-specific surface area (From Payne and Whittaker [102])

In particular, Payne and co-workers demonstrated that the method of compounding and surface activity of carbon black can greatly affect the magnitude of the Payne effect [95, 99, 102]. Figure 2.56 details the Payne effect measured for butyl rubber filled with a series of HAF carbon blacks at fixed volume loading. Hot milling of the carbon black is seen to dramatically reduce the small strain modulus and the magnitude of the Payne effect due to an improvement in filler dispersion. Attrition (ball milling) of carbon black leads to an increase in oxygen content and surface activity of the carbon black which results in a further reduction in small strain modulus and a substantially reduced Payne effect. Similar effects were also observed when increasing the mixing time of carbon black into rubber thereby improving the dispersion state of the filler (Figure 2.56).

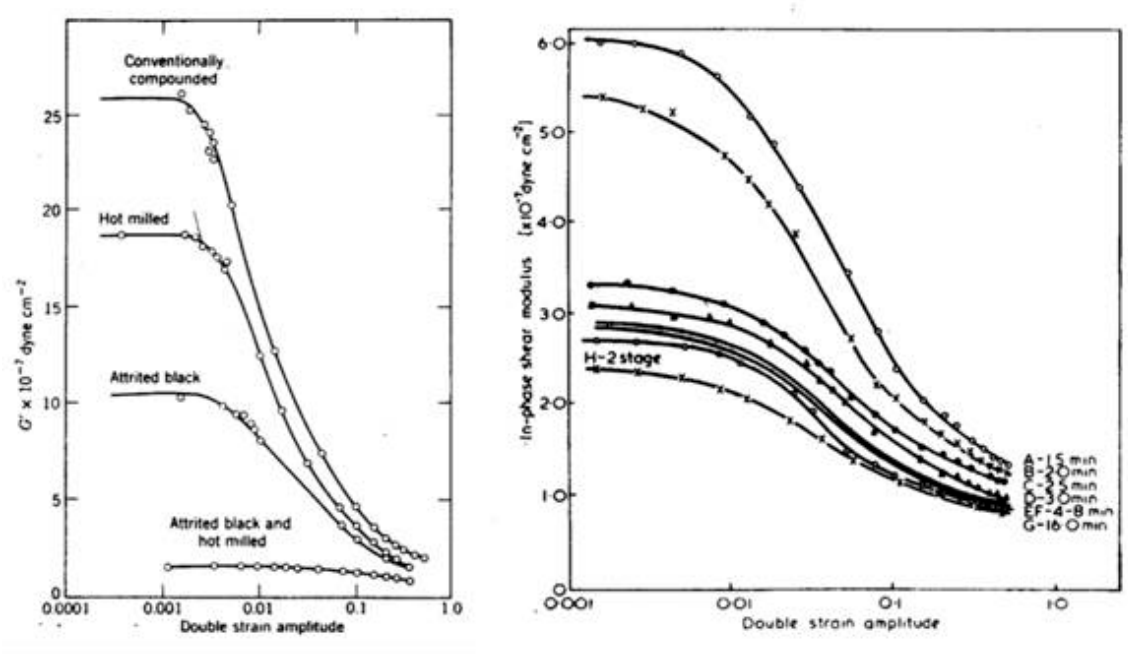

Figure 2.56: Left) the influence of processing and carbon black surface activity on the magnitude of the Payne effect. Right) the influence of mixing time (dispersion quality) on the Payne effect (From Payne [102])

Payne also examined a series of analogous systems, namely clay-water suspensions and carbon black-paraffin suspensions [100, 102]. His work demonstrated that even in the absence of the polymer phase, the same dynamic non-linearities are observed and that the small strain moduli for such systems are comparable (at least in the same order of magnitude) to equivalently filled elastomers. These findings prompted Payne to conclude that with increasing volume loading, a progressively connected filler network is formed which dictates the linear viscoelastic behaviour of the filler elastomer. The network of particles was proposed to be

connected via van de Waals forces which are overcome at higher strains resulting in filler structure breakdown, strain softening and increased viscous dissipation. Payne proposed a simple model for these effects which was widely accepted and is illustrated in Figure 2.57. Here the Payne effect is split into linear combinations of hydrodynamic, filler-rubber interaction and filler-filler networking interaction terms. As a crude approximation, improving the filler-rubber interaction improves dispersion of filler aggregates and reduces filler networking interactions, leading to reduced small strain moduli and reduced a Payne effect (and vice versa). This qualitative understanding of the filler networking process was subsequently used to describe observed trends in silica-reinforced elastomers. Payne's interpretation of this phenomenon remains widely accepted today, despite the proposal of several different physical mechanisms to account for the observed behaviour.

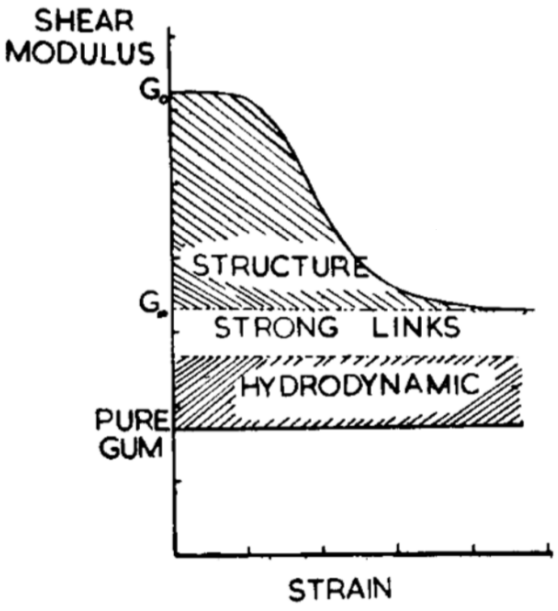

Figure 2.57: Payne's interpretation of small strain dynamic non-linearities in filled elastomers (From Payne [97])

Since Payne's work it has become clear that an 'infinite cluster' or permeating filler network only forms above a certain volume loading, which is unique for specific fillers and filler-rubber combinations. Such 'percolation thresholds' have been determined by both mechanical and electrical methods. For example Figure 2.58 from Meier and Klüppel [128] takes the original data of Payne and plots the small strain modulus versus volume loading of filler. Here a critical volume fraction, termed the 'gel point', is identified and related to the onset of cluster-cluster formation. The indicated power law exponent of 3.5 is predicted as an outcome of the fractal

geometry of the filler network. Alternatively many researchers have determined the electrical percolation threshold for conductive fillers by monitoring the DC conductivity of filled elastomers as a function of volume loading of filler [40]. A sharp rise in conductivity (typically of several order of magnitude) over a limited volume fraction range is related to the formation of conduction paths through the elastomer matrix by aggregate-aggregate contact or electron tunnelling between particles.

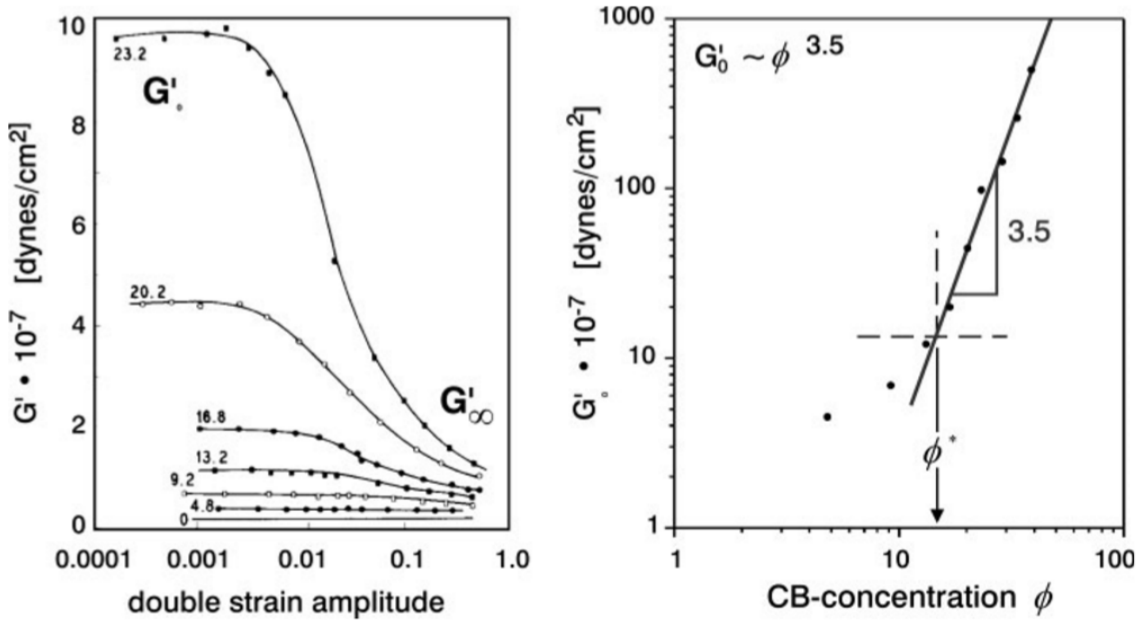

Figure 2.58**:** Re-plotting of Payne's data [84] by Maier and Klüppel [128] to illustrate the effect of filler aggregate percolation on small strain mechanical properties

A number of researchers [40, 92, 128, 129] have taken the concept of a filler network further and have described the elastic stored energy function, $W(\lambda)$, in terms of contributions from the elastomer phase, $\left(1-\varphi_{eff}\right)W_R(\lambda)$, and the filler network, $\varphi_{eff}W_A(\lambda)$,

$$W(\lambda)=\left(1-\varphi_{eff}\right)W_R(\lambda)+\varphi_{eff}W_A(\lambda) \qquad 2.54$$

In this situation, at small strains, the filler network is considered to be relatively flexible so that deformation of the sample results in elastic storage of energy in the 'bonds' between individual filler aggregates. This can be considered in terms of the stored energy density of a single cluster-cluster aggregate (CCA) - a filler network being composed of many such CCAs - as

shown in Figure 2.59. The Kantor-Webman model of elastic networks given as Equation 2.55 directly relates the elastic modulus G_A, of the CCA to the force constant of bonds between aggregates, $\bar{G}$, and the fractal dimension of the aggregate, d_f, where ξ is the cluster size, N_B is the number of aggregates in the cluster

$$G_A \cong \frac{k\bar{G}}{{d_f}^3}\left(\frac{d_f}{\xi}\right)^3 N_B(\xi)^{-1} \qquad 2.55$$

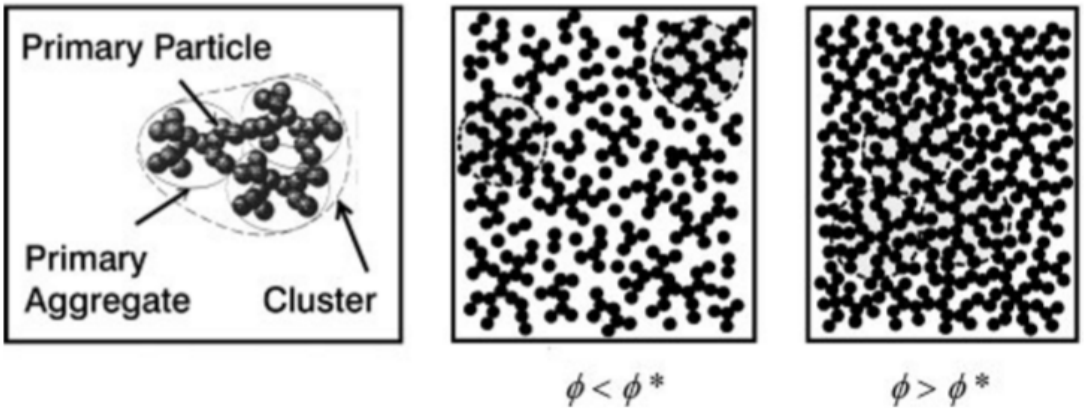

Figure 2.59: Development of cluster-cluster aggregation process below (ϕ < ϕ*) and above (ϕ > ϕ*) the gel or percolation point (ϕ*) (From Meier and Klüppel [122])

2.9.3.2.Filler network formation in the melt

The process of networking of filler particulates in rubber melts is of major industrial significance. What can broadly be termed the filler 'network' or 'structure' that evolves in filled rubber melts during shear and thermal processing is responsible for significant modifications of the melt rheology and processability of filled rubbers, the electrical properties of vulcanisates, the elastic stiffening and the strain-dependent viscoelasticity of filled elastomer products. Broadly, the nature of the filler network in crosslinked rubbers (elastomers) is dependent upon two key processes. Firstly the incorporation of filler into the rubber phase via mechanical mixing aims to break down agglomerated, often pelletised structures of the filler into individual rigid aggregates and then disperse these as effectively as possible throughout the rubber. Secondly, during subsequent thermal processing (vulcanisation), the tendency of the filler particles to flocculate promotes the development of an agglomerated filler network.

Many researchers have considered flocculation of carbon blacks and other particulate fillers in the polymer melt in terms of Brownian motion and particulate mobility via the particle diffusion coefficient given by the Stokes-Einstein equation

$$D = \frac{\mathbf{k}T}{\eta 6\pi r} \qquad 2.56$$

where D is the diffusion coefficient, $\mathbf{k}$ is the Boltzman constant, T is the temperature, η is the viscosity of the matrix and r is the particle radius. The viscosity term, η, can be viewed as the effective viscosity experienced by the particle and can be a function of particle shape, boundary condition at the particle surface and particle concentration [130].

Gerspacher et al. [52] studied flocculation of carbon black in natural rubber (NR) and solution styrene butadiene rubber (S-SBR) using resistivity measurements. They highlighted the dependence of flocculation on factors such as carbon black loading, particle size and particle structure. Mihara et al. [63, 64, 71] examined precipitated silica flocculation processes in S-SBR. They determined an Arrhenius dependence for the kinetics of flocculation and calculated activation energies for the process of about 10 kJ/mol. Wang [47] considered carbon black flocculation in terms of diffusion but also highlighted the influence of the non-spherical nature of carbon black aggregates and inter-aggregate distance on the effective diffusion coefficient. However Schwartz et al. [131] noted that carbon black flocculation may actually constitute several different physical processes. They found no evidence of filler particle mobility (Brownian motion) in the melt from TEM observations and so proposed that a contribution to the flocculation process arises from time-dependent bridging of adjacent filler particles by polymer chains whereby a single chain becomes attached to two filler aggregates in close proximity.

The physical process of filler networking has also been described using percolation theory and diffusion-limited cluster-cluster aggregation (CCA) processes which generate flocculated structures of characteristic fractal dimensions [40, 92, 128]. It was further proposed on the basis of dielectric spectroscopy measurements of carbon black flocculation in various rubber melts that the polymer between filler aggregates plays a key role in determining the mechanical properties of the filler network. Meier and Klüppel [128, 132] proposed that the gap size between aggregates dictates the dynamics of the entrapped polymer which effectively constitutes a filler-filler bond or a kind of viscoelastic glue between particles. They determined

gap sizes experimentally through measurements of the electron tunnelling process between filler aggregates using dielectric spectroscopy.

2.9.3.3.Modelling of filler networks and network breakdown

There have been many attempts to quantitatively model the breakdown of filler structure, the earliest of which was proposed by Kraus [40, 133]. Kraus derived a model to describe the breakdown and reformation of assumed van der Waals connections between filler aggregates by adapting the Langmuir isotherm for adsorption of gasses on surfaces. The Kraus equation describing the strain dependence of the storage and loss moduli is

$$\frac{G'(\gamma) - G'_{\infty}}{\Delta G'} = \frac{1}{1 + (\gamma/\gamma_C)^{2m}} \qquad 2.57$$

$$\frac{G''(\gamma) - G''_{\infty}}{G''_m - G''_{\infty}} = \frac{2(\gamma/\gamma_c)^m}{1 + (\gamma/\gamma_c)^{2m}}$$

where $\boldsymbol{G'(\gamma)}$ and $\boldsymbol{G''(\gamma)}$ are the strain-dependent storage moduli, $\boldsymbol{G'_{\infty}}$ and $\boldsymbol{G''_{\infty}}$ are the moduli apparent at large strain, $\boldsymbol{\Delta G'}$ is the magnitude of the Payne effect, $\boldsymbol{\gamma_C}$ is the critical strain at which half of the cluster-cluster contacts have broken, $\boldsymbol{G''_m}$ is the maximum in loss modulus and $\boldsymbol{m}$ is the power exponent relating to the strain sensitivity of the yielding process.

The Kraus equation is found to fit $\boldsymbol{G'}$ data very well but fails to accurately fit the corresponding $\boldsymbol{G''}$ data without empirical modification of the formula.

Various other models and concepts have been applied to describe networking and network breakdown in filled elastomers, including the Network Junction Model, the Link-Blob-Node model, the cluster-cluster aggregate model and the van de Walle, Tricot and Gerspacher (VTG) model. These are reviewed in detail by Heinrich and Klüppel [134].

2.9.4. Modified polymer dynamics at the interface/interphase

Over the past five and a half decades many researchers have proposed that polymer chains in the vicinity of particulate fillers behave significantly differently to polymer chains in the unfilled material or polymer far removed from the filler surface. Since the surface areas of

reinforcing filler particles are large, the fractional volume of polymer in contact with the filler surface has the potential to be significant and therefore substantially contribute to the bulk properties of the filled elastomers.

Qualitatively, the presence of an extended, broadened or shifted glass transition due to the presence of filler particles may be able to account for some of the phenomenology of filler reinforcement. Before considering work performed on elastomer composites, evidence from work performed on free standing or supported polymer thin films is reviewed.

2.9.4.1. Evidence from polymer thin films

Over the past 20 years, work performed on polymer thin films has demonstrated the significant effects that nanoscale confinement and surface interactions can have on polymer dynamics. Keddie et al. [27] demonstrated in their 1994 paper that thin films of polystyrene (PS) supported on silica wafers are observed to undergo a glass transition up to 60 K lower than that of the corresponding bulk polymer (Figure 2.60). This work was expanded by many others including Fryer et al. [135], Forrest et al. [136] and van Zanten et al. [137] who showed that the magnitude and even the sign of the T_g shift can be dictated by the degree of interfacial interaction between the polymer thin films and the supporting substrate. In a series of papers, Torkelson and co-workers subsequently demonstrated using a chemical fluorescence technique that a gradient of T_g exists in thin films which decays away from the substrate to bulk-like behaviour [30, 138-143]. There have been limited reports of quantitative equivalence between thermoplastic nanocomposite properties and those observed in model thin film analogues [144]. However this topic remains incompletely resolved both in experimental and theoretical terms as a recent review by Alcoutlabi et al. has highlighted [145].

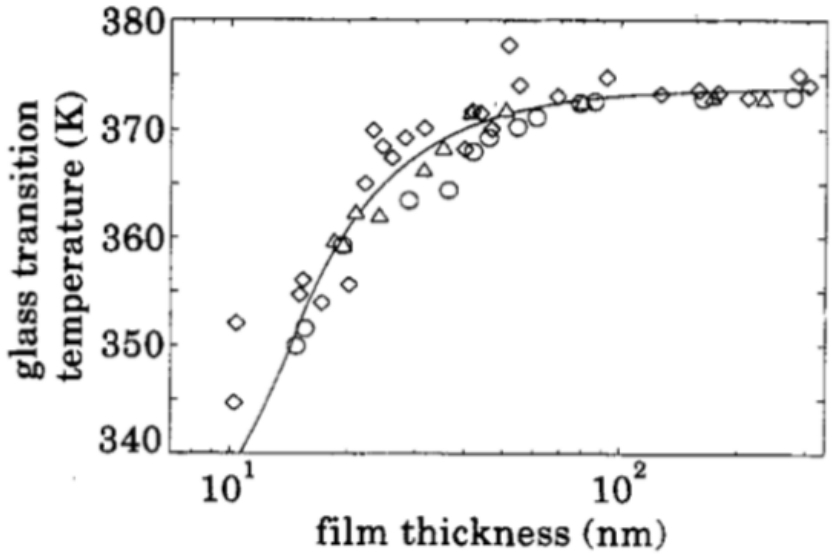

Figure 2.60: Film thickness dependence of the glass transition of PS (From Keddie et al. [27])

2.9.4.2. Direct evidence from filled elastomers

Early work to identify and characterise modified regions of polymer in proximity to filler surfaces was undertaken in the 1960s and 1970s and utilised NMR, thermal expansion and mechanical analysis techniques, the results of which were reviewed by Dannenburg in 1975 [50] and later by Kraus in 1978 [146]. The results of these early studies were often contradictory with some authors claiming no effect of filler particles on the molecular mobility of the elastomer phase and others claiming to have observed a layer (or layers, or a gradient) of restricted mobility polymer of defined thickness. To further complicate this, the interpretation of NMR data in these early papers has now been called into question by Robertson and Roland in their review of this topic [29].

More recent experimental work is very extensive, therefore only a selection of key papers on this topic are summarised in Table 2.2. Papers are highlighted light grey to indicate that glassy or immobilised polymer was reported. Dark grey highlighting indicates that the findings or conclusions of the paper have subsequently been called into question. As can be seen, a wide range of experimental techniques have now been used to characterise the dynamics of polymers in filled rubbers though consensus of opinion has yet to be reached. As has been highlighted in the literature, this may be due to the wide range of filler-polymer combinations studied by different groups.

Table 2.2: Review of papers addressing the immobilisation of polymer by filler particles

Author	Year	Technique(s)	Materials	Conclusion
Mason [147]	1960	Dilatometry	NR/CB	No change in T_g
Smit [148]	1966	Mechanical	SBR/CB	Absorbed, modified polymer layer. Thickness > 2 nm
Waldrop & Kraus [149]	1969	^{1}H-NMR	SBR/CB	No effect of filler on polymer segmental motion even for 'bound' rubber fraction
Kraus & Gruver [150]	1970	Thermal expansion	SBR/CBs	Little effect of carbon black on the T_g
Kaufman, Slichter & Davis [151]	1971	NMR	BR, EPDM/CB	Immobilised and constrained regions of polymer detected in 'bound' rubber fraction
Kraus, Rollmann & Gruver [152]	1971	Mechanical	SBR/PS	Modifications of dynamic properties are not associated with T_g effects
O'Brien et al. [153]	1976	NMR	BR/CB	Evidence of a glassy layer of polymer surrounding filler
Struik [154, 155]	1987	Mechanical	SBR/CB	Evidence of extended T_g in filled elastomers
Stacer & Husband [156]	1990	Mechanical	Various/AP, alumina	Interphase relaxation behaviour reported
Tsagaroupoulos and Eisenberg [157-159]	1995	DMA	PVA_C, PMMA, PS, P4VP /Silica	Interfacial layer of polymer with restricted mobility inferred from temperature dependence of loss tangent
Wang [47]	1998	Mechanical	SBR/CB	Gradient of T_g around filler particles
Berriot et al. [28]	2002	H-NMR	PEA/Silica	Identified gradient of T_g around filler particles
Fragiadakis et al. [160]	2005	DSC, TSDC & BDS	PDMS/Silica	Interfacial layer of polymer of 2.1-2.4 nm thickness with restricted mobility
Fragiadakis et al. [161]	2006	BDS	PDMS/Silica	Restricted interfacial layer of polymer of ~3 nm thickness. Layer decreases in thickness with increasing temperature
Amanuel et al. [162]	2008	DSC	PS/Silica	No alteration or broadening of T_g
Bogoslovov et al. [163]	2008	DSC, rheometry, BDS, dilatometry	PVA_C/Silica	No effect of filler on T_g or polymer segmental dynamics
Meier & Klüppel [128]	2008	DMA & DBS	Various elastomers/CB	Immobilisation of polymer between aggregate gaps
Robertson et al. [91]	2008	Rheometry, AFM	SBR/Silica	No effect of filler on dynamic loss modulus

				around T_g
Robertson et al. [29]	2008	DMA, DSC, BDS, Pressure dependence	PVA_C/silica	No change in temperature dependence of segmental relaxation
Göritz et al. [164]	2010	AFM	Polyisoprene droplets on graphitic substrate	No evidence of glassy or non-bulk behaviour in thin polyisoprene droplets
Fragiadakis et al. [165]	2011	DSC, TSDC & BDS	NR/Silica	Restricted interfacial layer detected for homogenously dispersed nanoparticles. No modification of dynamics detected for aggregated fillers
Fritzche & Klüppel [92]	2011	DMA & BDS	S-SBR/CB	Immobilisation of polymer between filler aggregates subject to temperature dependence
Robertson et al. [166]	2011	Rheometry	PB/CB	Concludes that 'second glass transition' of Tsagaroupoulos and Eisenberg (1995) is related to polymer terminal flow rather than T_g
Robertson et al. [26]	2011	Rheometry, DSC & AFM	SBR/Silica	No effect of commercial fillers on the polymer segmental dynamics
Vo et al. [167]	2011	BDS	SBR/mSBR, carbon black/silica/nanoclay	Slower interfacial relaxation for all filled samples. T_g of interfacial layer is up to 65K higher than bulk
Papon et al. [168]	2012	^{1}H-NMR & DSC	PEA/Silica	Gradient of T_g around filler particles
Marianella et al. [169]	2010 - 2012	BDS	NR, Graphene/Silica/Vulcanizing Additives	No evidence of a shift of T_g by introducing fillers or additives
Kummali et al. [170]	2013	Electric Force Microscopy (EFM)	SBR/Silica	Equivalent segmental relaxation dynamics between interfacial layer and bulk polymer
Wu et al. [171]	2013	BDS	VPR/Graphene oxide (GO)	Segmental dynamics depends on interfacial bonding and GO volume fraction
Mujtaba et al. [172]	2014	^{1}H-NMR	SBR/Silica	Glassy layer is detected and related to viscoelastic properties

As an example of such disagreement, the papers of Berriot et al. (2002) [28] and Robertson et al. (2011) [26] are compared. Berriot et al. reported a gradient of glass transition in the polymer in proximity to silica particles in model, silica-filled PEA elastomers. In their samples the filler particles were synthesised using the Stöber method and yield spherical silica filler particles of ~50 nm diameter with little to no particle flocculation or aggregation. Their primary evidence for a T_g shift is derived from fitting of proton NMR T_2 relaxation times obtained from Hahn spin echo experiments. They deconvoluted the filled material relaxation response in terms of rubbery and glassy responses (both measured in separate experiments on unfilled material above and below the T_g). Figure 2.61 shows the normalised time domain free induction decay ($M(t)/M_0$) of their silica-filled PEA (solid dark line). They fit their data, at long time scales, using an exponential function which describes the relaxation of the mobile elastomer above T_g. By subtracting this fitted function from the total T_1 relaxation, a rapid relaxation component is revealed which is found to correlate with the rapid relaxation measured for unfilled PEA below the T_g (inset in Figure 2.61).

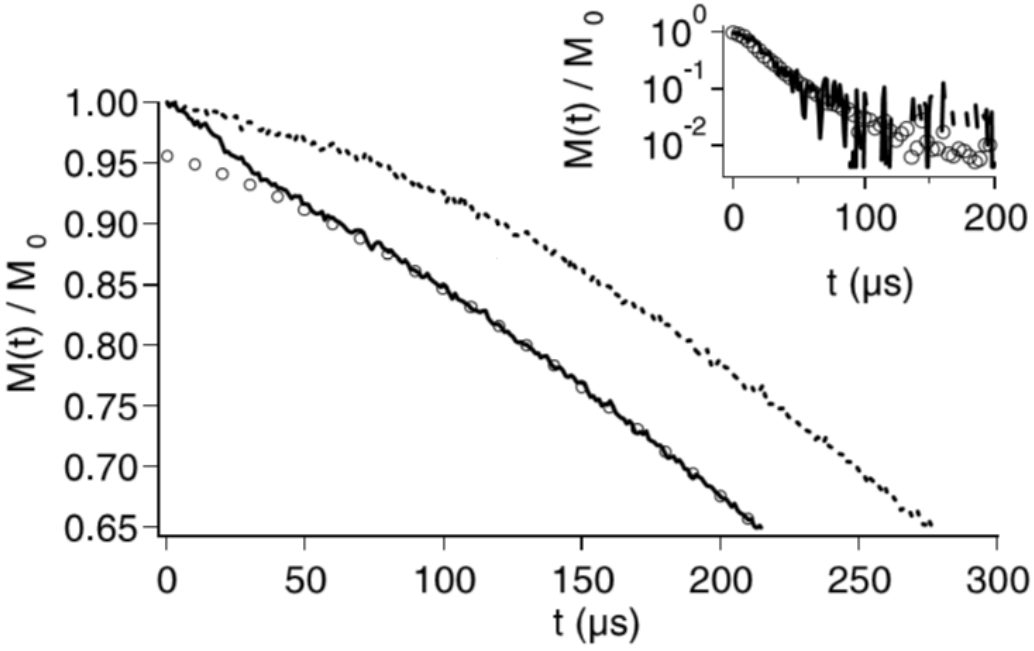

Figure 2.61: NMR T_2 relaxation of silica-filled PEA. The solid line is the decay of the filled material above T_g. The dotted line is the decay of the unfilled material above T_g. Open circles correspond to an exponential fit (performed at long timescales only) describing the unfilled matrix relaxation above T_g. Inset is the residual data compared with the relaxation of unfilled material measured below the T_g. (From Berriot et al. [28])

Thus they claim that a separate glassy layer exists around the filler particles which is subject to a temperature dependence (temperature dependence data not shown). They propose a gradient in T_g with respect to distance from the filler surface, z, which they describe as

$$T_g^{\omega}(z) = T_g^{\omega}\left(1 \pm \left(\frac{\zeta}{z}\right)^{1/v}\right) \qquad 2.58$$

where $T_g^{\omega}(z)$ is the local T_g, T_g^{ω} is the bulk T_g, ζ is a constant with units of dimension which relates to the nature of the attachment at the interface and v is an exponent related to 3D percolation (see the PFVD model of the glass transition). This equation in similar in form to that originally proposed by Keddie et al. [27] to account for the size dependence of the glass transition in polymer thin films.

This contrasts with the work of Robertson et al. [26] who studied commercial precipitated silica-filled SBR. In this case, the silica particles exist as particle aggregates. They found no evidence from dilatometry, calorimetric and mechanical testing of any modification of polymer dynamics due to the incorporation of filler. Figure 2.62 shows their calorimetric data showing no change in T_g and heat capacity step change from the glass to the rubber. It is important to note that these DSC experiments were performed on samples of filled rubber extracted with solvent prior to crosslinking. What remains after this process is the filler phase and the portion of polymer which is tightly bound to the filler particles (the so-called bound rubber). Even for measurement of just the polymer in intimate contact with the filler, no change in T_g calorimetric properties was detected. Figure 2.62 shows the dynamic loss modulus as a function of temperature. As can be seen, there is no shift or broadening of the mechanical dissipation resulting from the T_g.

In these investigations, diametrically opposed conclusions about the nature of the interfacial polymer were reached. It is worthwhile noting that a direct comparison between these studies may be difficult, as different polymer phases were used and, although both groups studied silica filler, the particle sizes and morphologies were very different.

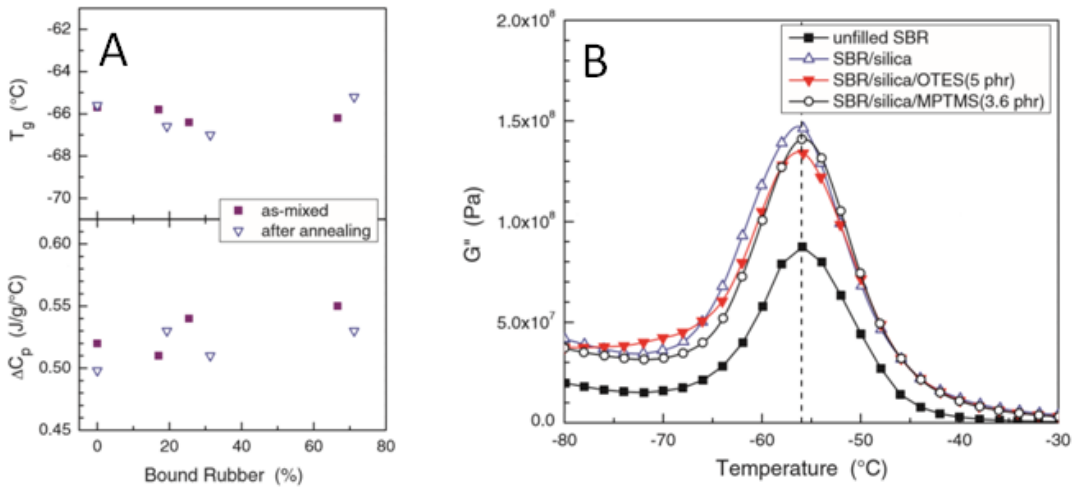

Figure 2.62: A) Calorimetric data of Robertson et al. [26] showing no deviation in T_g or heat capacity step as a function of bound rubber content. B) Dynamic mechanical dissipation from Robertson et al. [26]. As can be seen the shape of the peak in loss modulus is unaffected by the presence of filler

A highly relevant paper has also been published by Fragiadakis et al. (2011) [165] in which they investigated the role of silica particle morphology and dispersion on the formation of a glassy or immobilised layer of polymer. They studied natural rubber filled with silica prepared via the sol-gel method. In one series of samples the silica was precipitated into swollen NR networks and, in the second series, into NR melts in a toluene solution. In this way they prepared a series of well dispersed spherical silica-filled samples (with diameter = 10 nm) and a series of samples with aggregated silica particle structure (with the lower viscosity of the NR/toluene solution allowing for greater particle aggregation). Using a combination of DSC, BDS and Thermally Stimulated Depolarisation Current (TSDC) techniques they demonstrated that a distinct, immobilised phase is found in NR filled with near perfect dispersions of spherical filler particles which is absent from NR filled with silica aggregates (Figure 2.63). The state of particle dispersion and therefore polymer-filler contact appears to play a key role in the formation of an immobilised layer of polymer.

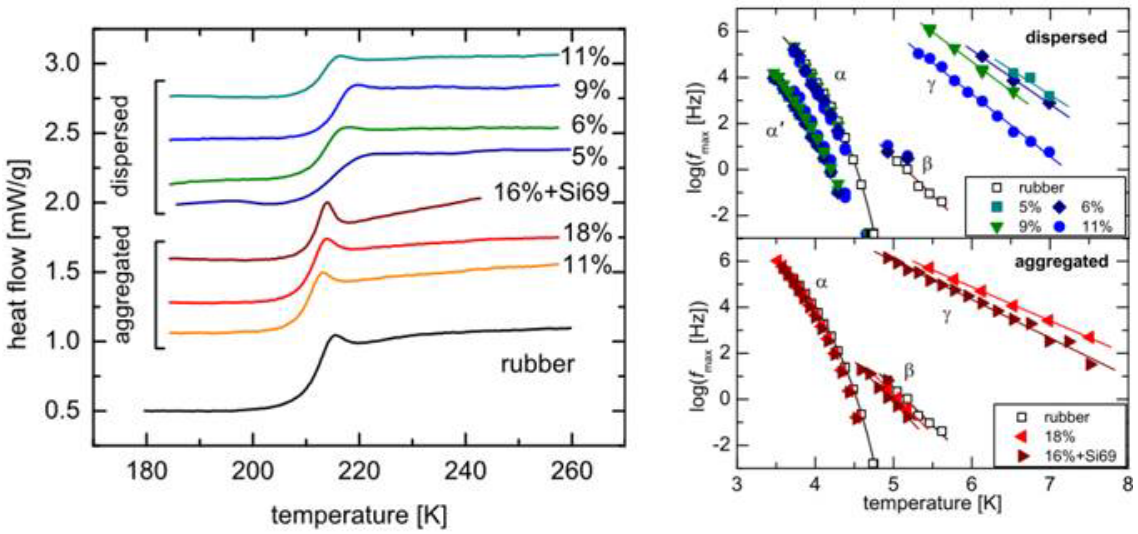

Figure 2.63: Calorimetric (left) and BDS (right) data for dispersed and aggregated silica-filed NR systems. For dispersed systems the calorimetric step change at the T_g is reduced in magnitude and broadened indicating a gradient of T_g. BDS data for the dispersed system shows the appearance of a secondary, slower α' relaxation associated with interphase polymer. Aggregated systems essentially behave like the unfilled material (From Fragiadakis [165])

2.9.4.3. Simulations and Microstructural Models

Several groups have developed microstructural models in an effort to connect macroscopic reinforcement phenomena with the mesoscale mechanics of filler-induced immobilisation of polymer. Merabia et al. [23, 24] and Papon et al. [173] have considered the temperature and strain dependence of glassy bridges connecting spherical filler particles and showed that some aspects of elastomer reinforcement such as the Payne and Mullins Effects can be recovered by modelling the rupture and recovery of glassy bridges. The 'glassy bridge' model of filler reinforcement of Merabia et al. considers reinforcement effects at both linear an non-linear strains [24]. Non-linear strain responses are addressed by considering the rupture and 'rebirth' of elastic glassy bonds between filler particles (Figure 2.64). By considering the breakdown of glassy clusters under strain and the gradual recovery of network connectivity at zero strain they are able to reproduce the phenomenology of the Payne Effect and the modulus recovery following stress softening associated with the Mullins Effect (Figure 2.65). Papon et al. [104] considered that dynamic response of model silica-filled elastomer nanocomposites which display a significant modified fraction of polymer and compared this with the model proposed by Merabia et al. They demonstrated that the breakdown and rebirth of glassy bridges between filler particles in the non-linear regime is able to account for the Payne Effect harmonic paradox.

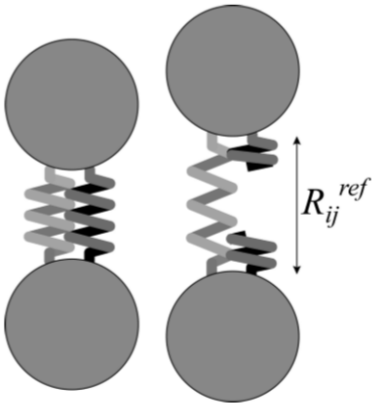

Figure 2.64: Schematic of the breakdown of elastic springs (representing glassy bridges) between filler particles. The dark coloured spring represents the glassy bridge connection between particles while the lighter spring represents the regular rubber matrix elasticity. R_{ij}^{ref} corresponds to the new particle displacement length following stress rupture of the glassy bridge (From Merabia et al. [24])

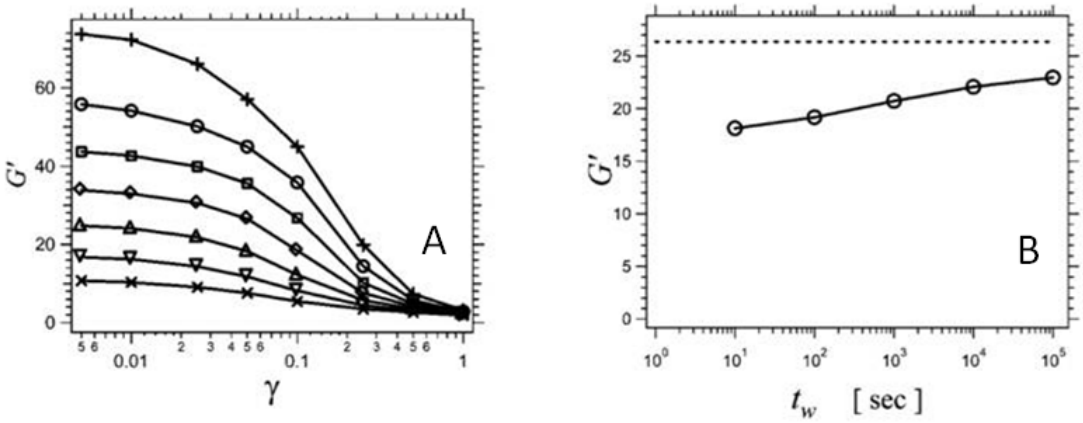

Figure 2.65: A) Simulations of the Payne effect over various temperatures with $\boldsymbol{\varphi}$ = 0.40. B) Recovery of glassy bridges following deformation leads to a time-dependent recovery of the small strain dynamic elastic modulus. From Merabia et al. [24]

Klüppel and co-workers have also considered glassy polymer bridges between filler aggregates in the 'Dynamic Flocculation Model' of rubber reinforcement [40, 51, 92, 128, 129]. Here the glassy bridges between filler particles are responsible for stress transfer between aggregates which can sequentially yield under strain. Underpinning the stiffness of filled elastomers is therefore the frequency distribution of aggregate cluster sizes with 'hard' and 'soft' mechanical characteristics (Figure 2.66) which depends on the strain history of the sample. In this model, the temperature dependence of the glassy bridges is characterised by an activation energy associated with the polymer-filler interaction (Figure 2.67). Klüppel and co-workers have proposed that this activation energy can be calculated either through an Arrhenius fit of the

temperature dependence of the storage modulus in the rubbery region (as shown in Figure 2.67) or through an Arrhenius fit of vertical shift factors required to produce mastercurves for highly filled materials in the rubbery region [92]. Fitzgerald and Ferry [103] and Arai and Ferry [174] have also observed such Arrhenius dependencies of mastercurve vertical shift factors but attributed this to a temperature dependence of the van der Waals bonds constituting the filler network.

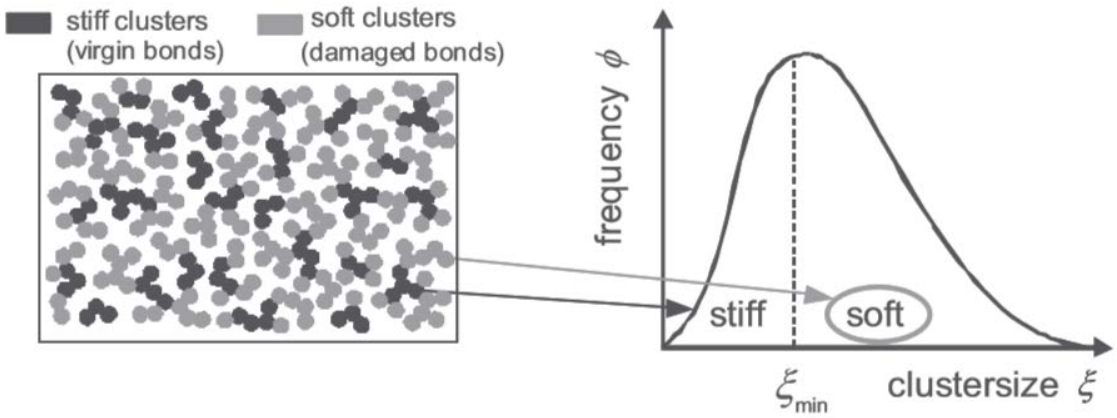

Figure 2.66: Schematic of the frequency distribution of hard and soft clusters of aggregates connected by glassy bridges which underpins reinforcement effects in the 'Dynamic Flocculation Model' (From Klüppel [40])

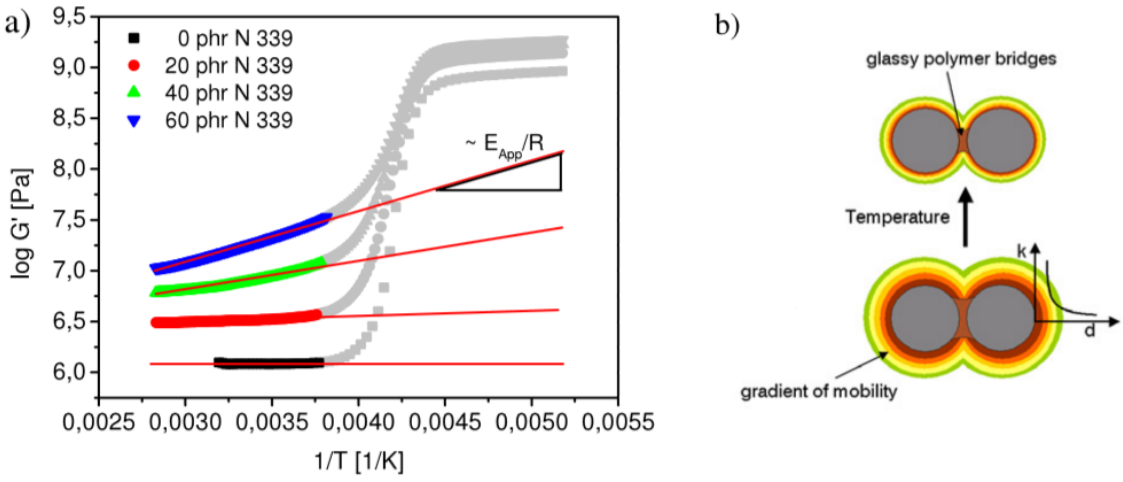

Figure 2.67: A) Effective activation energies for the glassy bridge filler structure determined from small strain, temperature-domain dynamic elasticity. B) Schematic of the temperature dependence of glassy bridges between filler aggregates. (From Fritzsche and Klüppel [92])

Strain dependent yielding of glassy bridges between filler particles has been further explored by Froltsov et al. [175] using a molecular dynamic simulation of coarse grained polymer chains between parallel plates. Performing non-equilibrium MD simulations to separate the plates illustrated potential yielding mechanisms of the glassy bridges (Figure 2.68). Gusev [176] and Gusev and Laurie [177] have explored viscous dissipation in glassy bridges between filler particles by implementing a finite element analysis. Their results indicated that the dynamic losses in such composites may be isolated entirely in the bridging polymer.

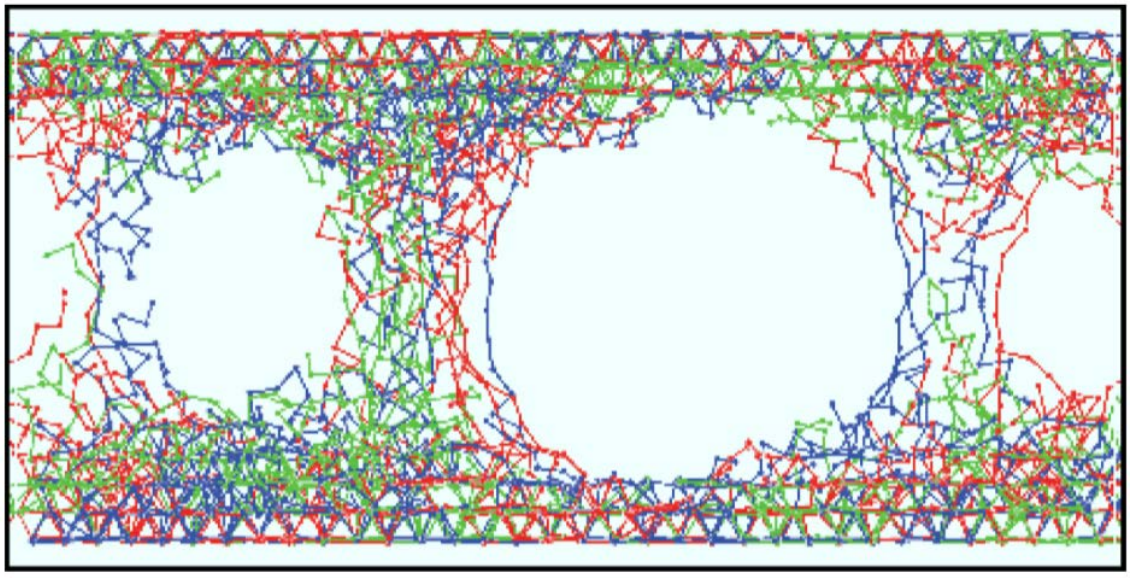

Figure 2.68: Rupture modes (cavity formation) of glassy polymer between separating interfaces from the non-equilibrium molecular dynamic simulations of Froltsov et al. [175]. The rigid walls are seen at the top and bottom of the simulation. The deformation is applied in the vertical direction

Long and Lequeux [21, 178, 179] have proposed that the immobilisation of polymer in the vicinity of filler surfaces and between aggregates can be understood in the context of the 'Percolation of Free Volume Distribution' model of the glass transition. Here small (~2 nm) dynamic heterogeneities or localised density fluctuations in the polymer phase are able to percolate between filler aggregates leading to a modification of the T_g in the local area.

2.9.5. Chain slippage/desorption mechanisms

A number of researchers have proposed that the bonding of polymer chains to the surface of filler aggregates may be labile and subject to a temperature and/or strain dependence. For example, as part of their theoretical consideration of the Payne Effect, Maier and Göritz [46,

180] proposed that in the linear viscoelastic regime, the storage modulus, $G'(\gamma,T)$, may be described in terms of the effective network density, $N(\gamma,T)$.

$$G'(\gamma,T) = N(\gamma)\mathbf{k}T \quad 2.59$$

$$N(\gamma,T) = N_C + N_{St} + N_L(\gamma,T) \quad 2.60$$

This comprises polymer network crosslinks, N_C, crosslinks arising from strong bonding of chains to the filler surface, N_{St}, (note that these crosslinks are not subject to a temperature or strain dependence) and those arising from thermally labile, weaker bonding of chains to the filler, N_L, which may desorb as a function of strain or temperature (Figure 2.69).

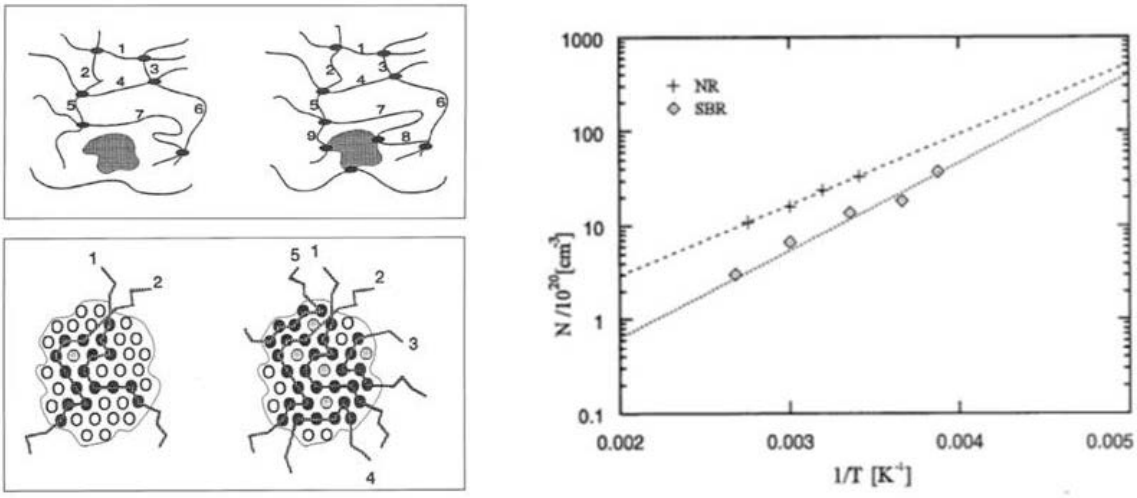

Figure 2.69: Maier and Görtiz's model of variable network density in filled rubbers. Left top: chains attached to filler particles increase the effective network density. Left bottom: chains attached to filler surfaces can be stably attached (solid attachment points) or attached to thermally and strain labile-sites (hollow attachment points). Right) Maier and Göritz's determination of activation energies for the thermally-activated desorption of chains from the filler surface. The plot is the concentration of network density, obtained from a fitting of the model to Payne effect data, plotted versus the inverse of temperature (From Maier and Göritz [180])

Maier and Göritz [180] proposed in their molecular model that labile bonding of polymer chains to the filler surface is subject to a strain dependence and derived a microstructural model of this concept based on the Langmuir desorption isotherm. The strain dependence of

$\nu_L(\gamma, T)$ is determined in terms of a steady state between absorbed and desorbed chains (analogous to the Langmuir adsorption of gases on solid surfaces), by the following [180]:

$$\Theta\Phi_a = \Theta_1\Phi_d \quad 2.61$$

where Θ is the fraction of occupied absorption sites on the carbon black surface, Φ_a is the rate of chain segment absorption, Θ_1 is the fraction of unoccupied sites and Φ_d is the desorption rate. The sum of the site fractions is unity:

$$\Theta + \Theta_1 = 1 \quad 2.62$$

The chain segment desorption rate is assumed to be a function of applied strain with β being a constant which is characteristic of the process:

$$\Phi_d = \beta\gamma \quad 2.63$$

By defining the process solely in terms of Θ_1, the strain dependence of the chain segment desorption process and therefore the strain dependence of crosslink density can be derived:

$$(1 - \Theta_1)\Phi_a = \Theta_1\Phi_d \quad 2.64$$

$$\Theta_1 = \frac{\Phi_a}{\Phi_d + \Phi_a} = \frac{1}{1 + \frac{\beta\gamma}{\Phi_a}} \quad 2.65$$

The constant c is defined as:

$$c = \frac{\beta}{\Phi_a} \quad 2.66$$

The strain dependence of the density of labile crosslinks can then be defined by multiplying through by the maximum number of interaction sites per unit volume:

$$N_L(\gamma, T) = \Theta_1 N_{L0} = \frac{N_{L0}}{1 + c\gamma} \quad 2.67$$

The parameter N_{L0} corresponds to the theoretical maximum number of adsorbed chains on the filler surface. From entropic elasticity (Equation 2.1) the following equations can be defined:

$$G'^{(\gamma)} = \left(N_C + N_{St} + \frac{N_{L0}}{1 + c\gamma}\right)\mathbf{k}T = G'_{St} + \left(\frac{G'_L}{1 + c\gamma}\right) \quad 2.68$$

where

$$G'_{St} = (N_C + N_{St})\mathbf{k}T \quad 2.69$$

and

$$G'_L = N_{L0}\mathbf{k}T \quad 2.70$$

By fitting this equation to various Payne effect data collected over a range of temperatures, Maier and Göritz were able to determine an Arrhenius temperature dependence for the desorption process, $N_L(T)$, and estimate characteristic activation energies (E_a) for the process of between 0.15-0.18 eVs per absorbed segment. This corresponds to the van der Waals energy range of interactions and results in the characteristic non-entropic temperature dependence of the small strain elastic modulus of highly filled rubbers. (N_{Lc} is a constant characterising the concentration of unstable chain-filler bonds).

$$N_L(T) = N_{Lc}\exp^{E_a/\mathbf{k}T} \quad 2.71$$

In this model, as the dynamic strain is increased, the rate of polymer chain desorption from the surface of the filler increases, resulting in an overall decrease in the effective network crosslink density (due to a decrease in effective crosslinks at the filler surface) and therefore modulus. Slippage of debonded chains along the filler surface results in the observed peak in viscous dissipation.

One issue arising from the Maier and Göritz model is the method which they use to rationalise the increase in small strain storage modulus of rubbers due to the presence of filler. It is assumed to originate solely from the increased crosslinked density associated with interaction of polymer chains with the filler surface. This ignores the effect of filler geometry and morphology on, for example, hydrodynamic reinforcement, strain amplification and occlusion of rubber. This limits the physicality of the Maier and Göritz model.

Sternstein and co-workers [181, 182] observed that *'dynamic non-linearites'* (Payne Effect) are apparent in filled polymer melts well below the particle percolation threshold for the development of an aggregated filler network. To account for this, they proposed that effective entanglements at the filler surface contribute significantly to the viscoelastic response of the composite firstly by acting as effective crosslinking points and secondly by altering the far field properties of the bulk polymer chains. They proposed that application of stress or strain results in debonding of trapped chains at the filler surface resulting in relaxation of polymer structure akin to the slippage phenomenon observed in melt-substrate interactions.

Jha et al. [125] and Busfield et al. [126] have implemental finite element analyses of rubbers reinforced by spherical carbon black fillers (Mid-thermal N990 grade). They modelled the experimentally-determined tensile mechanical properties using a random array of spherical particles in an hyperelastic continuum. They found that their initial boundary conditions of no slip between filler and polymer phases overestimated the tensile data at higher strains and so they introduced a strain dependent slippage mechanism at a critical stress which resulted in a more accurate description of experimental data. Similarly the finite element analyses of Akutagawa et al. of carbon black aggregate-filled rubber were found to overestimate the experimentally determined stiffness data [127]. They proposed that a slippage mechanism could be introduced into their simulations to account for this.

Both Bueche [9, 183] and Dannenberg [50] considered the stress softening Mullins Effect, observed in filled rubbers, in terms of chain rupture (Bueche) or chain slippage (Dannenburg) at the polymer-filler interface. They considered that filler particles are connected by polymer chains of various lengths and that under strain the shortest bridging chains must either rupture

or slip at the filler surface to accommodate the imposed deformation. Broken or slipped chains are no longer able to contribute to the observed stiffness upon a second extension cycle as they were upon initial deformation - resulting in a stress softening effect. They also proposed that if the strained sample is then left to recover, molecular motion of the polymer chains results in a randomisation of connected segments at the filler surface and therefore a slow recovery of the un-deformed mechanical properties. Dannenberg attributed the large hysteretic losses observed in the Mullins Effect to this chain slippage (viscous) mechanism.

The primary difference between Bueche's mechanism (Figure 2.70) and Dannenberg's mechanism (Figure 2.71) is that Dannenberg assumed physical (that is reversible) bonding of polymer to filler while Bueche proposed a chemical grafting of chains to the filler surface which once ruptured is irreversibly disconnected from the filler surface [9].

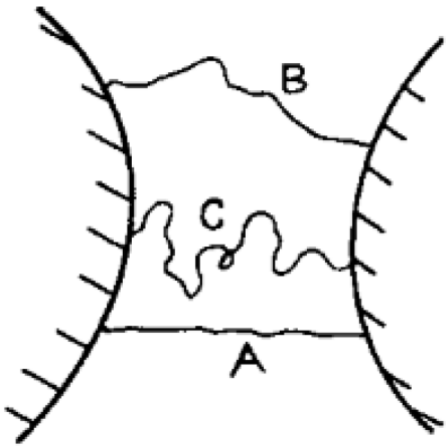

Figure 2.70: Bueche's model of filler particles connected by polymer chains of various length. (From Bueche [183])

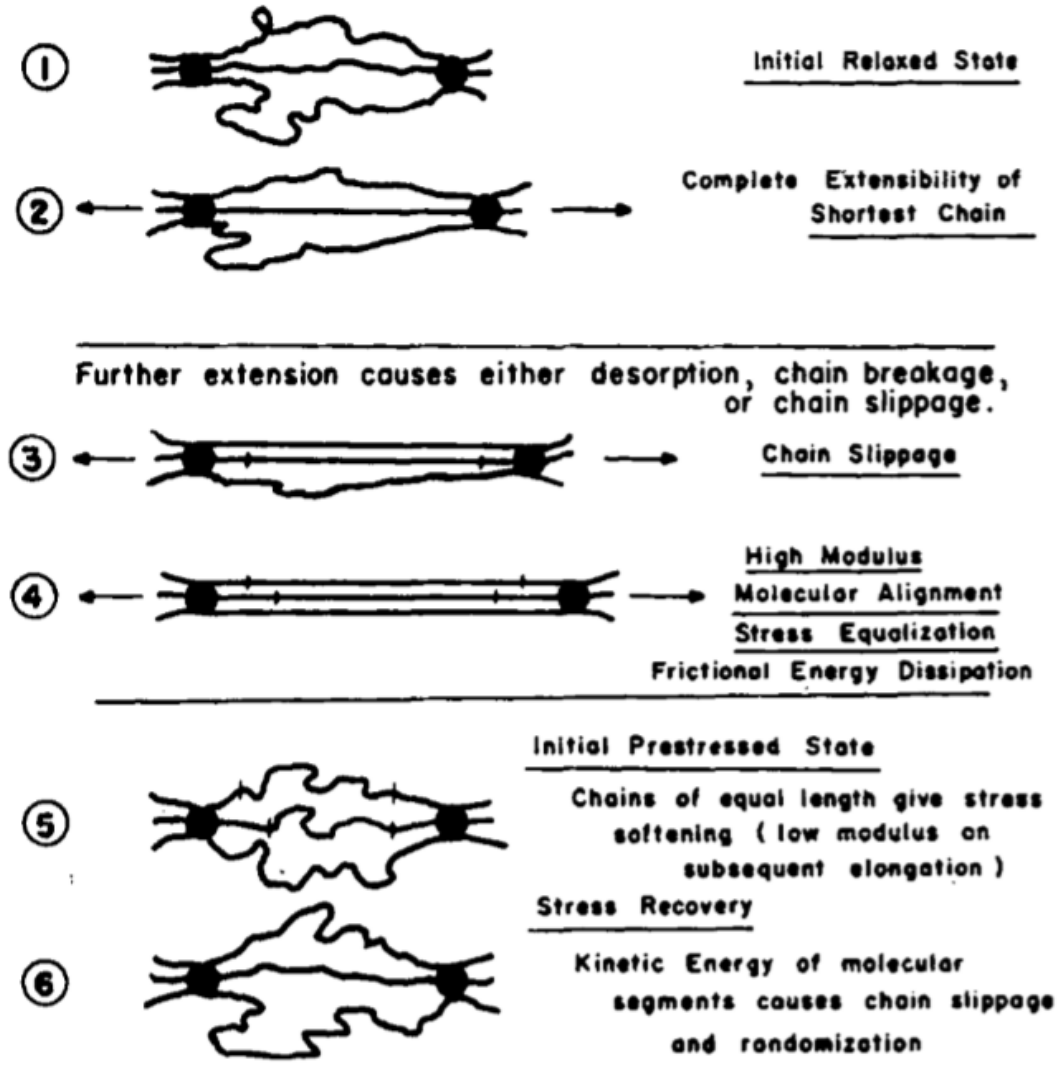

Figure 2.71: Dannenberg's model of the Mullins effect using chain slippage and breakage concepts (From Dannenberg [50])

2.9.6. Filler network as a jammed system and strain memory effects

Robertson and Wang [184] have considered the Payne Effect as part of the larger phenomenon of particle jamming/unjamming physics, which is equally applicable to granular systems, glass formation processes, colloidal and molecular systems. They noted that if rheological data for strain sweeps performed on carbon black-filled rubbers and silica-filled oils with a variety of filler volume fractions are plotted versus mechanical energy ($\sigma\gamma$) rather than strain then all data can be superposed on the x-axis independent of volume fraction (Figure 2.72). They found that the mechanical energy required to achieve an equivalent level of structure breakdown (taken at the peak in loss modulus) is independent of volume fraction of filler (Figure 2.73). Robertson and Wang claim that this equivalence of breakdown processes between filled rubber and filled oil is evidence for the Payne Effect's origin in particle unjamming processes.

However the universality of this equivalence has since been questioned by Richter et al. [185, 186]. Wang and Robertson [187] proposed a phase diagram to describe the transition from a jammed to an unjammed state in terms of the volume fraction, thermal energy and mechanical energy (Figure 2.74).

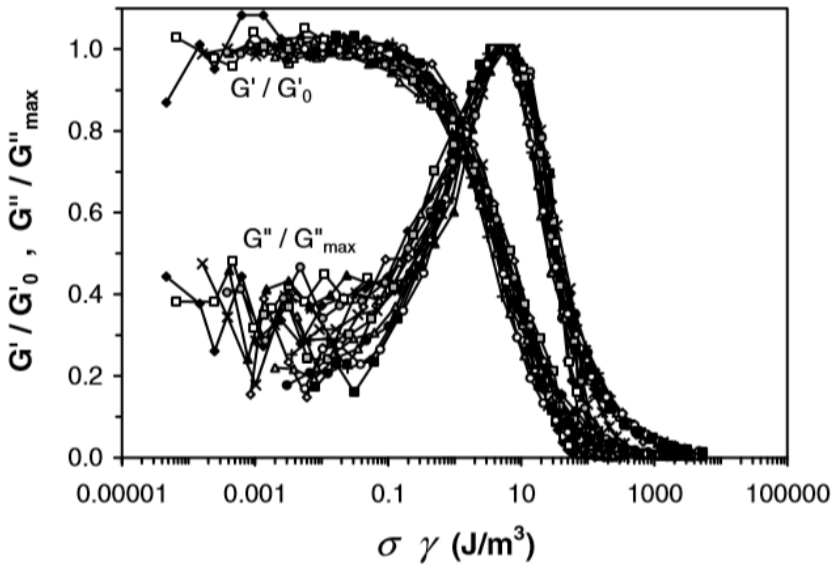

Figure 2.72: Equivalence of dynamic non-linearites for oil filled with varying volume fraction of silica plotted versus mechanical energy - yielding a constant breakdown energy [184]

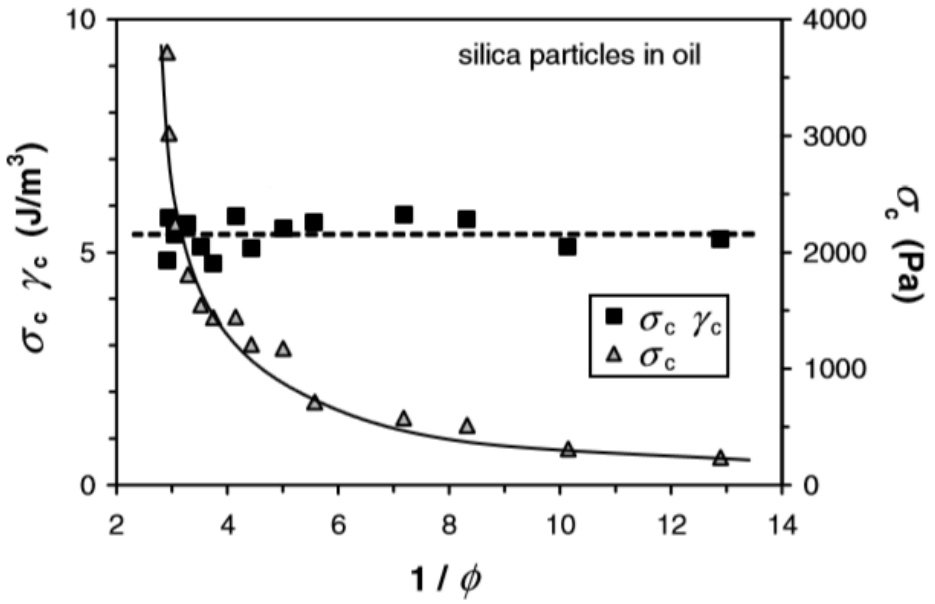

Figure 2.73: Plot of the dependence of the critical energy and critical stress of breakdown versus the reciprocal of volume fraction for silica filled oil (similar relationships were also noted using Payne's data for carbon black-filled butyl rubber) [184]

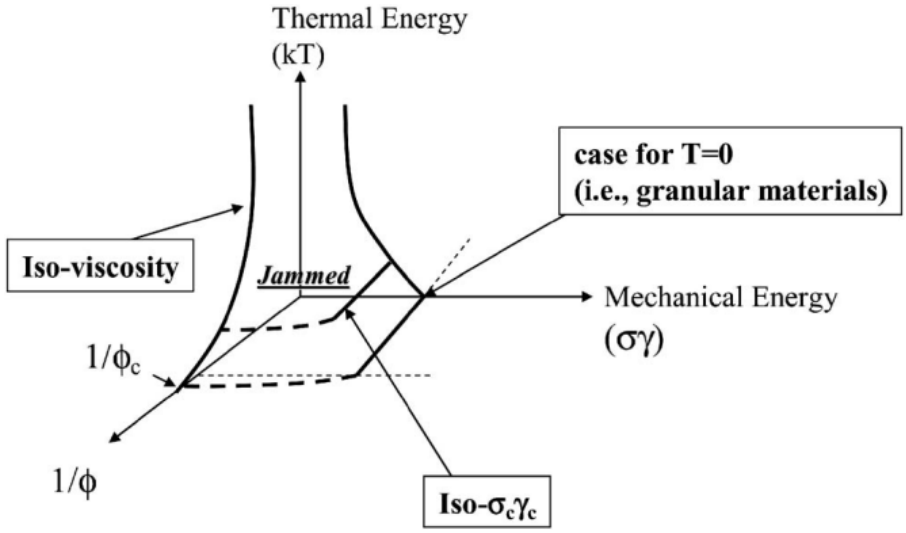

Figure 2.74: The phase diagram proposed by Wang and Robertson to describe the transition of a particulate system from a jammed to an unjammed state (From [187])

Robertson and Wang have also discovered and extensively reported on a new strain memory effect in filled rubbers specifically manifested at strains corresponding to the Payne Effect region of deformation [187-190]. They noted that if a filled, crosslinked rubber with a controlled and minimum strain history is 'aged' at a specific non-linear dynamic strain (say 1 %) then this results in a drop or 'spectral hole' in the loss modulus observed during a subsequently performed strain sweep (up to say 10 %) - roughly in the location of the aging strain. Also observed is a corresponding increase in the storage modulus around the aging strain during a strain sweep. Once the strain sweep to larger strains has been performed, the spectral hole memory is erased. They have observed the persistence of the spectral hole up to 10 days after aging at a specific strain before applying a strain sweep to higher strains. The full aging procedure is outlined in Figure 2.75. Examples of spectral holes are presented in Figure 2.76.

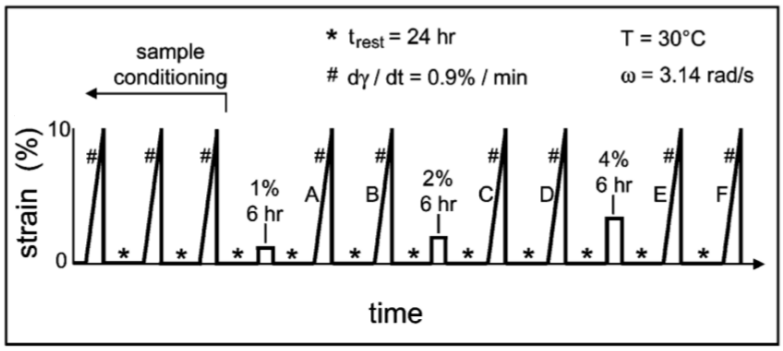

Figure 2.75: The full aging procedure used by Robertson and Wang to investigate memory effects in filled rubbers [188]

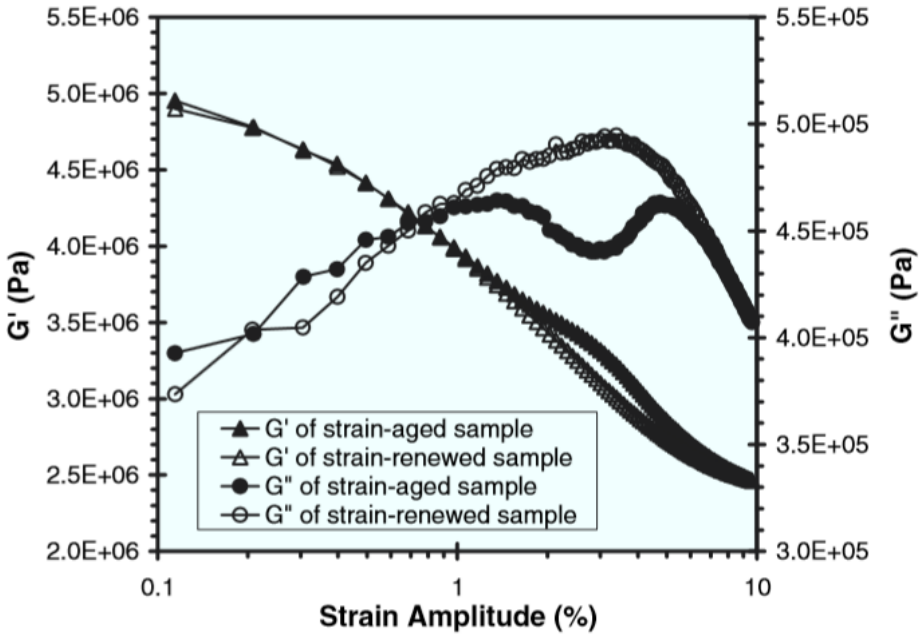

Figure 2.76: Memory effects measured in strain sweeps of filled rubbers. Data corresponding to strain aged samples show a significant drop in dissipation and increase in elastic modulus at around the aging strain - in this case 2 %. Once the strain sweep has been performed this information is lost (see strain-renewed data) [190]

Robertson and Wang have shown that the location and depth of the spectral hole is influenced by the aging strain, frequency of deformation and aging time (number of oscillations). By aging at a specific strain, the filled rubber becomes more elastic at that particular strain until that aging strain is subsequently exceeded. Robertson and Wang have interpreted this as evidence for structural heterogeneity in the filler structure meaning that the filler structure itself responds to deformation via a range of relaxation times associated with different structural conformations. They suppose that the effect of an ageing strain is equivalent to an ageing temperature - for example they point out the equivalence between these strain ageing effects in filled rubbers and physical aging effects in glassy materials. Here the ageing strain promotes particle exploration of different structural conformations just as thermally activated particle diffusion would in a low viscosity composite analogue.

2.10. Summary of the literature and identification of research opportunities

From the literature review presented in this chapter it is clear that although a significant amount has been learned about particulate reinforcement over the past 110 years since SC Mote's discovery of the reinforcing effect of carbon black, a comprehensive understanding of the underlying physical mechanisms is still outstanding. Though many theories have been proposed, some backed with extensive experimental evidence, none of the current theories are either i) universally accepted or ii) able to explain by themselves the full phenomenology of reinforcement as a function of time, temperature and strain.

This seems to be due in part to the complexity of the materials typically used in industrial applications. For example, passenger tyre treads are enormously complicated systems made of blends of different, often immiscible, rubbers with chemically and physically complex vulcanising systems and a range of filler particles of varying size, surface activity and dispersion states.

In situations where simplified materials are used or even when model systems - where variables can be strictly controlled - are employed, the main barrier to understanding reinforcement lies in the difficulty in correctly interpreting bulk measurements of material properties in terms of events occurring on the meso- or even nano-scale.

This investigation is predominantly mechanical analysis-based and aims to characterise and identify the underlying mechanisms contributing to reinforcement in silica and (primarily) carbon black filled natural rubbers. In order to simplify the problem as much as is possible, two phase compounds are used (that is a single filler phase and a single rubber phase). Additionally the work is restricted to small strains, below the onset of the Payne effect. This means that dynamic yielding of the filler networks is in general not considered. Furthermore one of the key variables of this study is the surface activity of the filler particles. For the case of silica-reinforced compounds, this is modified using silane chemistry and for the case of carbon black fillers using thermal modifications.

2.11. References

[1] H. Wolf, R. Wolf, Rubber - A story of greed and glory, JJ Little and Ives Company, New York, 1936 (reprint 2009).
[2] H. Morawetz, Rubber Chemistry and Technology, 73 (2000) 405-426.
[3] E.A. Hauser, India Rubber Journal, 94 (1937) 7-8.
[4] J. Cooper, The lost Kingdoms of Central America, Television program, BBC, 2014.
[5] S. Wolff, Rubber Chemistry and Technology, 69 (1996) 325-346.

[6] J.M.G. Cowie, V. Arrighi, Polymers: chemistry and physics of modern materials, 3rd ed., CRC Press, Boca Raton, 2008.
[7] L.R.G. Treloar, The physics of rubber elasticity, 3rd ed., Oxford University Press, Oxford, 2009.
[8] R. Simpson, Rubber Basics, Smithers Rapra Technology, Shawbury, 2002.
[9] J.E. Mark, B. Erman, F.R. Eirich, Science and Technology of Rubber, Elsevier, New York, 2005.
[10] A. Gent, Rubber Chemistry and Technology, 28 (1955).
[11] S. Toki, T. Fujimaki, M. Okuyama, Polymer, 41 (2000) 5423-5429.
[12] S. Toki, I. Sics, S.F. Ran, L.Z. Liu, B.S. Hsiao, S. Murakami, K. Senoo, S. Kohjiya, Macromolecules, 35 (2002) 6578-6584.
[13] S. Toki, B.S. Hsiao, Macromolecules, 36 (2003) 5915-5917.
[14] R.J. Young, P.A. Lovell, Introduction to Polymers, CRC Press, Boca Raton, 2011.
[15] A.N. Gent, Engineering with rubber. How to design rubber components, 2nd ed., Hanser, Cincinnati, 2001.
[16] L. Mullins, Rubber Chemistry and Technology, 21 (1948) 281-300.
[17] J. Ferry, Viscoelastic Properties of Polymers, Wiley, New York, 1961.
[18] C.M. Roland, Viscoelastic behaviour of rubbery materials, Oxford University Press, Oxford, 2011.
[19] G. Allegra, G. Raos, M. Vacatello, Progress in Polymer Science, 33 (2008) 683-731.
[20] C.M. Roland, Rubber Chemistry and Technology, 85 (2012) 313-326.
[21] D. Long, F. Lequeux, European Physical Journal E, 4 (2001) 371-387.
[22] S. Merabia, P. Sotta, D. Long, European Physical Journal E, 15 (2004) 189-210.
[23] S. Merabia, P. Sotta, D.R. Long, Journal of Polymer Science Part B-Polymer Physics, 48 (2010) 1495-1508.
[24] S. Merabia, P. Sotta, D.R. Long, Macromolecules, 41 (2008) 8252-8266.
[25] P.P. De, N. Roy Choudhury, N.K. Dutta, Thermal analysis of rubbers and rubbery materials, Smithers Rapra Technology Ltd, Shawbury, 2010.
[26] C.G. Robertson, C.J. Lin, R.B. Bogoslovov, M. Rackaitis, P. Sadhukhan, J.D. Quinn, C.M. Roland, Rubber Chemistry and Technology, 84 (2011) 507-519.
[27] J.L. Keddie, R.A.L. Jones, R.A. Cory, Europhysics Letters, 27 (1994) 59-64.
[28] J. Berriot, H. Montes, F. Lequeux, D. Long, P. Sotta, Macromolecules, 35 (2002) 9756-9762.
[29] C.G. Robertson, C.M. Roland, Rubber Chemistry and Technology, 81 (2008) 506-522.
[30] C.J. Ellison, S.D. Kim, D.B. Hall, J.M. Torkelson, European Physical Journal E, 8 (2002) 155-166.
[31] L. Bateman, Chemistry and Physics of Rubber-like Substances, The Garden City Press Ltd., Letchworth, 1963.
[32] M. Porter, Rubber Chemistry and Technology, 40 (1967) 16.
[33] C.M. Roland, Journal of Rheology, 34 (1990) 25-34.
[34] R.A. González L, Marcos A, Chamorro C, Rubber Chemistry and Technology, 69 (1995) 11.
[35] L. Loan, Rubber Chemistry and Technology, 40 (1967).
[36] J.L. Valentín, P. Posadas, A. Fernández-Torres, M.A. Malmierca, L. González, W. Chassé, K. Saalwächter, Macromolecules, 43 (2010) 4210-4222.
[37] P. Dluzneski, Rubber Chemistry and Technology, 74 (2001) 41.
[38] J.L. Valentín, J. Carretero-González, I. Mora-Barrantes, W. Chassé, K. Saalwächter, Macromolecules, 41 (2008) 4717-4729.
[39] J.B. Donnet, R.C. Bansal, M.J. Wang, (Eds), Carbon Black: Science and Technology, 2nd ed., Marcel Dekker Inc, New York, 1993
[40] M. Klüppel, Advances in Polymer Science, 164 (2003) 1-86.
[41] T.C. Gruber, C.R. Herd, Rubber Chemistry and Technology, 70 (1997) 727-746.
[42] ASTM, Standard classification system for carbon blacks used in rubber products, ASTM International, West Conshohocken, PA, 2014.

[43] N990 Physical and Chemical Properties PDF available from:, http://www.cancarb.com/docs/pdf/Physical_Chemical_Properties.pdf, Access Date: 19/6/15
[44] A. Schröder, M. Klüppel, R.H. Schuster, Macromolecular Materials and Engineering, 292 (2007) 885-916.
[45] J.B. Donnet, Rubber Chemistry and Technology, 71 (1998) 323-341.
[46] D. Göritz, H. Raab, J. Frohlich, P.G. Maier, Rubber Chemistry and Technology, 72 (1999) 929-945.
[47] M.J. Wang, Rubber Chemistry and Technology, 71 (1998) 520-589.
[48] E. Dannenberg, Rubber Chemistry and Technology, 48 (1975) 410-444.
[49] E.M. Dannenberg, Rubber Chemistry and Technology, 59 (1986) 512-524.
[50] E.M. Dannenberg, Rubber Chemistry and Technology, 48 (1975) 410-444.
[51] E. Geberth, M. Klüppel, Macromolecular Materials and Engineering, 297 (2012) 914-922.
[52] M. Gerspacher, L. Nikiel, H.H. Yang, C.P. O'Farrell, G.A. Schwartz, Kautschuk Gummi Kunststoffe, 55 (2002) 596-604.
[53] T. Gruber, T.W. Zerda, M. Gerspacher, Carbon, 32 (1994) 1377-1382.
[54] E.M. Dannenberg, Rubber Chemistry and Technology, 25 (1952) 843-857.
[55] E. Papirer, Adsorption on silica surfaces, Marcel Dekker Inc, New York, 2000.
[56] H. Luginsland, A review of the chemistry and the reinforcement of the silica-silane filler systems for rubber applications, Shaker Verlag, Aachen, 2002.
[57] V.V. Potapov, L.T. Zhuravlev, Glass Physics and Chemistry, 31 (2005) 661-670.
[58] L.T. Zhuravlev, Colloids and Surfaces a-Physicochemical and Engineering Aspects, 173 (2000) 1-38.
[59] L.T. Zhuravlev, Langmuir, 3 (1987) 316-318.
[60] N. Hewitt, Compounding precipitated silica in elastomers, William Andrew Publishing, Norwich, 2007.
[61] J. Ramier, L. Chazeau, C. Gauthier, L. Guy, M.N. Bouchereau, Rubber Chemistry and Technology, 80 (2007) 183-193.
[62] J. Fritzsche, M. Klüppel, J.G. Meier, Kgk-Kautschuk Gummi Kunststoffe, 62 (2009) 319-325.
[63] S. Mihara, R.N. Datta, W.K. Dierkes, J.W.M. Noordermeer, N. Amino, Y. Ishikawa, S. Nishitsuji, M. Takenaka, Rubber Chemistry and Technology, 87 (2014) 348-359.
[64] S. Mihara, R.N. Datta, J.W.M. Noordermeer, Rubber Chemistry and Technology, 82 (2009) 524-540.
[65] J. Ramier, C. Gauthier, L. Chazeau, L. Stelandre, L. Guy, Journal of Polymer Science Part B-Polymer Physics, 45 (2007) 286-298.
[66] S.C. Debnath, R.N. Datta, J.W.M. Noordermeer, Rubber Chemistry and Technology, 76 (2003) 1311-1328.
[67] L. Reuvekamp, J.W. Ten Brinke, P.J. Van Swaaij, J.W.M. Noordermeer, Rubber Chemistry and Technology, 75 (2002) 187-198.
[68] L. Reuvekamp, J.W. ten Brinke, P.J. van Swaaij, J.W.M. Noordermeer, Kautschuk Gummi Kunststoffe, 55 (2002) 41-47.
[69] R. Rauline, Michelin and Cie, 1992.
[70] X.D. Pan, Rheologica Acta, 44 (2005) 379-395.
[71] S. Mihara, University of Twente, Twnete, 2009.
[72] L. Bokobza, J.P. Chauvin, Polymer, 46 (2005) 4144-4151.
[73] D.J. Lowe, A.V. Chapman, S. Cook, J.J.C. Busfield, Macromolecular Materials and Engineering, 296 (2011) 693-702.
[74] D.J. Lowe, A.V. Chapman, S. Cook, J.J.C. Busfield, Rubber Chemistry and Technology, 86 (2013) 538-557.
[75] D.J. Lowe, A.V. Chapman, S. Cook, J.J.C. Busfield, Journal of Polymer Science Part B-Polymer Physics, 49 (2011) 1621-1627.
[76] L. Bokobza, T. Pflock, A. Lindemann, D. Kwiryn, P.D. Claro, Kgk-Kautschuk Gummi Kunststoffe, 67 (2014) 45-50.
[77] C. Harishkumar, R.H. Schuster, Kgk-Kautschuk Gummi Kunststoffe, 67 (2014) 22-28.

[78] A. Das, G.R. Kasaliwal, R. Jurk, R. Boldt, D. Fischer, K.W. Stöckelhuber, G. Heinrich, Composites Science and Technology, 72 (2012) 1961-1967.
[79] A. Shakun, J. Vuorinen, M. Hoikkanen, M. Poikelispaa, A. Das, Composites Part a-Applied Science and Manufacturing, 64 (2014) 49-69.
[80] F. Bueche, Rubber Chemistry and Technology, 34 (1961) 493-505.
[81] L. Mullins, N.R. Tobin, Rubber Chemistry and Technology, 39 (1966) 799-813.
[82] G. Kraus, Rubber Chemistry and Technology, 51 (1978) 297-321.
[83] W.P. Fletcher, A.N. Gent, Rubber Chemistry and Technology, 26 (1953) 181-187.
[84] A.R. Payne, Rubber Chemistry and Technology, 36 (1963) 422-431.
[85] S. Poompradub, M. Tosaka, S. Kohjiya, Y. Ikeda, S. Toki, I. Sics, B.S. Hsiao, Journal of Applied Physics, 97 (2005) 103529.
[86] N. Suphadon, Ph.D Thesis: Queen Mary Univeristy of ondon, London, 2010.
[87] Y. Fukahori, A.A. Hon, V. Jha, J.J.C. Busfield, Rubber Chemistry and Technology, 86 (2013) 218-232.
[88] A. Ten Brinke, Ph.D Thesis: University of Twente, Twente, 2002.
[89] A.N. Gent, Journal of Applied Polymer Science, 18 (1974) 1397-1406.
[90] H. Lorenz, M. Klüppel, Journal of the Mechanics and Physics of Solids, 60 (2012) 1842-1861.
[91] C.G. Robertson, C.J. Lin, M. Rackaitis, C.M. Roland, Macromolecules, 41 (2008) 2727-2731.
[92] J. Fritzsche, M. Klüppel, Journal of Physics-Condensed Matter, 23 (2011) 035104.
[93] M. Klüppel, Journal of Physics-Condensed Matter, 21 (2009) 10.
[94] W.P. Fletcher, A.N. Gent, Rubber Chemistry and Technology, 27 (1954) 209-222.
[95] A.R. Payne, Rubber Chemistry and Technology, 39 (1966) 365-374.
[96] A.R. Payne, Rubber Chemistry and Technology, 36 (1963) 432-443.
[97] A.R. Payne, Rubber Chemistry and Technology, 36 (1963) 444-450.
[98] A.R. Payne, Rubber Chemistry and Technology, 30 (1957) 218-241.
[99] A.R. Payne, Rubber Chemistry and Technology, 38 (1965) 387-399.
[100] A.R. Payne, W.F. Watson, Rubber Chemistry and Technology, 36 (1963) 147-155.
[101] A.R. Payne, E. Whittaker, Journal of Applied Polymer Science, 16 (1972) 1191-&.
[102] A.R. Payne, R.E. Whittaker, Rubber Chemistry and Technology, 44 (1971) 440-478.
[103] E.R. Fitzgerald, J.D. Ferry, Rubber Chemistry and Technology, 55 (1982) 1569-1577.
[104] A. Papon, S. Merabia, L. Guy, F. Lequeux, H. Montes, P. Sotta, D.R. Long, Macromolecules, 45 (2012) 2891-2904.
[105] A.M. Randall, C.G. Robertson, Journal of Applied Polymer Science, 131 (2014) 10.
[106] B. Meissner, Rubber Chemistry and Technology, 68 (1995) 297-310.
[107] J.L. Leblanc, Progress in Polymer Science, 27 (2002) 627-687.
[108] J.L. Leblanc, Journal of Applied Polymer Science, 66 (1997) 2257-2268.
[109] J.L. Leblanc, B. Stragliati, Journal of Applied Polymer Science, 63 (1997) 959-970.
[110] A. Einstein, Annalen der Physik, 19 (1906) 289.
[111] H.M. Smallwood, Rubber Chemistry and Technology, 18 (1945) 292-305.
[112] S. Wolff, J.-B. Donnet, Rubber Chemistry and Technology, 63 (1990) 32-45.
[113] E. Guth, Rubber Chemistry and Technology, 18 (1945) 596-604.
[114] E. Guth, Rubber Chemistry and Technology, 23 (1950) 635-643.
[115] G.G. Batchelor, JT, Journal of Fluid Mechanics, 56 (1972) 401.
[116] H.S. Chen, A. Acrivos, International Journal of Solids and Structures, 14 (1978) 349-364.
[117] H.S. Chen, A. Acrivos, International Journal of Solids and Structures, 14 (1978) 331-348.
[118] A.A. Gusev, M.G. Rozman, Computational and Theoretical Polymer Science, 9 (1999) 335-337.
[119] M. Klüppel, G. Heinrich, Rubber Chemistry and Technology, 68 (1995) 623-651.
[120] A.I. Medalia, Rubber Age, 104 (1972) 67-71.
[121] A.I. Medalia, Journal of Colloid and Interface Science, 32 (1970) 115-131.
[122] J.G. Meier, M. Klüppel, Macromolecular Materials and Engineering, 293 (2008) 12-38.
[123] G. Huber, T.A. Vilgis, Macromolecules, 35 (2002) 9204-9210.

[124] J.S. Bergström, M.C. Boyce, Rubber Chemistry and Technology, 72 (1999) 633-656.
[125] V. Jha, A.A. Hon, A.G. Thomas, J.J.C. Busfield, Journal of Applied Polymer Science, 107 (2008) 2572-2577.
[126] J.J.C. Busfield, V. Jha, A.A. Hon, A.G. Thomas, Conference Proceedings: Constitutive Models for Rubber IV, P.E. Austrell, L. Kari (Eds.), Balkema, Stockholm,
[127] Y.K. Akutagawa K, Yamamoto A, Heguri H, Jinnai H, Shinbori Y, Rubber Chemistry and Technology, 81 (2008) 182-189.
[128] J.G. Meier, M. Klüppel, Macromolecular Materials and Engineering, 293 (2008) 12-38.
[129] H. Lorenz, M. Freund, D. Juhre, J. Ihlemann, M. Klüppel, Macromolecular Theory and Simulations, 20 (2011) 110-123.
[130] F.B. Wyart, P.G. de Gennes, European Physical Journal E, 1 (2000) 93-97.
[131] G.A. Schwartz, S. Cerveny, A.J. Marzocca, M. Gerspacher, L. Nikiel, Polymer, 44 (2003) 7229-7240.
[132] J.G. Meier, J.W. Mani, M. Klüppel, Physical Review B, 75 (2007) 10.
[133] G. Kraus, Applied Polymer Symposia, (1984) 75-92.
[134] G. Heinrich, M. Klüppel, Advances in Polymer Science, 160 (2002) 1-44.
[135] D.S. Fryer, R.D. Peters, E.J. Kim, J.E. Tomaszewski, J.J. de Pablo, P.F. Nealey, C.C. White, W.L. Wu, Macromolecules, 34 (2001) 5627-5634.
[136] J.A. Forrest, K. Dalnoki-Veress, J.R. Stevens, J.R. Dutcher, Physical Review Letters, 77 (1996) 2002-2005.
[137] J.H. vanZanten, W.E. Wallace, W.L. Wu, Physical Review E, 53 (1996) R2053-R2056.
[138] C.J. Ellison, M.K. Mundra, J.M. Torkelson, Macromolecules, 38 (2005) 1767-1778.
[139] C.J. Ellison, J.M. Torkelson, Nature Materials, 2 (2003) 695-700.
[140] S. Kim, J.M. Torkelson, Macromolecules, 44 (2011) 4546-4553.
[141] R.D. Priestley, C.J. Ellison, L.J. Broadbelt, J.M. Torkelson, Science, 309 (2005) 456-459.
[142] P. Rittigstein, R.D. Priestley, L.J. Broadbelt, J.M. Torkelson, Nature Materials, 6 (2007) 278-282.
[143] P. Rittigstein, J.M. Torkelson, Journal of Polymer Science Part B-Polymer Physics, 44 (2006) 2935-2943.
[144] A. Bansal, H.C. Yang, C.Z. Li, K.W. Cho, B.C. Benicewicz, S.K. Kumar, L.S. Schadler, Nature Materials, 4 (2005) 693-698.
[145] M. Alcoutlabi, G.B. McKenna, Journal of Physics-Condensed Matter, 17 (2005) R461-R524.
[146] G. Kraus, Rubber Chemistry and Technology, 51 (1978) 297-321.
[147] P. Mason, Journal of Applied Polymer Science, 4 (1960) 212-218.
[148] P. Smit, Rheologica Acta, 5 (1966) 277-283.
[149] M.A. Waldrop, G. Kraus, Rubber Chemistry and Technology, 42 (1969) 1155-1166.
[150] G. Kraus, J.T. Gruver, Journal of Polymer Science Part a-2-Polymer Physics, 8 (1970) 571.
[151] S. Kaufman, W.P. Slichter, D.D. Davis, Journal of Polymer Science Part a-2-Polymer Physics, 9 (1971) 829-893.
[152] G. Kraus, K.W. Rollmann, J.T. Gruver, Rubber Chemistry and Technology, 44 (1971) 598-606.
[153] J. O'Brien, E. Cashell, G. Wardell, V. McBrierty, Macromolecules, 9 (1976) 653-660.
[154] L.C.E. Struik, Polymer, 28 (1987) 1521-1533.
[155] L.C.E. Struik, Polymer, 28 (1987) 1534-1542.
[156] R.G. Stacer, D.M. Husband, Rheologica Acta, 29 (1990) 152-162.
[157] G. Tsagaropoulos, A. Eisenberg, Macromolecules, 28 (1995) 6067-6077.
[158] G. Tsagaropoulos, A. Eisenberg, Macromolecules, 28 (1995) 396-398.
[159] G. Tsagaropoulos, A. Eisenberg, Abstracts of Papers of the American Chemical Society, 209 (1995) 20-MACR.
[160] D. Fragiadakis, P. Pissis, L. Bokobza, Polymer, 46 (2005) 6001-6008.
[161] D. Fragiadakis, P. Pissis, L. Bokobza, Journal of Non-Crystalline Solids, 352 (2006) 4969-4972.

[162] S. Amanuel, A.N. Gaudette, S.S. Sternstein, Journal of Polymer Science Part B-Polymer Physics, 46 (2008) 2733-2740.
[163] R.B. Bogoslovov, C.M. Roland, A.R. Ellis, A.M. Randall, C.G. Robertson, Macromolecules, 41 (2008) 1289-1296.
[164] D. Goeritz, R.W.P. Hofmann, H.H. Bissem, Rubber Chemistry and Technology, 83 (2010) 323-330.
[165] D. Fragiadakis, L. Bokobza, P. Pissis, Polymer, 52 (2011) 3175-3182.
[166] C.G. Robertson, M. Rackaitis, Macromolecules, 44 (2011) 1177-1181.
[167] L.T. Vo, S.H. Anastasiadis, E.P. Giannelis, Macromolecules, 44 (2011) 6162-6171.
[168] A. Papon, H. Montes, M. Hanafi, F. Lequeux, L. Guy, K. Saalwächter, Physical Review Letters, 108 (2012) 065702.
[169] M. Hernandez, M.D. Bernal, R. Verdejo, T.A. Ezquerra, M.A. Lopez-Manchado, Composites Science and Technology, 73 (2012) 40-46.
[170] M.M. Kummali, L.A. Miccio, G.A. Schwartz, A. Alegria, J. Colmenero, J. Otegui, A. Petzold, S. Westermann, Polymer, 54 (2013) 4980-4986.
[171] S.W. Wu, Z.H. Tang, B.C. Guo, L.Q. Zhang, D.M. Jia, Rsc Advances, 3 (2013) 14549-14559.
[172] A. Mujtaba, M. Keller, S. Ilisch, H.J. Radusch, M. Beiner, T. Thurn-Albrecht, K. Saalwächter, Acs Macro Letters, 3 (2014) 481-485.
[173] A. Papon, H. Montes, F. Lequeux, J. Oberdisse, K. Saalwachter, L. Guy, Soft Matter, 8 (2012) 4090-4096.
[174] K. Arai, J.D. Ferry, Rubber Chemistry and Technology, 59 (1986) 592-604.
[175] V.A. Froltsov, M. Klüppel, G. Raos, Physical Review E, 86 (2012) 041801.
[176] A.A. Gusev, Macromolecules, 39 (2006) 5960-5962.
[177] A.A. Gusev, S.A. Lurie, Macromolecules, 42 (2009) 5372-5377.
[178] F. Lequeux, D. Long, P. Sotta, K. Saalwachter, Angewandte Chemie-International Edition, 50 (2011) A63-A70.
[179] D. Long, P. Sotta, Macromolecules, 39 (2006) 6282-6297.
[180] P.G. Maier, D. Göritz, Kautschuk Gummi Kunststoffe, 49 (1996) 18-21.
[181] S.S. Sternstein, S. Amanuel, M.L. Shofner, Rubber Chemistry and Technology, 83 (2010) 181-198.
[182] S.S. Sternstein, A.J. Zhu, Macromolecules, 35 (2002) 7262-7273.
[183] F. Beuche, Jounal of Applied Polymer Science, 4 (1960) 107-114.
[184] C.G. Robertson, X.R. Wang, Physical Review Letters, 95 (2005) 075703.
[185] S. Richter, H. Kreyenschulte, M. Saphiannikova, T. Gotze, G. Heinrich, Polymer Networks, 306-307 (2011) 9.
[186] S. Richter, M. Saphiannikova, G. Heinrich, Conference Proceedings: Constitutive Models for Rubber VI, G. Heinrich, M. Kaliske, A. Lion, S. Reese (Eds.), Balkema, Boca Raton,
[187] X.R. Wang, C.G. Robertson, Physical Review E, 72 (2005) 031406.
[188] C.G. Robertson, X. Wang, Europhysics Letters, 76 (2006) 278-284.
[189] X.R. Wang, C.G. Robertson, Journal of Polymer Science Part B-Polymer Physics, 48 (2010) 859-869.
[190] X.R. Wang, C.G. Robertson, Rubber Chemistry and Technology, 83 (2010) 149-159.

Chapter 3

Materials and Compounding

Précis:

The filler materials examined in this work are all based on carbon black and precipitated silica particulates which are widely used in the tyre industry as reinforcing fillers. This chapter details the characterisation of the fillers 'as-received' from commercial suppliers, the subsequent thermal and chemical modifications of the filler particles, and the processes used to compound the filler materials with natural rubber. All the filler types studied are available from commercial suppliers at the time of writing or are surface modified versions of commercially available materials.

The carbon black fillers selected for this study have a range of aggregate morphologies and surface areas. Carbon black surface activity is modified by thermal treatment (graphitisation) which results in a dramatic reduction in surface free energy and bound rubber by promoting the growth of graphitic planes at the carbon black surface at the expense of higher energy sites.

Two grades of silica are selected to contrast with the carbon blacks: a conventional silica and a highly dispersible silica. Silane surface modifications are used to promote interactions between the silica surface and the polymer.

After compounding the fillers with natural rubber, a series of silica and carbon black-filled compounds varying not only in compounded filler aggregate morphology but also in terms of polymer-filler interactions are prepared for further experimentation.

Aspects of this work have been published in the peer reviewed journal *'Macromolecular Materials and Engineering*' as: LB Tunnicliffe et al. *'Flocculation and Viscoelastic Behaviour in Carbon Black-Filled Natural Rubber*', 299(12), 1474-1483, 2014

3.1. Carbon Black-based fillers

Carbon black fillers of various grades were obtained from commercial suppliers (Table 3.1). The carbon blacks grades were selected to provide a range of surface areas and particle morphologies. N990 (trade name Thermax N990) is a mid-thermal (MT) grade of carbon black which is categorised as '*...non-reinforcing...*' (Cancarb data sheets [1]). This is due to its very low surface area, relatively large particle size (diameter ~ 250 nm) and low aggregate structure. N990 is primarily used as a diluting filler in non-tyre tread applications. N330 (trade name Vulcan 3) is a high abrasion furnace (HAF) grade carbon black which is characterised as '*reinforcing*' and has a significantly higher surface area and structure than N990 (Cabot data sheets [2]). As such N330 is extensively used as a reinforcing carbon black for tyre tread applications Cabot claim that N330 is '*...an industry standard for many tire applications...*'. N134 (trade name Vulcan 10H) is a super abrasion furnace (SAF) grade of carbon black and has one of the highest surface areas among carbon blacks used for tyre tread applications. According to the Cabot technical data sheet [3], N134 imparts '*...exceptionally high levels of reinforcement...*' to tyre tread compounds .

In addition to these 'as-received' carbon blacks, graphitised analogues were produced. In the graphitisation process, approximately 200 g of carbon black were placed inside a Carbolite STF tube furnace which was connected to a nitrogen supply flushing at 400 ml/minute. The nitrogen was allowed to purge the samples and furnace chamber for a minimum of 6 hours in order to ensure a significant, near total, reduction of the oxygen content inside the furnace chamber. The temperature of the furnace was then ramped to 1250 °C at a rate of 10 K/min. The peak temperature was held for 1 hour before cooling to room temperature. The cooling process was uncontrolled and required around 12 hours. The inert atmosphere was maintained during the cooling process. The thermally modified carbon blacks were removed from the furnace, sampled for characterisation and then stored under a nitrogen atmosphere until they were compounded with rubber and sampled for characterisation. The possibility of thermal gradients within the furnace leading to different degrees of graphitisation was addressed simply by thorough mixing of the carbon black powder once removed from the furnace.

Table 3.1: Physico-chemical data for the carbon black fillers

Filler Code	Supplier	Commercial Grade	Surface Area / $m^2.g^{-1}$	L_A / nm	L_C / nm	L_A/L_C	Crystallinity %	Density / $g.cm^{-3}$	Surface Free Energy / $mJ.m^{-2}$	Bound Rubber %
N990	Cancarb	MT	8	2.06	1.65	1.25	32.2	1.80	17.5	N/A
N990g	Cancarb†	N/A	8	3.23	1.94	1.66	45.6	1.95	6.9	N/A
N330	Cabot	HAF	77	1.75	1.43	1.22	28.7	1.80	19.0	42.61
N330g	Cabot†	N/A	78	2.22	1.53	1.45	33.7	1.90	1.6	27.55
N134	Cabot	SAF	134	1.74	1.05	1.66	28.6	1.80	39.1	56.70
N134g	Cabot†	N/A	136	2.40	1.20	2.00	35.5	1.96	5.2	33.29

†Thermally modified (graphitised)

Having obtained a total range of six carbon black types, various analyses were performed on the samples to determine their physico-chemical properties.

3.1.1. Simultaneous Thermal Analysis (STA)

STA was performed for each carbon black sample using a Netzsch 449 F3 Jupiter STA using platinum sample crucibles and a flushing nitrogen atmosphere. A temperature ramp was performed from room temperature to 1250 °C at a ramp rate of 10 K/min - simulating the graphitisation process. The principle of STA is given in more detail in the Appendix. Data for each sample are presented in Figure 3.1. Note that the DSC heat flow is weight-normalised to the initial weight of the sample.

The TGA trace for the 'as-received' samples shows a significant drop in weight % at the peak temperature of 1250 °C in the range of 5-8 %. The weight % drop can be correlated with the loss of surface volatile content in the form of CO, CO_2 and H_2 ([4-7]). The corresponding DSC traces show significant exo- and endotherms notably between 650 and 850 °C and also at around 1150 °C.

These thermal events may relate to the volatilisation processes, but potentially also with crystallisation of amorphous carbon within the carbon black structure itself [6, 7]. For the graphitised carbon black series the total weight reduction at 1250 °C is substantially reduced to around 1-2 % indicating that graphitisation resulted in a removal of volatile content from the carbon blacks. The DSC traces show a significant depression or absence in the intensity of the thermal transitions throughout the temperature ramp; indicating that little crystallisation or volatilisation occurs.

3.1.2. Nitrogen-Specific Surface Area (SSA)

Nitrogen-specific surface areas were determined for each filler type using a Micrometrics BET-method surface area analyser (see Appendix for detail information). Samples were dried at 110 °C in an oven and then degassed at 110 °C in flowing nitrogen for 24 hours prior to analysis, in order to remove surface moisture. SSA values are given in Table 3.1, and show little variation between unmodified and graphitised carbon blacks. This suggests that little change to the fundamental aggregate morphology occurred during thermal treatment.

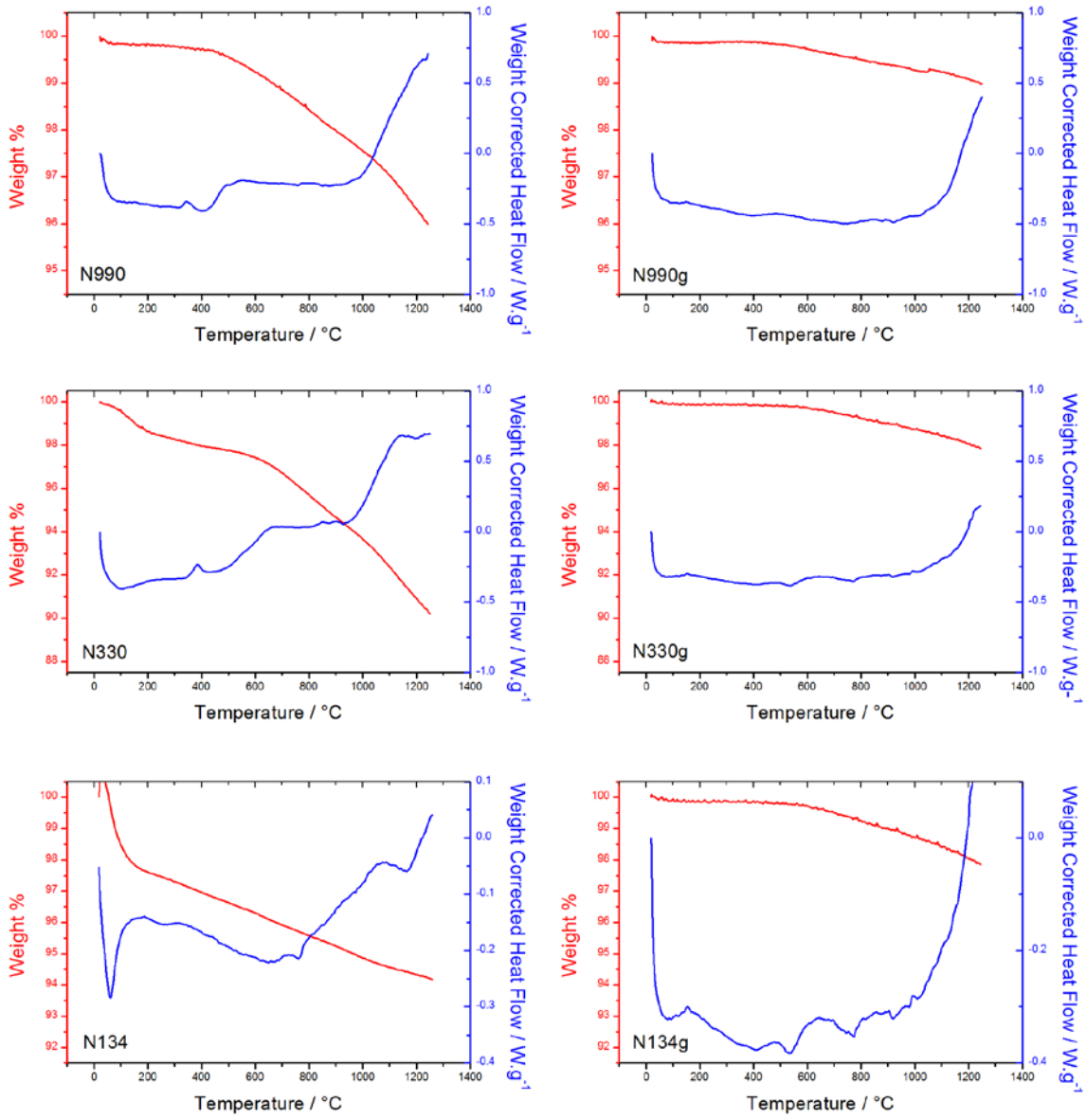

Figure 3.1: STA traces for carbon black fillers. Red data traces are TGA data. Blue data traces are the corresponding DSC data

3.1.3. Transmission Electron Microscopy (TEM)

The morphology of the carbon black filler particles was investigated qualitatively by TEM. Dilute particle dispersions were prepared by ultrasonic dispersion of small quantities of the particulates in ethanol for 10 minutes. A TEM grid was then dipped into the dispersion and the ethanol was evaporated prior to examination. A JEOL 2010 TEM was used to obtain the images.

TEM images for the N134 and N330-based carbon blacks are given in Figure 3.2. Note that due to the relative large size of the N990 grades, the particles were examined using the scanning electron microscopy (SEM) technique. Here a small amount of the filler was suspended in ethanol and ultrasonicated. Then a small amount of the resulting suspension was left to completely dry on a sheet of aluminium foil. The powders were then transferred to SEM stubs by pressing the conductive adhesive mounted on the stub onto a lightly covered area of the aluminium foil. The samples were examined using secondary electron imaging on an FEI Inspect SEM.

It is clear from examination of the images that in a qualitative sense the aggregated particle morphology of the high structure carbon blacks is unaffected by the thermal treatment. Primary particle and aggregate sizes remain consistent between 'as-received' and graphitised samples. Closer examination of the primary particle nodules on graphitised samples reveals substantial Fresnel fringing resulting from electron diffraction from regular spacings - indicative of crystalline regions (Figure 3.3).

Local electron diffraction patterns were collected by insertion of the Selected Area Diffraction (SAD) aperture and selecting the area of interest (typically a region of high carbon black aggregate density). The strength of the intermediate lens was then adjusted so as to focus the diffraction pattern into the screen. Local electron diffraction patterns of primary particle nodules indicate increased crystallisation post-graphitisation (Figure 3.3). Here the intense main 'halo' in the centre of the image results from direct transmission of electrons through the sample. Moving out from the central halo, a series of rings can be observed which arise from electron diffraction. The sharpening and intensification of these rings upon graphitisation indicates greater crystalline content.

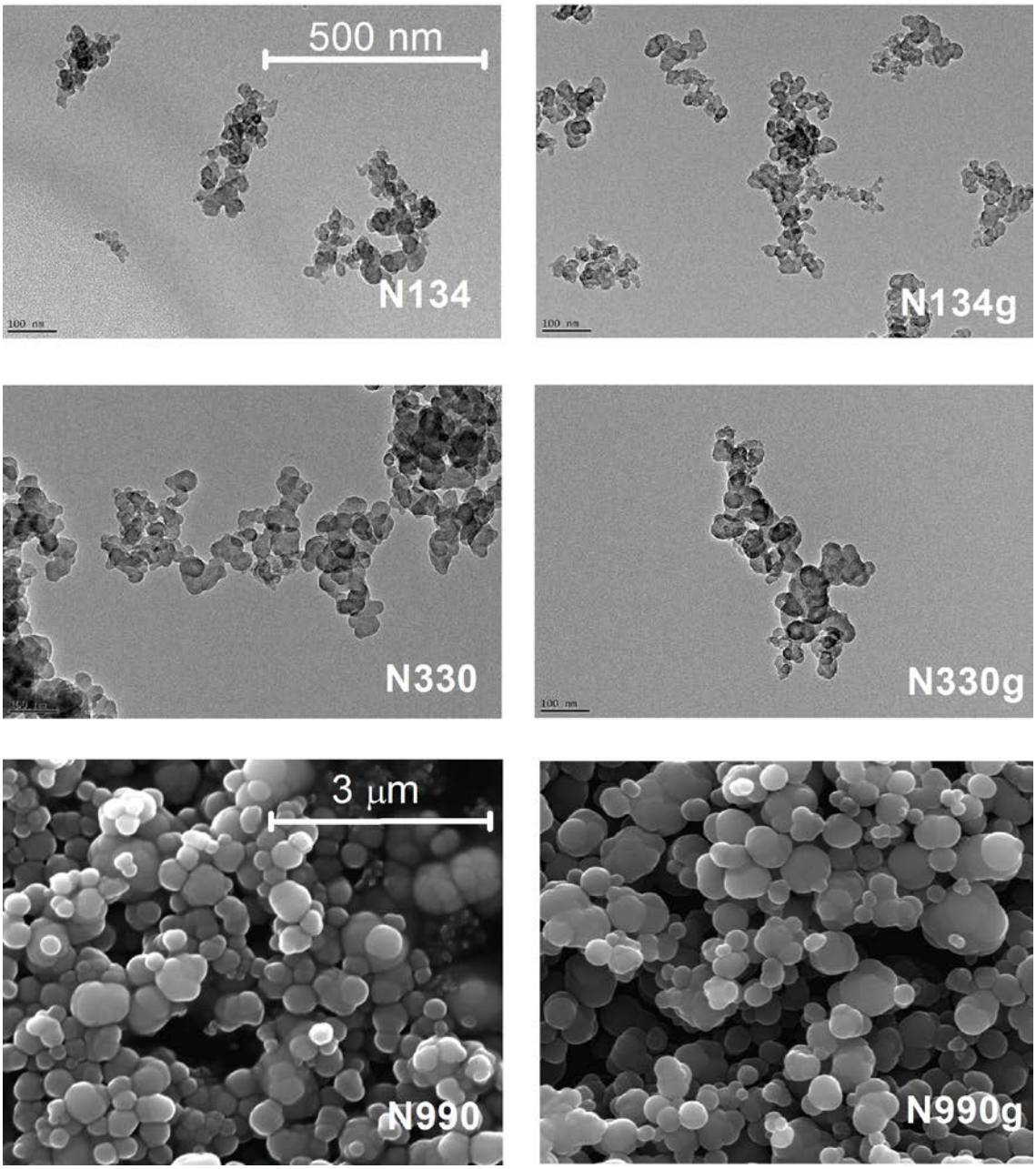

Figure 3.2: TEM and SEM images of carbon black filler particles. Scale bar plotted on N134 image is valid for all TEM images. Scale bar plotted on N990 image is also valid for the N990g SEM image

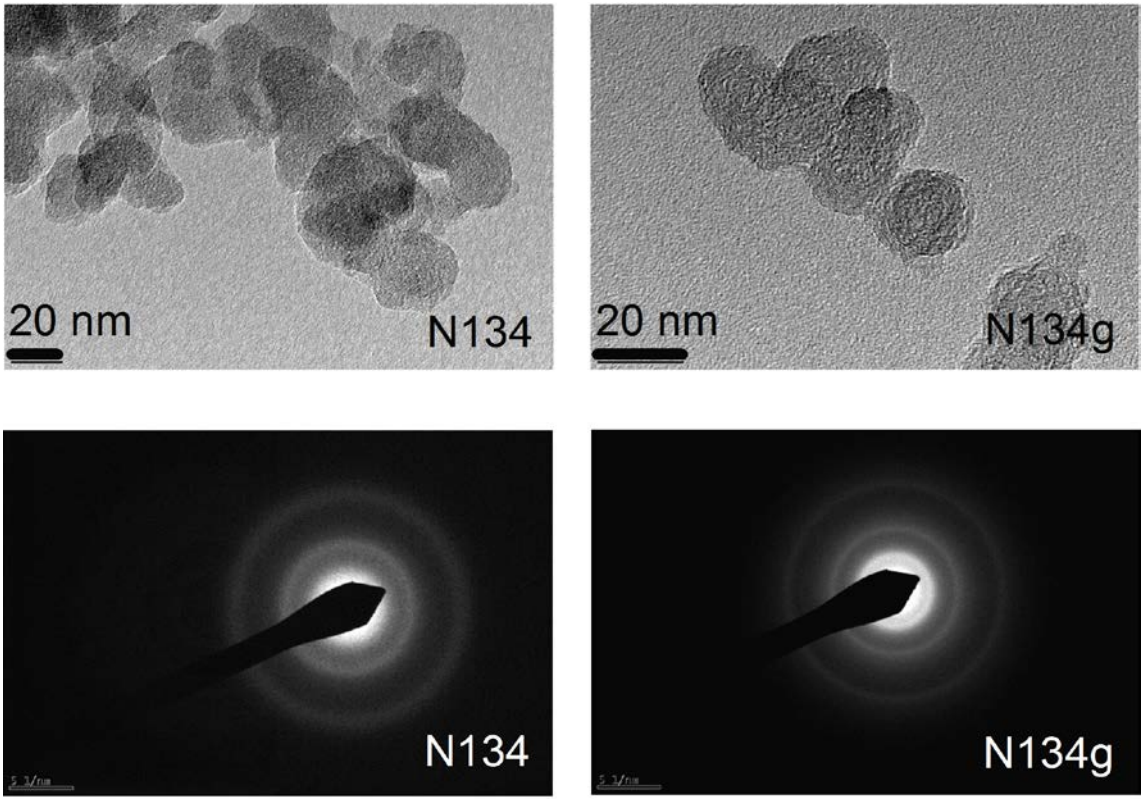

Figure 3.3: Top - high resolution images of primary particle nodules for N134 and N134g. Bottom -local electron diffraction patterns for N134 and N134g

3.1.4. Raman Spectroscopy

The literature background to this technique is provided in the Appendix. Total sample crystallinity was determined by measuring the relative intensities of the D band, centred around 1350 cm^{-1} and the G band, centred around 1580 cm^{-1}. The percentage crystallinity of the carbon was defined as: % crystallinity = I_G / (I_G + I_D) x 100, where I_G and I_D are the areas of the G and D bands. A calibration of this method of crystallinity determination with X-ray diffraction measurements has shown a correlation coefficient of 0.98 [8]. The in-plane crystallite dimension, L_A, was calculated using the formula, $L_A = 43.5(I_D/I_G)^{-1}$ derived by Tuinstra and Koenig [8] for graphite materials and shown to be applicable to microcrystalline carbon black materials by Gruber et al. [9].

Values for total crystallinity and lateral crystallite dimension are given in Table 3.1. Graphitisation results in an increase in total crystallinity and growth of the lateral crystallite size. In the 'as-received' samples crytallinity is higher for the lower surface area carbon blacks in line with the literature [4].

3.1.5. Powder X-ray Diffraction

Powder X-ray diffraction (XRD) patterns were obtained for each carbon black samples between 10° and 40° 2θ on a Bruker D8 Advance diffractometer using nickel-filtered Cu-K_α radiation (wavelength = 0.154 nm). Carbon black samples were back loaded into sample holders, to reduce preferential alignment of particles at the irradiated surface. In addition to carbon black samples, the diffraction pattern of pure graphite (from Sigma Aldrich cod 496588) was also obtained. Diffraction patterns for the carbon black samples are given in Figure 3.4.

The peak in intensity observed around 2θ = 25° results from X-ray diffraction from the basal plane (100) of the graphitic crystal. Figure 3.4 also shows the diffraction of pure graphite powder. As can be seen the graphite peak is significantly more intense than those observed for carbon blacks and apparent at slightly larger values of 2θ. In addition there is a significant background intensity apparent in the carbon black samples. These observations are accounted for as follows:

- The basal peak of graphite is more intense because the sample is entirely crystalline and the crystallites will always be slightly preferentially aligned (which amplifies the basal reflection) due to packing of plate-like particles against a flat surface. In contrast carbon black is only partially crystalline and not plate-like in structure.
- The carbon black basal peaks are shifted to lower values of 2θ because the inter-planar distance (d-spacing) in these samples is larger. 2θ values are related to d-spacing by

$$\sin\theta_{hkl} = \frac{\lambda}{2d_{hkl}} \qquad 3.1$$

  where θ is the Bragg angle, λ is the radiation wavelength and d_{hkl} is the basal spacing. Increased d-spacing in carbon black versus crystalline graphite arises due to interspersion of crystalline domains with amorphous carbon regions. The XRD pattern is an average measurement over all particles and therefore takes non-crystalline regions between graphitic planes into account.

- The additional background contribution to the XRD pattern for the carbon black samples arises from a broad scattering from the amorphous regions of carbon black.

Upon graphitisation the basal reflection of the carbon blacks is observed to narrow and shift to higher 2θ (smaller d-spacing). This is explained simply by an increase in sample crystallinity. Values of graphitic crystallite dimensions in the crystallographic *c*-axis were extracted from the basal reflection using the Scherrer equation [10]

$$L_{\mathrm{C}} = \frac{K\lambda}{\beta \cos\theta} \qquad 3.2$$

where L_C *is* the crystallite dimension along the c-axis, K is a shape factor taken as 0.9, β is the line broadening of the basal peak at half maximum, λ_{WL} is the radiation wavelength and θ is the Bragg angle.

These values are reported in Table 3.1. As can be seen the process of graphitisation results in an increase in crystallite dimension along the c-axis. If the ratio of the lateral and orthogonal crystallite dimensions (L_A/L_C) given in Table 3.1 is considered, it becomes apparent that crystallite growth during thermal treatment proceeds preferentially along the lateral dimension of the graphitic domains.

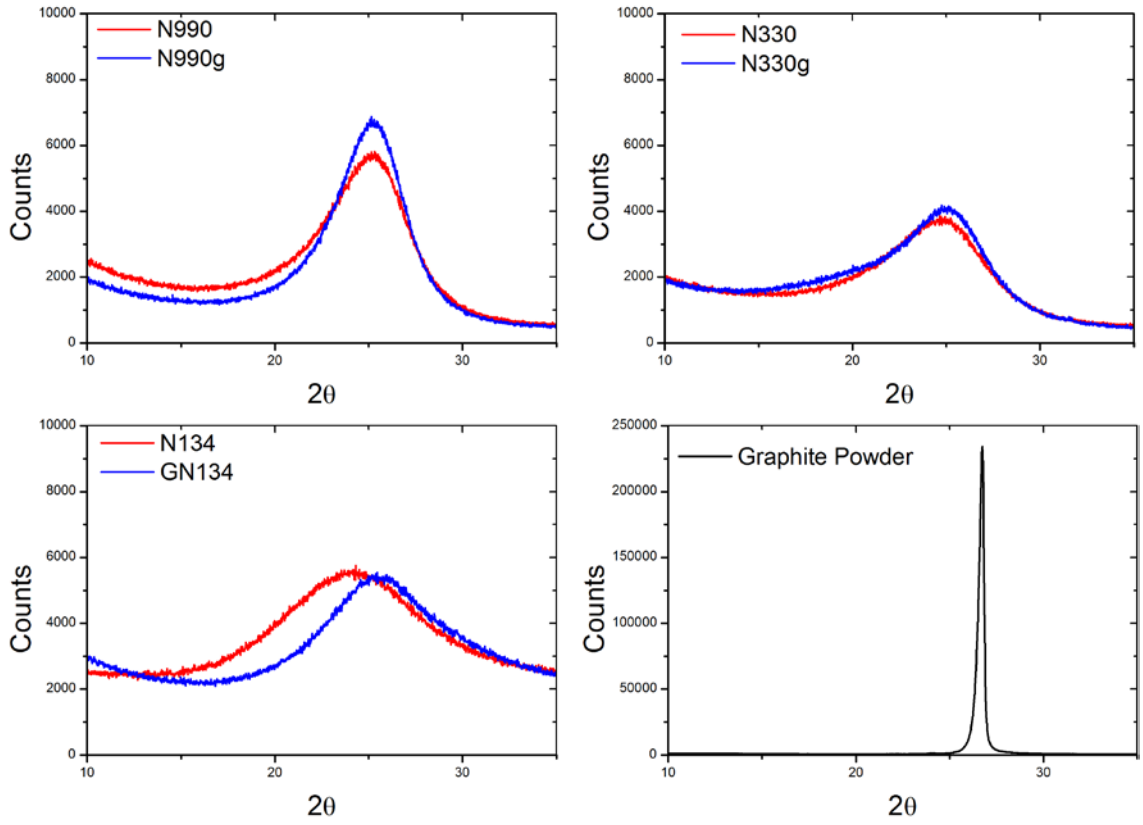

Figure 3.4: Powder X-ray diffraction patterns for carbon black fillers and a sample of pure graphite powder

3.1.6. Surface Free Energy Determination

Surface Free Energy (SFE) is defined in this case as the spreading pressure of water, π_e,

$$\pi_e = \frac{RT}{A}\int_0^{P_0} \Gamma d\ln P \qquad 3.3$$

where R is the gas constant, T is absolute temperature, A is the specific surface area of the test sample, Γ is the amount of adsorbed water in moles per gram, P is the partial pressure of water and P_0 is the saturation vapour pressure.

Adsorption was measured using a Dynamic Vapor Sorption Instrument, manufactured by SMS instruments. 11 partial pressures were used, between 5% and 92% relative humidity, with 20 minutes equilibration at each level. Results are the average of duplicate samples. SFE values are reported in Table 3.1. Surface free energy determination is addressed in more detail in

Appendix I. The SFE values determined by this methods for the unmodified carbon black materials show a slight positive trend as the particle size deceases (surface area increases). This is in line with previous observations [11]. The graphitised carbon blacks all display a significant drop in SFE versus the unmodified materials which is indicative of the graphitisation process significantly reducing the concentration of high surface energy sites.

3.1.7. Helium Displacement Pyconometry

Densities of the graphitized fillers were determined by helium displacement using a Micrometrics AcuPyc 1330 Pycnometer. Graphitised fillers were rapidly transferred from the nitrogen storage atmosphere to a helium displacement cylinder and 10 sequential density determinations were performed. There was no significant drift in the sequential density values obtained indicating that little adsorption of atmospheric moisture onto the filler surfaces had occurred. For the unmodified carbon black samples, a literature value of 1.80 $g.cm^{-3}$ obtained by Donnet [4] from X-ray diffraction measurements was used as this is representative of the skeletal density of the unmodified carbon blacks. Density values are reported in Table 3.1. The graphitisation process results in an increase in the density of the carbon blacks of between 5.6 % and 8.9 %.

3.2. Precipitated Silica-based fillers

Two types of precipitated silica were obtained from commercial suppliers. These silicas corresponded to conventional and highly dispersible precipitated silicas used in the rubber industry: Ultrasil VN2 (in this thesis referred to as CS) and Zeosil 1165mp (hereafter referred to as HDS) respectively.

Table 3.2: Physico-chemical data for the precipitated silica fillers

Filler Code	Manufacturer	Trade name	Surface Area / $m^2.g^{-1}$	Bound Rubber %
CS	Evonik	Ultrasil VN2gr	130	33.26
CS-TEVS	Evonik	Coupsil 6508	126	24.26
HDS	Solvay	Zeosil 1165mp	165	45.47
HDS-TEVS[A]	Solvay[A]	N/A	N/A	41.98

[A]Surface modified during the compounding process

Evonik classify their Ultrasil VN2 silica as a conventional silica and state that '*...due to [a] slightly lower specific surface area Ultrasil VN2 GR has a slightly lower reinforcing potential compared to [highly dispersible grades]...*' [12]. Solvay classify their Zeosil 1165mp product as highly dispersible silica and claim that it '*...is now the world benchmark for low rolling resistance tires...'* [13].

It is widely accepted that polar silica surfaces have a poor interaction with rubber polymer in terms of wettability and adhesion [14] In order to modify the surface activity of the silicas a tri-ethoxyvinyl silane (TEVS) surface treatment was used. The chemical structure of TEVS is given in Figure 3.5. TEVS contains a tri-ethoxy functional group which can react with silanol groups on the silica surface (as outlined in Chapter 2) and also contains a vinyl group which can react with available free radicals during the curing process.

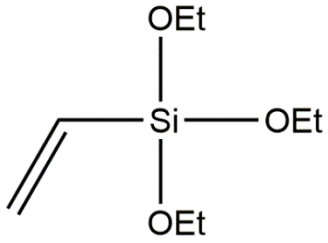

Figure 3.5: Chemical structure of tri-ethoxyvinyl siliane (TEVS)

For the CS sample obtained from Safic Alcan (UK suppliers of Evonik materials) a surface modified version was commercially available (Coupsil 6508). Evonik claim that this material is produced using their conventional silica material which is reacted with TEVS at a silane mass loading of 8 phr. Therefore Coupsil 6508 (hereafter referred to as CS-TEVS) should be expected to retain the morphology of the CS sample but have a different interaction with rubber polymer. In contrast to the CS material, no TEVS-modified analogue of the HDS material was commercially available at the time of writing. Several attempts were made to react HDS material with TEVS through wet chemistry routes (solvent reflux, pot-to-pot distillations etc.) which are not covered in detail. However these techniques were largely unsuccessful for a number of reasons - most commonly that the HDS formed a very compact gel with a number of solvents, rendering distillation and even vacuum distillation of the solvent post processing very difficult. In addition, an even application of TEVS to the silica surface could not be guaranteed using these methods.

In light of these findings it was decided to react the TEVS with the HDS material during compounding of the silica with the rubber in an internal mixer (as outlined in Chapter 2). This had a number of benefits and drawbacks. It was very easy to perform the *in-situ* reaction as will be detailed later; however, the process relies on migration of the silane to the silica surface during mixing. Also loss of silane due to evaporation from the hot mix could not be ruled out. Therefore, unfortunately it was not possible to analyse the effectiveness of the silane functionalisation of the HDS-TEVS surface to the same degree as for CS-TEVS. TEVS addition during compounding was adjusted to maintain the same theoretical surface area concentration as CS-TEVS.

Surface area values for the silicas were determined by the nitrogen BET method discussed earlier and are given in Table 3.2. The silane modification resulted in little change to the silica surface area. TEM images of the silica aggregate morphologies were taken as per the carbon black samples. Images of the silica aggregates are shown in Figure 3.6. Qualitatively, the CS and HDS aggregates appeared very similar. Despite the ultrasonication preparation step, the

non-silanised silica particles appeared to have clustered together, leaving individual aggregates hard to distinguish. In contrast, for the CS-TEVS sample, individual aggregates appear to be well dispersed on the TEM grid with little evidence of clustering. The primary particles and aggregates appear of similar size to those discernible in the CS TEM images.

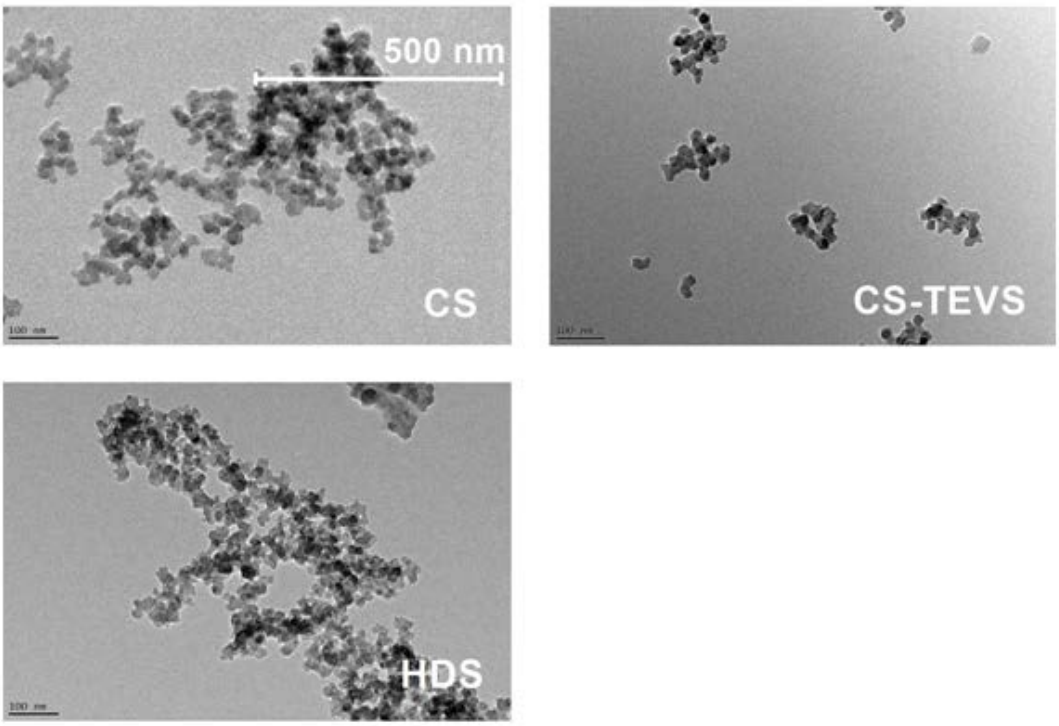

Figure 3.6: TEM images of precipitated silica filler particles. Scale bar is correct for all images.

3.3. Compounding of fillers with Natural Rubber

Following the thermal/surface treatments and characterisation of the carbon blacks and silica fillers they were compounded with CV60 grade NR. Masterbatch compounds were produced for each filler type at a volume fraction loading of 0.20. This is equivalent to a mass loading of 50 phr of unmodified carbon black. For the graphitised carbon blacks, a correction was made to accommodate the slight densification of the carbon black which occurred during thermal treatment. For the precipitated silicas, the density of the amorphous SiO_2 skeleton was taken as 2.0 $g.cm^{-3}$ and mass loadings were corrected to account for this. Corrections were also applied for surface moisture content (measured as percentage weight loss following 12 hours at 110 °C).

The carbon black fillers were all compounded in a Banbury-type Brabender internal mixer equipped with tangential rotors and a mixing chamber volume of 390 cm^3. A constant fill factor

of 0.7 was used for the compounding process. Cleaning and warm up mixes were performed prior to the compounding runs. Initially NR polymer was added at a rotor speed of 70 rpm then filler was added and mixed for 2 minutes. The rotors were stopped and any filler caught on the ram chute was swept down into the mixing chamber. The compounds were then mixed for a further 5 minutes prior to dumping. Dump temperatures ranged from 140 - 160 °C depending on the filler type used. The dumped compounds were then processed on a laboratory 2 roll mill for a further 5 minutes. When lower volume loadings of filler were required, sub-samples of the masterbatch were 'diluted' by back addition of the appropriate amount of NR CV60 on a laboratory 2-roll mill.

All silica samples, excepting HDS-TEVS, were compounded with NR on a laboratory 2-roll mill. During the compounding processes the roller differential ratio was set at 1.25. The HDS-TEVS sample was compounded using the appropriate amount ratio of NR, silica and TEVS in the Brabender internal mixer. To aid the migration of silane to the silica surface, TEVS was stirred into the silica prior to compounding. A 2 stage mix process was used; NR was added to the mix followed by approximately 50 % of the silica/silane mixture. Following a sweep step the remaining silica/silane mix was added and mixing continued for a further 5 minutes. This was done in order to keep the total mix temperature below 160 °C, which is the boiling point of TEVS, but suitably high (>120 °C) to promote the reaction of silane with the filler surface. Following dump at a temperature of 155 °C, the samples were processed on a laboratory 2-roll mill. Again, back addition of NR was performed on the 2-roll mill when samples with lower volume fractions of filler were required.

The dispersion of the filler phase throughout the rubber network was assessed qualitatively, using SEM. This analysis was performed on samples crosslinked after compounding as it was found that imaging of uncured compounds in the SEM tended to suffer from significant defocusing arising from the relaxation and creep of the compound induced by stresses and strains imposed during sample preparation. In order to assess the filler dispersion within the bulk of the compound, the crosslinked compounds were submerged in liquid nitrogen for 1 minute and then fractured with pliers. Fracturing below the polymer T_g provides a more representative surface for analysis as ambient temperature fracturing inevitably results in the application of large strains to the compound and can tear the surface. The fracture surface was mounted face-up on an SEM stub with conductive carbon cement then coated in gold and analysed using an FEI Inspect SEM using secondary electron imaging at a variety of magnifications.

Representative SEM images of the filler dispersions at the highest magnification level used are presented in Figure 3.7 for the carbon black-filled compounds. As can be seen for the high surface area carbon black fillers the compounded particle sizes were qualitatively broadly equivalent. Examination of the fracture surfaces at lower magnifications (not shown) showed almost no agglomerates of carbon black larger than 1 μm. The macrodispersions of these carbon blacks are seemingly equivalent. Note that due to the larger particle size of N990 carbon black the magnification factor in Figure 3.7 E&F is smaller for these compounds. Fracture surfaces for the silica-filled compounds are presented in Figure 3.8. For the non TEVS-treated compounds, the polymer appeared to have de-bonded from the silica surface during fracture, revealing the agglomerated filler microstructure below. For samples with a TEVS surface treatment the imaging suggested that the treated filler was better wetted by the polymer.

Prior to the addition of curatives the masterbatch compounds were analysed for 'bound rubber' content. As described in Chapter 2, the bound rubber content is defined as the total percentage of polymer in the uncured state, which cannot be extracted by solvent under stated conditions (temperature, time of extraction, solvent type etc.). The molecular origins of bound rubber are complex and appear to be related to topological constraints at the filler surface and physical binding of polymer chains to the filler surface [15-17] but the phenomenon correlates extremely well with the reinforcing potential of various fillers [18] and provides an indirect assessment of the rubber-filler interaction.

To assess bound rubber content in these compounds small (~1 g) samples were taken from the masterbatches, weighed on an analytical balance then cut into smaller sections. These were then loaded into small cages made from '200 mesh' steel gauze and immersed in 100 ml of toluene at room temperature for 5 days. After 2 days the solvent was refreshed. At the end of the 5 day extraction period, a gel formed of filler and non-soluble or 'bound' rubber remained. This gel was dried in air and then in a vacuum oven at 80 °C. Bound rubber was defined as the mass of non-extractable as a percentage of total rubber content of the samples. Three repeats were performed per compound and the averages of these results are reported in Table 3.1 for the carbon black-filled compounds and Table 3.2 for the silica-filled compounds. A number of studies have noted that post-mixing storage of filled compounds can significantly increase the amount of bound rubber. To avoid this complication in these tests, the masterbatch subsamples were run through the 2-roll mill three times and tested immediately following this high shear pre-treatment. It is clear from the bound rubber values for the carbon black-filled

compounds that the bound rubber decreases upon graphitisation - potentially indicating a reduced rubber-filler interaction.

The N990-filled compounds disintegrated when exposed to the solvent for 5 days, so their values cannot be reported. This was due to N990 being loaded substantially below its critical gel point [19], which is related to the formation of a percolating filler network. This topic will be addressed in more detail in Chapter 6.

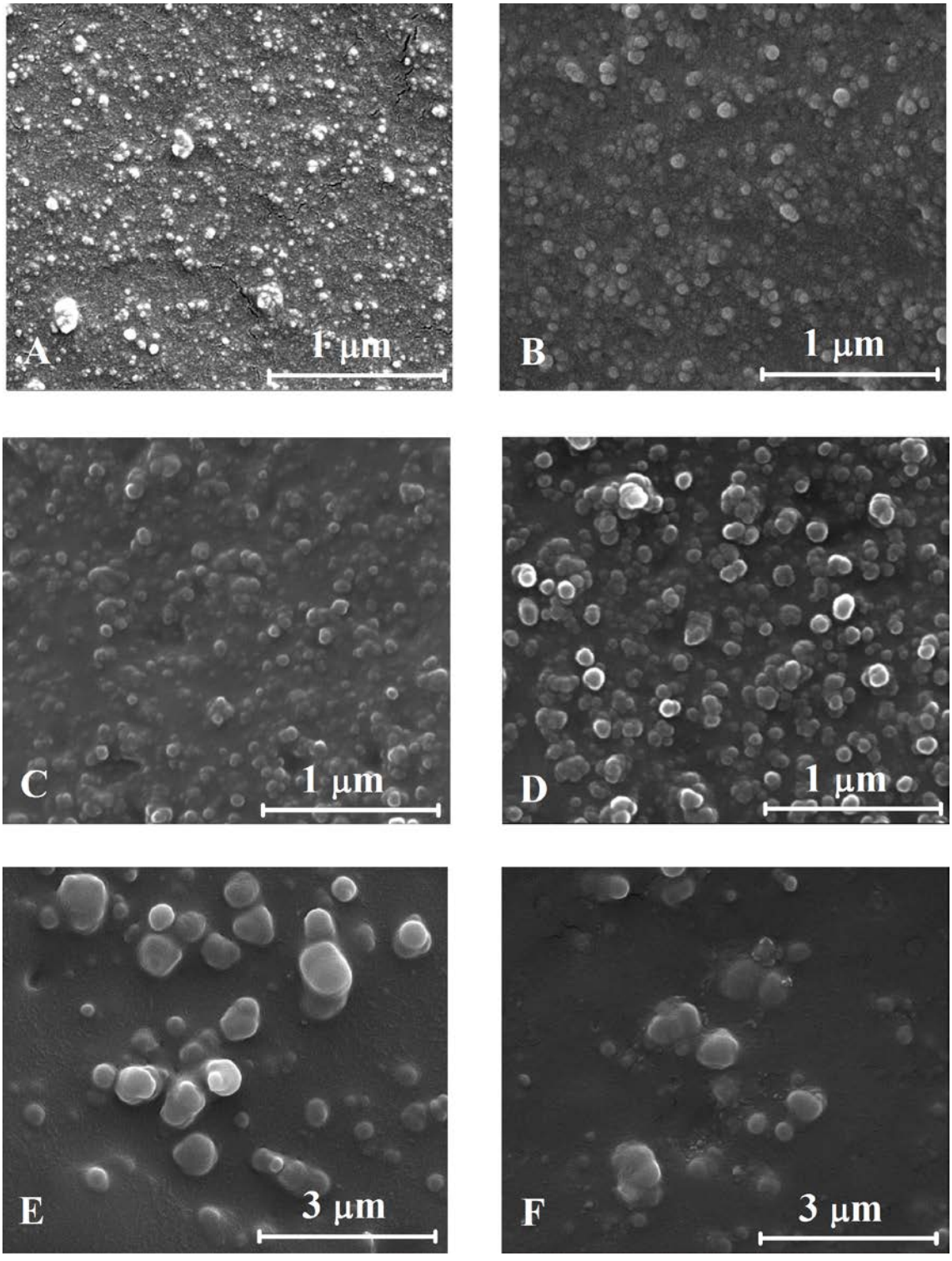

Figure 3.7: SEM images of carbon black-filled compound liquid nitrogen fracture surfaces**.** A) N134, B) N134g, C) N330, D) N330g, E) N990, F) N990g

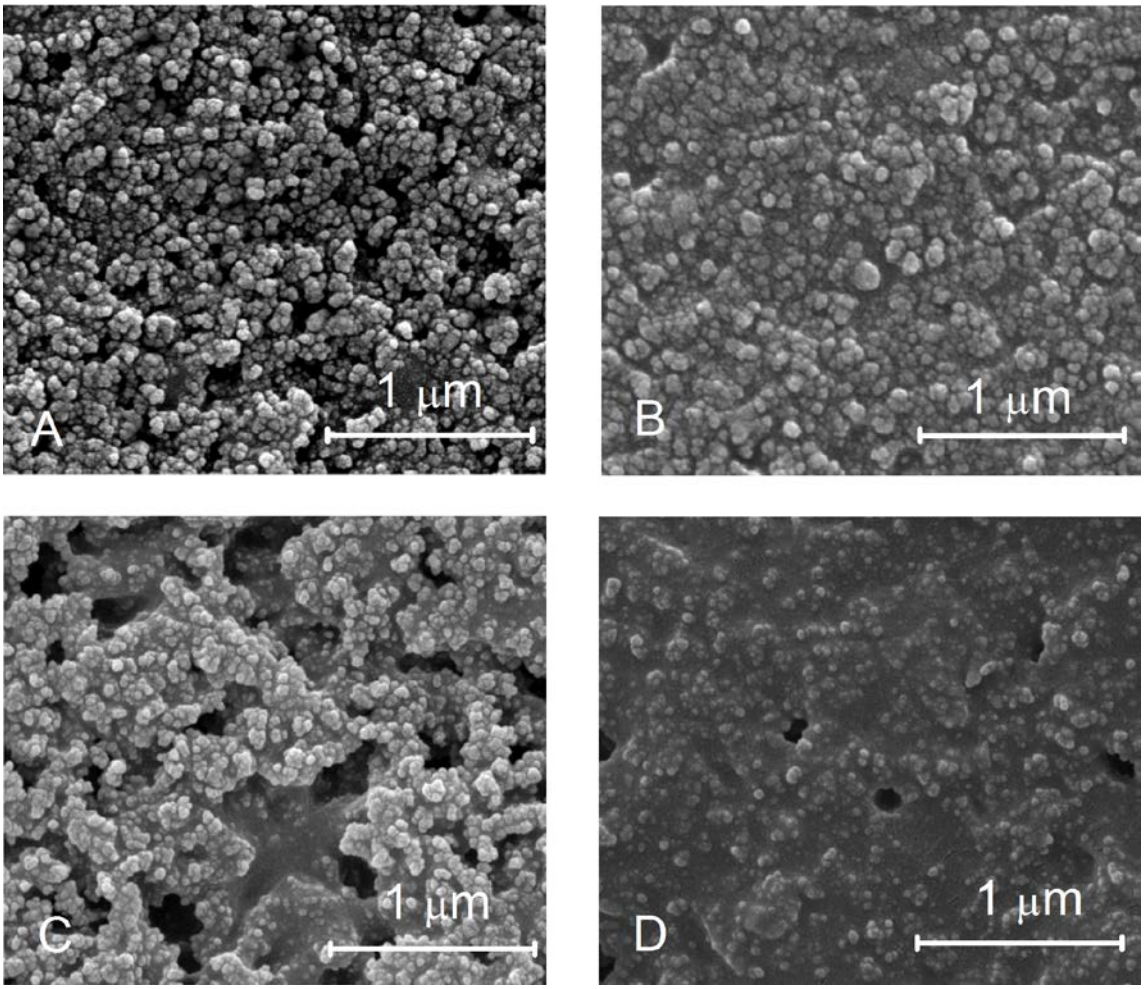

Figure 3.8: SEM images of precipitated silica-filled compound liquid nitrogen fracture surfaces

For the silica-filled compounds the amount of bound rubber was seen to decrease following TEVS surface treatment. This is perhaps unexpected, given that for the carbon black-filled compounds it was observed that a reduction in rubber-filler affinity (graphitisation) resulted in a decrease in bound rubber. One potential explanation for this observation might be the effect of TEVS on the nature of the filler structure formed in the compound. It is often reported that unmodified silica can form a tightly agglomerated network of particles in rubber melts and compounds. The mechanical strength of these networks often exceeds those of analogous carbon black networks as evidenced by the increase in the limiting strains for small strain linear elastic behaviour in quasi-static tensile testing [20].

One explanation for the strength of filler networks is the establishment of hydrogen bonds between the silanol groups of neighbouring silica particles. A consequence of the silane

treatment of silicas is that the concentration of surface silanol groups is reduced and the surface of silica is partially shielded by the silane tail - thereby reducing the attractive forces between particles in the melt. The origin of the unusual bound rubber results may be related to the degree of occlusion of rubber polymer from the solvent extraction process by the rigid, agglomerated silica network; upon treatment with TEVS the silica is far better dispersed throughout the rubber phase thus reducing the proportion of the polymer occluded from the extraction process.

3.4. References

[1] N990 Physical and Chemical Properties PDF available from:, http://www.cancarb.com/docs/pdf/Physical_Chemical_Properties.pdf, Access Date: 19/6/15
[2] VULCAN® 3 ASTM Industry Reference N330/HAF, http://www.cabotcorp.com/solutions/products-plus/carbon-blacks-for-elastomer-reinforcement/reinforcing, Access date 19/6/15
[3] VULCAN® 10H ASTM Industry Reference: N134, http://www.cabotcorp.com/solutions/products-plus/carbon-blacks-for-elastomer-reinforcement/reinforcing, Access date 19/6/15
[4] J.B. Donnet, Rubber Chemistry and Technology, 71 (1998) 323-341.
[5] W.D. Schaeffer, W.R. Smith, M.H. Polley, Industrial and Engineering Chemistry, 45 (1953) 1721-1725.
[6] W.D. Schaeffer, W.R. Smith, Industrial and Engineering Chemistry, 47 (1955) 1286-1290.
[7] R.W. DH Everett, Journal of Chemical Society: Faraday Transactions I, 82 (1986) 2915-2928.
[8] F. Tuinstra, J.L. Koenig, Journal of Chemical Physics, 53 (1970) 1126-&.
[9] T. Gruber, T.W. Zerda, M. Gerspacher, Carbon, 32 (1994) 1377-1382.
[10] P.Z. V. Pecharsky, Fundamentals of powder diffraction and structural characterisation of materials, 2nd ed., Springer, New York, 2009.
[11] J.B. Donnet, R.C. Bansal, M.J. Wang, (Eds), Carbon Black: Science and Technology, 2nd ed., Marcel Dekker Inc, New York, 1993
[12] ULTRASIL® VN 2, http://ultrasil.evonik.com/www2/uploads/productfinder/ULTRASIL-VN-2-EN.pdf, Access date 19/6/15
[13] Zeosil® http://www.solvay.com/en/markets-and-products/featured-products/zeosil.html, Access date 19/6/15
[14] K.W. Stöckelhuber, A.S. Svistkov, A.G. Pelevin, G. Heinrich, Macromolecules, 44 (2011) 4366-4381.
[15] J.L. Leblanc, Progress in Polymer Science, 27 (2002) 627-687.
[16] J.L. Leblanc, Journal of Applied Polymer Science, 66 (1997) 2257-2268.
[17] J.L. Leblanc, B. Stragliati, Journal of Applied Polymer Science, 63 (1997) 959-970.
[18] E.M. Dannenberg, Rubber Chemistry and Technology, 59 (1986) 512-524.
[19] S. Wolff, Rubber Chemistry and Technology, 69 (1996) 325-346.
[20] D.K. De, Ph.D Thesis: Queen Mary and Westfield College, London, 1994.

Chapter 4

Elastomer Network Characterisation

Précis:

This thesis is primarily concerned with the linear viscoelastic properties of filled rubber networks. Prior to a detailed examination of the viscoelastic properties of the filled compounds an effort is made to characterise the network structures of both filled and unfilled, peroxide-crosslinked rubbers to determine the key structure-property relationships in order to better understand the viscoelastic responses of such polymer networks.

Traditionally, information about the nature of the network structures of crosslinked rubbers has been obtained experimentally through quasi-static mechanical testing or equilibrium solvent swelling (reviewed in Chapter 2). However these types of analyses only provide a limited amount of information about the network structure and rely on assumptions implicit in the derivation of the respective models. For the case of filled networks this situation is complicated even further by the degree of interfacial restriction imposed on the elastomer network by the rigid inclusions. The Mooney-Rivlin analysis of tensile mechanical properties of entropically elastic networks, often used to determine the crosslink density of unfilled elastomers, fails to take into account the hydrodynamic and filler networking reinforcement effects of particulates on the bulk elasticity. De-convolution of crosslink-induced stiffening from filler-induced stiffening is very difficult if not impossible. Similarly the Flory-Rehner treatment of equilibrium solvent swelling of entropically elastic networks does not take into account any restriction of the three dimensional swelling capacity of elastomer in the vicinity of the filler particles. Thus application of these analyses to filled networks yields an 'apparent' crosslink density value which is in reality a concatenation of network structure, filler structure and filler-elastomer interaction effects.

In order to examine network structures in greater detail than these traditional techniques allow, a series of additional, complimentary experimental techniques are employed including *in-situ* DSC curing experiments, ^{13}C-NMR and a low field ^{1}H-NMR technique which allows

access to a wide range of quantitative information about rubber network structures; even when those networks incorporate filler particles.

This chapter is split into two sections. The first section (Section A) addresses the characterisation of unfilled rubbery networks in order to understand the crosslinking system in more depth and identify an optimum state of crosslinking with which to conduct further experiments. It is found that the NR-peroxide cure system produces networks with a high degree of inhomogeneity in terms of the spatial distribution of crosslinks. This was particularly pronounced when larger initial concentrations of peroxide curative are used. A loading of 2 phr peroxide is found to provide optimum mechanical properties and maximum network heterogeneity.

The second section (Section B) examines the influence of particulate fillers on the natural rubber network structures and assesses the affinity of the elastomer matrix for the filler surfaces by the evaluation of the degree of restriction in equilibrium swelling imposed upon the elastomer matrix by the filler-elastomer interface. Carbon blacks and silicas are found to have a detrimental impact on the final yield of crosslinks in peroxide systems. The severity of the reduction in crosslink yield depends on the surface area and surface activity of the particles. For the carbon black-filled series of samples, the degree to which the filler particles impose a restriction of the solvent swelling capacity in the vicinity of the particles does not scale as a function of the nitrogen surface area of the particles, but rather as a function of a reduced surface area calculated from TEM estimates of the average aggregate size. The results show clear differences between unmodified and graphitised carbon blacks in terms of the degree of adhesion of rubber to the filler surface.

Some of this work is in preparation for publication as: LB Tunnicliffe, JL Valentín, A González-Jiménez, AG Thomas, JJC Busfield, *Network Structures and Interfacial Properties of Filled, Peroxide-Crosslinked Natural Rubber,* 2015.

Some of this work is in preparation for submission to a peer reviewed journal as: LB Tunnicliffe, JL Valentín, A González-Jiménez, AG Thomas, JJC Busfield, *Inhomogeneities in the Network Structures of Peroxide-Crosslinked Natural Rubbers,* 2015.

Chapter 4: Section A - Unfilled networks

For all the samples reported on in this thesis, the crosslinked rubbery component comprised peroxide-crosslinked natural rubber (NR). The NR grade used was Standard Malaysian Rubber (SMR), constant viscosity, 60 Mooney viscosity units (CV60) obtained from the Tun Abdul Razak Research Centre (TARRC), Hertfordshire, England.

The peroxide used to crosslink the NR was dicumyl peroxide (DCP) obtained from Fisher Scientific at 99 % purity. The chemical structure of DCP is given in Figure 4.1. This particular peroxide has a 10 hour half-life of 114 °C meaning that thermal treatment of the peroxide at 114 °C for 10 hours results in 50 % decomposition of the peroxide [1]. DCP is thermally stable at room temperature (melting point = 40 °C) with decomposition occurring only at elevated temperature (i.e. under curing conditions). Decomposition of the peroxide during compounding with rubbers on the 2-roll mill (T < 80 °C) is also expected to be negligible. An initial investigation was performed in order to better understand the relationships between peroxide crosslinking reaction mechanisms, network structures and material mechanical properties, initially for unfilled networks.

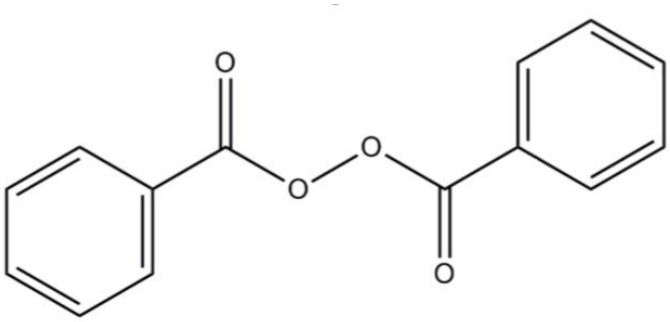

Figure 4.1**:** Chemical structure of dicumyl peroxide (DCP)

4(A).1. Compounding and crosslinking of unfilled samples

Unfilled NR was compounded on an open 2-roll mill with various loadings of DCP (Table 4.1). Following compounding, the samples' cure characteristics were determined on an Alpha Technologies Moving Die Rheometer (MDR) 2000. The MDR compresses an un-crosslinked rubber sample between two serrated plates and subjects the sample to a constant dynamic

Table 4.1: DCP loadings and corresponding concentrations. Crosslink densities determined via three experimental techniques

DCP Loading/ phr (parts per hundred rubber)	[DCP] x10^5 / mol.g^{-1}_{Rubber}	Tensile Crosslink Density, $\nu_{Tensile}$, x10^4 / mol.g^{-1}_{Rubber}	Swelling Crosslink Density, $\nu_{Swelling}$, x10^4 / mol.g^{-1}_{Rubber}	Average† NMR Crosslink Density, ν_{NMR}, x10^4 / mol.g^{-1}_{Rubber}
0	0	-	-	-
0.5	1.8	0.300 ± 0.007	0.1517 ± 0.0002	1.11
1.0	3.7	0.490 ± 0.002	0.3570 ± 0.0018	1.41
2.0	7.4	0.890 ± 0.040	0.7943 ± 0.0015	1.99
3.0	11.1	1.350 ± 0.012	1.2932 ± 0.0058	2.46
4.0	14.8	1.830 ± 0.082	1.8026 ± 0.0100	3.00
5.0	18.5	2.345 ± 0.047	2.3258 ± 0.0042	3.41

.

†In this sense the 'average' is the average crosslink density value of the spatial distribution of crosslinks rather than an average of experimental repeats

shear strain of 2.7 %. The plates are pre-heated to the temperature of interest and dynamic torque, S', is recorded as a function of time.

For the case of unfilled materials the increase in dynamic stiffness as a function of time can be directly related to the formation of network crosslinks within the sample. The resulting torque-time plots can be used to determine various curing parameters for the rubbers. Each of the unfilled compounds were tested using the MDR at a plate temperature of 150 °C and a frequency of 1.5 Hz for a total time of 3 hours. The recorded data traces are presented in Figure 4.2 and show a sharp increase in torque as a function of time following a short induction period followed by a pseudo-plateau stage where the torque increases very slowly with time. The pseudo-plateau stage corresponds to the near-complete decomposition of DCP and maximum formation of crosslinks. In reality the true torque plateau is only obtained at extremely long curing times, so here the torque measured at three hours was approximated to T_{100} (i.e. 100 % formation of crosslinks).

If the cure traces are suitably normalised (Figure 4.3) then it becomes apparent that there is little change in the overall kinetics of the process as a function of initial DCP concentration. Therefore a universal curing time for all samples of 100 minutes was selected which corresponds in each sample to $>T_{96}$. It is also worth noting that the magnitude of the torque in the pseudo-plateau stage scales linearly with initial peroxide content - indicating the expected increase in modulus with increasing crosslink density (Figure 4.4). The linear trend shown in Figure 4.4 extrapolates the plateau torque value down to a finite value of torque at [DCP] = 0 mol/g. Since $S' \propto G'$ this finite torque relates to a finite modulus in un-crosslinked rubber which is associated with network entanglements and the entropic elasticity of the un-crosslinked NR molecules.

Crosslinked samples for experimental investigations were then prepared on a laboratory hotpress at platen temperatures of 150 °C. Sheets of crosslinked sample (2 mm thick) were prepared via compression moulding at a pressure of 6.3 MPa (40 ton load on 8 inch diameter ram). The compression mould measured 230 x 250 mm in area and had cavities for 6 sheets of rubber measuring 100 x 25 x 2 mm. Experimental samples were stamped from these thin sheets as required.

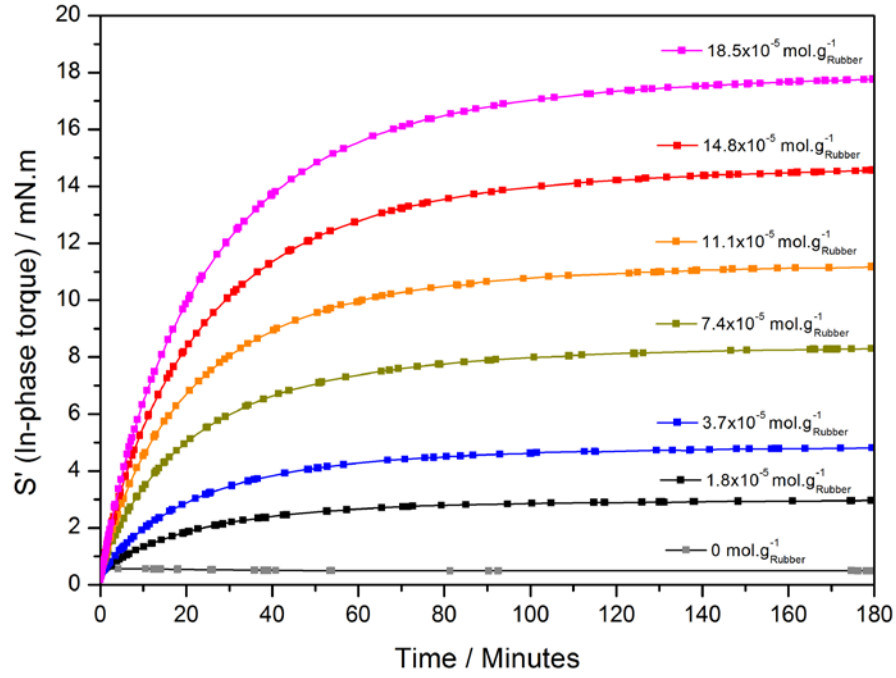

Figure 4.2: Cure rheometry of unfilled NR at 150 °C labelled with the corresponding initial concentrations of DCP

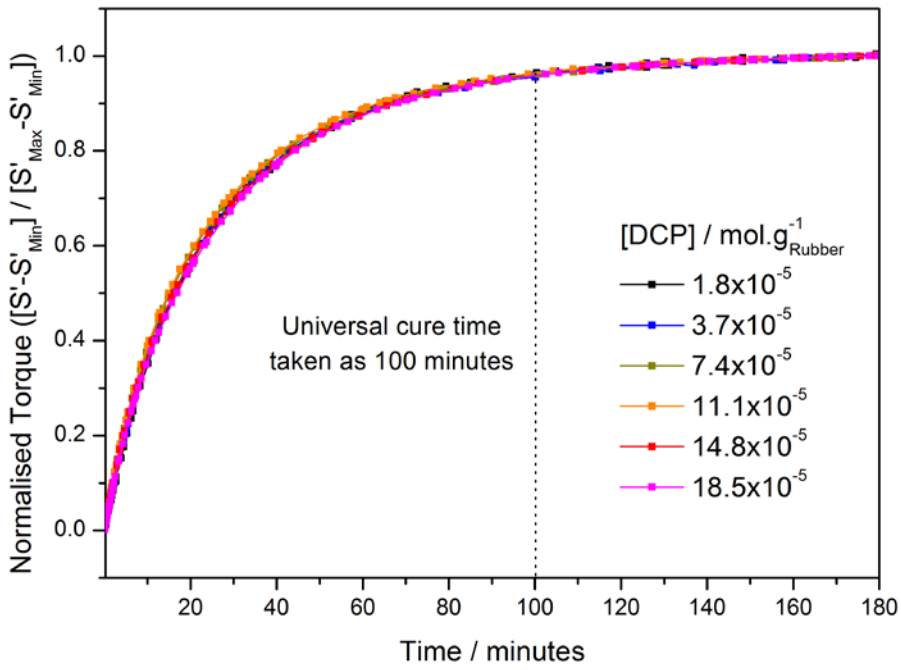

Figure 4.3: Normalised cure traces showing the universal cure time, T_{96}, of 100 minutes

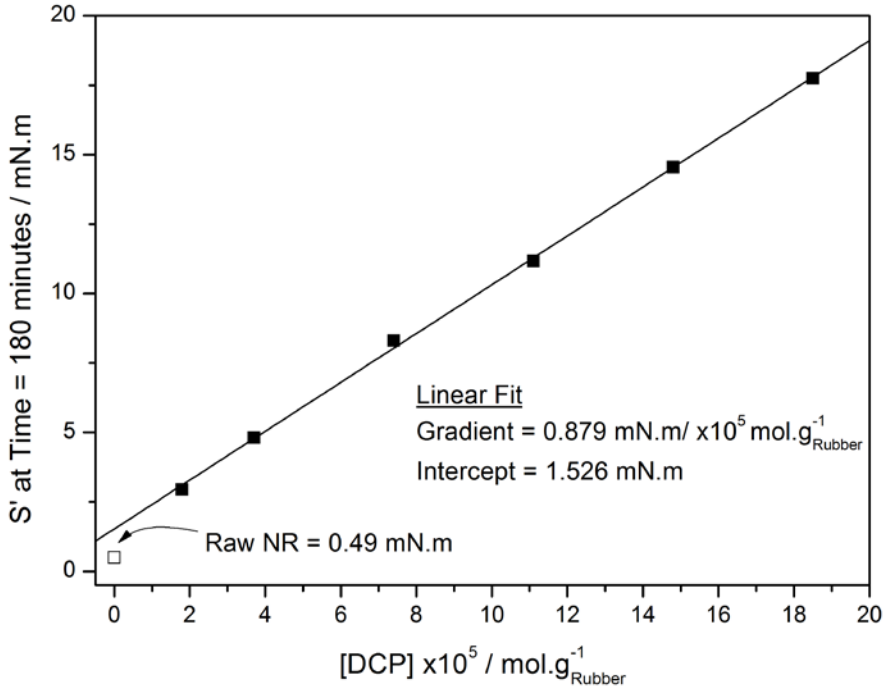

Figure 4.4**:** Pseudo-plateau torque from the cure traces plotted versus peroxide concentration. The solid line is a linear fit to the solid data points. The hollow symbol is the experimental datum for NR with no peroxide crosslinking agent which is not included in the linear regression

4(A).2. Crosslinking thermodynamics

In order to characterise the crosslinking reactions, DSC experiments were performed on samples of uncured material loaded with various amounts of DCP. Small samples (~10 mg) were heated in aluminium crucibles from room temperature to 250 °C at a rate of 5 K/minute under a nitrogen atmosphere. In the resulting heat flow-time (or heat flow-temperature) traces an exotherm is evident at around 175 °C. Example data are presented in Figure 4.5. It is likely that this exotherm corresponded to the formation of network crosslinks - note that the NR sample containing no DCP did not display this distinctive exotherm.

To confirm this, the samples were collected following the DSC experiments and immersed in excess toluene for 5 days. The samples were all observed to swell rather than dissolve; which is characteristic of crosslinked rubbers. After 5 days the swollen samples were removed and dried, first in air and then in a vacuum oven at 80 °C for 1 hour. The total weight loss for the samples during the swelling process was less than 5 % which is in line with values determined for traditionally crosslinked samples. Therefore substantial amounts of network crosslinks were formed during the DSC experiments. However, these DSC experiments do not fully

simulate the curing process outlined in the previous section as the DSC tests were a) non-isothermal and b) performed at atmospheric pressure. They can however be used to characterise and examine the crosslinking thermodynamics evident under the DSC experimental conditions.

The exotherms were integrated versus a time axis using consistent integration time axis limits. The resulting energy values were then normalised to the weight of NR in the samples. Weight of NR was calculated taking into account the theoretical weight of DCP present in each sample. Each loading of DCP was tested 5 times and average values were calculated. Variation in values between repeats was found to be around ±1 % of the average value.

It is possible to quantitatively assess these reaction enthalpy values using a simple bond dissociation model of the peroxide crosslinking process. Values of the relevant Bond Dissociation Energies (BDE's) were taken from Bach et al. [2], Dluzneski [1] and Atkins [3]. The full mechanistic details of the proton abstraction reaction mechanism are presented in Chapter 2 (Figure 2.24). This can also be viewed in terms of BDE's for each process to generate a theoretical reaction enthalpy on a DCP molar basis for formation of crosslinks (Figure 4.6). Note that this theoretical enthalpy corresponds to the idealised case of purely abstraction-route crosslink formation.

Experimental and theoretical reaction enthalpies are plotted versus DCP concentration in Figure 4.7. Note that maximum and minimum theoretical enthalpy trends are reported, corresponding to the upper and lower limits of the literature values for the bond dissociation values. It is clear from Figure 4.7 that although the experimental enthalpies were in good agreement with theory at lower DCP concentrations, there was an increasing positive divergence from theory at higher DCP concentrations. This may be due to the inability of the very simple reaction model to account for enthalpic transitions associated with side reactions such as chain scission and pseudo-polymerisation of polymer macro-radicals which follow very different thermal reaction profiles.

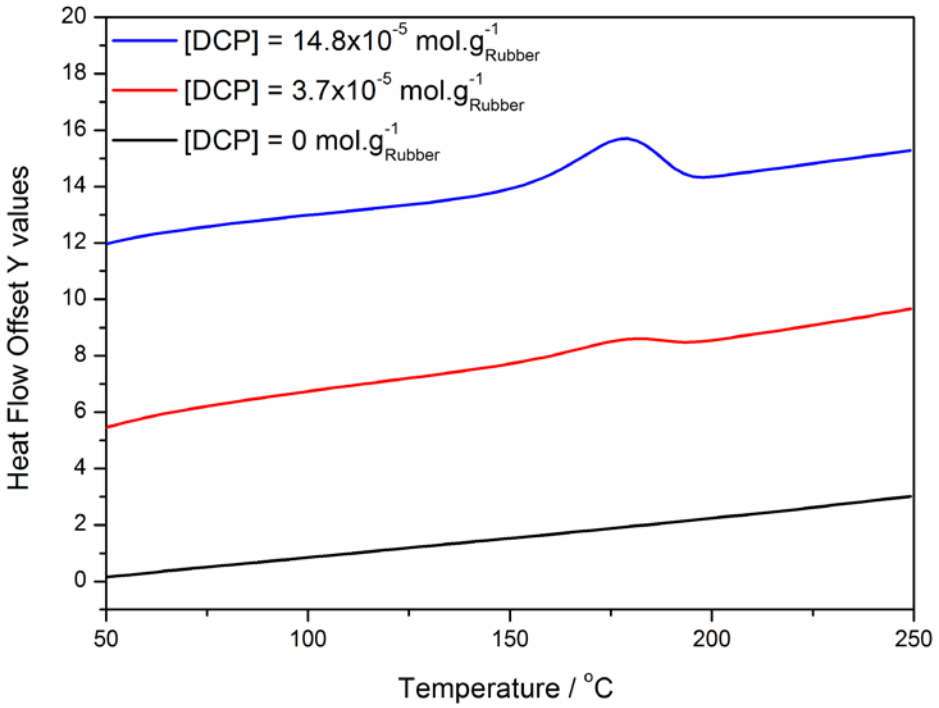

Figure 4.5: Example DSC traces for NR with various concentrations of DCP. Note that the symbols are a guide for the eye rather than data points.

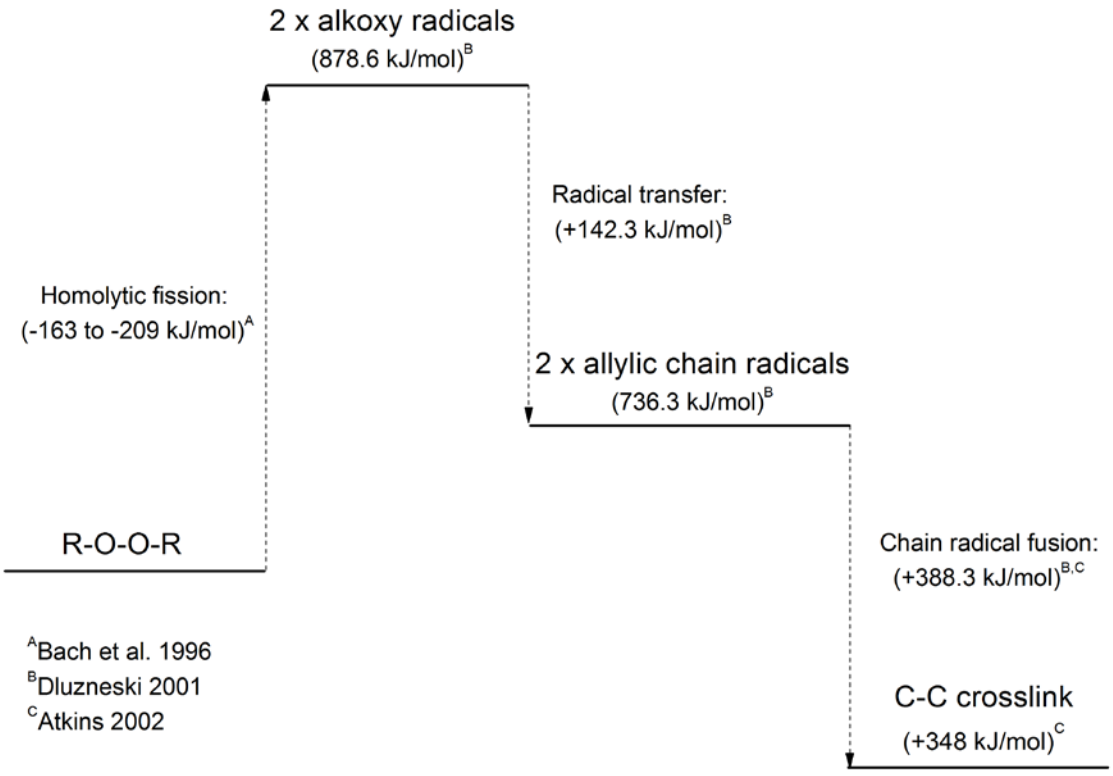

Figure 4.6: Schematic bond dissociation model of the abstraction mechanism of crosslink formation in unsaturated polyolefins (net exotherm = between +321.6 and +367.6 kJ/mol)

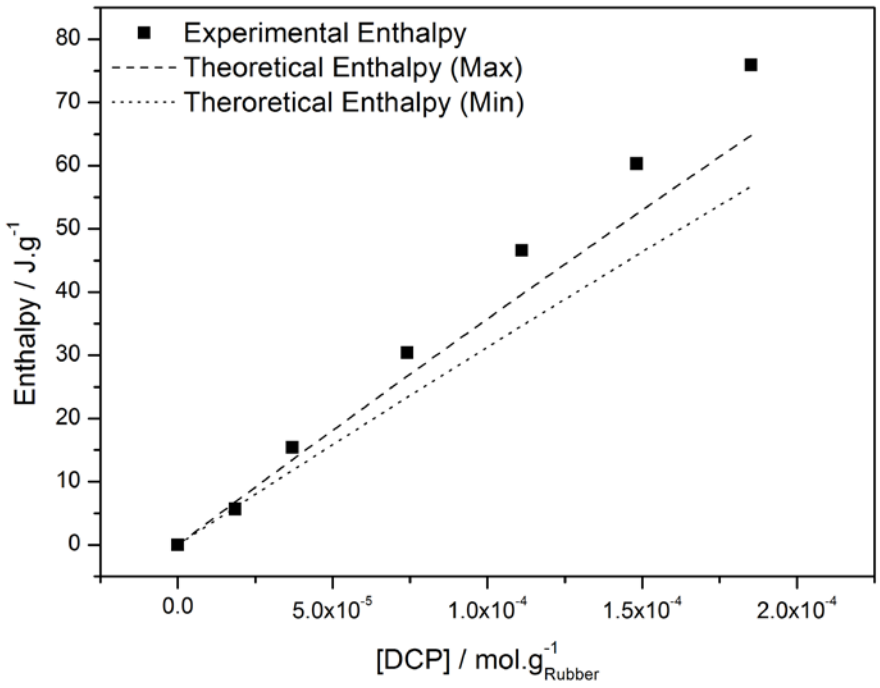

Figure 4.7**: E**xperimental and theoretical reaction enthalpies versus DCP concentration

4(A).3. Characterisation of network structures

4(A).3.1. Equilibrium solvent swelling

Average crosslink density values were determined using equilibrium solvent swelling experiments. The Flory-Rehner relationship was used to calculate the crosslink density from weight uptake data [4]. Swelling experiments were performed in a fumehood in a temperature controlled laboratory using toluene solvent. Samples of crosslinked rubber (~0.2 g) were immersed in 100 ml of toluene and then removed every 24 hours and weighed after ensuring that excess solvent at the sample surface was removed by lightly dabbing the surface with tissue. This process was repeated for 84 hours during which time solvent uptake equilibrium was reached. During this period the samples were stored in the dark to avoid photo-oxidative breakdown of the polymer networks [5]. Three repeats were performed per sample.

In order to define the crosslink density, ν, the affine description of network elasticity was used. The polymer-solvent interaction parameter for NR-toluene mixtures was taken as $\chi = 0.393$ [4] and NR density was taken to be $\rho = 0.92$ g.cm^{-3} [5]. Average crosslink density values were calculated from the Flory-Rehner equation (Equation 4.1) arranged to give ν in units of mol/g.

$$\nu = \frac{1}{2M_C} = \left(-\frac{1}{2V_S} \frac{\ln(1-\varphi_2) + \varphi_2 + \chi\varphi_2^2}{\varphi_2^{1/3} - \varphi_2/2} \right) \frac{1}{\rho_r} \quad 4.1$$

where M_C is the molecular weight between crosslinks, V_S is the molar volume of toluene, $\varphi_2$is the volume fraction of rubber in the swollen sample at equilibrium, χ is the polymer-solvent interaction parameter and $\rho_r$is the density of NR. Values are reported in Table 4.1 and, as expected, the crosslink density increases with increasing initial concentration of DCP curative.

4(A).3.2. ^{13}C-Magic Angle Spinning (MAS)-NMR

Solid state, proton-decoupled ^{13}C-MAS-NMR was used to investigate the specific chemical environments of NR backbone carbon atoms in fully cured samples. A theoretical background to this technique is given in the Appendix. A 600 MHz Bruker NMR spectrometer with a ^{13}C 4 mm solid state probe was used to collect NMR data. Samples of the crosslinked rubbers were loaded into tubes using glass beads as a packing material to fill air voids and reduce sample movement during magic angle spinning. Samples were spun at 800 Hz with high power proton decoupling for 512 scans with an 8 second relaxation delay. The tip angle was 90°.

Examples of the ^{13}C-NMR spectra are presented in Figure 4.8. The spectra have been arbitrarily normalised to the intensity of the allylic peak at 135.33 ppm. Peak positions are in exact correlation with previously published data [6] and have been assigned to NR backbone carbons in the inset of Figure 4.8. Closer examination of peaks in the alkyl region of the spectra shows the evolution with increasing peroxide concentration of peaks corresponding to the *trans* isomeric form of polyisoprene (16.53 ppm, 40.83 ppm) [6], indicating that substantial main chain modification and isomerisation has taken place.

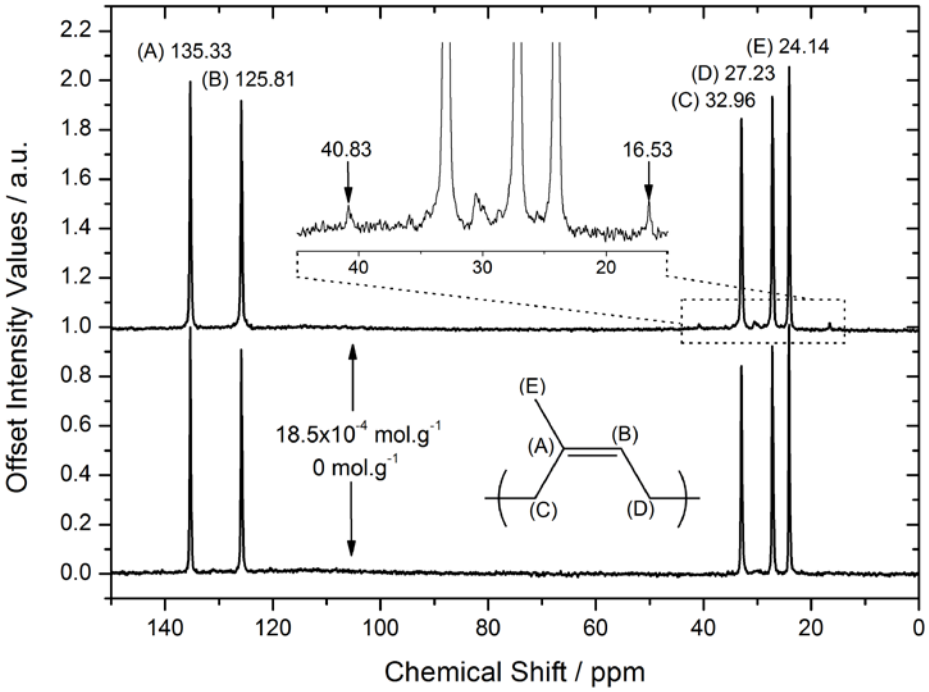

Figure 4.8**:** Example NMR spectra for un-crosslinked and highly crosslinked NR (concentration values refer to initial concentrations of DCP prior to curing). Insets: assignment of main peaks to the NR backbone carbon atoms and magnification of the alkyl region of the spectrum

4(A).3.3. ^{1}H-Double Quantum (DQ)-NMR

The theoretical background and data analysis principle for this NMR technique is presented in detail in the Appendix. The experimental procedure was as follows.

Time-domain ^{1}H NMR measurements were performed on a low-field Bruker Minispec mq20 spectrometer at 20 MHz proton resonance frequency (0.5 T) with 90° pulses of 3 µs length and a dead time of 12 µs. The sample temperature (80 °C) was controlled with a BVT3000 heater working with air.

In this high temperature regime, the normalisation procedure (widely detailed in the literature [7, 8]) allows for a separation of the temperature-independent network structure effect from the temperature dependent segmental dynamics that are convoluted within the experimental NMR data. In this way, the obtained normalized DQ intensity (I_{nDQ}) is analysed via a regularisation process to determine the actual distribution function of residual dipolar couplings for rubber samples, yielding information on their spatial distribution of cross-links [9]. The relationship between the measured residual dipolar couplings and the molecular weight between constraints (M_c) for natural rubber was determined by assuming a reasonable

model for the intrasegmental motions and applying spin dynamics simulations (obtaining apparent reference couplings for the NMR sub-molecule in static conditions) in addition to a proper definition for the statistical (Kuhn) segments between constraints (based on the definitions of Flory's characteristic ratio and the Kuhn segment length): $M_c = \frac{617\ \text{Hz}}{D_{\text{res}}/2\pi}$ kg/mol. Assuming tetra-functional junctions, the cross-link density was calculated according to the equation: $\nu_{NMR} = \frac{1}{2M_c}$. Average values of the obtained crosslink distributions are presented in Table 4.1. The average crosslink density values are seen to increase with increasing initial DCP curative concentration. They are also observed to be systematically larger than those determined from tensile and mechanical measurements.

The spatial distributions of crosslink density are presented in Figure 4.9 and Figure 4.10. From examination of the distributions plotted on a linear x-axis (Figure 4.9) it is clear that increasing concentrations of peroxide resulted in a more heterogeneous, broadened distribution of crosslinks. At the highest levels of peroxide loading, very densely crosslinked regions could be observed of nearly three times that of the average network crosslink density. Furthermore, examination of the distributions plotted using a logarithmic x-axis (Figure 4.10) also reveals a broadening towards lower crosslink densities at the highest levels of peroxide loading. This has been interpreted as indicative of chain scission during the crosslinking process [10] and is in good agreement with the finding of the ^{13}C-NMR investigation. Broadening is illustrated in Figure 4.11 where the relative distribution width (σ/D_{Res}) is plotted versus the peroxide concentration. The upturn in σ/D_{Res} at higher peroxide concentrations is indicative of the formation of regions of very high crosslink density. Figure 4.11 also plots the stored energy density at break - extracted from the tensile test data discussed in section 4(B).4. - versus peroxide concentration. The maximum in stored energy at break coincides with the narrowest crosslink density distribution (the most homogeneous network structure).

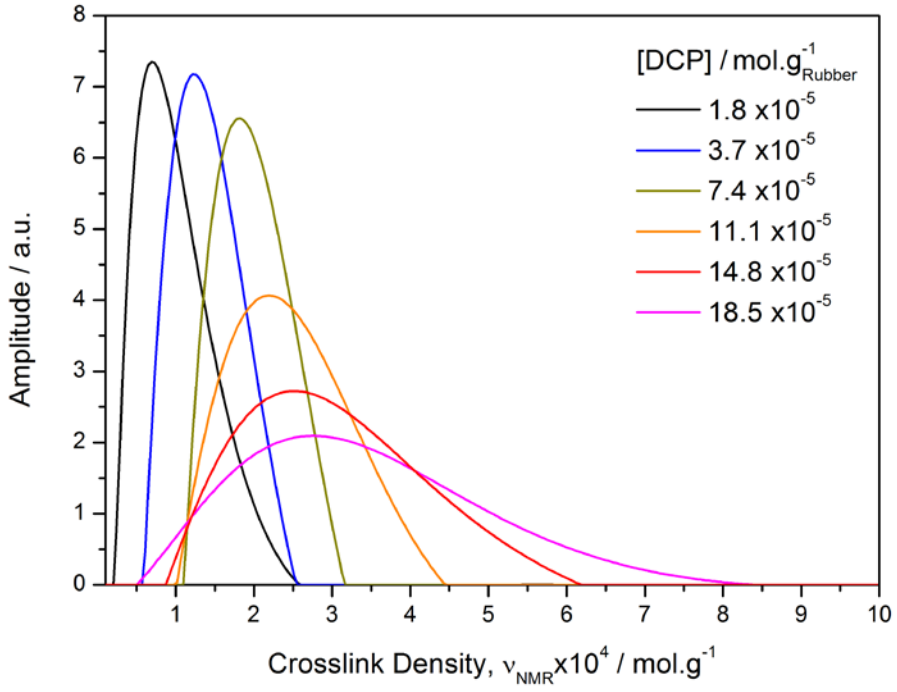

Figure 4.9: Crosslink density distributions plotted on a linear x-axis for unfilled networks

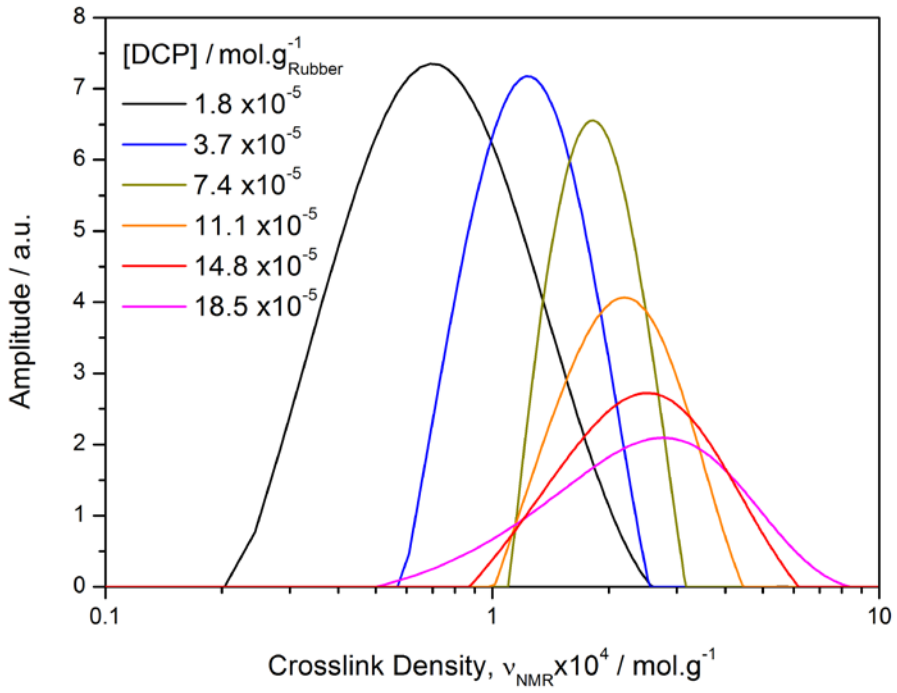

Figure 4.10: Crosslink density distributions from Figure 4.9 re-plotted on a logarithmic x-axis for unfilled networks

Figure 4.12 plots the average crosslink density obtained from NMR, swelling and tensile experiments against the initial concentrations of peroxide. The dashed line in Figure 4.12 corresponds to a theoretical relationship where the gradient is unity, corresponding to a direct molar equivalence between peroxide and crosslink yield (the idealised abstraction mechanism of Figure 4.6).

As can be seen the data obtained from swellings tests is in good agreement with this trend at lower peroxide concentrations (< 2 phr). Above this loading the crosslinking efficiency increases significantly due to formation of crosslinks via macro-radical addition to unsaturated backbone carbons. This is in good agreement with the thermodynamic data presented in Figure 4.7. In contrast, the NMR data displays a similar gradient to the swelling data but is offset by a positive intercept equivalent to M_C = 5556 mol/g. This results from the NMR test's sensitivity to physical as well as chemical restrictions imposed on the elastomer network such as chain packing or trapped entanglements which are less significant in the swollen state and are in line with previous observations reported in the literature [10].

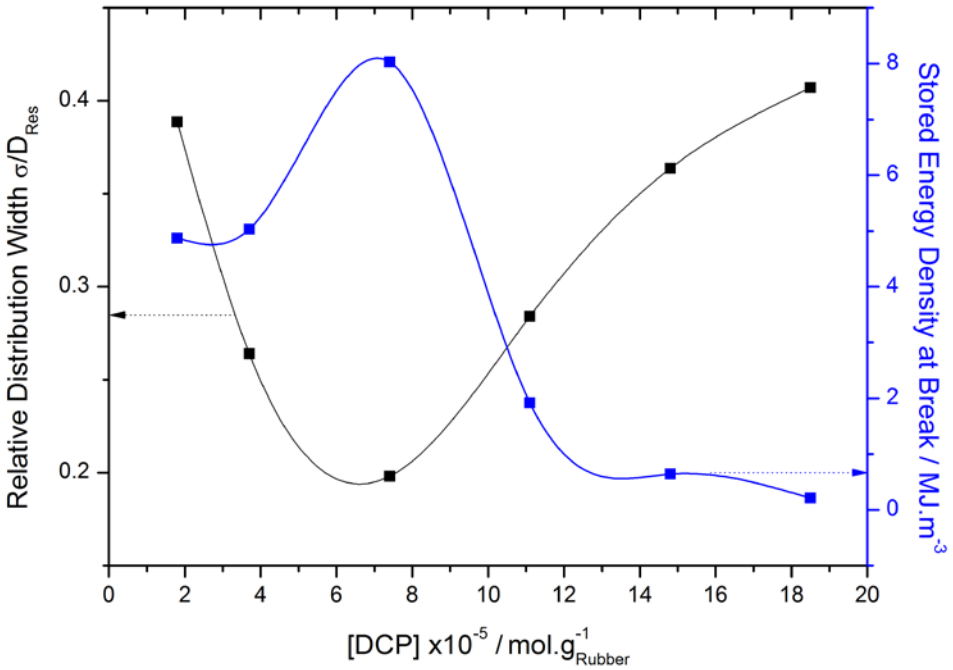

Figure 4.11**:** Crosslink density distribution width and maximum stored energy at break from tensile testing plotted versus the initial concentration of DCP in the compounds

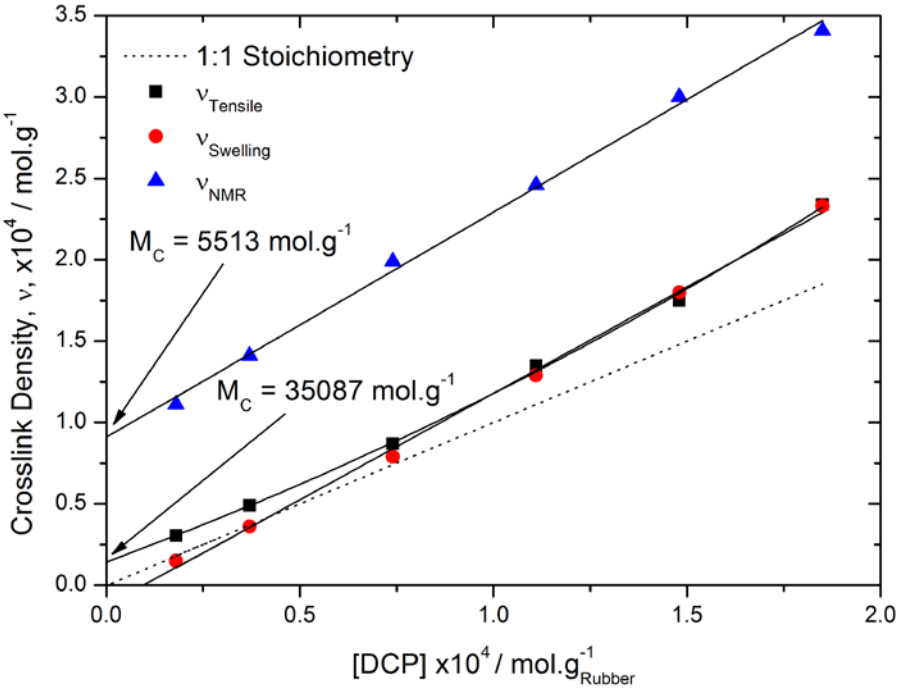

Figure 4.12: Comparison of crosslink density values determined via three different experimental techniques versus the initial concentration of DCP in each compound. The dotted line corresponds to a theoretical 1:1 stoichiometry of crosslink formation

4(A).4. Mechanical properties of unfilled networks

An Instron 5566 frame equipped with a 1 kN load cell and video extensometer was used to measure tensile properties of the unfilled samples. Dumbell-shaped specimens (dimensions given in Appendix I)were tested using a strain rate of ~0.03 /s. Tests were performed at room temperature and three repeat tests were performed for each sample.

Representative data are given in Figure 4.13 to Figure 4.15 and are fitted to the Neo-Hookean stored energy function

$$W = \frac{1}{2}G(\lambda_1^2+\lambda_2^2+\lambda_3^2-3) = \frac{\rho \mathrm{R}T}{2M_C}(\lambda_1^2+\lambda_2^2+\lambda_3^2-3) \qquad 4.2$$

where W is the stored energy, G is the small strain shear modulus, λ_i is the extension ratio along axis i, ρ is the density of NR, $\mathbf{R}$ is the gas constant, T is the temperature and M_C is the molecular weight between crosslinks. The values of M_C obtained from the different

experimental methods are used to fit the Neo-Hookean model as follows: equilibrium solvent swelling experiments (Figure 4.13), tensile data assuming incompressibility (Figure 4.14) and NMR experiments (Figure 4.15).

As can be seen from the tensile data, changing the average crosslink density dramatically affects the small strain modulus, extension to break and tensile strength of the NR networks. Tensile strength is found to peak at 2 phr DCP (7.4 x10^{-5} mol/g_{rubber}) addition. At large extensions some of the samples display the classical upturn in stiffness associated with finite network extensibility (FNE) and/or strain-induced crystallisation (SIC). The onset strains and stresses for this upturn in stiffness vary systematically with DCP loading. Samples with loadings of DCP higher than 2 phr fail before the onset of this phenomenon.

It is of interest to compare the predictions of the Neo-Hookean computed using M_C values determined from different experimental techniques. In Figure 4.13 the Neo-Hookean data is calculated using equilibrium swelling data and is seen to be generally in good correlation with the experimental behaviour at low strains. As expected, the Neo-Hookean model cannot capture the upturn in stiffness observed at large strains. In addition it is possible to observe that at medium strains the model actually *underestimates* the stiffness of the material.

In Figure 4.14 the model is calculated using M_C values from the small strain portion (1-7 % strain) of the tensile stress-strain data and assuming incompressibility of the rubber. Again there is a good correlation with the experimental behaviour at low strains and a failure to fit the stiffness inflexion at high strains. However the Neo-Hookean model is seen to slightly *overestimate* the stiffness at medium strains for the less densely crosslinked networks, in contrast to the model calculated with swelling data.

When the Neo-Hookean model is calculated using NMR data (Figure 4.15) there is a *dramatic overestimation* of the small strain modulus and therefore the stress-strain behaviour of all the NR networks.

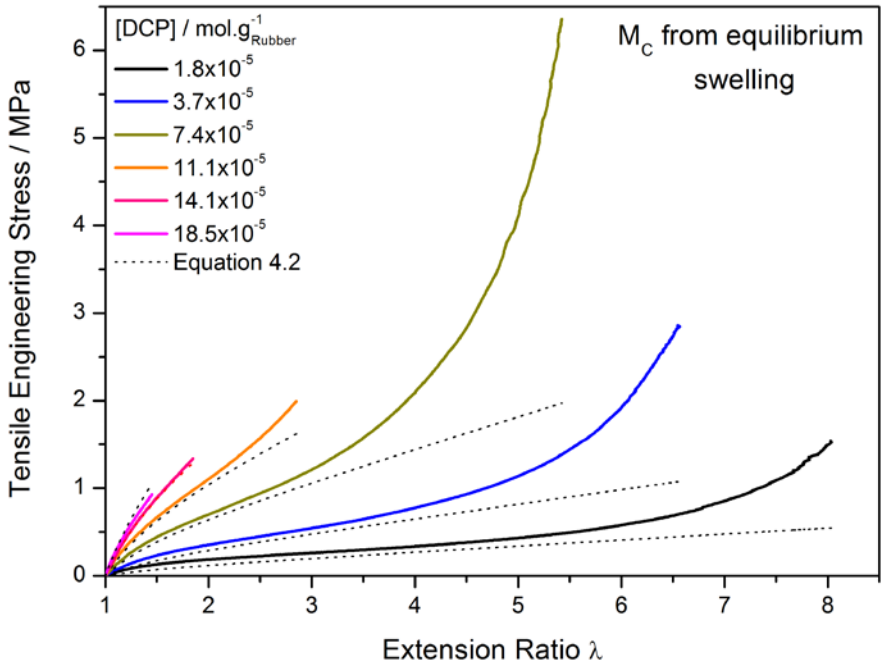

Figure 4.13**:** Tensile mechanical properties of the unfilled networks. The dashed lines are fits to the Neo-Hookean stored energy function using values of $\boldsymbol{M_C}$ calculated from equilibrium swelling experiments (Table 4.1)

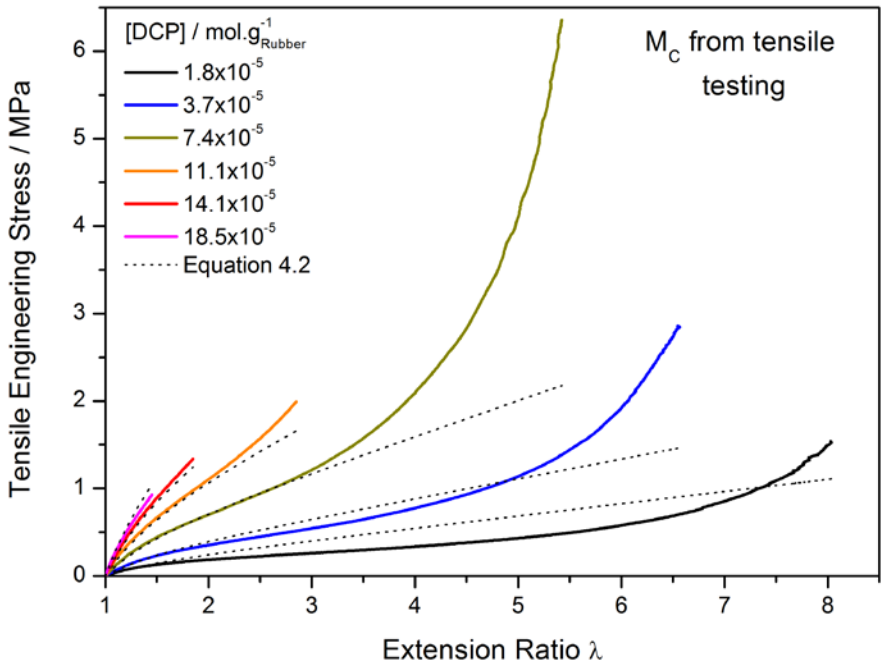

Figure 4.14**:** Tensile mechanical properties of the unfilled networks. The dashed lines are fits to the Neo-Hookean stored energy function using values of $\boldsymbol{M_C}$ calculated from tensile test small strain data (Table 4.1)

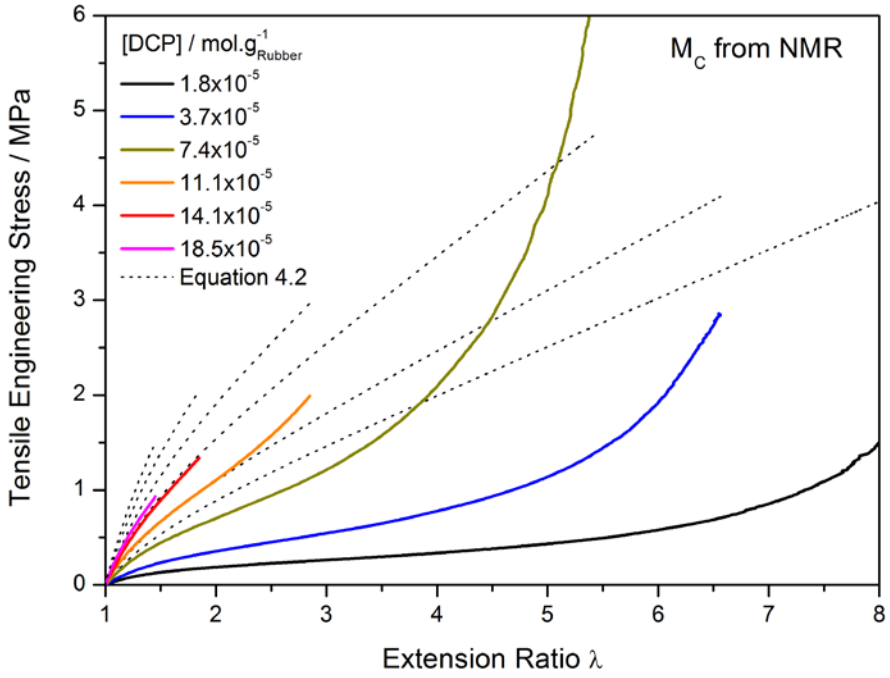

Figure 4.15**:** Tensile mechanical properties of the unfilled networks. The dashed lines are fits to the Neo-Hookean stored energy function using values of $\boldsymbol{M_C}$ calculated from NMR experiments (Table 4.1)

This difference in fitting behaviour relates to differences in sensitivity between techniques to macromolecular network structure. The NMR technique is sensitive to *all* topological restrictions imposed on the polymer chains. This includes chemical crosslinks but also contributions from physical entanglements of the polymer chains. In contrast, the equilibrium swelling approach assesses solely the contribution to elasticity arising from chemical crosslinks, since the under swollen conditions the network is expanded; therefore forcing the 'disentanglement' of some of the entangled chains (those which are not permanently entangled). Mechanical testing lies somewhere in-between since the contribution to elasticity arising from physical entanglements diminishes as a function of strain. The insensitivity of the swelling procedure to physical entanglements has been demonstrated by performing NMR crosslink density measurements on swollen samples. In this case it is found that the values from NMR and swelling experiments are in good agreement [11].

From Figure 4.12 it is clear that for more densely crosslinked networks, the crosslink density values determined from mechanical and swelling testing are in good agreement. However, for the lightly crosslinked networks the values from swelling experiments are measurably lower than those from mechanical testing. This may be due to the increasing mechanical significance

of physical entanglements in lightly crosslinked networks which is essentially ignored by the swelling procedure.

4(A).5. Discussion

The evidence presented here indicates that the use of high concentrations (> 2 phr) of peroxide curative in NR results in the formation of localised regions of very high crosslink density (up to 8 x 10^{-4} mol.g^{-1}). Such regions are formed via the promotion of direct chain macro-radical addition to chain double bonds in close proximity - generating a chain free radical able to repeat the process. This is evidenced by deviation of curing enthalpies from a simple thermodynamic model of the abstraction reaction process and the relative broadening of the crosslink density distributions in highly crosslinked samples from DQ ^{1}H-NMR experiments. In addition, there is evidence of significant main chain modification; with *cis-trans* isomerisation and chain scission becoming apparent when higher peroxide concentrations are used.

Considering the tensile mechanical data, it is apparent that at small strains Neo-Hookean elasticity can accurately describe the mechanical properties simply using an average value of M_C determined from swelling or mechanical testing - despite the fact that significant network heterogeneities have been observed. This implies that although significant broadening of the crosslink density distribution is present in the more heavily crosslinked samples, the net contribution of the localised regions of 'polymerised' NR to the total bulk elasticity is negligible. The physical reasoning behind this is that localised regions of high crosslink density act as a single effective network crosslinking point. While not contributing significantly to bulk elasticity at lower strains it has been proposed that such highly crosslinked regions act a stress raisers within the network, potentially contributing to the observed reduction in stored energy density at break of highly crosslinked natural rubbers [10, 12]. The inability of the Neo-Hookean model to describe higher strain elasticity prior to the onset of finite network extensibility and strain-induced crystallisation, especially in the lightly crosslinked samples, has been attributed to the presence of inelastic network defects such as closed loops and dangling chain ends [4].

From a practical perspective the optimum concentration of DCP was found to be 2 phr (7.4 x10^{-5} mol/g_{rubber}). This produced a crosslinked NR network which was mechanically tough and easy to handle and demould (higher peroxide concentrations resulted in substantial tearing of the material upon demoulding). Additionally networks formed with DCP loadings of 2 phr (7.4

$x10^{-5}$ mol/g_{rubber}) displayed a more homogeneous distribution of crosslinks. This loading of DCP was subsequently used to crosslink all materials, filled or otherwise, required for further

4(A).6. Future Work

During the course of this work Electron Paramagnetic Resonance (EPR) was used to investigate the free radical chemistry of the peroxide crosslinking process. EPR, often called electron spin resonance (ESR), is an analogue of the NMR technique and is sensitive to the electronic environments of spin-unpaired electrons.

As free radicals are spin-unpaired electrons, EPR is an ideal technique to investigate mechanistic details of free radical reactions. EPR has been used extensively for such purposes in polymer science, life sciences and chemistry amongst other disciplines [3]. Just as NMR is able to discriminate between chemical environments of nuclei, so EPR is able to discriminate between the electronic environments of free radicals. For the reaction mechanism in question here a number of potential free radical species may exist at some stage during the crosslinking process; alkoxy radicals, allylic radicals, secondary carbon radicals etc.

Some preliminary EPR experiments were undertaken during this work. Samples of rubber were taken at various stages the curing process and quenched in liquid nitrogen. These were then analysed by w band EPR. Example data taken at time = T_{50} during the curing process are presented in Figure 4.16 which plots the 1st derivative of the signal intensity versus the applied magnetic field in kGauss (in EPR the magnetic field is variable while the probe radiation is constant - the reverse of the procedure for NMR). Two discrete resonance signals can be isolated in samples containing both high and low initial concentrations of peroxide. One strong resonance signal is centred around 2.25 kG while the second weaker resonance signal is centred around 3.3 kG. The strong signal at 2.25 kG has been reported in SBR (synthetic) as a result of paramagnetic impurities arising from the catalysts used in synthesis. For the case of NR the likelihood of paramagnetic impurities being present in the sample is quite high as biological materials (proteins etc.) are often rich in paramagnetic complexes. However this does not explain the clear dependence of the resonance intensity on the initial peroxide concentration. The weaker signal at 3.3 kG is due to the presence of free radical electrons.

Although these experiments were not performed *in-situ* and are therefore subject to handling and processing uncertainties, the presence of a free radical signal does indicate that a more thorough investigation (potentially performed *in-situ*) may be insightful.

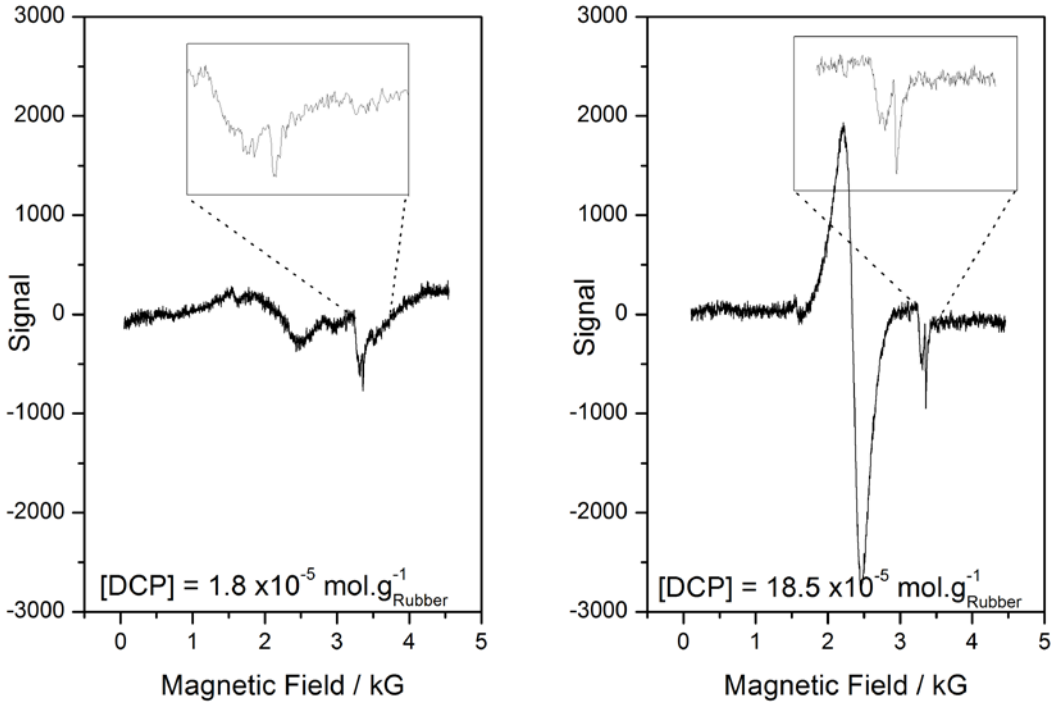

Figure 4.16**:** EPR spectra of NR specimens sampled at time = T_{50} during the curing reaction. Inset: the resonance associated with free radicals is highlighted

Chapter 4: Section B - Filled networks

Having extensively characterised the unfilled rubber networks and determined an optimal loading of DCP of 2 phr, a similar investigation was performed on the filled sample series to determine the effects of the various fillers on the peroxide crosslinking system.

Crosslinked samples were prepared from filled masterbatch material using a method analogous to the preparation of the unfilled materials. DCP was compounded with masterbatch at a mass loading of 2 phr on a laboratory 2-roll mill. The compounding temperature was significantly higher than for unfilled networks due to the increased viscosity of the masterbatch. Nevertheless, the maximum temperatures did not exceed 80 °C, meaning thermal decomposition of the peroxide during mixing was kept to a minimum. Samples were then tested on the MDR rheometer to obtain cure traces. The cure behaviour was found to be very similar to that of the unfilled material. A cure time of 100 minutes (~T_{98}) on a laboratory hotpress with plate temperatures of 150 °C was used to prepare sheets of crosslinked, filled rubber.

4(B).1. Crosslinking thermodynamics

The enthalpy associated with the vulcanisation process was determined using DSC experiments as detailed in the first half of this chapter. Five repeats were performed for each sample type. The only difference in data analysis between filled and unfilled materials was that for the filled materials the enthalpy value was normalised to the mass of NR is the sample. This meant that the mass loading of filler and initial peroxide was subtracted from the total sample weight prior to normalisation. By doing this the enthalpy of vulcanisation associated with the unfilled and filled networks could be directly compared.

Figure 4.17 plots the reaction enthalpy for the filled samples versus the specific surface area of the various filler materials. The dashed line which intercepts the y-axis at around 30 $kJ.g^{-1}$ corresponds to the crosslinking enthalpy measured for the corresponding unfilled material with an initial DCP loading of 2 phr. Deviation from the dashed line indicates differences in the enthalpy of the reaction process (note that for filled materials this value may now also include reaction heats associated with filler-peroxide interactions and so is not entirely related to the process of crosslinking).

The first issue of note in Figure 4.17 is the magnitude of the error associated with some of the measurements of the reaction enthalpy. For the unfilled materials considered in the first half

of this chapter these values deviated by less that 1 % from the averaged value of 5 repeats. However, for some of the filled materials the error bars are significantly larger. This may be due to an inhomogeneous dispersion of filler or curative throughout the rubber phase with the small sample size (~ 10 mg) resulting in sampling issues. Despite the increase in experimental scatter it is clear that the carbon black series of fillers results in an overall reduction in reaction enthalpy. This reduction in enthalpy scales with the surface area of the carbon blacks with no significant difference distinguishable between unmodified and graphitised carbon blacks.

The silica samples, despite having a higher specific surface area, have less of an effect on the total measured reaction enthalpy. It is noteworthy that both the TEVS treated silicas lie above the measured enthalpy associated with the corresponding unfilled network. These deviations in reaction enthalpy could be interpreted in terms of crosslinking reaction efficiency however, as mentioned previously, the possibility of thermal interaction between filler and peroxide is an added complication.

Additional information is required about the resulting network structures before the thermodynamic data can be fully interpreted. To this end DQ-NMR experiments were performed on the filled samples.

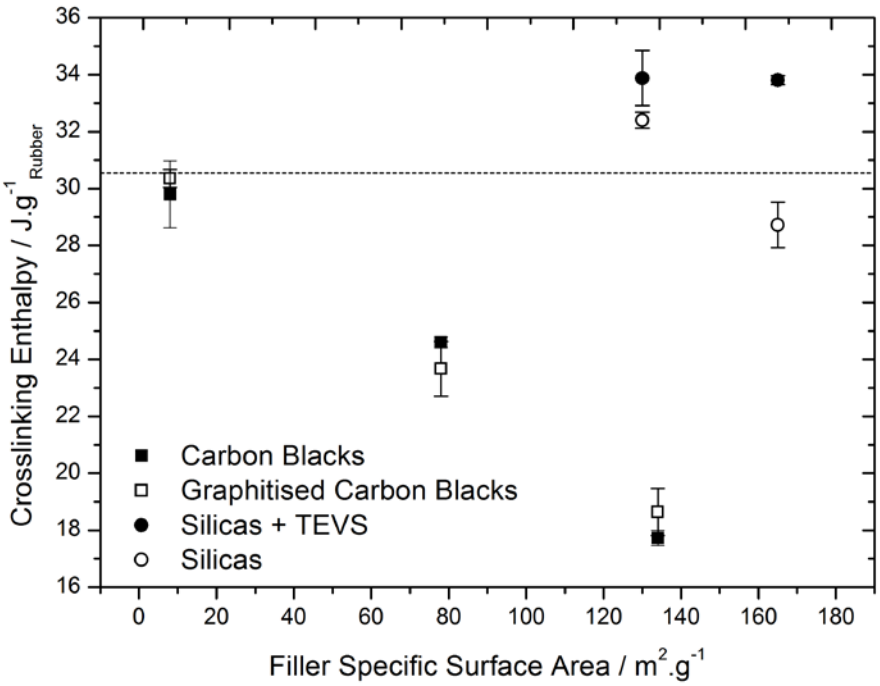

Figure 4.17**:** Reaction enthalpy versus filler specific surface area. The dashed line corresponds to the enthalpy measured for the unfilled material with an initial DCP loading of 2 phr

4(B).2. ^{1}H-Double Quantum (DQ)-NMR

DQ-NMR experiments were performed on the filled series of samples. Figure 4.18 shows the crosslink density distributions obtained from the NMR data analysis for the carbon black-filled series along with the corresponding unfilled material. It is clear from Figure 4.18 that the use of carbon black filler with peroxide cure systems results in 1) a reduction in the average and peak crosslink density and therefore efficiency of the crosslinking reaction and 2) a broadening of crosslink density distributions towards lower crosslink densities. These effects scale with the specific surface area of the carbon black.

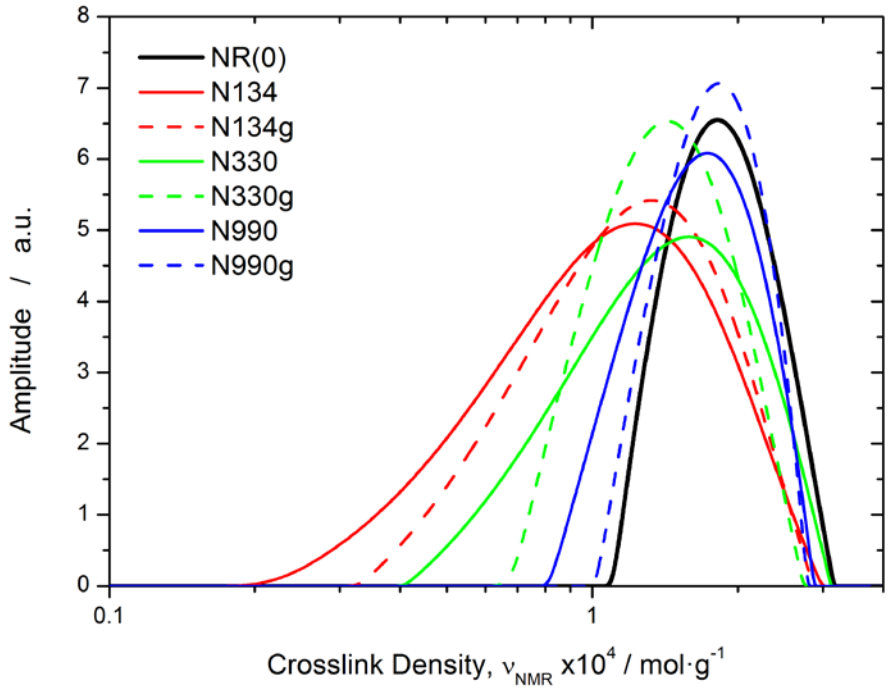

Figure 4.18**:** Crosslink density distributions for the carbon black-filled series obtained from low field ^{1}H-DQ-NMR experiments

This is due to the CB particles acting as strong radical scavengers during the vulcanisation process. The presence of oxygen and hydrogen-containing surface groups such as aromatic rings, phenolic hydroxyl and quinone groups [13] of CB act as free radical traps and consequently, CB particles are able to effectively inhibit radical polymerisation [14] and polymer oxidation [15], and provoke important effects on the efficiency of peroxide vulcanisation of rubber, as is shown in Figure 4.18 and Figure 4.20. These groups at the CB surface (preferentially formed at high-energy sites associated with the edge atoms of the

quasi-graphitic parallel layer groups [16]) trap free radicals by addition to form stabilised radicals in a termination reaction.

According to the simplest reaction pathways for the peroxide vulcanisation process, the thermal decomposition of dicumyl peroxide forms alkoxy radicals which react with NR chains forming polymer radicals. The combination of two polymer radicals results in a cross-link, whereas the addition of a polymer radical to a double bond of another NR chain creates a cross-link and a new, reactive polymer radical. Under certain experimental conditions (for example high initial peroxide concentrations), the addition reaction of polymer radicals can behave as a radical polymerisation process, creating local regions of higher cross-link density [10]. This means that the population of both alkoxy radicals and propagating polymer radicals may be affected.

In the situation where *polymer radicals* become trapped at the CB surface, a chain segment would be grafted to the particle surface in the same way in which radical combination reactions form a cross-link. As a consequence, a slight reduction in the cross-linking efficiency would be expected due to the minimisation of the addition reaction of polymer radicals - which should be visible as a symmetric shift of spatial cross-link distribution - corresponding to a random process without change to the cross-link distribution width. Or in the regions of higher cross-link density, in case of existence of polymerisation-type reaction.

Contrary to this statement, Figure 4.18 shows an important broadening in the spatial distribution of cross-links mainly caused by the presence of lower cross-linked regions in the rubber network. This scenario is better explained by the trapping of the *alkoxy radicals* at the carbon black surface and the consequent decrease in radical concentration available for the cross-linking reaction. As such the presence of carbon black affects radical concentrations during NR vulcanization with dicumyl peroxide, as is suggested by the observed reductions in vulcanisation enthalpies (Figure 4.17).

Graphitisation of the CB results in a slight reduction in the broadening of the crosslink distribution to lower crosslinked regions and the detrimental effect on the vulcanization efficiency. This is an interesting feature as graphitisation of carbon black is accompanied by the removal of surface chemical groups. According to Bansal and Donnet [13], and Schaeffer et al. [17] carbon-oxygen containing surface groups are completely removed from carbon blacks after heat treatment under inert atmosphere to a temperature of 1000 °C. However, the more stable carbon-hydrogen containing surface groups are still present on the CB up to a temperature of 1600 °C. Recalling that the graphitised CB materials used in this study were

heat treated at a temperature of 1250 °C, it would appear that the mechanism of radical scavenging for graphitised carbon blacks is associated with radical attack on the remaining carbon-hydrogen surface groups or even on exposed surface layers of the graphitic crystals [18, 19]. At the other extreme of the spatial cross-link distribution, the higher cross-linked areas are also affected by graphitisation of CB particles which is probably related with the disappearance of high energy sites (crystal edges) and the reduction of filler-rubber interactions (see the following section) in comparison with the unmodified CB.

Precipitated silicas have a less severe, though still measurable, effect on the crosslinking process (Figure 4.19). The effect of the TEVS surface treatment is to reduce the detrimental interaction of silica with the curative and to provide functional moieties (vinyl groups) that are able to react with the rubber chains during the peroxide vulcanisation. The TEVS treatment results in efficient modification of silica surface, witnessed by the improvement in vulcanisation efficiency - achieving values higher than 90% - with respect to the raw silica counterparts (Figure 4.20).

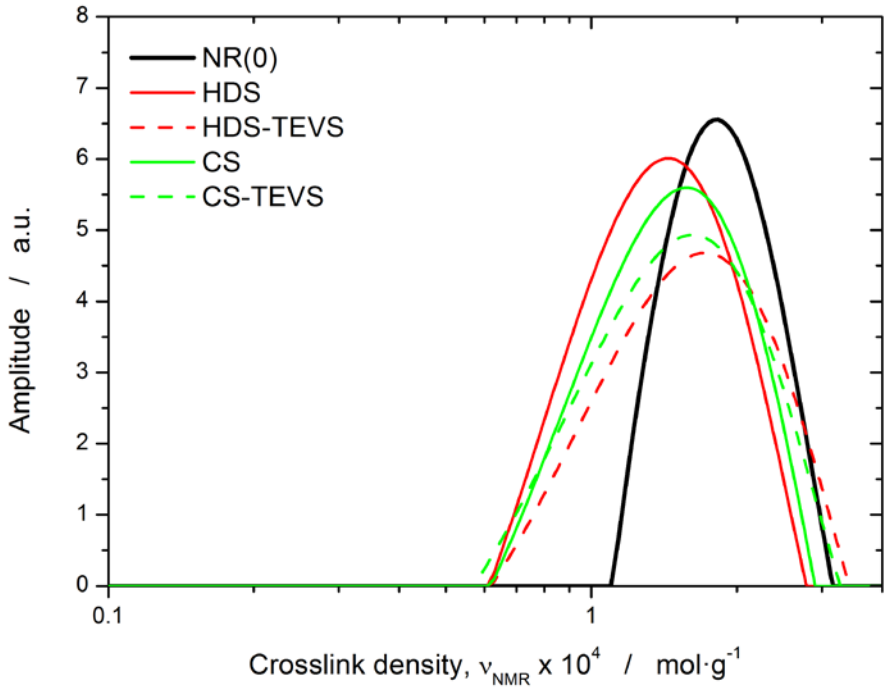

Figure 4.19: Crosslink density distributions for the silica-filled series obtained from low field ^{1}H-DQ-NMR experiments

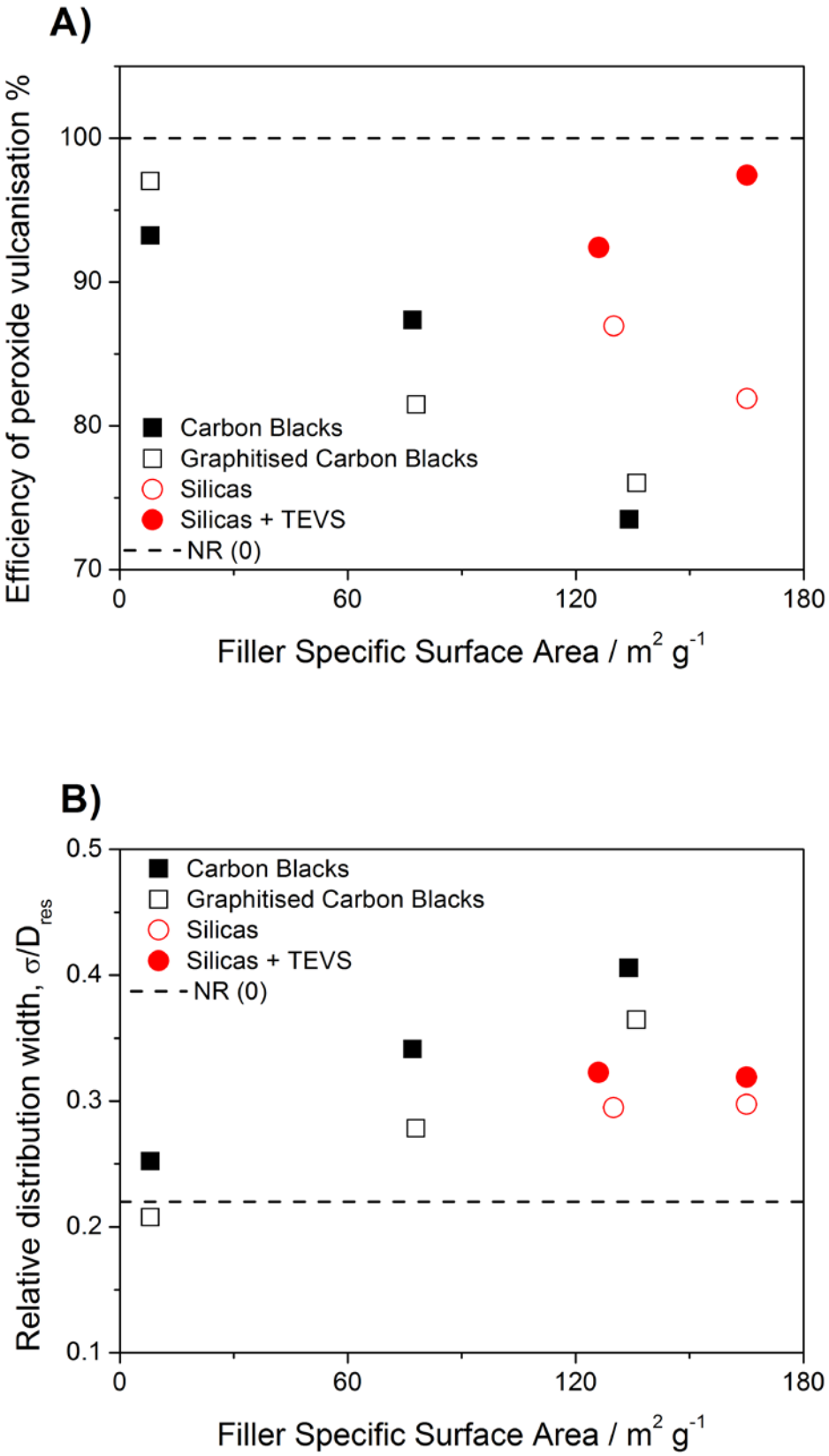

Figure 4.20 A: Efficiency of the peroxide vulcanisation reaction versus filler specific surface area. B: the relative distribution width of the crosslink distribution versus the filler specific surface area

A closer analysis of spatial cross-link distribution (Figure 4.19) reveals that surface modification does not have any effect on the areas with lower cross-link densities, but the vinyl silane promotes the formation of areas with higher cross-link densities with respect to the unfilled and raw silica counterparts. As a consequence, a slight broadening of the relative width of the spatial cross-link density distribution is detected - though it is still independent of the silica surface area.

This modification to the rubber network structure could be associated with a the higher concentration of free radicals and/or the modification on the vulcanisation pathway as it is suggested by the increment on the associated enthalpy shown in Figure 4.17. Existence of more reactive vinyl groups may enhance the addition reaction of polymer radicals, increasing the total amount of free radicals in the system and the efficiency of the cross-linking reaction (promoting the polymerisation-type reaction).

4(B).3. Equilibrium solvent swelling

Equilibrium solvent swelling experiments were performed for the filled samples according to the procedure detailed for the unfilled samples. For the filled sample data the mass of filler was subtracted from the total sample mass prior to the Flory-Rehner analysis. As mentioned previously the values of crosslink density for filled samples are 'apparent' crosslink densities which evaluate not only the swelling capacity of the crosslinked rubber network but also any reduction in swelling capacity of the matrix arising from strong adhesion between filler and rubber.

During the equilibrium swelling experiments, a slight leaching of carbon black from the sample surfaces was noted for the graphitised carbon black specimens. This became apparent when the sample surfaces were dried with tissue prior to weight measurement and small dark stains were left behind on the tissues. This was not apparent for any other filler type investigated. The total mass of carbon black leached from the samples was below the resolution of a 4 point analytical balance, so the results of the swelling tests are unlikely to be adversely affected. However, this leaching is indicative of the very weak interfacial bonding between graphitised carbon black and NR being ruptured by the stresses arising from solvent swelling of the elastomer network.

Valentín et al. [8] demonstrated that filler-matrix interactions can be evaluated by plotting the average crosslink density obtained from NMR experiments against the value of apparent crosslink density obtained from equilibrium swelling measurements (Figure 10). A swelling

'masterline' is shown in Figure 4.21 which represents the swelling behaviour for a series of unfilled rubber networks according to the actual cross-link density measured by NMR. For the unfilled samples the positive intercept of the 'masterline' trend arises from the NMR method's sensitivity to entanglements (in addition to any other chain restrictions, such as chemical cross-links and trapped entanglements) which are not present in the swollen state. This is in line with previous observations [8, 10]. Within the unfilled series, the datum corresponding to 2 phr loading of DCP is labelled. In Figure 4.21, vertical shifting corresponds to a change in the average crosslink density as measured by NMR (widely explained in the previous section), whereas horizontal shifting from the unfilled masterline behaviour corresponds to the degree of swelling restriction imposed by the rubber adhesion to the filler surface. These non-swelling particles act as macro-crosslinks and consequently, the more compatible reinforcing fillers (characterized by rubber-filler interfaces with higher number of interactions) will display larger horizontal shifts than the less compatible counterparts for a given cross-link density (note that in Figure 4.21 the filler pairs with different chemical surface are connected by dotted lines).

Fillers which are assumed to have a strong surface interactions with the polymer phase (unmodified CB and TEVS-treated silicas) all display a larger horizontal shift than their less compatible counterparts: proof of strong filler-matrix interactions (the filler pairs are connected by dotted lines). The trend within the carbon black series itself is more complex. Initially the degree of elastomer swelling restriction increases with carbon black surface area (N330>N990). However, for the N134-filled sample the degree of apparent swelling restriction falls below that of N990. This can be explained by considering the reduction in crosslink density apparent with higher surface area carbon blacks and the corresponding increase in swelling capacity of the elastomer networks of lower crosslink density. Standardising the apparent swelling crosslink density of the filled samples (ν_{filled}^{sw}) to the swelling behaviour of unfilled networks with corresponding NMR crosslink density ($\nu_{unfilled}^{sw}$ - which is interpolated from the unfilled trendline) gives a comparable evaluation of the degree of swelling restriction for each sample. This process is shown schematically for one of the carbon black-filled samples in Figure 4.21. The 'swelling restriction ratio' is defined according as

$$\text{Swelling Restriction Ratio} = \frac{\nu_{\text{filled}}^{\text{sw}} - \nu_{\text{unfilled}}^{\text{sw}}}{\nu_{\text{unfilled}}^{\text{sw}}} \qquad 4.3$$

and plotted versus filler surface area in Figure 4.22.

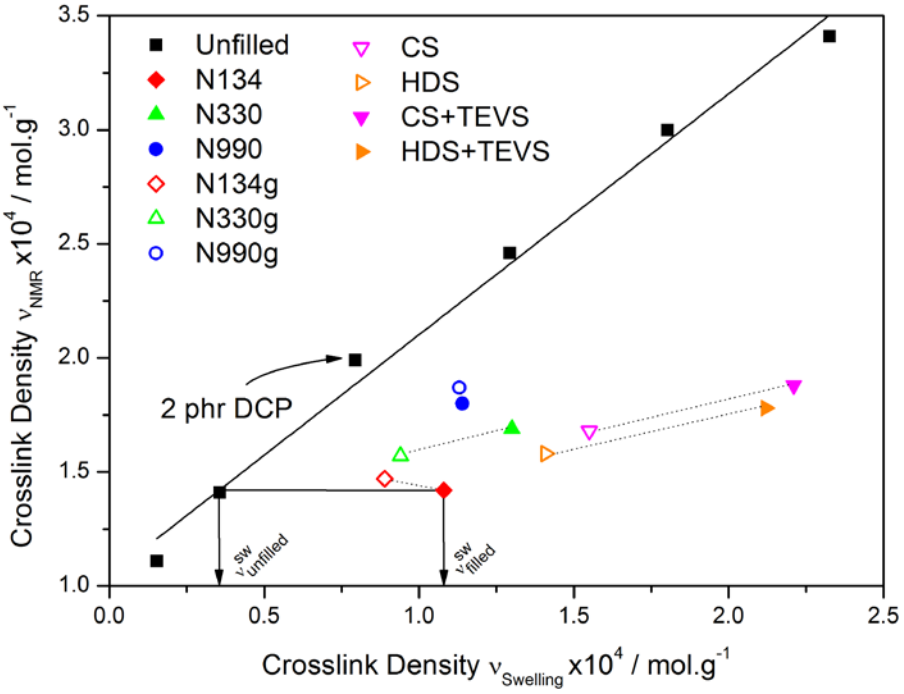

Figure 4.21: Crosslink densities for the filled and unfilled samples determined via NMR and swelling procedures. Dashed lines connect unmodified and surface modified filler pairs and the solid lines illustrate extraction of parameters required for the calculation of the 'Swelling Restriction Ratio'

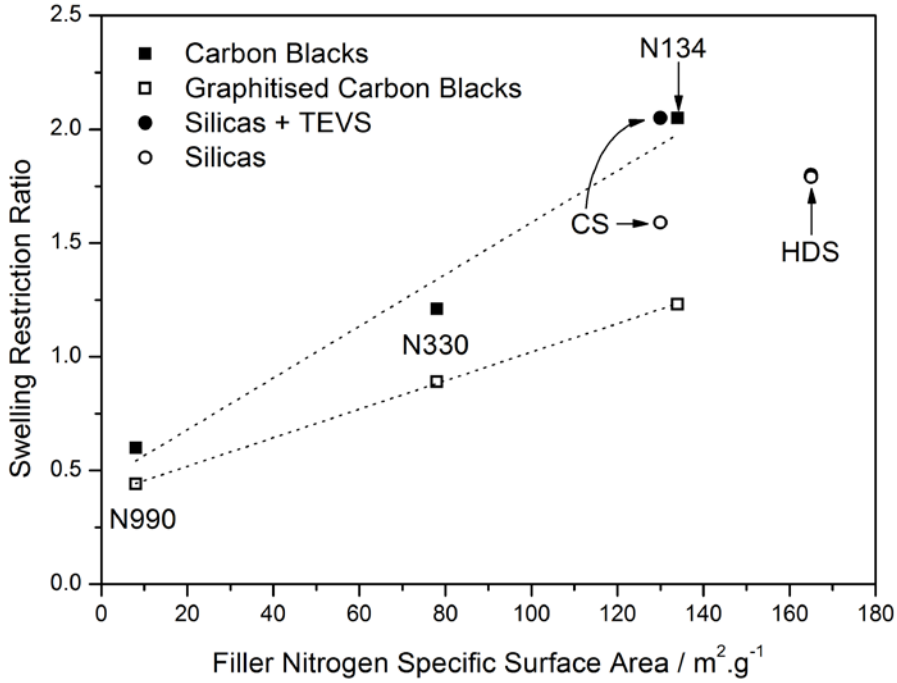

Figure 4.22: Swelling restriction ratio for each filler type versus the filler specific surface area. Dashed lines illustrate linear relationships for the carbon black and graphitised carbon black series

Plotted versus the nitrogen-specific filler surface area, the swelling restriction ratios for the carbon black-filled materials extrapolate back to a finite value at zero surface area. This is not physically realistic as it corresponds to an unfilled material - where the swelling restriction cannot be non-zero.

Two possibilities are apparent. First we may consider that the swelling restriction per unit surface area varies greatly between carbon black grades and that therefore the N990-based carbon blacks display a much greater interaction with the NR chains than the higher structured grades, resulting in a significant increase in the apparent density of rubber-filler interactions. However, the measurements of the surface free energy of the fillers (indicative of the rubber-filler interaction) do not support this explanation - in fact they are actually found to increase with increasing particle surface area and structure (Chapter 3 Table 3.1).

An alternative and more likely explanation is that the nitrogen-specific surface area does not properly define the interacting filler surface area in highly structured carbon blacks and consequently is not useful for the actual definition of rubber-filler interaction density. The nitrogen surface area measurement assesses the total surface area accessible to the nitrogen probe molecule. This includes all 'pseudo-pores' evident for fractal aggregates which may not be accessible to larger molecules.

N990-based carbon blacks are very low structured particles, tending towards a spherical morphology. For this extreme morphological case it is clear that the restriction of swelling should be directly proportional to the nitrogen-specific surface area of the near-spherical filler particles. For the higher structure carbon blacks this is no longer the case as the complex fractal geometry of the particles plays an important role and the absolute nitrogen-specific surface area loses its physical meaning when normalising the number of rubber interactions at the filler surface as measured by the swelling restriction ratio.

This is illustrated in Figure 4.23 which shows a two dimensional schematic of fillers embedded in a swollen rubber matrix. Due to the strong adhesion between carbon black and rubber, the extent of equilibrium swelling of rubber material in the vicinity of rigid filler is reduced. The fillers exhibit a finite spatial perturbation on the swelling capacity of interfacial rubber which is denoted in the illustration by the dashed lines. For the case of spherical, non-aggregated particles shown in Figure 4.23 A the degree of swelling restriction is directly proportional to the nitrogen surface area of the filler. In the case of Figure 4.23 B a single, highly structured filler aggregate is shown. Again the maximum extent of influence of the filler particle surface on the swelling capacity of the surrounding rubber is indicated by the dashed lines. However in

this case it is clear that there is considerable overlap of restriction of swelling due to the aggregate morphology and presence of pseudo-pores (essentially 'wasted' surface area), thereby underestimating the density of rubber-filler interactions. This means that the total swelling restriction is now no longer directly proportional to the nitrogen surface area of the aggregate but rather to some lower 'effective' surface area.

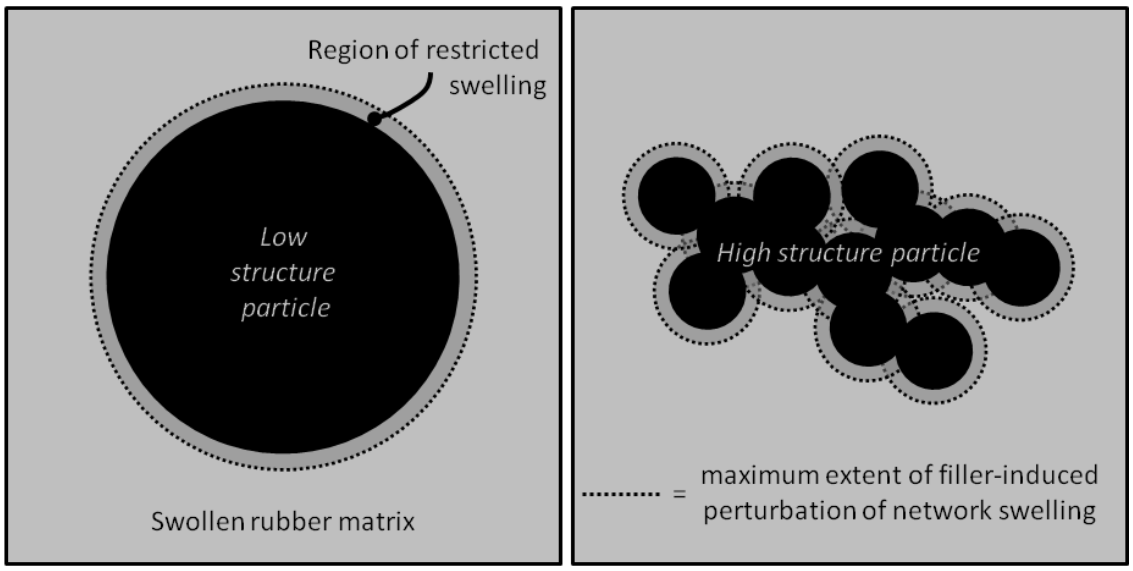

Figure 4.23**:** Two dimensional cross section schematic of carbon black filler particles swollen to equilibrium in a crosslinked rubber network. **A**) The left image illustrates the situation for near-spherical N990 carbon blacks where total restriction of matrix swelling is directly proportional to the surface are of the particle, and **B**) illustrates the case for an highly aggregated carbon black such as N330 or N134.

The two extremes of these effective surface areas are clear: the upper limit corresponds to the nitrogen-specific surface area while the lower limit may be approximated by calculating surface area values based on the fractal aggregate's projected spherical diameter and assuming the aggregate to be spherical and of a density specified in Chapter 3.

Numerous experimental techniques are available which can provide a measure of carbon black average aggregate size. For example, automated dimensional analysis of TEM images of dispersed carbon black aggregates is able to provide a range of information on the projected area of carbon blacks, aggregate sizes and size distributions [13]. Average aggregate sizes for the weight mean diameter of the carbon blacks used in this study are shown in Table 4.2.

Sedimentation techniques (disc centrifuge photosedimentometry) are also able to provide a measure of aggregate diameter. Sedimentation aggregate diameters are also shown in Table

4.2. As Donnet et al. [13] have pointed out, photosedimentometry is not a flawless descriptor of aggregate size, as the technique relies on centrifugal sedimentation principles. Size values are calculated based on the Stokes spherical particle sedimentation model and, due to the additional frictional drag apparent on fractal aggregates versus spheres, the technique tends to underestimate the true aggregate size (compared with TEM image analysis).

Table 4.2: Aggregate diameters determined from different experimental methods, the nitrogen-specific surface area and surface area values calculated from aggregate size measures using a spherical aggregate shape assumption

	Aggregate Diameters / nm		**Surface Areas / $m^2.g^{-1}$**		
	Sedimentation method	TEM method	N_2 BET	Sedimentation aggregate sphere	TEM aggregate sphere
N134	70[A]	124[A]	134	47.6	26.9
N134g	"	"	136	43.7	24.7
N330	133[B]	225[B]	78	25.1	14.8
N330g	"	"	79	23.7	14.0
N990	436[B]	811[B]	8	7.7	4.1
N990g	"	"	8	7.1	3.8

A) Data provided by Cabot Corp., Billerica, MA
B) Donnet et al. [13]

From the values of aggregate diameter taken from the literature, surface area values can be calculated based on the assumption of spherically shaped aggregate (Table 4.2). In Figure 4.24 the swelling restriction ratio is again plotted versus surface area. In this case three separate measures of surface area are plotted: I) the nitrogen surface area, N_s SA, II) the surface area calculated from sedimentation measures of aggregate diameters and III) the surface area calculated from automated TEM image analysis measures of aggregate diameters. Also plotted in Figure 4.24 as solid lines is the linear trend based upon N990 N_2 SA and swelling restriction ratio data extrapolated to the origin. This represents an idealised trend where surface area is directly proportional to the degree of swelling restriction.

As can be seen in Figure 4.24, both the surface area trends based on the spherical aggregate assumption result in a much better agreement with the idealised relationship between swelling restriction and surface area. Surface area values calculated from TEM image analysis data give the best correlation; although the agreement is still not perfect.

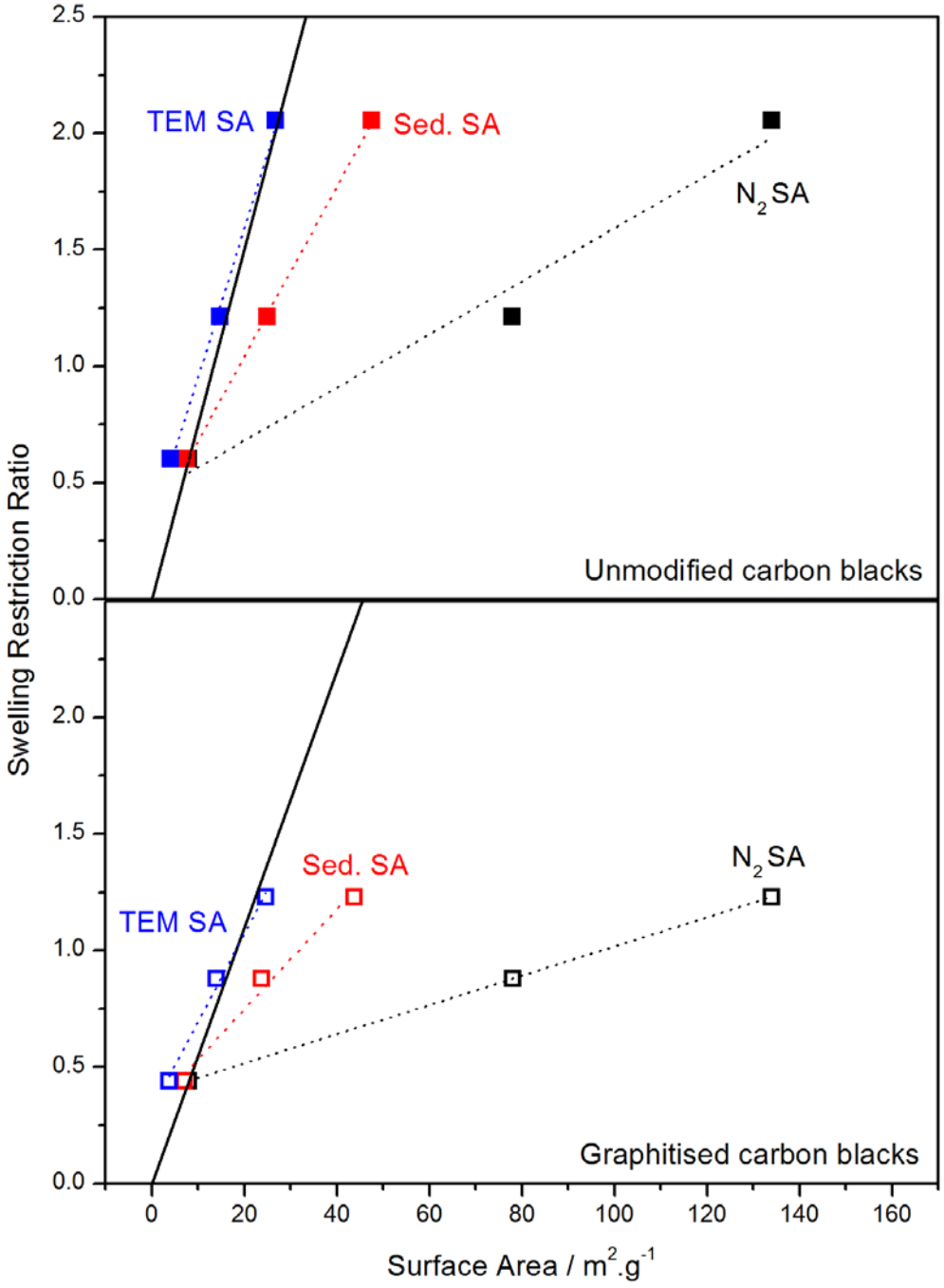

Figure 4.24**:** The swelling restriction ratios for the carbon black filled compounds plotted versus surface area. Three measures of surface area are plotted: the nitrogen BET surface area (N_2 SA), the surface areas calculated from aggregate diameters determined by centrifuge sedimentation experiments (Sed. SA) and the surface areas calculated from aggregate diameters determined by TEM automated image analysis (TEM SA). The solid lines correspond to a fit of the N990 data plotted versus nitrogen surface area through the origin.

In the context of this explanation it would appear that the swelling restriction ratio, which represents the number of interactions between the rubber segments and the filler surface, is highly sensitive to the filler aggregate structure and thus it is proportional to the effective aggregate surface area.

Further evidence to support this hypothesis is evident when the swelling restriction factor is plotted versus the dibutyl adipate absorption (DBPA) value of the filler particles (Figure 4.25). The DBPA value is widely used in the rubber industry to estimate the aggregate size and structure of carbon blacks. In both cases reasonably linear relationships with near-zero intercept of the extrapolations are obtained.

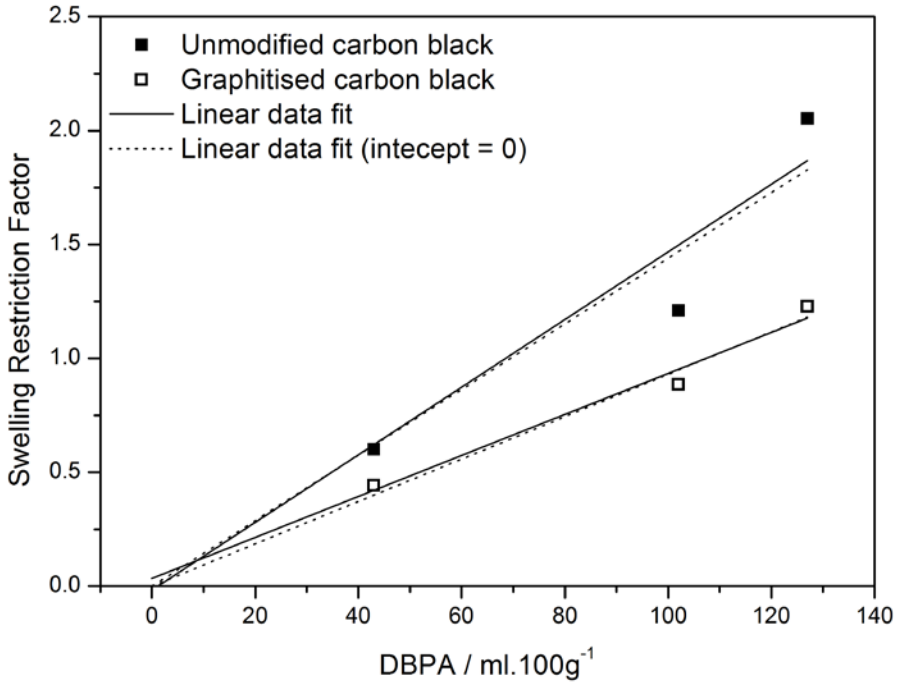

Figure 4.25**:** The swelling restriction ratio plotted versus the corresponding dibutyl adipate absorption (DBP) values of the carbon blacks which are typical taken as a measure of the aggregate structure

According to these results, the number of rubber-filler interactions (measured by the swelling restriction ratio) can be normalised by the effective aggregate structure (experimentally measured by the DBPA value).

For silica-filled samples the swelling restriction ratios imposed by the filler-rubber interactions are between the two extreme behaviours dictated by CB and graphitised CB particles, respectively (Figure 4.22). The surface modification of silica particles with vinyl silane increases

the interactions during the peroxide vulcanization with the NR matrix at the interface in the case of CS silica, but is completely ineffective in the case of HDS particles. This divergence could be related with the enhanced efficiency in the modification process for CS silica particles that were modified prior to the addition to the rubber matrix, in comparison with the HDS particles which react with the silane molecules *in-situ* during rubber compounding. This potentially leads to a reduced reaction efficiency, or more likely reflects a loss of silane in the hot mix through evaporation (the boiling point of TEVS is 160 °C compared to a mix temperature of ~150 °C).

According to Figure 4.22, the ranking of the interfacial interactions of fillers with NR is: Carbon black ≈ silica+silane (depending on silane reaction efficiency) > unmodified silica > graphitised carbon black.

4(B).4. Tensile mechanical analysis of filled networks

Tensile mechanical analysis was performed for the filled series of compounds on an Instron testing machine using the same testing conditions specified in the previous section. Figure 4.26 presents the tensile data for the carbon black-filled series of compounds. A clear difference can be discerned between the unmodified and graphitised carbon blacks. Incremental stiffness for the graphitised carbon black compounds is significantly lower than for the unmodifed counterparts - indicating a reduced polymer-filler interaction. The dramatic differences in the observed large strain quasi-static tensile behaviour between unmodified and graphitised carbon blacks are related to the nature of the interfacial interactions and have been interpreted in terms of strain-dependent slippage of polymer chains at the filler surface [20] and the strain dependent polymer confinement and filler structure breakdown [21]. A similar situation is evident for the silica-filled elastomers.

Tensile data for the silica-filled series is shown in Figure 4.27. At lower strains (magnified and inset in Figure 4.27) the unmodifed silicas display a high modulus up to a distinctive, psuedo-plastic yield point, followed by a modest increase in incremental stiffness to $\lambda = 3$. Such yield points have been observed in molecular dynamic simulations of filled polymer networks. They have been attributed to the fracture of the polymer-mediated fractal filler network [22]. In contrast, for the TEVS-treated silicas, the modulus is reduced at smaller strains versus the unmodified silicas and subsequent incremental stiffening at higher strains is much more dramatic. These features are typical for silica/silica-silane combinations and have been

explained in terms of silane-induced suppression of filler agglomeration at lower strains and a reduction in chain slippage at higher strains due to silane filler-polymer phase coupling.

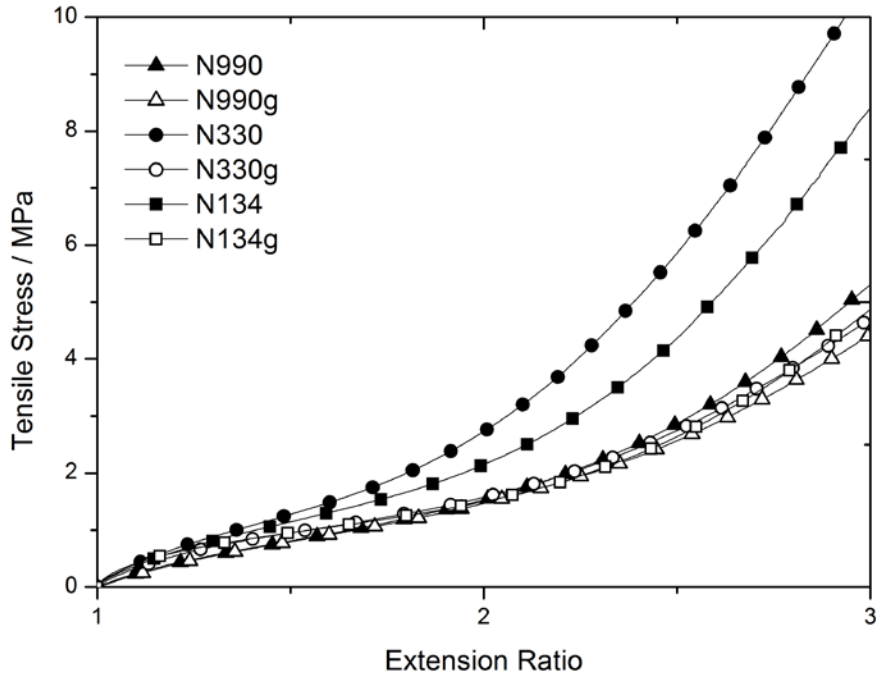

Figure 4.26**:** Tensile mechanical properties for the carbon black-filled series of compounds up to λ = 3.

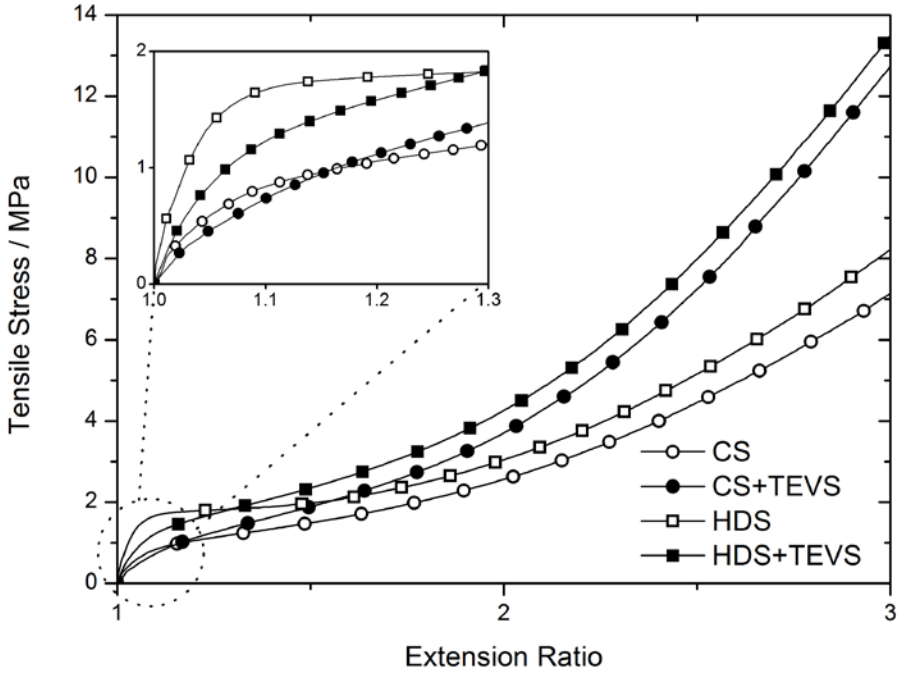

Figure 4.27**:** Tensile mechanical properties for the silica-filled series of compounds up to λ = 3. Inset: magnification of lower strain range λ = 1 - 1.25

4(B).5. Discussion

The second part of this chapter highlighted two key issues. Firstly that crosslinking of NR with peroxide in the presence of carbon blacks results in a crosslinked compound with reduced average crosslink density and greater heterogeneity of crosslink distribution versus the unfilled material. This effect scales with the surface area of the carbon black used. Secondly, by contrasting the values for crosslink density determined by NMR and equilibrium swelling techniques, it is possible to demonstrate the relative restriction of solvent swelling imparted by the presence of filler. It has been shown that graphitisation of carbon black results in a measurable reduction in the magnitude of the restriction of swelling capacity at the interface which is commensurate with a reduction in polymer-filler interaction. The silica fillers lie between the trends found for unmodified and graphitised carbon black depending on their surface treatment.

By considering an 'effective' surface area of the carbon black aggregates, it has been demonstrated that the degree of swelling restriction is not directly proportional to the nitrogen surface area of carbon blacks with higher aggregate structure. The best correlation between swelling restriction and surface area is found when the average aggregate diameter measured by TEM image analysis is used to compute the surface area based on the assumption of spherical aggregate shape (that is, a much reduced 'effective' surface area available for restriction of swelling capacity). The fact that the swelling restriction ratio shows a reasonably linear correlation on the DBPA values for the carbon blacks is added evidence for the density of the swelling restriction phenomenon on the aggregate structure.

It is also of note that peroxide-based cure systems are often viewed as 'clean' cure systems for scientific investigations. For example, much of the seminal work of Mullins was performed on dicumyl peroxide/NR vulcanisates [23]. However the interactions between carbon black and alkoxy radicals are almost never taken into consideration.

4(B).6. References

[1] P.R. Dluzneski, Rubber Chemistry and Technology, 74 (2001) 451-492.
[2] R.D. Bach, P.Y. Ayala, H.B. Schlegel, Journal of the American Chemical Society, 118 (1996) 12758-12765.
[3] P. Atkins, Atkins' Physical Chemistry, 7th ed., Oxford University Press, Oxford, 2002.
[4] L.R.G. Treloar, The physics of rubber elasticity, 3rd ed., Oxford University Press, Oxford, 2009.
[5] J.L. Valentín, J. Carretero-González, I. Mora-Barrantes, W. Chassé, K. Saalwächter, Macromolecules, 41 (2008) 4717-4729.

[6] F.H. Larsen, T. Rasmussen, W.B. Pedersen, N.C. Nielsen, H.J. Jakobsen, Polymer, 40 (1999) 7013-7017.
[7] K. Saalwächter, Progress in Nuclear Magnetic Resonance Spectroscopy, 51 (2007) 1-35.
[8] J.L. Valentín, I. Mora-Barrantes, J. Carretero-González, M.A. López-Manchado, P. Sotta, D.R. Long, K. Saalwächter, Macromolecules, 43 (2010) 334-346.
[9] W. Chassé, J.L. Valentín, G.D. Genesky, C. Cohen, K. Saalwächter, Journal of Chemical Physics, 134 (2011) 044907.
[10] J.L. Valentín, P. Posadas, A. Fernández-Torres, M.A. Malmierca, L. González, W. Chassé, K. Saalwächter, Macromolecules, 43 (2010) 4210-4222.
[11] S. Schlogl, M.L. Trutschel, W. Chasse, G. Riess, K. Saalwachter, Macromolecules, 47 (2014) 2759-2773.
[12] L. Gonzalez, A. Rodriguez, J.L. Valentin, A. Marcos-Fernandez, P. Posadas, Kgk-Kautschuk Gummi Kunststoffe, 58 (2005) 638-643.
[13] J.B. Donnet, R.C. Bansal, M.J. Wang, (Eds), Carbon Black: Science and Technology, 2nd ed., Marcel Dekker Inc, New York, 1993
[14] T.Q. Liu, S.J. Jia, T. Kowalewski, K. Matyjaszewski, R. Casado-Portilla, J. Belmont, Macromolecules, 39 (2006) 548-556.
[15] J. Mwila, M. Miraftab, A.R. Horrocks, Polymer Degradation and Stability, 44 (1994) 351-356.
[16] W. Smith, Polley, HR, Journal of Polymer Chemistry, 60 (1956) 689-691.
[17] W.D. Schaeffer, W.R. Smith, M.H. Polley, Industrial and Engineering Chemistry, 45 (1953) 1721-1725.
[18] P. Allongue, M. Delamar, B. Desbat, O. Fagebaume, R. Hitmi, J. Pinson, J.M. Savéant, Journal of the American Chemical Society, 119 (1997) 201-207.
[19] H.P. Boehm, Carbon, 50 (2012) 3154-3157.
[20] E. Dannenberg, Rubber Chemistry and Technology, 48 (1975) 410-444.
[21] E. Geberth, M. Klüppel, Macromolecular Materials and Engineering, 297 (2012) 914-922.
[22] J. Liu, S. Wu, L. Zhang, W. Wang, D. Cao, Physical Chemistry Chemical Physics, 13 (2011) 518-529.
[23] L. Mullins, N.R. Tobin, Rubber Chemistry and Technology, 39 (1966) 799-813.

Chapter 5

Reinforcement and Filler Network Dynamics

Précis:

One of the most immediately obvious results of particulate reinforcement of elastomers is the increase in compound stiffness measured either under dynamic, quasi-static or static conditions.

This chapter addresses the reasons as to why fillers increase the small strain modulus of elastomers. It starts by considering very simple model microcomposite systems where the stiffening can be entirely ascribed to 'geometrical' reinforcement - this is simply the stiffening effect arising from the incorporation of rigid, spherical inclusions into a soft elastomer matrix. In this situation there is no contribution from filler networking or the filler-elastomer interface. This is then contrasted with the corresponding data found for the carbon black-filled series of compounds. For carbon blacks there is a clear indication that additional stiffening mechanisms must arise due to the onset of filler networking and/or the immobilisation of polymer in proximity to the filler interface.

Further to this finding, the extent and nature of the filler network evident a small strains is examined using DC resistivity testing and melt rheology measurements. The polymer-filler interaction - inferred from the filler surface activity - dictates the magnitude and rate of melt thixotropy and therefore the extent of filler networking in the crosslinked material. The mechanisms underlying the apparent flocculation of filler particles in the melt are discussed in the context of the experimental findings.

Aspects of this work have been published in the peer reviewed journal *'Macromolecular Materials and Engineering*' as: LB Tunnicliffe et al. *'Flocculation and Viscoelastic Behaviour in Carbon Black-Filled Natural Rubber*', 299(12), 1474-1483, 2014

5.1. Temperature Dependence of the Elastic Modulus Amplification at Small Strains

5.1.1. Hydrodynamic and geometrical reinforcement in model microcomposites

The amplification of the small strain elastic modulus of rubber upon the introduction of filler particles has been extensively considered in terms of hydrodynamics, as was outlined in the literature review. In terms of dynamic deformations, hydrodynamic reinforcement can be considered theoretically, using linear viscoelastic theory by examining a single Maxwell element, modified to incorporate a finite modulus amplification at low frequencies.

Equation 5.1 gives the frequency response of a Maxwell element modified with a finite low frequency stiffening contribution (G'_R) which is expanded by the analytical hydrodynamic equations to account for the presence of a dispersion of solid, spherical particles within the Maxwell material.

$$G'(\omega) = \frac{g(\omega\tau)^2}{1+(\omega\tau)^2} + G'_{\mathrm{R}} \qquad 5.1$$

where $G'_R = \begin{cases} G'_0(1+2.5\varphi) & \text{……Einstein-Smallwood} \\ G'_0(1+2.5\varphi+5.0\varphi^2) & \text{……..Chen-Acrivos} \\ G'_0(1+2.5\varphi+14.1\varphi^2) & \text{……Guth-Gold} \end{cases}$

Within the Maxwell element, g is the modulus of the material in the glassy state, ω is the deformation frequency which is fixed at 1 Hz and τ is the relaxation frequency associated with the T_g and is arbitrarily fixed at 1 Hz. The modulus response is plotted in Figure 5.1 for the three hydrodynamic expansions given in Equation 5.1 and assuming I) a filler volume loading of 0.20 and II) that the T_g relaxation is unaffected by the presence of filler particles (i.e. $\tau_{\text{Filled}} = \tau_{\text{Unfilled}}$). As can be seen, at lower frequencies the finite hydrodynamic modulus amplification is recovered. If this is plotted in terms of the small strain 'reinforcement', defined by Berriot et al. [1] as $R(\omega,T) = G'_{Filled}/G'_{Unfilled}$, then a constant, temperature-independent level of reinforcement is observed (Figure 5.2).

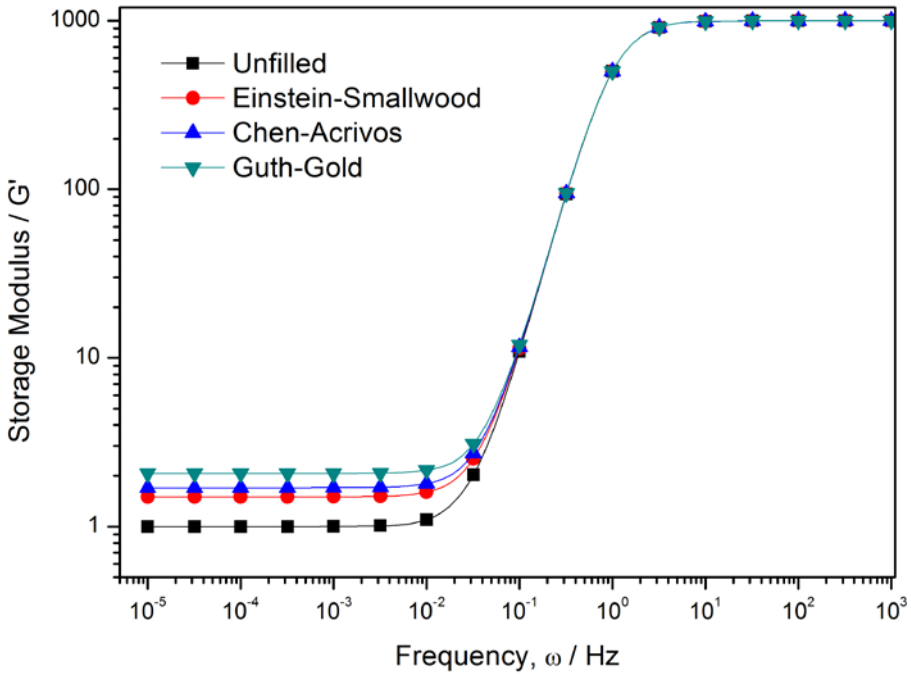

Figure 5.1: Frequency dependence of a single Maxwell element modified to account for a finite reinforcement at low frequency. Different levels of stiffening correspond to the analytical solutions to the hydrodynamic equation given in Equation 5.1 for a volume fraction loading of 0.20.

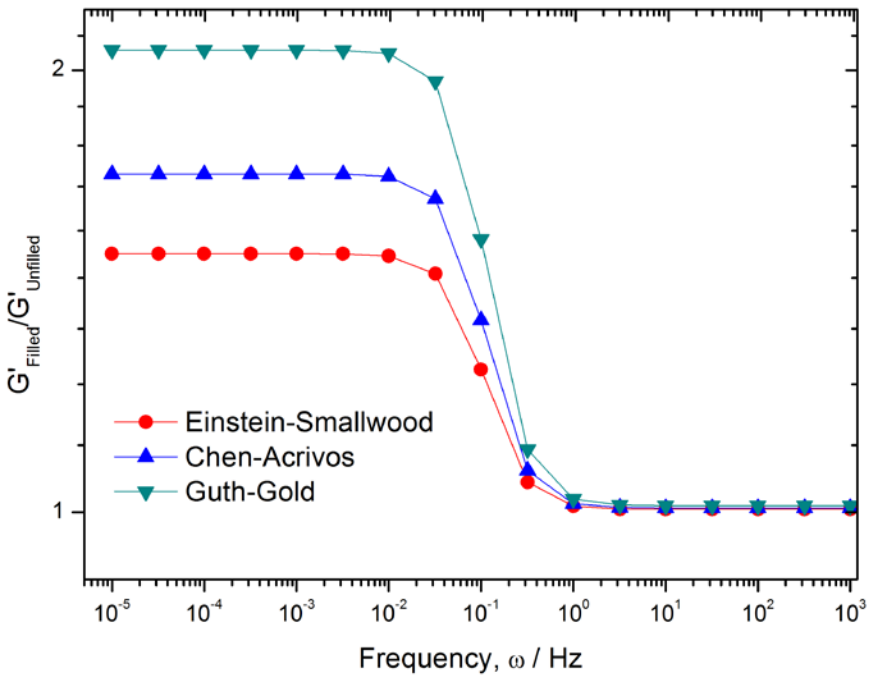

Figure 5.2: Frequency dependence of the modified, reinforced Maxwell material normalised to the frequency dependence of the unreinforced element.

Experimentally, this was explored in more detail by preparing a series of elastomers filled with model, microspheres of spherical particle morphology and variable particle sizes. These model microcomposites were prepared using solid glass microsphere fillers with a range of different particle size distributions (Potters Spheri-glass glass beads grade numbers 7010, 5000, 3000, 2530, 2227). The microspheres were not surface modified and the powders had a low moisture content (~1-3 %). The beads were dried in an oven at 100 °C for 48 hours prior to use. Low angle laser light scattering (Malvern Mastersizer) was used to determine the particle size distributions of the microspheres (see Appendix for more information on the technique). Nitrogen BET surface areas were determined using a Micrometrics pore size and surface area analyser. Particle size distributions and surface area values are given in Figure 5.3. The five different grades of microspheres were compounded with SMR CV60 grade natural rubber (NR) on an open 2-roll-mill. Microspheres were compounded at a mass loading of 50 parts per hundred rubber (phr). Components of a conventional sulphur-based cure system were then added on the open mill. The cure package consisted of elemental sulphur (1.5 phr), zinc oxide (5 phr), stearic acid (1 phr) and N-cyclohexyl-2-benzothiazol sulphenamide (CBS) accelerator (1.5 phr). Cure times corresponding to complete formation of sulphidic crosslinks (T_{100}) were obtained using an Alpha Technologies MDR 2000 at plate temperatures of 150 °C. Subsequently, 2 mm thick sheets of filled samples as well as an unfilled control were cured on a laboratory hot-press.

Temperature-domain dynamic mechanical properties of the model filled rubbers were measured on a TA Instruments Q800 DMA using a double shear clamp geometry. Rectangular samples of filled rubber material were mounted in the clamp using Loctite 480 cyanoacrylate adhesive. The deformation strain was 0.1 % (linear viscoelastic) at a frequency of 1 Hz and dynamic mechanical properties were recorded from 50 °C to -100 °C with a ramp rate of -5 K/minute. The temperature dependence of the storage moduli for model filled and unfilled samples are given in Figure 5.4. These temperature-domain data are comparable, in a general sense, with the theoretical frequency-domain Maxwell element plots of Figure 5.1 & Figure 5.2 by considering time-temperature equivalence (which is valid if no additional interfacial behaviour component is present). If the low surface areas of the model filler particles are taken into account (Figure 5.4) then this appears to be a reasonable assumption. The moduli are essentially independent of the presence of filler below the glass transition. Above the T_g, filler-induced amplification of the moduli is apparent and roughly scales with the average particle size of the microspheres. The storage moduli reinforcements are presented as an inset

in Figure 5.4. Rubber region reinforcement is apparent immediately after the glass transition but is not significantly temperature dependent. SEM micrographs of the fracture surface filler dispersion are presented in Figure 5.5 and show the spherical morphologies of the particles and the randomness of their dispersion states within the rubber matrix (contrasted to the regular body centred cubic packing dispersions considered by Chen and Acrivos [2, 3] and Guth and Gold [4, 5]). The temperature independence of the reinforcement shows that despite the random nature of the dispersion of the model filler particles, the amplification of the moduli can be fully ascribed to geometric reinforcement effects alone.

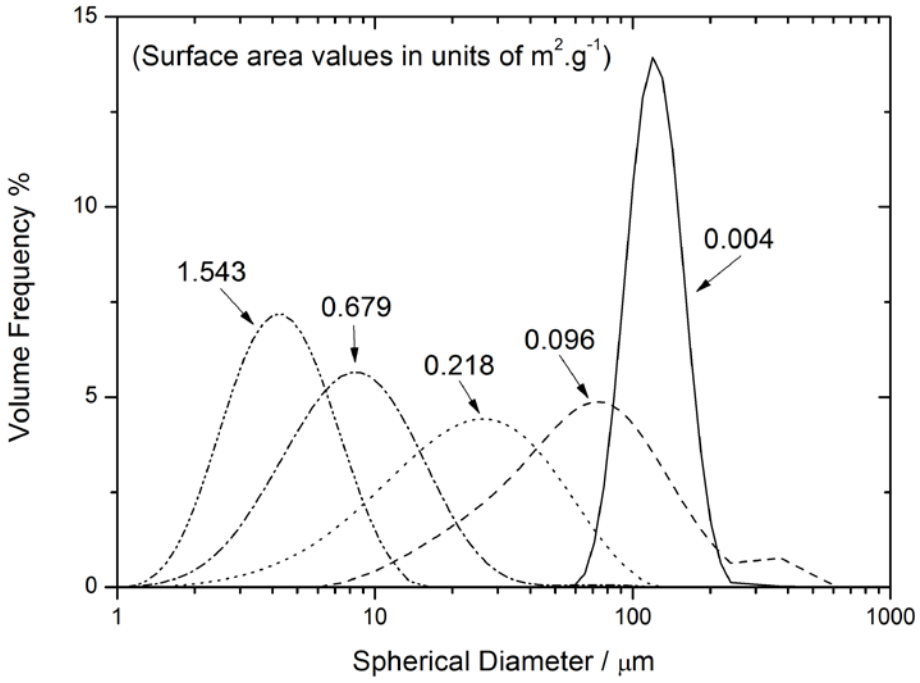

Figure 5.3: Particle size distributions of the glass bead fillers determined via light scattering experiments. Nitrogen-specific surface area values are indicated on the plot with units of m^2/g.

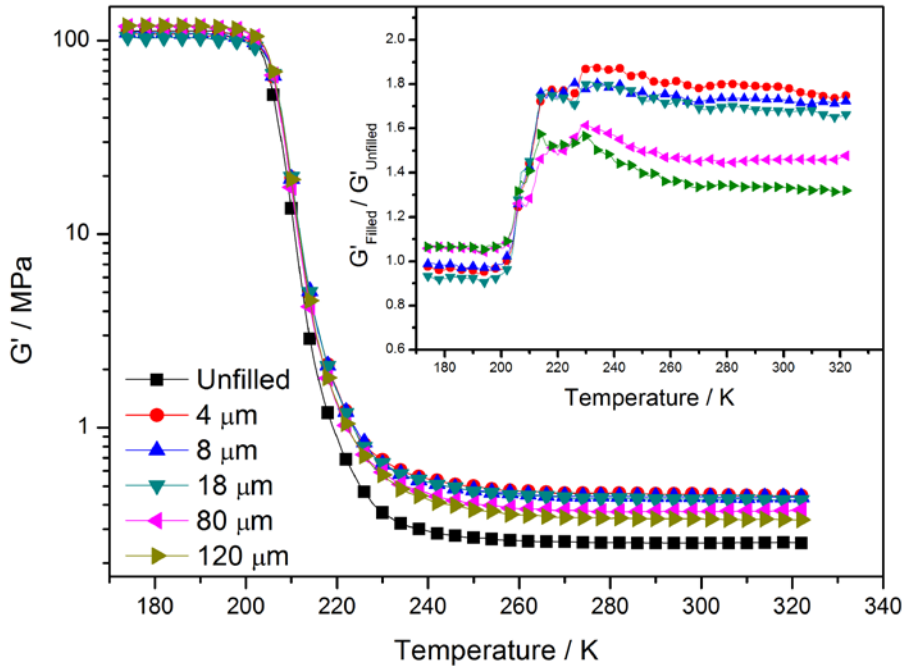

Figure 5.4: Temperature dependence of the linear viscoelastic storage modulus for glass bead-reinforced rubbers. Inset: filled sample data normalised to the unfilled material data

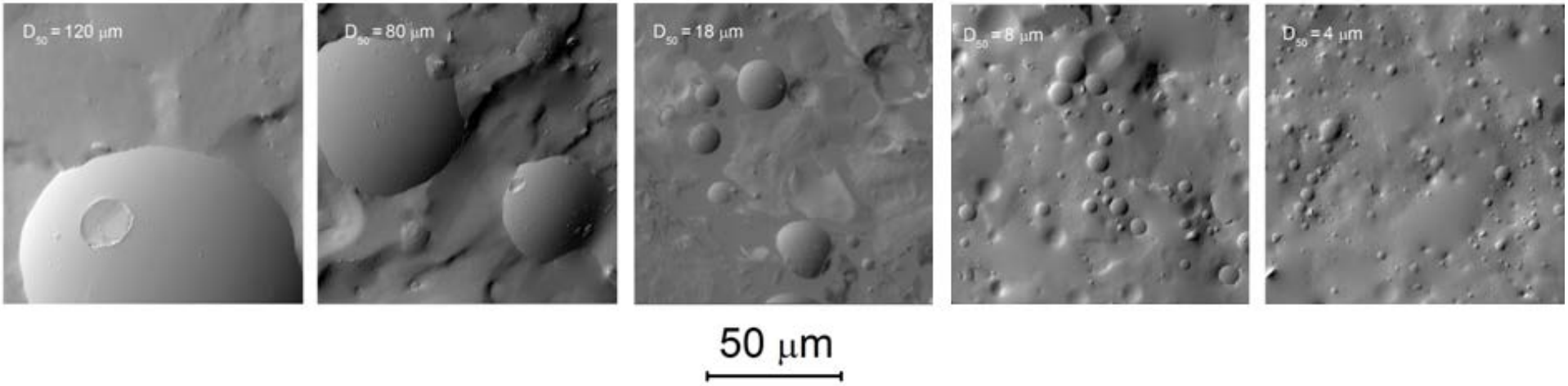

Figure 5.5: SEM images of glassy fracture surfaces of the glass bead-filled material. The reported D50 values are taken from the particle size distributions presented in Figure 5.3

5.1.2. Reinforcement in carbon black-filled compounds

Having considered the stiffening mechanisms evident for elastomers filled with model microcomposite particulates of spherical morphology, which display no tendency to form a filler network, it is now of interest to contrast these with the temperature-dependence of the small strain storage modulus of rubbers filled with much higher surface area, higher structured filler materials. For this purpose the carbon black-filled series of compounds was considered.

The dynamic mechanical properties of the carbon black filled compounds were measured using the DMA methodology described in the previous section. Figure 5.6 shows the small strain, dynamic mechanical storage moduli of the filled and unfilled crosslinked compounds as a function of temperature. Above the T_g the dramatic amplification of the storage moduli due to the presence of the filler phase is evident. It is apparent from Figure 5.6 that the reduction of modulus with temperature in the rubber region does not reflect the anticipated rise in entropic elasticity of the rubber network. Graphitised carbon blacks display significantly increased small strain moduli versus their unmodified counterparts.

Contrasting the plots of reinforcement for model filled compounds (Figure 5.5) with carbon black filled compounds (Figure 5.7), it is apparent that the independence of reinforcement on temperature, which is characteristic of hydrodynamic reinforcement, is no longer applicable to the carbon black-reinforced materials. A peak in reinforcement immediately following the T_g is apparent which decays to roughly 50 % of its initial value at T_g + 110 K. Normalised data for N990-based carbon black filled samples are plotted on a magnified ordinate in Figure 5.8 for clarity and also displays a marked, though less dramatic temperature dependence. This marked temperature dependence means that hydrodynamics alone cannot account for the stiffening of these materials.

Several temperature-dependent stiffening mechanisms have previously been proposed in the literature to account for this behaviour:

- Temperature dependence of an immobilised polymer phase (or gradient of polymer mobility) in proximity to the filler particles [1],
- Temperature-dependent slippage or desorption of polymer at the filler interface resulting in energy dissipation and reduction is stiffness [6-8], and
- A temperature dependence inherent to the mechanics of a percolating filler network [9].

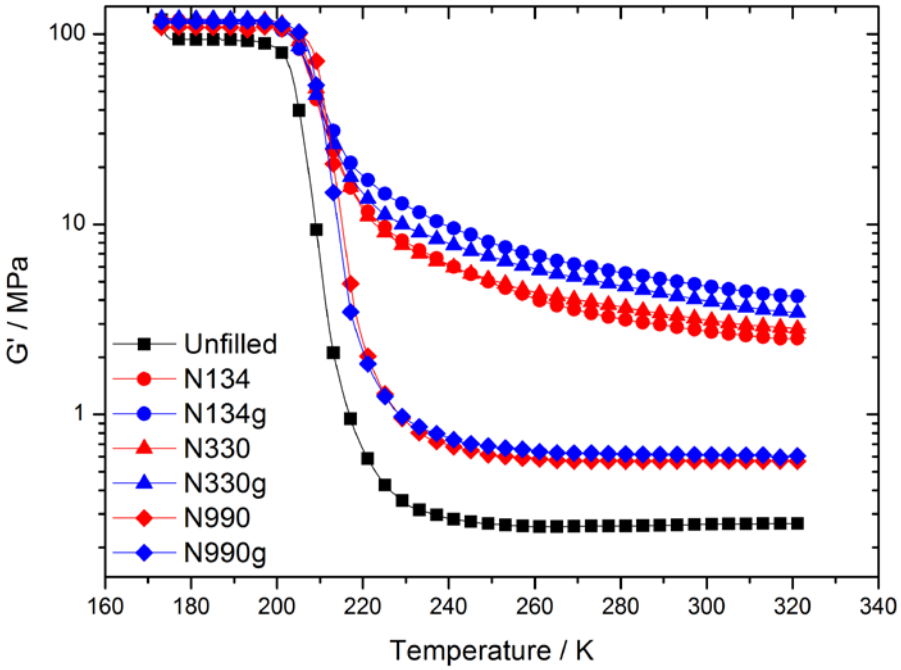

Figure 5.6: Temperature dependence of the linear viscoelastic storage moduli of unfilled and carbon black-filled NR.

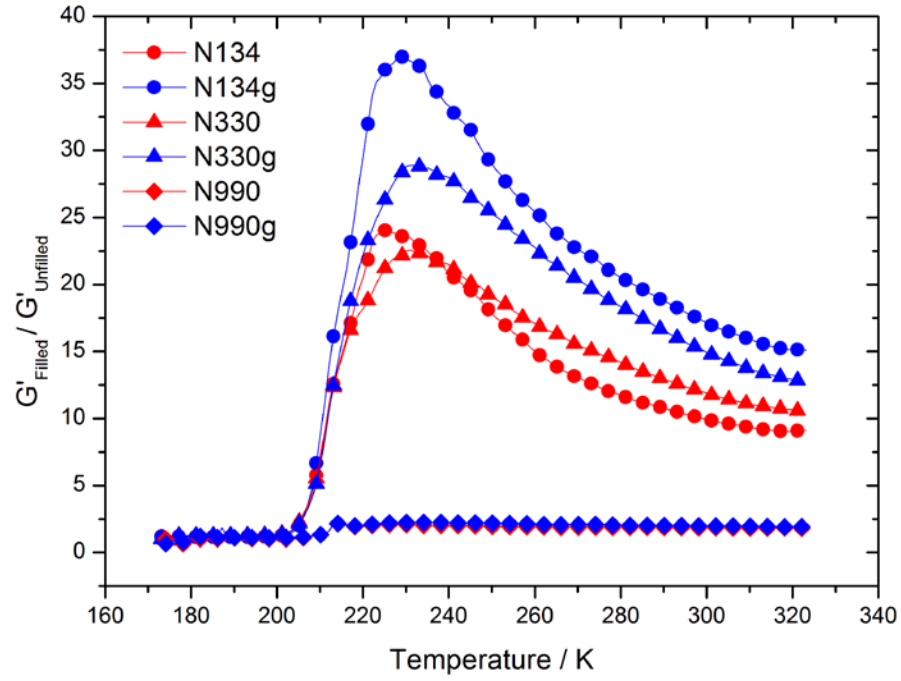

Figure 5.7: Linear viscoelastic storage moduli of carbon black reinforced rubbers normalised to the temperature dependence of the unfilled material

With respect to this final mechanism, it is noteworthy that the N990 series of fillers are effectively isolated spherical particles within an elastomer matrix and display no tendency for particle networking. Closer examination of the reinforcement of the N990 series (Figure 5.8) reveals that a marked temperature dependence is apparent even in samples without a networked, percolated filler structure. Therefore the physical mechanism underlying this temperature dependence in both high and low surface area carbon blacks appears to be, at least partially, if not wholly isolated at the filler-rubber interface rather than being related to the specific temperature-dependent mechanics of the filler network.

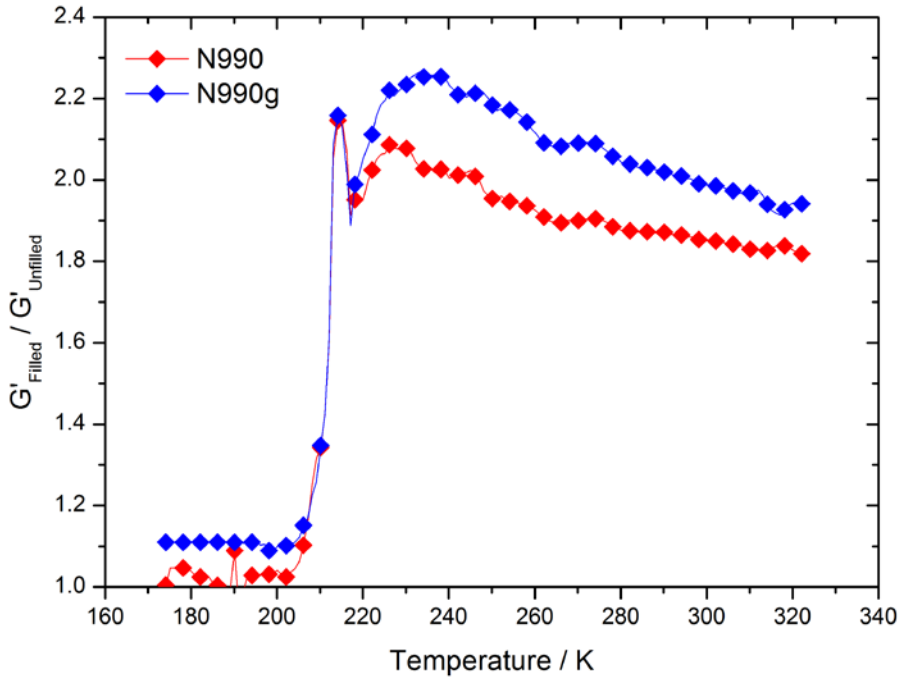

Figure 5.8: Normalised data for N990-based fillers plotted on a magnified ordinate

5.1.3. Contributions to the reinforcement peak in carbon black-filled compounds

In Figure 5.9 the average values of glass microsphere reinforcement above the T_g are plotted versus their spherical diameters on a log-log scaling. It is apparent that the reinforcement imparted by glass microsphere fillers follows a power law dependence on the particle size which is extrapolated to smaller particle sizes in Figure 5.9 (indicated by the solid line). The analytical solutions to the single term hydrodynamic equation of Einstein-Smallwood [10] and two term expansion of Chen-Acrivos [2, 3] are also plotted as dashed lines for the volume fraction corresponding to the volume loading of glass beads. As can be seen, the analytical

solutions can only account for the two largest particle sizes of microsphere. Considering the temperature independence of the reinforcement and also the micrometre length scale of the microspheres, nanoscale confinement-based modifications of the elastomer dynamics can be ruled out. Filler networking is also not relevant at these particular volume fractions. From the SEM observations of the filler microstructures (Figure 5.5) it is clear that higher expansion terms of the hydrodynamic polynomial series would be required to analytically account for the geometrical irregularity of the bead dispersions. The stiffening effect of the random placement of particles in an elastomer matrix has been addressed by Bergström and Boyce [11], Jha et al. [12], Gusev and Rozman [13] and Busfield et al. [8]. In their stochastic finite element simulations, they found that stiffening in these systems can be readily explained by a combination of hydrodynamics, strain amplification [14] and elastomer occlusion [15, 16]. In particular, Gusev and Rozman [13] identified that the geometry of the filler structure formed within the rubber phase (hexagonal, random, honeycomb, web-like) can have a dramatic effect on the resulting small strain stiffening observed. It is noteworthy that none of these mechanisms are likely to be temperature dependent - as supported by the data of Figure 5.4.

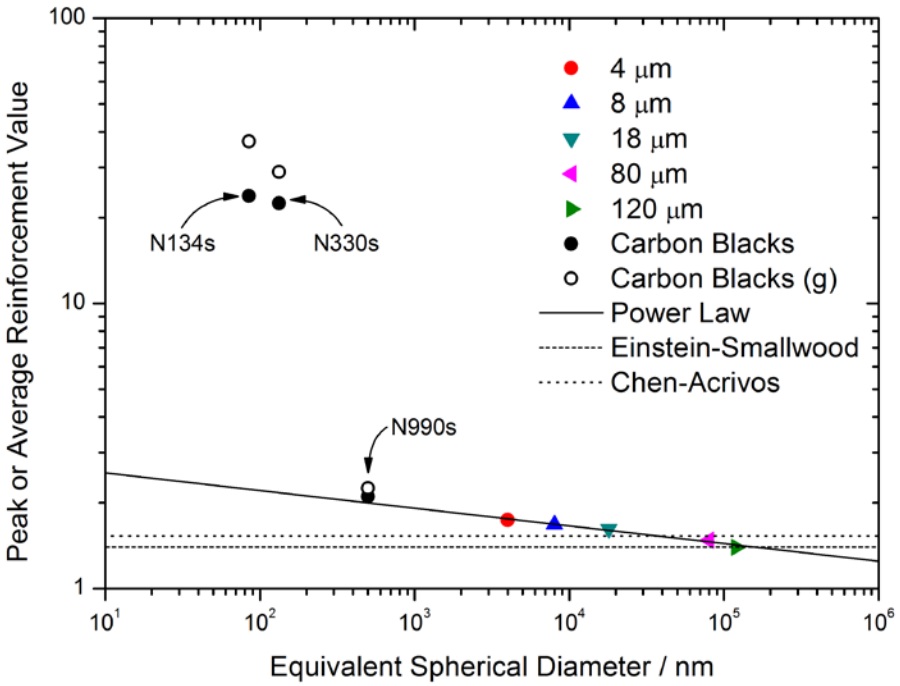

Figure 5.9: Average reinforcement value for temperature-independent samples or peak reinforcement value (typically located immediately following the glass transition) for temperature-dependent samples versus the filler spherical (or equivalent spherical) diameter. Note that the N330 and N134 data are plotted versus equivalent spherical diameters taken from Donnet et al. [17]

Figure 5.9 also plots the peak values for reinforcement observed just after the T_g versus the equivalent spherical diameter of the carbon black aggregates taken from Donnet [17] (the literature value for N110 is used for the N134 sample). The data for N990-based carbon black appears in relatively good agreement with the power law trend of the microspheres. The small discrepancy of around 10 % is almost exactly accounted for by the somewhat different volume fractions used for the glass microspheres (0.16) and the carbon black (0.20) fillers. Therefore the peak reinforcement imparted by N990 is attributable to hydrodynamics, strain amplification and elastomer occlusion processes. The slight difference in peak reinforcement observed between N990 and N990g-filled samples is probably due to differing placements (dispersions) of spherical particles within the elastomer - which is dictated by filler particle surface free energy [18] and the effectiveness of the mixing procedure.

It is therefore possible to qualitatively explain the stiffening effects imparted by spherical fillers of particle diameters down to ~300 nm. For the N990-based fillers this is particularly interesting in light of the observed temperature dependence of the reinforcement following the peak value post T_g. The mechanism for this temperature dependence cannot result from an immobilisation (stiffening) of polymer in the vicinity of the filler particles but is more likely to be related to a 'softening' or 'weakening' of the phase coupling at rubber-filler interface.

The levels of reinforcement for both the N330 and N134-based fillers lie an order of magnitude above the extrapolated trend of the larger particle sizes. It is clear that in the particle diameter range of between 300 - 100 nm, additional reinforcing mechanisms must be present. For example:

- Particle networking in the melt during shear processing and curing becomes more important as the filler particle size is reduced, due in part to the particle size dependence of the diffusion coefficient [19, 20]. The load bearing capacity of the filler network has been explored by numerous researchers and has been proposed to contribute significantly to the small strain modulus [21-23],
- Strain amplification and elastomer occlusion stiffening effects have also been shown to profoundly depend upon the degree of particle dispersion and fractal networking [24],
- Additionally the large filler surface areas and reduced inter-aggregate distances potentially promotes immobilisation (stiffening) of polymer in proximity to the filler surface which is not apparent in the microcomposite systems [1, 22].

From this work it can be concluded that the stiffening effects observed in the model microcomposites and for N990-based compounds can be attributed entirely to 'geometrical' reinforcement effects. There is no direct evidence to suggest that a modification in polymer dynamics is required to explain the levels of reinforcement observed. It is important to note that these compounds are filled far below the particle percolation thresholds, meaning that no filler networks are developed. As the following section will demonstrate, the N134 and N330-based fillers all form a percolated filler networks at φ = 0.20. This complicates the interpretation of the stiffening effects seen for these compounds, as the increase in reinforcement and the temperature dependence of the modulus can no longer be ascribed solely to the rubber-filler interface with full confidence. Therefore in the next chapter, an attempt is made to directly study the effects of the filler particles on the glass transition of the polymer phase to determine whether the observed jump in reinforcement seen in Figure 5.9 for the high surface area carbon blacks can be correlated with an immobilisation of the rubber phase by the polymer or if it is solely related to development of a filler network.

5.2. Extent of filler networking

The extent of filler networking in the N134 and N330-based samples was determined by electrical resistivity measurements as a function of the volume fraction of filler loading. Strips of crosslinked samples were tested on a DC electrical testing stage constructed according to ASTM D991-89 [25] standard to determine their static volume resistivity values. The testing stage measured 4 point contact resistance. From Ohmic current-voltage plots the resistance was calculated and transformed to sample volume resistivity according to Equation 5.2 where ρ is the volume resistivity, R is the measured resistance and A and L are the cross sectional area and sample length respectively.

$$\rho_{\mathrm{DC}} = \frac{RA}{L} \qquad 5.2$$

Figure 5.10 A & B shows plots of log conductivity versus volume fraction of filler for the various types of carbon blacks studied. Note that data for N990-based fillers are not shown as the maximum volume loading considered here falls substantially below the filler's percolation

volume fraction. The electrical behaviour of N990-filled elastomers at φ = 0.20 was found to be identical to that of the insulating unfilled material. Data was fitted to Equation 5.3, which is derived from percolation theory [26-28], to give the quantitative values of the percolation thresholds reported in Figure 5.10.

$$\sigma_{\mathrm{dc}} = \sigma_0 \left(\frac{\varphi - \varphi_{\mathrm{C}}}{1 - \varphi_{\mathrm{C}}}\right)^{\mu} \qquad 5.3$$

where σ_{dc} is the DC conductivity, σ_0 is the DC conductivity above the percolation threshold, φ is the volume fraction of filler loading, φ_C is the percolation volume fraction and μ is a power law exponent.

The percolation thresholds correspond to the formation of a continuous electrical conduction pathway through the sample. At a microstructural level this is achieved by proximity of conductive aggregates, either through direct contact or tunnelling through thin layers of polymer between aggregates [22]. The jump in conductivity of several order of magnitude observed for each sample at a critical volume fraction level is taken as proof of the formation of a filler network structure.

As can be seen in Figure 5.10 both larger particle surface areas and reductions in SFE significantly reduce the percolation thresholds of the carbon blacks in the crosslinked samples. This is as a direct result of melt thixotropy during the early stages of the crosslinking process and will be explored in the following section. Graphitisation of the carbon blacks results in a shifting of the percolation threshold to lower volume fractions.

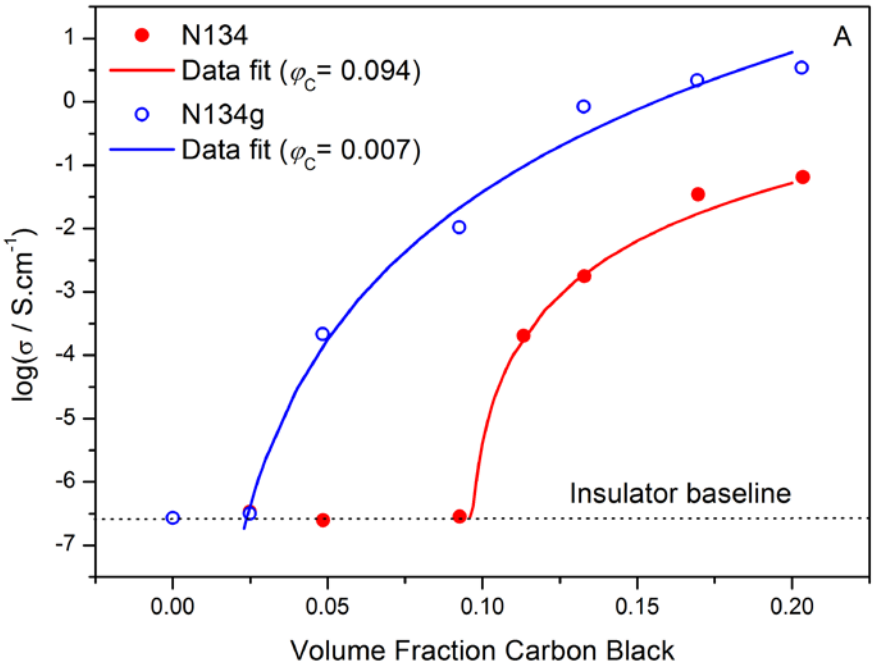

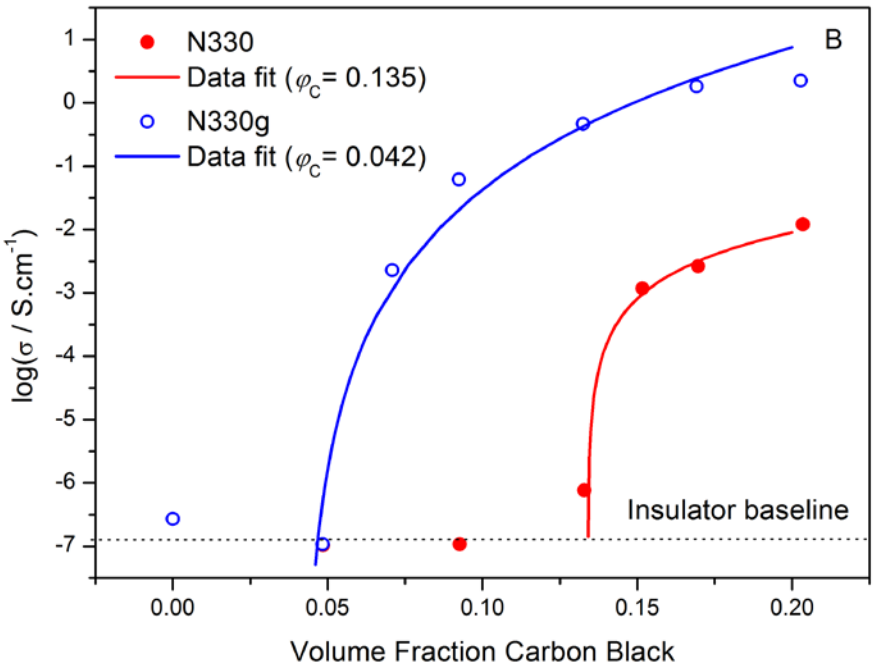

Figure 5.10 A & B: Conductivity versus filler volume fractions on a semi-log scale. Values of percolation threshold, φ_C, are determined from fits to Equation 3. The baseline conductivity value recorded for insulating materials is indicated by the dotted line

5.3. Filler Structure Dynamics in the Melt

The previous sections have concentrated on the filler-induced amplification of modulus observed in crosslinked compounds. However the absolute magnitude of this reinforcement is dictated by the melt rheology of filled compounds during processing. Above the T_g and prior to chemical crosslinking, filled rubbers can be classified as filled polymer melts. Melt rheology plays an important role in defining the processability of rubber compounds but is also indicative of the reinforcing characteristics of the filler material. Highly filled rubber melts are shear thinning, thixotropic viscoelastic materials where the filler loading, surface area and aggregate morphology all play a key role in dictating the rheology and the extent of 'filler network' development within the compound [29]. An illustrative example from the literature is given in Figure 5.11 [30] and shows the high temperature time dependent evolution of a filler network resulting in an initial stiffening of the melt prior to the onset of crosslink formation.

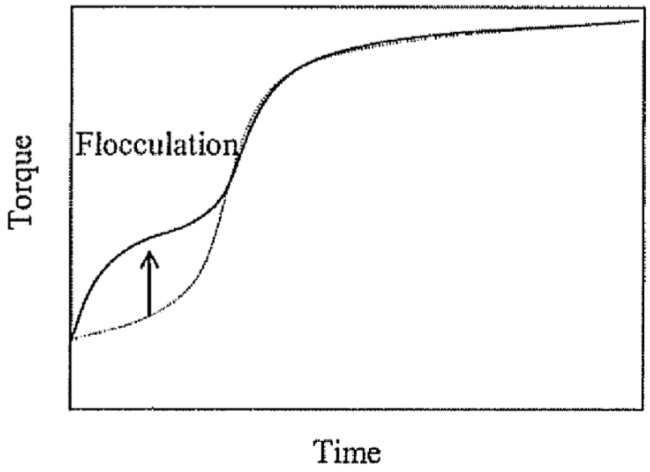

Figure 5.11: Literature example of flocculation evident in the initial stages of curing a silica filled material [30]

Rheological properties of the filled NR melts prior to the incorporation of curing chemicals were examined using a Rubber Process Analyser (RPA) from Alpha Technologies[1]. A simple

[1]Unfortunately the RPA equipment does not provide the individual sinusoidal waveform data. Therefore it is impossible to assess the contribution to the dynamic response in terms of higher harmonic contributions arising at large amplitude oscillatory strains. It is therefore assumed in this work that the response at higher strains is linear with a minimal contribution from higher order harmonics. This is actually in line with previous observations of the 'harmonic paradox' for the Payne effect in filled rubber materials.

experiment was performed in order to probe filler structure dynamics - specifically the breakdown and recovery dynamics - in the melt. Samples were loaded into the rheometer test chamber which had a preheated plate temperature of 150 °C. The samples were left to rest for 20 minutes in order to reach thermal equilibrium and ameliorate loading strains. Then they were subjected to a dynamic strain sweep from 0.1 to 10 % dynamic shear strain. Immediately following the strain sweep the dynamic excitation was dropped back to 0.1 % and viscoelastic properties were monitored for a further 20 minutes. This procedure is schematically illustrated in Figure 5.12. All deformations were performed at a fixed frequency of 1 Hz. This experimental procedure produces 2 sets of test data: one related to the strain softening of the melt and one related to the recovery of modulus post deformation.

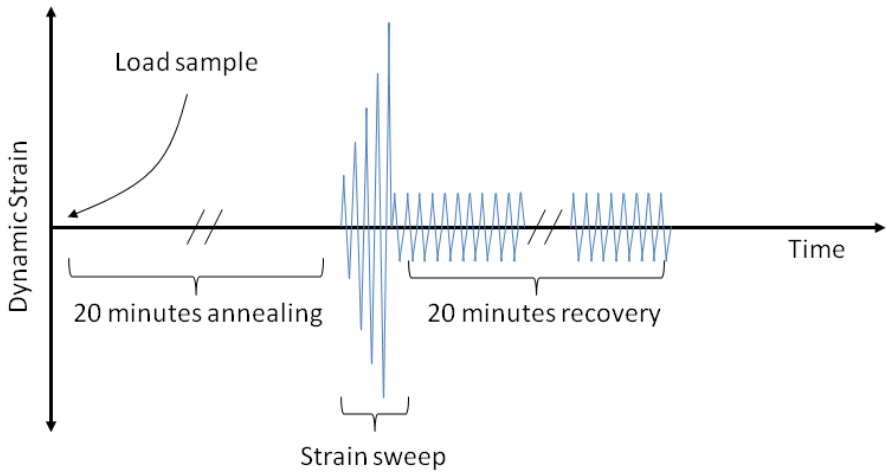

Figure 5.12: Schematic illustration of the RPA test procedure. The abscissa is the experimental timescale. Sweep amplitudes are for schematic purposes only

Rheological data for the carbon black and silica-filled series are presented in Figure 5.13 and Figure 5.14 respectively. For the carbon black-filled samples it is immediately clear that a change in surface free energy (SFE) has a dramatic effect on the rheological properties of the filled rubbers. Examination of the strain sweep data shows that graphitization of the filler results in an approximate trebling of the modulus at small strain. These effects seem to scale with surface area and particle size for N330 and N134-based grades. It is noteworthy that linear viscoelastic behaviour is not particularly pronounced especially for the graphitized carbon blacks, indicating that the filler structures in the melt are fragile when compared to their crosslinked analogues. This finding supports the previous conclusions of Wang [31]. Similarly the surface activity of the silica particles dictates the magnitude and extent of non-

linear behaviour in the melt. It is obvious that the silica filled rubbers are significantly stiffer at small strain than the carbon black-filled counterparts.

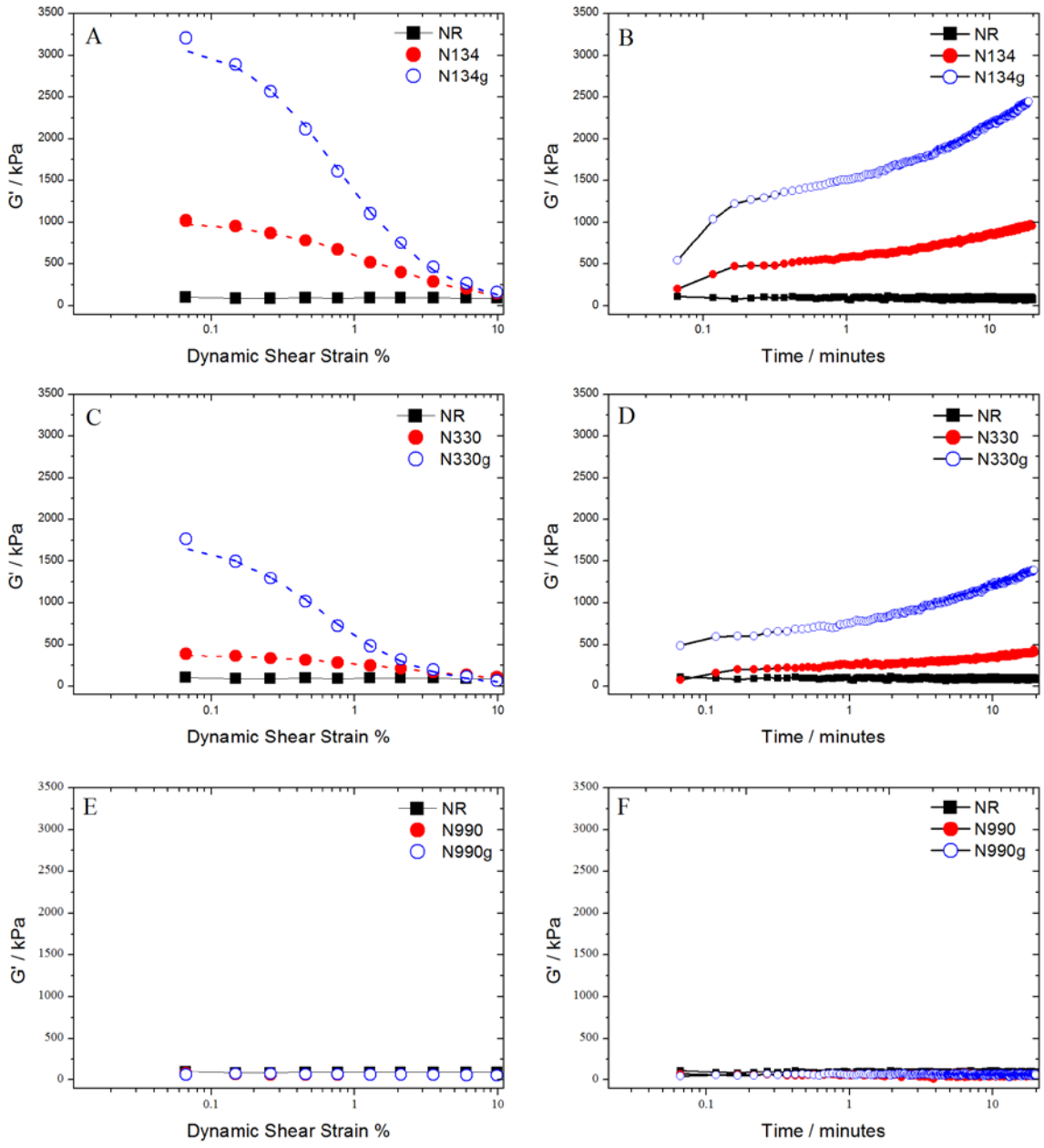

Figure 5.13: Rheological data for carbon black-filled NR melts. A, C & E) Strain yielding data (dashed lines are fits to the Kraus Equation). B, D & F) Thixotropic recovery data. Note that the thixotropic recovery data is plotted versus a logarithmic time scale to emphasise the initial recoveries of the moduli.

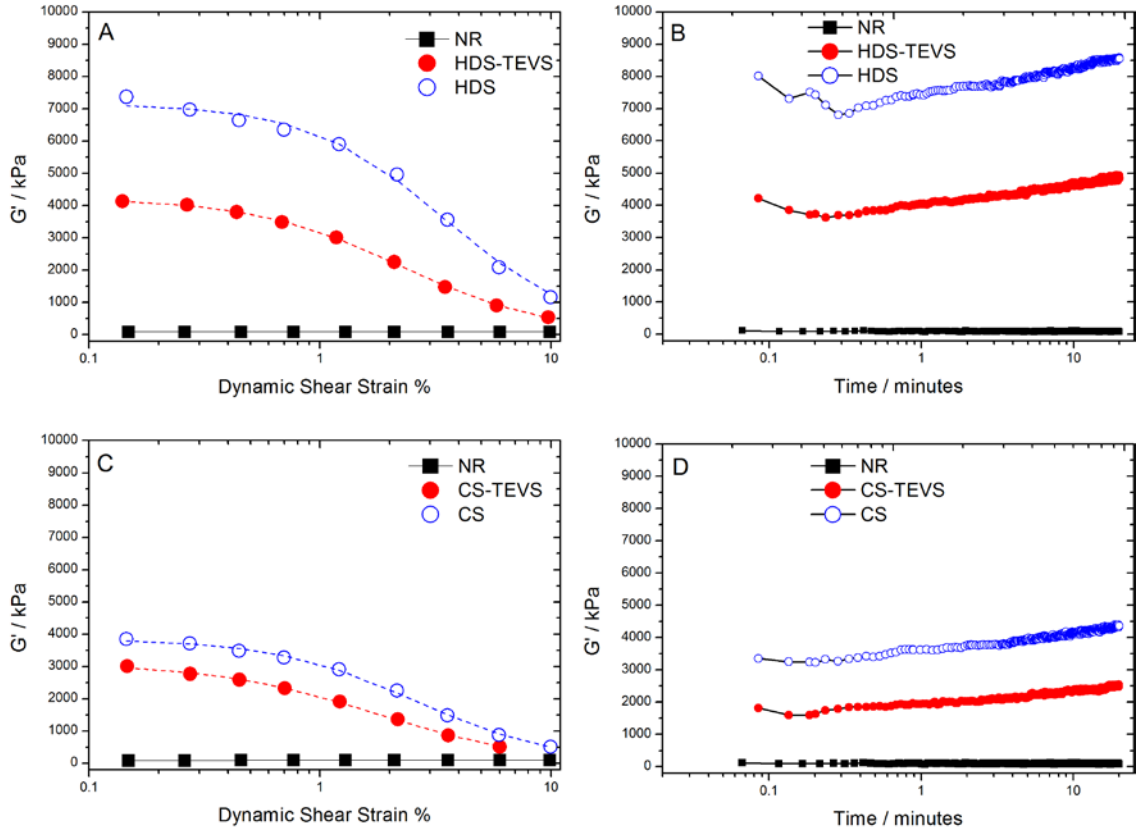

Figure 5.14: Rheological data for silica-filled NR melts. A, C & E) Strain yielding data (dashed lines are fits to the Kraus Equation). B, D & F) Thixotropic recovery data. Note that the thixotropic recovery data is plotted versus a logarithmic time scale to emphasise the initial recoveries of the moduli.

5.3.1. Filler structure breakdown

For a more quantitative analysis of the strain sensitivity of the filler structure in the melt, the data collected from the strain yielding process were fitted using the Kraus Equation [32, 33] which is based upon a physical concept of agglomeration and de-agglomeration of particulates connected via van der Waals forces

$$\frac{G'(\gamma) - G'_{\infty}}{\Delta G'} = \frac{1}{1 + \left(\frac{\gamma}{\gamma_C}\right)^{2m}} \qquad 5.4$$

where $G'(\gamma)$ is the storage modulus, G'_{∞} is the storage modulus at high strain, γ is the applied dynamic strain, γ_C is the critical strain and m is a power law exponent.

The fits to the data are presented in Figure 5.13 and Figure 5.14 as dashed lines. The Kraus Equation contains two fitting parameters: γ_C, which corresponds to the strain at which half of the proposed filler-filler contacts have been ruptured and a term, m, which describes the shear sensitivity of the yielding process. These fitting parameters are reported in Table 5.1 for both sets of fillers. For the carbon black-based fillers it is clear that a reduction in SFE of the carbon black results in an increased shear sensitivity of the filler structure and a more rapid yielding of the filler structure under the application of strain. For silica fillers, the modification of the surface with TEVS acts to reduce the small strain stiffness of the compounds, to decrease the shear sensitivity parameter, m, and also to decrease the critical strain γ_C. This is related to the silane's ability to suppress and shield strong filler-filler interactions arising from hydrogen bonds formed between silica aggregates.

Table 5.1: Fitting parameters from Equations 5.4 and Equation 5.5 plus the calculated fractional thixotropic recovery observed 20 minutes after the strain sweep

Carbon Black	$\gamma_{C\,\%}$	***m***	k_{fast} **/ s**	k_{slow} **x10^{-3} / s**	**Fractional thixotropic recovery[A]**
N134	1.439	0.514	0.14	1.6	0.39
N134g	0.783	0.616	0.16	1.7	0.47
N330	2.644	0.414	0.13	1.2	0.31
N330g	0.594	0.621	0.24	1.9	0.40
HDS-TEVS	2.263	0.676	N/A	N/A	0.70
HDS	3.479	0.734	N/A	N/A	0.77
CS-TEVS	1.749	0.632	N/A	N/A	0.61
CS	2.605	0.707	N/A	N/A	0.72

[A]Defined as: $(G''_{t=inital} - G'_{\gamma=10\%})/(G'_{t=20\,mins} - G'_{\gamma=10\%})$

From an examination of the high strain response of the carbon black-filled rubbers during the strain sweep experiment it is apparent that at the highest strain (10 %), the moduli of the unmodified fillers are broadly equivalent to those of the surface modified fillers. This can be understood in terms of hydrodynamics and strain amplification. As the filler morphologies and surface areas are essentially unchanged by the graphitisation process, their potential for hydrodynamic and strain amplification reinforcement should remain equivalent to their

unmodified counterparts. The majority of the filler structure is broken down at large strains leaving only the hydrodynamic and strain amplification reinforcing effect of the disaggregated particulates [34]. The dramatic differences in rheology observed at smaller strains are therefore the sole result of strain and temperature-induced flocculation. For silica-based fillers at 10 % strain there is still a significant modulus difference between surface modified and unmodified particles - particularly in the case of the HDS grade of silica. We should recall that the silicas and carbon blacks are not of comparable surface areas. It is therefore reasonable to assume that the filler structures apparent in HDS-based fillers are not completely broken down at this level of strain.

The N990 carbon black-based fillers displayed no strain or time dependent rheology. This is not surprising considering the size of the particles - approximately 280 nm in diameter - and the theoretical percolation threshold for N990 which is equivalent to a volume fraction loading of around 0.53. It is clear that for N990 no filler networking occurs.

5.3.2. Filler structure recovery

Considering the time dependence of the recovery of the dynamic modulus, *G'*, after the applied strain sweep (Figure 5.13 B, E & F. Figure 5.14 B & E) it is clear that there are significant strain-induced thixotropic effects apparent in all of the high structure, high surface area carbon black and silica filled melts. From these data it is apparent that the flocculation process operates across a broad range of timescales. The time axis is plotted logarithmically to highlight this. Within the initial minute of the experiment a substantial amount of structure (modulus) is recovered (note that data is lost in the initial few seconds of the experiment run due to the equipment response time). Over longer timescales a much slower contribution to the total recovery process is observed. Meier and Klüppel [23] have observed similar effects induced by thermal annealing of carbon black-filled S-SBR using a bi-exponential deconvolution

$$G' = G'_1\left(1 - e^{-k_{fast}t}\right) + G'_2\left(1 - e^{-k_{slow}t}\right) \quad 5.5$$

where t is the experimental time, k_{fast} is the rate constant corresponding to the initial rapid contribution and k_{slow} is the rate constant for the slower contribution).

Such a fitting process is also able to reasonably describe the data reported here for the higher surface area carbon black-filled compounds (Figure 5.15) indicating that there is a microstructural equivalence between flocculation effects induced by a step change in temperature (annealing) and those induced by pre-shearing. Rate constants corresponding to the fast and slow thixotropic processes extracted from the fitting de-convolution are given in Table 5.1. Upon graphitisation of the carbon blacks both rate constants are seen to increase.

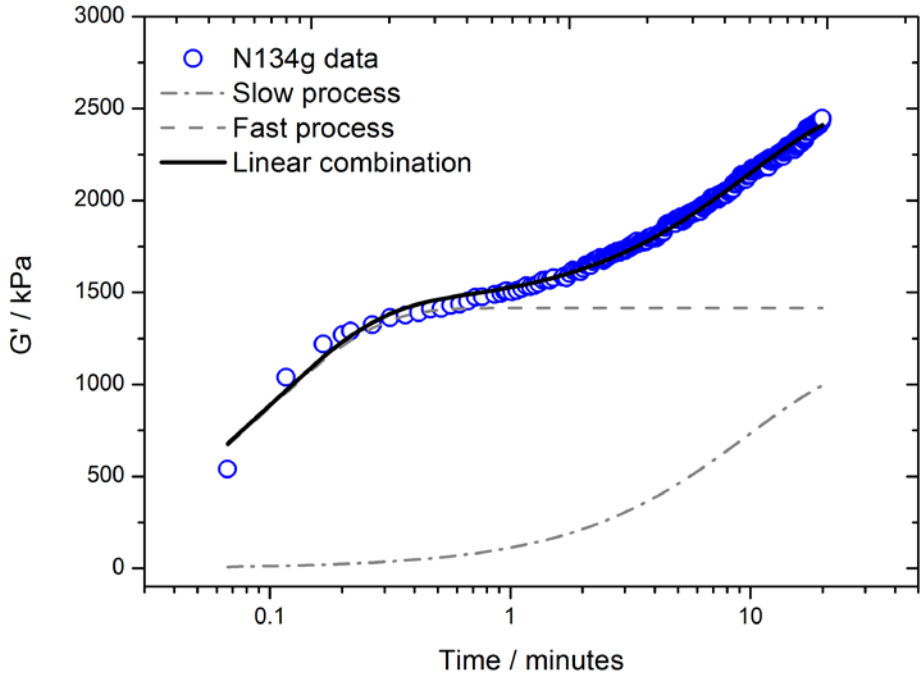

Figure 5.15: Example fit of thixotropic recovery behaviour to a bi-exponential model

For the silica-filled compound data the proposed bi-exponential process is harder to validate. For the carbon black compounds there is a very obvious two stage contribution to thixotropy even through some data was lost in the initial few moments of the experiment. Examining the corresponding data for silica-filled compounds (Figure 5.14 B & D), specifically the magnitude of the initial few data points, it is apparent that the vast majority of structure has been recovered even prior to the onset of measurement (that is, within the instrument dead time). Contrasting the magnitudes of this recovery defined as $(G''_{\mathrm{t=inital}} - G'_{\gamma=10\%})/(G'_{\mathrm{t=20\ mins}} - G'_{\gamma=10\%})$ in Table 5.1, it is clear that the initial thixotropic recovery occurs at a much more rapid rate in silica-filled compounds than carbon black-filled compounds. In the

initial 10 seconds of the experiment the storage modulus decreases somewhat prior to the onset of a more gradual rise in modulus with time. Note that the upturn in modulus at longer timescales observed for carbon black-filled compounds (when plotted logarithmically) is absent and that the data beyond the initial few seconds seem accurately described by a simple logarithmic fit. One possible explanation for these effects lies in the rapidity of the initial thixotropic recovery when contrasted with the experimental timescales. In the transition between the strain yielding experiment and the structure recovery experiment there is a finite instrument dead time during which the sample is subjected to no shear. During the dead time the structure is rapidly recovering to a zero shear state. When the small strain shear of the structure recovery step commences it is imposed over a sample which has recovered, to some extent, to the zero shear condition. It is possible therefore that the decrease in stiffness observed in the initial few seconds of measurement actually corresponds to a slight time dependent shear thinning of the material. At longer timescales the structure reaches steady state and the observed increase in modulus corresponds solely to structural recovery over a longer timescale. More precise instrumentation and experimentation would be required to confirm this hypothesis.

5.4. Discussion

These simple rheological experiments have probed a number of aspects of the phenomenology of the dynamics of filler networks in the melt. The general findings are as follows:

- Weaker rubber-filler interactions result in an increased small strain modulus,
- Altering the rubber-filler interaction via surface modifications has a significant effect on the shear sensitivity of the filler networks,
- The thixotropic shear recovery process operates across a range of timescales, highlighted by the bi-exponential behaviour of the thixotropic recovery of the carbon black-filled compounds,
- The rate of thixotropic recovery is influenced by the nature of the polymer-filler interaction, and
- The initial thixotropic recovery in silica-filled compounds proceeds at a much faster rate than in the carbon black-filled compounds.

A complete understanding of these phenomena in terms of microstructural origins in not possible without significant further work. However, with reference to the literature it is possible to draw some basic conclusions.

Due to the relatively high volume fraction of the networked carbon blacks and silica aggregates in the melt it is likely that the application of shear significantly disrupts the established filler network by overcoming the attractive forces between particles. Such forces have been proposed to result from van der Waals attractions between aggregates [9, 32], hydrogen bonding between aggregates for the case of silica fillers [30], bridging polymer chains adsorbed onto adjacent particulates [35] or immobilised, glassy polymer in gaps between aggregates [23]. Whatever the physical origin of the binding forces between particles, they must be overcome to some extent by mechanical deformation. Due to the crowded nature of the particulate filled system such attractive connections are rapidly re-established between particles in close proximity upon cessation of deformation resulting in the rapid initial recovery of modulus. Longer timescale effects may correspond to agglomeration or reorientation of structures with a larger length scale than that of the individual filler aggregates (flocs or cluster-cluster aggregates) as proposed by Maier and Klüppel [23].

The role of the diffusion coefficient of the filler aggregates in the recovery of modulus following shear has not yet been conclusively resolved in the literature. Many papers make reference to the Brownian diffusion of filler aggregates as the driving force behind melt thixotropy - that is thixotropy is apparent due to filler aggregate flocculation. The diffusion coefficient for particles of spherical morphology is [36]

$$D = \frac{\mathbf{k}T}{\eta 6\pi r} \qquad 5.6$$

where D is the diffusion coefficient, $\mathbf{k}$ is the Boltzman constant, T is the temperature, η is the viscosity of the matrix and r is the particle radius.

However, this has been questioned by the experimental results of Schwartz et al. [35]. Nevertheless, the data presented here can be interpreted in terms of an aggregate Brownian diffusion mechanism. It is clear that fillers with a reduced rubber-filler interaction display increased rates of thixotropic recovery (contrast the rate constants for the carbon black fillers

and the logarithmic pre-factor for the silica fillers). This could be rationalised by a reduced (effective) viscosity term in Equation 5.6 due to an easier detachment and slippage of polymer at the filler surface. However, this process does not consider any contribution to thixotropy from a time dependent contribution from the polymer phase. This could take the form of bridging polymer chains between filler aggregates stiffening the filler network as proposed by Schwartz et al. [35] or originate from an immobilisation and stiffening of polymer between filler aggregates. Future work on model compounds may help to evaluate the contributions.

5.5. Future work

This work has considered commercially relevant materials in terms of their filler structural dynamics in the melt. However, as alluded to in the discussion, more controlled test samples are required in order to attempt to deconvolute the contribution to total melt thixotropy from aggregate flocculation and polymer phase mechanisms. A further investigation is outlined below:

Polyvinyl acetate (PVA_C) is used as the polymer phase. PVA_C has a number of advantages over NR for use as a model rubber melt:

- Various molecular weights of PVA_C are commercially available,
- PVA_C contains fewer non-polymer impurities in comparison with NR,
- It is possible to produce filled samples of PVA_C though solution processes which minimises the scission of polymer chains arising from shear mixing of compounds, and
- PVA_C has a T_g typically just above ambient temperature - making characterisation of the T_g very simple in contrast to NR where cryogenic conditions are required.

Fumed silica is used as the filler phase:

- Certain fumed silicas have a broadly spherical morphology versus precipitated silica,
- Fumed silicas are available with relatively low surface areas (commercially down to 45 m^2/g),
- Fumed silicas can be compounded with PVA_C using a solution processing route. The route detailed by Sternstein et al. [6] has been shown to achieve very good dispersion of the individual silica filler particles in the PVA_C phase.

Such compounds could be used to study the role of bridging polymer chains between filler aggregates. For example, if the fumed silica was loaded at sufficiently low volumes so that the silica particles were essentially isolated in the melt and if the fumed silica used was of sufficiently large particle size so as to suppress Brownian motion of the particles then it would be possible to obtain a rough idea of inter-particle distances. This could be achieved qualitatively through SEM observations or by using a suitable radiation scattering technique. Coil sizes in the melt can be estimated and contrasted with the inter-particle gap size. By varying the PVA_C weight it should be possible to reach a point where the inter-particle gaps may be bridged be a single polymer chain. This provides a method for studying the mechanism proposed by Schwartz et al. [35] and may help to deconvolute the contributions to thixotropy in commercial filled melts.

5.6. References

[1] J. Berriot, H. Montes, F. Lequeux, D. Long, P. Sotta, Macromolecules, 35 (2002) 9756-9762.
[2] H.S. Chen, A. Acrivos, International Journal of Solids and Structures, 14 (1978) 331-348.
[3] H.S. Chen, A. Acrivos, International Journal of Solids and Structures, 14 (1978) 349-364.
[4] E. Guth, Rubber Chemistry and Technology, 18 (1945) 596-604.
[5] E. Guth, Rubber Chemistry and Technology, 23 (1950) 635-643.
[6] S.S. Sternstein, S. Amanuel, M.L. Shofner, Rubber Chemistry and Technology, 83 (2010) 181-198.
[7] P.G. Maier, D. Göritz, Kautschuk Gummi Kunststoffe, 49 (1996) 18-21.
[8] J.J.C. Busfield, V. Jha, A.A. Hon, A.G. Thomas, Conference Proceedings: Constitutive Models for Rubber IV, P.E. Austrell, L. Kari (Eds.), Balkema, Stockholm,
[9] K. Arai, J.D. Ferry, Rubber Chemistry and Technology, 59 (1986) 592-604.
[10] H.M. Smallwood, Rubber Chemistry and Technology, 18 (1945) 292-305.
[11] J.S. Bergström, M.C. Boyce, Rubber Chemistry and Technology, 72 (1999) 633-656.
[12] V. Jha, A.A. Hon, A.G. Thomas, J.J.C. Busfield, Journal of Applied Polymer Science, 107 (2008) 2572-2577.
[13] A.A. Gusev, M.G. Rozman, Computational and Theoretical Polymer Science, 9 (1999) 335-337.
[14] L. Mullins, N.R. Tobin, Rubber Chemistry and Technology, 39 (1966) 799-813.
[15] A.I. Medalia, Journal of Colloid and Interface Science, 32 (1970) 115-131.
[16] A.I. Medalia, Rubber Age, 104 (1972) 67-71.
[17] J.B. Donnet, R.C. Bansal, M.J. Wang, (Eds), Carbon Black: Science and Technology, 2nd ed., Marcel Dekker Inc, New York, 1993
[18] K.W. Stöckelhuber, A.S. Svistkov, A.G. Pelevin, G. Heinrich, Macromolecules, 44 (2011) 4366-4381.
[19] M. Gerspacher, L. Nikiel, H.H. Yang, C.P. O'Farrell, G.A. Schwartz, Kautschuk Gummi Kunststoffe, 55 (2002) 596-604.
[20] L.B. Tunnicliffe, J. Kadlcak, Y. Shi, M.D. Morris, A.G. Thomas, J.J.C. Busfield, Macromolecular Materials and Engineering, 299 (2014) 1474-1483.

[21] A.R. Payne, R.E. Whittaker, Rubber Chemistry and Technology, 44 (1971) 440-478.
[22] J. Fritzsche, M. Klüppel, Journal of Physics-Condensed Matter, 23 (2011) 035104.
[23] J.G. Meier, M. Klüppel, Macromolecular Materials and Engineering, 293 (2008) 12-38.
[24] Y.K. Akutagawa K, Yamamoto A, Heguri H, Jinnai H, Shinbori Y, Rubber Chemistry and Technology, 81 (2008) 182-189.
[25] ASTM, Standard Test Method for Rubber Property—Volume Resistivity Of Electrically Conductive and Antistatic Products, ASTM International, West Conshohocken, PA, 2014.
[26] S.R. Heinrich G, Klüppel M, Rubber Chemistry and Technology, 70 (1997) 243-255.
[27] M. Klüppel, G. Heinrich, Rubber Chemistry and Technology, 68 (1995) 623-651.
[28] M. Klüppel, Advances in Polymer Science, 164 (2003) 1-86.
[29] J.L. Leblanc, Progress in Polymer Science, 27 (2002) 627-687.
[30] S. Mihara, R.N. Datta, J.W.M. Noordermeer, Rubber Chemistry and Technology, 82 (2009) 524-540.
[31] M.J. Wang, Rubber Chemistry and Technology, 71 (1998) 520-589.
[32] G. Kraus, Applied Polymer Symposia, (1984) 75-92.
[33] G. Heinrich, M. Klüppel, Advances in Polymer Science, 160 (2002) 1-44.
[34] R. Pérez-Aparicio, A. Vieyres, P.A. Albouy, O. Sanseau, L. Vanel, D.R. Long, P. Sotta, Macromolecules, 46 (2013) 8964-8972.
[35] G.A. Schwartz, S. Cerveny, A.J. Marzocca, M. Gerspacher, L. Nikiel, Polymer, 44 (2003) 7229-7240.
[36] S. Mihara, R.N. Datta, W.K. Dierkes, J.W.M. Noordermeer, N. Amino, Y. Ishikawa, S. Nishitsuji, M. Takenaka, Rubber Chemistry and Technology, 87 (2014) 348-359.

Chapter 6

The Effect of Filler Particles on the Glass Transition of Natural Rubber

Précis:

Chapter 5 highlighted the significant amplification of the dynamic storage modulus of filled rubbers imparted by the presence of fillers. This amplification is at a maximum immediately after the glass transition and subsequently decays with increasing temperature. It has previously been proposed that this phenomenon is indicative of an extended or broadened glass transition within the polymer matrix which makes a significant contribution to the observed elastic stiffening in the transition and rubbery regions. Recent advances in the understanding of these effects are highlighted in Chapter 2 together with the debate in the literature surrounding the applicability of these concepts to commercial, filled elastomer materials.

It is clear from the literature review that any effect of the presence of filler on the polymer T_g would have a significant, potentially dominant, impact on the small strain viscoelastic properties of the compounds studied in this work. In order to address this issue a number of experimental techniques are employed to characterise the glass transition in these filled compounds. Many different experimental techniques have been used to characterise various aspects of the glass transition (Chapter 2, Table 2.2).

However for the purposes of observing a filler-induced broadening of the glass transtion in the compounds considered in this work, it is nescessary to use experimental techniques which have previously been demonstrated to be sensitive to such effects: differential scanning calorimetry, broadband dielectric spectroscopy and dynamic mechanical analysis.

None of these techniques are able to detect any significant, systematic effect of the filler particles used in this study on the glass transition and dynamics of the NR matrix. This finding is discussed in the context of the relevent literature. [1]

Aspects of this work are published in the peer reviewed journal '*European Polymer Journal*' as M Huang, LB Tunnicliffe et al. *'The Glass Transition, Segmental Relaxations and Viscoelastic Behaviour of Particulate-Reinforced Natural Rubber',* 67, 232-241, 2015

[1] *Note that many studies have examined the glass transition using deconvolutions of the proton NMR T_2 time domian relaxtion into fast and slow decaying components corresponding to immobilised and bulk-like polymer respectively. However it has been pointed out by Cohen-Addad and Frebourg [1] J.P.C. Addad, P. Frebourg, Polymer, 37 (1996) 4235-4242. and later by Robertson and Roland [2] C.G. Robertson, C.M. Roland, Rubber Chemistry and Technology, 81 (2008) 506-522. that this method of data analysis assumes that all protons within the sample belong to the polymer phase. For the case of natural rubber (and most commercial rubbers) this is clearly not the case as protons belonging to organic impurities (proteins etc.), residual curative chemicals (which may constitute 5-10 % of total sample mass) and filler surface functionalities (silanol groups etc.) that are present. Due to these issues, characterisations of T_g by ^{1}H NMR is not attempted in this work.*

6.1. Differential Scanning Calorimetry (DSC)

An obvious choice for direct T_g characterisation is DSC. DSC is sensitive to the step change in polymer heat capacity observed when passing through the T_g due to the onset of chain segmental motions [2]. From a typical DSC observation of the T_g (Figure 6.1) it is possible to characterise the T_g onset temperature via extrapolation of linear fits to the data at the point of onset. Additionally when the heat flow data is normalised to the weight of polymer in the sample, the amount of polymer material which actively participates in the transition can be estimated from the step change observed in the heat capacity jump [3] [4].

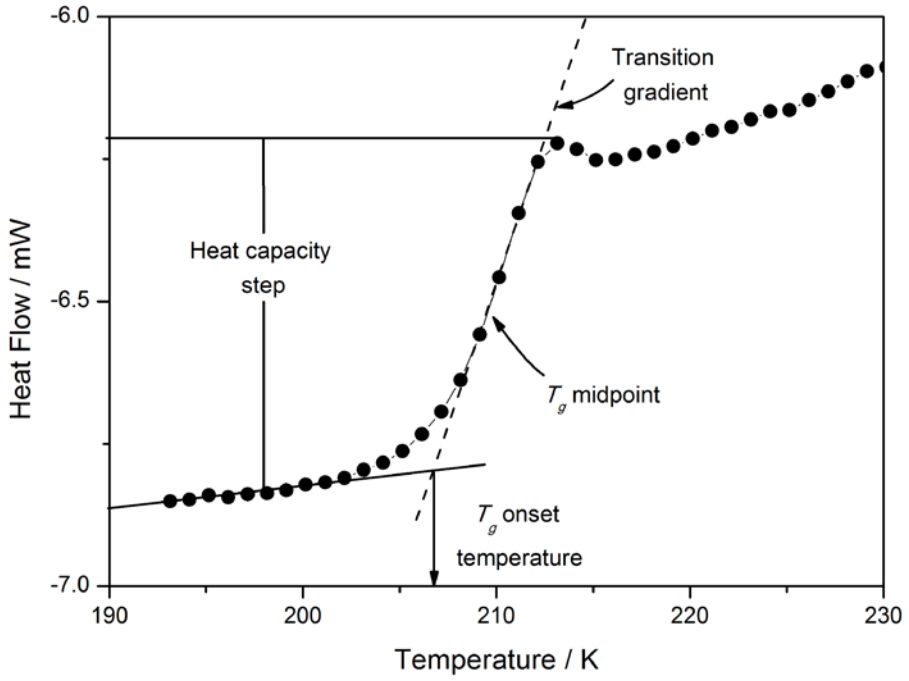

Figure 6.1: An example of a typical DSC trace showing the jump in heat flow upon traversing the glass transition. A number of evaluation parameters are indicated on the plot

A number of papers have shown that DSC is sensitive to a filler-induced broadening of the glass transition. A review of these papers is given in Chapter 2 but some of the key data are presented here in greater detail in order to demonstrate the sensitivity of the DSC technique to the glass transition. Papon et al. [5] have recently demonstrated the existance of a gradient of glass transition around spherical silica nanoparticles of near perfect dispersion within a Polyethyl acrylate (PEA) matrix using time domain ^{1}H NMR and were able to quantitatively

correlate this with a broadening of the step change in heat capacity observed in the DSC trace (Figure 6.2A). Furthermore, a number of other studies have shown a significant broadening of the DSC heat capacity step for nanocomposite materials which display a pronounced filler-induced immobilisation of the polymer phase. For example the DSC data of Fragiadakis et al. [4] shows a significant broadening through the T_g for dispersed silica-NR nanocomposites (Figure 6.2B), as do the data of Holt et al. [6] for nanosilica-filled poly-(2)-vinyl pyridine (P2VP) (Figure 6.2C) and the data of Bansal et al. [7] for nanosilica-filled PS (Figure 6.2D).

As such, the transition gradient is defined here as the gradient of a linear fit to the data at the mid point of the step in the heat capacity (Figure 6.1). The transition gradient may be expected to be sensitive to a filler-induced broadening of the T_g for the NR.

The working principles of DSC are reviewed in more detail in the Appendix. Calorimetry measurements were made using a Perkin Elmer Pyris Diamond DSC. Small samples (~10 mg) were cut from cured sheets and placed in aluminium crucibles. Samples were cooled at 10 K/min from the melt to the glass (193 K) and then heated at a rate of 10 $K.min^{-1}$ to 238 K under a flushing nitrogen atmosphere. Heat flow traces were weight-normalised to the weight of the elastomer in the samples (as opposed to the total sample weight). In Figure 6.3 to Figure 6.6 the parameters determined from the DSC traces are plotted versus the nitrogen specific surface area of the filler for all samples considered in this study. The filler type and surface activities are indicated on the plots. As can be seen from Figure 6.3 to Figure 6.6 neither the glass transition onset nor midpoint temperatures, the transition gradient nor the step change in heat capacity at the T_g depend significantly on the presence of filler, the filler surface area or the filler surface activity. A number of repeats were performed on the unfilled sample to determine the error associated with these values. As can be seen from examination of the error bar for the unfilled sample, most of the variation in the data lies within the repeatability of the measurement. The DSC data is therefore shows no effect on the filler on the T_g or may be not sufficiently accurate to indicate any slight dependence of the glass transition temperature or glass transition gradient on the incorporation of any of the filler particles used in this study at these volume fractions.

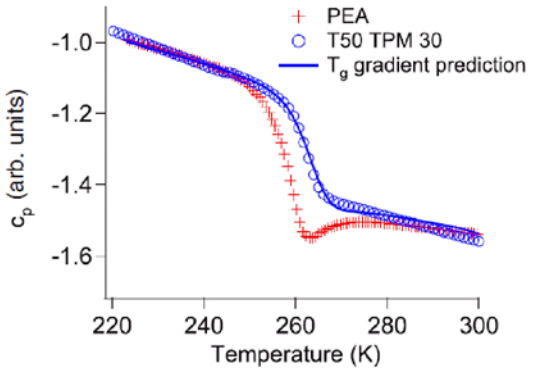

A) Papon et al., *Physical Review Letters*, 108, 065702, 2012

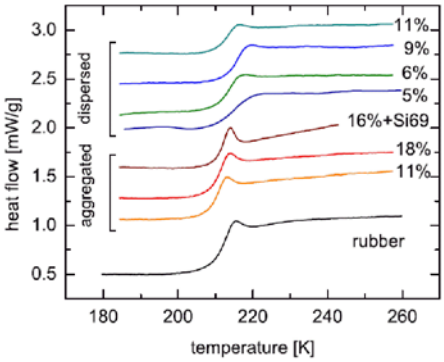

B) Fragiadakis et al., *Polymer*, 52, 3175-3182, 2011

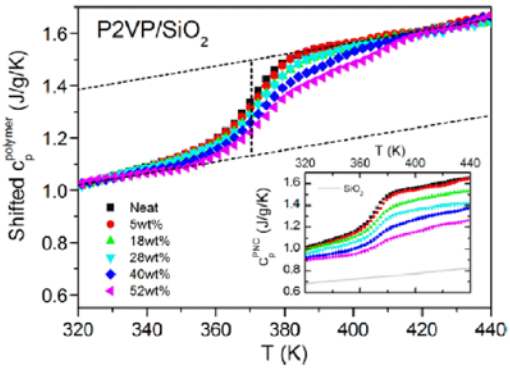

C) Holt et al., *Macromolecules*, 47, 1837-1843, 2014

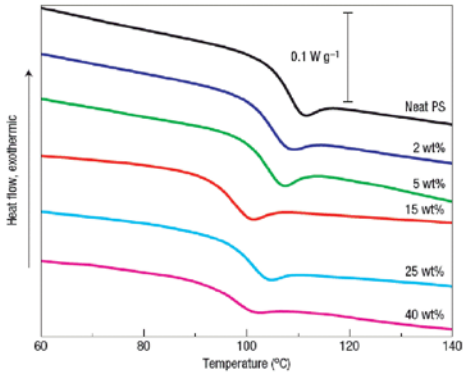

D) Bansal et al., *Nature Materials*, 4, 693-698, 2005

Figure 6.2 A-D: Various examples from the literature of a broadening or smearing of the step change in heat capacity at the glass transition and a reduction in the magnitude of the step in heat capacity upon the incorporation of filler nanoparticles particles. A) Data is shown for neat PEA (red crosses) and silica-filled PEA (blue circles). The blue line corresponds to DSC prediction from NMR data. B) DSC traces shown for NR filled with aggregated and dispersed silica particles. Samples filled with dispersed filler particles are claimed to exhibit modified polymer dynamics. C) P2VP filled with nanoscale silica. Inset is the raw DSC data. The main plot shows the DSC traces shifted to demonstrate broadening of the T_g. D) DSC data for nanosilica-filled PS showing a shift in T_g, a broadening of the transition and reduction in the heat capacity step.

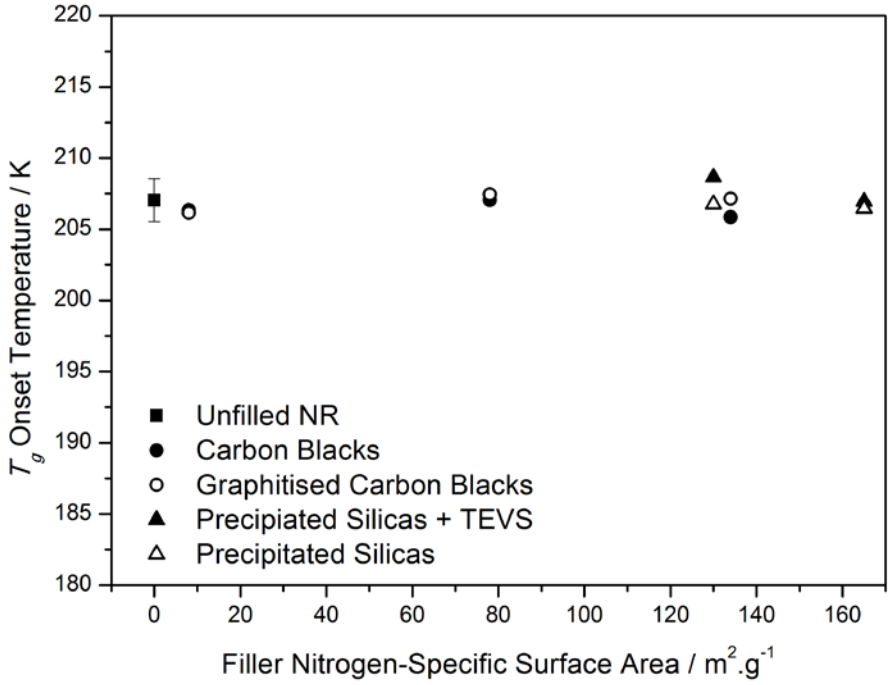

Figure 6.3: Dependence of the T_g onset temperature on the filler specific surface area

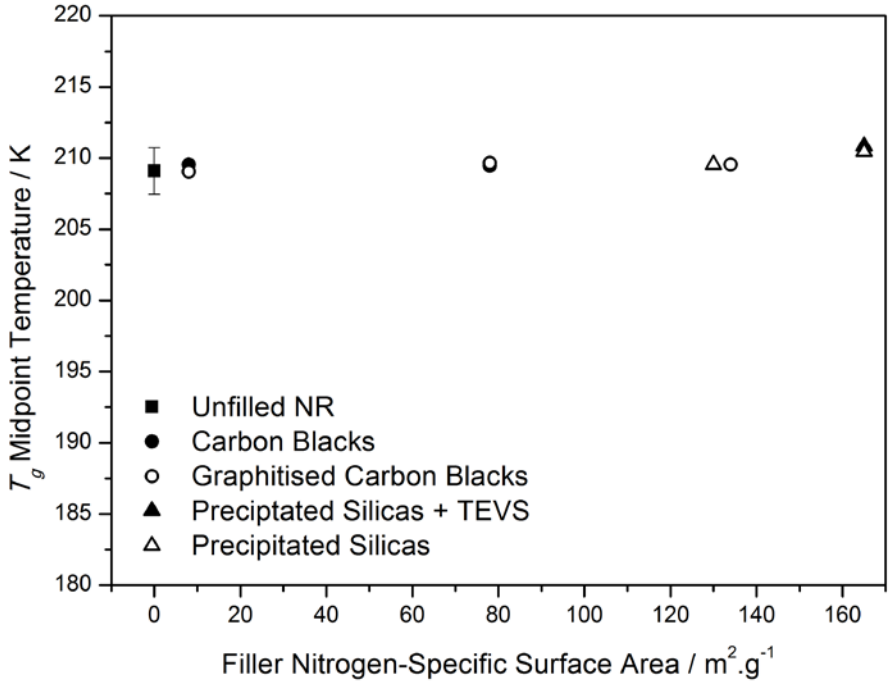

Figure 6.4: Dependence of the T_g midpoint temperature on the filler specific surface area

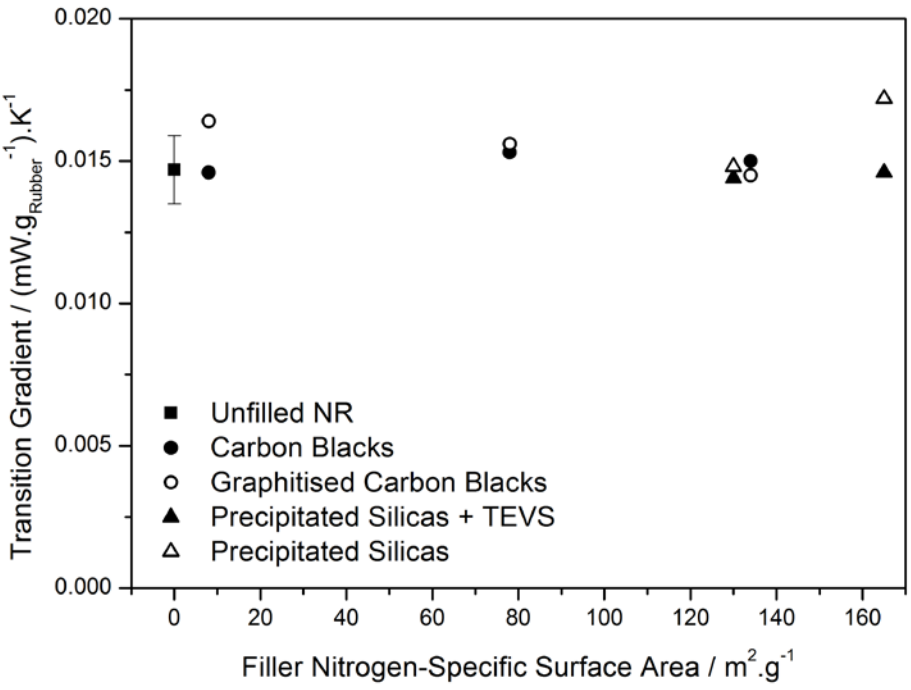

Figure 6.5: The dependence of the transition gradient (gradient of the step in heat capacity) at the T_g versus filler specific surface area

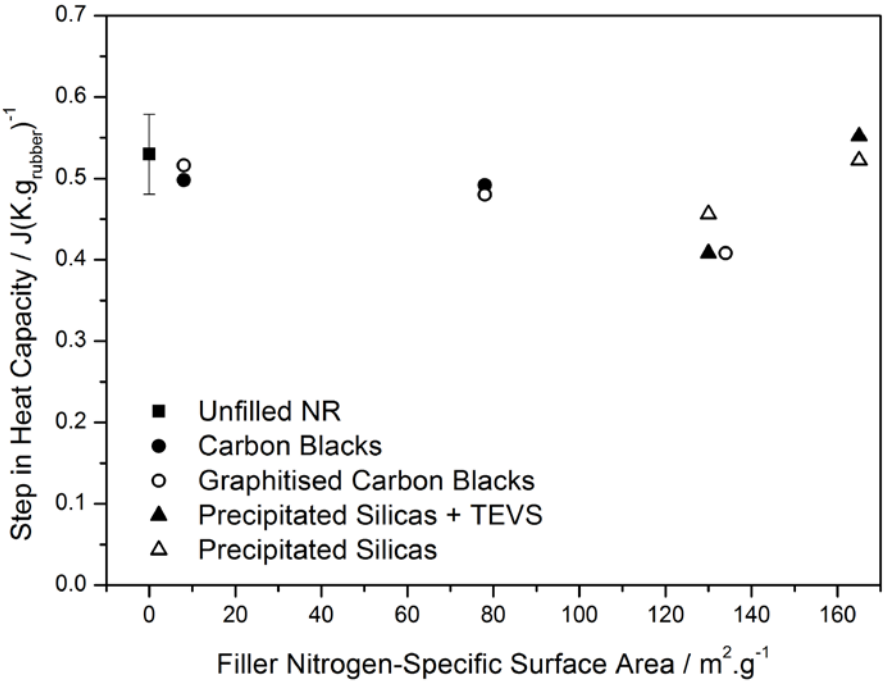

Figure 6.6: Plot of the heat capacity step versus filler specific surface area

6.2. Broadband Dielectric Spectroscopy (BDS)

BDS is another characterisation technique which has been extensively used to investigate the polymer dynamics in filled and unfilled polymer systems. BDS is sensitive to dipolar relaxations including the segmental α relaxation which underpins the glass transition. A review of the BDS technique is given in the Appendix and several experimental studies are reviewed in Chapter 2.

A selection of this relevant data from the literature is presented in more detail in Figure 6.7 to illustrate BDS measurements of the glass transition.

Figure 6.7 A presents the data of Fragiadakis et al. [4] and contrasts the segmental relaxation observed for unfilled and silica-filled NR. In samples with highly aggregated silica particles (bottom) the α relaxation is essentially the same as in the unfilled NR. When dispersed silica particles are incorporated (top), a significant broadening of the low frequency side of the relaxation is observed which the authors attribute to the appearance of a secondary slower relaxation belonging to interphase polymer with slower dynamics than the bulk.

Figure 6.7 B, presents BDS spectrum in the vicinity of the α relaxation of unfilled P2VP (top) from Holt et al. [6] which is deconvoluted in terms of a linear combination of a polymer relaxation (H-N function) and a low frequency conductivity terms. For their silica filled sample (bottom) they apply the same deconvolution but now require a slower contribution from a second H-N function in order to fit the data. They ascribe this to a layer of polymer surrounding the filler particles having slow dynamics.

Figure 6.7 C presents s a deconvolution of BDS data for silica-filled SBR from Vo et al. [8]. A secondary, slower α relaxation is observed which again is proposed to originate from interphase polymer.

Figure 6.7 D presents a BDS deconvolution for silica-filled Butyl-styrene vinyl pyridine rubber (VPR) from Wu et al. [9] with similar results and findings to the previous investigations.

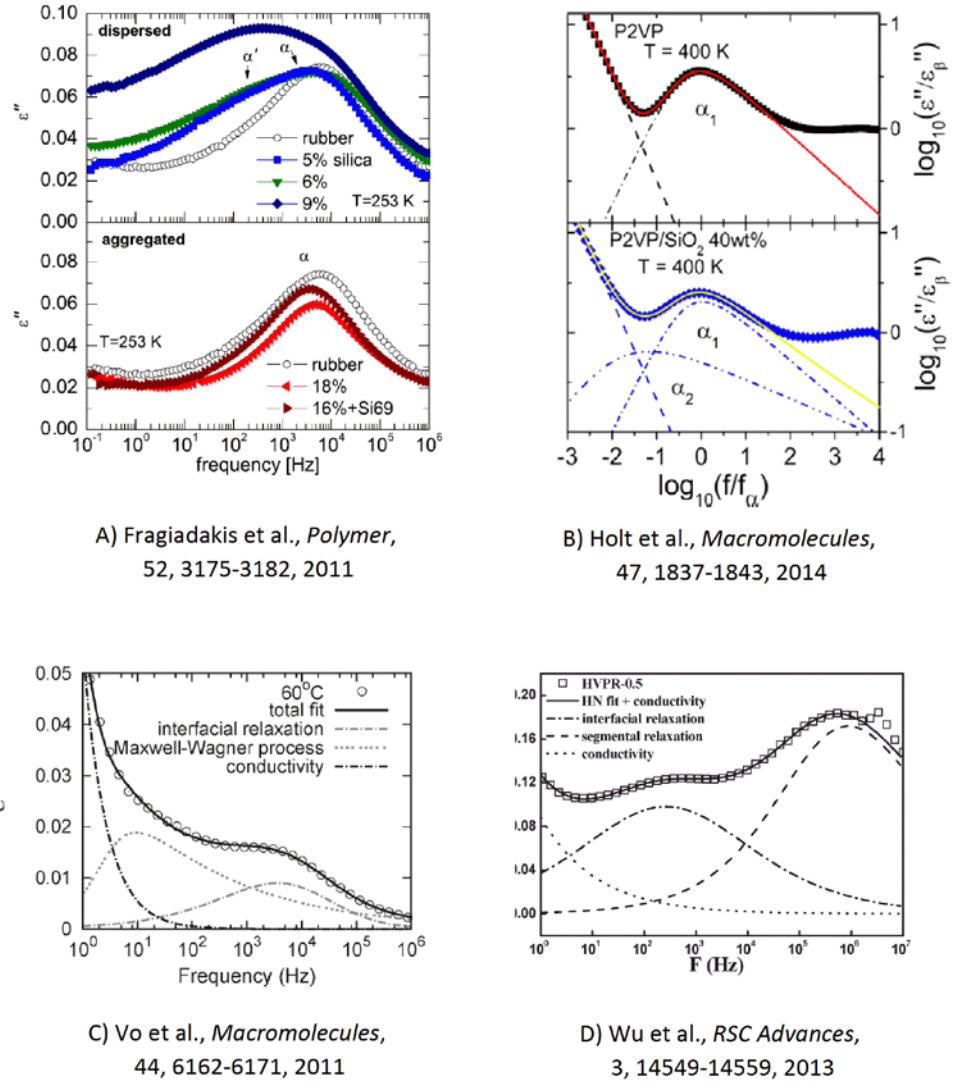

A) Fragiadakis et al., *Polymer*, 52, 3175-3182, 2011

B) Holt et al., *Macromolecules*, 47, 1837-1843, 2014

C) Vo et al., *Macromolecules*, 44, 6162-6171, 2011

D) Wu et al., *RSC Advances*, 3, 14549-14559, 2013

Figure 6.7: Example BDS from the literature showing a shifting, broadening or appearance of a slower secondary relaxation in the α relaxation of various filled polymers upon the incorporation of filler particles

Samples for BDS having a thickness of 0.7 mm were produced using the compression moulding method detailed in Chapter 4. Samples were cut into 25 mm x 25 mm x 0.7 mm square sheets. Gold electrodes were coated on both sides of each specimen by evaporation deposition. The diameter of the concentric gold circle electrodes was 22 mm. Due to the carbon black's inherent conductivity which, when the filler is loaded above the electrical percolation threshold, masks the polymer chain segmental relaxation process, the carbon black series of samples were not extensively investigated using BDS. However, as an example, one carbon black sample (N330) was prepared at one volume fraction (0.05) below the filler electrical percolation threshold for BDS testing. BDS was performed on a Novocontrol Concept 40

dielectric spectrometer. All coated samples were dried in a vacuum oven at 100 °C for 24 hours prior to testing. Experiments were performed over a frequency range from 0.1 Hz to 20 MHz and a temperature range from -100 °C to 50 °C. The accuracy of the temperature controlling system was ±0.1 °C. Frequency domain dielectric spectra were collected at temperature steps of 1 K with an isothermal dwell time of approximately 10 minutes.

Figure 6.8 A presents the frequency and temperature dependence of the dielectric losses for unfilled NR. The strong dielectric relaxations observed as a ridge in the 3D plot correspond to chain segmental (α) relaxations. Upon increasing the temperature, the α relaxation is first fully observed at around 213 K - above the glass transition and subsequently shifts to higher frequencies with increasing temperature. Figure 6.8 B shows as an example of a filled compound, temperature and frequency domain plots of the dielectric loss for, in this case, the HDS-TEVS filled NR compound. Several differences from the corresponding unfilled spectra are apparent. Firstly, tending towards lower frequencies, a gradual rise in the dielectric loss is observed. This may be attributable to Maxwell–Wagner–Sillars (MWS) polarization effects [10] or charge leakage (conductivity) [11]. In Figure 6.9 this low frequency dissipation is deconvoluted from the main segmental relaxation using two fitting functions - an Havriliak-Negami (HN) function

$$\varepsilon^*(f) = \varepsilon_\infty + \frac{\Delta\varepsilon}{(1 + (if/f_0)^\alpha)^\beta} \qquad 6.1$$

where $\Delta\varepsilon$ is the dielectric strength, f_0 is the characteristic peak relaxation frequency, α and β are shape parameters and f is the frequency,

Splitting the HN function into real and imaginary contributions gives the following function for the dielectric loss as a function of frequency [12]

$$\varepsilon''(f) = r^{-\beta/2}(\varepsilon_0 - \varepsilon_\infty)\sin\beta\theta$$

where

$$r = \left[1 + (f\tau_0)^{\alpha}\sin\left(\alpha\frac{\pi}{2}\right)\right]^2 + \left[(f\tau_0)^{\alpha}\cos\left(\alpha\frac{\pi}{2}\right)\right]^2$$

$$\theta = \arctan\left[\frac{(f\tau_0)^{\alpha}\cos\left(\alpha\frac{\pi}{2}\right)}{1 + (f\tau_0)^{\alpha}\sin\left(\alpha\frac{\pi}{2}\right)}\right]$$

where τ_0 is the characteristic relaxation time. A second term is also used to account for the low frequency dispersion

$$\varepsilon''(f) = a(2\pi f)^{-s} \qquad 6.2$$

where a and s are shape parameters and f is the frequency. From the deconvolution results it appears that there is no secondary, slower α relaxation detectable in these compounds.

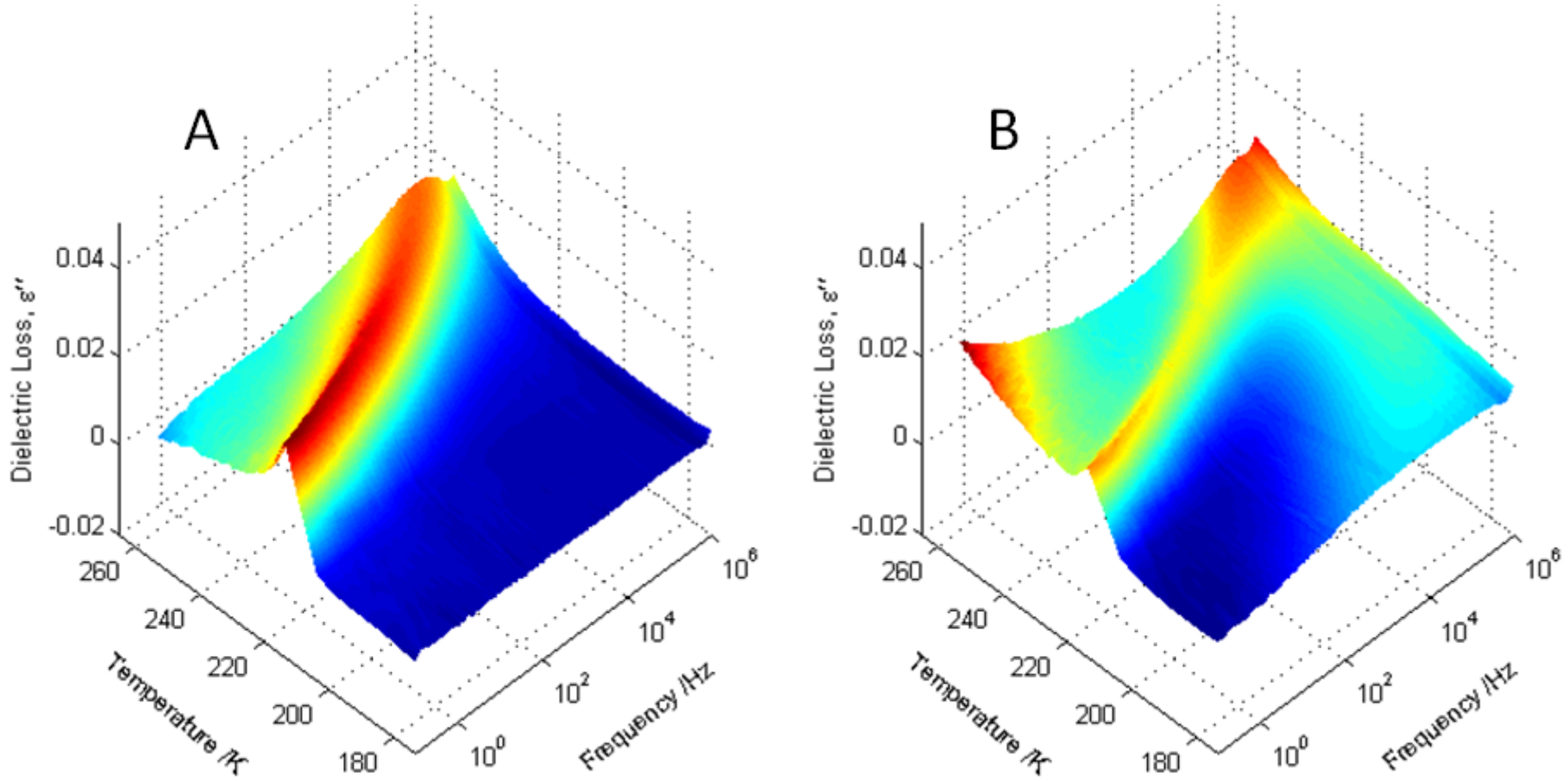

Figure 6.8: Temperature and frequency domain spectra of (A) unfilled NR and (B) HDS-TEVS filled NR

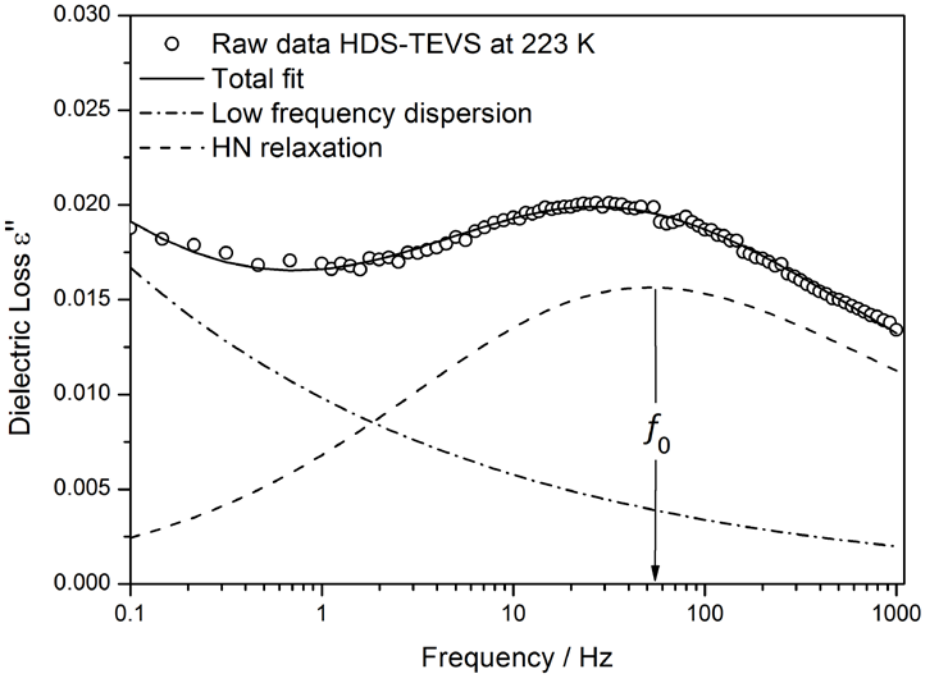

Figure 6.9: Example of a fit to the experimental data of a single HN function and a single conductivity term; indicating that no slower relaxations are apparent

Secondly at higher frequencies and lower temperatures another, non-polymer, dissipation is apparent (see the high frequency, low temperature region in Figure 6.8 B). This dissipation process appears to be a partially resolved relaxation that could potentially be attributed to the relaxation of confined, hydrogen bonded water molecules at the silica surface which has previously been detailed for silica-filled SBR compounds [13].

Of interest here is the temperature dependence of the α relaxation. The characteristic frequency of the relaxation process was determined for each temperature step using an HN fit to each frequency domain spectrum as in Figure 6.9. A Vogel−Fulcher−Tammann (VFT) fitting procedure was performed on the extracted relaxation frequency data in order to determine quantitatively the glass transition temperatures from Arrhenius-type plots

$$\log f_{p,\alpha} = \log f_I - \frac{A}{T - T_0} \qquad 6.3$$

where f_I and A are fitting parameters, T_0 is the Vogel temperature (ideal glass transition temperature) which is generally 30-70 K below the glass transition temperature, T_g and $f_{p,\alpha}$ is the frequency of the α relaxation peak at temperature T.

The VFT plot and extracted T_g values (T_g is defined from the VFT equation at the temperature at which the relaxation time of the polymer exceeds 100 seconds) are presented in Figure 6.10 which also includes the data obtained for the low volume fraction N330-filled compound. Glass transition temperatures for these compounds are found to vary only slightly (maximum ±~1 K) and non-systematically from that of the unfilled elastomer. The T_g values determined from dielectric spectroscopy are in reasonable agreement with those from the DSC experiments.

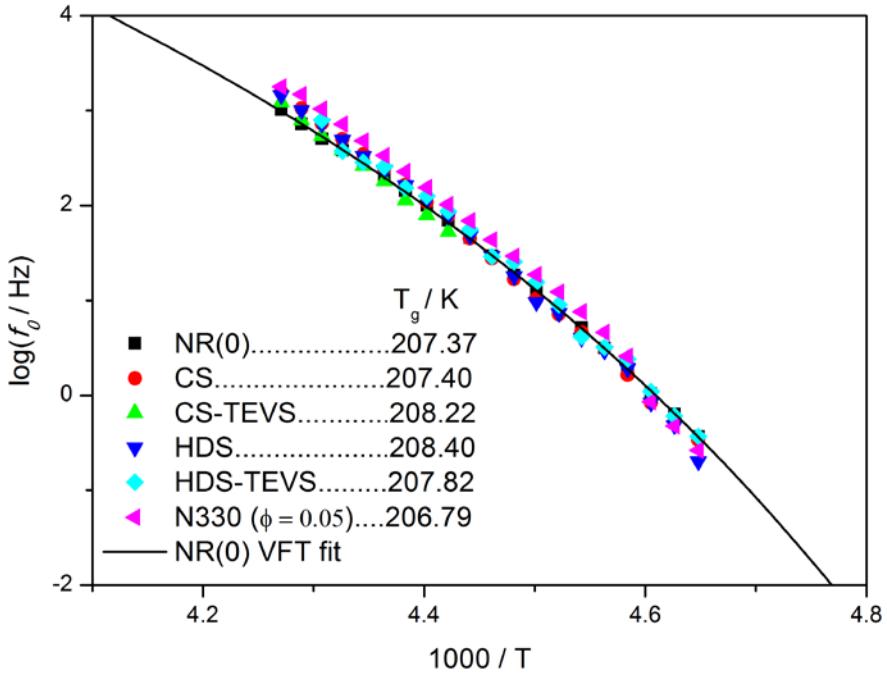

Figure 6.10: Arrhenius plot of the relaxation frequencies of the various samples. Inset are the T_g values determined by VFT fitting. The solid line is a VFT fit for unfilled NR

6.3. Dynamic Mechanical Analysis (DMA)

For unfilled elastomers DMA is a suitable technique to evaluate the glass transition since the measured phase angle is solely related to the dynamics of the network sub-chains and the changes in chain segmental mobility. When filled rubbers are considered, the interpretation of DMA data in terms of the T_g becomes more ambiguous. Within the transition and rubbery regions, hydrodynamic and filler network amplification of the storage modulus have been

incorrectly interpreted as a broadening of the T_g. Robertson et al. [14] noted that the peak in loss modulus at the T_g - reflecting the chain segmental dynamics - is unaffected by the presence of filler [3]. Care therefore has to be taken when interpreting the results of DMA experiment performed on filled samples.

Temperature-dependent dynamic mechanical properties of the filled elastomers were measured using a Perkin Elmer DMA 8000 in tensile deformation mode. Rectangular test strips were cut from sheets of the elastomer compounds and mounted into the test clamps. The test clamps were fully tightened under cryogenic conditions when the sample was in the glassy state. Data were collected in temperature steps of -2 K from 237 to 197 K with an isothermal step dwell time of 5 minutes. The dynamic tensile strain was 0.1 % (within the linear viscoelastic domain) at a frequency of 1 Hz with a small static pre-load of 0.1 N.

The temperature dependence of the storage modulus in the glass transition region of the silica-filled samples is shown in Figure 6.11 A. The onset of the glass transition at ~218 K is apparent in all the samples and is broadly independent of the presence of filler particles. This is in line with the trends of the corresponding DSC measurements shown in Figure 6.3. The absolute values of T_g determined from DMA are somewhat higher than those from DSC experiments. This is due to the different measurement techniques being sensitive to different aspects of the transition phenomenon (e.g. mechanical versus heat capacity). For the filled samples the storage modulus is significantly amplified on the rubbery side of the T_g.

The interpretation of this amplification of storage modulus in the rubbery region in terms of a broadening of the glass transition is difficult and so it is useful to consider the temperature dependence of the storage moduli of filled samples in relation to the NR segmental relaxation time. The polymer segmental relaxation time, τ, was calculated From the characteristic relaxation frequency

$$\tau = \frac{1}{2\pi f_0} \qquad 6.4$$

where f is the relaxation shown schematically in Figure 6.9. Polymer relaxation times determined through this procedure are in line with values computed from previously published data [15]. The segmental relaxation times for the unfilled and silica-filled compounds are plotted as a function of temperature in Figure 6.11 B. There is no appreciable difference in the polymer segmental mobility of the filled rubber compared and that of the

unfilled rubber in the transition and rubbery regions. There is no correlation between the storage modulus reinforcement in the transition region and any modification of the polymer dynamics (contrast Figure 6.11 A with Figure 6.11 B).

The independence of the segmental relaxation time from the presence of filler would suggest that the amplification of the storage modulus on the rubbery side of the glass transition is determined by the composite nature of the filled rubbers rather than through any slowing down of the chain dynamics by the filler particles.

Figure 6.12 shows the corresponding viscous moduli data. As can be seen, the dissipation peak does not appear to systematically depend on the presence of filler particles in terms of the peak position or breadth.

$$\tau = \frac{1}{2\pi f_0} \qquad 6.5$$

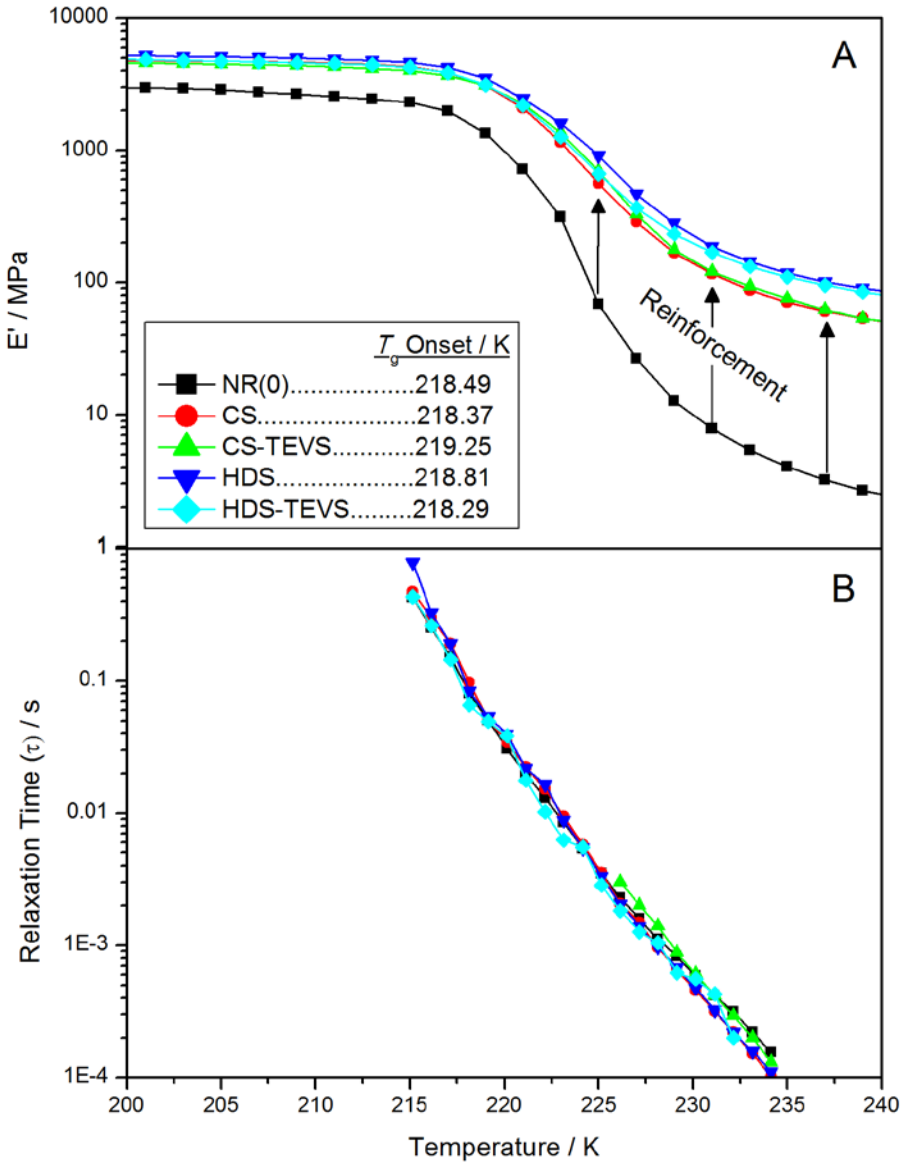

Figure 6.11: A) Linear viscoelastic storage moduli for unfilled and silica-filled NR compounds. B) corresponding segmental relaxation time from BDS. Lines are guides for the eye

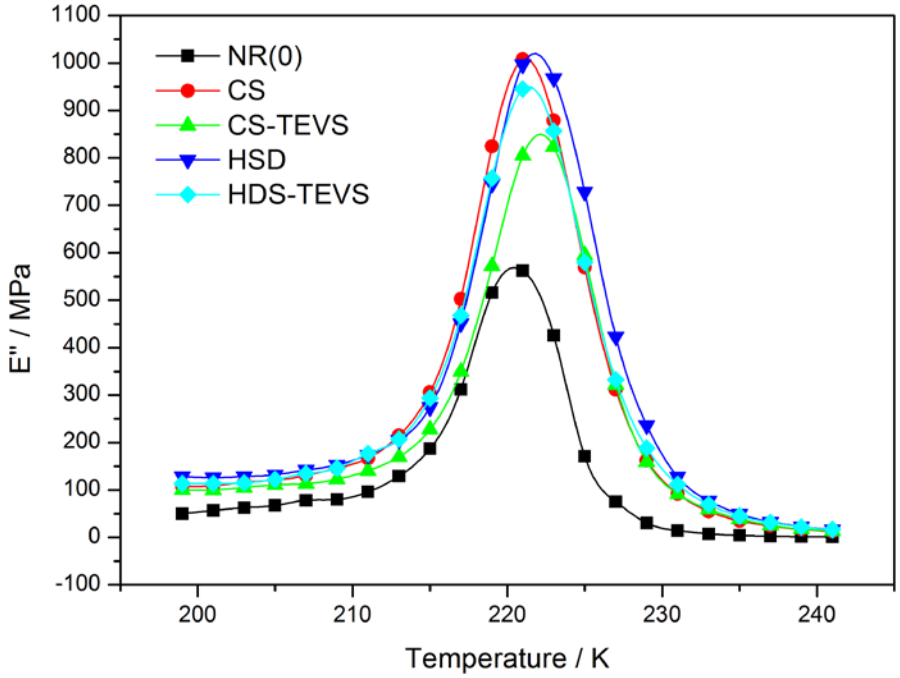

Figure 6.12: Linear viscoelastic loss moduli for unfilled and silica-filled NR compounds. Lines rae guides for the eye

6.4. Discussion

The data presented and analysed here suggest that the dynamics of the polymer phase in these samples are not significantly modified by the presence of the various filler particles. The DSC data show no filler-induced changes in the T_g. Previously, DSC analyses of filled elastomer nanocomposites which display a pronounced polymer interphase have been shown to be sensitive to the broadening and magnitude of the step change in heat capacity at the T_g [4-6]. In light of this, the DSC data indicate that if such an interphase exists in the samples studied here, then the total volume fraction of modified polymer is small and that the associated thermal transitions are within the measurement error of this particular instrument.

The temperature dependence of the dielectric α relaxation in the vicinity of the glass transition for filled samples shows little variation from that of the unfilled material, at least in terms of the peak relaxation frequency, for all silica-filled samples and for a carbon black-filled sample below the electrical percolation threshold loading. Filled sample storage moduli measured using DMA are significantly amplified on the rubbery side of the T_g by the presence of the filler phase. The initial softening temperature of the glassy material - which is indicative of the onset of the glass transition - is unchanged upon incorporation of filler. The lack of any systematic

correlation of the substantial stiffening of the material in the rubbery regime with changes in the underlying polymer dynamics (measured thorough BDS and through consideration of the temperature dependence of the small strain viscous modulus) suggests that this amplification may be associated with the mechanical nature of the filler network within the sample. Note that a simple rule of mixtures can give reinforcement values of the correct order of magnitude if the modulus of silica and rubber are taken as 70 GPa and 1-100 MPa respectively. However this approach is flawed in this case as it assumes that the filler phase is present as continuous fibres through the matrix. Although the filler is present as a percolated network, the modulus of such a network is ill-defined and so the elastic modulus of the composite cannot be related to a simple rule of mixtures.

In the context of previous investigations the fact that the filler particles do not appear to significantly alter the rubber T_g may not be so surprising. For example Fragiadakis et al. demonstrated the sensitivity of the polymer interphase to the degree of filler particle aggregation [4]. The filler particles studied in this paper are all industrial grade fillers (or derived thereof) and as such display a significant degree of primary particulate aggregation. These particles cannot therefore be classed as true nanoparticles, but rather as nanostructured aggregates - with correspondingly reduced filler-polymer contact areas. In addition, upon shear processing and thermal curing of the samples, filler particle re-agglomeration (flocculation) may occur, which can act to further deplete the surface area of filler in intimate contact with the polymer and detrimentally affect the degree of filler dispersion. Therefore the nature of confinement of polymer in these systems may be very different to previously published reports of filled elastomers and thermoplastics where near-perfect dispersions of isolated spherical nanoparticles have been shown to significantly alter the dynamics of the polymer in proximity to the filler [4-6, 16]. Example TEM and SEM micrographs of individual silica aggregates and fracture surface filler morphology are presented in Figure 6.13 and serve to illustrate the aggregated and agglomerated nature of the filler particles and filler particle networks studied in this work. The precise role of particle dispersion or aggregation in dictating a local modification of the T_g is beyond the scope of this thesis but may in part explain why no significant volume of interphase can be detected for the commercially relevant compounds studied here.

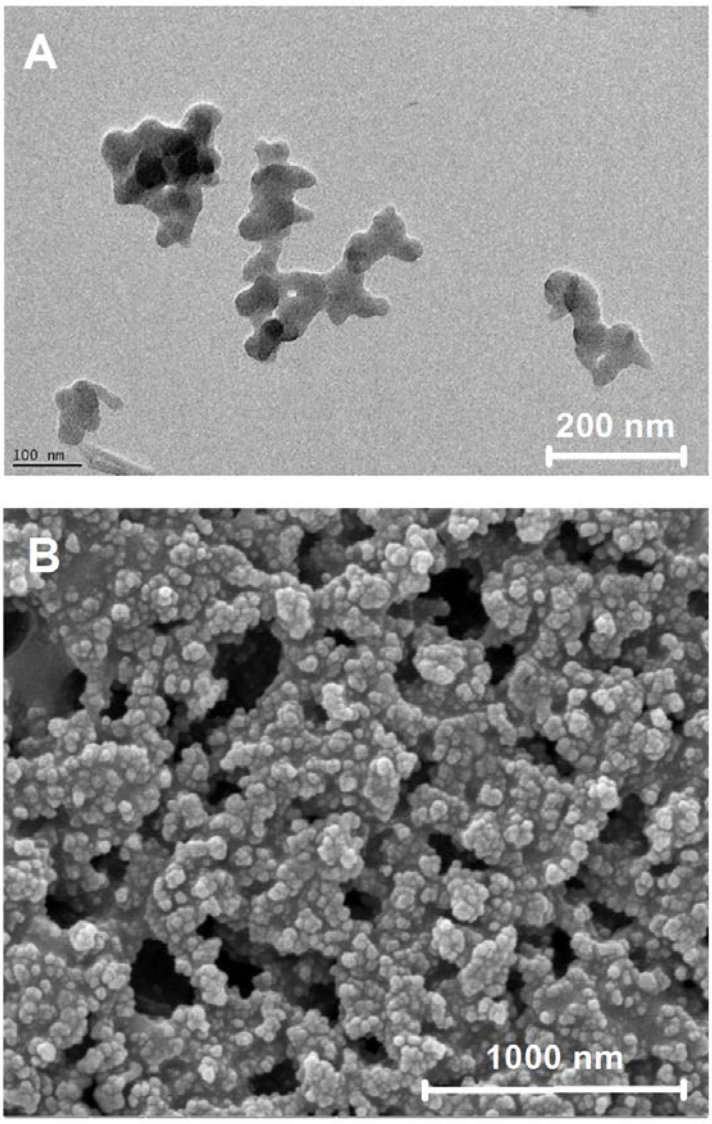

Figure 6.13: A) TEM image of individual silica aggregates. B) SEM image of filler microstructure at a sample fracture surface

It is pertinent at this point to discuss mechanisms other than a broadening of the T_g which could possibly account for the observed trends in small strain modulus amplification. It has previously been proposed that occlusion or shielding of a part of the total volume of polymer from the globally applied strain by the fractal filler network increases the 'effective' volume fraction of solid phase [17, 18]. Additionally strain amplification due to the presence of rigid filler inclusions raises the average stored energy density in the polymer phase upon deformation [19]. Accordingly the presence of a geometrically complex filler network can act to amplify the storage modulus significantly above that determined analytically via the Einstein-Smallwood and Chen-Acrivos hydrodynamic equations [20-23].

Unfortunately it is very difficult to experimentally verify whether or not these effects alone could account for the modulus amplification observed for the systems studied here. Bergström and Boyce [24] have demonstrated using stochastic 3D finite element simulations that random dispersions of fillers can accurately match, and in some cases exceed, the stiffening at small strains observed in experimental data. Both occlusion of the elastomer phase and strain amplification mechanisms are apparent in their simulation results. Furthermore the finite element analyses Akutagawa et al. [25] of three dimensional representations of real filler dispersions (determined experimentally using a microtomography technique) embedded in an hyperelastic continuum have demonstrated that such mechanisms can in fact significantly overestimate the magnitude of stiffening observed experimentally. Importantly both the aforementioned simulations did not incorporate any alteration of the dynamics of the elastomer phase by the filler and yet were still able to approximate the appropriate stiffening magnitude - suggesting that stiffening can be explained by the nature of filler networking. Gusev and Rozman [26] performed finite element simulations of rigid particles of various dispersion geometries in an hyperelastic matrix. They examined various particle arrangements including hexagonally close packed spheres, randomly placed spheres and 'honeycomb' and 'web-like' dispersion states. Interestingly they found that the honeycomb and web-like arrays were able to reach stiffness values of up to 100 times that of the unfilled matrix (see Figure 6.14). These dispersion states could be considered as crudely representative of the real life situation of packed fractal aggregates. This may be one explanations for the peak in reinforcement seen immediately after the glass transition in highly filled rubbers (if not the subsequent temperature dependence).

In fact in Payne's original work [27, 28] on filler reinforcement he demonstrated that at small strains the shear moduli of carbon black-filled oil approaches that of equivalently filled rubber - indicating that the observed filler-induced stiffening of rubber may in fact be relatively unrelated to the rubber phase and instead may be more dependent the mechanical properties of the filler network.

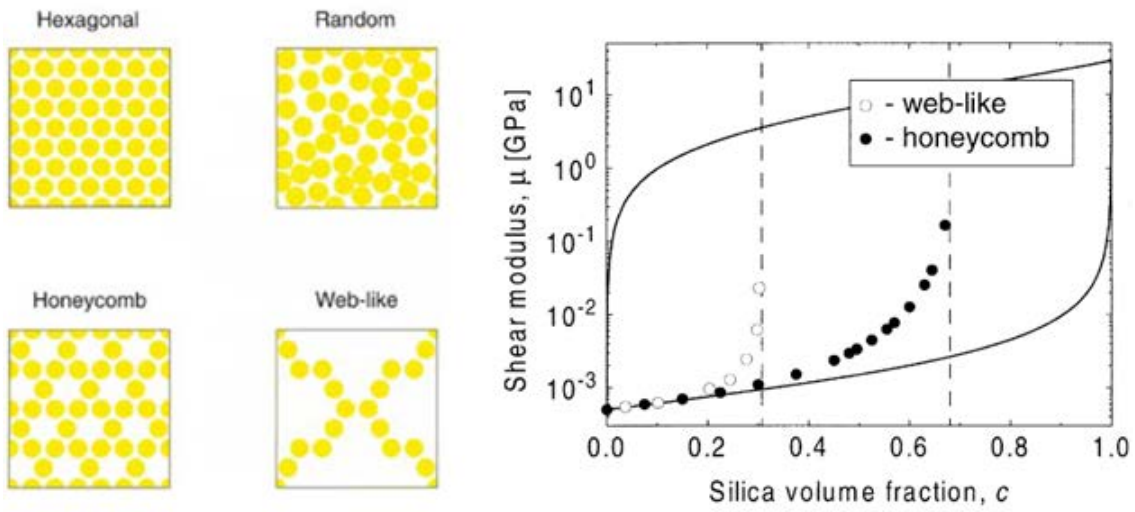

Figure 6.14: Overview of the simulations performed by Gusev and Rozman. The images to the left are the dispersion states examined by FEA in their study. The data to the right plots the shear modulus determined from simulations versus the volume fraction of 'virtual' silica filler. the solid lines refer to theoretical bounds which are defined in the paper. Their data shows that complex particle packing arrays are capable of increasing the stiffness of elastomers by up to 100 times that of the unfilled material (Adapted from Gusev and Rozman [26]).

In the previous chapter the small strain storage moduli reinforcement of filled compounds was shown to be markedly temperature dependent following a peak immediately after the glass transition. According to the data presented in this chapter the temperature dependence is seemingly unrelated to polymer immobilisation effects. Two alternative mechanisms for this temperature dependence are apparent from the literature 1) a temperature dependence associated with the mechanics of the filler network and 2) temperature dependent phase coupling at the rubber-filler interface. In the previous chapter it was demonstrated that reinforcement temperature dependence is observable in compounds filled below the percolation threshold - meaning that a temperature dependent mechanism must be located at the interface. The next two chapters explore this temperature dependence in more detail.

6.5. Comments on some recently published studies

Recently Pérez-Aparicio and co-workers have studied materials which are reasonably similar to those described here. They have demonstrated, using a combination of various experimental techniques, that the linear viscoelastic storage modulus amplification observed for their compounds exceeds the experimentally-discriminated levels of stiffening arising from strain

amplification effects alone [29]. One explanation for this may be development of a load bearing filler network. However, they have proposed that this discrepancy may be accounted for by an immobilised layer of polymer surrounding the filler aggregates.

Additionally Mujtaba et al. [30] have recently published a report in which they claim to have identified, using ^{1}H-NMR relaxometry, a very small volume of immobilised, glassy phase in commercial silica-filled SBR. They report a volume of glassy material at 25 °C of between 2.5 and 3.5 %. However, they have proposed that the immobilised phase may not exist as a 'layer' or 'shell' (which would necessitate a larger volume fraction) but rather as regions found only under conditions of high confinement. They propose that this confinement is most dramatic between aggregates and therefore in the context of an elastic filler network (Kantor-Webman network) small volumes of glassy material between filler aggregates are capable of dominating the bending modulus of agglomerated particles and therefore mechanical properties of the composite. Figure 6.15 illustrates their findings.

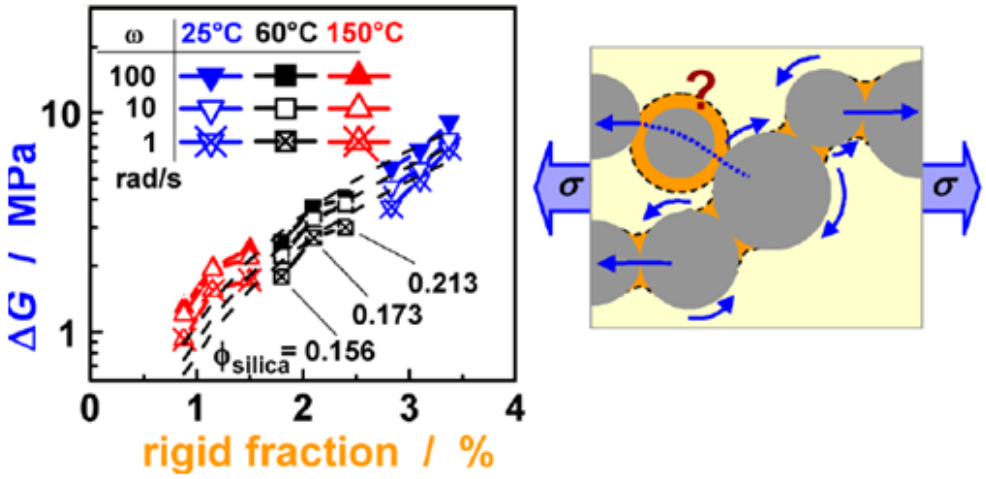

Figure 6.15: Data of Mujtaba at el. showing, left) the magnitude of the Payne effect, Δ*G*, versus the volume of immobilised polymer detected from ^{1}H-NMR relaxometry at different temperatures and frequencies. Right) their concept of immobilised polymer between aggregates dictating the bending modulus of aggregate clusters. (From Mujtaba et al. [30])

Given these findings, it is plausible that the volume of immobilised rubber - seemingly less than 3.5 % for a silica volume fraction of 0.156 - is sufficiently small as to be within the sensitivity limits of the techniques used here. Mujtaba et al. [30] postulate that such a small volume of immobilised polymer material is capable of dominating the mechanical response of the composite.

It is worthwhile noting that from the literature reviewed in chapter 2 and in this chapter, DSC and BDS have been shown to be sensitive to immobilised polymer in *nanocomposite* materials - where the total volume of immobilised material is relatively large. As discussed previously, the commercial materials studied here are far removed from true nanocomposite materials in terms of filler aggregate structures, filler dispersion states and levels of polymer confinement. Two conclusions may be drawn from the data presented here in the context of the finding of Mujtaba et al. [30]:

- Commercial materials lack the polymer confinement conditions for the development of immobilised interphase polymer. Therefore BDS and DSC do not detect any changes to the T_g.
- Commercial materials lack the polymer confinement conditions for the development of *large volumes of* immobilised interphase polymer. Therefore BDS and DSC do not detect any changes to the T_g.

Unfortunately it is not possible to distinguish between these two conclusions based on the current data sets and it is not possible to discount the role played by small volumes of immobilised material on viscoelastic reinforcement as envisaged by Mujtaba et al.

6.6. Conclusion

From the evidence presented in this chapter it may be concluded that the carbon black and silica filler particles have a negligible effect on the glass transition of the NR. Certainly there is enough evidence from DSC and DMA measurements to firmly claim that there is no bulk shifting of the T_g upon incorporation of filler (that is a significant shift in the T_g onset). Furthermore, the lack of any systematic broadening of the T_g observed in the DSC traces and the apparent independence from the presence of filler of the temperature dependence of the α-relaxation in the transition and rubbery regions (from BDS data) suggests that the T_g is not significantly broadened into the rubbery region and does not significantly contribute to the observed reinforcement effects. However, it is necessary to incorporate two caveats into this conclusion:

- The conclusion is predicated upon the assumption that the equipment used (particularly DSC and BDS) is suitably sensitive to a broadening of the glass transition. Literature work suggests that this is the case for nanocomposite materials but it is less certain for the case of commercial materials as discussed in the previous section.

- The conclusion assumes that the analysis techniques applied to the experimental data are robust enough to indentify and correctly interpret any broadening of the glass transition. Previous literature supports this assumption.

Although the conclusions of this chapter are in disagreement with some of the findings of other studies on different rubber-filler combinations, they are in broad agreement with the findings of Robertson et al. [14]. They studied SBR filled with commercial silica and determined that immobilisation of polymer in such commercial systems is negligible. As a more general conclusion they proposed that filler-induced immobilisation of polymer does not play a significant role in the reinforcement of commercially relevant materials. This is in line with the findings presented here.

6.7. References

[1] J.P.C. Addad, P. Frebourg, Polymer, 37 (1996) 4235-4242.
[2] C.G. Robertson, C.M. Roland, Rubber Chemistry and Technology, 81 (2008) 506-522.
[3] C.G. Robertson, C.J. Lin, R.B. Bogoslovov, M. Rackaitis, P. Sadhukhan, J.D. Quinn, C.M. Roland, Rubber Chemistry and Technology, 84 (2011) 507-519.
[4] D. Fragiadakis, L. Bokobza, P. Pissis, Polymer, 52 (2011) 3175-3182.
[5] A. Papon, H. Montes, M. Hanafi, F. Lequeux, L. Guy, K. Saalwächter, Physical Review Letters, 108 (2012) 065702.
[6] A.P. Holt, P.J. Griffin, V. Bocharova, A.L. Agapov, A.E. Imel, M.D. Dadmun, J.R. Sangoro, A.P. Sokolov, Macromolecules, 47 (2014) 1837-1843.
[7] A. Bansal, H.C. Yang, C.Z. Li, K.W. Cho, B.C. Benicewicz, S.K. Kumar, L.S. Schadler, Nature Materials, 4 (2005) 693-698.
[8] L.T. Vo, S.H. Anastasiadis, E.P. Giannelis, Macromolecules, 44 (2011) 6162-6171.
[9] S.W. Wu, Z.H. Tang, B.C. Guo, L.Q. Zhang, D.M. Jia, Rsc Advances, 3 (2013) 14549-14559.
[10] J. Otegui, G.A. Schwartz, S. Cerveny, J. Colmenero, J. Loichen, S. Westermann, Macromolecules, 46 (2013) 2407-2416.
[11] R.B. Bogoslovov, C.M. Roland, A.R. Ellis, A.M. Randall, C.G. Robertson, Macromolecules, 41 (2008) 1289-1296.
[12] P. Ortiz-Serna, R. Diaz-Calleja, M.J. Sanchis, G. Floudas, R.C. Nunes, A.F. Martins, L.L. Visconte, Macromolecules, 43 (2010) 5094-5102.
[13] J.G. Meier, J. Fritzsche, L. Guy, Y. Bomal, M. Klüppel, Macromolecules, 42 (2009) 2127-2134.
[14] C.G. Robertson, C.J. Lin, R.B. Bogoslovov, M. Rackaitis, P. Sadhukhan, J.D. Quinn, C.M. Roland, Rubber Chemistry and Technology, 84 (2011) 507-519.
[15] M. Hernandez, M.D. Bernal, R. Verdejo, T.A. Ezquerra, M.A. Lopez-Manchado, Composites Science and Technology, 73 (2012) 40-46.
[16] J. Berriot, H. Montes, F. Lequeux, D. Long, P. Sotta, Macromolecules, 35 (2002) 9756-9762.
[17] A.I. Medalia, Journal of Colloid and Interface Science, 32 (1970) 115.
[18] A.I. Medalia, Rubber Age, 104 (1972) 67-71.
[19] L. Mullins, N.R. Tobin, Rubber Chemistry and Technology, 39 (1966) 799-813.
[20] Y. Fukahori, A.A. Hon, V. Jha, J.J.C. Busfield, Rubber Chemistry and Technology, 86 (2013) 218-232.
[21] H.M. Smallwood, Rubber Chemistry and Technology, 18 (1945) 292-305.

[22] S. Wolff, J.-B. Donnet, Rubber Chemistry and Technology, 63 (1990) 32-45.
[23] H.S. Chen, A. Acrivos, International Journal of Solids and Structures, 14 (1978) 331-348.
[24] J.S. Bergström, M.C. Boyce, Rubber Chemistry and Technology, 72 (1999) 633-656.
[25] Y.K. Akutagawa K, Yamamoto A, Heguri H, Jinnai H, Shinbori Y, Rubber Chemistry and Technology, 81 (2008) 182-189.
[26] A.A. Gusev, M.G. Rozman, Computational and Theoretical Polymer Science, 9 (1999) 335-337.
[27] A.R. Payne, Rubber Chemistry and Technology, 38 (1965) 387-399.
[28] A.R. Payne, R.E. Whittaker, Rubber Chemistry and Technology, 44 (1971) 440-478.
[29] R. Pérez-Aparicio, A. Vieyres, P.A. Albouy, O. Sanseau, L. Vanel, D.R. Long, P. Sotta, Macromolecules, 46 (2013) 8964-8972.
[30] A. Mujtaba, M. Keller, S. Ilisch, H.J. Radusch, M. Beiner, T. Thurn-Albrecht, K. Saalwächter, Acs Macro Letters, 3 (2014) 481-485.

Chapter 7

Linear Viscoelastic Mechanical Analysis

Précis:

The initial part of Chapters 5 and all of Chapter 6 focused on reinforcement effects within the glass transition region of the filled elastomer compounds. This chapter shifts the focus of the investigation and details a characterisation of the small strain linear viscoelastic properties of the carbon black filled series of compounds in the higher temperature rubbery region.

The model microcomposite compounds introduced in Chapter 5 are revisited and it is shown that the small strain loss tangents of these compounds are identical to that of the unfilled control. This is in agreement with the findings of Chapter 5 in that the energy of deformation is demonstrated to be stored and dissipated solely within the elastomer phase.

A custom built torsion pendulum is constructed to very precisely measure the linear viscoelastic properties of the carbon black filled compounds in the temperature range of T_g + 50 K to T_g +150 K. Firstly it is apparent that all the carbon black-filled compounds displayed tanδ values in excess of the unfilled material - indicating an additional source of dissipation at small strain. However the key finding of this chapter is the appearance in the data collected for the graphitised carbon black-filled compounds, of an increasing tanδ with increasing temperature. This cannot be explained by the temperature dependence of the dynamics of the underlying elastomer matrix.

This finding is discussed in the context of similar data found in the literature which suggest some generality of this feature in filled polymer materials where the polymer-filler interactions are particularly poor. This is the first observation of such secondary dissipation effects for carbon black-based fillers.

7.1. Consideration of hydrodynamic reinforcement in terms of linear viscoelastic damping

It is worthwhile at this point re-examining the hydrodynamic theory of reinforcement in terms of its implications for linear viscoelastic damping in filled compounds. It is apparent from Chapter 2 that a number of assumptions underpin the various analytical hydrodynamic equations:

- The filler particles and agglomerated filler network structure are rigid versus the matrix,
- The matrix material in the filled samples has the same underlying properties as that of the unfilled material, and
- The boundary condition between filler and matrix phases is non-slip.

The implications of such assumptions mean that, so long as the applied strains remain small enough to ensure that there is no mechanical disruption of the filler network, reinforcement of the moduli should be independent of temperature above the glass transition. Furthermore, upon small strain deformation, elastic storage and viscous dissipation of mechanical energy should occur entirely within the elastomer phase. In this context, the presence of a geometrically complex, rigid filler structure acts to amplify the dynamic moduli according to hydrodynamics, strain amplification and elastomer occlusion - termed here 'geometrical reinforcement'. The precise magnitudes of such amplification are impossible to ascertain due to the complexity in determining the coefficients of a hydrodynamic series expanded to describe the geometry of a fractal filler structure; however, the ratio of the moduli, tanδ, should be independent of the presence of filler and equal to that of the unfilled elastomer.

This can be demonstrated by defining the loss tangent for filled compounds in terms of hydrodynamics

$$\tan\delta_{filled} = \frac{G''_{filled}}{G'_{filled}} = \frac{G''_{unfilled}(1 + a\varphi + b\varphi^2 + \cdots)}{G'_{unfilled}(1 + a\varphi + b\varphi^2 + \cdots)} = \tan\delta_{unfilled} \qquad 7.1$$

where φ is the filler volume fraction and a and b are the series expansion coefficients.

Here we see that the series expansions for the storage and loss moduli cancel; meaning that tanδ of the filled compound should be equal to that of the unfilled compound (at any volume loading of filler and at any temperature and frequency in the rubbery region). This is demonstrated graphically in Figure 7.1. Here the experimental storage and loss moduli measured at 25 °C of an unfilled NR cured with 2 phr DCP are expanded as a function of filler

volume fraction using the Chen-Acrivos hydrodynamic equation [1, 2]. Although the absolute magnitudes for both the dynamic moduli scale with the theoretical incorporation of filler, the loss tangent is independent of the filler volume fraction.

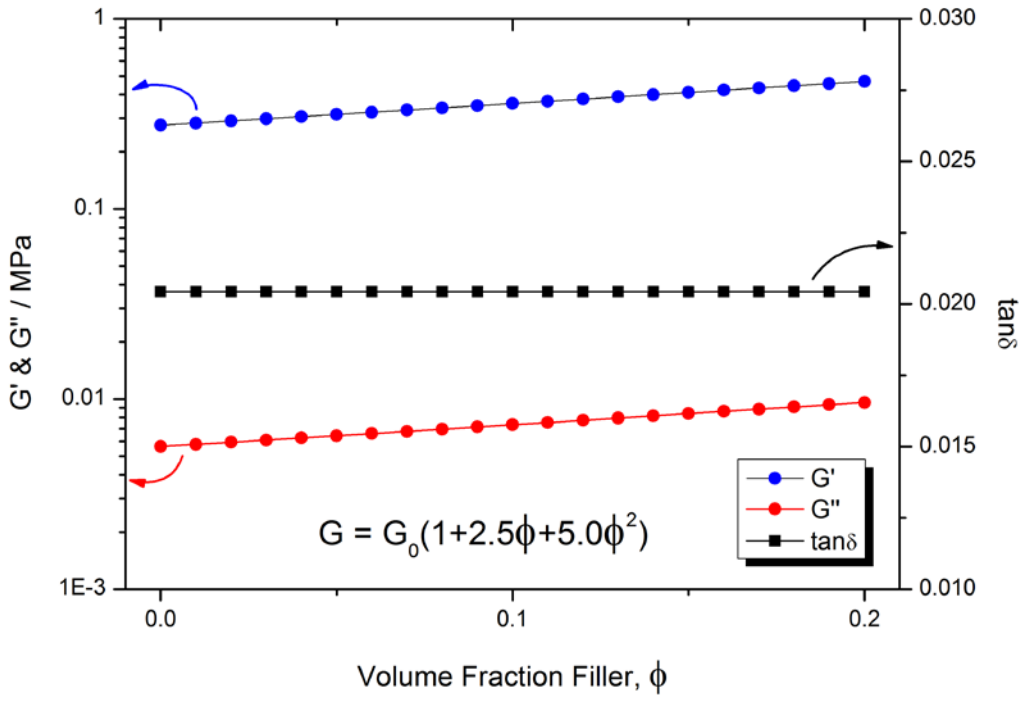

Figure 7.1: Viscoelastic moduli of unfilled, peroxide-cured NR at 25 °C expanded in terms of the Chen-Acrivos hydrodynamic equation as a function of filler volume fraction. Note that although the moduli are amplified due to the presence of the filler particles the ratio of the moduli, tanδ, is independent of the filler loading

This independence of the loss tangent of filled compounds from the presence of filler can be seen in the dynamic mechanical properties of the glass microsphere-filled rubbers introduced in Chapter 5. In Chapter 5 the reinforcement mechanisms for these compounds were ascribed to hydrodynamics, strain amplification and elastomer occlusion mechanisms ('geometrical reinforcement'). Examining the small strain loss tangent of the model filled rubbers as a function of temperature (Figure 7.2), we see that in the rubbery region, above the glass transition, the loss tangents of the glass microsphere-filled rubbers are indistinguishable from each other and from the unfilled control material.

Consider the peak in damping around the glass transition apparent at ~210 K. The maximum of this peak in damping is sensitive to both the presence of filler and the filler particle size (see the inset in Figure 7.2). This can be related to the stiffening of the material just after the glass transition as discussed in Chapter 5. Robertson et al. [3] pointed out that the small strain loss

tangent around the T_g constitutes contributions from both the damping dynamics of the polymer phase and the hydrodynamic stiffening (additional non-polymer contribution to G') associated with the presence of a fractal filler phase in the rubbery region.

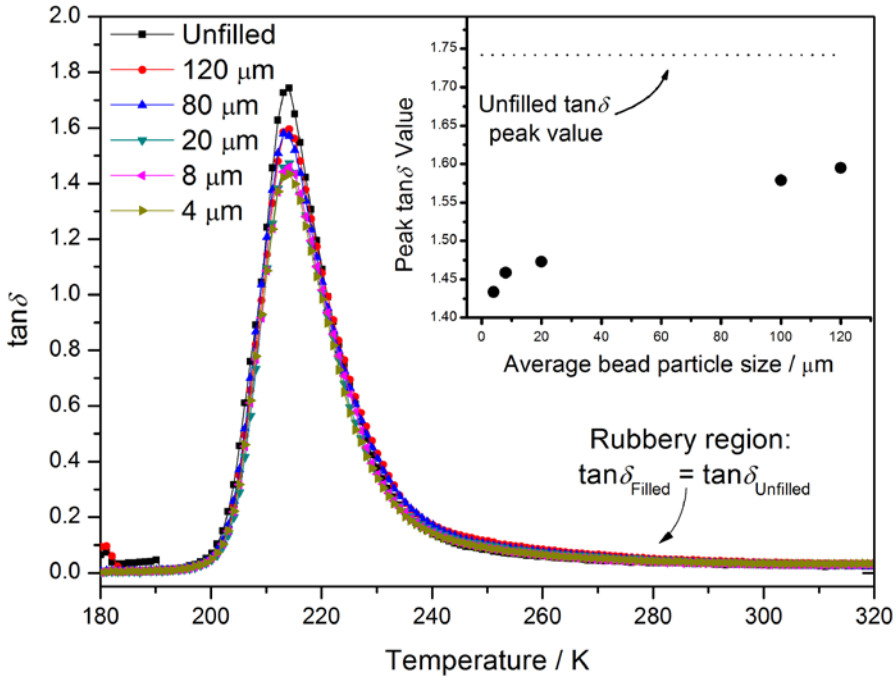

Figure 7.2: Linear viscoelastic tanδ as a function of temperature for glass microsphere-filled NR. In the rubbery region the tanδ values of the filled compounds are indistinguishable from the unfilled material. The inset shows the decrease in damping peak as a function of microsphere diameter. The legend gives the average microsphere diameter determined from light scattering experiments

The independence of the loss tangent of filled compounds from that of the corresponding unfilled compound holds for simple, model filled rubbers. It is therefore of interest to examine loss tangents of commercially relevant filled rubbers in a similar way. In fact, examination of some of Payne's original data in the linear viscoelastic regime - where tanδ appears to depend on the volume loading of carbon black - suggests that this independence of the loss tangent is no longer valid for materials of commercial interest. Furthermore, work by Roland [4] on the dynamic properties of filled elastomers at very small strains indicates an anomalously large viscous dissipation at small strains which Roland postulated to originate from frictional drag between neighbouring aggregates within the filler network. The dynamic data from Payne [5], Roland [4] and Wang [6] are presented in Figure 7.3. This chapter details an attempt to

precisely determine the loss tangent and dynamic moduli for the commercially relevant compounds at vanishingly small strains.

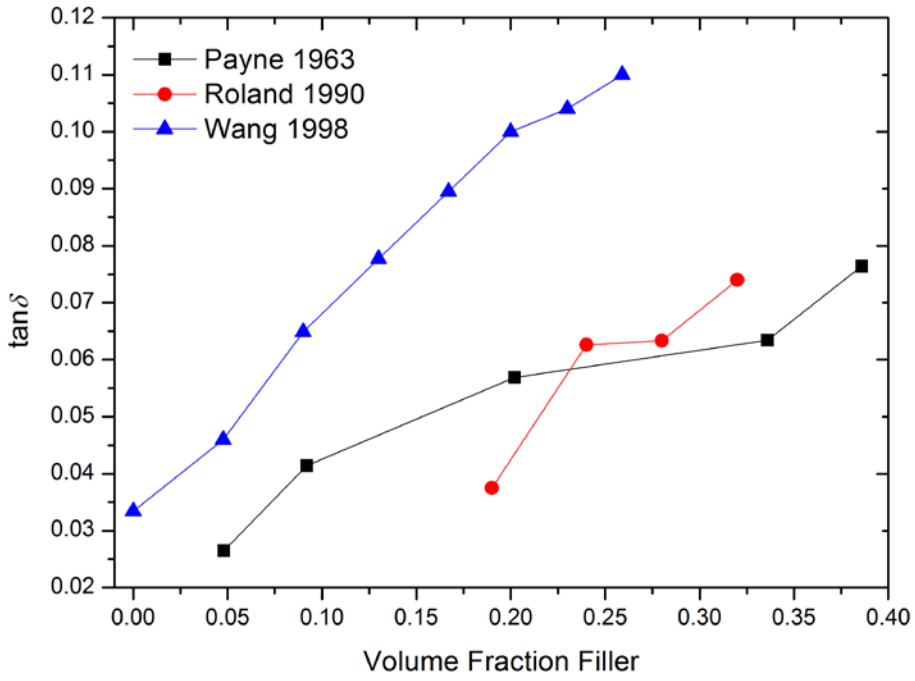

Figure 7.3: tanδ data from the literature (data points have been digitised using Digplot software - available from http://polymerphysics.net/software.html at the time of writing). For cases where tanδ was not explicitly reported, it has been calculated from the dynamic moduli). The plot shows tanδ as a function of filler volume fraction taken from three papers[1]. The data of Payne [5, 7, 8] from 1963 refers to an HAF carbon black/butyl rubber combination with a deformation frequency of 0.5 Hz. Roland [4] studied peroxide crosslinked IR filled with N110 carbon black with a deformation frequency of 0.1 Hz. The data of Wang [6] refers to an SBR-N234 carbon black combination with a deformation frequency of 10 Hz.

7.2. Free vibration dynamic mechanical analysis

When considering samples filled with high structure, high surface area particles, the incorporation of a strain-sensitive filler network complicates mechanical testing. Substantial pre-straining of the samples, for example by clamping samples into test geometries, or simply the deformation of sample test specimens under their own weight, must be avoided or minimised. For highly filled elastomers, the limit of linear viscoelasticity is generally found at small strains typically of around 0.1 %. Linear viscoelastic testing must therefore be conducted with equipment capable of accurately resolving dynamic losses at strains below 0.1 % while

[1] Wang used a 5 % dynamic strain which is probably outside of the material's linear response. Both Payne and Roland reported values within their material's linear viscoelastic regions.

imposing a minimum strain history on the sample. A number of issues arise from using the forced oscillation Q800 DMA for this purpose:

- The DMA requires the use of small samples (typically 5x5x2 mm^3 dimensions). This means that material deformations imposed simply by handling (demoulding, cutting and sample preparation) of the samples result in quite large and unquantifiable pre-straining,
- The most reliable mode of testing for strain sensitive filled rubber compounds is double shear rather than tension since there are no sample buckling or preloading issues. For the DMA double shear clamp setup as manufactured by TA Instruments, the two shear specimens are compressed into the clamps in order to hold them in place. Such pre-straining is undesirable. Gluing of the samples in place is one solution but is not ideal since again the sample must be handled considerably and the possibility of swelling of the rubber by the glue cannot be discounted,
- In the double shear setup, the specimen thickness is fixed at room temperature by locking the clamps around the mounted samples. If a sufficiently wide temperature sweep is performed then the discrepancy in thermal expansion coefficients between the rubber material and the metallic clamps results in relative compressive or tensile deformation of the samples along the axis orthogonal to the applied shear during the temperature cycling.
- Even though small deformations can be precisely imposed upon the specimen using the DMA, the resolution of the forces and the calculated viscous dissipations at very small strains is more problematic. Typically viscous properties of rubbers measured at very small strains (<0.01%) are extremely noisy. The resolution of dissipations is noticeably increased if testing is performed at strains of 0.1% or greater - however this is very close to the typical limit of linear viscoelasticity. Medalia [9], Davies et al. [10] and Akutagawa [11] have previously commented on this testing issue and have proposed that in certain circumstances a free vibration technique may be more suitable for precise linear viscoelastic characterisation of rubber compounds.

To this end a purpose-built torsion pendulum was developed based on the free vibration principle. A schematic of the torsion pendulum setup is given in Figure 7.4. The filled elastomers were compression moulded into cylinders of 150 mm length and 12 mm diameter. To minimise straining due to sample handling, the mould design included thin flanges of excess crosslinked material attached to either side of the sample cylinder. This allowed the sample to be removed from the mould and subsequently handled without excessive pre-straining. Silicone-based mould release agent was also applied to the sample moulds prior to curing, to lubricate removal of the samples from the mould. Cylindrical samples were then bonded by

one end face to a steel plate and by the other to a threaded screw using Loctite 480 adhesive. The flanges could then be trimmed from the sample using a scalpel once it was bonded in place. The samples were attached to the inertia bar via the screw thread and located and fixed to the bottom of the pendulum using an electromagnet locator system. Two aluminium plates were located at each end of the inertia bar and the bar was counter balanced in the vertical direction using a pulley system.

The central cylinder of the inertia bar seen in Figure 7.4 had a diameter of 15 mm and a length of 65 mm. The arms and sensor target panels were constructed of stainless steel giving the inertia bar a total length of 240 mm. The total mass of the inertia bar for dynamic experiments was 97.48 g.

A nearly instantaneous torsional deformation was applied across the samples using a short burst of lightly compressed air directed at the opposing faces of both aluminium plates. To apply the compressed air to the aluminium plates, flexible tubing was connected at one end to a 20 ml syringe. The tubing was then split by a 3-way T piece connector. The two free tubing ends were then mounted on retort stands about 5 mm away from the aluminium target plates on opposite ends of the inertia bar. To supply the compressed air actuation, the syringe was rapidly depressed. This assembly is schematically illustrated in Figure 7.5.

The subsequent torsional damping of the imposed strain was recorded by monitoring the displacement of the aluminium plates over time using a non-contact displacement sensor. The sensor was calibrated and linearity was confirmed by collecting voltage-displacement data using an Instron frame to accurately control the displacement of the aluminium target plate from the sensor. Calibration data was collected over a range of temperatures. Figure 7.6 shows the sensor output voltage as a function of target distance from the sensor face. There is an initial standoff distance of ~1.5 mm before an output voltage is detected. Thereafter the relationship between voltage and displacement is linear up to about 6 V (5 mm). The effect of temperature cycling is minimal in this region. The working linear region is illustrated in Figure 7.6 by the dotted lines. For all measurements the output voltage was kept within these limits.

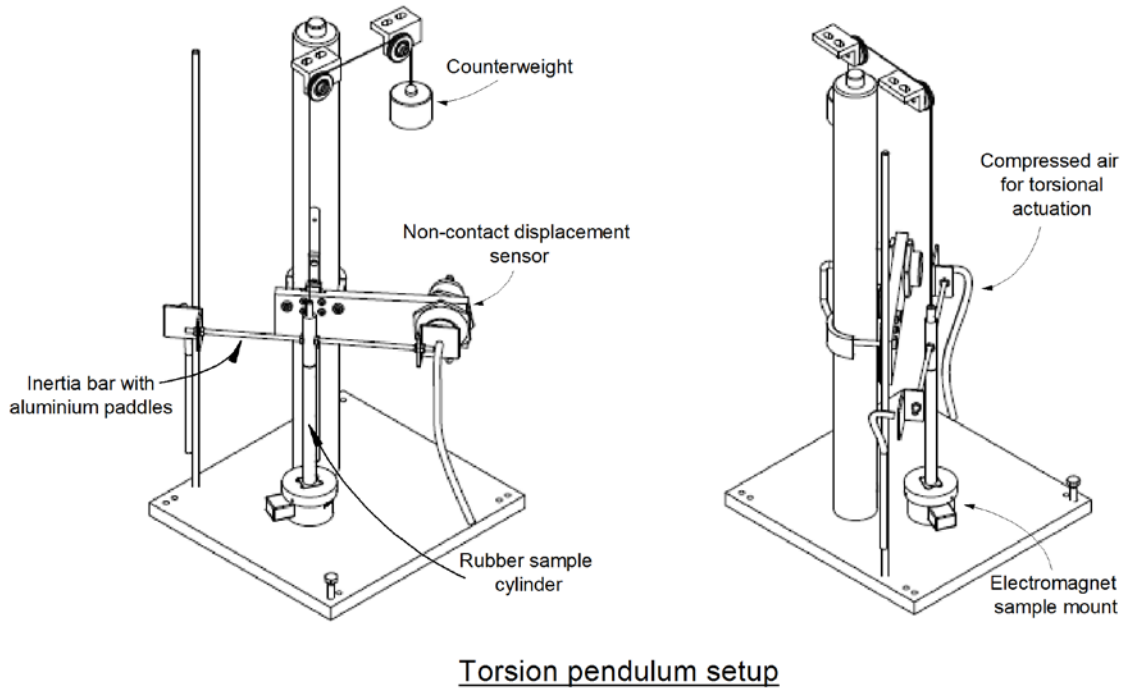

Figure 7.4: Schematic of the set up of the small strain test equipment in dynamic (pendulum) mode The equipment is shown from two perspectives.

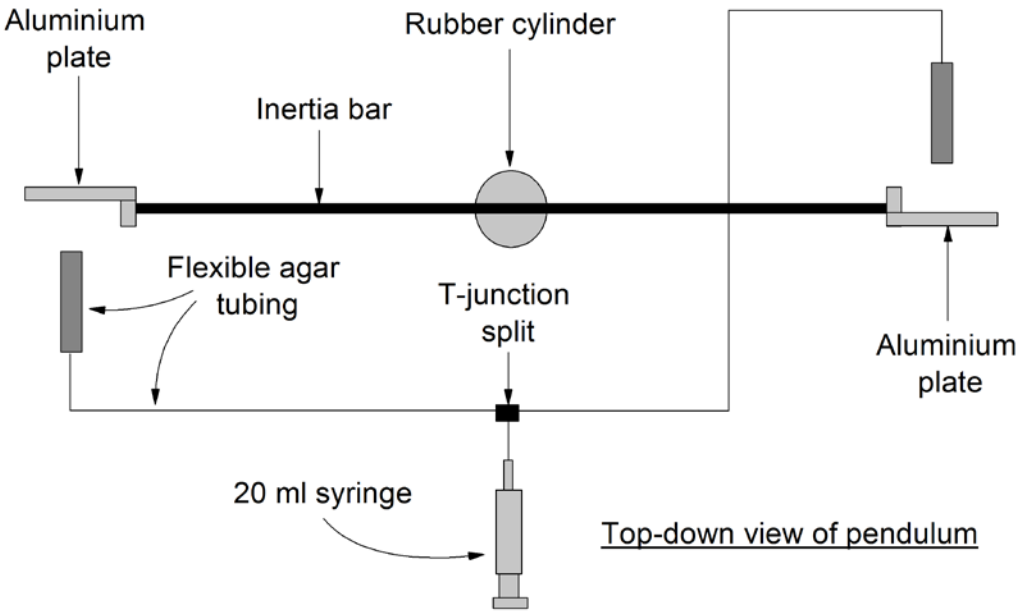

Figure 7.5: Compressed air actuation of the pendulum. The torsional rotation is in the plane of the page. Flexible agar tubing was connected to the syringe and then split and positioned perpendicular to the two aluminium plates. Depressing the syringe plunger supplied an equal blast of air to each extremity of the inertia bar - thereby inducing a balanced, in-plane and near instantaneous torsional excitation.

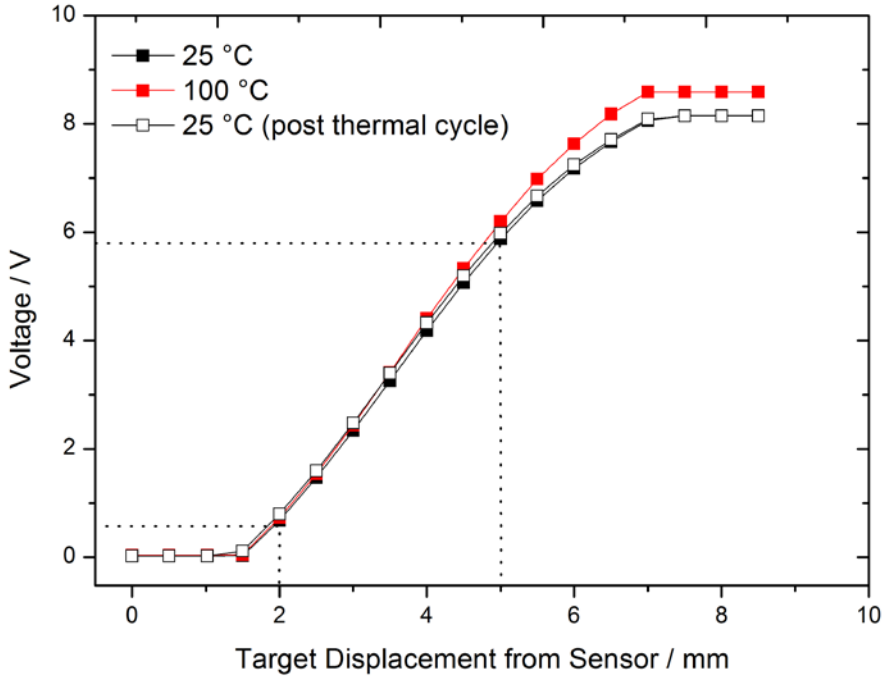

Figure 7.6: Non-contact displacement sensor calibration. Data taken at 25 °C, 100 °C and again at 25 °C. The dotted lines correspond to the linear voltage-displacement range in which all experimental data were collected

A damped oscillating waveform, typical of the data collected from the free vibration experiment, is presented in Figure 7.7. The arbitrary voltage values of the ordinate are directly proportional to the position of the aluminium plate relative to the sensor.

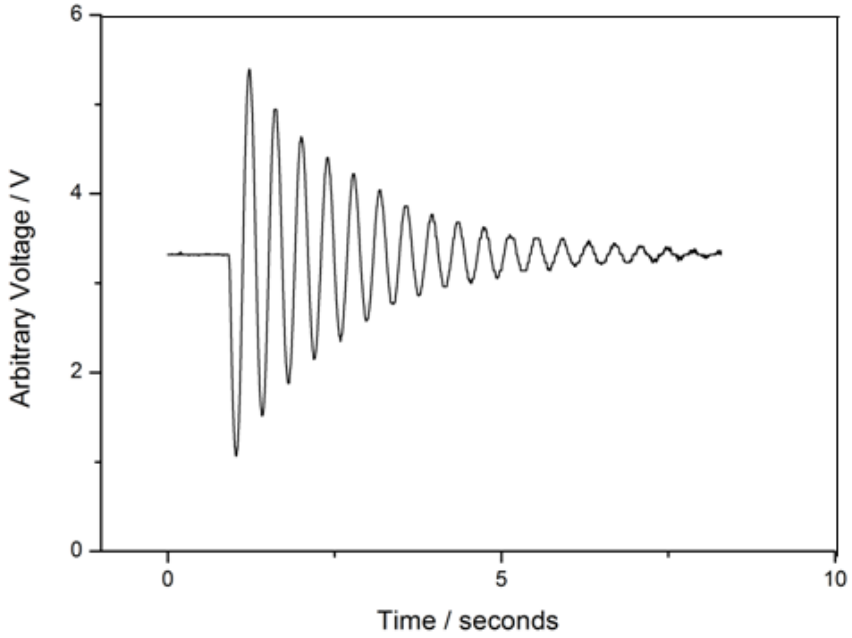

Figure 7.7: A typical damped waveform from the pendulum setup showing the decay in free vibration amplitude with time. The arbitrary voltage is produced by the non-contact displacement sensor and is directly proportional to displacement.

Dynamic mechanical properties can be extracted from such waveforms using Equations 7.2 - 7.4. [12, 13].

$$\tan\delta = \left(\frac{\Delta}{\pi\left(1+\frac{\Delta}{4\pi^2}\right)}\right) \qquad \text{where} \qquad \Delta = \frac{1}{n}\ln\left(\frac{x_i}{x_{i+n}}\right) \tag{7.2}$$

where Δ is the logarithmic decrement of oscillation amplitude between sequential oscillations, x_i is the oscillation amplitude at oscillation i, x_{i+n} is the oscillation amplitude at oscillation $i+n$.

$$G'' = \left(\frac{2If^2\Delta}{\pi^2}\right)\left(\frac{l_0}{r^4}\right)\lambda_0^3 \tag{7.3}$$

$$G' = \left(\frac{2If^2}{\pi}\right)\left(\frac{l_0}{r^4}\right)\lambda_0^3 \tag{7.4}$$

where I is the inertia of the inertia bar, f is the frequency of the oscillation, Δ is the logarithmic decrement of oscillation amplitude, l_0 and r refer to the length and radius of the cylinder sample respectively, λ_0 is the pre-strain applied to the cylinder which in this case is zero, therefore $\lambda_0 = 1$

To ensure that all the measurements were collected in the linear viscoelastic region, dynamic properties were plotted versus strain (or oscillation number). For all measurements, linear viscoelasticity (that is, independence of dynamic properties from strain) was confirmed. The typical maximum strain subjected to the edge of the sample cylinder upon initial deformation was found to be between 0.02 % and 0.001 %. It is worthwhile noting that due to the dependence of torsional strain on the sample radius, the bulk of the samples were subjected to smaller strains and that this strain decays by at least an order of magnitude during the damping process.

The inertia of the inertia bar was calculated by suspending the bar from either end with nylon wire. The bar was then lightly tapped on one side to initiate a torsional oscillation. This oscillation was recorded using a non-contact displacement sensor and PC oscilloscope. The frequency of the torsional oscillation was determined and the inertia of the bar, I, was calculated from [14]

$$I = \frac{mga^2}{4l\pi f^2} \qquad 7.5$$

where m is the mass of inertia bar, g is the acceleration due to gravity, a is half of the length of the bar, l is the length of nylon string and f is the torsional frequency of oscillation.

As can be seen from Equation 7.4 the frequency of the torsional deformation is dictated by the modulus of the material and the setup (inertia) of the inertia bar. As the same inertia bar setup was used for the whole series of experiments over the entire temperature range considered, the frequency of the deformation varied slightly between samples and within each temperature sweep data set due to temperature dependent changes in the material modulus.

As rubber materials are highly frequency dependent, this had the potential to complicate the data interpretation. However it was found that the maximum variation in deformation frequency over the temperature range studied was less than a factor of two. It has previously been demonstrated for this type of equipment that within such a limited range of frequency the dynamic properties are broadly independent of the applied frequency [11, 15, 16].

However, in the glass transition region the modulus is extremely sensitive to changes in temperature and can change by an order of magnitude as a result of changes of just a few Kelvin. Therefore, around the T_g the changes in deformation frequency could be substantial. For this reason and due to excessive torsional damping in the T_g region, the temperature range of investigation was restricted to a minimum of -20 °C which is well within the rubbery region for all of the materials studied. Therefore there is a broad independence of the dynamic properties from the slight change in deformation frequency. Deformation frequencies were of the order of 2 Hz depending on filler type.

The entire pendulum apparatus was placed inside an Instron environmental test chamber (ETC), allowing a temperature range for testing of between +100 °C and -20 °C (Figure 7.8). The test temperatures and temperature stabilities were confirmed using an independent

thermocouple as well as the ETC's built-in thermocouple. Prior to testing, samples were conditioned *in situ* at 100 °C for three hours in an attempt to anneal any unintentional pre-straining. Dynamic properties were then monitored at 100 °C for a minimum of 90 minutes to check for any pre-strain-induced time dependence. Once the dynamic readings were stable the temperature inside the chamber was dropped in steps of 10 K with a 40 minute isothermal equilibration period at each step. Three repeat free vibration measurements were taken at each temperature.

The ETC uses a fan system to circulate air around the chamber. The vibration caused by the fan resulted in very slight disturbance to the sample. However, the deformations recorded from this vibration were very small and well within the linear region of the material's response. In order to obtain an acceptable signal from the free vibration experiments, the fan was switched off just prior to testing. Testing took on average 30 seconds to obtain 3 repeats and then the fan was switched back on. During this test period no measurable change in the chamber temperature was recorded either by the built-in thermocouple (sensitive to 0.1 °C) or by a second thermocouple placed in the chamber close to the sample (sensitive to 0.05 °C).

Gent and Mifune [17] used a torsional pendulum apparatus to investigate the viscoelasticity of unfilled rubbers. They reported that their home-made pendulum gave a value of tanδ of 0.02 for unfilled SMR-L NR crosslinked with 2 phr DCP at a plate temperature of 150 °C for 130 minutes. This material is very similar to the unfilled materials investigated in this work (here SMR CV60 grade NR is used with a crosslinking time of 100 minutes). Using the torsion pendulum apparatus outlined in this chapter, a value of tanδ for the unfilled NR sample considered in this work was found to be 0.022 at 22 °C (note Gent and Milfune [17] tested materials at 25 °C). This indicates that the pendulum designed and built for this work is capable of producing precise measures of linear viscoelasticity which are in line with literature values.

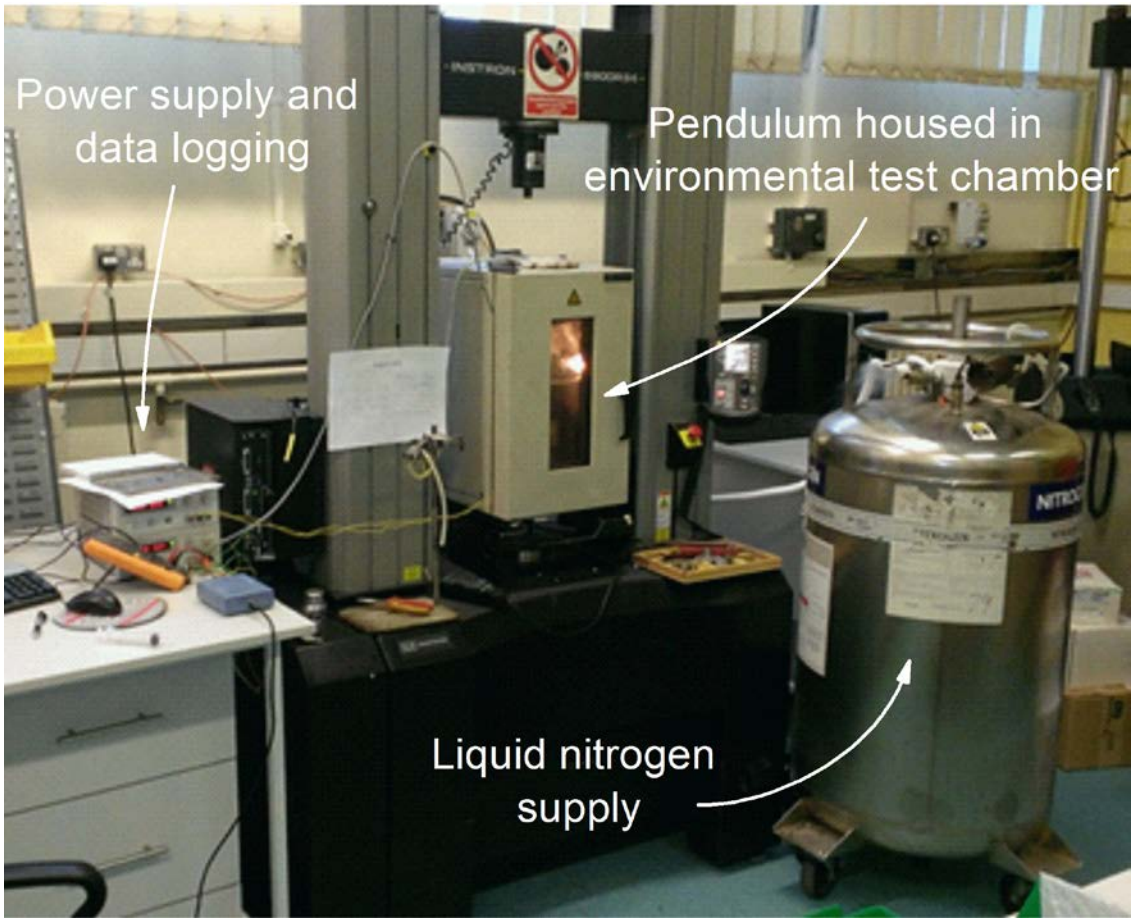

Figure 7.8: Test setup for torsion pendulum. The pendulum was housed in an Instron environmental test chamber.

7.3. Loss tangents as a function of filler volume fraction at a fixed temperature

The linear viscoelastic loss tangents of the various carbon black-filled materials were examined as a function of filler volume fraction at a fixed temperature (room temperature ~22 °C) for each filler type. For all filler types, irrespective of particle surface area and surface activity, an increase in tanδ relative to the unfilled material was observed. A linear relationship between tanδ and filler volume fraction was found for all the materials as shown in Figure 7.9. Fitted linear trends are shown in Figure 7.9. There is some scatter of data around the linear fits but this could potentially be ascribed to slight compounding errors.

The DC electrical percolation thresholds determined in Chapter 5 are indicated on the linear fits by the change in line style from dotted to solid lines. It is of interest here that there is no discontinuity present in the small strain damping response at the percolation threshold. Below the percolation threshold tanδ is seen to increase linearly in magnitude with increasing volume fraction (see in particular the data of N990 and N990g-filled materials and N330-filled material). This indicates that there must be some non-hydrodynamic, viscous dissipation

evident which depends upon the surface area of interaction between the carbon black and the natural rubber. Above the percolation threshold, where a filler network is developed, a change or additional contribution to the reinforcement mechanisms may have been expected. For example Meier and Klüppel [18] and Fritzsche and Klüppel [19] have proposed that above the percolation threshold, the level of reinforcement depends upon the stiffness of filler aggregates clusters connected by regions of immobilised polymer. This is distinct from that observed below the percolation threshold which is essentially dominated by hydrodynamics.

However, the data collected cannot be reconciled with a dramatic change in the reinforcement mechanism at the percolation threshold. This suggests that actually, rather than being flexible at small strains, the aggregate clusters which form the percolated filler network are rigid and the amount of non-hydrodynamic viscous dissipation instead depends upon the filler-polymer interaction area which would broadly be expected to increase with filler loading (even above the percolation threshold). Stated another way: the energy of small strain deformation is not stored/dissipated in aggregate clusters above the percolation threshold but is instead isolated in the rubber phase and at the filler interface.

There is, however, an alternative and more mundane explanation for this data. As shown in Chapter 4, the carbon black fillers act to reduce the crosslinking efficiency of the peroxide cure system in proportion to the filler surface area. A reduction in crosslink density results in an increase in linear viscoelastic damping as seen in Figure 4.14 in Chapter 4. Therefore the data may simply reflect the level of crosslinking in the compounds versus the unfilled material which is dependent upon the amount of carbon black filler in the material and also the surface activity of the carbon black. Without further work it is not possible to distinguish between the reinforcement and crosslink density interpretations of the data. Examining the previous data of Payne, Roland and Wang (Figure 7.3) we can note that both Payne and Wang worked on materials crosslinked using sulphur-based systems and that their data also demonstrates a linear increase in small strain tanδ.

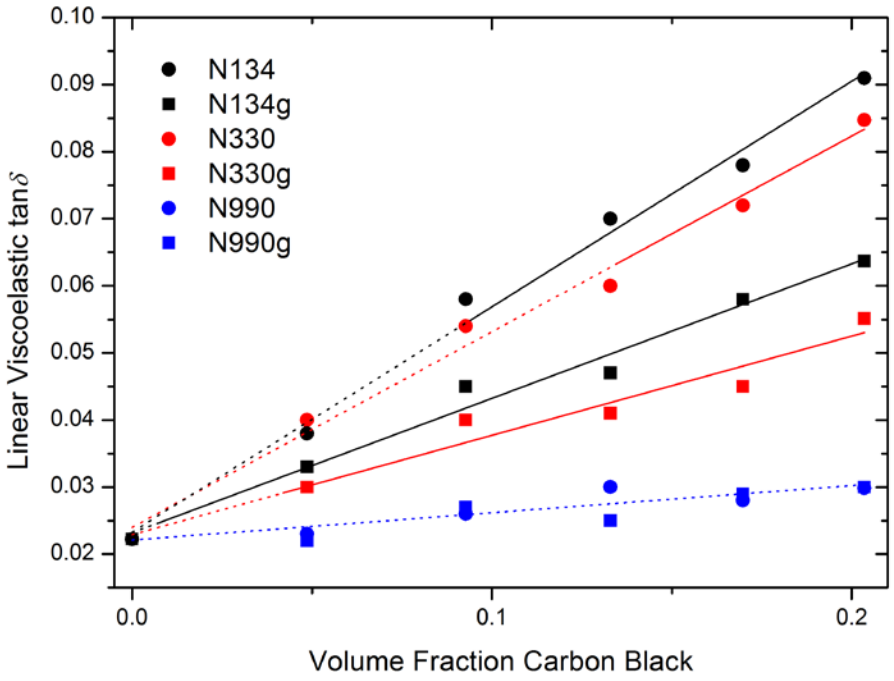

Figure 7.9: Linear viscoelastic tanδ values as a function of filler volume fraction for each carbon black filler type. Linear relationships are indicated by a regression fit. The point of change of the fitted line from dotted to solid graphic indicates the percolation threshold determined from electrical measurements. The test temperature was 22 °C

7.4. Dynamic mechanical properties as a function of crosslink density

The previous section raises some questions about the filler network and its role in dictating the mechanics of compounds at small strains. In order to probe the mechanical nature of the percolated carbon black network in more detail, a series of simple experiments were performed on the N134-filled compound which, when incorporated at a volume loading of 0.20, is loaded significantly above its electrical percolation threshold (Chapter 5, Figure 5.10 A).

In this experiment, samples of N134-filled natural rubber were prepared with varying levels of crosslink density using the masterbatch material which was prepared in a Banbury internal mixer (Chapter 3). Six different levels of crosslink density were prepared corresponding to DCP loadings of 0.5, 1, 1.5, 2, 2.5 and 3 phr. During processing of the compounds an attempt was made to keep the total compounding shear experienced by each sample equivalent. This was done by keeping the number of mill passes during compounding on the 2-roll-mill the same. From the compounded materials, cylindrical test samples were produced for dynamic torsion testing and a series of rubber sheets were also produced from which tensile dumbbell samples were stamped. The viscoelastic moduli of the materials at very small strains were measured

using the torsion pendulum equipment while larger strain mechanical properties were extracted from each material's tensile stress-strain curves.

Figure 7.10 plots the small strain storage modulus versus the initial concentration of DCP cross-linker, which is proportional to the crosslink density[2]. Also plotted in Figure 7.10 are the tangent moduli (reported as G=E/3) determined at 10 % tensile strain for the filled materials and data for the corresponding unfilled materials which are determined from small strain tangent moduli from tensile tests. As can be seen from Figure 7.10 both the small and large (10%) strain moduli of the filled materials strongly depend on the crosslink density of the rubber matrix. Such dependence means that at small strain the energy of deformation must be stored, at least partially, in the rubber phase. For example, if the small strain moduli were found to be independent of the rubber network elasticity then this would imply that all the deformation energy is stored in an elastic filler structure - the mechanics of which are independent of the rubber phase. This is not the case. Accordingly the small strain loss moduli and tanδ values depend significantly on the rubber phase as shown in Figure 7.11.

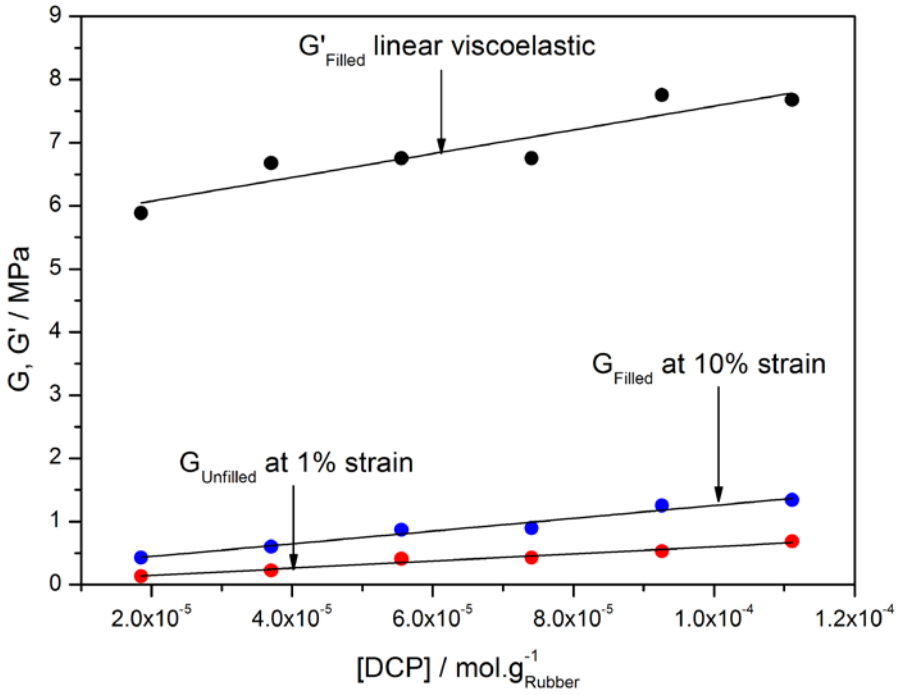

Figure 7.10**:** Plot of moduli versus initial peroxide concentration for N134-filled NR. Linear viscoelastic G' values were determined from torsion pendulum tests while moduli values taken at higher strains and for unfilled materials are converted from tensile test data.

[2]Note that the influence of carbon black on the crosslink density yield observed in Chapter 4 is not considered here. The important issue here is the general dependence of mechanical properties on crosslink density. Determination of the true crosslink density may be expected to shift the values along the *x*-axis somewhat but not to alter the trend

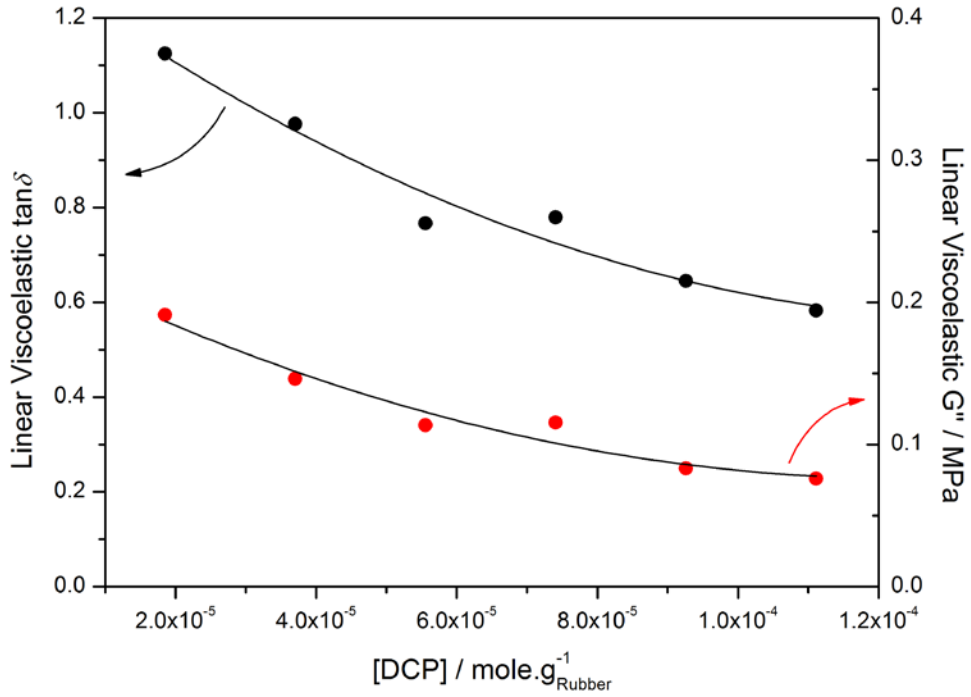

Figure 7.11**:** Small strain tanδ and G'' plotted versus the initial concentration of peroxide crosslinker

7.5. Loss tangents as a function of temperature at fixed volume fraction

Figure 7.12 shows the temperature dependence of the linear viscoelastic loss tangents for the unmodified carbon black-filled series of samples and the unfilled control, measured using the free vibration apparatus. For these experiments the volume fractions were fixed at 0.20. The temperature axis is presented as T-T_g using the value of T_g for the unfilled material determined from isothermal dielectric testing in Chapter 6 to standardise the temperature scale. The unmodified N134 and N330-filled samples display a large increase in tanδ versus the unfilled sample at all testing temperatures. However, in a general sense, the temperature dependence of the tanδ trace appears to follow that of the underlying viscoelastic rubber (that is a decreasing dissipation with increasing thermal distance from the T_g). Unmodified N990 results in a more modest increase in viscous damping but again follows the temperature dependence of the underlying polymer matrix.

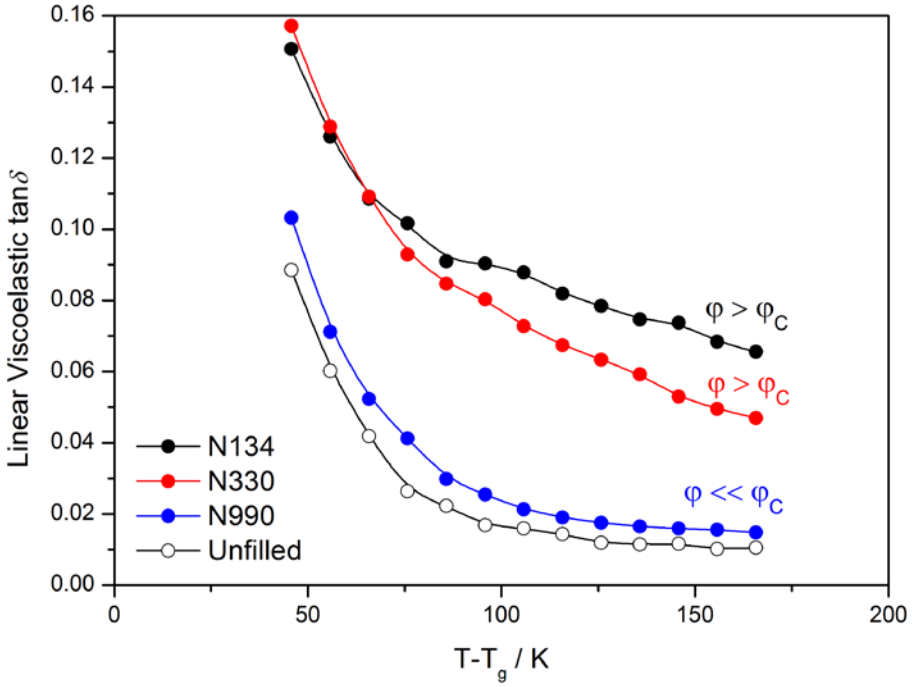

Figure 7.12: Temperature dependence of the linear viscoelastic loss tangent for natural rubber filled with unmodified carbon black and the unfilled control sample. The glass transition temperature corresponds to 0 K on the standardised axis

Figure 7.13 shows the temperature dependence of the linear viscoelastic loss tangents for the graphitised carbon black-filled series of samples and the unfilled control. Here the N134g and N330g -filled samples display a marked upturn in tanδ evident from approximately T_g + 100 K as indicated on the plot by the dashed line. N990g does not display an upturn in tanδ at higher temperatures but is measurably increased over the unmodified N990 in the higher temperature range. This is indicated by the inclusion of the unmodified N990 data and the blue arrow. Therefore all graphitised carbon black-filled materials show a temperature-dependent increase in linear viscoelastic dissipation in the region T_g + 80-170 K. This is independent of the state of filler networking in the compounds (i.e. whether they are above and below their percolation thresholds).

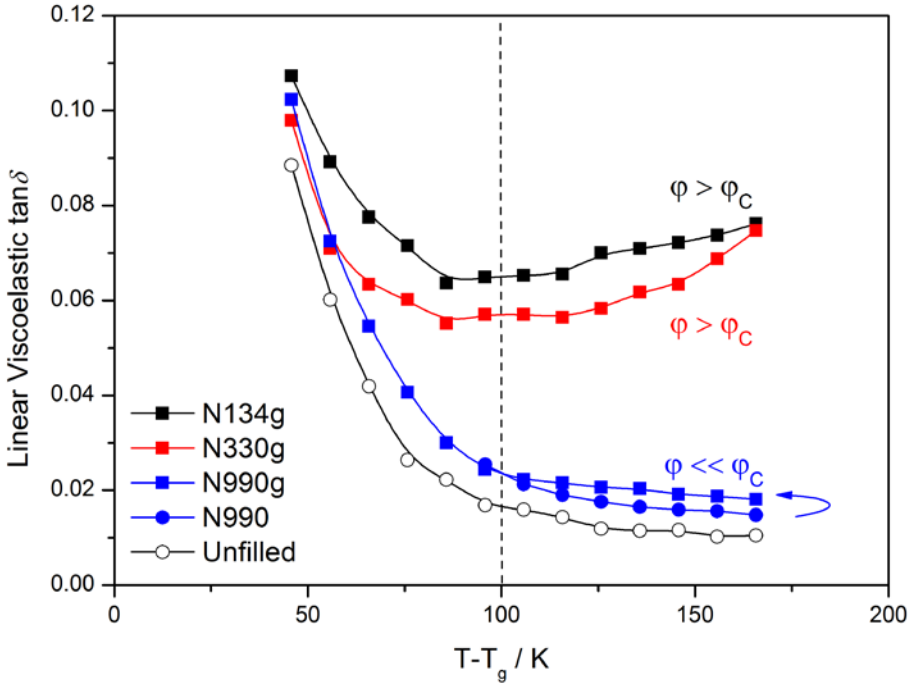

Figure 7.13: Temperature dependence of the linear viscoelastic loss tangent for natural rubber filled with graphitised carbon black and the unfilled control sample. The glass transition temperature corresponds to 0 K on the standardised axis. The onset temperature of the secondary increase in tanδ is indicated by the dashed line. The blue arrow indicates the additional dissipation at higher temperatures induced by graphitisation of the N990 materials.

It is clear that all the carbon black-filled compounds display larger hysteresis at small strains than would be expected from hydrodynamic theory as outlined in the previous section. As the applied strains used were vanishingly small it is apparent that this additional viscous dissipation is unrelated to the dynamic dissipations associated with undefined mechanisms underpinning the Payne effect. The origin of these non-hydrodynamic dissipations must therefore be associated with 1) the effect of filler particles on the crosslinking process and final state of cure within the compounds, 2) the interface between filler and elastomer, 3) the dynamics and temperature dependence of the filler network. Of key importance in these data sets is the upturn in hysteresis at higher temperatures observed for the graphitised N330 and N134 samples and to a lesser extent for graphitised N990. This upturn in hysteresis becomes apparent at roughly T_g + 100 K and cannot be explained in terms of the physics of the elastomer matrix, which in the rubbery region is dictated by thermal proximity to the glass transition, the crosslinked network structure and its associated entropic elasticity. No

physically reasonable combination of these rubber matrix effects can lead to an upturn in dissipation as a function of temperature:

- The work in Chapter 4 showed that the presence of carbon black during curing can significantly reduce the average crosslink density in the filled compounds versus the unfilled control. In such heterogeneously crosslinked systems, viscous dissipation still *decreases* systematically as thermal proximity to the glass transition is increased.
- Chapter 6 concluded that there was no significant, measurable effect of the filler particles on the glass transition of NR. Subsequent DSC measurements of this higher temperature region for the graphitised samples reveal no trace of secondary[3] T_g effects which have occasionally been reported in the literature (Figure 7.14). The first derivative of the DSC traces is presented in Figure 7.15. A secondary glass transition should appear as a distinct positive peak. No such peak is observed.

The high temperature upturn in loss tangents for the graphitised carbon black-filled compounds is therefore the result of either a temperature dependence of the filler structure (note that no filler structure is present in the N990g-filled compound) and/or a temperature dependence associated with the rubber-filler interface. Busfield et al. [20-22] have previously used resistivity and equilibrium swelling measurements to show that an increase in temperature equates to a reduction in the affinity of the elastomer to the filler surface. This is explored in more detail in the following chapter.

[3] The term 'secondary' T_g or loss tangent effect is used in this case to describe a peak or rise in loss tangent on the rubbery side of the T_g which is significantly separated in terms of temperature and frequency from the main T_g relaxation.

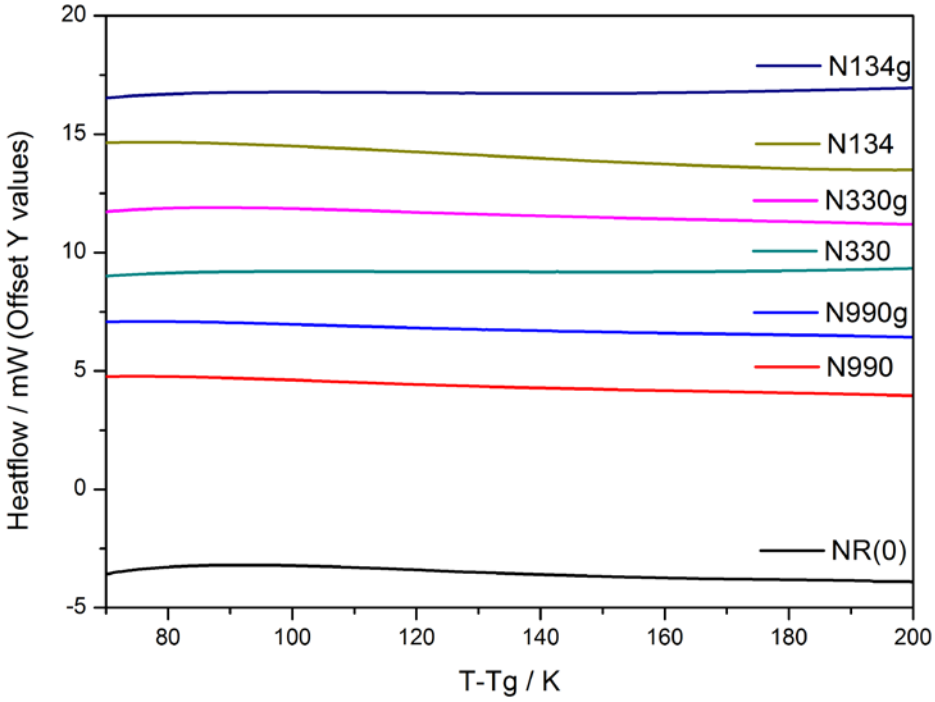

Figure 7.14: DSC traces for the carbon black-filled compounds in the temperature range corresponding to the temperature range of the observed secondary dissipation effects. The data are offset for clarity

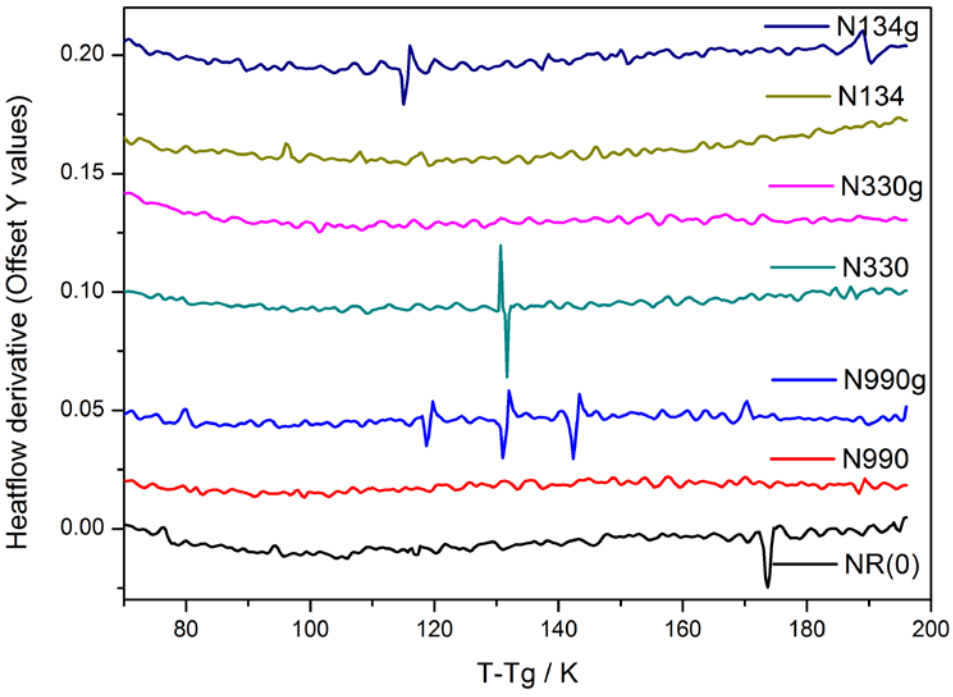

Figure 7.15: First derivatives of the DSC traces. The data traces are offset from each other for clarity. Spikes in the data trace correspond to random noise rather than thermal events.

The secondary higher temperature (or lower frequency) peaks or increases in hysteresis are seen frequently in the appropriate literature, notably where weak filler-elastomer combinations are considered. For example, Ganter et al. [23], Menghetti et al. [24] and Lowe et al. [25, 26] observed such effects in various organoclay-reinforced NR, BR and SBR compounds. Wang [6] reported hysteresis upturns in silica-reinforced SBR which he proposed were due to a weakening of the filler structure with increasing temperature. Ramier [27] and Ramier et al. [28] observed the appearance of a secondary peak in tanδ in silica filled SBR treated with dispersing agents of various chain length and surface coverage. Ratner [29] observed a secondary peak in the small strain dissipation of SBR filled with novel, experimental grades of silica. Tsagaropoulos and Eisenberg [30-32] have shown that filled polymer melts (uncrosslinked) can also display secondary increases in dissipation. They interpreted this as evidence for an immobilisation of polymer at the filler surface having a T_g much higher than that of the bulk. Robertson and Rackaitis [33] studied the appearance of a secondary maximum in tanδ at temperatures well above the T_g in various filled (though uncrosslinked) rubber melts. They related this to the terminal flow of the un-crosslinked polymer and the pseudo-crosslinking restriction effects imposed by the fillers. Ionic elastomers are also known to shows such secondary tanδ effects which have been ascribed, in this case, to immobilised polymer [34, 35]. Figure 7.16 presents some example data from the literature to illustrate the issue.

Of course different testing conditions and filler-matrix interactions in these studies mean they these secondary increases in loss tangent may not all originate from the same physical process but this is nonetheless a widespread and interesting phenomenon.

To the author's knowledge the data presented in this chapter is the first time such secondary dissipation effects have been observed for carbon black-filled materials. This is probably due to the fact that most literature studies have been performed on commercial carbon black-filled systems. Graphitised carbon blacks represent an extreme case where the surface concentration of poor polymer-filer interactions associated with the basal planes of graphitic sheets are promoted over higher energy sites. A key question is whether or not the secondary dissipation effect observed for the graphitised carbon black-filled materials represents an amplification of the same mechanism occurring in commercial carbon black-filled materials which has previously not been detected.

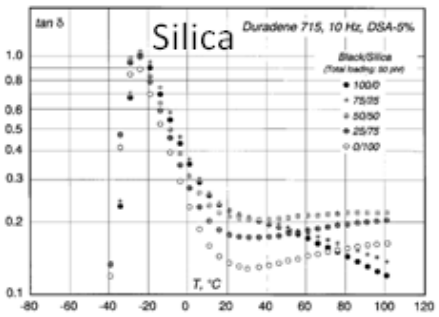

Wang, *Rubber Chem. Technol.*, 71, 250 (1998)

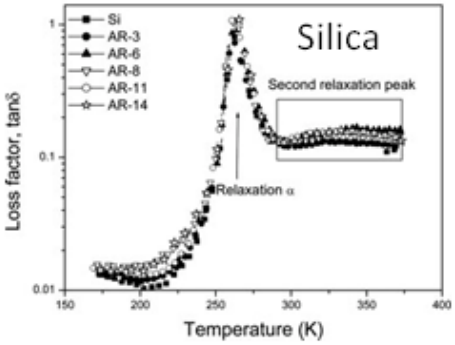

Ramier et al. *J. Polym.Sci: B Polym. Phys.*, 45, 286-298 (2007)

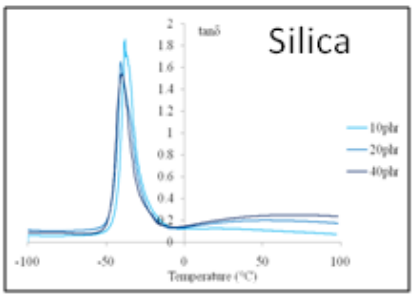

A Ratner, MScThesis, QMUL (2010)

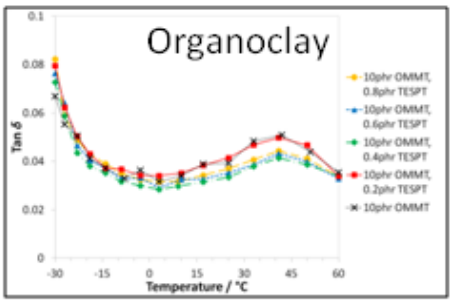

Lowe et al., *Rubber Chem. Technol.* 86, 4 (2013)

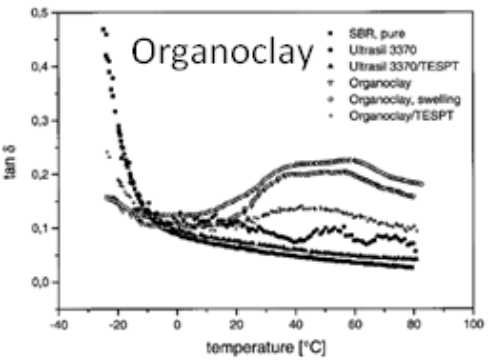

Ganter et al., *Rubber Chem. Technol.*, 74, 221 (2000)

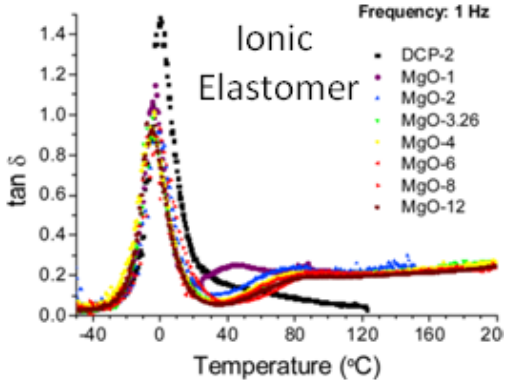

Malmierca et al., *Macromolecules*, 47, (2014)

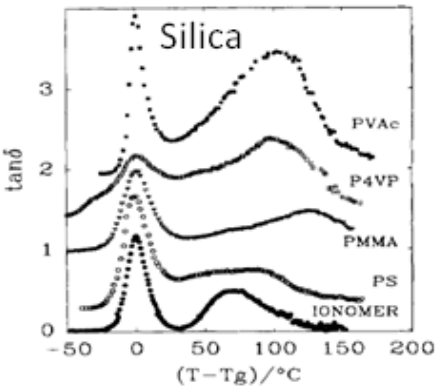

Tsagaropoulos & Eisenberg, *Macromolecules*, 28, 18, (1995)

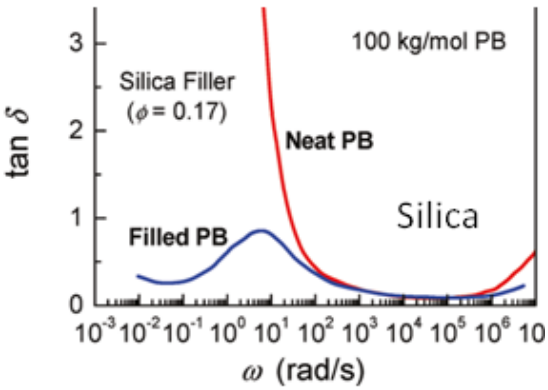

Robertson & Rackaitis, *Macromolecules*, 44, (2011)

Figure 7.16: Example data from the literature showing an upturn in viscous dissipation at higher temperatures/lower frequencies. In some cases a full, secondary relaxation is observed

7.6. Temperature dependence of the dynamic moduli

The loss tangents of the carbon black-filled compounds can be decomposed into elastic and viscous components in order to better understand the origin of the secondary dissipation observed in the graphitised carbon black-filled materials. Figure 7.17 A-D shows the moduli as a function of temperature. Graphitisation results in a dramatic increase in the small strain storage and loss moduli for the high surface area carbon black filled compounds which is discussed in more detail in Chapter 5.

For the N990-carbon black-filled compounds, the magnitude of moduli amplification is more modest, primarily due to the inability of N990 to form a percolating filler network at this volume fraction. Unlike the higher surface area carbon blacks, graphitisation of N990 makes no difference to the magnitude of the storage moduli (in Figure 7.17 D the data are plotted on a linear axis to emphasise the storage moduli). However, if the loss moduli are considered, it is apparent that graphitisation results in a slight but measureable increase in the magnitude of viscous dissipation at higher temperatures. This is significant as now, due to the lack of a filler network in these compounds, the viscous dissipation must be isolated at the filler-rubber interface.

In order to extract more information from the dynamic moduli of the N134 and N330 based compounds, the moduli of each material were normalised to their values apparent at -20 °C[4]. The results are given in Figure 7.18 A-C. Here it is possible to discern that graphitisation of the high surface area carbon blacks results in a relative decrease in storage moduli and concomitant rise in loss moduli with increasing temperature compared with the unmodified filler materials.

[4] This is somewhat arbitrary. A preferable normalisation would be of the moduli immediately after the T_g - however that data is not available

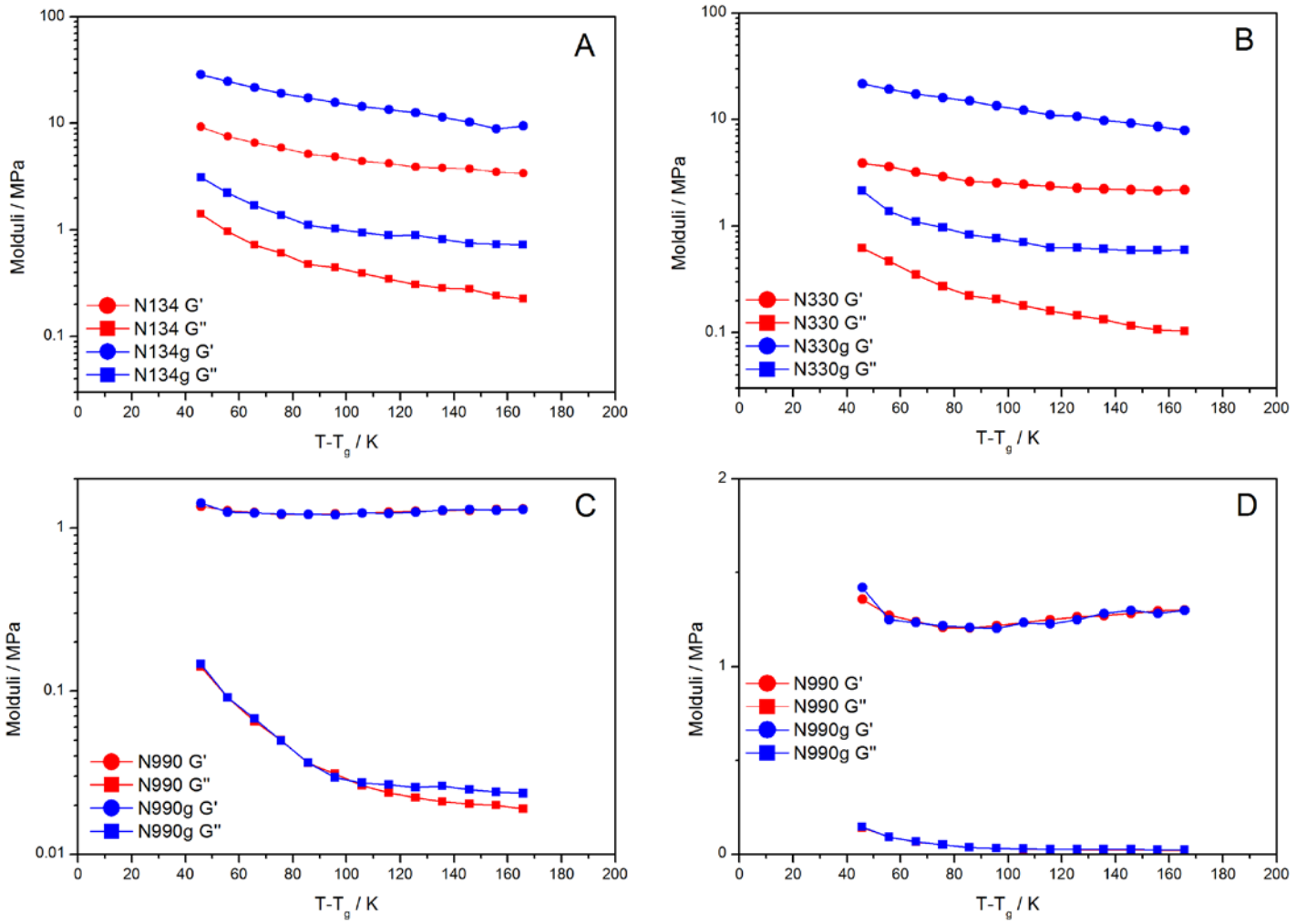

Figure 7.17 A-D: Storage and loss moduli of the carbon black-filled compounds as a function of T-T_g on log-normal scales. D is plotted on a linear scale to emphasise the relatively small changes in storage moduli with temperature

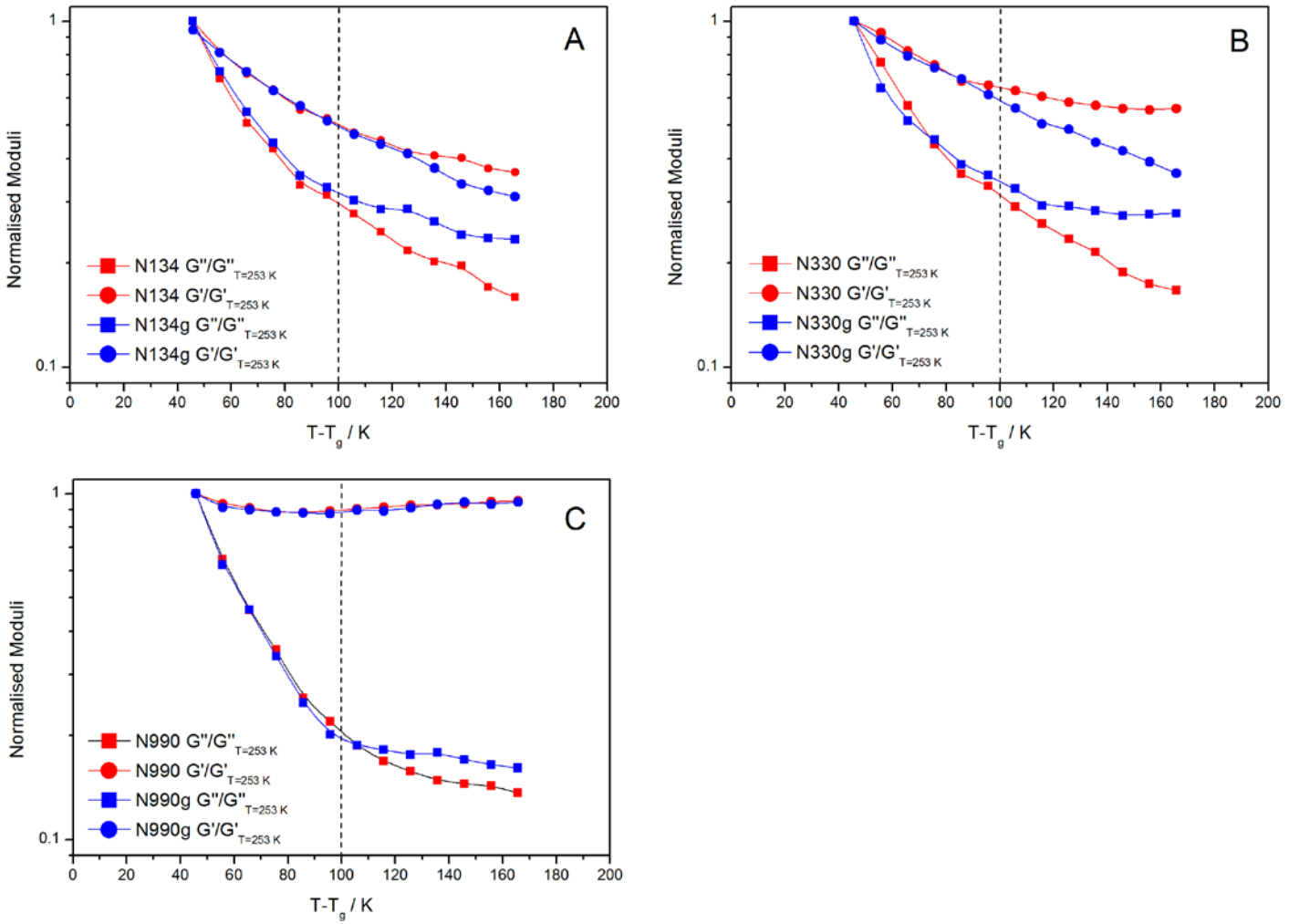

Figure 7.18 A-C: Storage and loss moduli normalised to the values apparent at T-T_g = 37 K highlighting the effect of graphitisation resulting in a relative reduction in G' and an increase in G'' as a function of increasing temperature versus the unmodified filler materials. The onset of the rise in tanδ is indicated with a dashed line

7.7. Discussion

It is apparent from the loss tangent data presented here that reinforcement effects in these materials cannot be explained using the principles of geometric reinforcement (hydrodynamics, strain amplification, matrix occlusion). Of particular interest is the observation that upon graphitisation of carbon black a secondary dissipation process is observed in the resulting compounds at temperatures of the order of T_g +100 K. This process is observed in both the high surface area graphitised carbon black-filled compounds where a percolating filler network is present and to a lesser extent in the graphitised N990-filled compounds which do not form percolating networks.

From the dynamic moduli data it is clear that this process results from a reduction in the elastic, and increase in the viscous nature of the compound as a function of temperature, that is, an apparent secondary relaxation. For the high surface area compounds it is impossible to discern whether or not this dissipation is associated with a decrease in stiffness of the filler network or a separate viscous phenomenon isolated at the filler-rubber interface. However, in the case of the N990-based compounds, no filler network is present. Here we can note a relative increase in the viscous modulus as a function of temperature with almost no comparable change in the storage moduli. This would indicate that the dissipation is at least partially associated with the filler-rubber interface.

7.8. References

[1] H.S. Chen, A. Acrivos, International Journal of Solids and Structures, 14 (1978) 349-364.
[2] H.S. Chen, A. Acrivos, International Journal of Solids and Structures, 14 (1978) 331-348.
[3] C.G. Robertson, C.J. Lin, M. Rackaitis, C.M. Roland, Macromolecules, 41 (2008) 2727-2731.
[4] C.M. Roland, Journal of Rheology, 34 (1990) 25-34.
[5] A.R. Payne, Rubber Chemistry and Technology, 36 (1963) 422-431.
[6] M.J. Wang, Rubber Chemistry and Technology, 71 (1998) 520-589.
[7] A.R. Payne, Rubber Chemistry and Technology, 36 (1963) 432-443.
[8] A.R. Payne, Rubber Chemistry and Technology, 36 (1963) 444-450.
[9] A.I. Medalia, Rubber Chemistry and Technology, 64 (1991) 481-492.
[10] C.K.L. Davies, A.G. Thomas, K. Akutagawa, Progress in Rubber and Plastics Technology, 12 (1996) 174-190.
[11] K. Akutagawa, Department of Materials, Ph.D Thesis: Queen Mary and Westfield College, London, 1995.
[12] R. Brown, Physical Testing of Rubber, Springer, New York, 2005.
[13] N. Suphadon, A.G. Thomas, J.J.C. Busfield, Journal of Applied Polymer Science, 117 (2010) 1290-1297.
[14] N. Suphadon, A.G. Thomas, J.J.C. Busfield, Journal of Applied Polymer Science, 113 (2009) 693-699.
[15] N. Suphadon, A.G. Thomas, J.J.C. Busfield, Polymer Testing, 29 (2010) 440-444.

[16] N. Suphadon, Ph.D Thesis: Queen Mary Univeristy of ondon, London, 2010.
[17] A.N. Gent, N. Mifune, Rubber Chemistry and Technology, 64 (1991) 661-667.
[18] J.G. Meier, M. Klüppel, Macromolecular Materials and Engineering, 293 (2008) 12-38.
[19] J. Fritzsche, M. Klüppel, Journal of Physics-Condensed Matter, 23 (2011) 035104.
[20] J.J.C. Busfield, A.G. Thomas, K. Yamaguchi, Journal of Polymer Science Part B-Polymer Physics, 43 (2005) 1649-1661.
[21] J.J.C. Busfield, A.G. Thomas, K. Yamaguchi, Journal of Polymer Science Part B-Polymer Physics, 42 (2004) 2161-2167.
[22] K. Yamaguchi, J.J.C. Busfield, A.G. Thomas, Journal of Polymer Science Part B-Polymer Physics, 41 (2003) 2079-2089.
[23] M. Ganter, W. Gronski, H. Semke, T. Zilg, C. Thomann, R. Muhlhaupt, Kautschuk Gummi Kunststoffe, 54 (2001) 166-171.
[24] P. Meneghetti, S. Shaikh, S. Qutubuddin, S. Nazarenko, Rubber Chemistry and Technology, 81 (2008) 821-841.
[25] D.J. Lowe, A.V. Chapman, S. Cook, J.J.C. Busfield, Macromolecular Materials and Engineering, 296 (2011) 693-702.
[26] D.J. Lowe, A.V. Chapman, S. Cook, J.J.C. Busfield, Rubber Chemistry and Technology, 86 (2013) 538-557.
[27] J. Ramier, Ph.D Thesis: l'Ecole Doctorale Matériaux de Lyon, Lyon, 2004.
[28] J. Ramier, C. Gauthier, L. Chazeau, L. Stelandre, L. Guy, Journal of Polymer Science Part B-Polymer Physics, 45 (2007) 286-298.
[29] A. Ratner, Queen Mary University of London, 2010.
[30] G. Tsagaropoulos, A. Eisenberg, Macromolecules, 28 (1995) 6067-6077.
[31] G. Tsagaropoulos, A. Eisenberg, Macromolecules, 28 (1995) 396-398.
[32] G. Tsagaropoulos, A. Eisenberg, Abstracts of Papers of the American Chemical Society, 209 (1995) 20-MACR.
[33] C.G. Robertson, M. Rackaitis, Macromolecules, 44 (2011) 1177-1181.
[34] M.A. Malmierca, A. Gonzalez-Jimenez, I. Mora-Barrantes, P. Posadas, A. Rodriguez, L. Ibarra, A. Nogales, K. Saalwächter, J.L. Valentín, Macromolecules, 47 (2014) 5655-5667.
[35] I. Mora-Barrantes, M.A. Malmierca, J.L. Valentín, A. Rodriguez, L. Ibarra, Soft Matter, 8 (2012) 5201-5213.

Chapter 8

Small Strain Creep Behaviour of Filled Elastomers

Précis

The previous chapter has shown that upon reducing the interaction between carbon black and the rubber polymer via graphitisation, a secondary increase in dissipation occurs at temperatures significantly higher than the T_g. This observation was made using dynamic frequencies of around 5 Hz. It is of interest to probe this dissipation in more detail by performing additional testing in this thermal region. In order to do this the pendulum apparatus is modified to perform small strain creep testing.

The small strain creep data presented in this chapter clearly demonstrate that graphitisation of the carbon black filler results in a substantial increase in material inelasticity and that the magnitude of this inelasticity increases with increasing temperature - reflecting the findings of Chapter 7. Furthermore the observation that graphitisation of carbon black results in an *apparent* upturn in creep rate at longer timescales is rationalised by considering the total creep response of the compounds as a combination of creep of the polymer network combined with an underlying viscous flow phenomenon. In this case the 'viscous flow' is postulated to be related to a viscous sliding of polymer chain segments at the graphitic planes of the carbon black surface or to a small strain structural reorganisation of the filler network

8.1. Development of torsional creep experimental methodology

In order to examine the inelastic behaviour of the filled elastomers over longer timescales, the torsion pendulum setup was adapted to perform small strain torsional creep experiments over a range of elevated temperatures (Figure 8.1). Small steel side arms were attached at the extremities of the inertia bar projecting along the torsional plane of motion. One of these side arms was passed through a wound copper coil. Passing a small, constant current through the coil induced a small, constant torsional force across the sample. The consequent elastic and inelastic displacements were measured by the non-contact displacement sensor for 1000 seconds. After this the force was removed by cutting the current to the coil and the resulting creep recovery behaviour was recorded for a further 1000 seconds. The magnitude of the applied current depended on the sample in question. For the more compliant samples (N990-based fillers) a current of 20 mA was required to produce an initial elastic deformation and creep behaviour that could be resolved by the sensor. For the stiffer samples (graphitised carbon blacks and all silica-filled samples) a current of 80 mA was required.

In order to accurately control the temperature of the creep testing, the torsion rig was placed inside a Gallenkamp Plus II forced convection oven (the fan in the Instron ETC used for the dynamic measurements was found to significantly interfere with the creep experiments). The Gallenkamp Plus II oven operates by circulating air heated by a single heating element coil around the oven chamber using a large inbuilt fan. The inbuilt fan caused substantial vibration within the oven and was therefore disconnected and the side panelling of the oven chamber was stripped back to expose the heating element. A small desk fan was mounted inside the oven on a retort stand passed through a vent hole in the top of the oven. The vibrations from the fan were therefore isolated from the main structure of the oven. The desk fan was directed at the heating element and set to its lowest fan speed setting. The setup was checked at this point using the oven thermostat and two separate thermocouples to ensure that the oven chamber reached the desired temperature and that the temperature could be maintained for long periods of time. The torsion rig was placed inside the oven on a stable concrete slab and threaded bolts at the base of the rig were adjusted to level the equipment. At this stage it was found that even with the vibration-isolated fan in place, the movement of air throughout the chamber still interfered with the creep data. Therefore the rig was isolated from the moving air using a cardboard screen. Small holes were punched into the screen to allow air to pass slowly between the isolated rig chamber and the main oven chamber. This was found to

remove noise artefacts from the creep signal associated with movement of air inside the chamber. The temperature was checked again; this time with one thermocouple placed in the main oven chamber and one within the isolated rig chamber. The rig chamber was found to reach the same temperature as the main oven chamber - albeit with a short lag time. This lag time was compensated for in the experimental procedure. The temperature in the rig chamber was found to be stable to within ±0.5 °C. The temperature range for the investigation was 30-70 °C in 10 °C steps. The testing procedure involved mounting the sample in to the pendulum at room temperature. The sample was then left in place for 24 hours to allow the sample to settle in to its zero strain position. The temperature was then increased to 30 °C and held for 5 hours to allow the material to reach thermal equilibrium. The creep and creep recovery testing was then performed and then the temperature of the chamber was increased by 10 °C. Again an equilibration period of 5 hours was observed before the next set of creep tests. This equilibration period was >20 times longer than the creep experiment period and so it is assumed that the resulting inelastic deformations from the previous creep test are fully recovered and that the material is fully relaxed prior to starting a new test. Note that at a maximum temperature of 70 °C and a creep time of 1000 seconds, chemical creep, which is associated with breakdown of the rubber network is negligible [1]. A schematic of the oven set up is given in Figure 8.2.

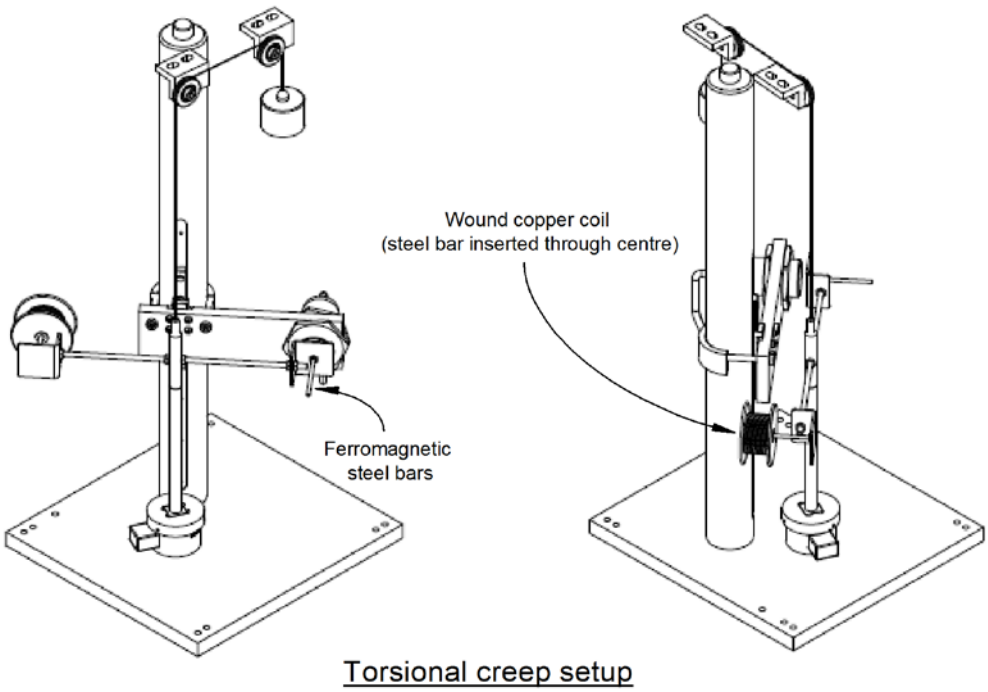

Figure 8.1: Schematic of the set up of the small strain test equipment in static (creep) mode

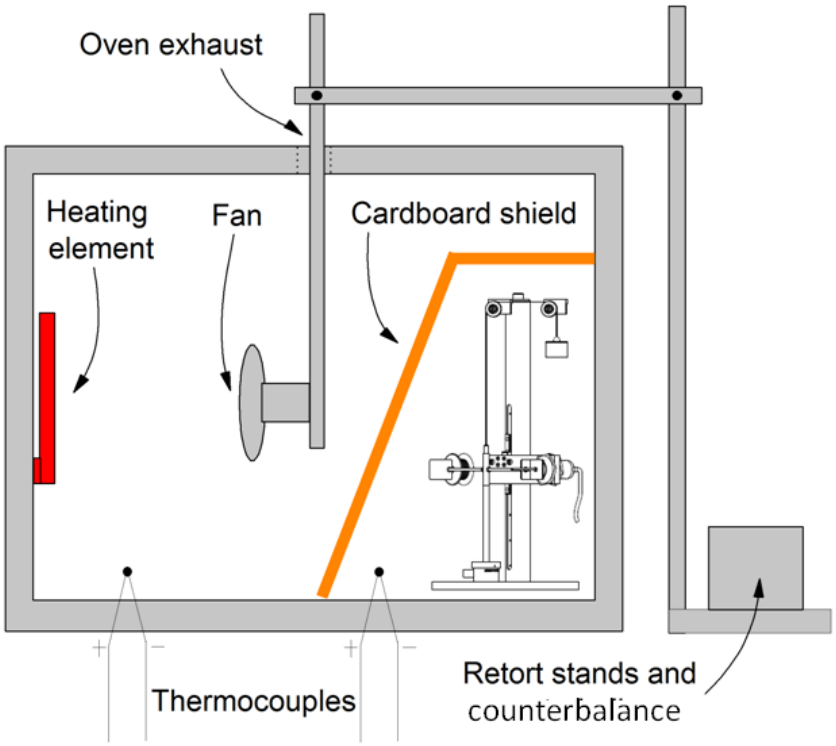

Figure 8.2: Setup of the modified Gallenkamp Plus II oven used for elevated temperature creep testing

Prior to the main creep experiments a number of calibrations were performed in order to validate the equipment and resulting measurements.

8.1.1. Determination of relevant forces, stresses and strains

By applying a constant current through the rig coil, a constant torsional force and therefore torsional stress is applied across the sample cylinder inducing a torsional displacement. In order to determine the magnitudes of these forces, stresses and deformations, a series of calibration experiments were performed. Initially the electromotive force exerted by the coil upon the steel side arm at the extremity of the inertia bar was determined.

The experimental setup to do this is detailed in Figure 8.3. One of the steel side arms was attached to one end of a steel beam (a steel ruler) and passed through the wound coil. The

modulus of the steel beam was found to be 198 GPa[1]. The other end of the steel beam was clamped securely to a table top. Passing a current through the coil induced a deflection in the beam and the deflection at the non-clamped end of the beam was monitored using the non-contact displacement sensor. The resulting displacement data could be used to determine the electromotive force exerted by the coil upon the steel side arm via the appropriate beam bending equation.

$$\delta = \frac{FL^3}{3EI_x} \qquad \left(\text{where} \quad I_x = \frac{bh^3}{12}\right) \tag{8.1}$$

where, δ is the beam deflection at the loaded edge, F is the applied force, L is the beam length, E is the experimentally determined Young's modulus of the beam, I_x is the second moment of area of the beam in the plane of the deformation, b and h are the width and height of the beam respectively

Figure 8.4 plots the force versus the square of the current. This linearises the relationship which is in agreement with the theoretical relationship between electromotive force and applied coil current given as

$$F = \frac{I^2}{2}\frac{dL}{dx} \tag{8.2}$$

where force, F, defined in terms of the applied coil current, I, and the change in inductance, L, with beam displacement, x [2].

[1]This was determined by hanging weights from one end of the beam, measuring the subsequent deflection and using the appropriate beam bending equation.

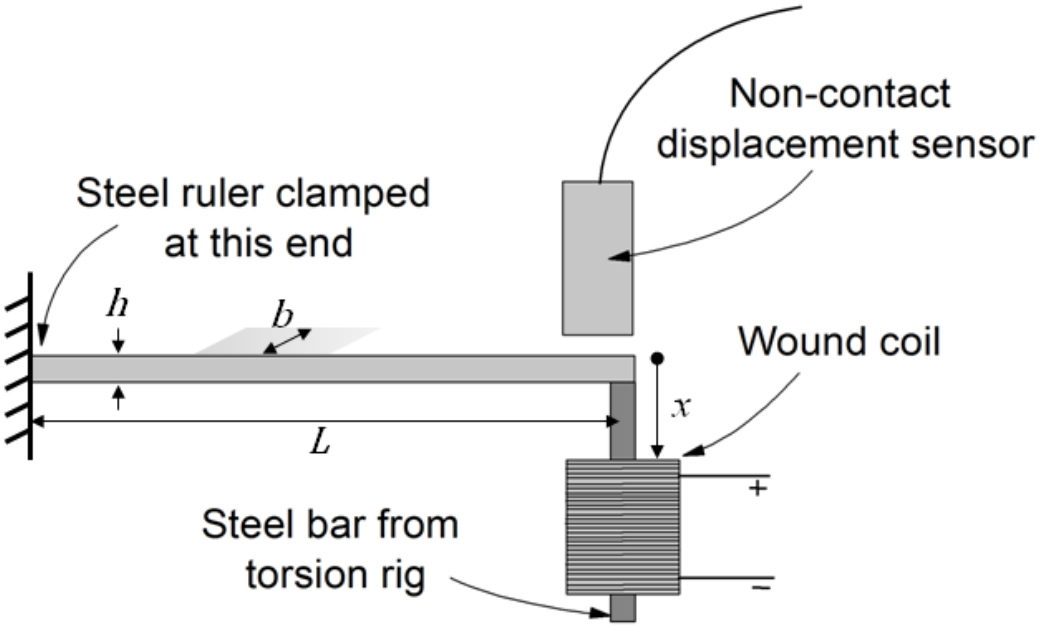

Figure 8.3: Experimental setup to determine the electromotive force applied to the steel torsion bar by the wound coil

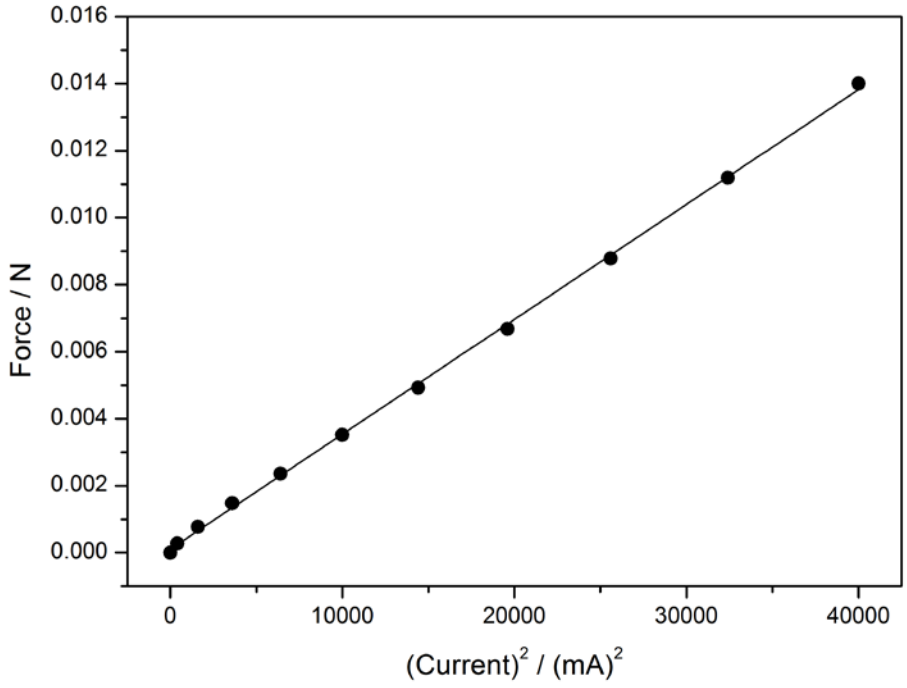

Figure 8.4: Calculated force plotted versus the square of the current as per Equation 8.2

The torsional shear stress can be calculated from the applied force. However due to the cylindrical sample geometry the stress (and strain) are inhomogenously distributed across the radius of the cylinder. Torsional stress can be calculated via Equation 8.3.

$$\tau = \frac{T_{\mathrm{Q}} d}{2 I_{\mathrm{C}}} \qquad \left(\text{where} \quad T_{\mathrm{Q}} = F.D, \quad I_{\mathrm{C}} = \frac{\pi d^4}{32} \right) \tag{8.3}$$

where T_{Q} is the torque and I_{C} is the second moment of area of the cylinder, F is the torsional force, D is the half length of the inertia bar and d is the diameter of the cylinder. The radius value is taken as the extremity of the cylinder so all reported stress values relate to the maximum stress experienced at the sample edge.

Similarly the shear strain is non-homogeneous throughout the sample. Strain is determined as

$$\gamma = \frac{\theta d}{2h} \tag{8.4}$$

where the strain is defined as the maximum strain at the sample edge where d is the cylinder diameter and h is the cylinder height. θ is the angular deflection in radians which is calculated from trigonometry using the half length of the inertia bar and the measured deflection values.

This allowed the determination of the quasi-static shear stress-shear strain behaviour of the samples. Samples were loaded onto the rig at room temperature and left for 30 minutes to settle. Then the coil current was increased in 10 mA steps every minute from 0 up to 100 mA and the inertia bar displacement was monitored for the duration of the test. Typical strain-time data are shown in Figure 8.5 where the steps in strain correspond to sequential increases in coil current. Creep behaviour is evident following the initial elastic deformations. These data can be transformed into shear stress-shear strain plots as in Figure 8.6 (here the initial displacements, i.e. the finial data point post imposition of force, of Figure 8.5 are considered). There is a linear relationship between stress and strain meaning that creep experiments performed within this stress-strain region do not disrupt the filler network and induce non-linear behaviour.

An issue with this testing arises when working with the very compliant unfilled material. Because the torsional force is applied on only one side of the inertia bar, very compliant samples are preferentially deformed off the rotational axis resulting in apparent non-linear behaviour (an apparent increase in modulus with strain which is non-physical). A simple way to observe these effects is to apply a fixed force deformation across the sample and then cut the current to the coil. For the unfilled material the resulting damped oscillation was notably off axis and the collected signal was non-sinusoidal with evidence of off-axis beats. For the stiffer samples the damped oscillation was entirely torsional and symmetrical.

In future, to avoid this issue, the sample dimensions of the compliant materials could be changed in order to stiffen the cylinder, or the torsional creep force could be applied to both ends of the inertia bar - though this would require a balancing of the electromotive forces of 2 separate coils.

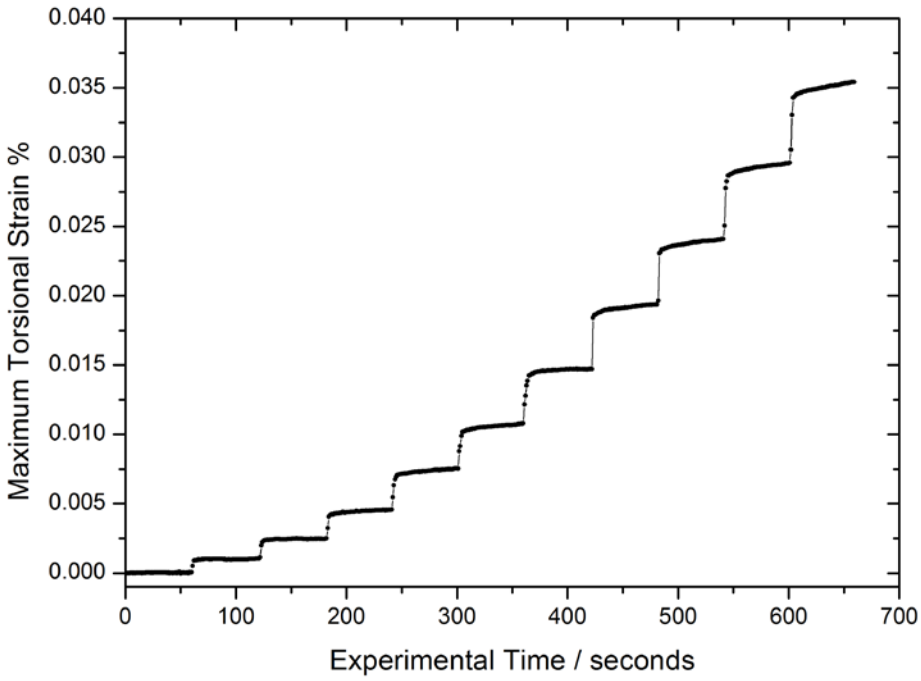

Figure 8.5: Calculated maximum torsional strain in the cylindrical sample as a function of experimental time for the N134-filled compound at room temperature. The jumps in strain occur at 10 mA jumps in coil current

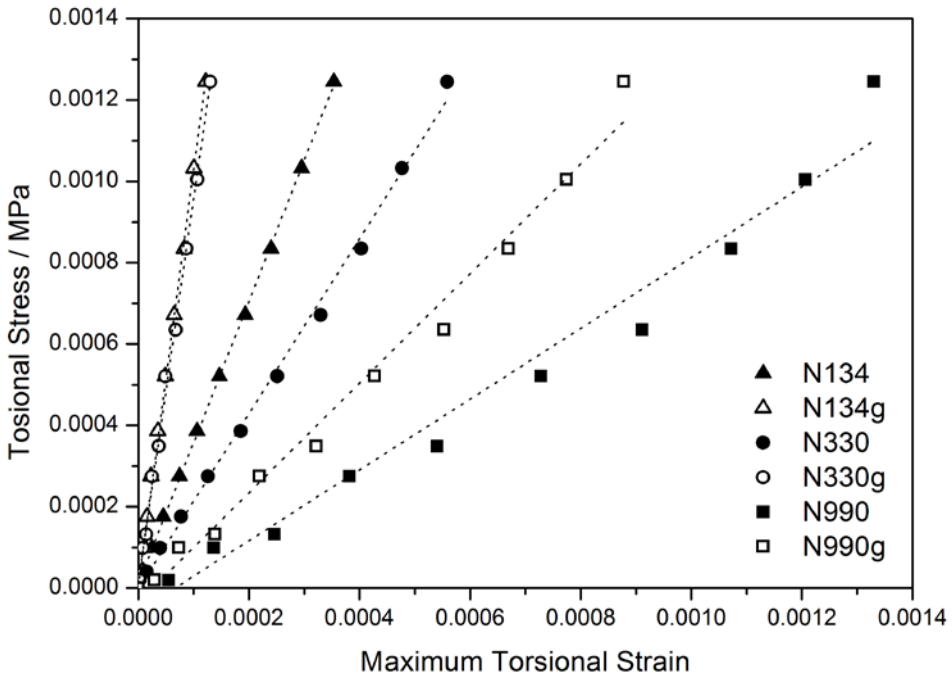

Figure 8.6: Instantaneous (first data point) elastic strain data (abscissa) plotted versus the corresponding torsional stresses (ordinate). Room temperature data

To illustrate the difference in strain range between the torsional testing and typical quasi-static tension testing, the results of the torsion test and the corresponding tensile test (Chapter 4, Figure 4.26) are plotted on the same graph in Figure 8.7 for the N134 series of carbon black fillers. Here the chord modulus from both tests is plotted versus strain % on a log-log scale. The torsional shear modulus is converted to a tensile modulus by taking advantage of the near incompressibility of rubber via $G = E/2(1 + v_{\mathrm{P}})$ where v_{P} is the Poisson's ratio of rubber which is taken to be 0.5. As can be seen the torsion equipment can be used to access stress-strain behaviour up to 4 orders of magnitude smaller than that of typical tensile testing. The independence of the elastic modulus from strain in the small strain region is lost between the strains of 0.01 % and ~1 % (note that data are missing in the intermediate strain region where we would expect to see the Payne effect softening). The material continues to soften up to strains of around 100% due in part to geometrical effects associated with tensile deformations. At strains of around 100% a marked upturn in moduli for both materials marks the onset of strain induced crystallisation and/or finite network extensibility. By coupling both torsional and tensile data it is possible to examine the quasi-static properties of the rubber materials over 7 orders of magnitude of strain if required.

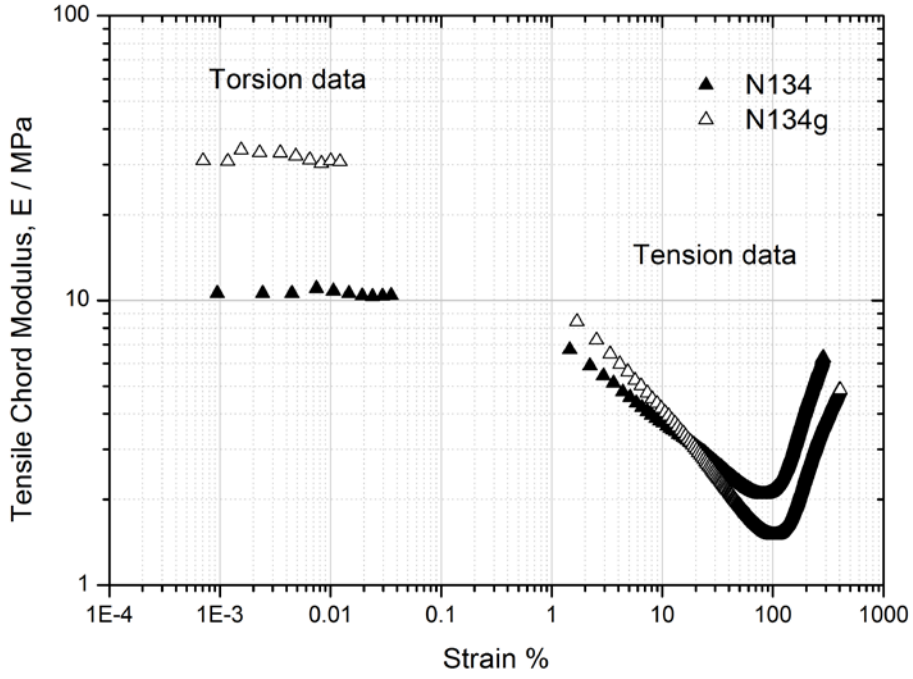

Figure 8.7: Tensile elastic moduli plotted as a function of shear strain. The plot combines chord moduli values from torsional and tensile testing. Data collected at room temperature

8.2. Temperature dependence of the relaxation behaviour of unfilled NR

Due to the off-axis deformation issue relating to the unfilled material, it was necessary to characterise the unfilled material on a more conventional mechanical test rig. As the modulus of the unfilled material is insensitive to strain up to large extensions, it is valid to compare the general trends determined for unfilled materials at larger strains with trends determined for filled materials at much small strains. To characterise the temperature and time dependence of the static inelastic behaviour of peroxide-cured NR, stress relaxation experiments were performed using an Instron 5900R 84 mechanical test frame with a 100 N capacity load cell. Rectangular sample strips measuring 50 x 5 x 2 mm, were clamped securely in tensile clamps mounted in an Instron environmental test chamber (ETC). Samples were strained to $\lambda = 2$ at a strain rate of ~ 0.1 /s and held at this displacement for 1000 seconds. The resulting force was measured at 0.5 second intervals. Samples were tested at 20, 40, 60 and 80 °C. Samples were equilibrated at each temperature for 1 hour prior to testing.

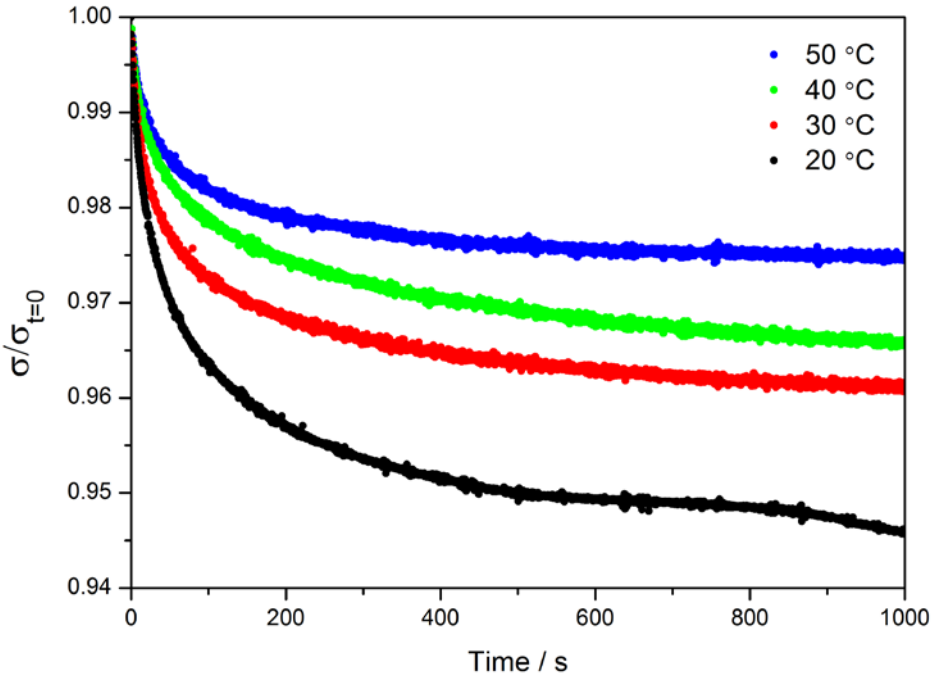

Figure 8.8: Stress relaxation data for unfilled NR crosslinked with 2 phr DCP. Normalised stress plotted versus linear time axis, λ = 2

Figure 8.8 shows the stress relaxation data for NR crosslinked with 2 phr DCP plotted as normalised stress ($\sigma/\sigma_{t=0}$). The relative degree of relaxation of stress decreases as the test temperature increases. The inelastic behaviour of the unfilled material (relaxation rate, relaxation magnitude) decreases with increasing temperature. This can be understood by considering entropic elasticity effects and the test temperatures relative to the glass transition. For unfilled rubbers the primary source of dissipation is the thermal proximity to the glass transition. An increase in temperature relative to the T_g results in a reduction in the network inelasticity. Additionally, the elasticity of the network is increased proportionally with the absolute temperature since from the kinetic theory $E \propto T$.

8.3. Numerical processing of the creep data

Typical creep and recovery data obtained from the torsional apparatus is presented in Figure 8.9. In order to obtain data in this format, the voltage output from the displacement sensor was converted first to displacement and then to maximum torsional strain. Conversion from voltage to displacement was achieved using the sensor calibration data described in Chapter 7.

Figure 8.6 showed that the small strain moduli vary significantly between samples depending on carbon black surface area and surface activity. To account for this in the analysis of the creep data it was necessary to suitably normalise the inelastic part of the data to the initial elastic strain ($\gamma_{\mathrm{in}}/\gamma_{\mathrm{e}}$). This accounted for the variation in small strain compliance between materials and allowed the inelastic creep magnitude and time dependence between materials to be compared. In order to perform this normalisation it was necessary to determine, in a systematic way, the initial elastic deformation. Some data were always lost in the initial few seconds following the application of the load due to the limited sampling frequency of the sensor. In addition, the application of the load via the coil was not truly instantaneous and, due to the fact that the load was applied in a non-contact fashion, there were always artefacts in the initial few seconds of data due to inertial effects.

Therefore it was not possible to use the initial data point(s) as an accurate measure of the initial deformation. In order to circumvent this problem the initial 40 data points were fitted to a logarithmic trend. The initial few data points - which suffered from considerable noise - were systematically removed until a reasonable fit (taken as $R^2 > 0.95$) to the remaining data was obtained. From the logarithmic relationship an estimate for the displacement at time = 0.1 seconds could be obtained. The validity of this extrapolation was confirmed by checking that the normalised data projected back to $\gamma_{\mathrm{in}}/\gamma_{\mathrm{e}} = 1$ at time ~ 0. This process is shown in Figure 8.10.

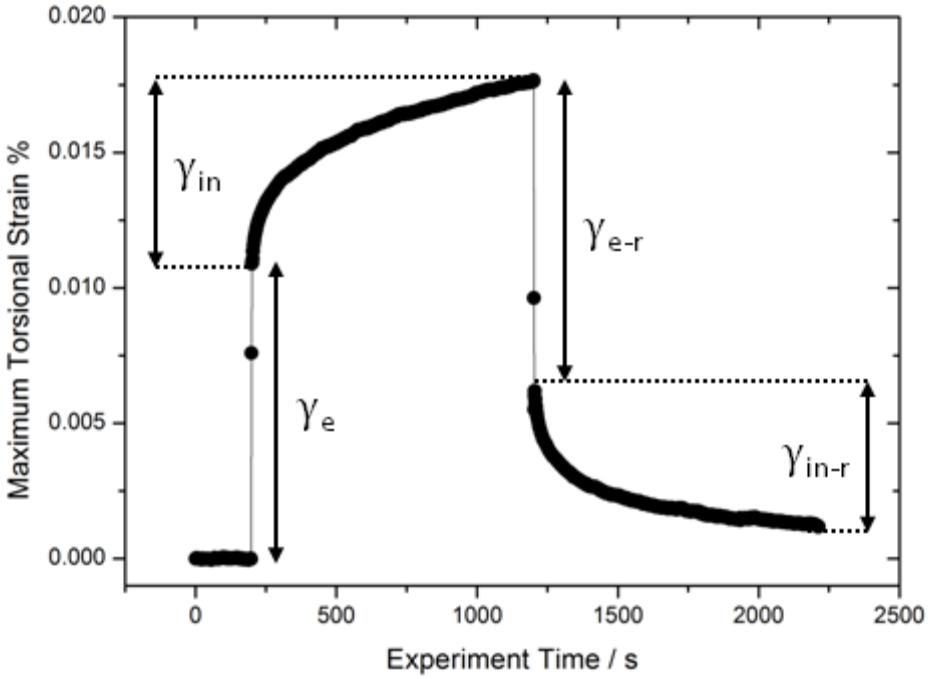

Figure 8.9: Typical creep and recovery data. Creep is constituted of the initial instantaneous elastic strain, γ_{e}, followed by inelastic, time dependent strain, γ_{in}. Recovery is again initially elastic, $\gamma_{\mathrm{e-r}}$, and then inelastic $\gamma_{\mathrm{in-r}}$

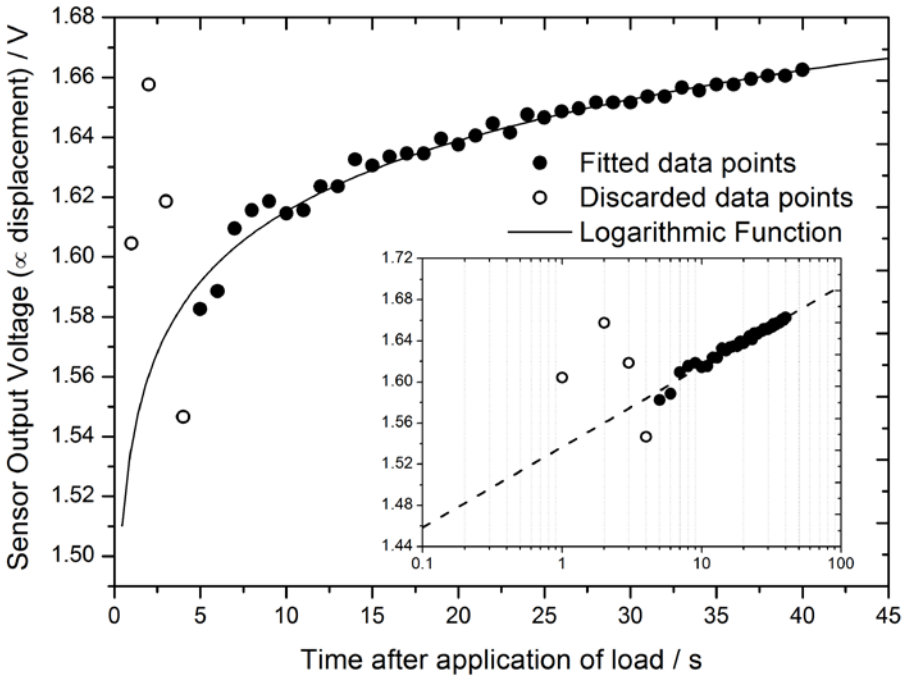

Figure 8.10: Schematic of the process used for the determination of the initial elastic displacement at time = 0.1 s in the creep data sets. Inset is the data plotted versus a logarithmic x-axis

8.4. Comparison of isothermal creep behaviour of carbon black filled compounds

Figure 8.11 A and B show the creep behaviour recorded at 40 °C for unmodified carbon black-filled materials. As can be seen the magnitude of the inelastic creep scales with the surface area of the carbon black, with the higher surface area carbon black (N134) displaying the largest inelastic deformations. When the data are plotted versus a logarithmic time axis, a broadly logarithmic dependence of creep on time is observed. At longer time scales (between 100 and 1000 seconds) there appears to be a very slight increase in creep rate for the higher surface area carbon blacks.

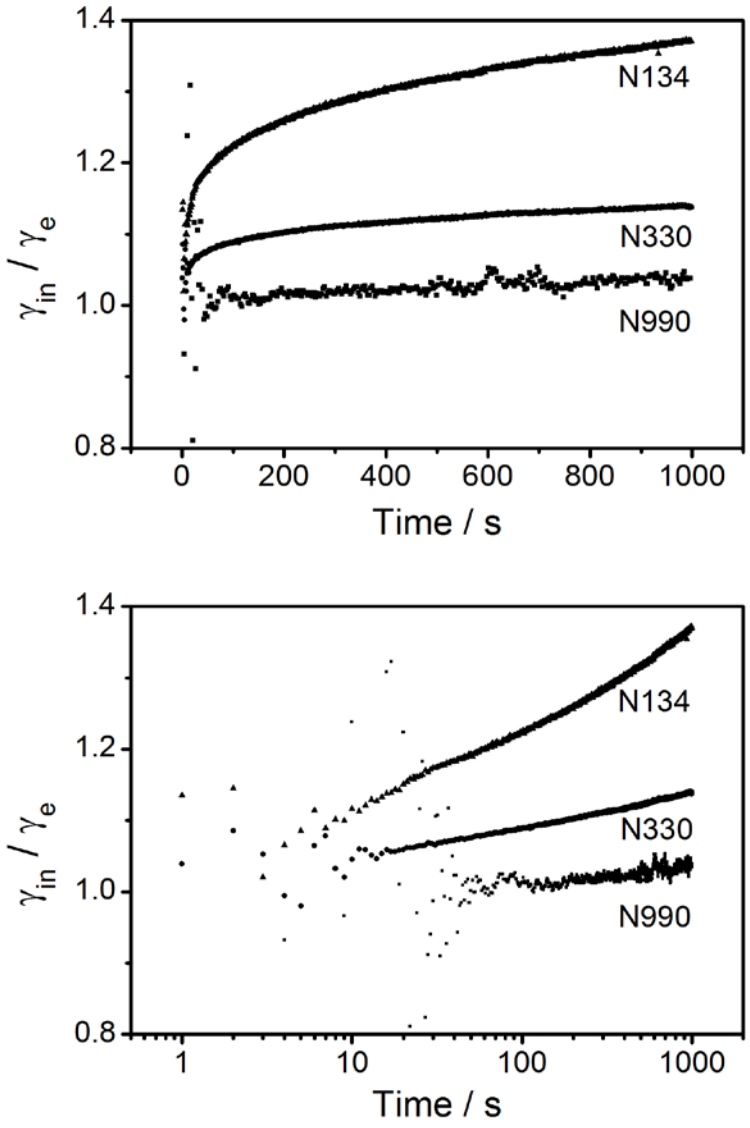

Figure 8.11**:** Creep data for the unmodified carbon black-filled compounds at 40 °C. The top plot is versus a linear time axis, the bottom plot is versus a logarithmic time axis

Figure 8.12 A and B plots the data for the graphitised analogues again at a temperature of 40 °C. Some major differences between the graphitised and unmodified carbon blacks are evident. Firstly the creep rates are much higher for graphitised carbon back than for unmodified carbon black (note the difference in axis scales between Figure 8.11 and Figure 8.12). Secondly the upturn in creep rate at longer timescales noted for the unmodified carbon blacks is much more pronounced for the graphitised materials.

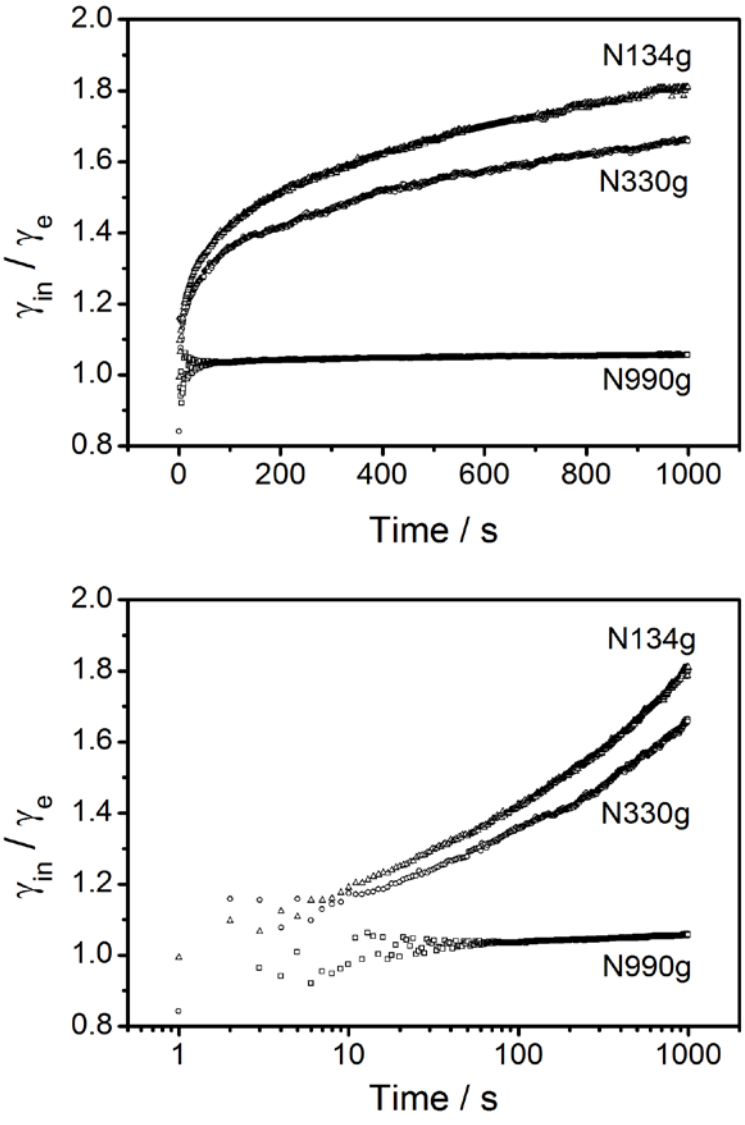

Figure 8.12: Creep data for the graphitised carbon black-filled compounds at 40 °C. The top plot is a linear time axis, the bottom plot is a logarithmic time axis

8.5. Temperature dependence of the creep behaviour of carbon black-filled compounds

The temperature dependence of the creep behaviour of the filled materials was examined between 30 and 80 °C. This is within the temperature range in which the upturn in tanδ was observed during dynamic testing in Chapter 7. As an example of this temperature dependence, the creep behaviours for the N134 and N134g-filled materials are shown in Figure 8.13. The data are shown plotted versus a logarithmic time axis in Figure 8.14.

As a general trend, the process of graphitisation of the carbon black results in a greater magnitude and rate of inelastic creep of the compounds at small strains. The temperature dependence of the creep of unmodified carbon black-filled materials is very slight.

When the filler is graphitised, the creep behaviour becomes far more dependent on the test temperature. The creep magnitude and rate increase systematically between 30 and 60 °C before dropping off at 70°C . Figure 8.14 plots the creep data against a logarithmic time axis. As can be seen, the acceleration in creep rate at longer timescales is pronounced for the graphitised carbon black-filled materials but much more subtle (if present at all) in the unmodified carbon black-filled materials. Repeat tests were performed for N134, N134g, N330 and N330g-filled materials. The full set of creep data is presented in Appendix II.

One method for analysis of this type of data is analogous to that employed for analysis of chemical degradation effects in the high temperature, long term creep behaviour of rubber compounds. As outlined by Gent [1], high temperature, long term creep behaviour can be deconvoluted into a logarithmic time dependence and a linear time dependence. The logarithmic time dependence corresponds to the physical creep of the polymer network while the linear contribution corresponds to chemical creep arising from oxidative breakdown of the network. Mathematically this amounts to [1]

$$\text{creep } \% = Alog_{10}\left(\frac{t}{t_0}\right) + B(t - t_0) \qquad 8.5$$

where A and B are the physical and chemical creep rates respectively.

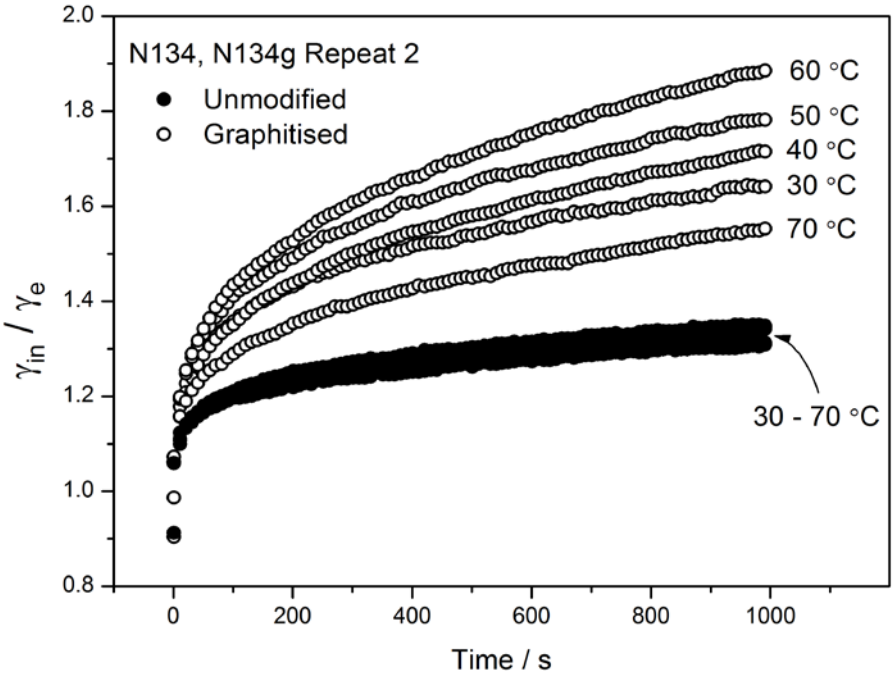

Figure 8.13: Creep data for the N134 and N134g-filled series of compounds measured over a temperature range of between 30 and 80 °C. All data are plotted versus a linear time axis. 1 in 10 of the collected data points per trace are shown to improve clarity

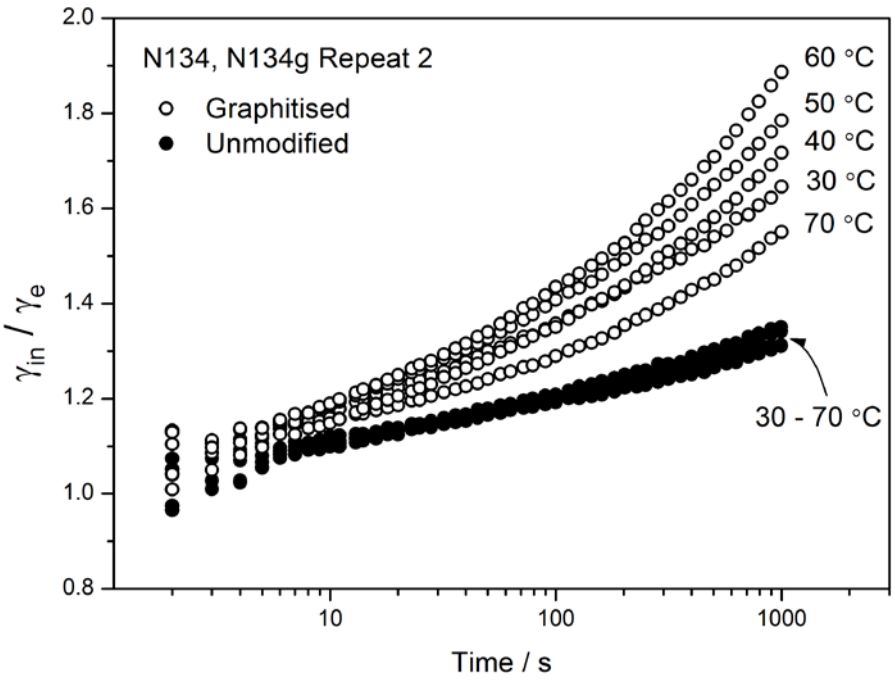

Figure 8.14: Creep data for the N134 and N134g-filled series of compounds measured over a temperature range of between 30 and 80 °C. All data are plotted versus a logarithmic time axis. Data have been selected logarithmically to improve clarity

The creep tests performed in this work were conducted under conditions where chemical creep effects are negligible (chemical creep is only observed in NR networks at temperature greater than 90 °C and over timescales of hours or days). However the general principle of data analysis is used to further investigate the creep data presented here.

As an example of this type of deconvolution, the creep data of N134g at 40 °C was fitted by linear and logarithmic functions. In order to ensure that the fits to the data were appropriate and unique, two fitting processes were examined and the results were compared:

- In the first method the error between the data and model was minimised using a least squares approach with the log and linear function parameters being free to fit over the whole data range. However it was found that this method tended to over-fit the data at long timescales at the expense of the first 100-200 seconds of data - particularly for the graphitised carbon black filled materials where the acceleration in creep rate is very pronounced.

- In the second method the data was first fitted with a log function over the time period 1-100 seconds. The fit parameters of this log function were then used to define the main log function over the whole data set. This forces the solver to then fit for the upturn in creep rate over longer times using only the linear function. After the linear function was fitted the whole data was fitted again using the previously determined parameters but this time allowing the log function parameters to vary as well. It was found that this method gave the most reliable deconvolution of data sets and was adopted for the rest of this work.

The resulting deconvolution of the N134g 40 °C data set is shown in Figure 8.15. This demonstrates that the small strain creep data can apparently be successfully described as a combination of a logarithmic and a linear process.

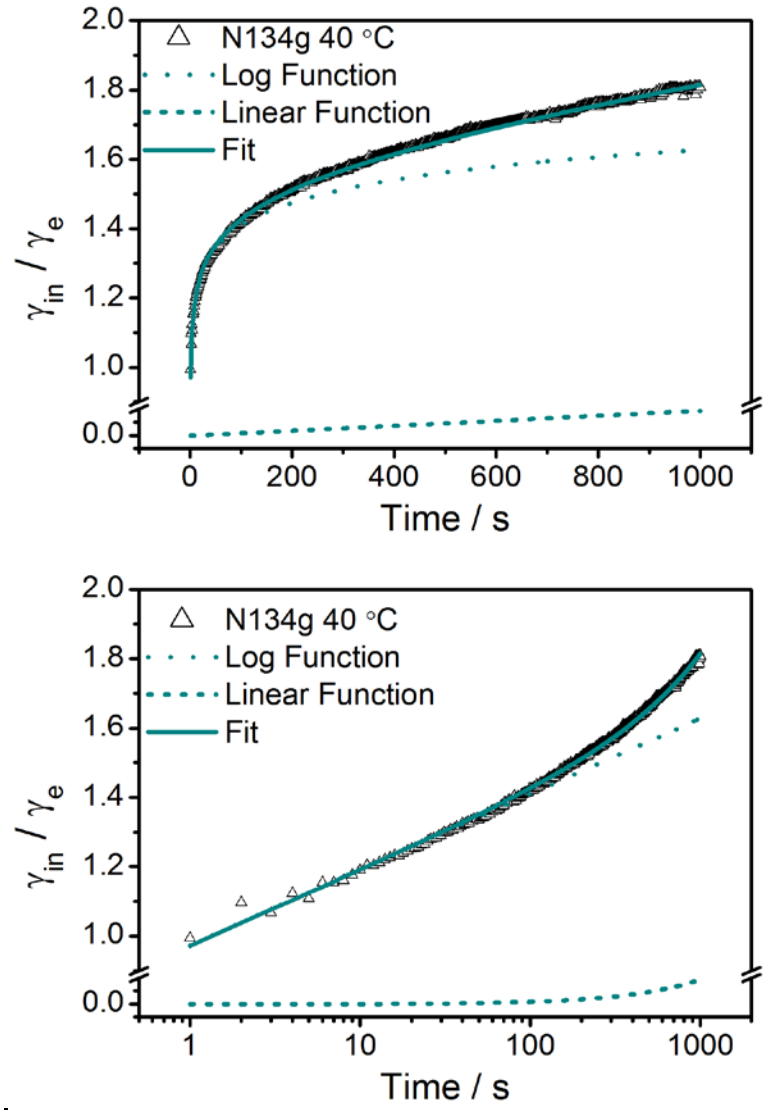

Figure 8.15: Example of the deconvolution of creep (N134g at 40 °C) data into linear and logarithmic contributions. The incorporation of a linear creep terms is able to account for the apparent increase in creep rate observed at longer timescales.

All the creep data sets were deconvoluted into logarithmic and linear contributions. For the following samples a clear linear time contribution could be extracted from the creep data: N134, N134g, N330, N330g. Over the timescale of the creep experiments neither N990 nor N990g displayed any linear time inelastic contribution to the creep behaviour. Note that for N990 and N990g filled materials the total creep behaviour was very small and subsequently was rather poorly resolved by the instrumentation. The gradients of the extracted linear functions are plotted versus temperature in Figure 8.16. Note that the gradient has units of

rate (s^{-1}). From Figure 8.16 it is clear that the extracted linear contribution to creep has a strong, positive temperature dependence - although there is some scatter in the data which is presumably related to inherent errors in the deconvolution process and in determining the exact value of the initial elastic deflection. For graphitised carbon black materials the rate is almost an order of magnitude larger than that of the unmodified carbon black materials, indicating that it is promoted by the process of graphitisation.

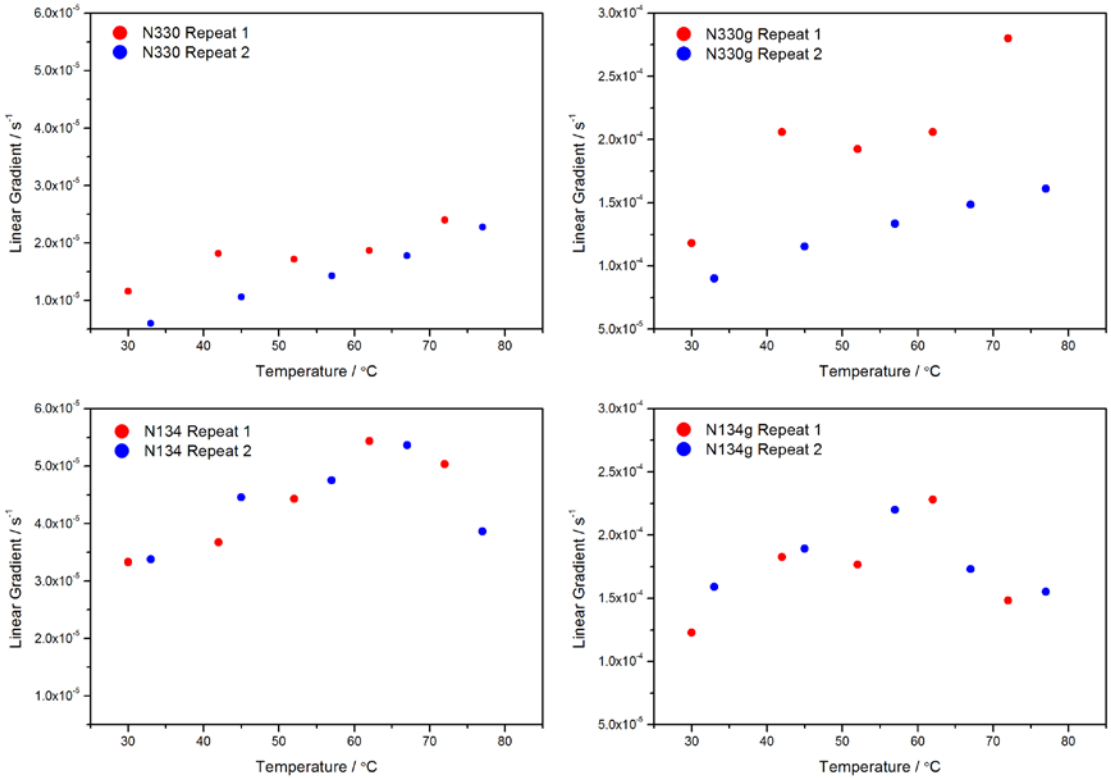

Figure 8.16: Temperature dependence of the linear functions extracted from creep data sets. Repeat measurements are indicated in the legends. Note the difference in scale between the unmodified and graphitised data sets

For the N134 and N134g materials the linear rate appears to pass through a maximum at around 60 °C - although more data would be required to confirm this. Note also that the repeat data for most of the materials are in reasonable agreement with the initial data set - thereby indicating good repeatability, with the exception of N330g. It is possible to calculate an apparent activation energy for the linear time creep process by plotting the data according

to the Arrhenius equation (Equation 8.6 and Figure 8.17) and fitting the initial positive temperature dependence portion of the data. Calculated values for the apparent activation energy are given in Table 8.1. With the exception of one the N330 sample repeats, the activation energies are very similar, regardless of filler surface activity and lie between 10 and 15 kJ/mol. Therefore the magnitude of the linear contribution to creep is seen to depend on the surface activity of the filler (being small in magnitude for carbon black with a good rubber-filler interaction and very pronounced for graphitised carbon blacks). However, the temperature dependence, E_a, of the linear contribution is identical for all filler types. The exception to this are the N990-based materials where no linear contribution to creep can be identified.

$$ln(k) = ln(A_0) - \frac{E_a}{R}\left(\frac{1000}{T}\right) \qquad 8.6$$

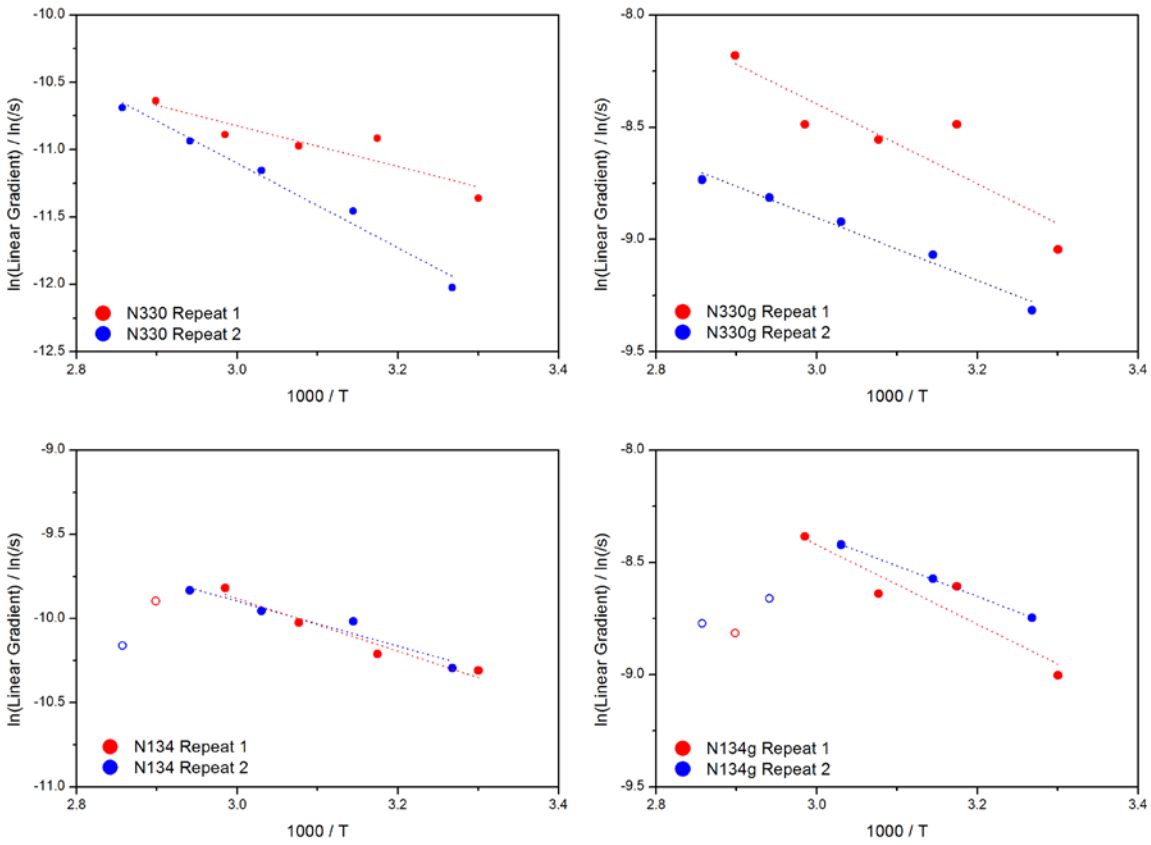

Figure 8.17: Arrhenius plots of the linear functions extracted from creep data collected over a range of temperatures. Data points not included in the linear regressions are indicated as hollow symbols.

Table 8.1: Apparent activation energies calculated from Arrhenius plots. Values in brackets refer to activation energies determined from the repeat experiments

Filler	Repeat 1 E_a / kJ.mol^{-1}	Repeat 2 E_a / kJ.mol^{-1}
N134	11.1	12.9
N134g	11.4	14.7
N330	26.0	12.6
N330g	11.6	14.7

8.6. Discussion of Microstructural Interpretations

The creep tests reported in this chapter were performed in the linear region for each material. According to conclusions of Payne [3] and Kraus [4], this is below the strain levels at which breakdown of the 'filler network' contributes significantly to viscous energy dispersion within the material. We can conclude therefore that the unusual inelastic behaviour of the rubbers filled with unmodified and graphitised carbon black of high surface area and structure is in some way related to the interface between filler and rubber or the filler structure (that is filler aggregate interactions).

A noteworthy observation is that the N990-based fillers display a purely logarithmic time dependent creep behaviour over the experimental timescale. This is important for two reasons: firstly the N990-based fillers are loaded significantly below their percolation thresholds, and secondly the N990-based fillers are of very low surface area relative to N330 and N134. Based on this, two possible conclusions are postulated:

- Since this additional inelasticity is not observed for filled materials in the absence of a filler network, the additional inelasticity observed in the creep behaviour of high structure/surface area carbon black-filled rubbers is related to viscous dissipation within the filler network
- The additional inelasticity is associated with the filler-rubber interface and so, due to the low surface area of the N990-based fillers is not evident over the timescales examined in this work.

Unfortunately, without further experiments it is not possible to firmly distinguish between these two conclusions based on the data presented here. Attempts were made to run longer creep tests for the N990 filled materials however, as can be seen from Figure 8.13 and Figure 8.14, the creep behaviour of N990-filled materials is very slight and, as such the issue of experimental noise became a significant issue at longer experimental timescales. Further work could examine fillers of higher surface area but still below their percolation thresholds - for example an N660 or N550 grade of carbon black would allow a significant loading of filler ($\phi \sim 0.15$) before the percolation threshold is reached [5]. This would amplify the creep magnitude and reduce issues with experimental noise.

In the context of these findings, if the results of the dynamic oscillation testing are revisited (See Chapter 7, Figures 7.12 and 7.13) it can be seen that there is a clear correlation between the high temperature upturns in $\tan\delta$ for the high surface area carbon blacks and the additional inelasticity observed in the creep behaviour over the same temperature range. Examining the data for N990 versus N990g it is possible to distinguish a small, though measurable, increase in viscous dissipation at higher temperatures upon graphitisation of the carbon black. This evidence would appear to support the second conclusion over the first and indicates that the no additional linear contribution to creep could be distinguished for N990-based samples because the low surface area of the filler reduces the measureable contribution of the interface inelasticity to the bulk material properties. To provide a balanced discussion and interpretation of this data, both of the aforementioned conclusions are discussed in more detail.

8.1.2. Inelasticity of the filler network at small strains

One explanation for the creep data presented here is the inelasticity associated with the filler network. Put another way, if the filler network is imagined to be loaded with a constant force - small enough so as not to rupture the network - then the viscoelastic nature of the 'bonds' or interactions between aggregates becomes of paramount importance. If these bonds are somehow time-dependent (for example, able to yield and then re-establish themselves) then they will contribute to the total creep of the composite material. The physical origins of such interactions between aggregates are the subject of much debate - as highlighted in Chapter 5. They may arise from direct contact between aggregates, physico-chemical interactions such as van der Waals or hydrogen bonding forces [6, 7] or immobilisation of polymer confined in gaps

between the aggregates [8, 9]. Without a precise understanding of the nature of interactions between aggregates, a deeper understanding of such a phenomenon is currently intractable.

Robertson and Wang [10] and Wang and Robertson [11] have proposed that non-linearities in filled rubbers can be understood in terms of an unjamming process. Figure 8.18 is reproduced from one of their papers [11] and presents a tentative phase diagram showing the transition from jammed to unjammed states as a function of volume fraction (plotted as 1/ϕ), thermal energy (kT) and mechanical energy (σγ).

For the case of linear viscoelasticity the mechanical energy input is minimal so it is possible to consider only the kT versus 1/ϕ plane. It is clear from this that sufficient thermal energy can result in an unjamming of the filler network in an analogous fashion to the application of larger strains which induce the observed Payne effect. Hypothetically one could consider that the kT versus 1/ϕ trends for unmodifed and graphitised carbon black networks are significantly different as a result of differing polymer-filler and filler-filler interactions Figure 8.19. Thus the observation of a secondary dissipation process in graphitised carbon black-filled materials may arise from a partial thermal unjamming of the filler network.

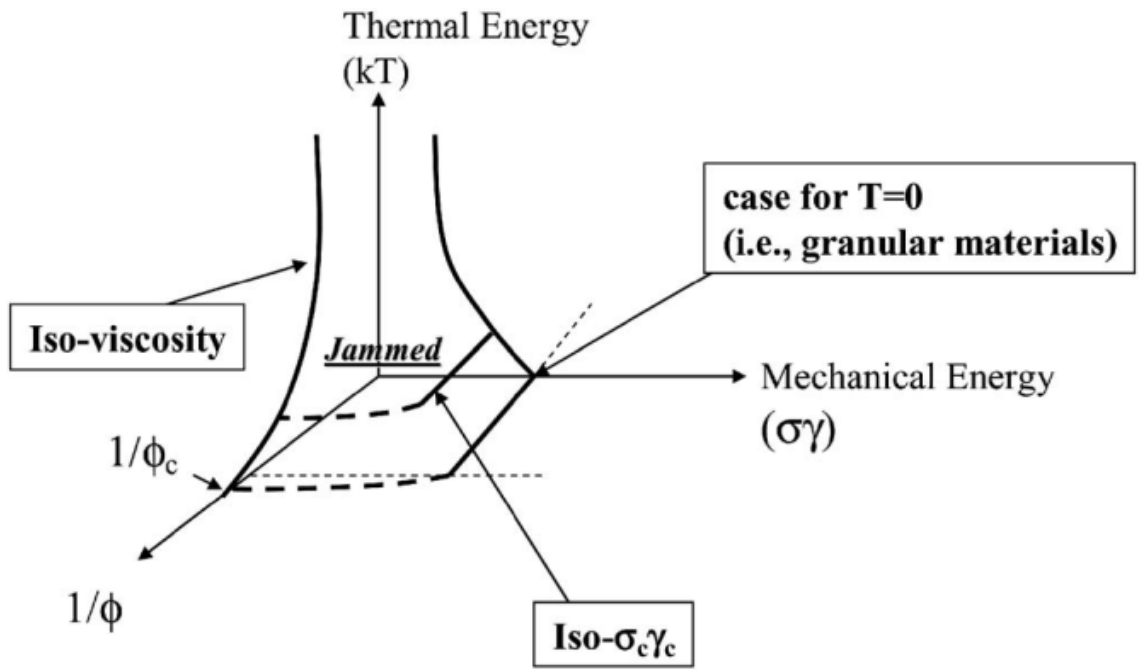

Figure 8.18: The phase diagram for unjamming of filler networks proposed by Wang and Robertson [11]

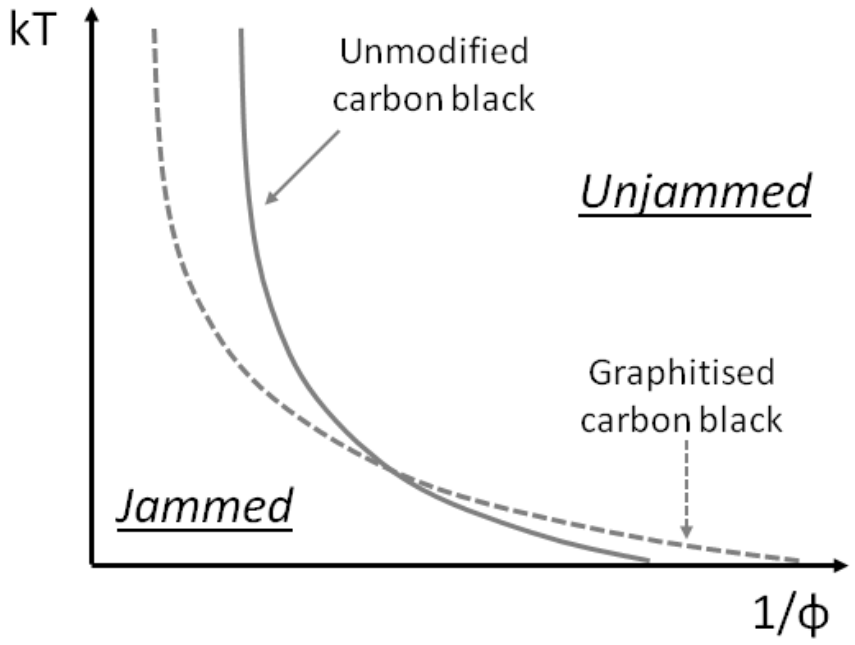

Figure 8.19: Speculative plot of the kT versus 1/ϕ relationships for carbon black networks of different polymer-filler and filler-filler interactions

8.1.3. Viscous dissipation at the filler-rubber interface

As discussed in the literature review, a number of different researchers have previously proposed that slippage or desorption of polymer from the particle surface may play a role in viscous energy dissipation and in reinforcement more generally [12-17]. In this sense, the local 'slippage' of an individual chain segment across a filler surface may appear insignificant by itself in terms of energy dissipation, but, given the large surface area of the carbon black filler particles, it may be of more significance to the bulk material properties.

However, it is important to connect what is meant by 'desorption of polymer segments' in the context of the Maier and Göritz model [13] and the less well defined concept of polymer slippage at the interface as discussed by Jha et al. [16], Busfield et al. [15] and others [14, 17].

Maier and Göritz proposed that, in the linear viscoelastic region, the role of temperature is simply to change the kinetic balance between empty and occupied chain segment absorption sites on the filler surface. They assume that bonding of the polymer macromolecules to labile

sites on the filler surface is at equilibrium at a given temperature but that there is a continuous desorption and absorption of chain segments across the filler surface. In the papers of Jha et al. [16] Busfield et al. [15] and Akutagawa et al. [17], the authors discuss this process from a mesoscopic or continuum-level viewpoint and assume that 'slippage' of polymer chains gives rise to increased energy dissipation and reduction in composite stiffness. In these papers the exact molecular mechanisms of slippage are left undefined. Sternstein and Zhu [14] have made a connection between Maier and Görtiz's molecular-level mechanism and continuum-level considerations. They have highlighted the applicability of wall slip equations, such as those proposed by Yarin and Graham [18], to the reinforcement of rubbers.

At the core of the model proposed by Yarin and Graham is the dependence of the lifetime of bonds between the polymer and the substrate on a number of factors. These are given in Equations 8.10 and 8.11 from [18]. In Equation 8.7 the probability of bond breakage is proportional to the lifetime of the filler-polymer bond, t_1, the temperature and an effective activation energy, E_a^{eff}. This in turn is proportional to the activation energy of the polymer-substrate bond, E_a, minus the external force applied to the polymer chain, F, multiplied by a characteristic length, β. t_* is a time constant inserted to ensure that detachment of chain segments does not occur on timescales shorter than the Brownian motion of the chain segments themselves (Equation 8.8).

$$t_1 = t_\star + t_0 \exp\left[\left(E_a^{eff}\right)/\mathbf{k}T\right] \tag{8.7}$$

$$E_a^{eff} = E_a - \beta F \tag{8.8}$$

Assuming that there is a labile bonding of rubber chains to the surface of the carbon black filler particles which gives rise to viscous dissipation upon deformation - presumably by a desorption/adsorption of chain segments at the interface to relieve the locally developed stresses - then it should be possible to account for the observed Arrhenius plots for the creep data (Figure 8.17) in terms of an interfacial slippage mechanism.

Table 8.1 showed that the linear-time contributions to creep have similar activation energies regardless of the average particle surface energy. However, from an examination of the

magnitudes of the linear process in the Arrhenius plots of Figure 8.17 it is apparent that the magnitude of the contribution of the linear-time process to the total inelastic behaviour is dramatically amplified - by nearly an order of magnitude - upon graphitisation. Therefore it appears that the same physical process underpins the linear-time creep contribution in both unmodified and graphitised carbon blacks but the magnitude of the process is related the surface activity or degree of graphitisation of the carbon black aggregates.

In rationalising these observations in terms of an interfacial polymer chain slippage mechanism, it is important to recall the contrasting heterogeneous surface structures and activities of unmodified and graphitised carbon blacks. Unmodified carbon blacks have a comparatively low surface concentration of graphitic crystallite planes interspersed with higher surface energy regions of amorphous carbon. The high surface energy amorphous carbon regions as well as the graphitic crystal edges are thought to be the points of strongest interaction of the particle surface with the polymer chain segments. Upon graphitisation of carbon black the surface concentration of these high surface energy sites is reduced by the growth of the graphitic crystalline regions. This is therefore accompanied by an increase in the surface concentration of graphitic planes at the filler particle surface.

Maier and Göritz proposed in their model that the interaction of chain segments with the carbon black surface is either permanent or labile depending on the mode of interaction. This may be an oversimplification as the distribution of energetic sites on carbon black surfaces has been determined by IGC studies to be broad rather than bi-modal [19, 20]. However the general principle of more stable and less stable interactions is feasible. In this sense it is clear that slippage (desorption/adsorption) of chain segments under small strain conditions would occur preferentially at the low surface energy graphitic planes rather than at sites where the chain segments are tightly bound to the surface. Therefore the same underlying temperature dependence of the physical process is apparent in both unmodified and graphitised carbon blacks but the contribution to inelasticity scales with the surface concentration of graphitic planes.

The activation energies given in Table 8.1 are in units of kJ/mol, obtained directly from the Arrhenius plots. If we assume that the normalisation of the energy refers to the energy per mole of chain (Kuhn) segments weakly attached to the graphitic portions of the carbon black surface, then this gives an average value (excluding the apparently erroneous first E_a value for N330) of 0.13 ± 0.01 eV per chain segment. This is in reasonable agreement with the values

extracted by Maier and Görtiz's fits of their molecular model to literature data for the temperature-dependent desorption of chain segments from the surface of carbon black [13] (0.15 eV for NR-carbon black [HAF CB at $\phi = 0.324$] and 0.18 eV for SBR-carbon black [N339 CB at $\phi = 0.189$]). Similarly, the activation energy values are in reasonable agreement with the surface energy of the absorption sites on the graphitic surfaces of carbon black determined by Schröder et al. [19] to be of the order of 16 kJ/mol (0.17 eV per site).

Recently Balzer et al. [21, 22] have published a series of papers which have a significant bearing on this topic. They have developed an AFM-based method to perform nanoscale investigations on the stick-slip lateral motion of polymer chains along substrates. In their technique a single linear polymer chain is covalently grafted to an AFM tip and absorbed at the substrate of interest by bringing the chain and tip into contact with the substrate (their experiments were performed in a liquid medium). Absorption of the polymer chains was confirmed by *z*-axis pull off experiments. They then dragged the polymer chain in the *x*-*y* plane and measured the frictional behaviour. They observed a range of different slippage mechanisms depending on the polymer-substrate interaction and also upon the sliding velocity. In their papers they distinguish between slip and so-called desorption stick-slip and cooperative stick-slip motion. These mechanisms are illustrated in Figure 8.20.

Desorption stick-slip is proposed to occur when polymer chain segments preferentially desorb from the substrate into the *z* plane under the application of a lateral force rather than translates across the surface of the substrate. For the case of cooperative stick-slip, which is observed for the case of stronger polymer-substrate interactions (for example hydrogen bonding), the polymer segments between the AFM tip and the those absorbed onto the substrate are strained significantly until the stored energy is equal to the binding energy between the chain segments to the substrate. At this point whole chain desorbs and translates laterally across the surface.

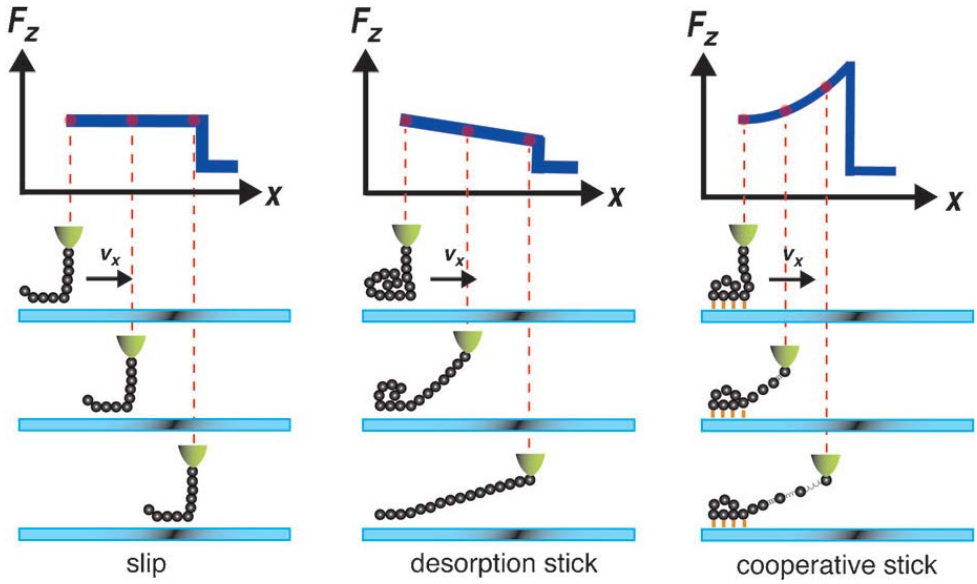

Figure 8.20: Schematic showing the proposed slip, desorption and cooperative stick-slip behaviour of individual polymer chains under the application of a lateral force. The top diagrams indicate the corresponding forces measured by the AFM in the *z* axes (From [21])

8.7. Interfacial slippage and the secondary tanδ phenomenon

Finally it worth considering how an interfacial slippage mechanism could manifest itself as a secondary peak in tan*δ* on the rubbery side of the glass transition. Numerous examples of this phenomenon are seen in the literature and while it is quite obvious that increasing slippage with temperature must give rise to an increase tan*δ,* it is less obvious why the dissipation should appear to decrease following a maximum in tan*δ*. This peak-like appearance of the phenomenon has led to it being described as a 'relaxation' process [23, 24] by previous researchers.

Taking into account the models of Yarin and Graham and Maier and Göritz, it is clear that the desorption/slippage of chain segments, which is correlated with mechanical energy dissipation, at the surface must reach a maximum magnitude at higher temperatures. However, these models do not describe the often observed peak and decrease in dissipation. An explanation for this effect is presented here.

It is postulated that temperature dependence of the underlying elastomer matrix plays and important role in shaping this phenomenology. Take as an example the case of a single filler particle embedded in a viscoelastic rubber matrix. Theoretically the bulk viscoelasticity may be described as the sum of dissipation arising from the matrix and from the interface. Assuming

that slippage (and therefore dissipation) is initiated at the surface at a given temperature and reaches a saturation value at some higher temperature where all the chains are fully mobile at the surface, then the dissipation at the interface may be arbitrarily represented as a sigmoidal function (Figure 8.21). The effect of the temperature dependence of the viscoelasticity of the matrix can then be investigated.

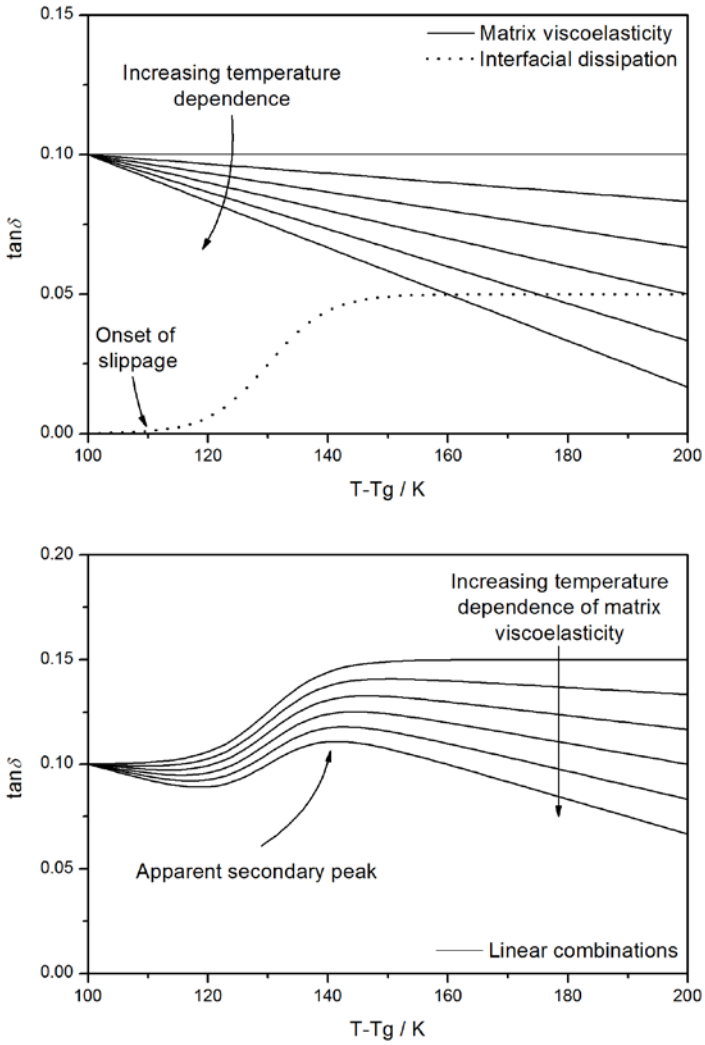

Figure 8.21: Schematic explanation for the appearance of a secondary peak in tanδ in terms of an interfacial dissipation mechanism. The top figure shows the dissipation arising from the elastomer matrix viscoelasticity (the temperature dependence of which is varied as indicated), the bottom figure shows the combination of interfacial and matrix dissipation and the appearance of an apparent secondary relaxation with an increasing temperature dependence of the matrix

Figure 8.21 shows the effect of changes to the underlying temperature dependence of the rubber matrix viscoelasticity by examining linear combinations of functions associated with

matrix viscoelasticity and a sigmoidal function associated with dissipation at the interface. When the matrix viscoelasticity is independent of temperature - as may be the case for rubbers with a very low T_g such as polybutadiene or PDMS measured around room temperature - then the sigmoidal-shaped dissipation associated with the interface is fully recovered in the bulk material response. However, as the temperature dependence of the matrix viscoelasticity increases, the sigmoidal dissipation associated with the interface is lost and replaced with an apparent peak in tanδ. In Figure 8.21 the tanδ associated with the elastomer matrix is approximated as a linear function of temperature. Arbitrary values for tanδ have been chosen and a sigmoidal function describing the surface dissipation is centred on $T-T_g$ = 130 K with an arbitrary broadness constant of 0.2. Figure 8.21 clearly shows that a secondary peak in tanδ may be the expected outcome for cases where the elastomer matrix displays some temperature dependence.

8.8. References

[1] A.N. Gent, Engineering with rubber. How to design rubber components, 2nd ed., Hanser, Cincinnati, 2001.
[2] R.J. Smith, Circuits devices and systems: a first course in electrical engineering, 2nd ed., John Wiley, New York, London, 1971.
[3] A.R. Payne, R.E. Whittaker, Rubber Chemistry and Technology, 44 (1971) 440-478.
[4] G. Kraus, Applied Polymer Symposia, (1984) 75-92.
[5] M. Klüppel, Advances in Polymer Science, 164 (2003) 1-86.
[6] K. Arai, J.D. Ferry, Rubber Chemistry and Technology, 59 (1986) 592-604.
[7] E.R. Fitzgerald, J.D. Ferry, Rubber Chemistry and Technology, 55 (1982) 1569-1577.
[8] J. Fritzsche, M. Klüppel, Journal of Physics-Condensed Matter, 23 (2011) 035104.
[9] J.G. Meier, M. Klüppel, Macromolecular Materials and Engineering, 293 (2008) 12-38.
[10] C.G. Robertson, X. Wang, Europhysics Letters, 76 (2006) 278-284.
[11] X.R. Wang, C.G. Robertson, Physical Review E, 72 (2005) 031406.
[12] D. Göritz, H. Raab, J. Frohlich, P.G. Maier, Rubber Chemistry and Technology, 72 (1999) 929-945.
[13] P.G. Maier, D. Göritz, Kautschuk Gummi Kunststoffe, 49 (1996) 18-21.
[14] S.S. Sternstein, A.J. Zhu, Macromolecules, 35 (2002) 7262-7273.
[15] J.J.C. Busfield, V. Jha, A.A. Hon, A.G. Thomas, Conference Proceedings: Constitutive Models for Rubber IV, P.E. Austrell, L. Kari (Eds.), Balkema, Stockholm,
[16] V. Jha, A.A. Hon, A.G. Thomas, J.J.C. Busfield, Journal of Applied Polymer Science, 107 (2008) 2572-2577.
[17] Y.K. Akutagawa K, Yamamoto A, Heguri H, Jinnai H, Shinbori Y, Rubber Chemistry and Technology, 81 (2008) 182-189.
[18] A.L. Yarin, M.D. Graham, Journal of Rheology, 42 (1998) 1491-1504.
[19] A. Schröder, M. Klüppel, R.H. Schuster, Macromolecular Materials and Engineering, 292 (2007) 885-916.

[20] J.B. Donnet, R.C. Bansal, M.J. Wang, (Eds), Carbon Black: Science and Technology, 2nd ed., Marcel Dekker Inc, New York, 1993
[21] B.N. Balzer, M. Gallei, M.V. Hauf, M. Stallhofer, L. Wiegleb, A. Holleitner, M. Rehahn, T. Hugel, Angewandte Chemie-International Edition, 52 (2013) 6541-6544.
[22] B.N. Balzer, S. Kienle, M. Gallei, R. von Klitzing, M. Rehahn, T. Hugel, Soft Materials, 12 (2014) S106-S114.
[23] J. Ramier, Ph.D Thesis: l'Ecole Doctorale Matériaux de Lyon, Lyon, 2004.
[24] J. Ramier, C. Gauthier, L. Chazeau, L. Stelandre, L. Guy, Journal of Polymer Science Part B-Polymer Physics, 45 (2007) 286-298.

Chapter 9

Summary, Conclusions and Future Work

9.1. Summary of the findings of this thesis

This thesis addressed the topic of particulate reinforcement of elastomers, paying special attention to the linear viscoelastic properties of filled compounds. General themes of the thesis were to keep experiments and compounds as simple as possible - for example by using two phase composites as opposed to more complex industrial compounds. The general objective was to build an understanding of reinforcement mechanisms in carbon black and precipitated silica filled natural rubber.

Chapter 2 reviewed the literature pertaining to rubber physics and filler reinforcement. The review highlighted the extensive existing work in these areas and, in particular, the fact that many microstructural theories which attempt to explain filler reinforcement are incomplete or inconsistent with one another. Potential areas of investigation were proposed.

Chapter 3 detailed the physico-chemical characteristics of the various fillers used in this study. As well as unmodified carbon black, a series of carbon black fillers were thermally modified (graphitised) which resulted in a reduction in particle surface activity with little to no change in particle aggregate structure. Silica fillers were surface modified using a silane coupling chemical. The surface modifications were quantified using a variety of techniques.

Chapter 4 demonstrated that the natural rubber/peroxide cure combination results in polymer networks which are inhomogeneously crosslinked in terms of the spatial distribution of chain-chain links. This becomes more apparent when high initial concentrations of peroxide are used. Furthermore Chapter 4 demonstrated that the NR/peroxide cure system when used in combination with reinforcing fillers in not ideal in terms of maintaining a stoichiometric crosslink yield. There is an interaction between the filler surfaces and the free radical cure system. This is significant as the peroxide cure system is often seen a 'clean' cure system for scientific work. These results should be borne in mind as an inherent drawback of this cure system when designing future experiments and when revisiting the literature (the point was emphasised that much of the seminal work of Mullins and co-workers was conducted on NR/peroxide/carbon black combinations). In addition, inferences about the nature of the restriction of swelling of interfacial rubber and its dependence on filler aggregate structure were made.

In Chapter 5 it was demonstrated that in very simple reinforced systems - model microcomposites - the observed stiffening at small strain could be attributed to the stiffening

arsing from the random incorporation of rigid spheres into the elastomeric matrix (hydrodynamics, strain amplification, matrix occlusion). For carbon black aggregates of high aggregate structure and surface area, additional reinforcing mechanisms are apparent. This is inferred from the temperature dependence of the amplification of the storage modulus. The presence of a percolated filler network in some of the carbon black-filled materials was determined by DC resistivity testing and the dynamics of the filler structure in the melt (flocculation) were found to depend significantly on the polymer-filler interaction.

In Chapter 6 no measurable effect of the various filler particles used in this study on the glass transition and segmental dynamics of natural rubber could be detected using DSC, BDS and DMA. These finding were placed in the context of the relevant literature.

Chapter 7 initially revisited the model microcomposites introduced in Chapter 5 and examined their small strain loss tangents. It was found that in the rubbery region the loss tangents of the filled microcomposites were identical to those of the unfilled control. This means that the energy applied to the composites upon deformation is entirely stored and dissipated in the elastomer phase. Very precise measurements of the loss tangents of the carbon black-filled rubbers were made at small strains and for the graphitised carbon black-filled materials, a secondary rise in dissipation as a function of increasing temperature was observed. This was found to be the case for all graphitised carbon blacks independent of whether they were loaded at volume fractions above or below the electrical percolation threshold. Such effects are readily observed in the literature - although incompletely understood. Based on the author's knowledge of the literature, this is the first time that secondary dissipation effects have been reported for fully crosslinked polymers containing carbon black-based fillers.

Chapter 8 investigated the same thermal region in which the secondary dissipation effects were observed. In this chapter creep experiments were performed for the carbon black series of compounds. It was found that graphitisation of the carbon black filler dramatically increases the magnitude of creep inelasticity of the compounds. The creep data were found to follow the trend of the dynamic data of Chapter 7 in that the relative inelasticity of the compounds increased with increasing temperature. An apparent upturn in the creep rate of the graphitised carbon black filled compounds was noted at longer time scales. Similar effects were also observed in the unmodified carbon black-filled materials, though to a less pronounced extent.

9.2. Conclusions

The key conclusions of this thesis are as follows:

Deviations from reinforcement observed for model microcomposites that are seen in NR reinforced with carbon black fillers are related to the formation of a filler network (the mechanical nature of which is not currently understood) and to the role of the interface between the polymer and filler. This conclusion was reached based on the following observations:

(I) Reinforcement of the small strain elastic modulus in NR filled with high structure, high surface area carbon blacks loaded above their electrical percolation thresholds was found to be temperature dependent and at a maximum just after the glass transition. The maximum value of the reinforcement was found to be roughly an order of magnitude larger than that predicated by extrapolation of the particle size dependence of the temperature-independent reinforcement measured in the model microcomposites (i.e. geometrical reinforcement effects alone).

(II) For carbon black filler of roughly spherical morphology (N990), loaded well below the electrical percolation threshold (no filler network is present), the observed maximum in reinforcement was in good correlation with that predicted from the model microcomposites. This implies that just after the glass transition the reinforcement for these materials can be completely ascribed to geometrical stiffening effects.

(III) For the same material, a measurable decay in reinforcement with increasing temperature is observed following the peak value measured after the T_g. This means that a temperature dependent softening mechanism must be present which cannot be associated with filler networking.

For the materials studied in this work, no interphase polymer could be detected. Certainly large volumes of interphase polymer are not present in these compounds, however small volumes of interphase polymer may be within the detection limits of the equipment used and cannot be ruled out. The possible role of very small volumes of interphase polymer in dictating the mechanical properties of percolated filler networks has been speculated on in the literature.

The observation of a secondary dissipation effect in the dynamic mechanical and creep measurements of Chapters 7 and 8 relates to a phenomenon either at the polymer-filler interface or is associated with a viscous effect within the filler structure. The fact that these effects are observed in graphitised N990 carbon black below the percolation threshold, indicates that there is at least some contribution from the interface. This is likely accounted for by a mechanism of viscous sliding or the desorption/adsorption of chain segments to relieve local shear stress at the interface. The observation of what appears to be an underlying Newtonian viscous contribution to creep behaviour is very evident in graphitised materials but is also detectable for commercial carbon blacks. This implies that sliding may still occur between high energy regions on the surface of the carbon black particles. More data is required to confirm this.

9.3. Future Work

The key question raised by this thesis is the origin of secondary dispersion effects in carbon black-filled rubbers. Do similar events occur in commercial systems but on a reduced scale? The proposal made in this thesis is that chain segment sliding occurs at graphitic region on the surface of the carbon black. Potentially this same mechanism may occur at graphitic regions between higher energy sites on the surface of commercial carbon black.

Future work on this topic could include:

- Collecting more data on samples loaded below the percolation threshold so as to confirm the independence of the secondary dissipation effect from the presence of a filler structure.
- Collecting more data for carbon black materials at differing levels of graphitisation. This may enable the extrapolation of secondary dissipation effects back to commercial carbon black materials.
- Examining the effect of rubbers with different glass transitions but similar backbone chemistry. Does the effect depend on thermal separation from the T_g in a systematic way?
- How do secondary dissipation effects behave under the application of larger strains outside of the linear viscoelastic region?
- Can sliding experiment of rubber on model surfaces such as graphite or glassy carbon corroborate the bulk compound measurements of this thesis?

If a solid link can be made between these dissipation effects and commercial carbon blacks then it represents a previously unidentified and unquantified source of dissipation in carbon black-elastomer composites.

An experimental issue arising from the custom built torsion testing rig was noted in chapter 8. The current design of the rig used when performing creep experiments actuated the sample by the application of a torsional load at one end of the inertia bar. This was appropriate for materials with low initial compliance but was problematic for softer materials such as unfilled NR or NR filled with non-reinforcing N990 carbon black. In this case a significant off-axis deformation was observed in the sample which limited the validity of creep testing on the N990-filled materials. A future iteration of the rig could incorporate two wound coils applying the load across both ends of the inertia bar. This would balance any off-axis forces during the experiment.

Further to this, it was highlighted that critical information could be obtained by exploring dynamic and creep behaviour below the percolation threshold. In future materials could be prepared for examination using lower structure, lower surface area carbon black such as N700 series fillers. This would enable high volume fraction loadings comparable to those used in this study (predominantly $\phi = 0.20$) but no filler networking effects. Thus dissipation effects at the filler-rubber interface could be directly studied.

In order to validate the chain segment slippage mechanism, it may be informative to perform model sliding experiments on substrates which approximate the surface of carbon black particles. On option would be to use graphite however graphite sheets are generally not homogeneous substrates and tend to delaminate along the basal crystal layer upon the application of shear forces. An alternative would be to perform model experiments on glassy carbon substrates. Glassy carbon is a form of inexpensive, non-graphitising carbon which is found to bear a reasonable similarity to the surface of carbon black.

A sample of Siguradur G glassy carbon plates measuring 25x25x3 mm was obtained from HTW Hochtemperatur-Werkstoffe GmbH, Germany. Surface characteristics were analysed and are presented in Figures 9.1-9.3. AFM analysis (Figure 9.1) shows that the substrate is essentially atomically smooth, with an average surface roughness of ~3 nm. XRD studies (Figure 9.2) show that N330 carbon black and glassy carbon have very similar diffraction patterns. The TEM image - which is reproduced from the suppliers' website - shows that glassy carbon is made up

of fullerene-type random graphitic layers. Furthermore surface energy analysis (Figure 9.3) by the sessile drop technique obtains the polar and dispersive parts of the surface free energy of glassy carbon. These values are found to be in very good agreement with previously published values for carbon black. Stockelhuber et al. [1] used a modified Wilhelmy method to measure contact angles of fluids on carbon black powders. They obtained values of 0.0 and 26.4 mJ/m^2 for the polar and dispersive parts of N330 surface energy respectively. Values obtained by sessile drop analysis are 6.4 and 20.1 mJ/m^2 for the polar and dispersive parts of glassy carbon respectively. Note that this gives total surface free energy values of 26.4 mJ/m^2 for N330 carbon black and 26.5 mJ/m^2 for glassy carbon.

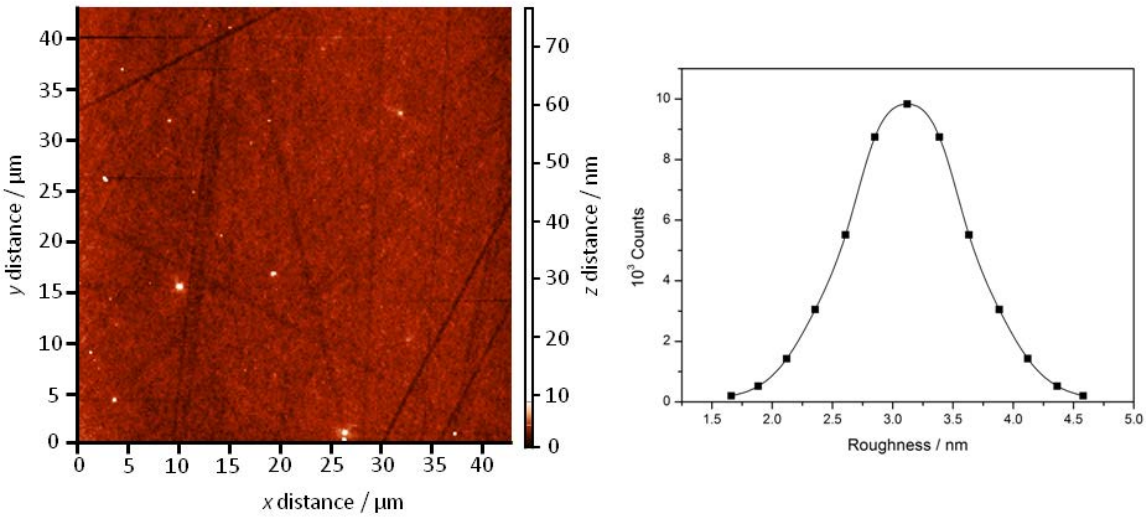

Figure 9.1: AFM image (contact mode) and roughness histogram of the surface of glassy carbon

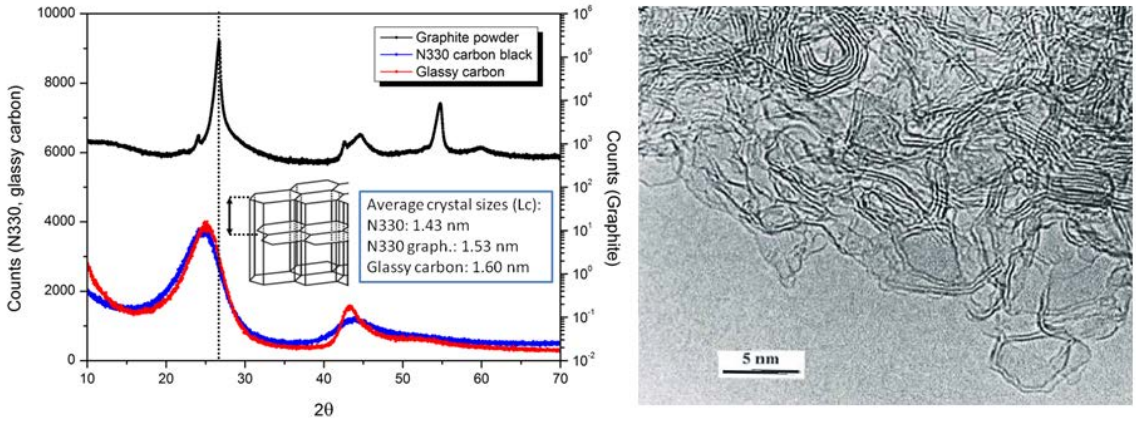

Figure 9.2: XRD patterns of glassy carbon, carbon black N330 and graphite power. Note the similarity between glassy carbon and N330. TEM image of glassy carbon structure from [2]

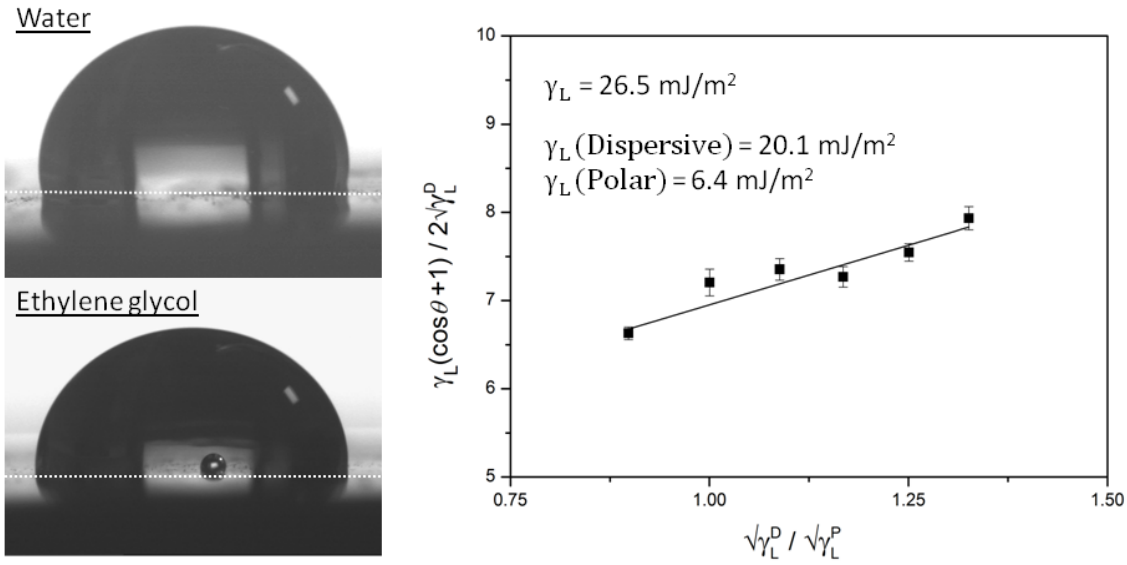

Figure 9.3: Surface energy analysis of glassy carbon by sessile drop technique. The plot is a typical Owens-Wendt plot for determination of polar and dispersive components of the surface free energy from linear regression

The type of experiments that could be performed to validate the chain slippage mechanism could range from long term sliding or peeling experiments of bulk unfilled rubber on the glassy carbon substrate, or nanomechanical, AFM-based experiments such as those performed by Balzer et al. [3, 4].

Future work relating to network structure characterisation and flocculation dynamics have been proposed in detail in Chapters 4A and 5 respectively.

9.4. References

[1] K.W. Stöckelhuber, A.S. Svistkov, A.G. Pelevin, G. Heinrich, Macromolecules, 44 (2011) 4366-4381.
[2] http://www.htw-germany.com/technology.php5?lang=en&nav0=2&nav1=15, Access date 19/6/15
[3] B.N. Balzer, M. Gallei, M.V. Hauf, M. Stallhofer, L. Wiegleb, A. Holleitner, M. Rehahn, T. Hugel, Angewandte Chemie-International Edition, 52 (2013) 6541-6544.
[4] B.N. Balzer, S. Kienle, M. Gallei, R. von Klitzing, M. Rehahn, T. Hugel, Soft Materials, 12 (2014) S106-S114.

Appendix I

Theory and Details of Experimental Techniques

This appendix details some of the experimental procedures and background information in more detail than was possible in the main chapters. References to the theory and development of these methods are given at the end of each section where appropriate.

A.1. Mechanical Testing and Rheometry

A.1.1. Tensile Testing

Tensile mechanical testing was performed on an Instron 5566 screw driven mechanical testing frame with a 1kN load cell and video strain gauge. Samples of material for tensile testing were cut into dumbbell shapes using a pneumatic die cutter and ASTM D412 type C die. Dumbbell dimensions are shown in Figure A.1. The dumbbell test piece shape has the advantage that it allows a large surface area of sample to be clamped at each end, reducing the potential for slippage, while leaving a smaller rectangular section of known dimensions between which deforms during testing. A number of uncertainties in the tensile test procedure were addresses as follows:

- Buckling of the dumbbells during clamping of the specimens was rectified by applying a 0.5 N pre-load to the samples prior to testing.
- 5 repeat specimens were tested for each type of material investigated to highlight any issues arising from non-representative random flaws within or at the surface of the specimens leading to non-representative mechanical behaviour.
- Slippage of samples from the clamps was minimised by using screw action-type clamp grips which are optimal for testing of rubber materials. In addition, the use of the video extensometer to define the strain, rather than crosslink displacement, meant that any unavoidable slippage was accounted for in the recorded strain. Figure A.2 plots the imposed crosshead displacement against the true strain in the material measured by the optical strain gauge for unfilled NR crosslinked with 2 phr DCP. The distinct non-linear relationship at the highest strains is indicative of slippage of the sample which is compensated for by the true strain measurement.
- A 1 kN load cell was found to provide the optimum calibrated load range for sample testing out of the load cell facilities available at QMUL.

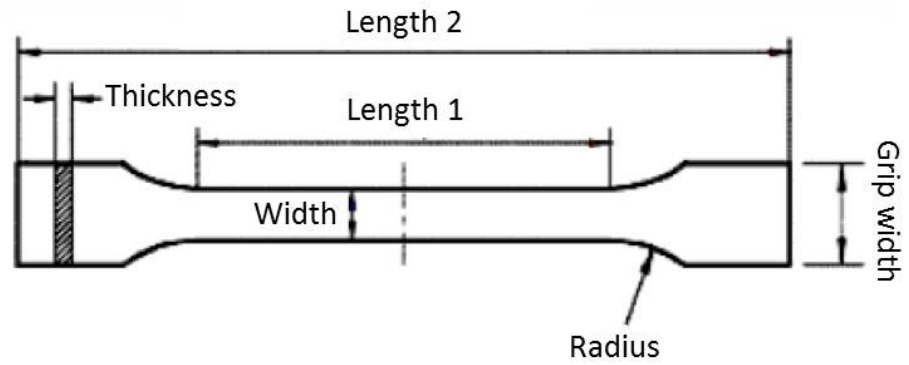

Figure A(I).1: Schematic of ASTM D412 type C dumbbell shape and dimensions used in this work. Length 1 = 33 mm, length 2 = 115 mm, width = 6 mm, grip width = 25 mm, radius = 14 mm and the thickness was typically 2 mm. During testing the width was determined as the average of 3 Vernier calliper measurements along the sample. The thickness was determined as the average of 3 measurements along the sample from a 2 decimal place drop gauge.

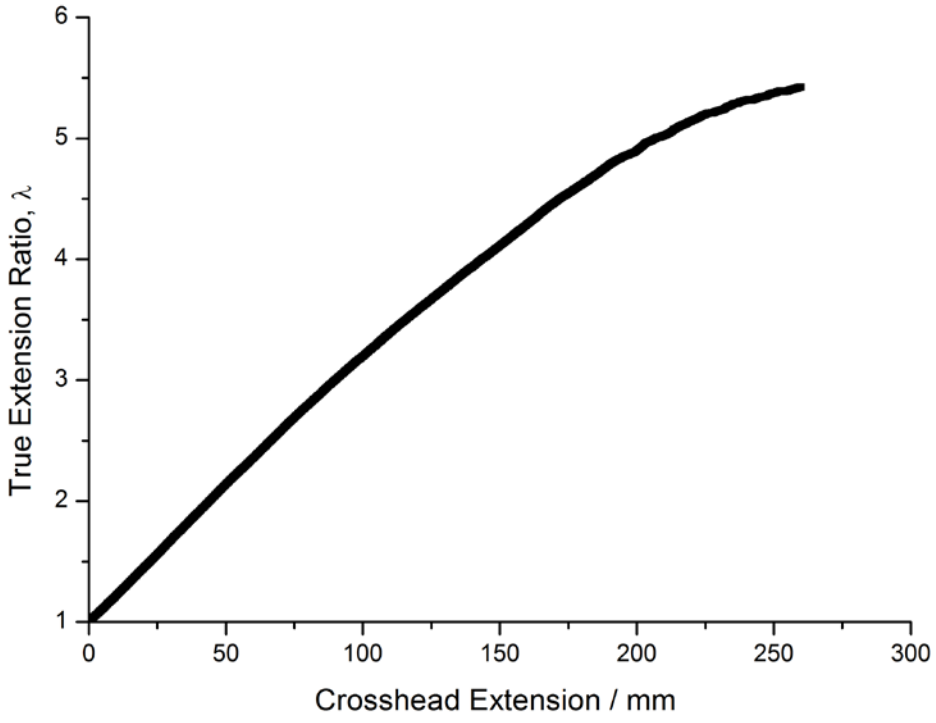

Figure A(I).1: Plot of the true extension ratio measured from the axial video strain gauge versus the crosshead displacement during the tensile testing of a sample of NR crosslinked with 2 phr DCP

A.1.2. Dynamic Mechanical Analysis

The basic principles of DMA were outlined in the literature review. Two types of deformation modes were used in this work; shear (Chapter 5) and tension (Chapter 6).

Shear testing was performed on a TA Instruments Q800 DMA using a double shear clamp geometry. This particular DMA has a maximum load capacity of 18 N. It was found in practise that when testing was performed at small strain from the rubbery region through to the glassy region, large sized samples would result in overloading of the load cell. The optimum size for samples was found to be 5x5 mm square width with a thickness of around 2 mm. These samples were mounted into the shear clamp in one of two ways. For unfilled samples, the independence of modulus from applied strain meant that the samples could be compressed into the clamps using a 5 % compressive strain. For strain-sensitive, filled samples, the specimens were loaded by gluing the faces of the specimens to the clamps using Loctite 480 adhesive. The Loctite Adhesive required a 24 hour drying period before it was fully cured and ready for testing.

Tensile deformation mode was performed on a Perkin Elmer DMA 8000. Rectangular samples were lightly gripped in the clamps and then crash cooled to -90 °C (well below the T_g). Tensile clamps were then fully tightened onto the glassy materials and testing was performed from the glass to the rubbery state as outlined in Chapter 6.

A.1.3. Rheometry

Two types of equipment were used to examine the rheological properties of the filled rubber melts. The most basic form of testing was the monitoring of the crosslinking process. For this an Alpha Technologies Moving Die Rheometer (MDR) 2000 rheometer was used which compressed un-crosslinked rubber compounds (which incorporated dicumyl peroxide curative) between two serrated plates heated to a temperature of 150 °C. A 2.5 % torsional strain was applied across the sample in shear and the resulting in and out of phase torque (S' and S'') were reported as a function of temperature.

An Alpha Technologies Rubber Process Analyser (RPA) was used to perform more complex rheological investigations on filler networking dynamics. The RPA uses the same sample geometry as the MDR but allows user control of the strain level and frequency. Details of the specific strains and frequencies used are given in Chapter 5.

A.2. Electron Microscopy

A.2.1. Scanning Electron Microscopy

Scanning electron microscopy (SEM) was used to observe the quality of filler dispersion in rubber compounds. Details of the sample preparation techniques are given in Chapter 3. Optical microscopy was not suitable for studying the features of interest here as, in general, radiation-based microscopy techniques are limited in terms of resolution by the wavelength of the radiation used. Optical microscopy is therefore theoretically limited at around 400 nm - the wavelength of blue light.

The wavelength of an electron however, is limited only by its momentum as defined in the de Broglie equation (Equation A1 - the de Broglie equation for the wavelength of an electron where λ_{WL} is the wavelength, $\mathbf{h}$ is the Planck's constant and p_{e} is the electron momentum)[1]. The momentum of the electron can be increased by accelerating the electron across a potential difference (Equation A2 - where v_{e} is the electron speed, e is the charge on the electron, V_{A} is the accelerating voltage and m is the electron mass)[1].

$$\lambda = \frac{\mathbf{h}}{p_{\mathrm{e}}} \qquad \text{A.1}$$

$$p_{\mathrm{e}} = \mathrm{m}v_{\mathrm{e}} \quad \text{where} \quad v_{\mathrm{e}} = \sqrt{\frac{2eV_{\mathrm{A}}}{\mathrm{m}}} \qquad \text{A.2}$$

Therefore the resolution of electron-based imaging techniques is dictated by the accelerating voltage which is typically of the order of several thousand kV. In this work an FEI Inspect SEM was used to collect the SEM images. The Inspect generated electrons from a lanthanum hexaboride (LaB_6) source.

Secondary electrons were used to collect the image data. Secondary electrons are electrons which are ejected from the electron shells of the material under investigation (i.e. they are not beam electrons) and as such can give a topographic representation of the material surface.

A.2.2. Transmission Electron Microscopy

Transmission electron microscopy (TEM) was used to image individual filler aggregates. TEM utilises the same physics outlined above in order to generate high resolution images. However TEM differs from SEM in that the sample under investigation is usually thin enough to allow the electron beam to 'transmit' through the material. The electron beam is focused onto the sample using electromagnetic 'lenses' which are controlled by current levels.

Images may be constructed from the transmitted electrons by considering the levels of attenuation of electron beam intensity (i.e. the levels of electron absorption throughout the material) this is termed 'bright field' imaging and was used in this thesis to image the filler aggregates.

TEM can also be used to collect electron diffraction patterns resulting from amorphous and crystalline diffraction of electrons as they pass through the sample. To achieve this the electron beam is focused so that the focal length of the back of the lens is placed onto the imaging equipment. The resulting diffraction pattern for polycrystalline materials such as carbon black consists of an array of diffraction halos which vary in terms of their sharpness, intensity and angular position relative to the axis of the electron beam depending on the crystalline nature of the sample.

References

[1] P. Atkins, Atkins' Physical Chemistry, 7th Ed. Oxford University Press, Oxford, 2002

A.3. Surface Area Analysis

In this thesis the surface area of the particulate fillers has been characterised by application of the Brunauer-Emmet-Teller (BET) theory [2] for adsorption of non-interacting gas molecules on surfaces to nitrogen adsorption isotherms. The BET theory is a modification the Langmuir isotherm for monolayer adsorption of gas molecules and is given in Equation A.3 where v is the volume of gas adsorbed by the sample, p_0 is the saturation pressure of the gas, p is the equilibrium gas pressure, v_{m} is the volume of gas involved in monolayer coverage, E_1 and E_{L} are the heats of adsorption for the first layer and subsequent layers of molecules. Plots of $1/v[(p_0/p)-1]$ versus (p/p_0) allow the calculation of the amount (volume) of gas adsorbed as a monolayer. If the adsorption cross-section and the molar volume of the molecule are known, the specific surface area can be calculated using Equation A.4 where $\mathbf{N}$ is Avagadro's number, s is the adsorption cross-section of the gas molecule, $V$is the molar volume of the probe gas and a is the weight of the sample. Units are therefore $m^2.g^{-1}$.

$$\frac{1}{v[(p_0/p)-1]} = \frac{c-1}{v_{\mathrm{m}}c}\left(\frac{p}{p_0}\right) + \frac{1}{v_{\mathrm{m}}c} \qquad \text{where} \qquad c = \exp\left(\frac{E_1 - E_{\mathrm{L}}}{\mathbf{R}T}\right) \tag{A.3}$$

$$SSA_{\mathrm{BET}} = \left(\frac{(v_{\mathrm{m}}\mathbf{N}.s)}{V}\right)\left(\frac{1}{a}\right) \tag{A.4}$$

In practise, data for surface area determination is collected using specialised equipment such as a Micrometrics pore and surface area analyser (Figure A.3). In such equipment powdered sample (which is usually dried and de-gassed using an inert atmosphere) is weighed and placed into glass vials which are connected to a pressurised gas supply. The volume of gas absorbed is measured at equilibrium steps in pressure. The whole experiment is performed at liquid nitrogen temperature to promote adsorption of gas at the sample surface. The BET isotherm is applied to the linear section of resulting BET plot. In this thesis nitrogen was used as the probe molecule so reported surface area values relate to nitrogen-specific adsorption.

Figure A(I).2: A commercial surface area analyser. The dewar (blue cylinder) contains cryogenic liquid, typically liquid nitrogen, into which the sample vessels are submerged [3].

References

[2] S. Branauer, P.H. Emmett, E. Teller, Journal of the American Chemical Society, 60 (1938), 309-319

[3] Image taken from *http://www.micromeritics.com/Product-Showcase/Gemini-VII-2390-Series-Surface-Area-Analyzers.aspx*. Correct at time of writing.

A.4. Surface Free Energy

Surface free energy (SFE), commonly denoted as γ_s, is defined by Wang and Wolff [4] as *'...the Work, W, required to create a new surface of liquid or solid...'*. Typically the surface free energy is assessed in terms of polar, γ_s^p, and dispersive, γ_s^d contributions (Equation A.5).

$$\gamma_s = \gamma_s^p + \gamma_s^d \quad \text{A.5}$$

Determination of the SFE of carbon blacks can be achieved using inverse gas chromatography [4] or the modified Wilhelmy method [5]. These methods allow the determination of the relative contributions from polar and dispersive contributions. In this thesis the total surface free energy, including polar and dispersive components, was determined through a method developed at Cabot Corporation's research and development lab, Boston, USA. SFE is defined here as the spreading pressure of water, π_e, in Equation A.6 where $\mathbf{R}$ is the gas constant, T is absolute temperature, SSA is the specific surface area of the test sample, Γ is the amount of adsorbed water in moles/g, P is the partial pressure of water and P_0 is the saturation vapour pressure. The integral of the isotherm gives the energy associated with absorption of the probe molecules. Normalising this value to the specific surface areas of the carbon blacks allows a direct comparison of the surface energies. The resulting values of SFE are therefore specific to water absorption and therefore include contributions from both the dispersive and polar components of the SFE.

$$\pi_e = \frac{\mathbf{R}T}{SSA}\int_0^{P_0} \Gamma d \ln P \quad \text{A.6}$$

Water adsorption isotherms were measured using a Dynamic Vapor Sorption Instrument, manufactured by SMS Instruments. 11 partial pressures were used, between 5% and 92% relative humidity, with 20 minutes equilibration at each level. Results are the average of duplicate samples.

References

[4] Wang and Wolff in: J.B. Donnet, R.C. Bansal, M.J. Wang, Carbon Black, 2nd ed., Marcel Dekker Inc., New York, 1993

[5] K.W. Stöckelhuber, A.S. Sviskvok, A.G. Pelevin, G. Heinrich, Macromolecules, 44 (2011), 4366-4381

A.5. Low Angle Laser Light Scattering

Low angle laser light scattering (LALLS) is a technique which is commonly used for determination of particle size and size distribution. LALLS takes advantage of the phenomenon of light scattering which occurs at discontinuities in refractive index. Rayleigh addressed the simplest form of scattering for the case where the scattering particles are significantly smaller than the wavelength of incident light - the so-called Rayleigh scattering regime [6]. The Rayleigh equation relates the intensity of light scattered from a single small particle to the refractive index contrast between the medium and the particle, the wavelength of incident light and the particle size (Equation A.7 where I is the intensity of scttered light, I_0 is the intensity of incident light, R is the distance to the particle from obervation of scattered intensity, θ is the angle at which the scattered light is observed, λ_{WL} is the wavelength of the incident light, n is the refractive index and $d$is the diameter of the particle). In practise there is no angular dependence to scattered light intensity in the Rayleigh scattering regime.

$$I = I_0 \frac{1+\cos^2\theta}{2R^2}\left(\frac{2\pi}{\lambda}\right)^4\left(\frac{n^2-1}{n^2+2}\right)^2\left(\frac{d}{2}\right)^6 \qquad \text{A.7}$$

Equation A.7 demonstrates the sensitivity of the scattered intensity on the wavelength of incident light $\left({\lambda_{WL}}^{-4}\right)$ and the scattering particle diameter (d^6). When particle size and wavelength of light are similar in size, light is no longer scattered according to Equation A.7. A significant angular dependence to the scattered intensity is introduced leading to the need to collect angular intensity data in LALLS particle sizing. Solutions for the angular intensity become significantly more complicated and require the application of Lorenz-Mie theory which are detailed in the literature [7].

LALLS was used in this thesis to characterise the particle size distributions of spherical glass bead particles. Malvern Mastersizer 2000 LALLS equipment was used to collect and process the data. The dispersing liquid was distilled water with a refractive index of 1, and the refractive index of the glass beads was 2.62. Less than 0.5 g of each glass bead were first dispersed in 50 ml distilled water stirred by a magnetic stirrer bar with a drop of sodium silicate added to suppress any flocculation or aggregation effects. 2 ml of the resulting suspension was sampled and added to the Malven Matersizer sample reservoir (liquid volume

of ~0.5 l). The sample reservoir was ultrasonicated for 60 seconds before the sample was measured. These steps ensured that the glass beads were at sufficiently low concentration to suppress multiple scattering effects and that the individual glass beads were dispersed. Blue light was used as the incident radiation. Application of the Lorenz-Mie theory was performed directly by the equipment to give the particle size distributions reported in this thesis.

References

[6] F. Träger, Springer handbook of lasers and optics, 2nd ed., Springer, New York, 2012

[7] H.C. van de Hulst, *Light scattering by small particles*, Dover, New York, 2003

A.6. Powder X-ray Diffraction

Powder X-ray diffraction (Powder XRD) is a technique which takes advantage of the small wavelength of X-rays[1] to probe the symmetry of arrangements of atoms within materials and is a powerful technique for the evaluation of polycrystallinity in powdered samples, for example carbon blacks.

The Bragg equation describes the diffraction of radiation from a series of evenly spaced planes (Equation A.8 where n is the path length integer of the X-ray wavelength λ_{WL}, d is the inter-planer distance and θ is the incidence angle of the X-rays - called the Bragg angle. This is illustrated in Figure A.4). Constructive interference and therefore a maximum in diffracted radiation intensity occurs when the angle of incidence is such that the path lengths of the radiation passing between the planes are equal to a multiple of the wavelength of the radiation meaning that the diffracted radiation is in phase. The intensity of diffracted radiation therefore varies as a function of incidence angle with inter-planer distances, d, having discrete maxima in angular diffraction intensity depending on their magnitude. For the case of layered crystalline domains within a material, this level of interpretation of the resulting diffraction patterns is enough to provide significant insight into the crystalline nature of the sample. Inter-planer spacing is calculated using Equation A.8 [9].

$$n\lambda = 2d\sin\theta \qquad \text{A.8}$$

Powder XRD experiments are therefore conducted as a function of Bragg angle. A typical XRD diffractometer setup is shown in Figure A.5 Diffractometers consist of an X-ray source (typically CuKα) which is mounted onto a rotating arc whose focus point is the centre of the sample holder. The X-rays are filtered to achieve an entirely in-phase X-ray beam. The detector is located as a mirror image of the X-ray source and moves in tandem with the source to collect diffracted radiation at the same Bragg angle as the source. With this setup an angular range of just over 0° and just under 90° can be examined.

[1] X-rays from a standard laboratory CuKα source have a wavelength of 1.54 Å

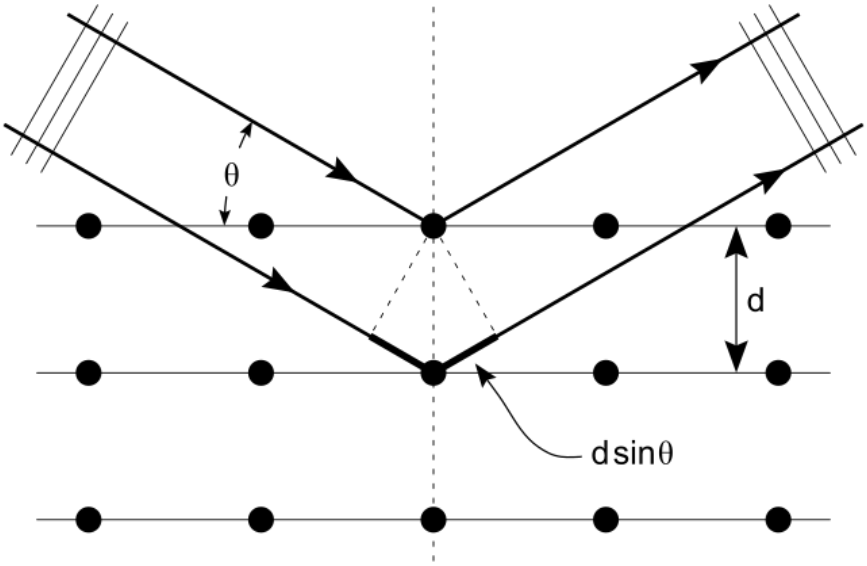

Figure A(I).3: Pictorial representation of the Bragg equation. Here the angle of incidence, θ, is such that the radiation path length at the point of diffraction is divisible by the wavelength, λ, resulting in constructive interference.

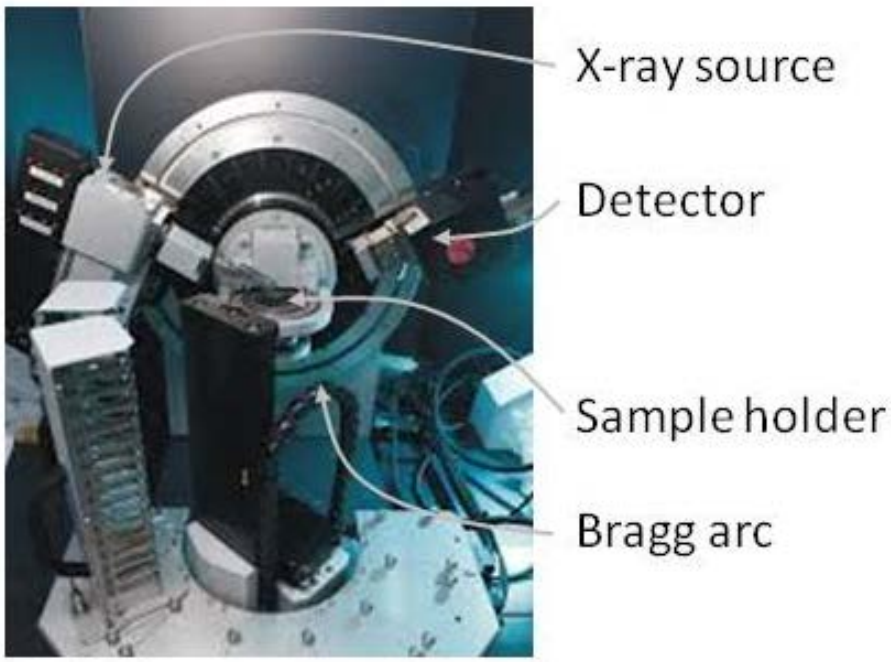

Figure A(I).4: Picture of a typical XRD diffractometer setup showing sample holder, X-ray source, detector and the Bragg arc.

Sample preparation is simple; powder is back-loaded into circular sample holders in order to avoid preferential alignment of particles at the sample holder surface. Sample holders are then

mounted in position at the centre of the Bragg arc. Resulting diffraction data usually contains an experimental artefact at very low angles where very high intensity tending towards 0° is seen to decay rapidly towards the background intensity level. This results from saturation of the detector at very low angles. Fortunately, very low angle analysis was not required in this work.

References

[9] V. Pecharsky & P Zavalij, Fundamentals of powder diffraction and structural characterisation of materials, 2nd edition, Springer, New York, 2009

A.7. Thermal Analysis Techniques

Two related thermal analysis methods were used in this work. Differential Scanning Calorimetry (DSC) and Simultaneous Thermal Analysis (STA) which combines DSC with Themogravimetric Analysis (TGA) [10]. DSC is concerned with the measurement of thermal events or transitions within a material. DSC is typically used to study melting, crystallisation, reaction events and glass transition temperatures by measuring their associated endo/exotherms under dynamic thermal conditions. A typical DSC setup consists of a thermal chamber containing two small crucibles (usually made from aluminium, platinum or ceramic). The temperature of the thermal chamber can be accurately controlled under cryogenic or high temperature conditions using a combination of furnace elements, cryo-chiller or liquid nitrogen apparatus. The crucibles are nominally identical in terms of thermal properties and sit on top of thermocouples. One crucible is the reference crucible and remains empty during experiments. The other crucible is loaded with a small quantity of the sample of interest - typically around 10 mg. Both crucibles are subjected to thermal cycling and the measured difference in temperature between the sample and reference crucibles is corrected for by altering the heat flow over the sample crucible. The heat flow required to maintain equivalent temperatures between the crucibles is directly related to any thermal transitions and the heat capacity of the sample material. Typically DSC experiments are performed under inert atmosphere.

Themogravimetric analysis is concerned with the measurement of changes in sample weight during thermal ramps. A typical TGA setup consists of a sample crucible connected (usually via suspension) to a highly precise balance. Samples are loaded into the crucible, weighed and subjected to a thermal ramp. Reactions within the sample which result in a change in weight (e.g. oxidation, dehydration or thermal decomposition) can be correlated with the recorded weight-temperature data. STA combines these two techniques.

References

[10] P.P. De, N. Roy Choudhury, N.K. Dutta, Thermal analysis of rubbers and rubbery materials, Smithers RAPRA Technology Ltd., Shawbury, 2010

A.8. Raman Spectroscopy

Raman spectroscopy works on the principle of inelastic scattering of radiation from materials [11]. This means that there is an energy exchange between the incident photon and the sample material. For Stokes-Raman scattering this involves the transfer of energy from the photon to the materials. As such the scattered photon contains information (a shift in wavelength) about the samples material.

For the case of single crystal graphite, Tuinstra and Koenig [11] demonstrated that the Raman spectrum contains a single peak at 1575 cm^{-1} (called the G band). Upon disruption of the crystalline structure of graphite, an additional peak at 1355 cm^{-1} called the D band and corresponding to defects within the graphite structure, is evident. The experimental results of Tuinstra and Koenig are shown in Figure A.6. Tuinstra and Koenig also developed the empirical formula which relates the intensity of the D and G bands to the lateral crystallite size.

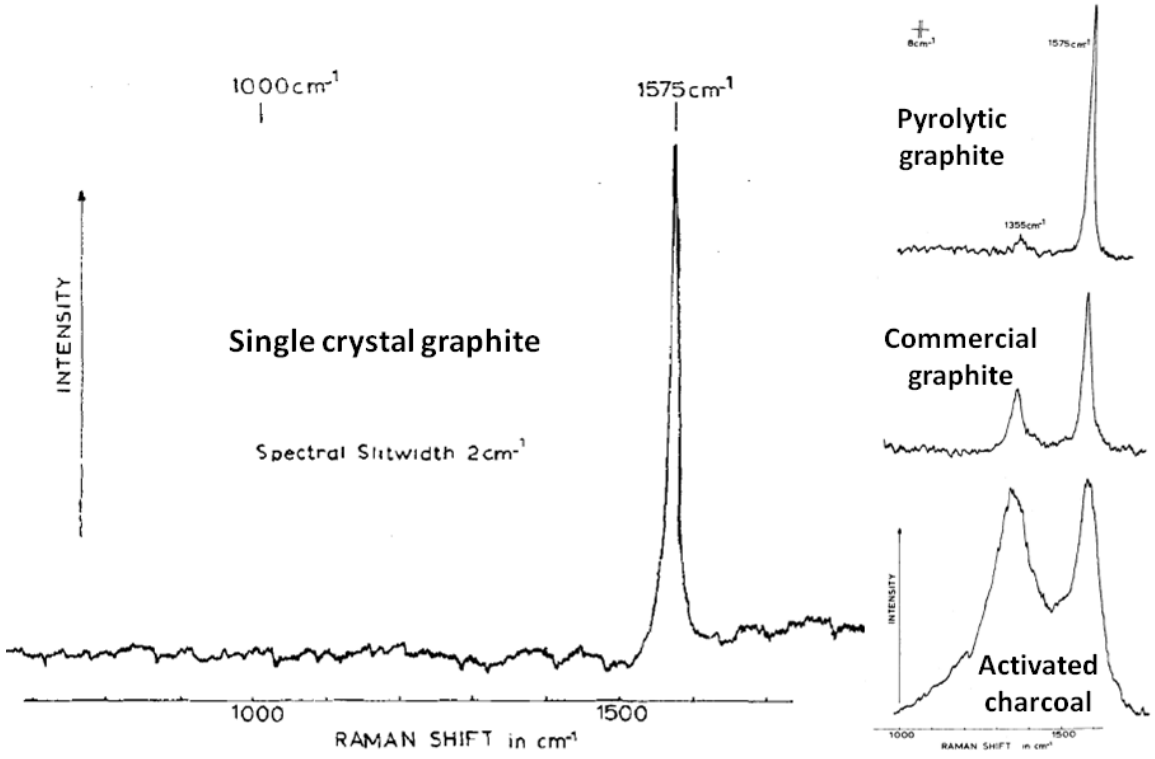

Figure A(I).6: Raman data of Tuinstra and Koenig [12]. The main spectrum shows a single peak (G band) corresponding to inelastic scattering from single crystal graphite. The smaller images to the right show the effects of microcrystallinity and crystal irregularity on the Raman spectrum; namely the appearance of a second peak (D band).

Gruber et al. [13] later studied the effects of heat treatment of carbon black materials on the Raman spectrum. They found that upon graphitisation of the carbon blacks the D band reduces in intensity - corresponding to the formation of a more crystalline structure (Figure A.7).

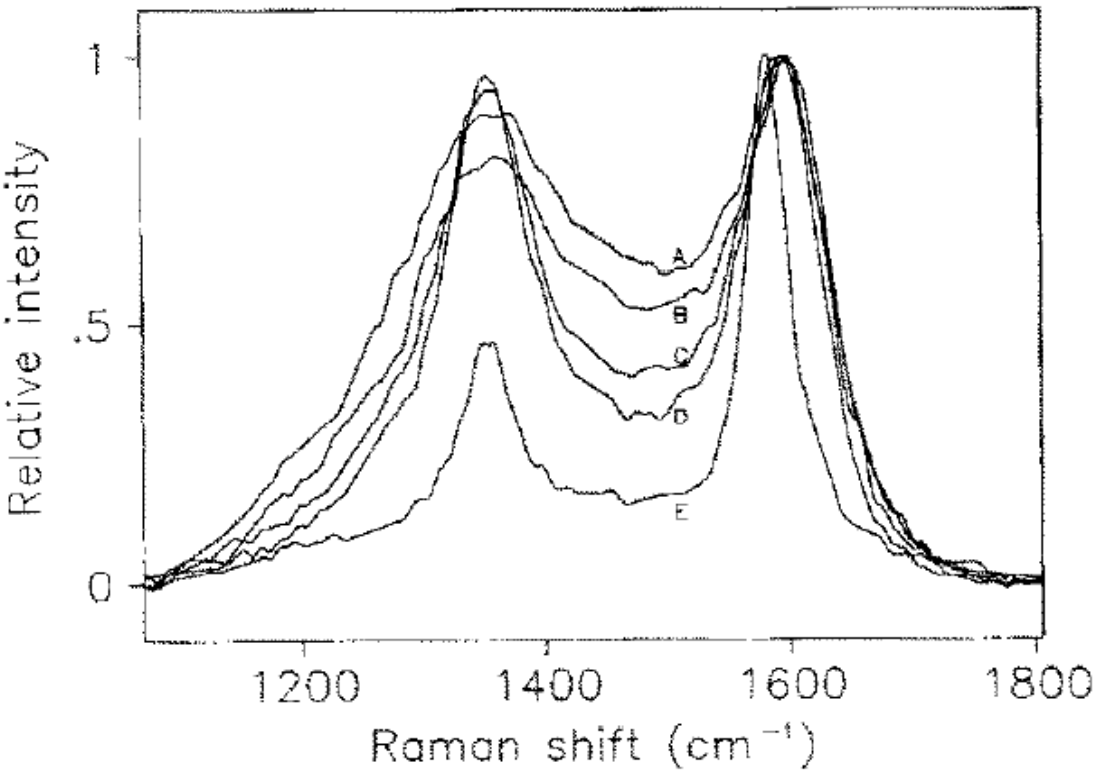

Figure A(I).7: The influence of thermal treatment on the magnitudes of the D and G bands in the Raman spectra of N234 carbon black. In the figure A: 300K thermal treatment (untreated), B: 1300 K, C: 2100 K, D: 2600 K, E: 3000 K (From Gruber et al. [13])

References

[11] P. Atkins, Atkins' Physical Chemistry, 7th Ed. Oxford University Press, Oxford, 2002

[12] F. Tuinstra, J.L. Koenig, The Journal of Chemical Physics, 53 (1970), 1126-1130

[13] T. Gruber, T.W. Zerder, M. Gerspacher, Carbon, 32 (1994), 1377-1382

A.9. Nuclear Magnetic Resonance (NMR) Techniques

A.9.1. ^{13}C-Magic Angle Spinning (MAS)-NMR

In Chapter 4, ^{13}C-MAS-NMR was used to examine the chemical environments of backbone carbons in various crosslinked NR networks. ^{13}C-MAS-NMR is a magnetic resonance technique useful for examining solid state materials, however it shares it's theoretical basis with the more common solution state techniques [14-16]. Atomic nuclei which have an angular momentum when placed in a magnetic field, all posses a quantum mechanical property called nuclear spin. Angular momentum is a quantised property according to Equation A.9 where

$$P_0 = m\frac{\mathbf{h}}{2\pi}; \quad m = \pm n\frac{1}{2}; \quad n = 0, 1, 2, \ldots \tag{A.9}$$

m is also limited by the total spin quantum number, I_{Q}, which is determined by the makeup of the nucleus.

$$m = I_{\mathrm{Q}}, I_{\mathrm{Q}} - 1, \ldots, -I \tag{A.10}$$

All nuclei with non-zero spin quantum numbers, $I_{\mathrm{Q}} \neq 0$, interact with magnetic fields because of their non-zero magnetic moments, μ, according to Equation A.11 where γ_{g} is the gyromagnetic ratio. This means that it is possible to consider some nuclei (e.g. ^{1}H and ^{13}C) as very small bar magnets.

$$\mu = \gamma_{\mathrm{g}} p \tag{A.11}$$

The energy, E, of the magnetic moment in a magnetic field B_0 is given by Equation A.12 where $\mathbf{h}$ is the Planks constant and I_{Q} is the spin quantum number.

$$E = -\mu_0 B_0 = -\gamma_g \frac{\mathbf{h}}{2\pi} I_Q B_0 \quad \text{A.12}$$

Quantum mechanical rules mean that nuclei with spin quantum number I_Q may occupy $(2I_Q + 1)$ energy levels. For ^{1}H and ^{13}C nuclei I_Q = ½. Therefore when the nuclei are place into a magnetic field the nuclear spins are split into two different energy levels denoted +½ and -½ and shown schematically in Figure A.8. The energy difference between these levels can be derived using Equation A.13-15.

$$E_{+½} = -\mu_0 B_0 = -\frac{1}{2}\left(\gamma_g \frac{\mathbf{h}}{2\pi} B_0\right) \quad \text{A.13}$$

$$E_{-½} = \mu_0 B_0 = \frac{1}{2}\left(\gamma_g \frac{\mathbf{h}}{2\pi} B_0\right) \quad \text{A.14}$$

$$\Delta E = E_{-½} - E_{+½} = 2\mu_0 B_0 = \gamma_g \frac{\mathbf{h}}{2\pi} B_0 \quad \text{A.15}$$

This energy difference corresponds to the frequency of nuclear magnetic resonance. The NMR technique probes this frequency by inducing resonance through radio wave irradiation of the sample and measuring the recovery of the system to equilibrium. The observable signal from NMR measurements is the time-domain Free Induction Decay (FID) which is detected via a system of wound coils in the spectrometer. Fourier Transform of the FID allows examination of the frequency-domain resonance spectrum.

$$\Delta E = \boldsymbol{h}\nu_{res} \quad \text{A.16}$$

$$\nu_{res} = \frac{\gamma_g}{2\pi} B_0 \qquad \text{A.17}$$

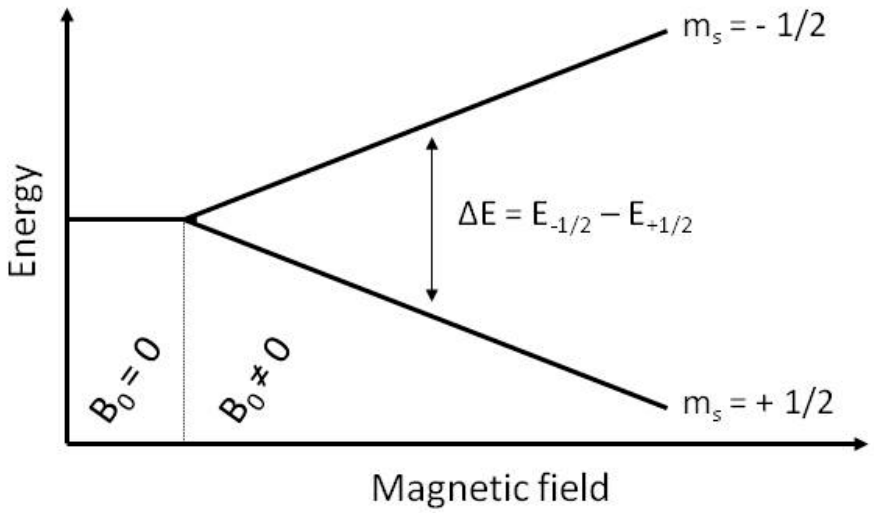

Figure A(I).8: Schematic of the splitting of aligned spins under application of a magnetic field

NMR is able to distinguish between identical nuclei in different chemical environments due to the phenomenon of shielding. Shielding occurs due to the interaction of local electrons with the applied magnetic field, B_0, inducing a local current which changes the *effective* magnetic field at the nucleus. The additional magnetic field, $\delta_{\mathrm{CS}}B$, is defined by the sheilding contant of the nuclei, σ_{NMR}

$$\delta_{\mathrm{CS}}B = -\sigma_{\mathrm{NMR}}B_0 \qquad \text{A.18}$$

These slight differences in the local magnetic fields experienced by nuclei due to their chemical environments means that the corresponding resonance frequencies are different. Therefore the frequencies of resonances of, for example ^{13}C, enable the discrimination of the various chemical configurations of the element with a sample. Figure A.9 plots the positions of typical ^{13}C resonances against the shift factor, δ_{CS}, in units of ppm, which is calculated from the resonance frequency of the specimen nuclei, ν_{S}, and that of a reference nuclei, ν_0, according to Equation A.19.

$$\delta_{CS} = \frac{\nu_S - \nu_0}{\nu_0} \text{ x } 10^6 \qquad \text{A.19}$$

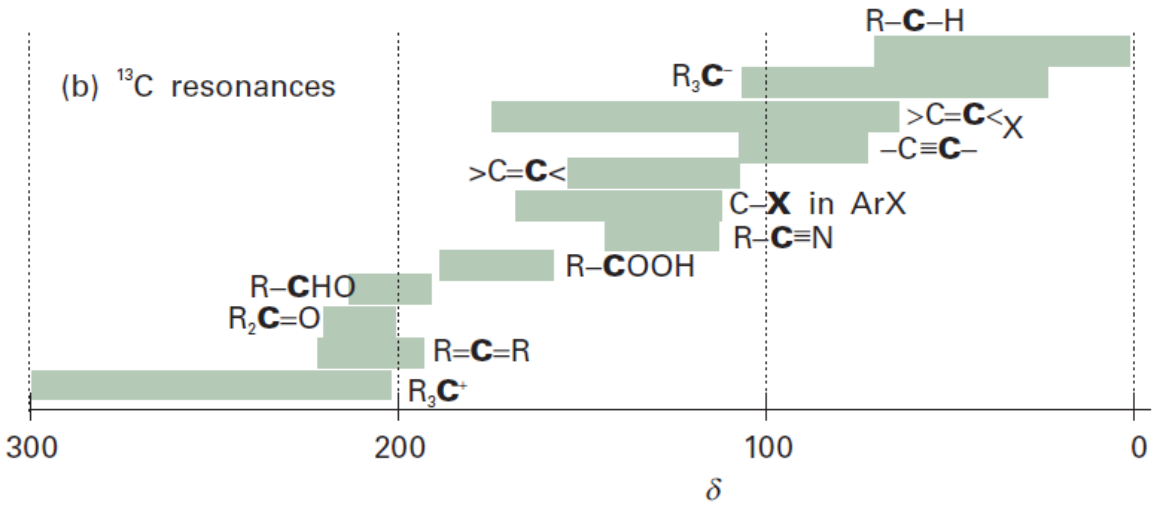

Figure A(I).9: The position of different ^{13}C resonances (chemical environments) in terms of the chemical shift, δ_{CS}, in ppm.

Complications arise when solid sate samples are considered. In the solid state, line broadening due to non-relaxed dipolar couplings tends to smear out spectral information. This arises from interactions between nuclei separated in space (i.e. not chemically bonded) and results in the establishment of local magnetic fields along a given axis. In the solution state this is not a problem as rapid motion of the solute in the solvent leads to a spatial averaging of the dipolar coupling effect to zero.

The is not the case for solid state samples where spatial orientation is extremely slow if not non-existent[2]. Solid state samples analysed using solution state methods suffer from dramatic line broadening - most information in the spectrum is lost. However Magic Angle Sample Spinning (MAS) is able to reduce the line width broadening seen in solid state samples by rapidly spinning the sample at the 'magic angle' of 54.74° where the dipolar couplings are reduced to zero [14].

[2] Interestingly, in NMR terms, rubber lies somewhere between liquid and solid state - just as in rheology. Line broadening is apparent in rubber samples but is not as dramatic as for a crystalline solid [16].

A.9.2. ^{1}H - Multiple Quantum (MQ) - NMR

Theoretical Background:

Proton NMR may be used to probe the crosslink density and network heterogeneity of crosslinked rubber compounds. Proton NMR techniques are sensitive to dipolar couplings between chain protons. In fact proton NMR measurements taken across the entire timescale of chain motion are sensitive to the autocorrelation function (ACF) describing polymer chain modes and motions [17, 18].

Figure A.10 schematically illustrates the ACF for a range of polymers and crosslinked networks. At shorter timescales (which are accessed experimentally by collecting data at low temperatures) the polymer dynamics and therefore dipolar couplings become increasingly localised and segmental couplings become apparent. At larger mode timescales (and therefore higher temperatures), the measured dipolar coupling tends towards a constant, time and temperature independent value for the case of polymer networks. At this point the measured dipolar coupling relates to larger cooperative modes (i.e. chain lengths between crosslinks).

Note also that in Figure A.10 the dipolar coupling measured at times and temperatures far removed from the glass transition temperature is several orders of magnitude smaller than that measured around T_g. Hence the measured dipolar coupling associated with the polymer network structure is termed the 'residual dipolar coupling' (RDC).

Figure A.11 illustrates the origin of the RDC in crosslinked polymers well above the T_g. Between crosslink points the chain is free to move through a vast number of possible configurations. In liquid specimens the RDC and associated finite magnetic field, would average to zero. Due to the imposition of crosslinking points in rubber compounds, a finite RDC remains at long relaxation timescales. The RDC constant, D_{Res}, and the chain order parameter, S_b, are related to the chain length in terms of physical segments which in turn is related to chain molecular weight between crosslinks (Equation A.20) Therefore D_{Res} is directly proportional to the crosslink density.

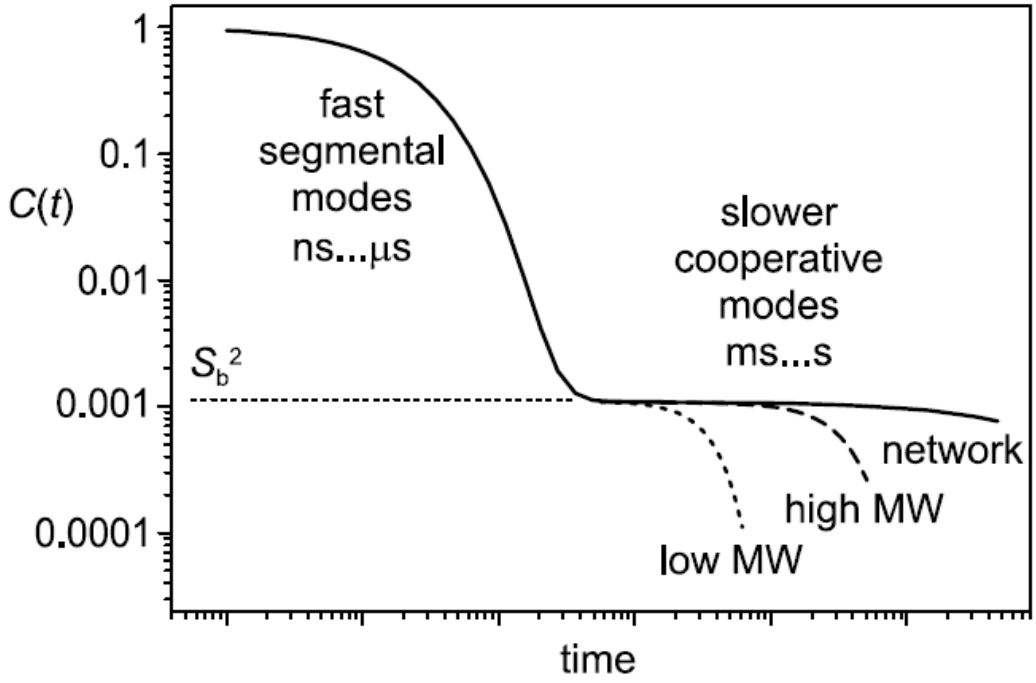

Figure A(I).10: Schematic of the autocorrelation function for polymer melts and networks. NMR is sensitive to dipolar couplings across a range of timescales. When far removed from the T_g the residual dipolar coupling is a constant for crosslinked networks and is indicative of the topological restrictions to the polymer chains (From Saalwächter [17]).

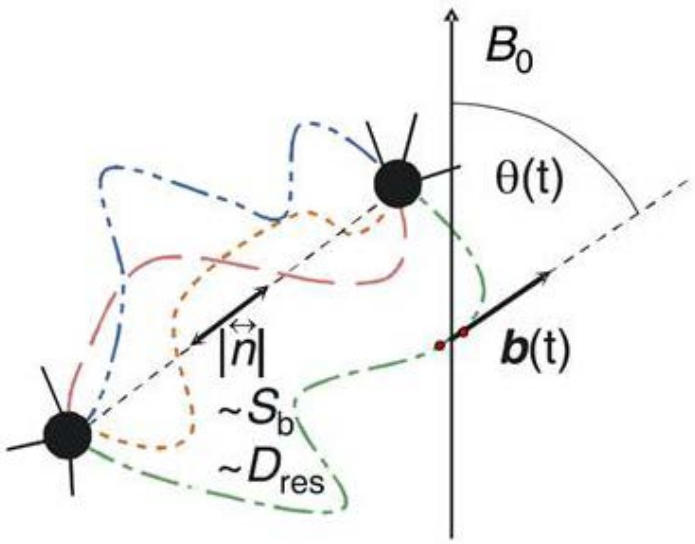

Figure A(I).11: Possible configurations of a rubber chain between crosslink points (black circles). The time-averaged finite dynamic order parameter, S_B, is related to both the number of physical segments between the crosslink points and the residual dipolar coupling constant. $|\overleftrightarrow{n}|$ is the time-averaged order tensor between crosslinks (From Saalwachter [18]).

$$S_b = \frac{D_{Res}}{(D_{Stat}/k)} = \frac{3}{5N} \quad \text{A.20}$$

A number of different NMR pulse techniques and setups (e.g. Hahn-Echo T_2 relaxometry) have been previously been used to obtain D_{Res} however, the technique of choice is Multiple Quantum (MQ) NMR. The advantages of the MQ-NMR method over other techniques is reviewed in Saalwächter [17, 18] but the key point is the generation of MQ data which can be analysed directly in terms of D_{Res} without having to account for the convolution of D_{Res} with polymer dynamic effects.

Data collection:

Data collection for the MQ-NMR tests starts by indentifying the proton magnetisation saturation time. This is the magnetic field exposure time required for all the rubber protons to align with the magnetic field. this is achieved by examining the magnitude of the FID at short timescales as a function of field exposure time. MQ experiments are performed on fully saturated materials. The sample is then held at 80 °C as this is the temperature required to access solely the residual dipolar coupling section of the autocorrelation function. The sample is then exited by the spectrometer. This selectively excites the protons at different multiple quantum timescales. The MQ pulse signal is not discussed in detail here but is described in detail in the literature [18].

The raw data from the experiments consists of two parts which are collected simultaneously during the experiment; the reference intensity curve I_{ref} and the double quantum build-up curve, I_{DQ}, which is constructed by plotting the values of the FIDs collected at different MQ excitation timescales extrapolated to time = 0 versus DQ excitation time. Examples of the raw data are presented in Figure A.12.

Data Processing and Analysis:

The raw data collected from the MQ experiments contains information about D_{Res}, network defects and the relaxation dynamics of the polymer chains. In order to directly access D_{Res} and therefore the crosslink density, a number of analysis steps must be performed. First the intensity of the signals are normalised by extrapolating the I_{ref} signal back to time = 0 and using this intensity value for signal normalisation (as seen in Figure A.13).

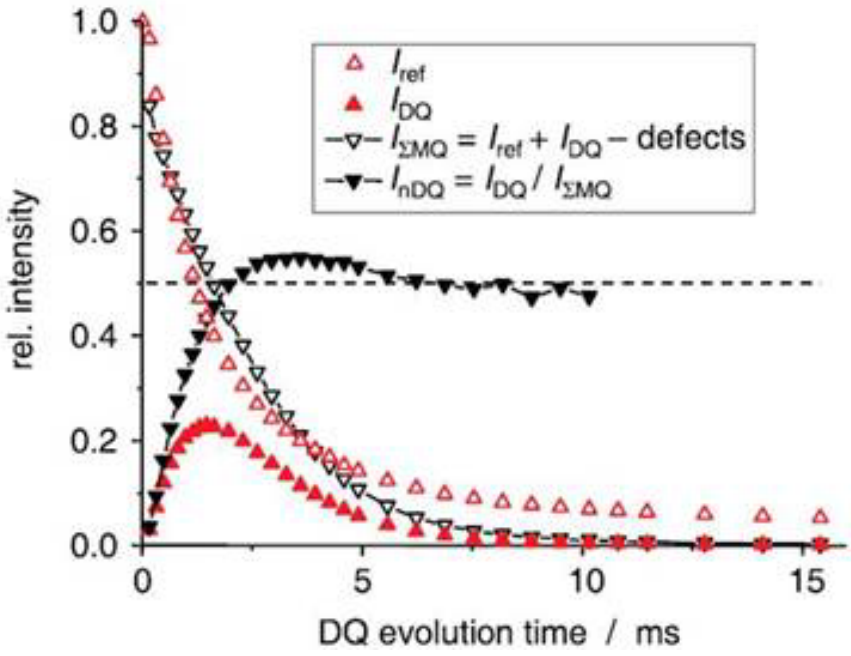

Figure A(I).12: Plot of the raw data obtained from MQ NMR experiments (I_{ref} and I_{DQ}) versus DQ evolution time. Also included are the summatory of Multiple Quantum function, $I_{\sum \mathrm{MQ}}$, and the normalised double quantum build-up function I_{nDQ}. Note that the normalised DQ build-up reaches an intensity of 0.5 at longer evolution times (From Saalwächter [18])

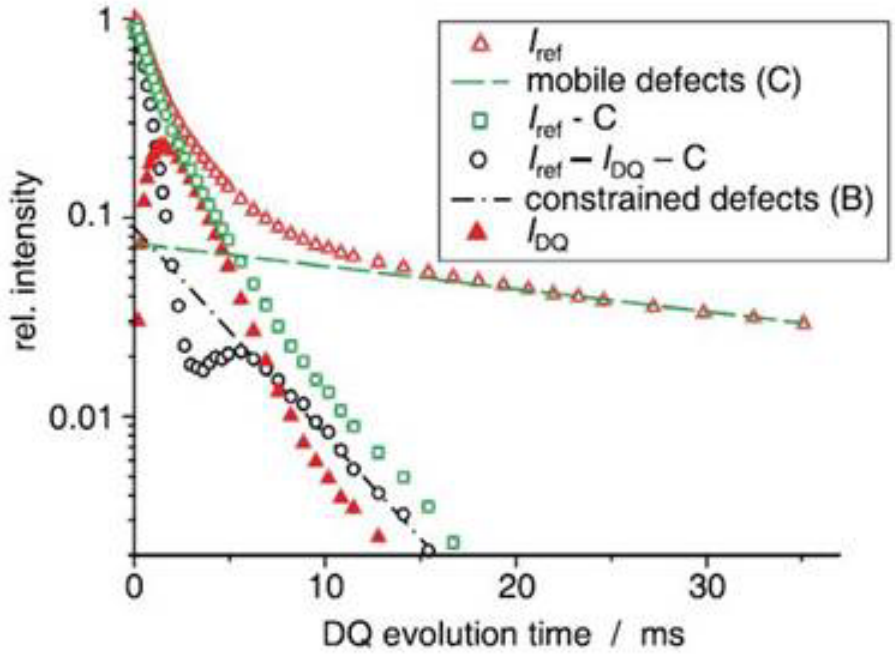

Figure A(I).13: Process for indentifying network defects. The function I_{ref} - I_{DQ} contains a clear inflection which separates the DQ evolution relating to network defects at DQ evolution times and network DQ evolution at shorter DQ evolution times. A fit to the tail of I_{ref} - I_{DQ} results in a measure of the total concentration of network defects and a DQ evolution function relating to the defect portion of the sample (From Saalwächter [18])

The network defects are then identified and quantified by calculating I_{ref} - I_{DQ}. The resulting function contains an inflection which separates the network DQ build-up information from the defect intensity. Fitting the longer time scale portion of the I_{ref} - I_{DQ}. function and extrapolating back to time = 0 gives a quantification of the total concentration of network defects (a a fraction of total signal intensity) and also a function relating to the network defects which can be subtracted from the raw data to yield data relating to the network structure only (Figure A.13).

The DQ build-up curve which can be directly analysed to obtain the average crosslink density and distributions is constructed by first calculating the summatory of multiple quantums ($I_{\sum \mathrm{MQ}} = I_{\mathrm{ref}} + I_{\mathrm{DQ}} - \mathrm{defect\ function}$). I_{DQ} is then normalised to $I_{\sum \mathrm{MQ}}$ to give the normalised DQ build-up curve (I_{nDQ}). This last normalisation step removes the dynamics information from the data and gives the normalised DQ build-up function solely in terms of structure. At this point the data is quality checked by ensuring the I_{nDQ} reaches a plateau intensity at longer MQ timescales of 0.5. This is essential as the DQ function represents the intensity arising from 50% of the quantum.

Extraction of Network Information:

The $I_{\mathrm{nDQ}}\left(\tau_{\mathrm{DQ}}\right)$ function can be analysed in terms of the average and distributions of D_{Res}. In the first instance this is achieved assuming a single value of D_{Res} - indicating a very homogeneous network structure - and the data is fitted to Equation A.21. This makes use of the second moment approximation [18].

$$I_{\mathrm{nDQ}}\left(\tau_{\mathrm{DQ}}, D_{\mathrm{Res}}\right) = 0.5\left(1 - \exp\left\{-\left(\frac{2}{5} D_{\mathrm{Res}}^2 \tau_{\mathrm{DQ}}^2\right) 1.5\right\}\right) \qquad \text{A.21}$$

However in most crosslinked rubber networks the distribution of D_{Res} is non-homogeneous. In this case it is possible to fit the $I_{\mathrm{nDQ}}\left(\tau_{\mathrm{DQ}}\right)$ function using an assumed Gaussian distribution of D_{Res} as given in Equation A.22, or using a Tikhonov regularisation process to generate the best fit function to describe the spatial distribution of D_{Res}. Examples of Tikhonov regularisation fits to the $I_{\mathrm{nDQ}}\left(\tau_{\mathrm{DQ}}\right)$ function and the resulting D_{Res} distribution functions for PDMS networks of varying network inhomogeneity are shown in Figure A.14.

$$I_{\mathrm{nDQ}}\left(\tau_{\mathrm{DQ}}, D_{\mathrm{Res}}, \sigma\right) = \frac{1}{2}\left(1 - \frac{\exp\left\{-\frac{\frac{2}{5}{D_{\mathrm{Res}}}^2{\tau_{\mathrm{DQ}}}^2}{1+\frac{4}{5}\sigma^2{\tau_{\mathrm{DQ}}}^2}\right\}}{\sqrt{1+\frac{4}{5}\sigma^2{\tau_{\mathrm{DQ}}}^2}}\right) \quad \text{A.22}$$

The correlation between D_{Res} and M_{C} is evidenced by plotting the shear modulus of unfilled sulphur crosslinked SBR versus the corresponding measured D_{Res} values (Figure A.15). A linear relationship is found.

To quantitatively relate the experimentally measured D_{Res} to M_{C} , a conversion factor based on the dipolar couplings within an individual polymer Kuhn segment is required. This clearly varies between polymer types and for the case of random copolymers, does not exist. The conversion factor for NR is given in Equation A.23.

$$M_{\mathrm{C}}^{\mathrm{NR}} = \frac{617\ \mathrm{Hz}}{D_{\mathrm{Res}}/2\pi}\,\mathrm{kg/mol} \quad \text{A.23}$$

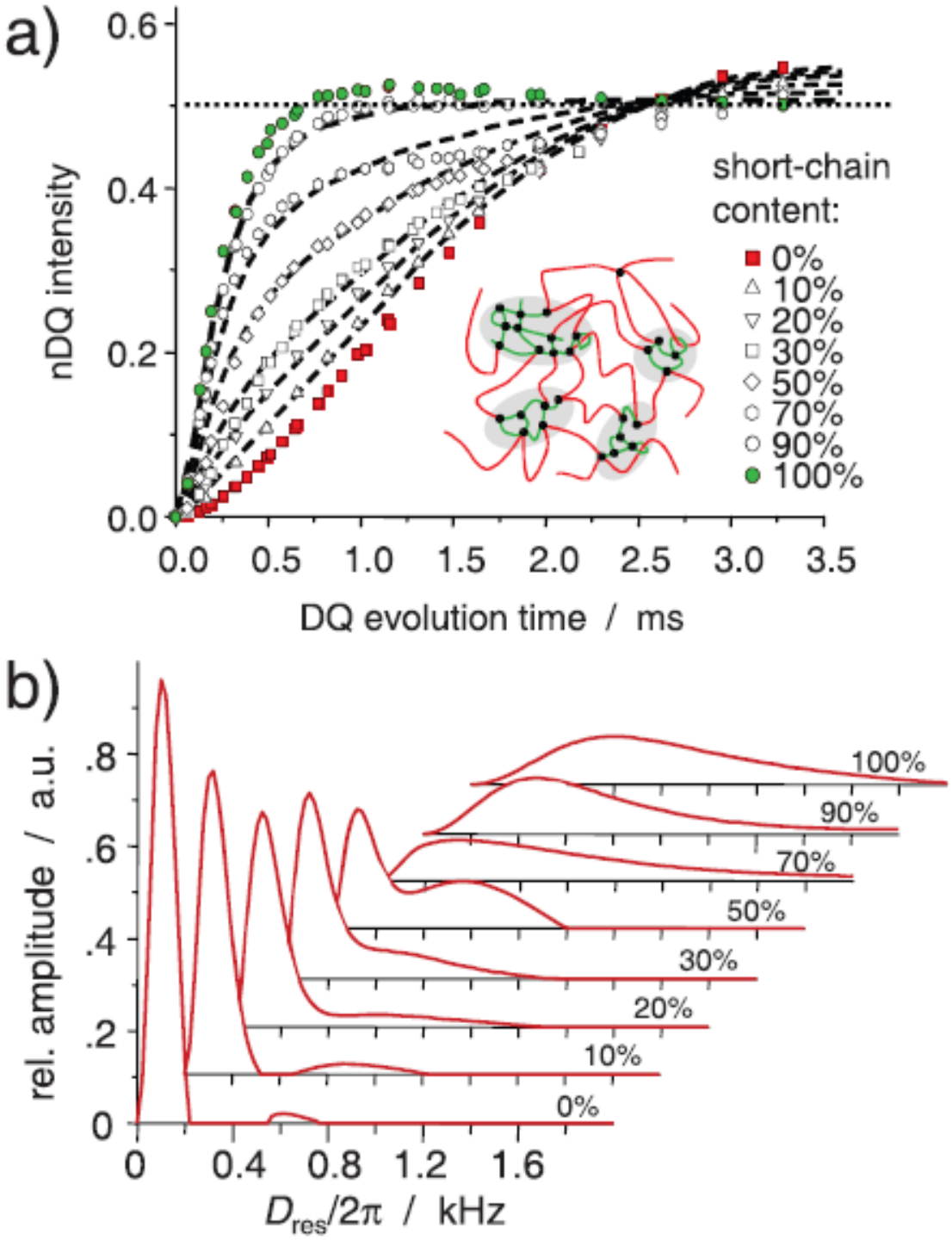

Figure A(I).14:A) example normalised DQ functions for PDMS materials with varying network heterogeneities. B) the corresponding distributions of D_{Res} obtained after regularisation (From [18])

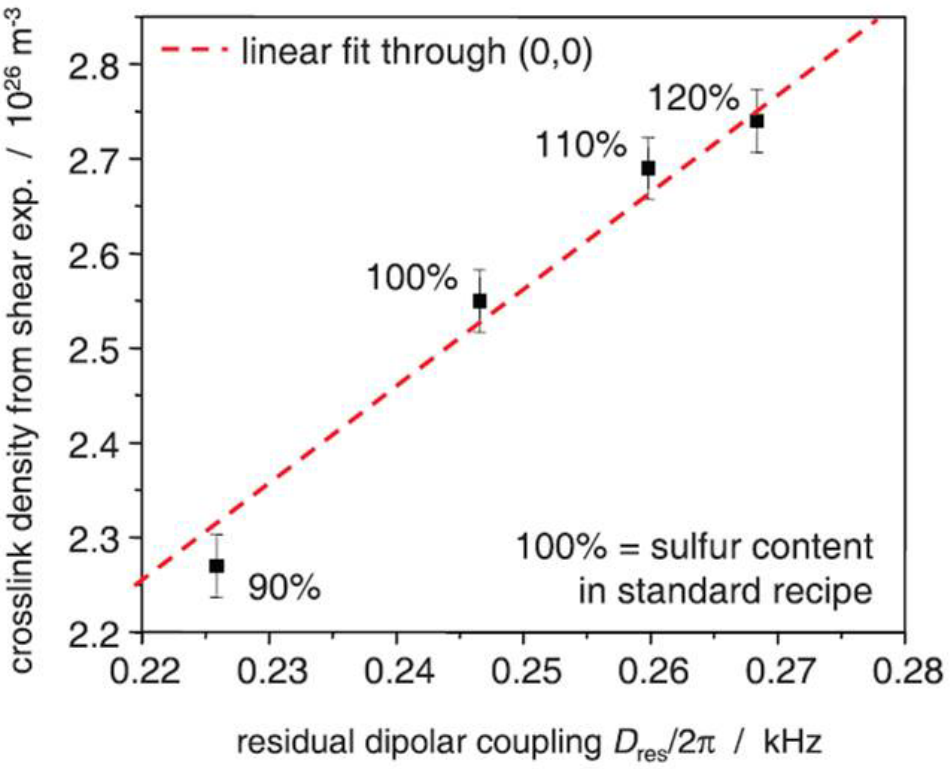

Figure A(I).15: Relationship between the crosslink density of vulcanised rubber samples from mechanical tests and the measured residual dipolar coupling (From [18])

References

[14] P. Atkins, Atkins' Physical Chemistry, 7th Ed. Oxford University Press, Oxford, 2002

[15] E. Breitmaier, W. Voelter, Carbon-13 NMR Spectroscopy, 3rd Ed, VCH, Weinheim, 1987

[16] J.L. Koenig, Spectroscopy of polymers, 2nd Ed, Elsevier, New York, 1999

[17] K. Saalwächter, Progress in Nuclear Magnetic Resonance Spectroscopy, 51 (2007), 1-35

[18] K. Saalwächter, Rubber Chemistry and Technology, 83 (2012), 350-386

[19] W. Chassé, J.L. Valentín, G.D. Genesky, C. Cohen, K Saalwächter, The Journal of Chemical Physics, 134 (2011), 044907

A.10. Dielectric Spectroscopy

Dielectric spectroscopy is concerned with examining the dielectric properties of materials as a function of electrical field frequency. Typically, samples are placed between two parallel electrodes, an electric field is applied across the sample material which alternates at a set frequency. From the induced alternating current, the dielectric properties of the material can be derived. If the oscillation frequency is the varied systematically the dielectric response of the material can be recorded as a function of broadband frequency.

In the experiments in Chapter 6, the capacitance, C_p, of the samples is calculated from the imaginary part of the measured impedance, Z, where Z' and Z'' and the real and imaginary part respectively.

$$Z = Z' + iZ'' \quad \text{A.24}$$

$$C_p = \frac{-1}{2\pi f Z''} \quad \text{A.25}$$

The tangent of the phase lag is calculated by direct analogy with mechanical spectroscopy

$$\tan\delta = \frac{-Z''}{Z'} \quad \text{A.26}$$

The real part of the permittivity is the calculated from the capacitance, the permittivity of a vacuum, ε_0, and the sample dimensions (where A is the sample area and d is the sample height)

$$C_p = \varepsilon' \varepsilon_0 \frac{A}{d} \quad \text{A.27}$$

Giving the imaginary part of the permittivity from tanδ

$$\frac{\varepsilon''}{\varepsilon'} = \tan\delta \qquad \text{A.28}$$

The alternating current induced in a material is related to the mobility of permanent and induced dipoles within the sample. At very low frequencies, currents are induced by the motion of all possible dipole reorientations within the material; for example the reorientation of chain segments in polymer systems. As the field frequency is increased, dipole reorientation timescales of the slowest motions cannot 'keep up' with the alternating field and undergo a relaxation process before they eventually cannot make a contribution to induced current in the material. Broadband dielectric spectroscopy is able to sweep through all the relevant dipolar reorientations within a material, observing a relaxation process where the field frequency exceeds the reorientation timescale. This is very useful for certain polymer systems whose chains are constituted of a series of weak permanent dipoles. For example, for case of natural rubber, the repeat unit is not chemically symmetrical. Due to the inherent electron withdrawing properties of alkyl groups, a slight asymmetry in electron density along the repeat unit is apparent. Reorientation of this slight permanent dipole in an alternating electrical field allows for the application of dielectric spectroscopy to probe chain relaxations across a range of time scales; for example segmental relaxations underpinning the glass transition and chain end-to-end relaxations (which may not be apparent in crosslinked NR).

Numerous investigations have studied the dielectric relaxation processes apparent for NR and various other rubber polymers, examples of which are presented in Chapter 6.

Appendix II

Creep Data

Creep data described in Chapter 8 are presented in this appendix. Data for N990 and N990g - filled materials are omitted due to the high levels of noise in the creep traces as described in Chapter 8. Each material was tested twice in order to confirm repeatability. Data are shown plotted versus a linear time axis and versus as logarithmic time axis.

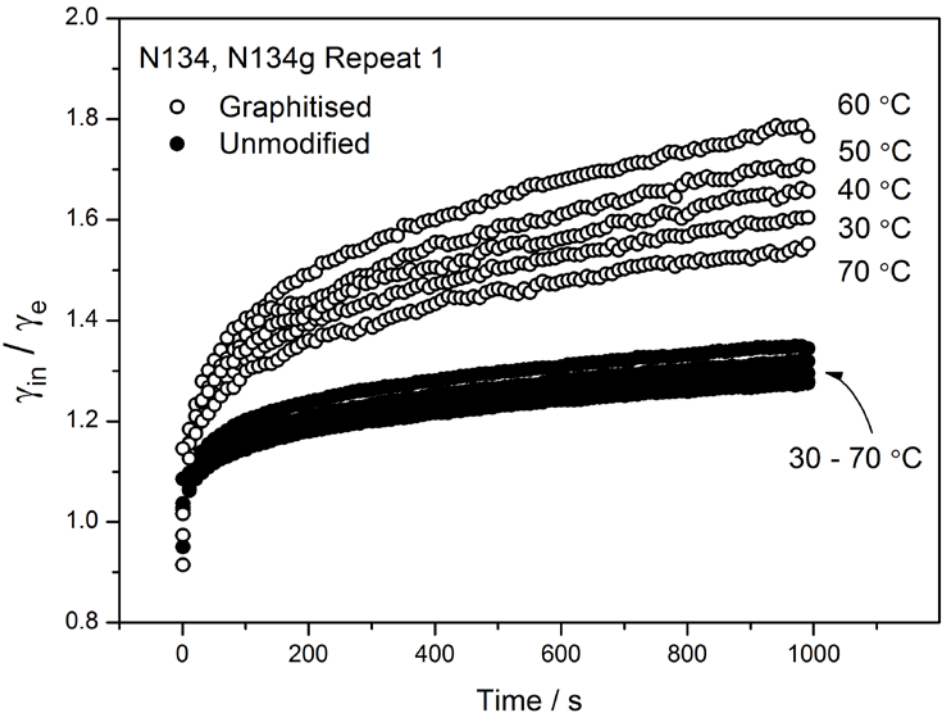

Figure A(II).1: N134 and N134g-filled materials. Repeat 1 plotted versus linear time axis

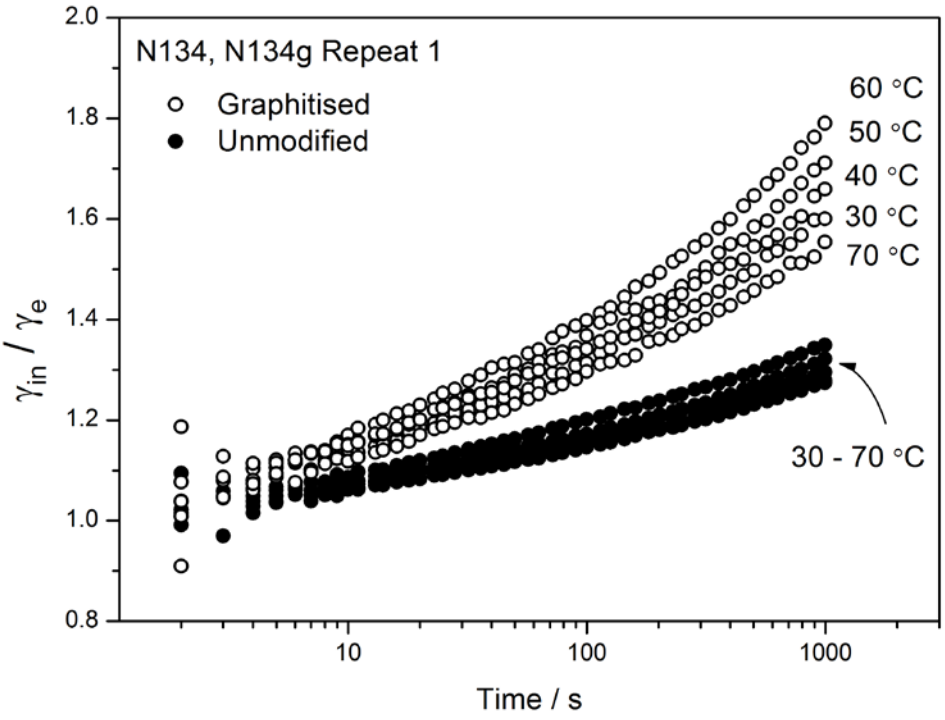

Figure A(II).2: N134 and N134g-filled materials. Repeat 1 plotted versus logarithmic time axis

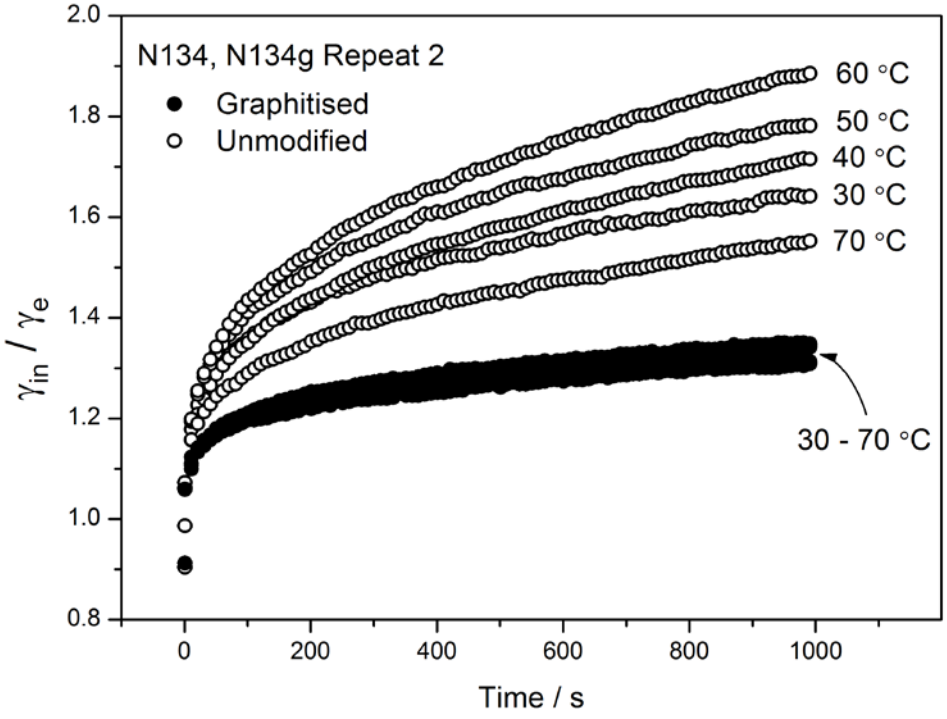

Figure A(II).3: N134 and N134g-filled materials. Repeat 2 plotted versus linear time axis

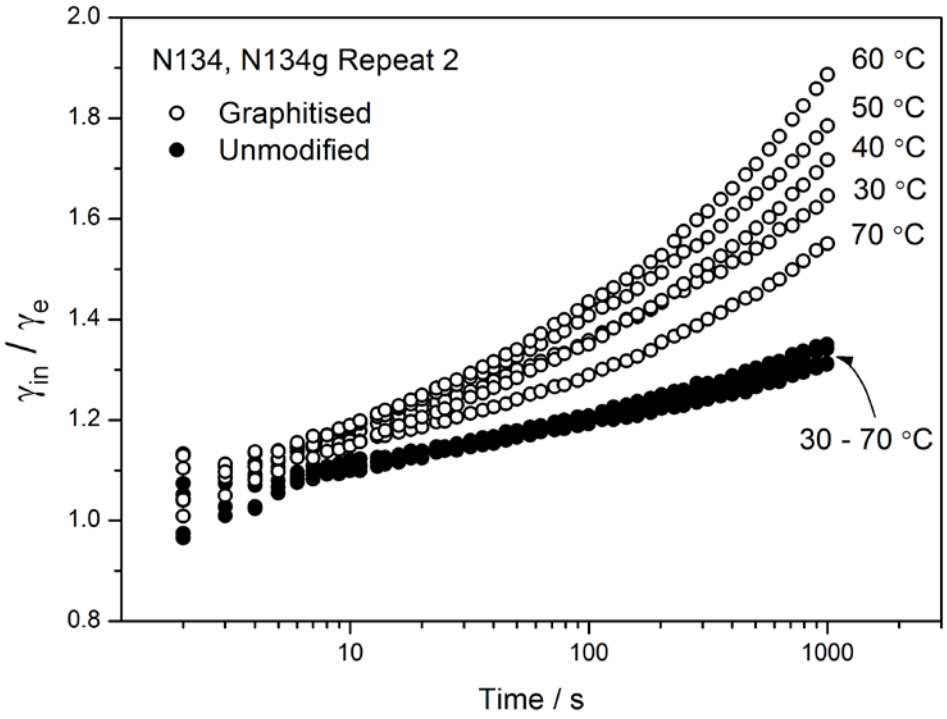

Figure A(II).4: N134 and N134g-filled materials. Repeat 2 plotted versus logarithmic time axis

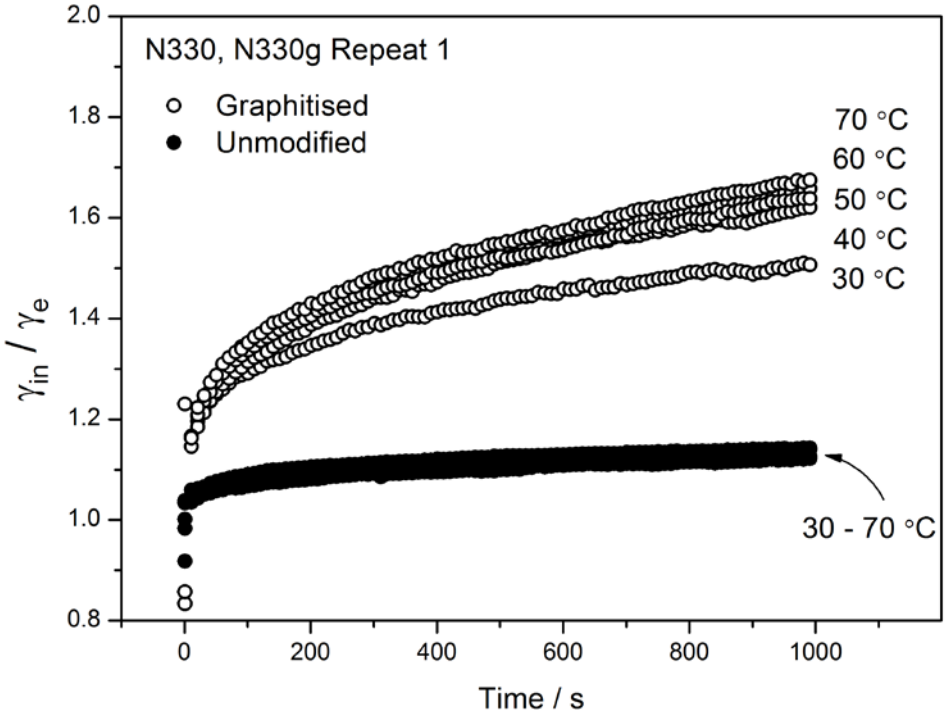

Figure A(II).5: N330 and N330g-filled materials. Repeat 1 plotted versus linear time axis

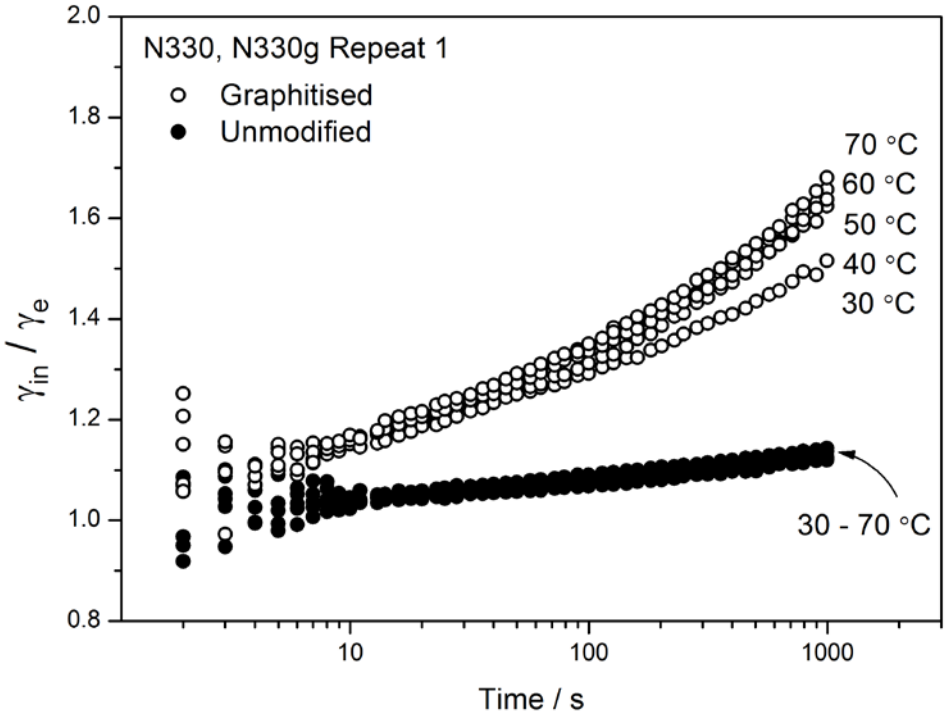

Figure A(II).6: N330 and N330g-filled materials. Repeat 1 plotted versus logarithmic time axis

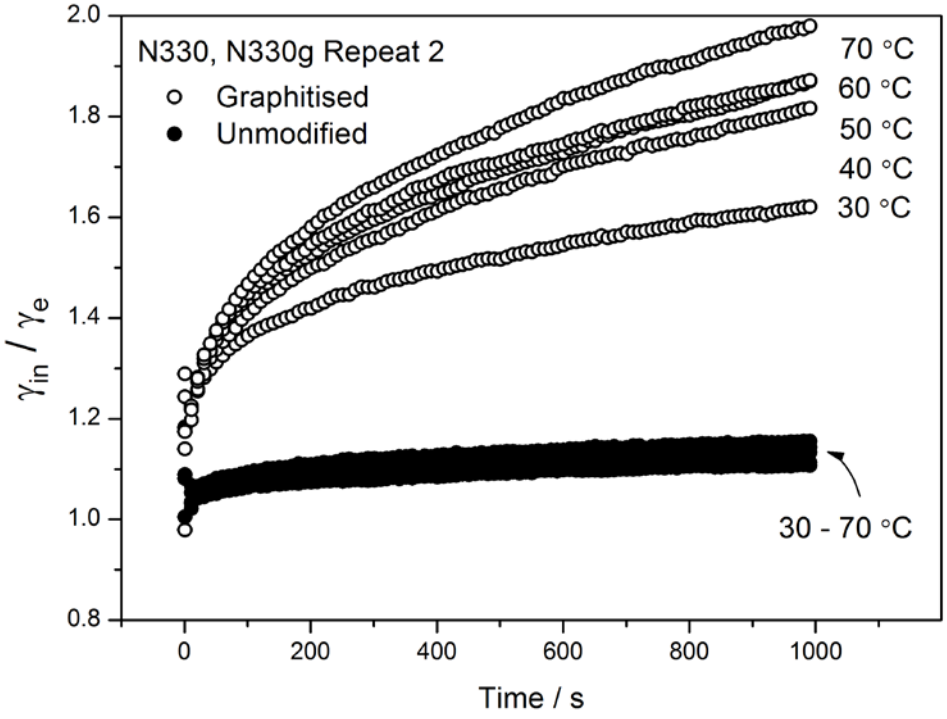

Figure A(II).7: N330 and N330g-filled materials. Repeat 2 plotted versus linear time axis

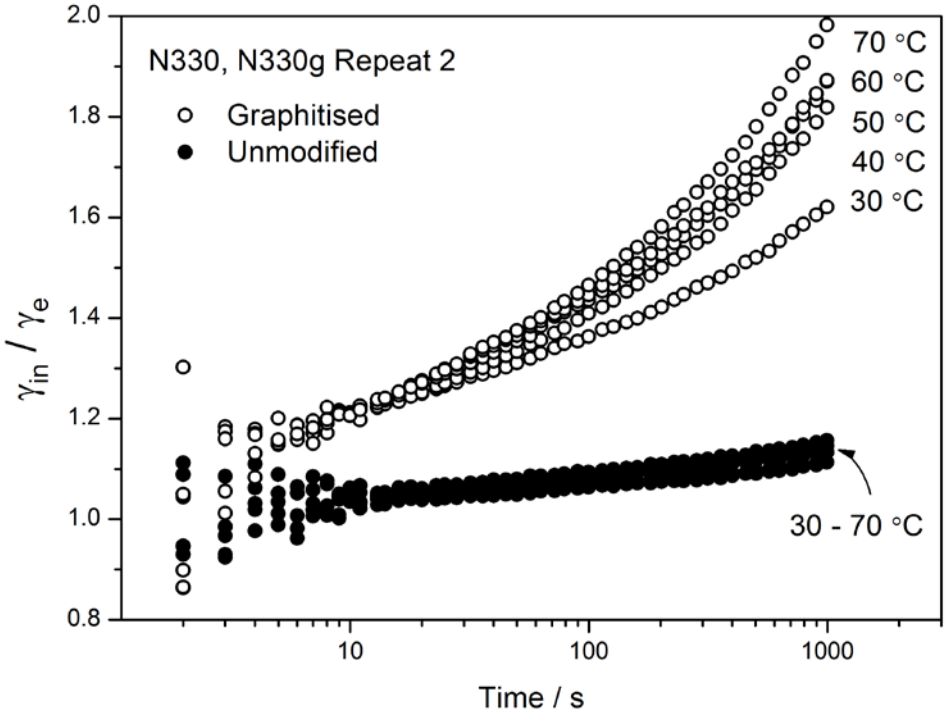

Figure A(II).8: N330 and N330g-filled materials. Repeat 2 plotted versus logarithmic time axis